University of Bath

PHD

Control of solid form and particle morphology using additives and crystallisation conditions

Payne, Pollyanna

Award date:
2021

Awarding institution:
University of Bath

Link to publication

Alternative formats
If you require this document in an alternative format, please contact:
openaccess@bath.ac.uk

General rights
Copyright and moral rights for the publications made accessible in the public portal are retained by the authors and/or other copyright owners and it is a condition of accessing publications that users recognise and abide by the legal requirements associated with these rights.

- Users may download and print one copy of any publication from the public portal for the purpose of private study or research.
- You may not further distribute the material or use it for any profit-making activity or commercial gain
- You may freely distribute the URL identifying the publication in the public portal ?

Take down policy
If you believe that this document breaches copyright please contact us providing details, and we will remove access to the work immediately and investigate your claim.

Download date: 18. Sep. 2021

Control of solid form and particle morphology using additives and crystallisation conditions

Pollyanna Payne

A thesis submitted for the degree of Doctor of Philosophy
University of Bath
Department of Chemistry

Supervisor: Professor Chick Wilson
April 2021

COPYRIGHT

Attention is drawn to the fact that copyright of this thesis rests with the author. A copy of this thesis has been supplied on condition that anyone who consults it is understood to recognise that its copyright rests with the author and that they must not copy it or use material from it except as permitted by law or with the consent of the author.

This thesis may be made available for consultation within the University Library and may be photocopied or lent to other libraries for the purposes of consultation.

Abstract

The research presented in this thesis concerns the improvement of the particle morphology of pharmaceutically relevant materials, focussing largely on the use of additives in crystallisations. The work fits into the wider context of the research carried out at the Future Manufacturing Hub in Continuous Manufacturing and Advanced Crystallisation (CMAC), funded by the EPSRC.

Opening chapters provide an introduction to the general research area, including the background of the project. A general overview of the analysis techniques used and methodology employed are also detailed in chapters 2-3.

Chapter 4-5 pertain to the experiments carried out to improve the morphology of the primary Active Pharmaceutical Ingredient (API) being investigated, isoniazid (IZN). Chapter 4 focuses on the use of different solvents and intentionally added impurities (additives). Additives chosen include both size-matched molecules and polymers. The effect of the additives is related to the crystallisation method and dependent on the concentration added. This chapter also reports the successful transfer of solvent effects into a continuous crystallisation platform, the Kinetically Regulated Automated Input Crystalliser (KRAIC). Face indexing and analysis of the crystal structure were used to rationalise the effects of the additives. In chapter 5, additives are used as co-formers with the aim of producing new multi-component crystals with favourable morphologies. The properties of each new co-crystal were determined and the improvements to morphology discussed with respect to experimental face indexing.

Chapter 6 applies the methodology used in the IZN research to a second API, pyridoxine (PYR). The effects of solvent, additives and formation of multi-component materials are discussed in terms of their influence on the crystal morphology achieved. Face indexing analysis was carried out to aid the comparison of crystal shapes produced.

Chapter 7 details the benchmarking of a workflow, produced by Dr. Lauren Hatcher, using CMAC target molecules fenamic acid (FA) and mefenamic acid (MFA).

Acknowledgments

Firstly, I would like to thank Prof. Chick Wilson for the opportunity to study this PhD. Thank you for the guidance throughout the research and constant reassurance that I do know what I'm talking about. I can't imagine having achieved this without your never ending support of all my crazy endeavours, both academically and, more importantly, personally. Thank you for never trying too hard to convince me to stay in academia, I hope I will make the great teacher you believe me to be. You gave my first ever university lecture at my applicant day in 2012, and I've always thought it must have somehow led me to here. My mum and I thought you were fab then and, I am so glad to say, I still think you are awesome now.

A huge thank you to Dr. Lauren Hatcher. You were the best thing to happen to my PhD and invaluable when it came to crystallography knowledge. I think I would still have no idea what I was doing if it wasn't for your input and expertise. Thank you also for keeping me company at CMAC events and being a great friend and colleague.

I want to extend a big thank you to everyone in the Wilson group, past and present, for making my PhD so enjoyable. Thank you to Alex Cousen for encouraging me to stick around after my masters' project. To Ruth Lunt, for always being there and providing so many laughs, and Dan Rixson, for being the best Ruth replacement once she had left! To Lois Wayment for sneaking in my vTPXRD sample on one of our many trips to Diamond. A big thank you to friends Anna Kinsella and Ciaran Sanford, long may our three hour lunches and cheerleading chats continue. And finally, Aneesa Al-Ani, thank you for being the best company over the last year; I don't know what I would have done without you. I am so sorry to be leaving you in your last 6 months but I know you will smash it!

Thank you to CMAC, for not only the opportunity to carry out this research, but for introducing me to three of my favourite people; Oliver, Laura and David. You guys are friends for life and I am so glad to have met you. Thank you also to CMAC and Roche for the internship opportunity. Although unfortunately cut short due to coronavirus, I am grateful for the experience.

I must also thank my family for all their support and encouragement. Mum, Dad, Maisie and Alfie, I hope you are proud of me, despite having no idea what it is I have done! Finally, Harry: thank you for pretending to be interested, pretending to understand and for always being my biggest supporter, I love you.

Table of Contents

List of figures XI

List of tables XXIV

List of abbreviations XXV

Chapter 1 Introduction 1

1.1 Research context 1

1.2 Crystallisation theory 2

1.2.1 Supersaturation 2

1.2.2 Nucleation 4

1.2.2.1 Primary nucleation 4

1.2.2.2 Secondary nucleation 6

1.2.3 Growth 7

1.3 Crystal morphology 10

1.3.1 Effects of impurities on crystal morphology 11

1.3.2 Choosing effective additives 13

1.3.2.1 Structurally similar and size-matched additives 13

1.3.2.2 Polymeric additives 14

1.3.3 Effect of additive concentration 16

1.3.4 Surface interactions and solution interventions 17

1.3.5 Effects of solvent on crystal morphology 19

1.3.6 Morphology prediction methods 22

1.4 Crystallisation methods 23

1.4.1 Evaporative crystallisations 23

1.4.2 Cooling crystallisations 24

1.4.3 Anti-solvent crystallisations 25

1.4.4 Mechanochemical grinding 25

1.4.5 Slurry crystallisation 26

1.5 Industrial crystallisation 26

1.5.1 Batch crystallisation 26

1.5.2 Continuous crystallisation 27

1.6 Crystal engineering 30

1.6.1 Intermolecular interactions 31

1.6.1.1 Hydrogen bonds 31

1.6.1.2 π-stacking 33

1.6.1.3 Weak interactions 33
1.6.2 Multi-component crystallisations 34
1.6.3 Molecular complementarity calculations 34
1.7 Types of crystalline solids 36
1.7.1 Polymorphism 36
1.7.2 Salts 39
1.7.3 Co-crystals 39
1.7.4 Solvates/hydrates 40
1.8 Aims and objectives 41
1.8.1 Isoniazid (IZN) 41
1.8.2 Pyridoxine (PYR) 47
Chapter 2 Analytical methods 53
2.1 Crystallography 53
2.1.1 Crystalline state 53
2.1.2 Molecular symmetry 55
2.1.3 X-ray diffraction 57
2.1.4 Bragg's Law 57
2.1.5 Diffraction patterns and reciprocal space 58
2.1.6 Scattering factors 59
2.1.7 Data collection 60
2.1.8 Structure solution 61
2.1.8.1 Direct methods 61
2.1.8.2 Patterson methods 61
2.1.8.3 Dual-space iterative methods 62
2.1.9 Structure completion and refinement 62
2.1.9.1 Least-squares refinement method 63
2.1.9.2 R-Factors 64
2.1.9.3 Structure completion 64
2.1.10 Powder X-ray Diffraction (PXRD) 65
2.2 Thermal analysis 66
2.2.1 Differential Scanning Calorimetry (DSC) 66
2.2.2 Thermogravimetric Analysis (TGA) 68
2.2.3 Hot-stage Microscopy (HSM) 68
2.3 Optical microscopy 69
2.4 Fourier Transform Infra-red spectroscopy (FTIR) 69

2.5 Nuclear Magnetic Resonance spectroscopy (NMR) 70

Chapter 3 Experimental methods and analysis equipment 73

3.1 Solubility and metastable zone width measurements 73

3.1.1 Gravimetric solubility determination 73

3.1.2 Solubility and metastable zone width determination via observation 74

3.2 Crystallisation methods 76

3.2.1 Evaporative crystallisation 76

3.2.2 Cooling crystallisation 76

3.2.2.1 Uncontrolled crash cooling 76

3.2.2.2 Controlled cooling 77

3.2.3 Grinding (mechanochemical) 77

3.2.4 Slurrying 78

3.2.5 Continuous crystallisation 78

3.2.6 Temperature cycling 80

3.3 Stability measurements 80

3.3.1 Slurry 81

3.3.2 Competitive slurrying 81

3.3.3 Elevated temperature 81

3.3.4 Humidity 81

3.4 X-ray diffractometers 82

3.4.1 Single Crystal X-ray Diffraction (SCXRD) 82

3.4.2 Powder X-ray Diffraction (PXRD) 84

3.5 Thermal analysis 84

3.5.1 Hot-stage Microscopy (HSM) 84

3.5.2 Differential Scanning Calorimetry (DSC) 85

3.5.3 Thermogravimetric Analysis (TGA) 85

3.6 Other analysis techniques 85

3.6.1 Fourier Transform Infra-red spectroscopy (FTIR) 85

3.6.2 Nuclear Magnetic Resonance spectroscopy analysis (NMR) 85

Chapter 4 Morphology changes observed in pure isoniazid 87

4.1 Introduction and aims 87

4.2 Solvent effects on isoniazid morphology 87

4.2.1 Experimental information 88

4.2.1.1 Choice of solvents for isoniazid crystallisations 88

4.2.1.2 Evaporative screening of isoniazid in different solvent systems 89

4.2.1.3 Cooling crystallisations of isoniazid in different solvent systems 89
4.2.1.4 Isoniazid cooling crystallisations in the KRAIC continuous platform 90
4.2.1.5 Temperature cycling crystallisation of isoniazid from ethyl acetate 91
4.2.1.6 Supersaturation experiments with isoniazid 91
4.2.1.7 Analytical methods 92
4.2.2 Effects of solvent on isoniazid morphology 92
4.2.3 Transfer of isoniazid solvent experiments into the KRAIC continuous crystallisation platform 101
4.2.4 Temperature cycling effects on isoniazid morphology crystallised from ethyl acetate 106
4.2.5 The effect of supersaturation on isoniazid morphology 107
4.2.6 Morphology changes of isoniazid in evaporative crystallisations with solvent mixtures 109
4.2.6.1 Ethyl acetate:propan-2-ol mixtures 109
4.2.6.2 Ethyl acetate and ester mixtures 110
4.3 Additive experiments with isoniazid 113
4.3.1 Selection of additives for isoniazid 114
4.3.2 Experimental information 116
4.3.2.1 Evaporative screening of isoniazid with different additives 116
4.3.2.2 Cooling crystallisation of isoniazid with different additives 117
4.3.2.3 Transfer of isoniazid additive crystallisations into the KRAIC continuous platform 117
4.3.2.4 Analytical methods 118
4.3.3 Effect of size-matched and structurally similar additives on isoniazid morphology achieved via evaporative crystallisation 119
4.3.4 Effect of size-matched and structurally similar additives on isoniazid morphology achieved via cooling crystallisation 122
4.3.4.1 Cooling crystallisations at 10 g solvent scale 122
4.3.4.2 Cooling crystallisations at 150 g solvent scale 123
4.3.4.3 Transfer of successful additive experiments into the KRAIC continuous platform 129
4.3.5 Effect of polymer additives on isoniazid morphology achieved via evaporative and cooling crystallisation 131
4.4 Conclusions 133
Chapter 5 Morphology changes observed in multi-component crystals of isoniazid 137
5.1 Introduction 137
5.2 Selection of co-formers for isoniazid 137

5.3 Experimental information ... 140
  5.3.1 Evaporative screening for isoniazid co-crystals ... 140
  5.3.2 Crash cooling of isoniazid co-crystals ... 141
  5.3.3 Isoniazid single crystal structures ... 141
  5.3.4 Further preparations of isoniazid co-crystals ... 144
    5.3.4.1 Isoniazid co-crystal production using mechanochemical grinding ... 144
    5.3.4.2 Isoniazid co-crystal production via slurrying ... 144
    5.3.4.3 Scale up of isoniazid co-crystals using controlled cooling ... 144
  5.3.5 Solubility determination of isoniazid co-crystals ... 145
  5.3.6 Stability testing of isoniazid co-crystals ... 145
  5.3.7 Analytical methods ... 146
    5.3.7.1 Variable temperature Powder X-ray Diffraction (vtPXRD) ... 146
5.4 Crystallisation of isoniazid with tartaric acid enantiomers ... 146
  5.4.1 Crystallisation of isoniazid with (L)-tartaric acid and (D)-tartaric acid ... 147
  5.4.2 Crystallisation of isoniazid with (DL)-tartaric acid forming a hydrate ... 155
  5.4.3 Dehydration of isoniazid and (DL)-tartaric acid hydrate to give an anhydrous form ... 167
5.5 Crystallisation of isoniazid with 3,4-dinitrobenzoic acid ... 175
5.6 Conclusions ... 185
Chapter 6 Changing the morphology of pyridoxine ... 187
6.1 Introduction ... 187
6.2 Selection of co-formers and additives for pyridoxine ... 187
6.3 Experimental information ... 191
  6.3.1 Additive and solvent experiments with pyridoxine ... 191
    6.3.1.1 Evaporative screening of pyridoxine with different solvents and additives ... 191
    6.3.1.2 Cooling crystallisation of pyridoxine with different solvents and additives ... 191
6.4 Multi-component experiments with pyridoxine ... 192
  6.4.1 Evaporative screening for pyridoxine co-crystals ... 192
  6.4.2 Pyridoxine single crystal structures ... 192
  6.4.3 Further pyridoxine co-crystal preparation ... 195
    6.4.3.1 Mechanochemical grinding of pyridoxine co-crystals ... 195
    6.4.3.2 Pyridoxine co-crystal production via slurrying ... 195
    6.4.3.3 Scale up of pyridoxine co-crystals using controlled cooling ... 195
  6.4.4 Solubility determination of pyridoxine co-crystals ... 195
  6.4.5 Analytical methods ... 196

6.5 Solvent effects on pyridoxine morphology 196
6.6 Effect of additives on pyridoxine morphology 197
6.6.1 Effect of size-matched and structurally similar additives in evaporative and cooling crystallisation 197
6.6.2 Effect of polymeric additives in evaporative and cooling crystallisation 197
6.7 Multi-component crystallisations with pyridoxine 199
6.7.1 Crystallisation of pyridoxine with 2,4-dinitrobenzoic acid 199
6.7.2 Determining the structure of the second polymorph of the PYR:2,4-DNBA co-crystal 206
6.7.3 Identifying the thermodynamically stable polymorphic form of the PYR:2,4-DNBA co-crystal 213
6.7.4 Crystallisation of pyridoxine with 3,5-dinitrobenzoic acid 215
6.7.5 Crystallisation of pyridoxine with trimesic acid 222
6.7.6 Crystallisation of pyridoxine with phthalic acid 229
6.7.7 Crystallisation of further multi-component materials of pyridoxine 234
6.8 Conclusion 234
Chapter 7 Benchmarking CMAC workflows 239
7.1 Introduction 239
7.2 Importance of workflows 239
7.3 Outline of workflows 240
7.3.1 Multi-component (MC) workflow 240
7.3.2 Additive workflow 242
7.4 Multi-component workflow benchmarking 245
7.5 Additive workflow benchmarking 245
7.5.1 Fenamic acid (FA) and mefenamic acid (MFA) 245
7.5.2 Workflow benchmarking for fenamic acid and mefenamic acid 248
7.6 Conclusions 254
Chapter 8 **Conclusions and future work** 257
8.1 Conclusions 257
8.2 Future work 262
Bibliography 265
Appendix 273

List of figures

Figure 1.1. Solubility curve, metastable zone and metastable boundary [4] 3
Figure 1.2. Differences in primary and secondary nucleation processes.[6] 4
Figure 1.3. Two alternative pathways for nucleation. Top: classical nucleation theory (CNT) Bottom: two-step nucleation theory. 5
Figure 1.4. Free energy change as a function of cluster size. (a) at low supersaturation, (b) at high supersaturation 6
Figure 1.5. Crystal growth surface showing potential growth sites: a surface only site, a step surface site and a kink site. 7
Figure 1.6. Crystal growth free energy barriers to be overcome 8
Figure 1.7. Spiral growth model as a result of screw dislocations[19] 9
Figure 1.8. Effect of crystal morphology on filtration: block-like crystals filter well (left), plate-shape crystals are less efficient, creating an impermeable layer (centre) and needles block pores in filter medium (right). [4] 11
Figure 1.9. Sites of impurity adsorption on a growing crystal: (a) kink site, (b) surface steps and (c) ledge 17
Figure 1.10. Generation of supersaturation in evaporative crystallisation methods (orange arrow). Variation of solute concentration throughout the evaporative process is depicted by the double headed arrow between supersaturated and metastable zone regions (purple arrow) 24
Figure 1.11. Ideal profile for a cooling crystallisation, including initial spontaneous nucleation, shown on a solubility diagram.[7] 25
Figure 1.12. Set up of COBC at the University of Bath. (a) input of feed solution via peristaltic pump, (b) output of solvent and crystalline product, (c) motor driven bellows to set up oscillation and (d) direction of flow along temperature gradient represented by colour change (red to blue shows hot to cold) 28
Figure 1.13. Illustrations of different flow mechanisms; (a) laminar flow, (b) turbulent flow and (c) plug flow 29
Figure 1.14. Typical hydrogen bond motifs (synthons); in the definition of hydrogen bond donors given above, the DH donor fragment here has D = O or N. (a) carboxylic acid dimer homo-synthon, (b) amide···acid hetero-synthon 31
Figure 1.15. Different hydrogen bonding interactions where D is the donor and A is the acceptor. (a) a two-centred hydrogen bond, (b) a bifurcated hydrogen bond between one donor and two acceptors and (c) a bifurcated hydrogen bond between two donors and one acceptor. 33
Figure 1.16. Face-centred stacking, (b) off-centre parallel stacking, (c) edge-to-face interactions.[130] 33
Figure 1.17. Illustration of possible crystalline forms for single and multi-component systems; (a) polymorphs, (b) salts (c) co-crystal and (d) solvate/hydrate. The counter-ion in the salt case can be a simple ion or a molecular ion, the latter is often generated by proton transfer during the crystallisation process. 36
Figure 1.18. Crystal packing of two paracetamol polymorphs: Form I viewed along crystallographic a axis showing herringbone structure (left) and form II viewed along the crystallographic b axis showing the layered packing (right) 37
Figure 1.19. Plots showing the free energy relationship with temperature for enantiotropic systems (left) and monotropic systems (right). G is the free energy, T is the temperature, A, B and

Liq refer to polymorphs A, B and liquid phase and T_m and T_t correspond to temperature of melt and transition respectively. 38
Figure 1.20. Solubility curves showing the relationship between two polymorphs enantiotropically related (left) and monotropically related (right) over a defined temperature range 38
Figure 1.21. Labelled IZN molecule (left) and unit cell projection for IZN (INICAC02) (right) 42
Figure 1.22. Packing of an IZN (INICAC02) crystal as viewed along the b axis (left) and a axis (right) 43
Figure 1.23. Hydrogen bonds present in IZN (INICAC02) crystal structure 43
Figure 1.24. BFDH predicted morphology of IZN (INICAC02) (left) and associated packing (right) .. 44
Figure 1.25. BFDH morphology schematic of IZN obtained from Sigma Aldrich, generated from face-indexing. 45
Figure 1.26. PXRD patterns of IZN: (a) form I calculated from SCXRD data (INICAC02), (b) form II calculated from SCXRD data (INICAC04) and (c) measured IZN starting material 45
Figure 1.27. DSC trace of IZN material obtained from Sigma Aldrich 46
Figure 1.28. Solubility curves for IZN: Crystallised from (a) H_2O, (b) EtOH, (c) IPA and (d) EtOAc 46
Figure 1.29. Labelled PYR molecule (left) and unit cell projection for PYR (BITZAF) (right) 47
Figure 1.30. Packing in PYR (BITZAF) crystal 47
Figure 1.31. Hydrogen bonds present in PYR (BITZAF) crystal structure 48
Figure 1.32. BFDH predicted morphology for PYR (BITZAF) (left) and associated packing (right) 49
Figure 1.33. PXRD data for PYR: (a) calculated from SCXRD data (BITZAF) and (b) measured PYR starting material 50
Figure 1.34. DSC trace for PYR starting material obtained from Sigma Aldrich 50
Figure 1.35. Solubility curves for PYR. Crystallised from (a) IPA, (b) EtOH and (c) H_2O 51
Figure 2.1. Unit cell defined by lengths (a, b, c) and angles (α, β, γ). The molecular components that comprise the crystal are contained within the unit cell. 54
Figure 2.2. The four lattice types. P = primitive, I = body-centred, C = centred and F = face-centred 54
Figure 2.3. Pictorial representations of (a) non-translational symmetry elements: (i) rotation, (ii) inversion, (iii) reflection and (iv) rotary-inversion. (b) translational symmetry elements: (i) screw-axis and (ii) glide plane. 56
Figure 2.4. Schematic of Bragg's law. X-ray diffraction shown between parallel Miller planes (hkl) separated by a distance d_{hkl} 58
Figure 2.5. Representation of X-ray scattering factors fj for atoms A and B. 59
Figure 2.6. Cones of reflection observed when irradiating a polycrystalline sample during a powder X-ray diffraction experiment. 65
Figure 2.7. DSC schematic showing some commonly observed thermal events in pharmaceutical solids. (a) glass transition, (b) recrystallisation or decomposition, (c) desolvation or phase transition and (d) melting or decomposition.[190] 67
Figure 2.8. Typical TGA graph showing mass loss from a sample 68
Figure 3.1. Cambridge Reactor Designs Polar Bear Plus crystalliser set up. Left: Polar Bear with overhead stirrer set up. Right: Different sized inserts for Polar Bear (top, left to right: 1 mL + 50 mL; bottom, left to right: 10 mL + 250 mL) 75
Figure 3.2. Adapted KRAIC set up. 1. Air pump; 2. Galden pump; 3. Solution pump; 4. Feed/solution vessel; 5. Submerged cross piece; 6. Crystallisation coil; 7. Outlet; 8. Crystal collection; 9. Galden recovery. 78
Figure 3.3. Humidity chamber set up with unsealed 1 mL vial inside an unsealed 20 mL vial 82

Figure 3.4. Rigaku Oxford Diffraction Gemini A Ultra diffractometer. 1. CCD area detector; 2. Goniometer; 3. Cryostream; 4. Cu and Mo X-ray tubes; 5. Camera. Backstop can be seen between the X-ray tubes and area detector 83
Figure 4.1. Ester solvents used (a) methyl acetate, (b) isopropyl acetate, (c) isobutyl acetate, (d) ethyl propionate, (e) ethyl butyrate, (f) ethyl valerate, (g) ethyl hexanoate and (h) ethyl heptanoate 88
Figure 4.2. Temperature profiles for temperature cycling experiment 1 (left) and 2 (right) 91
Figure 4.3. IZN crystals from evaporative crystallisations at 40 ^oC from solvents (a) H_2O, (b) EtOH, (c) IPA, (d) EtOAc and (e) ACN 93
Figure 4.4. IZN crystals from cooling crystallisations at a rate of 1 ^oC/minute from (a) H_2O, (b) EtOH, (c) IPA, (d) EtOAc and (e) ACN 93
Figure 4.5. Top: BFDH predicted morphology for IZN (INICAC02). Bottom: Molecular packing with respect to BFDH morphology 95
Figure 4.6. Top: Face indexed morphologies for IZN crystallised from EtOH (left) and IPA (right). Bottom: Molecular packing with respect to morphology for EtOH (left) and IPA (right). 96
Figure 4.7. Hydrogen bonds contributing to elongation of plate crystals in IPA: viewed from (-100) face (top) and (0-10) face (bottom) 97
Figure 4.8. Top: Face indexed morphology for IZN crystallised from EtOAc. Bottom: Molecular packing with respect to morphology 98
Figure 4.9. Top: Face indexed morphology for IZN crystallised from ACN. Bottom: Molecular packing with respect to morphology 100
Figure 4.10. Crystallisation in feed pump outlet (left) and crystals in solution slugs in KRAIC tubing (right) for IZN crystallisation from IPA 101
Figure 4.11. Crystals produced from continuous cooling crystallisations in IPA in the KRAIC set up 102
Figure 4.12. Face indexed crystals of IZN crystallised from IPA in the KRAIC continuous cooling (left) and batch cooling (right) 102
Figure 4.13. PXRD data for (a) IZN (INICAC02) and (b) IZN crystallised from IPA in the KRAIC continuous platform 103
Figure 4.14. Crystallisations in the feed pump outlet (left) and crystals in solution slugs in KRACI tubing (right) for crystallisations of IZN from EtOAc. 104
Figure 4.15. Crystals produced from continuous cooling crystallisations from EtOAc in the KRAIC set up 104
Figure 4.16. Face indexed crystals produced from EtOAc in KRAIC continuous cooling (left) and batch cooling (right) 105
Figure 4.17. PXRD data for (a) IZN (INICAC02) and (b) IZN crystallised from EtOAc in the KRAIC continuous cooling platform 106
Figure 4.18. IZN crystals produced in temperature cycling experiment 1 where a 30 minute hold was included between cycles (left) and experiment 2 where no hold was utilised between heating and cooling (right) 107
Figure 4.19. Evaporative experiments to investigate the effects of saturation and evaporation temperature on the morphology of IZN crystallised from IPA 108
Figure 4.20. Evaporative experiments to investigate the effects of saturation and evaporation temperature on the morphology of IZN crystallised from EtOAc. 109
Figure 4.21. Evaporative experiments carried out at 20 ^oC (top) and 40 ^oC (bottom) to investigate effects of solvent mixtures of IPA:EtOAC on IZN morphology 110

Figure 4.22. Evaporative experiments to investigate the effects of solvent mixtures of IPA and assorted esters (percentages given) on the morphology of IZN 111
Figure 4.23. Evaporative experiments to investigate the effects of solvent mixtures of IPA and assorted esters (percentages given) on the morphology of IZN 111
Figure 4.24. Evaporative experiments to investigate the effects of solvent mixtures of EtOAc and assorted esters (percentages given) on the morphology of IZN 112
Figure 4.25. Evaporative experiments to investigate the effects of solvent mixtures of EtOAc and assorted esters (percentages given) on the morphology of IZN 113
Figure 4.26. Additives list for screening with IZN (a) benzoic acid, (b) 3-hydroxybenzoic acid, (c) 2,4-dihydroxybenzoic acid, (d) 3,4-dihydroxybenzoic acid, (e) 3,5-dihydroxybenzoic acid, (f) 2,6-dihydroxybenzoic acid, (g) 4-cyanobenzoic acid, (h) 3-cyanobenzoic acid, (j) 2,4-dinitrobenzoic acid, (k) 3,4-dinitrobenzoic acid, (l) 3,5-dinitrobenzoic acid, (m) trimesic acid, (n) isonicotinamide, (p) nicotinamide, (q) pyridoxine, (r) vanillin and (s) L-tartaric acid 115
Figure 4.27. Polymeric additive list for screening with IZN (a) polybutadiene, (b) polyvinylpyrrolidone, (c) poly(ethylene glycol), (d) poly(propylene glycol), (e) pluronic P123 and (f) poly(ethylene glycol) diglycidyl ether 116
Figure 4.28. Face indexed crystals of IZN crystallised from IPA in the presence of 1% 3-HBA (left) and in the absence of additives (right) 119
Figure 4.29. Face indexed crystals of IZN crystallised from IPA in the presence of 1% 3,4-DNBA (left) and in the absence of additives (right) 121
Figure 4.30. Microscope images comparing the morphology of IZN crystallised from IPA with 3-HBA additive in 150 g cooling with overhead stirring (top and middle) and evaporative crystallisations (bottom) 123
Figure 4.31. PXRD data for (a) IZN (INICAC02), (b) 3-HBA form I (BIDLOP), (c) 3-HBA form II (BIDLOP01), (d) 3-HBA hydrate (BOMCAJ), (e) IZN 1% 3-HBA, (f) IZN 5% 3-HBA and (g) IZN 10% 3-HBA 124
Figure 4.32. Face indexed crystals of IZN from 150 g cooling crystallisation (left) and evaporative crystallisations (right) in IPA with 1% 3-HBA additive 125
Figure 4.33. Microscope images comparing the morphology of IZN crystallised from IPA with 3,4-DNBA additive in 150 g cooling with overhead stirring (top and middle) and evaporative crystallisation (bottom 126
Figure 4.34. PXRD data for (a) IZN (INICAC02), (b) 3,4-DNBA (YADKOF), (c) IZN 1% 3,4-DNBA, (d) IZN 5% 3,4-DNBA and (e) IZN 10% 3,4-DNBA 127
Figure 4.35. Face indexed crystals of IZN from 150 g cooling crystallisation (left) and evaporative crystallisations (right) in IPA with 1% 3,4-DNBA additive... 128
Figure 4.36. Microscope images of crystals achieved from IPA KRAIC crystallisations with different additive percentages of 3-HBA 129
Figure 4.37. Microscope images of crystals achieved in IPA KRAIC crystallisations with different additive percentages of 3,4-DNBA 130
Figure 4.38. Cooling crystallisations of IZN with 1% polymer additives in IPA at a rate of 0.1°C/minute. (a) PP123, (b) PEG, (c) PPG, (d) PBD, (e) PVP and (f) PDE 131
Figure 4.39. Cooling crystallisations of IZN with 0.1% polymer additives in IPA at rate of 0.1 °C/minute. (a) PP123, (b) PEG, (c) PPG, (d) PBD, (e) PVP and (f) PDE 131
Figure 4.40. 40 °C evaporative crystallisations of IZN with 1% polymer additives from IPA. (a) PP123, (b) PEG, (c) PPG, (d) PBD, (e) PVP and (f) PDE 132

Figure 4.41. 40 °C evaporative crystallisations of IZN with 0.1% polymer additives from IPA. (a) PP123, (b) PEG, (c) PPG, (d) PBD, (e) PVP and (f) PDE 132
Figure 5.1. Supramolecular synthons observed in IZN co-crystals in the CSD [203] 139
Figure 5.2. Structure of co-formers determined from initial molecular complementarity calculations with IZN (a) malic acid, (b) citric acid, (c) sorbic acid, (d) (L)-tartaric acid, (e) pyridoxine, (f) trimesic acid, (g) glutamic acid, (h) (L)-pyroglutamic acid, (j) 3,5-dinitrosalicylic acid, (k) 3,5-dinitrobenzoic acid, (l) 3,4-dinitrobenzoic acid, (m) D-mannitol.. 140
Figure 5.3. Structure of IZN and TA showing the numbering system used in hydrogen bonding discussions. 147
Figure 5.4. View along the crystallographic a axis of IZN:LTA (left) and IZN:DTA (right)............... 148
Figure 5.5. View along the crystallographic b axis of IZN:LTA (left) and IZN:DTA (right)............... 148
Figure 5.6. Hydrogen bonding interactions formed with IZN molecules in the LTA co-crystal structure (left) and DTA co-crystal structure (right) 149
Figure 5.7. Hydrogen bonding interactions between TA molecules: LTA co-crystal (left) and DTA co-crystal (right) 150
Figure 5.8. PXRD data for IZN:LTA (left) and IZN:DTA (right): (a) IZN (INICAC02), (b) LTA (TARTAL), (c) IZN:LTA co-crystal calculated from SCXRD, (d) IZN:LTA co-crystal from H_2O crash cooling, (e) DTA (TARTAC), DTA form II (TARTAC24), (g) IZN:DTA co-crystal calculated from SCXRD and (h) IZN:DTA co-crystal from H_2O crash cooling experiment 151
Figure 5.9. DSC data for IZN:LTA co-crystal (left) and IZN:DTA co-crystal (right). IZN melting point = 171-174 °C [163], TA melting point = 170-172 °C [205].. 152
Figure 5.10. Solubility plot for IZN:TA co-crystal (purple circle marker) and pure IZN (black square marker) measured by observation in H_2O 153
Figure 5.11. PXRD data for (a) IZN (INICAC02), (b) LTA (TARTAL), (c) IZN:LTA co-crystal calculated from SCXRD, (D) IZN:LTA co-crystal slurry 1 week, (e) IZN:LTA co-crystal 50 °C 3 weeks and (f) IZN:LTA co-crystal 70% humidity 9 weeks 153
Figure 5.12.Plate-shaped crystals of IZN:LTA co-crystal (left) and IZN:DTA co-crystal (right) crystallised from H_2O 154
Figure 5.13. Predicted BFDH morphology for IZN:TA (left); observed morphology for IZN:LTA (middle) and IZN:DTA (right).. 154
Figure 5.14. Unit cell for IZN:DLTA:H_2O co-crystal structure 156
Figure 5.15. Hydrogen bonding interactions present in the IZN:DLTA:H_2O co-crystal showing the alternating nature of the IZN stacking and the chains of DLTA 157
Figure 5.16. Schematic demonstrating (a) an isolated site hydrate, where H_2O molecules do not interact. (b) a channel hydrate, where H_2O molecules hydrogen bond to each other in a channel (orange dashed line). (c) an ion-associated hydrate, where the H_2O molecules are ion coordinated with the API (green dashed lines) 158
Figure 5.17. PXRD data for (a) IZN (INICAC02), (b) DLTA (ZZZDUI01), (c) DLTA monohydrate (TARTDL), (d) IZN:DLTA:H_2O co-crystal calculated from SCXRD and (e) IZN:DLTA:H_2O co-crystal from H_2O crash cooling.. 159
Figure 5.18. DSC trace for IZN:DLTA:H_2O co-crystal. IZN melting point = 171-174 °C [163], DLTA melting point = 210-212 °C [207] 160
Figure 5.19. Solubility plot for IZN:DLTA:H_2O co-crystal (purple circle marker) and pure IZN (black square marker) measured by observation in H_2O 161
Figure 5.20. TGA trace for IZN:DLTA:H_2O co-crystal showing the mass loss with increasing temperature... 162

Figure 5.21. FTIR scan of IZN:DLTA:H_2O co-crystal 163
Figure 5.22. Variable temperature PXRD data obtained from beamline I11 at Diamond light source showing the conversion from the hydrated co-crystal to a secondary crystal structure. (a) initial collection at 75 °C, (b) collection at 79 °C, (c) collection at 81 °C showing the transition, (d) collection at 83 °C and (e) collection at 85 °C 164
Figure 5.23. PXRD data for (a) IZN (INICAC02), (b) DLTA (ZZZDUI05), (c) DLTA monohydrate (TARTDL), (d) IZN:DLTA:H_2O co-crystal calculated from SCXRD, (d) IZN:DLTA:H_2O slurry 1 week, (e) IZN:DLTA:H_2O co-crystal 50 °C 24 hours, (f) IZN:DLTA:H_2O co-crystal 50 °C 1 week and (g) IZN:DLTA:H_2O co-crystal 70% humidity 9 weeks 165
Figure 5.24.Plate-shaped IZN:DLTA:H_2O co-crystals crystallised from H_2O 165
Figure 5.25. Predicted BFDH morphology for IZN:DLTA:H_2O (left); observed morphology for IZN:DLTA:H_2O (right) 166
Figure 5.26. Unit cell of IZN:DLTA anhydrous co-crystal 167
Figure 5.27. Hydrogen bonding interactions present in IZN:DLTA co-crystal showing the alternating nature of the IZN stacking and chains of the DLTA molecules 168
Figure 5.28. PXRD data for (a) IZN (INICAC02), (b) DLTA (ZZZDUI05), (c) DLTA monohydrate (TARTDL), (d) IZN:DLTA co-crystal calculated from SCXRD and (e) IZN:DLTA co-crystal produced by dehydrating the hydrated form at 50 °C 169
Figure 5.29. DSC trace for IZN:DLTA co-crystal. IZN melting point = 171-174 °C [163], DLTA melting point = 210-212 °C [207] 170
Figure 5.30. TGA trace for IZN:DLTA co-crystal confirming the absence of H_2O in the structure ... 170
Figure 5.31. FTIR scan of IZN:DLTA co-crystal 171
Figure 5.32. Left: Solubility plot for IZN:DLTA co-crystal (purple circle marker) and pure IZN (black square marker) measured by observation in H_2O. Right: comparison of IZN:DLTA co-crystal solubility (purple circle marker) and IZN:DLTA:H_2O co-crystal (black square marker) 172
Figure 5.33. PXRD data for (a) IZN (INICAC02), (b) DLTA (ZZZDUI05), (c) DLTA monohydrate (TARTDL), (d) IZN:DLTA co-crystal calculated from SCXRD, (e) IZN:DLTA co-crystal slurry 48 hours, (f) IZN:DLTA co-crystal 50 °C 3 weeks and (g) IZN:DLTA co-crystal 70% humidity 9 weeks 173
Figure 5.34. Images isolated from HSM video footage showing the morphology retention when IZN:DLTA:H_2O co-crystal (left) transforming to IZN:DLTA co-crystal (right) upon heating 174
Figure 5.35. Predicted BFDH morphology for IZN:DLTA (left); observed morphology for IZN:DLTA (right) 174
Figure 5.36. Structure of IZN and 3,4-DNBA showing the numbering system used in hydrogen bonding discussions 175
Figure 5.37. Unit cell of co-crystal IZN:3,4-DNBA 176
Figure 5.38. Hydrogen bonding and close interactions of IZN:3,4-DNBA co-crystal 177
Figure 5.39. Offset of dimeric hydrogen bonding interactions 177
Figure 5.40. PXRD data for (a) IZN (INICAC02) (b) 3,4-DNBA (YADKOF), (c) IZN:3,4-DNBA calculated from SCXRD and (d) IZN:3,4-DNBA crystals from evaporative crystallisation in IPA 179
Figure 5.41. DSC trace for IZN:3,4-DNBA co-crystal. IZN melting point = 171-174 °C [163], 3,4-DNBA melting point = 165 °C [210] 180
Figure 5.42. TGA trace for IZN:3,4-DNBA co-crystal 181
Figure 5.43. Solubility plot for IZN:3,4-DNBA co-crystal (purple circle marker) and pure IZN (black square marker) measured by observation in IPA 182

Figure 5.44. PXRD data for (a) IZN (INICAC02), (b) 3,4-DNBA (YADKOF), (c) IZN:3,4-DNBA calculated from SCXRD, (d) IZN:3,4-DNBA co-crystal slurry 1 week, (e) IZN:3,4-DNBA co-crystal 50 ^{o}C 3 weeks and (f) IZN:3,4-DNBA co-crystal 70% humidity 9 weeks 183
Figure 5.45. Plate-shaped IZN:3,4-DNBA co-crystals crystallised from IPA 183
Figure 5.46. Predicted morphology for IZN:3,4-DNBA (left); observed morphology for IZN:3,4-DNBA (right) 184
Figure 6.1. Labelled PYR molecule showing the functional groups present 187
Figure 6.2. Additive list for screening with PYR (a) benzoic acid, (b) trimesic acid, (c) imidazole, (d) benzimidazole, (e) 2,4-dinitrobenzoic acid, (f) isonicotinamide, (g) isonicotinic acid, (h) nicotinic acid, (j) nicotinamide, (k) 3,5-dinitrobenzoic acid, (l) 2-aminobenzoic acid, (m) barbituric acid, (n) tartaric acid, (p) 2,2’-bipyridine and (q) 4,4’-bipyridine 188
Figure 6.3. Supramolecular synthons observed in PYR co-crystals in CSD 189
Figure 6.4. Co-formers used in multi-component crystallisation screening (a) isonicotinamide, (b) nicotinamide, (c) nicotinic acid, (d) imidazole, (e) benzimidazole, (f) 2,4-dinitrobenzoic acid, (g) 3,4-dinitrobenzoic acid, (h) 3,5-dinitrobenzoic acid, (j) phthalic acid, (k) trimesic acid and (l) barbituric acid 190
Figure 6.5. Polymer additives used (a) Polybutadiene, (b) polyvinylpyrrolidone, (c) poly(ethylene glycol), (d) poly(propylene glycol), (e) pluronic P123 and (f) poly(ethylene glycol) diglycidyl ether 190
Figure 6.6. PYR morphology achieved in cooling crystallisations carried out in (a) H_2O, (b) EtOH and (c) IPA 196
Figure 6.7. PYR morphology achieved in evaporative crystallisations carried out in (a) H2O, (b) EtOH and (c) IPA 196
Figure 6.8. Cooling crystallisations of PYR with 0.1% polymer additives in IPA at rate of 0.1 ^{o}C/minute. (a) PP123, (b) PEG, (c) PPG, (d) PBD, (e) PVP and (f) PDE 198
Figure 6.9. 40 ^{o}C evaporative crystallisations of PYR with 1% polymer additives in IPA. (a) PP123, (b) PEG, (c) PPG, (d) PBD, (e) PVP and (f) PDE 198
Figure 6.10. 40 ^{o}C evaporative crystallisations of PYR with 0.1% polymer additives in IPA. (a) PP123, (b) PEG, (c) PPG, (d) PBD, (e) PVP and (f) PDE 198
Figure 6.11. Structure of PYR and 2,4-DNBA showing the numbering system used in hydrogen bonding discussions 199
Figure 6.12. Unit cell of co-crystal PYR:2,4-DNBA 200
Figure 6.13. Hydrogen bonding interactions present in PYR:2,4-DNBA co-crystal showing the nature of the stacking 200
Figure 6.14. PXRD data for (a) PYR (BITZAF), (b) 2,4-DNBA (BAQLUD), (c) PYR:2,4-DNBA co-crystal calculated from SCXRD data and (d) PYR:2,4-DNBA co-crystal from evaporative crystallisation in IPA 201
Figure 6.15. DSC trace of co-crystal PYR:2,4-DNBA. PYR melting point = 159-162 °C [166], 2,4-DNBA melting point = 182 °C [210] 202
Figure 6.16. Solubility plot for PYR:2,4-DNBA co-crystal (purple, circle marker) and pure PYR (black, square marker) from observation in IPA 204
Figure 6.17. PXRD data for (a) PYR (BITZAF), (b) 2,4-DNBA (BAQLUD), (c) PYR:2,4-DNBA form I calculated from SCXRD, (d) PYR:2,4-DNBA form I slurry 1 week, (e) PYR:2,4-DNBA form I 50dc 3 weeks and (f) PYR:2,4-DNBA form I humidity 9 weeks 204
Figure 6.18. Thickened crystals of PYR:2,4-DNBA form I co-crystal crystallised from IPA 205

Figure 6.19. Predicted BFDH morphology for PYR:2,4DNBA form I (left); observed morphology for PYR:2,4-DNBA form I (right) 205
Figure 6.20. Unit cell of PYR:2,4-DNBA form II co-crystal 206
Figure 6.21. Hydrogen bonding interactions present in PYR:2,4-DNBA form II co-crystal showing the ring interactions formed between the API and co-former and the chain links between the rings. 207
Figure 6.22. PXRD data for (a) PYR:2,4-DNBA form I calculated from SCXRD, (b) PYR:2,4-DNBA form II calculated from SCXRD and (c) PYR:2,4-DNBA form II co-crystal from slurry of PYR:2,4-DNBA form I in H_2O 208
Figure 6.23. DSC trace of co-crystal PYR:2,4-DNBA form II (solid black line) compared to form I (dotted purple line). PYR melting point = 159-162 °C [166], 2,4-DNBA melting point = 182 °C [210] 209
Figure 6.24. PXRD data for (a) PYR (BITZAF), (b) 2,4-DNBA (BAQLUD), (c) PYR:2,4-DNBA form II co-crystal calculated from SCXRD data and (d) PYR:2,4-DNBA co-crystal form II from cooling crystallisation in H_2O 210
Figure 6.25. Solubility plot for PYR:2,4-DNBA form II co-crystal (purple, circle marker) and pure PYR (black, square marker) from observation in H_2O 211
Figure 6.26. PXRD data for (a) PYR (BITZAF), (b) 2,4-DNBA (BAQLUD), (c) PYR:2,4-DNBA form II calculated from SCXRD, (d) PYR:2,4-DNBA form II slurry 1 week, (e) PYR:2,4-DNBA form II 50dc 3 weeks and (f) PYR:2,4-DNBA form II humidity 9 weeks 211
Figure 6.27. Irregular shaped crystals of PYR:2,4-DNBA form II from cooling in H_2O 212
Figure 6.28. Predicted BFDH morphology for PYR:2,4-DNBA form II (left); observed morphology for PYR:2,4-DNBA form II (right) 212
Figure 6.29. Solubility of PYR:2,4-DNBA form I (black) and form II (purple) in H_2O (left) and IPA (right) from observation methods 213
Figure 6.30. PXRD data for (a) PYR:2,4-DNBA form I calculated from SCXRD, (b) PYR:2,4-DNBA form II calculated from SCXRD, (c) competitive slurry of 1:1 form I:form II mixture in IPA and (d) competitive slurry of 1:1 form I:form II mixture in H_2O 214
Figure 6.31. PXRD data for (a) PYR:2,4-DNBA form I calculated from SCXRD, (b) PYR:2,4-DNBA form II calculated from SCXRD, (c) mixture of form I and form II after 3 months and (d) co-grinding experiment of 1:1 form I:form II PYR:2,4-DNBA co-crystal 215
Figure 6.32. Structure of PYR and 3,5-DNBA showing the numbering system used in hydrogen bonding discussions 215
Figure 6.33. Unit cell of co-crystal PYR:3,5-DNBA 216
Figure 6.34. Hydrogen bonding interactions present in PYR:3,5-DNBA co-crystal showing the discrete layers of hydrogen bonded molecules and the overlap of the aromatic rings (left) and the stacking of the discrete planes of molecules (right) 216
Figure 6.35. PXRD data for (a) PYR (BITZAF), (b) 3,5-DNBA form I (CUKCAM01), (c) pure 3,5-DNBA form II (CUKCAM02), (d) 3,5-DNBA hydrate (OKEMAT), (e) PYR:3,5-DNBA co-crystal calculated from SCXRD data and (f) PYR:3,5-DNBA co-crystal from evaporative crystallisation 218
Figure 6.36. DSC trace of PYR:3,5-DNBA co-crystal. PYR melting point = 159-162 °C [166], 3,5-DNBA melting point = 204-206 °C [213] 218
Figure 6.37. Solubility plot for PYR:3,5-DNBA co-crystal (purple, circle marker) and pure PYR (black, square marker) from observation in H_2O 220
Figure 6.38. PXRD data for (a) PYR (BITZAF), (b) 3,5-DNBA form I (CUKCAM01), (c) 3,5-DNBA form II (CUKCAM02), (d) 3,5-DNBA hydrate (OKEMAT), (e) PYR:3,5-DNBA co-crystal calculated from

SCXRD, (f) PYR:3,5-DNBA co-crystal slurry 1 week, (g) PYR:3,5-DNBA 50 ^oC 3 weeks and (h) PYR:3,5-DNBA 70 % humidity 9 weeks. 220
Figure 6.39. Fat, plate-shaped crystals of PYR:3,5-DNBA co-crystal crystallised from H_2O........ 221
Figure 6.40. Predicted BFDH morphology for PYR:3,5-DNBA form II (left); observed morphology for PYR:3,5-DNBA form II (right) 221
Figure 6.41. Structure of PYR and TRI molecules and positions in the co-crystal showing the numbering system used in hydrogen bonding discussions 222
Figure 6.42. Unit cell of 2:1 PYR:TRI co-crystal 223
Figure 6.43. Hydrogen bonding interactions present in PYR:TRI co-crystal: All hydrogen bonds for PYR molecule (right) and all hydrogen bonds to a central TRI molecule (left) 223
Figure 6.44. PXRD data for (a) PYR (BITZAF), (b) TRI (BTCOAC), (c) PYR:TRI co-crystal calculated from SCXRD and (d) PYR:TRI co-crystal from IPA evaporative crystallisation 225
Figure 6.45. DSC trace of PYR:TRI co-crystal. PYR melting point = 159-162 °C [166], TRI melting point = >300 °C [214] 225
Figure 6.46. Solubility plot for PYR:TRI co-crystal (purple, circle marker) and pure PYR (black, square marker) from observation in IPA 227
Figure 6.47. PXRD data for (a) PYR (BITZAF), (b) TRI (BTCOAC), (c) PYR:TRI co-crystal calculated from SCXRD, (d) PYR:TRI slurry 1 week, (e) PYR:TRI 50 ^oC 3 weeks and (f) PYR:TRI 70% humidity 9 weeks. 227
Figure 6.48. Plate-shaped crystals of PYR:TRI co-crystal crystallised from IPA 228
Figure 6.49. Predicted BFDH morphology for PYR:TRII (left); observed morphology for PYR:TRII (right) 228
Figure 6.50. Structure of PYR and PtA showing the numbering system used in hydrogen bonding discussions 229
Figure 6.51. Unit cell of 1:1 PYR:PtA co-crystal 229
Figure 6.52. Hydrogen bonding interactions present in PYR:PtA co-crystal 230
Figure 6.53. PXRD data for (a) PYR (BITZAF), (b) PtA (PHTHAC), (c) PtA hydrate (WODVAN), (d) PYR:PtA co-crystal calculated from SCXRD data and (e) PYR:PtA co-crystal from EtOH evaporative crystallisation 231
Figure 6.54. DSC trace of PYR:PtA co-crystal. PYR melting point = 159-162 °C [166], PtA melting point = 210-211 °C [216] 232
Figure 6.55. Solubility plot for PYR:PtA co-crystal (purple, circle marker) and pure PYR (black, square marker) from observation in EtOH 233
Figure 6.56. PXRD data for (a) PYR (BITZAF), (b) PtA (PHTHAC), (c) PtA hydrate (WODVAN), (d) PYR:PtA co-crystal calculated from SCXRD, (d) PYR:PtA slurry 1 week, (e) PYR:PtA 50 ^oC 3 weeks and (f) PYR:PtA 70% humidity 9 weeks. 233
Figure 6.57. Plate-shaped crystals of PYR:PtA co-crystal produced from IPA 234
Figure 7.1 CMAC MCM screening workflow driven by the decision points capturing key elements to indicate successes. Decision 1: is crystallinity retained following evaporation?; Decision 2: is there evidence for a new product from the PXRD and DSC analysis?; Decision 3: are there single crystals formed from the evaporation?; Decision 4: is there good diffraction from the single crystal and can a structure be solved?; Decision 5: is the product material stable to slurrying in solution?; Decision 1a: is crystallinity retained after grinding?; Decision 2a: is there evidence for a new product from the PXRD and DSC analysis?; Decision 3a: is the new product pure, or is there a mixture of product and starting materials present? 241

Figure 7.2. CMAC additive screening workflow driven by the decision points capturing key elements to indicate successes. Decision 1: are the chosen additives soluble in the solvents used for optimised non-additive API crystallisation process? (i.e. can a co-solvent be found easily?); Decision 2: does the API solubility/MSZW remain the same in the presence of each additive candidate?; Decision 3: does the analysis indicate a change in targeted property (e.g. solid-form/morphology/PSD etc.) in the presence of each additive candidate?; Decision 4: does the crystallisation process chosen for the product proceed unchanged following a change in additive ratio? 243
Figure 7.3. Dimeric hydrogen bonding interaction between FA molecules 246
Figure 7.4. Face indexed morphology for FA crystallised from IPA and molecular packing with respect to morphology 246
Figure 7.5. PXRD data for (a) MFA form I, (b) MFA form II, (c) MFA form III and (d) MFA crystallised from IPA 247
Figure 7.6. Dimeric hydrogen bonding interaction between MFA molecules 247
Figure 7.7. Face indexed morphology for MFA crystallised from IPA and molecular packing with respect to morphology 248
Figure 7.8. Structure of target molecules used in ConQuest structure search with all the hydrogens explicitly assigned: FA (left), MFA (right) 249
Figure 7.9. The morphology of FA crystals from IPA observed in the presence of additives. (a) absence of additive, (b) nicotinamide, (c) isonicotinamide, (d) flufenamic acid, (e) tolfenamic acid, (f) adipic acid, (g) 4,4’-bipyridine, (h) 2,2’-bipyridine and (j) sorbic acid 252
Figure 7.10. The morphology of MFA crystals from IPA observed in the presence of additives. (a) absence of additive, (b) isonicotinamide, (c) nicotinamide, (d) flufenamic acid, (e) tolfenamic acid, (f) adipic acid, (g) 4,4’-bipyridine, (h) 2,2’-bipyridine and (j) sorbic acid 252
Figure 7.11. PXRD data for (a) MFA form I calculated for SCXRD, (b) MFA crystallised from IPA in absence of additive, (c) with isonicotinamide, (d) with nicotinamide, (e) with flufenamic acid, (f) with tolfenamic acid, (g) with adipic acid, (h) with 4,4’-bipyridine, (k) with 2,2’-bipyridine and (l) with sorbic acid 253

A 1. PXRD data for (a) IZN (INICAC02), (b) IZN crystallised from H_2O, (c) IZN crystallised from EtOH, (d) IZN crystallised from IPA, (e) IZN crystallied from EtOAc and (f) IZN crystallised from ACN 273
A 2. PXRD data for (a) IZN (INICAC02), (b) IZN crystallised from EtOAc, (c) IZN temperature cycling experiment 1 in EtOAc and (d) IZN temperature cycling experiment 2 in EtOAc 273
A 3. Evaporative crystallisations at 40 ^{o}C with 1% additives (a) benzoic acid, (b) 3-hydroxybenzoic acid, (c) 2,4-dihydroxybenzoic acid, (d) 3,4-dihydroxybenzoic acid, (e) 3,5-dihydroxybenzoic acid, (f) 2,6-dihydroxybenzoic acid, (g) 4-cyanobenzoic acid, (h) 3-cyanobenzoic acid, (j) 2,4-dinitrobenzoic acid, (k) 3,4-dinitrobenzoic acid, (l) 3,5-dinitrobenzoic acid, (m) trimesic acid, (n) isonicotinamide, (p) nicotinamide, (q) pyridoxine, (r) vanillin and (s) L-tartaric acid 274
A 4. PXRD data for (a) IZN (INICAC02), (b) 3-HBA form I (BIDLOP), (c) 3-HBA form II (BIDLOP01), (c) 3-HBA hydrate (BOMCAJ) and (d) IZN evaporative with 1% 3-HBA from IPA 274
A 5. PXRD data for (a) IZN (INICAC02), (b) 3,4-DNBA (YADKOF) and (c) IZN evaporative with 1% 3,4-DNBA from IPA 275
A 6. Cooling crystallisations of IZN with 3-HBA additive. Scale: 10 g, cool rate: 1 ^{o}C/minute, final dwell: 1 hour 275

A 7. Cooling crystallisations of IZN with 3-HBA additive. Scale: 10 g, cool rate: 1 ^{o}C/minute, final dwell: 5 hour 276
A 8. Cooling crystallisations of IZN with 3-HBA additive. Scale: 10 g, cool rate: 1 ^{o}C/minute, final dwell: 10 hour 276
A 9. Cooling crystallisations of IZN with 3-HBA additive. Scale: 10 g, cool rate: 0.1 ^{o}C/minute, final dwell: 1 hour 277
A 10. Cooling crystallisations of IZN with 3-HBA additive. Scale: 10 g, cool rate: 0.1 ^{o}C/minute, final dwell: 5 hour 277
A 11. Cooling crystallisations of IZN with 3-HBA additive. Scale: 10 g, cool rate: 0.1 ^{o}C/minute, final dwell: 10 hour 278
A 12. Cooling crystallisations of IZN with 3,4-DNBA additive. Scale: 10 g, cool rate: 1 ^{o}C/minute, final dwell: 1 hour 278
A 13. Cooling crystallisations of IZN with 3,4-DNBA additive. Scale: 10 g, cool rate: 1 ^{o}C/minute, final dwell: 5 hour 279
A 14. Cooling crystallisations of IZN with 3,4-DNBA additive. Scale: 10 g, cool rate: 1 ^{o}C/minute, final dwell: 10 hour 279
A 15. Cooling crystallisations of IZN with 3,4-DNBA additive. Scale: 10 g, cool rate: 0.1 ^{o}C/minute, final dwell: 1 hour 280
A 16. Cooling crystallisations of IZN with 3,4-DNBA additive. Scale: 10 g, cool rate: 0.1 ^{o}C/minute, final dwell: 5 hour 280
A 17. Cooling crystallisations of IZN with 3,4-DNBA additive. Scale: 10 g, cool rate: 0.1 ^{o}C/minute, final dwell: 10 hour 281
A 18. DSC trace for IZN crystallised via 200 mL cooling crystallisation in IPA with 1% 3-HBA additive. IZN melting point = 171-174 °C [163], 3-HBA melting point = 200-203 °C [220] 281
A 19. NMR spectroscopy experimental data for IZN crystallised via 200 mL cooling crystallisation in IPA with 1% 3-HBA additive (red) compared to pure IZN (green) and pure 3-HBA (blue). 282
A 20. DSC trace for IZN crystallised via 200 mL cooling crystallisation in IPA with 1% 3,4-DNBA additive. IZN melting point = 171-174 °C [163], 3,4-DNBA melting point = 165 °C [210] 282
A 21. NMR spectroscopy experimental data for IZN crystallised via 200 mL cooling crystallisation in IPA with 1% 3,4-DNBA additive (red) compared to pure IZN (green) and pure 3,4-DNBA (blue). . 283
A 22. Cooling crystallisations of IZN with 1% polymer additives from IPA at a rate of 1^{o}C/minute. (a) PP123, (b) PEG, (c) PPG, (d) PBD, (e) PVP and (f) PDE 283
A 23. Cooling crystallisations of IZN with 0.1% polymer additives from IPA at a rate of 1^{o}C/minute. (a) PP123, (b) PEG, (c) PPG, (d) PBD, (e) PVP and (f) PDE 284
A 24. 20 ^{o}C evaporative crystallisations of IZN with 1% polymer additives in IPA. (a) PP123, (b) PEG, (c) PPG, (d) PBD, (e) PVP and (f) PDE 284
A 25. 20 ^{o}C evaporative crystallisations of IZN with 0.1% polymer additives from IPA. (a) PP123, (b) PEG, (c) PPG, (d) PBD, (e) PVP and (f) PDE 284
A 26. PXRD data for (a) IZN (INICAC02), (b) LTA (TARTAL), (c) 1:1 IZN:LTA grinding, (d) 1:1 IZN:LTA LAG with H_2O and (e) IZN:LTA co-crystal produced via crash cooling from H_2O 285
A 27. DSC trace for (a) 1:1 IZN:LTA grinding, (b) 1:1 IZN:LTA LAG with IPA and (c) IZN:LTA co-crystal produced via crash cooling from H_2O 285
A 28. PXRD data for (a) IZN (INICAC02), (b) DTA (TARTAC), (c) DTA (TARTAC24), (d) 1:1 IZN:DTA grinding, (e) 1:1 IZN:DTA LAG with H_2O and (f) IZN:DTA co-crystal produced via crash cooling from H_2O 286

A 29. DSC trace for (a) 1:1 IZN:DTA grinding, (b) 1:1 IZN:DTA LAG with H_2O and (c) IZN:DTA co-crystal produced via crash cooling from H_2O 286
A 30. PXRD data for (a) IZN (INICAC02), (b) LTA (TARTAL), (c) IZN:LTA co-crystal calculated from SCXRD, (d) 10 g cooling in H_2O, (e) 30 g cooling in H_2O and (f) 60 mL slurry in H_2O 287
A 31. PXRD data for (a) IZN (INICAC02), (b) DTA (TARTAC), (c) DTA (TARTAC24), (d) IZN:DTA co-crystal calculated, (e) 10 g cooling in H_2O and (f) 30 g cooling in H_2O 287
A 32. PXRD data for (a) IZN (INICAC02), (b) DLTA (ZZZDUI01), (c) DLTA monohydrate (TARTDL), (d) 1:1 IZN:DLTA grinding, (e) 1:1 IZN:DLTA LAG with H_2O and (f) IZN:DLTA co-crystal produced via crash cooling from H_2O 288
A 33. DSC trace for (a) 1:1 IZN:DLTA grinding, (b) 1:1 IZN:DLTA LAG with H_2O and (c) IZN:DLTA co-crystal produced via crash cooling from H_2O 288
A 34. PXRD data for (a) IZN (INICAC02), (b) DLTA (ZZZDUI01), (c) DLTA monohydrate (TARTDL), (d) IZN:DLTA co-crystal calculated, (e) 10 g cooling in H_2O, (f) 30 g cooling in H_2O and (g) 60 mL slurry in H_2O 289
A 35 DSC trace for IZN:DLTA:H_2O cycled experiment 289
A 36. PXRD data for (a) IZN (INICAC02), (b) 3,4-DNBA (YADKOF), (c) 1:1 IZN:3,4-DNBA grinding, (d) 1:1 IZN:3,4-DNBA LAG with IPA and (e) IZN:3,4-DNBA co-crystal produced via crash cooling from IPA 289
A 37. DSC trace for (a) 1:1 IZN:3,4-DNBA grinding, (b) 1:1 IZN:3,4-DNBA LAG with IPA and (c) IZN:3,4-DNBA co-crystal produced via crash cooling from IPA 290
A 38. PXRD data for IZN:3,4-DNBA co-crystal scale up. (a) IZN (INICAC02), (b) 3,4-DNBA (YADKOF), (c) IZN:3,4-DNBA co-crystal calculated, (d) 10 g cooling in IPA, (e) 200 g cooling in IPA and (f) 200 g slurry in IPA 290
A 39 PXRD data for (a) PYR (BITZAF), (b) PYR crystallised from H_2O, (c) PYR crystallised from EtOH and (d) PYR crystallised from IPA 291
A 40. Evaporative crystallisations for PYR in IPA at 40 ^{o}C with 1 % additive (a) benzoic acid, (b) trimesic acid, (c) imidazole, (d) benzimidazole, (e) 2,4-dinitrobenzoic acid, (f) isonicotinamide, (g) isonicotinic acid, (h) nicotinic acid, (j) nicotinamide, (k) 3,5-dinitrobenzoic acid, (l) 2-aminobenzoic acid, (m) barbituric acid, (n) tartaric acid, (p) 2,2'-bipyridine and (q) 4,4'-bipyridine. 291
A 41. Cooling crystallisations of PYR with 1% polymer additives from IPA at rate of 0.1 ^{o}C/minute. (a) PP123, (b) PEG, (c) PPG, (d) PBD, (e) PVP and (f) PDE 291
A 42. 20 ^{o}C evaporative crystallisations of PYR with 1% additives from IPA. (a) PP123, (b) PEG, (c) PPG, (d) PBD, (e) PVP and (f) PDE 292
A 43. 20 ^{o}C evaporative crystallisations of PYR with 0.1% additives from IPA. (a) PP123, (b) PEG, (c) PPG, (d) PBD, (e) PVP and (f) PDE 292
A 44. PXRD data for (a) PYR (BITZAF), (b) 2,4-DNBA (BAQLUD), (c) 1:1 PYR:2,4-DNBA grinding, (d) 1:1 PYR:2,4-DNBA LAG with IPA and (e) PYR:2,4-DNBA form I co-crystal produced from evaporative from IPA 292
A 45. DSC trace for (a) 1:1 PYR:2,4-DNBA grinding, (b) 1:1 PYR:2,4-DNBA LAG with IPA, (c) 1:1 PYR:2,4-DNBA LAG with H_2O and (d) PYR:2,4-DNBA co-crystal produced via evaporative from IPA 293
A 46. PXRD data for (a) PYR (BITZAF), (b) 2,4-DNBA (BAQLUD), (c) PYR:2,4-DNBA form I co-crystal calculated from SCXRD, (d) 10 g cooling in IPA, (e) 30 g cooling in IPA and (f) 10 g slurry in IPA ... 293
A 47. PXRD data for (a) PYR (BITZAF), (b) 2,4-DNBA (BAQLUD), (c) 1:1 PYR:2,4-DNBA grinding, (d) 1:1 PYR:2,4-DNBA LAG with H_2O and (e) PYR:2,4-DNBA form II co-crystal produced from cooling in H_2O 294

A 48. PXRD data for (a) PYR (BITZAF), (b) 2,4-DNBA (BAQLUD), (c) PYR:2,4-DNBA form II co-crystal calculated from SCXRD, (d) 10 g cooling in H_2O, (e) 30 g cooling in H_2O and (f) 10 g slurry in H_2O 294
A 49. PXRD data for (a) PYR (BITZAF), (b) 3,5-DNBA form I (CUKCAM01), (c) 3,5-DNBA form II (CUKCAM02), (d) 3,5-DNBA hydrate (OKEMAT), (e) 1:1 PYR:3,5-DNBA grinding, (f) 1:1 PYR:3,5-DNBA LAG with H_2O and (g) PYR:3,5-DNBA co-crystal produced via evaporative from H_2O 295
A 50. DSC trace for (a) 1:1 PYR:3,5-DNBA grinding, (b) 1:1 PYR:3,5-DNBA LAG with H_2O and (c) PYR:3,5-DNBA co-crystal produced via evaporative from H_2O... 295
A 51. PXRD data for (a) PYR (BITZAF), (b) 3,5-DNBA form I (CUKCAM01), (c) 3,5-DNBA form II (CUKCAM02), (d) 3,5-DNBA hydrate (OKEMAT), (e) PYR:3,5-DNBA co-crystal calculated from SCXRD, (f) 10 g cooling in H_2O, (g) 30 g cooling in H_2O, and (h) 10 g slurry in H_2O........................ 296
A 52. PXRD data for (a) PYR (BITZAF), (b) TRI (BTCOAC), (c) 2:1 PYR:TRI grinding, (d) 2:1 PYR:TRI LAG with IPA and (e) PYR:TRI co-crystal produced via evaporative from IPA....................................... 296
A 53. DSC trace for (a) 2:1 PYR:TRI grinding, (b) 2:1 PYR:TRI LAG with IPA and (c) PYR:TRI co-crystal produced via evaporative from IPA 296
A 54. PXRD data for (a) PYR (BITZAF), (b) TRI (BTCOAC), (c) PYR:TRI co-crystal calculated from SCXRD, (d) PYR:TRI co-crystal calculated from SCXRD, (e) 10 g cooling in IPA and (f) 10 g slurry in IPA 297
A 55. PXRD data for (a) PYR (BITZAF), (b) PtA (PHTHAC), (c) PtA hydrate (WODVAN), (d) 1:1 PYR:PtA grinding, (e) 1:1 PYR:PtA LAG with EtOH and (f) PYR:PtA co-crystal produced via evaporative from EtOH 297
A 56. DSC trace for (a) 1:1 PYR:PtA grinding, (b) 1:1 PYR:PtA LAG with EtOH and (c) PYR:PtA co-crystal produced via evaporative from EtOH.. 297
A 57. PXRD data for (a) PYR (BITZAF), (b) PtA (PHTHAC), (c) PtA hydrate (WODVAN), (d) PYR:PtA co-crystal calculated from SCXRD, (e) PYR:PtA 10 g cooling in IPA, (f) PYR:PtA 30 g cooling in IPA and (g) PYR:PtA 10 g slurry in IPA 298

List of tables

Table 1.1. Properties of different strength hydrogen bonds [127] 32
Table 1.2. Hydrogen bond distances and angles for IZN form I crystal structure 44
Table 1.3. Hydrogen bond distances and angles in PYR crystal structure 48
Table 2.1. Seven crystal systems, their unit cell restrictions and the distribution of lattice types ... 55
Table 4.1. Conditions for crystallisations carried out in the KRAIC continuous platform in solvents IPA and EtOAC 90
Table 4.2. Conditions for crystallisations carried out in the KRAIC continuous platform in solvents IPA and EtOH 118
Table 5.1. Crystallographic parameters for newly discovered co-crystal structures formed with IPA IZN 143
Table 5.2. Hydrogen bond distances and angles for IZN:LTA 150
Table 5.3. Hydrogen bond distances and angles for IZN:DTA 151
Table 5.4. Hydrogen bond distances and angles for IZN:DLTA:H_2O co-crystal 158
Table 5.5 Hydrogen bond distances and angles for IZN:DLTA co-crystal 169
Table 5.6. Hydrogen bond distances and angles for co-crystal IZN:3,4-DNBA 178
Table 5.7. Distances and angles for interactions between nitro groups 178
Table 6.1. Crystallographic parameters of newly discovered co-crystal structures formed with API PYR 194
Table 6.2. Hydrogen bond distances and angles for PYR:2,4-DNBA co-crystal 201
Table 6.3. Table of distances and angles for PYR:2,4-DNBA form II co-crystal 208
Table 6.4. Hydrogen bond distances and angles for PYR:3,5-DNBA co-crystal 217
Table 6.5. Hydrogen bond distances and angles for PYR:TRI co-crystal 224
Table 6.6. Hydrogen bond distances and angles for PYR:PtA co-crystal 231

List of abbreviations

2,4-DNBA	2,4-dinitrobenzoic acid
3-HBA	3-hydroxybenzoic acid
3,4-DNBA	3,4-dinitrobenzoic acid
3,4-DNBA	3,5-dinitrobenzoic acid
ACN	Acetonitrile
API	Active pharmaceutical ingredient
ATR	Attenuated total reflectance
BCF	Burton-Cabrera-Frank
BCS	Biopharmaceutics classification system
BFDH	Bravais-Friedel-Donnay-Harker
CAM	Competitive adsorption model
CAMUS	Competitive adsorption model under unsteady-state conditions
CCD	Charge coupled device
CCDC	Cambridge Crystallographic Data Centre
CMAC	Continuous Manufacturing and Advanced Crystallisation
CNT	Classical nucleation theory
COBC	Continuous Oscillatory Baffled Crytalliser
CSD	Cambridge Structural Database
cSTR	Continuous stirred tank reactor
D_2O	Deuterium oxide
DLTA	DL-tartaric acid
DMSO	Dimethyl sulfoxide
DSC	Differential scanning calorimetry
DTA	D-tartaric acid
ESD	Estimated standard deviation
EtOAc	Ethyl acetate
EtOH	Ethanol
FA	Fenamic acid
FBRM	Focussed beam reflectance measurement
FDA	Food and Drug Administration
FDC	Fixed dose combination
FEP	Fluorinated ethylene polypropylene
FNO	Fraction of N and O
FTIR	Fourier transform infra-red
GRAS	Generally regarded as safe
H_2O	Water
^{1}H-NMR	Proton NMR
HPLC	High performance liquid chromatography
HSM	Hot stage microscope
IPA	Isopropyl alcohol
IZN	Isoniazid
KRAIC	Kinetically Regulated Automated Input Crystalliser

LAG	Liquid assisted grinding
LTA	L-tartaric acid
MC	Multi-component
MCM	Multi-component material
MIAM	Multi-impurity adsorption model
MFA	Mefenamic acid
MSMPR	Mixed-suspension mixed-product removal
MSZ	Metastable zone
MSZW	Metastable zone width
NaCl	Sodium chloride
NMR	Nuclear magnetic resonance
PAT	Process analytical technology
PBC	Periodic bond chain
PBD	Polybutadiene
PDE	Poly(ethylene glycol) diglycidyl ether
PEG	Polyethylene glycol
PP123	Pluronic P123
PPG	Polypropylene glycol
PSD	Particle size distribution
PtA	Phthalic acid
PTFE	Polytetrafluoroethylene
PVP	Polyvinylpyrolidone
PXRD	Powder X-ray diffraction
PYR	Pyridoxine
rpm	Rotations per minute
SCXRD	Single crystal X-ray diffraction
STR	Stirred tank reactor
TA	Tartaric acid
TB	Tuberculosis
TGA	Thermogravimetric analysis
TG-MS	Thermogravimetric mass spectrometry
TRI	Trimesic acid
Tsat	Saturation temperature
wt%	Weight percentage
z_c	Critical nucleus size

Chapter 1 Introduction

1.1 Research context

Crystallisation is an integral step in the processing of pharmaceutical products, with more than 80% of market drugs being formulated in crystalline form.[1] Comprehensive screening is necessary to fully characterise the solid forms of each drug and their related physical properties in order to improve the safety and effectiveness of a treatment. Poor understanding of the solid state behaviour of crystals produced can result in unwanted phase transitions and, therefore, a change in the properties, such as stability and solubility. As a consequence of such changes, the final product will not perform in the expected way, for example affecting bioavailability of formulated products. Crystallisation conditions can also be invaluable in the control of particle attributes of the crystalline material, such as particle size distribution and crystal morphology.

The research carried out here focuses particularly on controlling the shape (morphology) of the crystals produced, a physical property often considered important later in processing. The morphology of a crystal largely affects the downstream processing steps required to produce the final drug product, often leading to extra steps being required. The downside of such extra steps is the added time required and the associated extra costs. As a result, research into controlling the morphology of a crystal during the initial crystallisation stage of the process is of distinct interest to the pharmaceutical industry.

This project is carried out in the broader context of the CMAC Future Manufacturing Hub, an academic-industrial collaboration with a specific research focus on the development of crystalline materials and particles (single or multi-component) and the transfer of their manufacture in continuous flow environments. Small molecule systems with challenging physical properties or performance limitations are chosen for development to help inform new approaches for advanced predictive design and integrated manufacturing.[2] Collaborations within CMAC across multiple disciplines allows for research to occur into the processing of materials from initial discovery through to formulated end products. Research at the University of Bath spoke of the CMAC Hub programme is strongly related to multi-component crystallisations and the use of additives to control solid form at the molecular and primary particle level. Multi-component crystallisations can be very beneficial for tuning the solid-state properties of small pharmaceutically active molecules.

The key areas of interest at Bath are targeting the formation of co-crystals and other multi-component crystalline systems, primary particle control and the alteration of morphology and habit. All of these areas can be controlled by changing crystallisation conditions (including choice of co-former molecules) and using appropriate additives in the crystallisation process. A second focus of the Bath strand of the CMAC Hub is the development of transfer from lab scale batch to small scale continuous crystallisations and the operation of the continuous crystallisation platforms. Implementing lab scale batch crystallisations in continuous platforms often poses many problems and work is carried out to minimise this disruption in transferring from lab scale tests to continuous systems available at Bath.

1.2 Crystallisation theory

Crystallisation is an important technique utilised in industry for the separation and purification of chemical mixtures, and for producing solid form materials for further processing and application. Crystals are favoured in the production of pharmaceuticals due to the ease of processing and characterisation coupled with the possibility to control their specific properties.[3]

The crystallisation method chosen is key to achieving desired properties, through controlling the crystalline structure and the macroscopic characteristics of crystalline particles, such as shape. There are several methods for forming crystals, including crystallising from solution and solidification of melts.[4] In the pharmaceutical industry the main focus is on growing crystals from solution, and this forms the major focus of the work discussed here. The crystallisation process, whilst complex, can be described in general terms by considering three distinct stages: supersaturation, nucleation and crystal growth.

1.2.1 Supersaturation

Figure 1.1 shows the relationship between temperature and the saturation solubility of a solution. A typical solubility curve shows an increase in solubility as temperature rises. The solution is saturated at a given temperature along the solubility curve. A solution whose concentration lies below the solubility line is undersaturated, where the solute is more stable in solution, and solutions that lie above the curve are supersaturated. A supersaturated solution contains a greater concentration than can ordinarily be dissolved at that given temperature.[5] This supersaturation of systems provides the driving force for crystal formation.

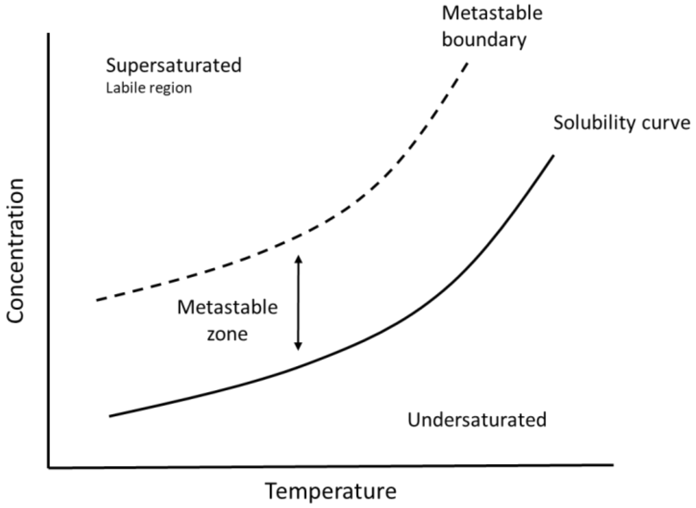

Figure 1.1. Solubility curve, metastable zone and metastable boundary [4]

It is not possible to maintain supersaturation over an infinite concentration range, as new phases will ultimately be induced. However, spontaneous nucleation does not tend to occur within the metastable zone (MSZ) indicated in figure 1.1; only existing crystals will grow in this region.[6] The temperature at which spontaneous nucleation can occur can be determined for a specific saturation concentration and marks the limit of the metastable region (metastable boundary marked with black dotted line). The width of the MSZ is dependent on the nature of the system being studied and can vary depending on conditions used such as scale, cooling rate or impurities present.[7] Once a solution lies beyond the metastable boundary it is termed labile, and spontaneous, uncontrolled nucleation can occur.[4]

Supersaturation is the driving force for the crystallisation process, a fundamental parameter. There are different ways of defining supersaturation. Calculating the difference between the concentration of the solution (c) and the concentration at equilibrium (c*) at the same temperature gives a value for the concentration driving force of the crystallisation (equation 1.1). The supersaturation can also be calculated by a ratio of the two concentrations (equation 1.2) or take into account the relative supersaturation (equation 1.3).[8]

$$\Delta c = c - c^{*} \qquad \text{Equation 1.1}$$

$$S = \frac{c}{c^{*}} \qquad \text{Equation 1.2}$$

$$c_{ss} = \frac{c - c^{*}}{c^{*}} \qquad \text{Equation 1.3}$$

$$\Delta\mu = \mu - \mu^{*} = kT\, ln\frac{c}{c^{*}} \qquad \text{Equation 1.4}$$

It is also possible to define supersaturation thermodynamically. The driving force is therefore defined as the dimensionless difference between chemical potential between the molecule in its equilibrium state (μ) and its supersaturated state (μ^*) (equation 1.4) where k is the Boltzmann constant and T is the absolute temperature.[4, 8]

In industry processes it is possible to achieve supersaturation via evaporating the solvent, cooling the solution, adding an anti-solvent to decrease solubility or performing a chemical reaction (where a reaction results in a less soluble product which is supersaturated upon formation).

1.2.2 Nucleation

The process by which new solid phases are created from supersaturated solution or super-cooled liquids, i.e. melt crystallisation, is known as nucleation.[4] Nucleation plays a decisive role in defining the initial population of crystals and can influence the initial state of succeeding processes, such as crystal growth.[9] Therefore, nucleation plays a significant role in determining the final crystal product quality. There are two types of nucleation: primary and secondary (figure 1.2).

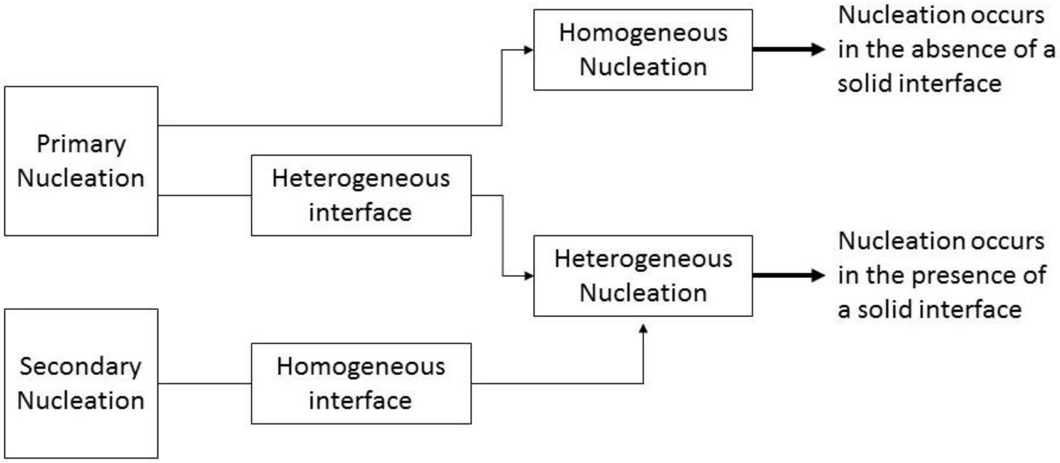

Figure 1.2. Differences in primary and secondary nucleation processes.[6]

1.2.2.1 Primary nucleation

Primary nucleation can occur homogeneously or heterogeneously, distinguishable by the absence or presence of a solid interface. Homogeneous nucleation is spontaneous formation of solid phases as a result of supersaturation with no solid interface required. In practice heterogeneous nucleation, where there is a solid interface present, is observed more often; homogeneous nucleation is generally not observed in larger volumes.[10]

The mechanism behind nucleation is not fully known, however, there are two widely accepted theories used to describe the events occurring. These are known as classical nucleation theory (CNT) and the two-step mechanism. Both theories start with a supersaturated solution and both consider that clusters are forming/disintegrating through the attachment/detachment of building units.[11]

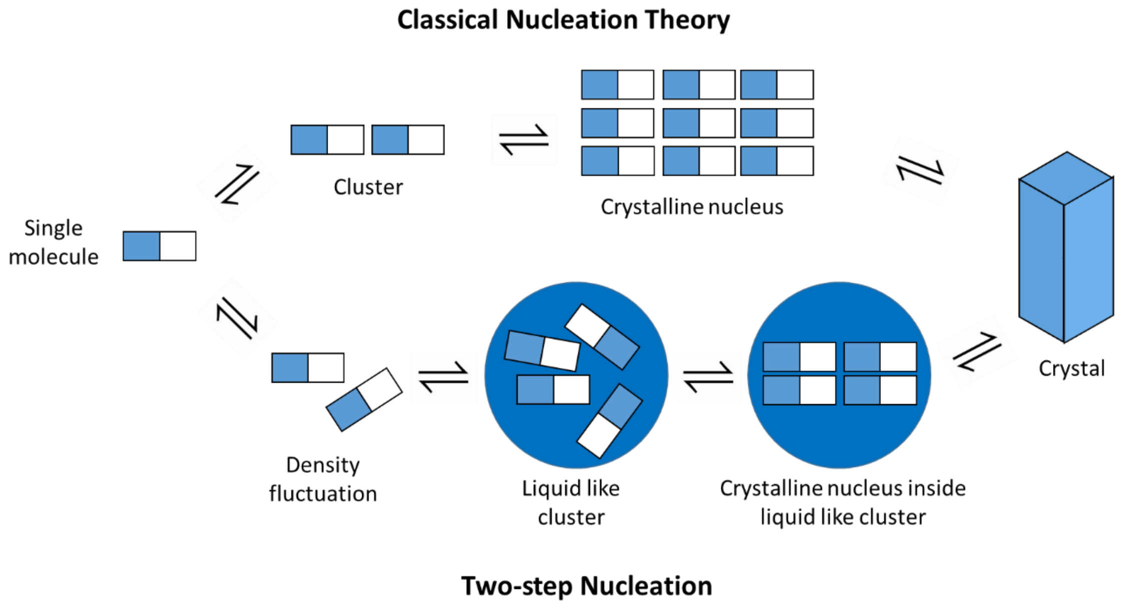

Figure 1.3. Two alternative pathways for nucleation. Top: classical nucleation theory (CNT) Bottom: two-step nucleation theory.

CNT assumes the addition of single growth units to the cluster until a critical size is reached (figure 1.3, top).[12] Further molecular additions to a cluster after the critical cluster size has been reached result in nucleation and subsequent growth of crystals.[13] Clusters that reach a critical size are known as critical nuclei and their likelihood of forming depends on the free energy barrier that must be overcome (figure 1.4). The maximum of the curve, z_c, corresponds to the size required to achieve a decrease in free energy with further growth of the cluster. If the cluster is smaller than this critical size the only way to reduce free energy is dissolution. Increasing supersaturation serves to reduce not only the height of the free energy barrier but also the critical size of the clusters required. Eventually, increasing supersaturation will lower the barrier enough to achieve spontaneous nucleation.[4]

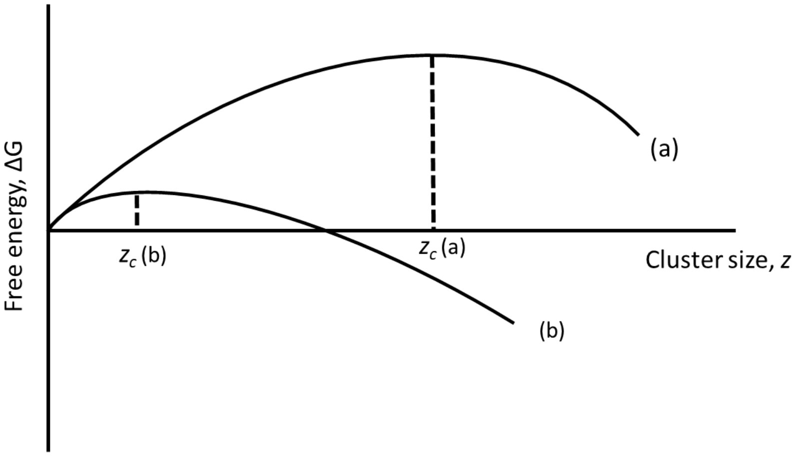

Figure 1.4. Free energy change as a function of cluster size. (a) at low supersaturation, (b) at high supersaturation

In the alternative two-step mechanism, a dense, disordered liquid phase precedes the crystal formation (figure 1.3, bottom). The ordered crystalline clusters observed in CNT are formed from these liquid phase droplets in the second step of this mechanism. When the critical cluster size – creating critical nuclei – is reached, further attachment of building units is energetically favoured, thus leading to the formation of macroscopic crystals.[11, 14]

Primary nucleation more often occurs through heterogeneous routes, with homogeneous nucleation being uncommon in practice.[15] Heterogeneous nucleation is also spontaneous nucleation but requires a foreign particle, such as dust from the wall of the crystallisation vessel or inherent impurities in the crystallisation solution, to induce the process.[16] The presence of these foreign particles allows heterogeneous nucleation to occur at lower supersaturation than homogeneous nucleation by reducing the free energy barrier of the system.[4]

1.2.2.2 Secondary nucleation

Secondary nucleation can only occur via heterogeneous nucleation and requires the presence of undissolved solute particles or crystals of the solute to act as nucleation sites.[12] The presence of solute particles can occur through a number of different mechanisms. Attrition of crystals is considered the most likely cause of secondary nucleation in industrial processes. Mechanical force applied to most solution mediated crystallisations can induce a number of different collisions; between crystal and crystalliser wall, crystal-crystal collisions and crystal-impellor attrition. These collisions result in crystal breakage and the formation of new nucleation sites.[14] There is also evidence to suggest the shear forces imposed on a crystal by the solution flowing past are sufficient to produce secondary nucleation: this effect is known as shear nucleation. Generally, nucleation via this mechanism can occur at much lower supersaturation than both primary homogeneous and heterogeneous nucleation.[4]

In crystallisation it is necessary to strike a balance between nucleation and growth in order to control particle size and other structural properties of the crystal.

1.2.3 Growth

The growth of a crystal occurs when a nucleus reaches a critical size and is exposed to a supersaturated environment. There are a number of different theoretical pathways by which a solute molecule can adsorb to the face of a crystal from a supersaturated solution. The ability of a crystal face to integrate growth units into the lattice is dependent on the number and strength of interactions available between the incoming solute and the surface.[4] Three types of crystal faces can be defined depending upon the interactions they can form with an incoming growth unit;[4, 6, 12] a surface only site has one attachment, a step surface has two attachments and a kink site has three attachments (figure 1.5). Energetically kink sites are the most favoured as solute molecules joining here are able to form three interactions. This is followed by a step surface attachment with two interactions and then the surface site with only one point of contact.[12]

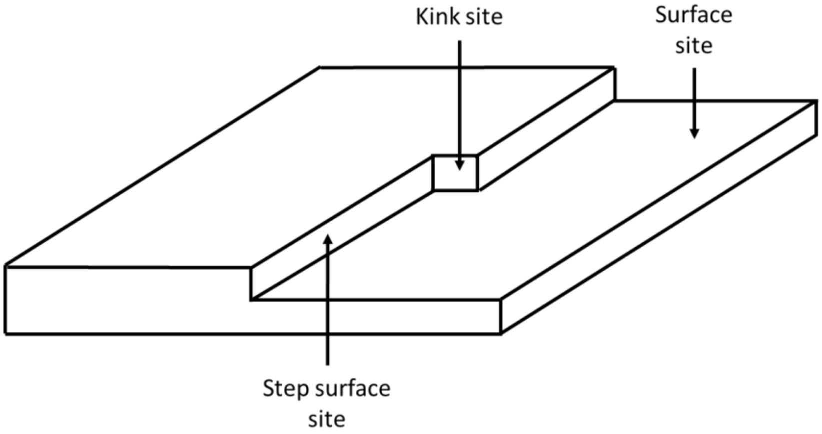

Figure 1.5. Crystal growth surface showing potential growth sites: a surface only site, a step surface site and a kink site.

Crystal growth is often thought of as occurring in layers. It was suggested by Volmer (1939) that growth was a discontinuous process, taking place layer by layer via adsorption to the crystal surface.[17] First, growth units need to be transferred from a solution to a solid state. This can be described by a schematic of free energy barriers that need to be overcome during the crystallisation process (figure 1.6).[4]

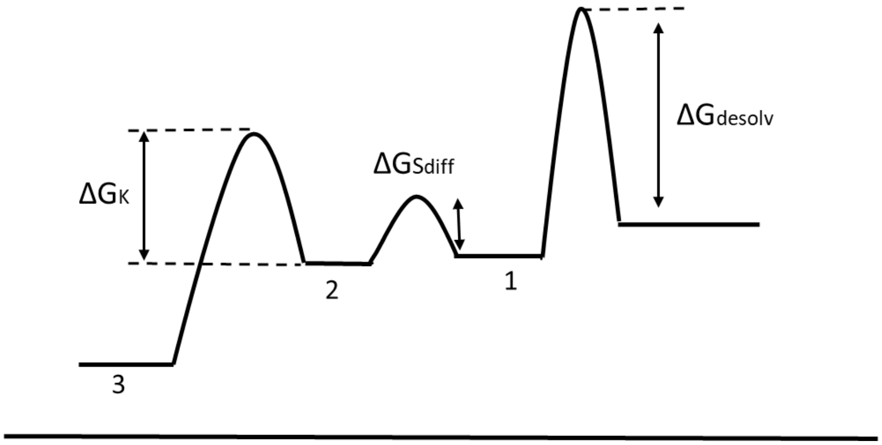

Figure 1.6. Crystal growth free energy barriers to be overcome

This requires an initially solvated solute molecule to shed the solvent layer before it can adsorb to a growth surface (ΔG_{desolv}). After this desolvation has occurred, the growth unit will enter the adsorption layer (position 1) and then diffuse across the surface (ΔG_{Sdiff}) to a step position (position 2). At this point further desolvation is necessary in order for the molecule to further diffuse across the surface to a final kink site at position 3 (ΔG_{K}).[4, 12]

Crystalline materials with high surface roughness grow via continuous growth mechanisms. There are enough kink and step sites for all approaching growth units to be incorporated efficiently, as every approaching growth unit will find a vacant growth site. This mechanism follows a linear growth rate with respect to supersaturation. Many materials do not have sufficiently rough surfaces to achieve continuous growth mechanisms. As a result, steps on the surface need to be created to facilitate incoming growth units.[4, 12] One mechanism for step creation is known as two-dimensional nucleation. Clusters of growth units form on the surface of the crystal, forming nuclei on the surface. The clusters must reach a critical size in order for further growth to be favoured.[18] Several models have been developed to describe the continued growth.

The simplest model for layer completion is known as the mononuclear model. This model assumes the surface nuclei spread across the surface at an infinite velocity. The growth rate of each face is therefore proportional to its area. This growth velocity indicates larger faces grow faster than small faces, contradicting the observation that the fastest growing faces on a crystal have the smallest areas. This model can therefore be eliminated from serious consideration. The contrasting polynuclear method assumes the spreading velocity of the surface nuclei is zero. In this second model, layer completion is achieved by the formation of enough critical size surface nuclei to cover the layer. Nucleation is the rate determining step of this model, with the growth rate increasing with the increased nucleation rate. However, the growth rate will decrease with decreasing critical nuclei size. As a result, the model indicates that crystal growth rate does not increase continuously with supersaturation. The final model is known as the birth and spread model. This model suggests nuclei spread at a finite, constant rate that is assumed to be independent of size. Nuclei can form at any location on the surface, including as incomplete layers, and no intergrowth between the nuclei occurs. This model predicts the growth rate increases with increasing supersaturation and temperature, making it more suitable than the other two models. The rate determining step in all three models discussed above is the formation of the two-dimensional crystal nucleus, making these models for discontinuous growth. [12, 18]

The above models all fail to account for growth rates at low supersaturation; addressing this resulted in the development of the Burton-Cabrera-Frank (BCF) model. This model proposes growth is self-perpetuating as a result of screw-dislocations. A dislocation results from stresses occurring during crystal growth: one part of the lattice becomes misaligned with the rest of the crystal. Screw dislocations create steps at the point of emergence on which growth occur. Molecules adsorb on the surface and diffuse to the top step creating a 'spiral staircase' feature (figure 1.7). Once a layer is complete, the dislocation is still present on the higher layer. In this model surface nucleation is not required, allowing growth to occur at a finite rate at low supersaturation. Surface diffusion is now assumed to be the rate determining step.[4, 18]

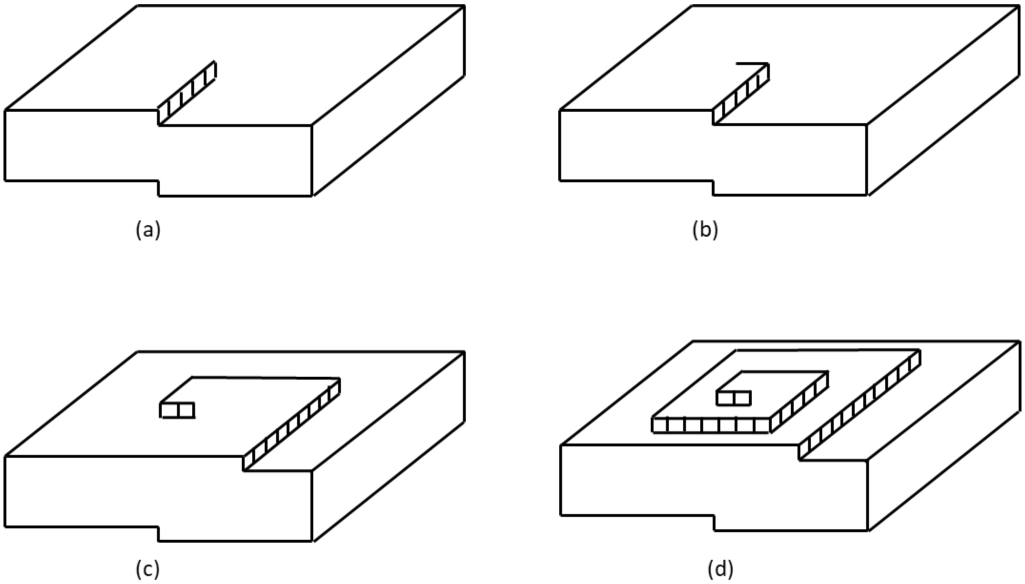

Figure 1.7. Spiral growth model as a result of screw dislocations[19]

1.3 Crystal morphology

Crystal morphology is used to describe the overall shape of a crystal, governed by the external faces present. It can be defined as either growth or equilibrium morphology. Equilibrium morphology is observed when the surface free energies associated with each crystal face are minimised and equilibrium is achieved between the crystal and its surroundings. Growth morphologies arise as a direct result of crystal growth kinetics in the system; this type of morphology is much more commonly observed.[4, 20]

The morphology of a crystal largely affects the downstream processing steps required to produce the final drug product, such as filtration, drying and compaction.[18, 21, 22] A poor morphology can often lead to extra processing steps being required, resulting in a more expensive process for pharmaceutical companies. For most manufacturing procedures, crystals with a needle shape are considered a hindrance. Needles often filter poorly due to their ability to align with the mother liquor as it flows and block the pores of the filter (figure 1.8). Suspensions containing needle crystals tend to have an increased viscosity making it difficult to pump the solution from the initial vessel to the filter.[18] Needles are also prone to agglomeration, resulting in poor drying efficiency and the potential for solvent and impurities to become trapped.[23] Needle-shaped crystals can also result in issues for tableting processes due to their poor flowability, creating the potential for unpredictable dosage quantities.[24-26] In an attempt to reduce the impact of needle crystals on the manufacturing procedure, extra milling steps are often introduced to break the crystals, creating more equant aspect ratios. The downside of this extra step is the added time required and the associated extra costs. Plate-shaped crystals are also a less desirable morphology due to inefficient filtration and washing steps. This arises as a result of their tendency to pack into impermeable layers on filter beds (figure 1.8).[4, 18] As a result, block-shaped crystals are much more favourable for the large scale processing required in industry due to their lower packing efficiency and significantly improved flow properties.

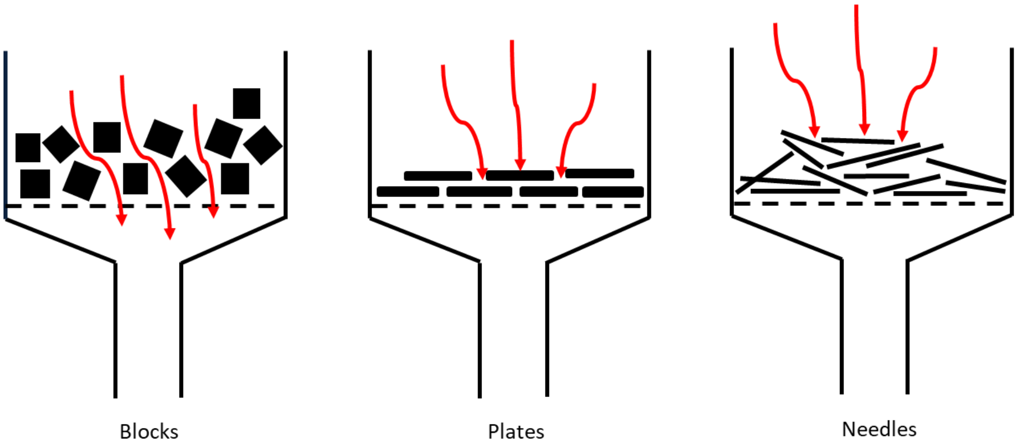

Figure 1.8. Effect of crystal morphology on filtration: block-like crystals filter well (left), plate-shape crystals are less efficient, creating an impermeable layer (centre) and needles block pores in filter medium (right). [4]

Methods attempting to alter morphology during crystallisation generally focus on influencing the crystal growth. Crystal morphology is mainly governed by the relative growth rates of the crystal faces; those with faster growth rates will have a smaller area than those faces that grow more slowly. Growth rates are influenced not only by the internal structure of the material but also by external factors, such as solvent choice, mixing conditions, degree of supersaturation, seeding and the presence of impurities.[27] The presence of impurities in crystallisations often has a significant effect on the nucleation and growth kinetics of the system. This can be of substantial benefit for modifying the morphology (shape) of crystals produced. The mechanism by which impurities influence growth is still debated, but the majority of researchers in the area agree that selective reduction of growth rates caused by impurities is responsible for the changes in morphology observed.[17, 18]

1.3.1 Effects of impurities on crystal morphology

Impurities are inherently present in pharmaceutical crystallisations. They are often generated during process chemistry and retained through to crystallisation processes. The FDA names organics, inorganics and residual solvents as likely impurities in a pharmaceutical product. Possible impurities resulting from storage and manufacture include: those present in starting materials; by-products and intermediates of the process; degradation products and other reagents, solvents, ligands, catalysts and stereoisomers present in the manufacturing process. Any impurities, actual or potential, that could arise during synthesis, purification and storage must be noted in any new drug specifications.[28] Whilst impurities need to be tightly controlled in the pharmaceutical industry to maintain the safety of products, additives are often intentionally added to improve certain properties of the final drug product.

There are a number of different ways in which impurities can affect the structure of an API. They can influence the primary structure of a molecule and induce a specific polymorph to form. Research suggests that using impurities with a similar conformation, within their crystal structure, to the desired polymorph can influence nucleation kinetics and growth to achieve a desired metastable polymorph or avoid an undesirable form of the crystal structure.[29, 30] This change in polymorphism often results in a change in morphology, as the primary crystal structure and shape of a crystal are inherently linked. Impurities are often structurally similar to the target molecule for the crystallisation. As a result, if present in large enough quantities, these impurities can sometimes become incorporated into the primary crystal structure, producing a co-crystal.[31, 32] Co-crystals often possess altered morphologies, again due to their inherently different crystal structure. However, this incorporation can cause problems with pharmaceutical regulation; if the impurity is not Generally Regarded as Safe (GRAS) for use in food and medicine its combination into the crystal structure would pose a health risk. Impurities also have to potential to affect the microstructure of a crystal, causing point defects to occur, by blocking potential growth sites and altering growth mechanisms. Most point defects arise due to the potential for molecules to be missing or orientated irregularly in the structure. Impurity defects are also possible, with foreign molecules either replacing some of the API molecules making up the solid or locating into interstices. This is particularly likely when the impurity is structurally similar to the crystallising molecule.[33, 34] In some crystallisations, impurities are deliberately added in order to produce a crystal with a desired morphology; these are known as additives.

Additives are notably used in drug formulation, in their role as excipients, to produce the final tablet form and improve the related properties.[35] The use of additives is also considered in early crystallisation steps to exert control over specific physical properties, including solid form and crystal size and shape.[30] Whilst there are different categories of additive, defined by how they are used, chemically they are the same; one molecule can be an impurity, an additive or a co-former depending on the application.

1.3.2 Choosing effective additives

Additives can have major effects on crystal morphology by disrupting growth mechanisms and inhibiting growth rates on particular faces.[36] Additives are often chosen based on the likelihood of their binding preferentially to desired faces to inhibit growth in a chosen direction. By designing an additive to block the fast growing faces in crystals with a needle morphology, for example, a more equant shape can be achieved.[4, 37] The presence of additives even at low concentrations can have significant effects on crystal morphology.[4]

Several factors must be considered when choosing additives as growth inhibitors in multi-component crystallisations, such as size and structural similarity to target. It is particularly important to consider functional groups on the target and choose additives which will form complementary interactions. However, designing additives to inhibit growth is often not fully reliable at present and the process relies on empirical approaches and a degree of trial and error.[38]

Generally, additives fall into one of three categories: size-matched, structurally similar or polymeric.

1.3.2.1 Structurally similar and size-matched additives

There are many examples of structurally similar additives being used in crystallisations to control primary particle attributes. Structurally similar additives are inherently size-matched, therefore these types of additives fall into very similar categories. A series of experiments were carried out by Berkovitch-Yellin et al. in the early 1980s to study systematically the effect of additives on the crystal growth and resulting shape.[27, 39-43] Using the relationship between the structure of the target crystal, the additives used and the affected surfaces, a mechanism was derived to explain the changes observed in the shape. It is suggested that the additive selectively adsorbs to the target crystal on the faces where the structurally similar part emerges from the crystal surface. The additive is bound in a very similar way to a substrate molecule as a result of the interactions possible due to the related structure. This adsorption disturbs the regular deposition of oncoming crystal layers, interrupting normal growth to these faces and resulting in an overall retardation of the growth. This generally leads to a relative increase in the surface area of the affected face, and therefore a change in morphology.[43]

Extensive research has been carried out on the effect of additives on paracetamol morphology.[44, 45] One example uses the structurally related molecule metacetamol as an additive in the crystallisation. Progressive morphology changes were observed, from tabular crystals to columnar habits, with increasing concentrations of metacetamol in the crystallisation. A significant effect from the solvent system used is also noted in this experiment.[46] Previous research suggests the metacetamol affects the nucleation of paracetamol, therefore, altering the resulting growth mechanism and final crystal shape.[45]

Another industrially important example involves the reduction of needle growth of urea in the presence of biuret. Urea strongly hydrogen bonds at the (001) face, causing the elongation of the morphology. The biuret (100) face is indistinguishable from that of urea and so can easily become attached at growth sites on this face. The NH_2 groups needed by urea to maintain growth through hydrogen bonding on this face are no longer accessible, resulting in reduced growth and a shorter crystal morphology. This example further illustrates the usefulness of structurally similar additives in modifying growth mechanisms and the resulting morphology. This example also suggests the most useful additives are those that are able to bind effectively to a growth surface and then successfully prevent any further growth from occurring.[17, 38, 47]

Another class of structurally similar additives are known as ‘tailor-made’ additives. Tailor-made additives are ‘designed’ to resemble the target system but with differences that will allow the growth mechanism to be affected in a desired way. Additives are usually modified versions of the target molecule, designed by analysis of the crystal structure and growth faces. Parts of the molecule that interact with chosen faces are maintained with the function of the opposite end of the molecule being changed. As a result, the additive can bind at specific surface sites but blocks any further growth from occurring as it is no longer compatible with the target crystal growth.[46] Best results have been reported when the modifications are minor, for example, methyl or chlorine substituents instead of hydrogen atoms. A specific example, investigated by a number of researchers, is the effect of benzoic acid on benzamide crystals.[41, 46] The additive, benzoic acid, is related to benzamide by replacing an NH_2 with a hydroxyl group. The usual plate morphology becomes rod-like in the presence of benzoic acid due to retardation of growth along the crystallographic *b* axis.[41] This small change in structure in the additive thus influences a large change in the crystal growth and resulting morphology.

A large number of examples of using structurally similar additives to control polymorphism can also be found in the literature.[29, 32, 48-53]

1.3.2.2 Polymeric additives

Crystal morphology can also be controlled using non-size-matched additives. A major benefit of using non-size-matched additives is the reduction in potential for them to become incorporated into the crystal structure. Generally, polymers are used due to their common occurrence in processing steps, such as their use as excipients in drug formulation, and their extreme dissimilarity in structure and size to target molecules. Polymer additives are particularly successful in reducing crystal growth rates when added to the medium, often referred to as poisoning crystals.[54-56] The success of polymers in reducing crystal growth largely depends on their ability to adsorb to the target molecule and the level of surface coverage achieved.[57, 58] An example of this is seen in experiments carried out on ibuprofen by Vetter et al. A reduction in crystal growth rate in the presence of co-block polymer Pluronic F127 was observed with binding of the polymer indiscriminately to all crystal faces, hindering the diffusion of solute molecules.[59] A series of experiments were also carried out on ritonavir by Ilevbare et al. to determine the effect of polymers on the crystallisation.[56, 60] The effective polymer in these experiments is hydroxypropyl methyl cellulose, which behaves as a growth inhibitor and binds non-preferentially to the crystal faces. Although these polymers appear to be influencing nucleation and crystal growth, no major changes in macroscopic properties are observed. It is possible for a polymer to impede the growth of specific faces, allowing growth to continue on certain crystallographic planes, resulting in an altered morphology.[54, 61] An early example of this effect was reported in 1965 by Holder and Winkler, who observed a change in the morphology of paraffin wax from lozenge shaped plates to dendrites with increasing amounts of block co-polymer impurities.[61] Experiments carried out on salbutamol sulphate display a change in morphology from needles to plates in the presence of polyvinylpyrrolidone (PVP). In this investigation, it was hypothesized that the polymer preferentially binds to a specific surface based on the hydrogen bonding available between the polymer and the crystal structure.[62] A more recent success in changing crystal morphology using polymers involved an investigation on succinic acid. Pluronic P123 (PP123), a triblock co-polymer, in small quantities successfully modified the morphology of crystals obtained from water, from plates to blocks. The investigation also determines the effect of the polymer to be dependent on both the concentration of succinic acid and the concentration of PP123 in solution.[63, 64] In the majority of published studies on polymeric additives, nucleation and growth are not discussed as separate phenomena. As a result, it is difficult to deduce a specific mechanism of interference for the additives chosen.[59]

Polymeric additives can also be used to control the polymorph produced in a crystallisation.[65, 66] In experiments with tolfenamic acid, a screening mechanism known as polymer induced heteronucleation was used to show that at least five polymorphic forms exist where before it was believed there were only two. This technique, unlike those in the examples previously discussed, utilizes insoluble polymers as heterogeneous growth sites.[67-69]

1.3.3 Effect of additive concentration

The concentrations of additives in the system can have a major impact on the outcomes of the crystallisation. Additives in crystallisations in larger concentrations are likely to have an effect on the solubility profile of the system. It has been reported that high concentrations of additives can reduce the supersaturation and metastable zone width of a system, and therefore the nucleation temperature of the solution.[70, 71] There is little discussion in the literature discussing the optimal amount of additive to use, however, all reports agree they can have significant effects in small concentrations. Lower concentrations of additives are not only favoured due to their limited effects on solubility profiles, but also to prevent incorporation into the crystal structure, especially in the case of size-matched additives.

Size-matched additives have been reported to have an influence on the crystallisation in small percentages, below 10 mol%. Structurally similar and size-matched additives are successful in altering morphology at concentrations between 1-4 mol%.[44, 45, 72] Similarly, structurally related additives at a concentration of up to 6 mol% have successfully altered the growth morphology of biuret.[47] However, there are examples of much higher percentages of additives. In templating experiments used to control the polymorph of paracetamol, in an attempt to stabilise the metastable polymorph, a concentration of 25 wt% metacetamol is required to achieve the desired outcome.[52] However, despite examples of much higher percentages used, it is generally found that morphology modifications can often be achieved with low concentrations of size-matched and structurally similar additives.

Polymeric additive concentrations used in crystallisations also tend to be low. This is important, since as concentrations of polymers in crystallisations increase they can have effects on the solution viscosity and on the equilibrium solubility of the system[37]. Polymer adsorption onto the growing surface is thought to follow the Langmuir adsorption isotherm. However, at low polymeric concentrations it is believed deviations occur due to significant size differences between the polymer and solvent.[55, 56, 73] In the case of succinic acid noted above, additive concentrations used were seen to have an effect on the morphology achieved. Weight percentages of 0.17%, 0.25% and 0.5% were used, with lower percentages giving a better modification. Polymer concentrations used are often chosen in regions where micellar formation is favoured, however, it is unclear how this might influence the possible interaction with the growing crystal faces.[63, 64] Low concentrations of polymeric additives are also often favoured in an attempt to reduce their impact on the solution kinetics. Due to the large difference in sizes between polymers and target molecules, incorporation into the crystal structure is unlikely and is not a consideration that needs to be made for polymeric additives.

1.3.4 Surface interactions and solution interventions

Impurities are thought to inhibit growth by adsorbing to crystal faces and preventing further growth from occurring. This adsorption changes the relative surface energies of the faces and can block sites essential to the incorporation of solute into the lattice. These effects often result in changes to growth kinetics and therefore can be useful for changing crystal morphology.[74] Many different mechanisms of interaction have been theorized, with the first most widely regarded mechanism suggested in 1958. Cabrera and Vermilyea published their ‘pinning mechanism’, suggesting the progress of growth layers on a surface is blocked by impurities adsorbing. It was proposed that growth would completely stop when the adsorbed impurities were less than twice the critical radius from one another. Larger distances than this would allow growth layers to continue through the gaps, thus only slowing the growth and, significantly, not stopping it all together.[17] In 1974, Davey and Mullin summarized the potential sites of additive and impurity adsorption to effect growth kinetics: these possible sites include surface steps, kinks and ledges (figure 1.9).

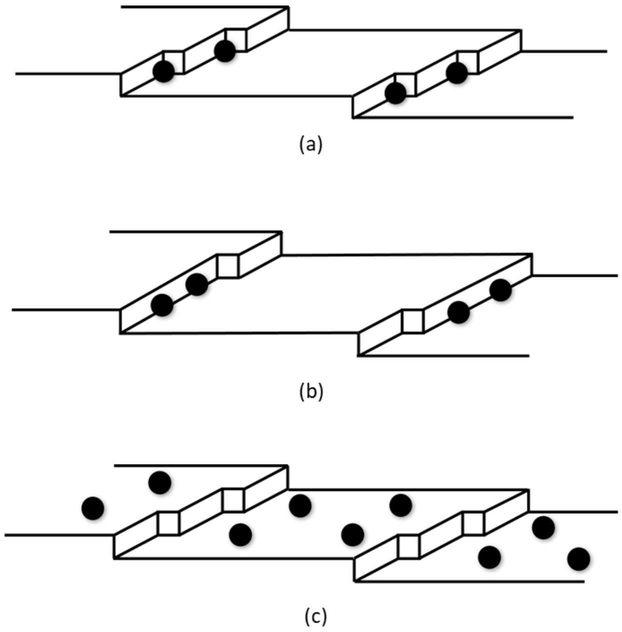

Figure 1.9. Sites of impurity adsorption on a growing crystal: (a) kink site, (b) surface steps and (c) ledge

Adsorption of the impurity at a kink site would effectively reduce the number of kinks present on a growing crystal surface. These sites are considered one of the most important for solute incorporation into the lattice and, as a result, their reduction would reduce the velocity of the growth. This reduction of growth causes ‘dead zones’ to occur on crystal surfaces where solute molecules are sufficiently blocked, preventing further propagation. Similar arguments can be used for adsorption to steps. Again, this would reduce the number available for solute molecules and reduce the velocity of growth. However, in this example it is believed that if adsorption falls below that of monostep coverage growth could squeeze between blocking impurities with relative ease, reducing their effectiveness. A critical concentration of additive or impurity is, therefore, implied in this example, with the layer velocity being relatively unaffected below this concentration.[74, 75] The relationship between the concentration of impurity and the blockage of surface sites can be described by a simple Langmuir isotherm.[17] The final point of adsorption, the ledge, will only have a strong effect on the crystal growth when the growth mechanism is strongly contributed to by surface processes, particularly diffusion. Adsorption at this location would decrease the surface area of the ledge causing a decrease in surface flux of growth units and, therefore, a reduction in step velocity.[74, 75] These concepts were revised in 1995 by Kubota and Mullin to incorporate the impurity effectiveness into calculations, offering the opportunity to explain anomalous patterns of behavior.[17, 76] The adsorption discussed is believed to occur via a modified version of the original pinning mechanism.[77]

Whilst the original pinning mechanism model is widely accepted, it does not accurately describe results observed in many investigations. Many commonly investigated systems do not exhibit the predicted behaviour.[78-80] This suggested a new model was required to describe the anomalous results being observed.

A new model emerged in 2006 known as the competitive adsorption model (CAM). This model differs considerably from the pinning mechanism previously discussed. This method gave new perspectives on the impurity adsorption mechanism and also gave an alternative description of the impurity effect on the crystal growth rate. The CAM considers the kinetic effect of impurities in the system, not the modifications their presence may induce on solution properties. Crystal growth in the presence of impurities is viewed as a competition between crystallising solute and the foreign additive for the adsorption sites.[81] Three of the stages involved in crystal growth can be affected by the kinetic effect of the impurity in solution: surface adsorption of molecules diffusing from solution, migration of molecules across the surface and step/kink adsorption of migrating molecules.[82] The CAM mechanism is assumed when the crystallising solute and the impurity dispute the coverage of the crystal surface and the occupation of energetically favourable places at surface steps. This model introduces a new variable, impurity concentration, which plays an important role in crystal growth from impure solutions and, arguably, improves the accuracy above those based on the original pinning mechanism.[81] A further adaptation of this model was developed for unsteady-state conditions (CAMUS). The CAM model assumes adsorption equilibrium is achieved instantaneously, which is not an accurate assumption for all systems. The CAMUS model describes experimental observations arising as a result of dynamic equilibrium between impurity and solute molecules. The impurity is adsorbed first at the crystal surface and then is gradually replaced by the solute target molecules until a steady-state is reached. These small changes made to the model for systems which take a period of time to reach equilibrium can successfully explain previously reported unusual growth rate trends.[83]

A further model was developed in 2016 to describe the effects of multiple impurities in the crystallisation on the final product. The multi-impurity adsorption model (MIAM) extends the CAM and pinning mechanism models to allow for simultaneous modelling of multiple impurities in a crystallisation that have the potential for different adsorption mechanisms to be present. The MIAM model is able to describe the different effects of multiple impurities on certain characteristic properties, such as crystal purity and shape and size distribution, using a mechanism of multi-component and multi-site adsorption.[84]

Computational models were developed as early as 1973, devoted to understanding and predicting the external crystal shape in terms of the internal solid state structure.[27, 85, 86] There are now a number of computational models that exist to determine the effect of external factors on the crystal morphology predicted from the internal structure. These models combine early calculations to predict the morphology with calculations of attachment and lattice energy to help determine the effects of solvent and additives on the growth morphology of target molecules.[87, 88] Despite the number of computational models developed, there is no complete agreement between them. In addition, the models are often not available to researchers outside the groups in which they were developed.

1.3.5 Effects of solvent on crystal morphology

Choice of solvent is often considered the most crucial design decision for solution based crystallisations.[89] Solvent can play an important role in the structure and morphology of a crystalline material. The choice of solvent can often allow the manipulation of crystal morphologies without changing the intrinsic packing of the crystal growth units, maintaining the crystal structure of the compound.[90-92] However, in some crystallisations the solvent can have significant effects on the crystal structure by changing the molecular packing. This change in packing could result in a new polymorphic form or the solvent could enter the crystal lattice creating a solvated form, often inaccurately termed a pseudopolymorph. Changing the form also influences the final morphology of the crystalline material.[93-96]

Different morphologies can often be accessed in different solvents for similar reasons to those seen with additives. Solvent molecules have the potential to form favourable interactions with functional groups exposed on crystal faces, resulting in inhibited growth and slowed growth rates on selected faces. Since crystal shape is largely determined by the relative growth rates of the various faces, determined primarily by the binding strength of the particles arriving at the surface, any factor which may alter the rate of deposition, such as solvent, will influence the crystal morphology. Due to differences in the functional groups present on specific faces preferential adsorption of solvent molecules can occur. The solvation layer needs to be removed from the surface of a crystal in order for growth units to bind. If solvent-surface interactions are stable enough to compete with the incoming solute molecules they can exert a significant influence over the final crystal morphology.[27] Due to these surface specific interactions it is possible for crystallisation from different solvents to result in different growth mechanisms, therefore causing a morphology change of the crystal. However, other factors also need to be considered, such as the physical properties of the solvent, crystal surface properties and supersaturation.[89, 97]

Most common crystal morphology prediction methods use the bulk crystal properties, such as interplanar distance or attachment energy (discussed further in section 1.3.6). These methods do not take into account the effect of a solvent on the crystal morphology. As a result, other parameters must be introduced to the models in order to accurately predict the effects of solvent on the system.[98] Many models have been created in order to simulate the effects of solvent on crystal morphology. Critical to the models developed are the interaction energetics. The presence of solvent alters surface interactions due to the solvation of a crystal surface. In order to predict the effects of the solvents correctly, the modification of the interactions must be determined.[89] Molecular dynamics simulations can focus on different parameters to achieve the prediction of solvent effect on morphology. These include modelling a solvent layer against the crystal surfaces[98], calculating lattice energies[99] and using chemical potential calculations[100] to deduce which faces will be most affected by the solvent system chosen. Molecular simulations are the most accurate method to obtain the relevant free energies, however, the often complex modelling involved limits the advantages of this modelling over experimental screening.[89] Other theoretical calculations often use attachment energy as a basis for the models and assume the attachment energy is proportional to the growth rate of the crystal surface. The development of activation energy models simulates the interactions of solvent with growing crystal faces to predict the resulting crystal morphologies. This method seems to achieves good agreement between calculations and experimental results and is argued to be the most effective model for quick solvent screening.[90, 92, 96]

Computational modelling and investigative experiments have suggested solvent polarity is an important consideration when choosing a solvent to affect the growth morphology achieved. Experimental research and computational simulations suggest the aspect ratios of resulting crystals can be directly altered by changing the polarity of the solvent system used. Studies carried out with benzoic acid found the aspect ratio decreased with increasing solvent polarity: a linear relationship was determined.[90] Experiments carried out on ibuprofen agree with the hypothesis determined from the findings for benzoic acid. Ibuprofen crystals grown from polar protic solvents, such as ethanol, produced less needle-like crystals than those prepared in less polar and aprotic solvents.[99] However, investigation into the influence of solvent polarity on isoniazid suggests the opposite relationship. Crystallisation experiments show a more needle-like crystal is achieved from water, compared to more rod-shaped crystals from alcohols. This suggests a decrease in aspect ratio resulting from a decrease in solvent polarity.[100] These differences are likely the result of different growth mechanisms in the crystal systems. Polarity affects the interactions between solvent and solute molecules at the different crystal faces leading to specific faces having different growth rates.[92] Polar solvents are thought to interact preferentially with polar faces, with non-polar solvents interacting more favourably with non-polar faces.[27] As a result, the effect of solvent polarity on the aspect ratio of the final modified crystal morphologies will depend on the specific interactions on the faces of the system being investigated.

The solubility of the solute in a particular solvent is also thought to affect significantly the ability to create more equant morphologies from needle-like crystals, by directly impacting the time it takes to reach the steady-state crystal shape. Although the solvent system will not alter the steady-state shape classification of the crystal system, a solvent system that slows down the creation of steady-state morphologies could result in a less needle-like crystal.[21]

Crystalline systems that form needles can be categorised into two different groups: ‘absolute’ needles are formed irrespective of the solvent whereas ‘conditional’ needles only form in specific solvents. For absolute needles, the solvent choice will not be driven by morphologies achieved. Attempts to reduce the impact of absolute needles will lie in additional processing steps, e.g.

mechanical milling or chemical temperature cycling. For conditional needles, attempt to improve crystal morphology via solvent selection merits consideration.[21]

1.3.6 Morphology prediction methods

Prediction of theoretical growth morphology is possible as a relationship exists between morphology and the crystal packing. The first methods developed for predicting growth rates of crystal faces relied exclusively on the crystal structure, interactions within it and their relation to the energies of the crystal faces.[20]

In this work the Bravais-Friedel-Donnay-Harker (BFDH) prediction method is the simplest model used. Bravais and Friedel initially established the relationship between the internal crystal structure and the external shape achieved. This work was expanded by Donnay and Harker by adding the influence of screw axes and glide planes to establish the BFDH rule.[101-103] The method assumes the binding energy of faces is inversely proportional to the interplanar spacing, where closer molecules will have larger interaction energies. As a result, the growth rate of the (hkl) face is proportional to the inverse of the distance between the (hkl) planes within the structure. Therefore, relative growth rates can be determined purely using the knowledge of the crystal structure.[4] The BFDH prediction approach does not take into account detail of intermolecular interactions nor the effects of external influences that may be present during growth steps, relying solely on the crystal structure data.

A model relating the interaction energies between building units and the external shape was developed by Hartman and Perdok.[104] Their model identified periodic repeated chains of strong, non-bonding interactions within the crystal structure, named periodic bond chains (PBC). These chains were hypothesised to determine the external shape of a crystal. Hartman and Perdok also classified crystal faces in a similar way to those discussed in section 1.2.3. The number of PBCs found in the plane parallel to a face determine the type of face and speed at which it grows: flat (F) faces are the slow-growing, followed by the step (S) faces, with kink (K) faces growing most rapidly.[104] Hartman and Bennema extended the model by introducing a proportionality relationship between attachment energy and growth rate. The hypothesis suggests faces with smallest attachment energies grow slowest, therefore, having the most morphological importance.[102, 103]

Both models discussed can provide good predictions for crystals grown from vapour, however, neither can account for any external interactions from the growth medium.[27, 86] Most crystallisations, especially those carried out in an industrial setting, involve solvent media, where interactions between the solvent and solute are inevitable. The presence of impurities in the system will also have an effect on the interactions present in the crystallisation. These external interactions significantly decrease the accuracy of the models discussed.

1.4 Crystallisation methods

In order for crystallisation to occur from solution, supersaturation must be achieved. There are a number of techniques able to generate supersaturation including evaporation, cooling and the use of an anti-solvent. Mechanochemical methods, such as grinding, can facilitate the formation of multi-component crystal systems without the need to generate supersaturation.

1.4.1 Evaporative crystallisations

Evaporative crystallisations involve supersaturation being generated by allowing solvent to evaporate at a constant temperature. This evaporation causes the concentration of the solution to increase and pass through the MSZ becoming supersaturated. At higher supersaturations, the system moves beyond the metastable limit (dotted line in figure 1.10) into the so-called labile region. In this region spontaneous nucleation can occur and this results in the concentration of solute decreasing in the solution. Constant evaporation allows the solution concentration to increase and again reach increased supersaturation. Further nucleation and growth occurs, reducing the concentration again. The cycle (figure 1.10) continues to repeat until complete evaporation occurs or the crystallisation is halted and crystals isolated from solution. Evaporative crystallisations are a good screening mechanism to use in materials discovery experiments. They are easy to set up and do not require any further intervention. Variables, such as temperature and solvent medium, can be easily altered. Slow evaporation can provide a good environment for single crystal growth.

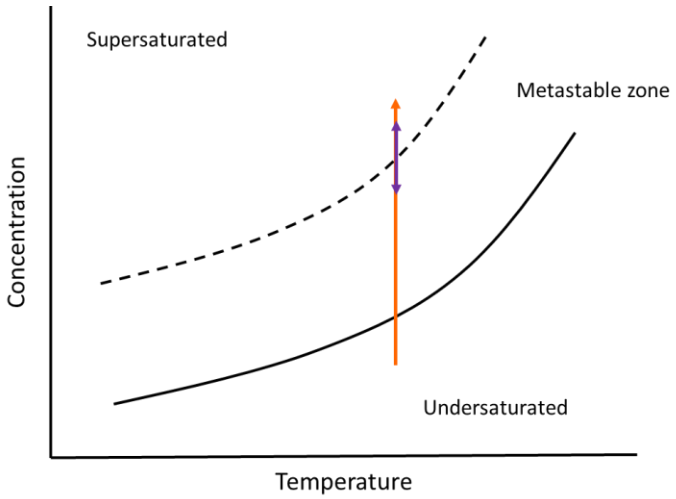

Figure 1.10. Generation of supersaturation in evaporative crystallisation methods (orange arrow). Variation of solute concentration throughout the evaporative process is depicted by the double headed arrow between supersaturated and metastable zone regions (purple arrow)

1.4.2 Cooling crystallisations

In cooling crystallisation methods, supersaturation is achieved by slowly cooling an undersaturated solution from an elevated temperature. This cooling decreases the solubility of the solute in the solvent system and drives the process to supersaturation. The temperature decrease moves saturation across the metastable zone and towards spontaneous nucleation in the labile region, and subsequently crystal growth (figure 1.11). Initially the solution is cooled to exceed the metastable zone and promote spontaneous primary nucleation, this generates a drop in concentration. After initial spontaneous nucleation further cooling repeats the same process until a final temperature is reached and the crystals are isolated. Controlled cooling is favoured in industrial processes to prevent uncontrolled primary nucleation. When the MSZW is known, the process can be controlled to maintain the concentration within this determined zone where following initial nucleation, only growth of existing crystals is possible, as shown in figure 1.11. By limiting the primary nucleation in this way, particle properties can be more tightly controlled.

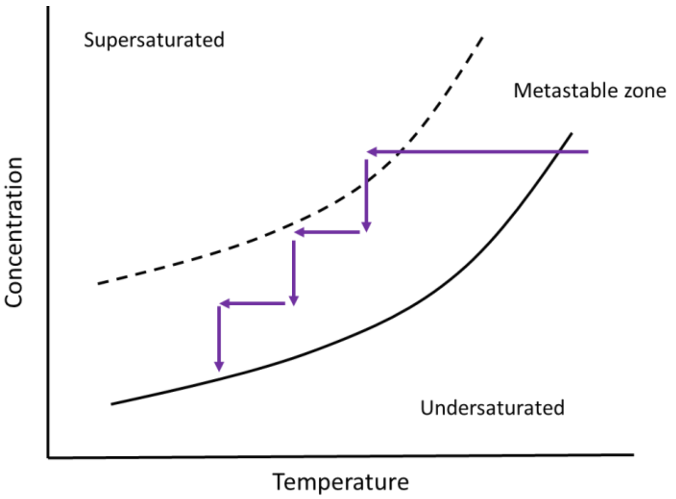

Figure 1.11. Ideal profile for a cooling crystallisation, including initial spontaneous nucleation, shown on a solubility diagram.[7]

1.4.3 Anti-solvent crystallisations

Another method to achieve supersaturation involves the addition of an anti-solvent. The solubility of the desired product decreases with the addition of a second solvent in which it is sparingly soluble or insoluble (the anti-solvent). This crystallisation method is often used for solutes whose solubility shows little change with temperature or to further decrease solubility towards the end of a cooling crystallisation to improve the yield achieved.[105]

1.4.4 Mechanochemical grinding

Mechanical methods for the creation of co-crystals is becoming a popular line of research; the most notable technique being used is grinding.[106] It differs from other crystallisation techniques as it does not require supersaturation to be achieved, as nucleation and growth do not occur. There are two methods by which this can be done, by grinding two components in a pestle and mortar either with the addition of solvent (liquid assisted grinding – LAG) or without. By grinding together components in this way, with the input of mechanical energy, it is hoped that a new co-crystal phase will form. Addition of a small amount of solvent is believed to play a catalytic role in the co-crystal formation before evaporating during the process.[106] The energy put in by the mechanochemical process allows for the breaking of intermolecular interactions, allowing rearrangement to form new interactions between multiple components. This mechanochemical based alternative is advantageous over solution based methods for screening multi-component crystal systems due to its rapidity, avoidance of solubility effects and solvent competition as well as being an inherently green process, with little to no waste being created.[106, 107]

1.4.5 Slurry crystallisation

Slurry crystallisation is a solvent-mediated method that does not require in-depth knowledge of solubility profiles of the solute. This method is useful for the formation of new crystalline phases and encouraging the transformation to the most stable forms.[95, 108] In slurrying, a suspension of starting materials is set up in a solvent with each dissolving until it reaches its solubility limit in the solvent system chosen. The suspension is stirred continuously to aid the establishment of an equilibrium of the solid materials and those dissolved in solution: the solutes continually move in and out of solution, continually making and breaking interactions. If favourable interactions between the two materials in the system exist a new co-crystalline form could be formed, reducing the concentration of individual components in the system. Once the individual components concentration is reduced, the equilibrium is disrupted and further dissolution occurs. After enough time has elapsed, full conversion of all starting materials will have occurred. A similar principle can be applied to metastable polymorphs, with full conversion to the more stable form being achieved after equilibrium is reached and enough time has elapsed. Varying conditions such as the solvent medium or the temperature can alter whether the transformation is favoured or not.

1.5 Industrial crystallisation

Crystallisation is widely applied in a number of different fine chemical industries and is essential for the production of many pharmaceuticals. The equipment and methods used vary from multi-purpose batch crystallisers to highly specialised equipment specific to particular processes and products.[109]

1.5.1 Batch crystallisation

Batch crystallisation methods are the most widely utilised processes within a number of different industries to produce crystalline products. The platform largely employed in production and purification of pharmaceuticals is the stirred tank reactor (STR). An STR consists of a jacketed batch vessel with a motor-controlled impeller to allow mixing to occur. Although widely used in the pharmaceutical industry, STRs present a range of difficulties with regards to control of crystallisation conditions at larger scales. With an STR it is harder to maintain consistent heat transfer throughout the whole volume as the scale increases, often resulting in longer reaction times. Mixing is a critical success factor during the crystallisation process and, as a result, when reactions are scaled up the optimisation of mixing conditions becomes paramount.[110] Due to the difficulties maintaining consistent conditions throughout the whole STR the control of product specifications, such as size distribution, polymorphic form and morphology, can be difficult, resulting in inconsistency and causing problems for downstream processes.[7, 111] STRs require a large amount of solvent and take up a substantial amount of space due to their large volumes and pose difficulties when it comes to cleaning vessels between batches, causing an increase in downtimes of processing plants.

1.5.2 Continuous crystallisation

Whilst batch techniques are well-established in the pharmaceutical industry, there is significant interest in continuous methods of crystallisation. This involves feed solution being continuously pumped into a crystalliser whilst product is continually being removed at the same rate. Continuous techniques are often more difficult to develop but they offer the potential for enhanced reproducibility and control of crystal physical properties.[112] In addition, continuous methods can allow for better efficiency with respect to reagents, solvents, energy and space as well as minimising waste production and reactor downtime, for cleaning and maintenance.[7] By allowing better control of physical properties, such as particle size and shape, it is possible to eliminate some downstream corrective processes, for example milling to produce a more homogeneous particle size.[112] In comparison to STRs, scale up of an existing crystallisation method is simpler as the process simply requires running for longer, therefore having no effect on variables such as solution concentration or mixing. Continuous crystallisers have the potential for the establishment of fully integrated processes involving flow chemistry, purification and final formulation.

There are various platforms with which to carry out continuous crystallisation. An STR can be adapted to allow for continuous feed of solution into the vessel and product removal at the same rate, a mixed-suspension, mixed-product removal (MSMPR) crystalliser. Additional vessels can be added to create a series of STRs (as an STR cascade (cSTR) or multi-stage MSMPR) to allow for an increase in the length of time a solution spends within the crystalliser cascade (residence time), although this will increase the running costs of the process.[7]

Tubular flow platforms can also be used to achieve continuous crystallisation. This is the method utilised in continuous oscillatory baffled crystallisers (COBCs). The use of COBCs can help overcome a number of problems faced when using batch processing techniques.[7] The COBC set up at the University of Bath is shown in figure 1.12. The tube has a number of 'restrictions' (baffles) equally spaced along its length to ensure equal volumes in each.[113] Between each restriction mixing is provided by oscillatory motion as an additional flow mechanism superimposed on the net flow of the feed solution.[7] The combination of restrictions in the tube and oscillatory pressure generates whirlpools in each section of the tube, optimising mixing.[113]

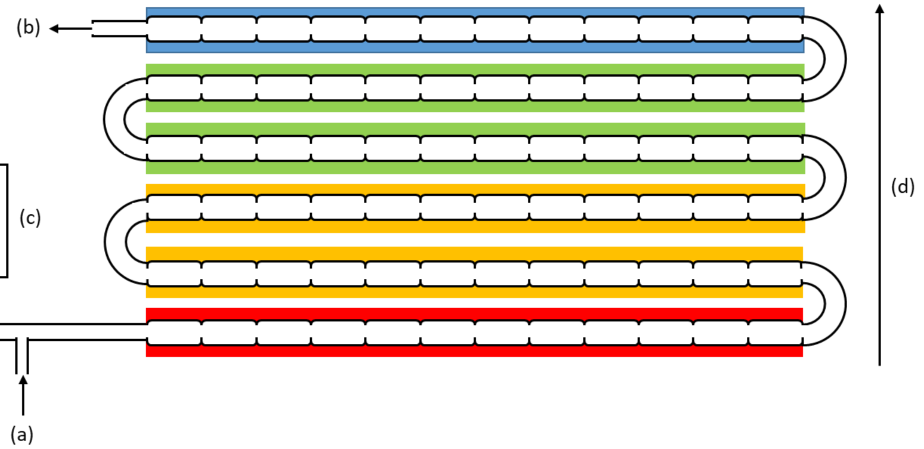

Figure 1.12. Set up of COBC at the University of Bath. (a) input of feed solution via peristaltic pump, (b) output of solvent and crystalline product, (c) motor driven bellows to set up oscillation and (d) direction of flow along temperature gradient represented by colour change (red to blue shows hot to cold)

A solution is fed into the crystalliser via a peristaltic pump, the continuous feed drives the flow of the solution through the length of the crystalliser. Motor driven bellows also help pump the feed solution through the baffled tubing, providing the oscillatory flow and aiding mixing. Controlled cooling is possible using jacketed tubing attached to temperature-control circulators: supersaturation is achieved due to the establishment of this temperature gradient. The jacketed tubing allows for improved heat transfer when compared to the MSMPR set up. Once cooling crystallisation is complete, with the feed solution having travelled through the length of the crystalliser, the crystalline product is filtered from the solution and isolated.

The nature of the flow through continuous crystalliser systems is important as it can affect vital parameters throughout the system. Ideally, they would operate under plug flow (figure 1.13) to provide ideal mixing profiles as well as consistent heat transfer, though this is often hard to achieve.[7] Carrying out continuous crystallisations as close to plug flow as possible is vital for production of crystals with uniform properties. Near plug flow conditions can be obtained by using very high flow rates in a tubular reactor to create a turbulent flow environment (figure 1.13).[7] Laminar flow, on the other hand, provides unfavourable conditions for consistent heat transfer and ideal mixing profiles, and reduces the homogeneity of the conditions throughout the length of the crystalliser.

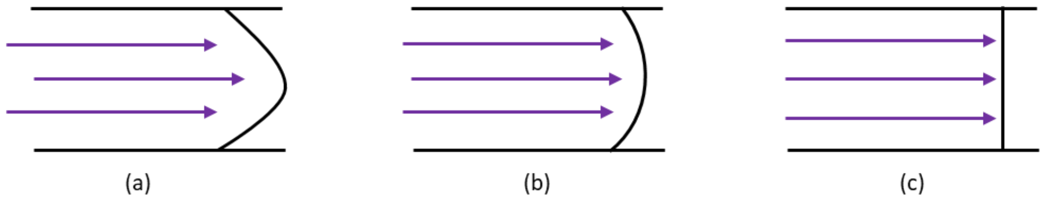

Figure 1.13. Illustrations of different flow mechanisms; (a) laminar flow, (b) turbulent flow and (c) plug flow

A further example of a tubular crystalliser is the KRAIC (Kinetically Regulated Automated Input Crystalliser), developed at the University of Bath. This is a mesoscale flow reactor that works on the basis of segmented flow, in which individual segments (slugs) of feed solution are separated by air and carrier fluid. The creation of discrete solution slugs allows each slug to act as its own micro-batch reactor; importantly, no back mixing can occur. A carrier fluid is chosen with favourable wetting properties to coat the inside of the tube and prevent the solution segment from touching the walls, thus removing this as a nucleation site and preventing encrustation. The carrier fluid and solvent used must be immiscible to allow for segmentation and to create a non-slip boundary between the two, generating bolus flow to provide mixing within each slug throughout the length of the crystalliser.[114] More in depth discussion about the KRAIC set up is provided in chapter 3.

Microscale continuous reactors are also available. Microfluidic continuous platforms have the benefits of well-defined laminar flow characteristics and enhanced heat and mass transfer. They are closed systems so also protect from undesired nucleation resulting from the presence of foreign particles.[115] Due to their size they have a low consumption of reagents, an attribute that is particularly attractive in research on expensive pharmaceutical materials. However, due to the small internal diameter there is an increased risk of sedimentation and blockages occurring in the reactor. So far microfluidics has not been widely used for the continuous crystallisation of APIs.

Despite the potential benefits of using continuous crystallisation, its uptake in the pharmaceutical industry has been slow. The majority of industrial scale production is still carried out using batch crystallisation methods, such as cooling and anti-solvent crystallisations.[112] The slow uptake of continuous processes in industrial production is largely due to the significant research already available for batch crystallisation. Batch methods have been implemented for many years with substantial capability for mass production already available to pharmaceutical companies. The well-established processes allow rapid development of new pharmaceutical products and efficient production. There is considerably less understanding of continuous crystallisation processing which could result in long development times, presenting a significantly increased risk to the companies.

Another hurdle the industry must overcome to see increased implementation of continuous crystallisation is the strict regulatory framework imposed on the pharmaceutical industry. Quality control can be simplified in batch processes. The introduction of powerful process analytical techniques (PAT) that can be used in-situ during a continuous crystallisation is key to overcoming the regulatory barriers and allowing wider scale use of continuous crystallisation.[116]

Research within the CMAC Future Manufacturing Research Hub is aimed at developing continuous manufacturing processes and exploring the extent to which these platforms can improve control of production, looking to establish these as a competitor to batch approaches for pharmaceutical manufacturing. It is important to understand that the crystallisation method chosen is based on the specific requirements for the particular product being developed. Continuous crystallisation is not always the most suitable method to choose and a number of different factors need to be considered when making the decision.

1.6 Crystal engineering

Multi-component systems are an interesting area of research, particularly for pharmaceuticals, as they allow for the possibility of property manipulation of crystalline solids. The difficulty is predicting the interactions components may have with each other and, therefore, the resulting multi-component crystals they may form. Crystal engineering is a means by which to attempt to combat these unknowns. Crystal engineering was first coined in literature in 1955 but has been largely associated with a paper published by G. M. J. Schmidt in 1964. The paper correlated the solid-state reactivity of trans-cinnamic acid with their crystal structures.[117-119]

The primary focus of crystal engineering is to establish reliable intermolecular interactions between molecular structures.[73] Interactions between molecules are broken down into supramolecular synthons, kinetically defined units that contain the essential features of the crystal structure. Supramolecular synthons are developed to closely resemble the functional groups within the molecules. Designing synthons requires a strong understanding of the intermolecular interactions within a structure.[120] Crystal engineering focuses on interactions between molecules and, therefore, mainly focusses on the manipulation of the intermolecular forces. Due to their collective strength, reliability and, importantly, directionality, the most widely utilised intermolecular force in crystal engineering is hydrogen bonding.[119, 121] Other molecular interactions can be utilised, such as van der Waals or π-interactions, but hydrogen bonds are considered the strongest, non-ionic intermolecular interactions that can exist within a structure.[122]

1.6.1 Intermolecular interactions

Crystalline solids are held together by a variety of different bonds and interactions. They can be strongly ionically or covalently bonded (for example the bonding within molecules) and involve a range of intermolecular interactions. In order to apply crystal engineering principles to design new crystalline forms an in-depth understanding of hydrogen bonding and other intermolecular interactions is required.[11, 118, 120] There are many possible intermolecular interactions to consider, including hydrogen bonds, halogen bonds, π-π interactions and van der Waals interactions. Once those present are recognised they can be categorised and applied to crystal design.

1.6.1.1 Hydrogen bonds

Hydrogen bonds can be described as "*an attractive interaction between a hydrogen atom from a molecule or a molecular fragment, D-H, in which D is more electronegative than H, and an atom or a group of atoms in the same or a different molecule, in which there is evidence of bond formation*".[123] For the design of extended crystal structures, considerations of hydrogen bonds between two different molecules are more important than those within a molecule. The relative strength of hydrogen bonds often depends on the electronegativity of the hydrogen bond donor (D atom), but also the acceptor atom with which the hydrogen bond is being formed. These interactions are often considered to be electrostatic between a covalently bonded hydrogen (with a partially positive charge) and a lone pair on the hydrogen bond acceptor. However, it is not always possible to rationalise the interactions this way as stronger interactions often point towards more covalent contributions.[124] Typically hydrogen bonds are considered the strongest, non-ionic intermolecular interactions that can exist within a structure.[122]

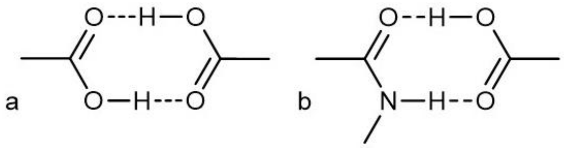

Figure 1.14. Typical hydrogen bond motifs (synthons); in the definition of hydrogen bond donors given above, the DH donor fragment here has D = O or N. (a) carboxylic acid dimer homo-synthon, (b) amide···acid hetero-synthon

The components forming the hydrogen bonds often form in identifiable and repeatedly occurring patterns known as supramolecular synthons; the directionality of hydrogen bonds is key in allowing potential rationalisation of these. These synthons represent an intermolecular building block involving more than one molecule (hence supramolecular), held together by interactions that are not covalent. These can then be considered as a supramolecular building block that helps define the interactions within the crystal packing. Hydrogen bonds can form between homo-synthons, two or more of the same molecules, or hetero-synthons, two or more chemically distinct organic molecules (figure 1.14).[125] In order to define the interactions forming such synthons, hydrogen bond graph set notation was established by *Etter et al.*; the symbolic representation of this is shown in equation 1.5.[126] There are four types of hydrogen bonding interactions in this classification: a ring (R), a chain (C), a non-cyclic dimer (D) and an intramolecular interaction (S). A hydrogen bond acceptor (A) is the molecule that accepts the proton whereas the hydrogen bond donor (D) donates it (in this nomenclature, DH is the equivalent of XH in the definition given above). In the equation describing Etter rules for naming hydrogen bond interactions, X denotes the type of hydrogen bond, A represents the number of hydrogen bond acceptors and D represents the number of hydrogen bond donors. (n) designates the total number of atoms involved in the interaction pattern being described

$$X^{A}{}_{D}(n) \qquad \text{Equation 1.5}$$

Hydrogen bonds can vary in strength depending on the atoms present in the hydrogen bonds (table 1.1). The strength is characterised by the distances between the donor and acceptor involved.

Table 1.1. Properties of different strength hydrogen bonds [127]

	Strong	Moderate	Weak
A-H··D interaction	Mostly covalent	Mostly electrostatic	Electrostatic
Bond lengths	A-H ≈ H··D	A-H < H··D	A-H << H··D
H··D (Å)	~ 1.2 – 2.5	~ 1.5 – 2.2	2.2 – 3.2
A··D (Å)	2.2 – 2.5	2.5 – 3.2	3.2 – 4.0
Bond angles (°)	175 - 180	130 – 180	90 – 150
Bond energy (kcal mol^{-1})	14 - 40	4 – 15	< 4

As well as more commonly observed intermolecular hydrogen bonds, it is also possible to form intramolecular hydrogen bonds between donors and acceptors within the same molecule. These hydrogen bonding interactions can fix a molecular conformation and therefore influence the crystal structure and packing. Hydrogen bonds primarily occur between one donor and acceptor group, known as two-centred interactions. However, multiple interactions are also possible between donors and acceptors, forming bifurcated or three-centred hydrogen bonds. These generally involve one acceptor and two donor hydrogens or two acceptors and one donor hydrogen atom (figure 1.15).[128]

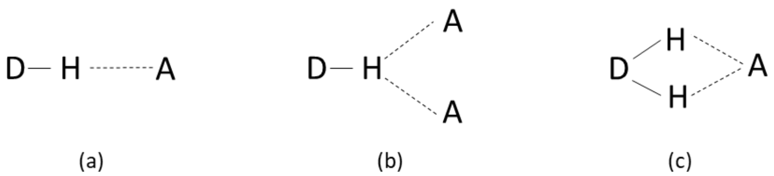

Figure 1.15. Different hydrogen bonding interactions where D is the donor and A is the acceptor. (a) a two-centred hydrogen bond, (b) a bifurcated hydrogen bond between one donor and two acceptors and (c) a bifurcated hydrogen bond between two donors and one acceptor.

1.6.1.2 π-stacking

When two or more aromatic rings are within close proximity to each other they can form interactions known as π-π interactions or π-stacking. These interactions occur when the attraction of the π-electrons and the σ-framework outweighs any unfavourable interactions, such as π-repulsions.[129] Different arrangements of neighbouring aromatic rings are possible, with each potentially leading to significant π-stacking interactions (figure 1.16). The geometry of the interaction between the rings is influenced by their substituents, whose presence alters the electron cloud polarisation. For example, the use of an electron-withdrawing substituent will decrease the π-electron density in the ring, reducing repulsions and allowing a stacked geometry to occur.[129]

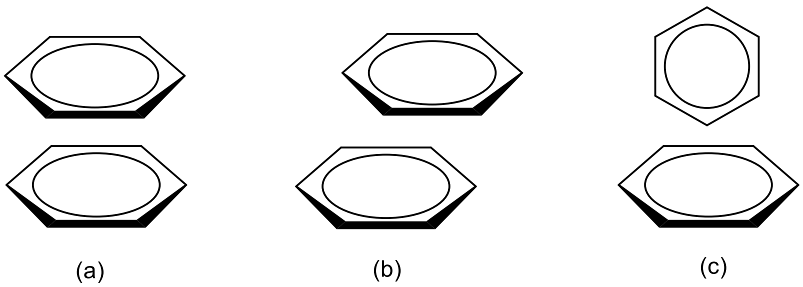

Figure 1.16. Face-centred stacking, (b) off-centre parallel stacking, (c) edge-to-face interactions.[130]

1.6.1.3 Weak interactions

Further weak interactions are also present in crystal structures but are often not considered in crystal engineering as they are less easy to predict. These weak interactions can be both attractive and repulsive and are often known as van der Waals interactions. This umbrella term includes dipole-dipole, dipole-induced dipole and London dispersion (instantaneous dipole) forces.[131]

Dispersion forces arise between non-polar species, where neither possesses a permanent dipole. Fluctuations of electron density result in the formation transient dipoles and an interaction is possible between the molecules. If a polar molecule is present, dipole-induced dipole interactions can occur. The presence of a molecule with a permanent dipole can influence the electron cloud of a nearby non-polar molecule and induce a dipole. If both molecules have a permanent dipole, dipole-dipole interactions can occur between molecules. These interactions are dependent on the orientation of the molecules present and the distance between them in the structure.[132]

1.6.2 Multi-component crystallisations

The materials of interest in crystallisation studies have increasingly broadened their scope from single-component systems to an enhanced focus on the use of multi-component crystallisations to manipulate the properties of the desired products, without affecting the biological activity of the API itself. Multi-component crystallisations require the active ingredient to be crystallised in the presence of one or more other components to change the conditions of the crystallisation and, hopefully, the final product. The effect of the secondary component on the system depends on its properties and the interactions it can achieve with the API. When crystallising from a solution containing two separate molecular solutes the most common outcome, when no chemical reaction occurs, is the recrystallisation of the two separate molecular crystals. In such cases, the presence of the secondary molecule can sometimes act as a 'template', causing changes in properties such as crystal morphology and the polymorphic form of the target component.[51, 133]. The second outcome involves the incorporation of the secondary element (the co-former) and the formation of a multi-component crystalline system – often termed co-crystallisation (further explanation in section 1.7).

Co-crystallisation attempts to bring two different molecular species together within one crystalline lattice without making or breaking covalent bonds.[134] Co-crystals are often formed due to hydrogen bond interactions between the two separate molecules. Thus, hydrogen bond interaction prediction can be utilised to determine the likelihood of a co-crystal forming. The CCDC software Mercury[135-137] offers the ability to run these calculations for interactions between a target molecule and a list of potential additives or co-formers identified by the user. The molecular complementarity check gives an indication of which molecules have the potential to form sufficiently strong hydrogen bonds to create a new co-crystalline phase.

1.6.3 Molecular complementarity calculations

Molecular complementarity is a co-crystal design element incorporated into the CCDC Mercury software, utilising informatics approaches to identify common features/patterns in previously published structures. Co-crystals presented significant research interest due to the potential for modifying and tailoring physiochemical properties of the target molecule, including the potential to influence morphology. The calculations carried out to assess the likelihood of co-crystallisation could be useful in developing a list of potential additive candidates for morphology modifications.

Calculations are based on quantitative structure-activity relationship molecular descriptors.[138-141] Molecules that tend to co-crystallise have similar properties, such as shape and polarity. Molecular descriptors have been given defined threshold values based on the majority of co-crystals entered into the CSD database.[142] This allows co-formers that are unlikely to interact effectively with the target molecule to be filtered out before experimental screening. Libraries of potential co-formers can be developed for analysis to fit the outcomes required by the investigation. This type of analysis has been particularly effective in cases where co-crystal formation is difficult. In the example of artemisinin, 75 co-formers were screened experimentally with only two successful outcomes. Using the complementarity calculations, 33 of the 75 co-formers would have been eliminated as potential candidates.[143] This 44% reduction in co-formers to screen not only increases the efficiency of the experimental steps taken, by reducing time and costs associated with the screening, but also the success rate of the experiments carried out.

The outcomes of the calculations can be analysed with respect to each molecular descriptor individually. Statistical analysis shows molecules with similar shapes and polarities tend to co-crystallise more effectively.[142] This analysis led to five different descriptors being chosen for calculations of molecular complementarity. There are two molecular polarity descriptors, dipole moment and the fraction of N and O atoms (FNO). Dipole moments of molecules in co-crystals show a strong correlation to each other, while the FNO of a molecule is calculated by dividing the total number of N and O in the molecule by the number of heavy atoms.[142] Size and shape descriptors were defined using the box model of crystal packing. The box model defines a crystal as being made up of identical boxes with three unequal sides denoted large (L), medium (M) and small (S), L> M>S. These boxes are stacked with faces touching and edges aligned, in a close-packed arrangement.[144] These lengths refer specifically to the size of the molecule, whereas ratios of these lengths describe the shape of the molecule. In planar molecules, S/L ratios are small. Small M/L ratios describe rod-shaped molecules. The size descriptors used in molecular complementarity calculations are S axis, S/L ratio and M/L ratio. It is believed the shape descriptors are much more important for co-crystallisation than the individual dimensions of the molecules.[142]

1.7 Types of crystalline solids

Crystalline solids can exist in many different distinct solid forms, namely polymorphs, co-crystals, solvates/hydrates and salts (figure 1.17).

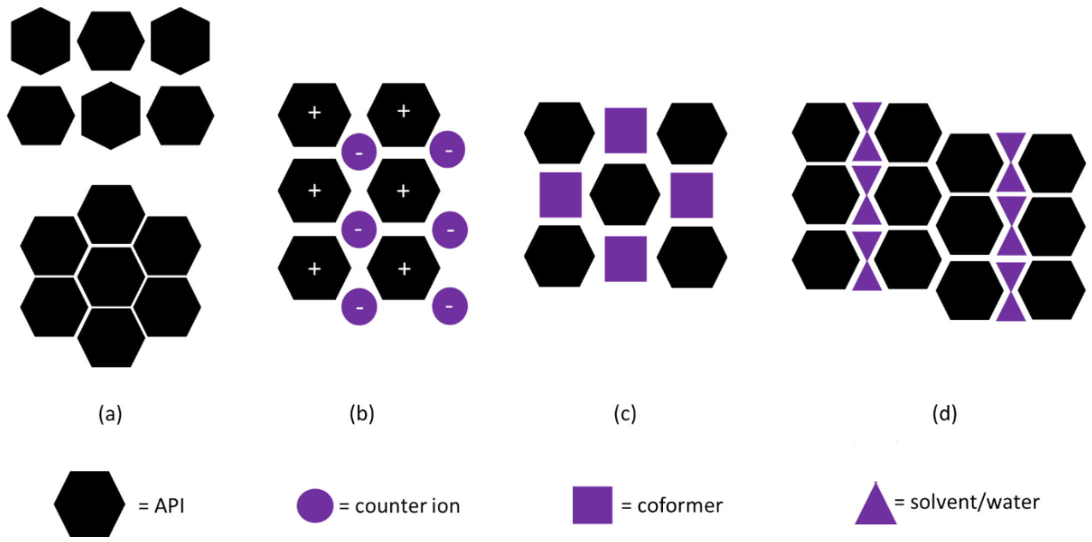

Figure 1.17. Illustration of possible crystalline forms for single and multi-component systems; (a) polymorphs, (b) salts (c) co-crystal and (d) solvate/hydrate. The counter-ion in the salt case can be a simple ion or a molecular ion, the latter is often generated by proton transfer during the crystallisation process.

1.7.1 Polymorphism

Polymorphism is observed when a solid crystalline phase of a compound has the ability to form in two or more different crystalline structures.[145] By definition polymorphs have the same elemental composition but differ in their unit cell and crystal packing, giving rise to differences in the physical properties they exhibit. As a result, polymorphism is of great interest in the pharmaceutical industry as the differing properties often have implications on processing steps, formulation and drug availability.[146]

An example of a pharmaceutical polymorph is paracetamol, which can exist in at least three polymorphic forms and is an example of packing polymorphism. Form I shows the molecules packing in a herringbone arrangement whereas form II shows a layered structure (figure 1.18). The layering observed in form II gives the paracetamol more favourable physical properties, allowing for better solubility and compressibility.[133]

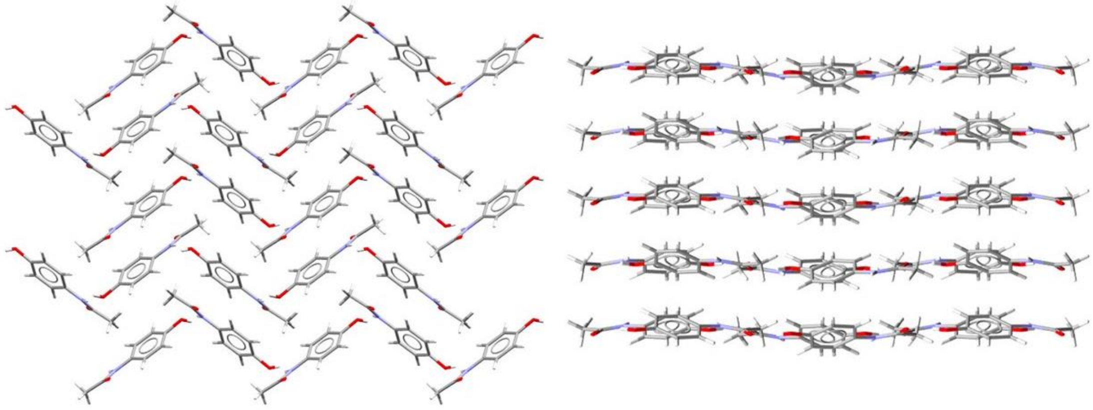

Figure 1.18. Crystal packing of two paracetamol polymorphs: Form I viewed along crystallographic a axis showing herringbone structure (left) and form II viewed along the crystallographic b axis showing the layered packing (right)

Investigating and understanding polymorphism is crucial in the pharmaceutical industry. Intensive screening of new drug molecules is essential under a range of crystallisation conditions. Typically, the most stable polymorph is required to prevent any unwanted phase transitions during production or whilst the final product is being stored. An example highlighting the importance of thorough polymorph screening is Ritonavir. Initially only one solid form of the molecule was determined and a formulation developed and sold as Norvir for the treatment of AIDS. A few years later several batches of the drug failed a dissolution test. Screening of the contents of the capsules showed a new polymorph of ritonavir had formed, form II. This new phase dominated production, as the more stable polymorph, and immediate reformulation was necessary. This cost the company huge sums of money and threatened the lives of those dependent on the drug. Ritonavir differs from paracetamol as it exhibits conformational polymorphism with the different conformational isomers crystallising as distinct polymorphic forms.[147]

The relative stabilities of polymorphs depend on their free energies, with the most stable polymorph having the lowest free energy. The lowest energy polymorph is termed the thermodynamic form, with the other forms termed metastable. Often metastable forms are desirable due to their favourable properties. Metastable forms are more soluble, for example, and can offer improved bioavailability. They can also offer other favourable properties, under grinding and compression for example, but have the tendency to transform to the thermodynamic polymorph. This transformation can be detrimental in terms of efficacy, such as discussed with ritonavir.[10]

Thermodynamically there are two types of polymorphism: enantiotropy and monotropy (figure 1.19). In monotropic polymorphs, one form is stable over the entire temperature range, until the melting point is reached: no solid-solid transition exists below the melting point. Enantiotropic polymorphs exhibit a solid-solid transition at a temperature below the melting point of either polymorph: each has a defined temperature range over which it is the most thermodynamically stable.[145]

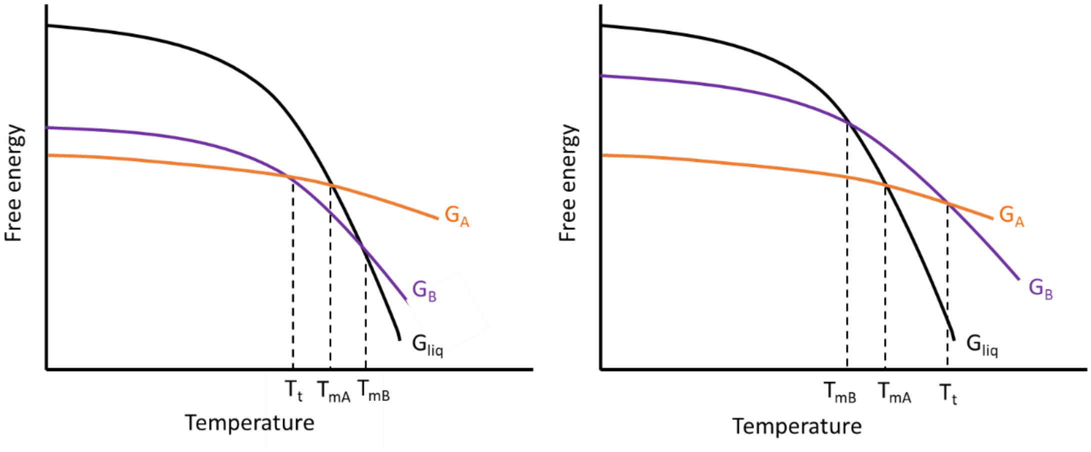

Figure 1.19. Plots showing the free energy relationship with temperature for enantiotropic systems (left) and monotropic systems (right). G is the free energy, T is the temperature, A, B and Liq refer to polymorphs A, B and liquid phase and T_m and T_t correspond to temperature of melt and transition respectively.

The solubility of polymorphs is also affected by enantiotropism and monotropism: in an enantiotropic system the solubility curves cross whilst in a monotropic system they do not (figure 1.20). The temperature at which the curves cross is the temperature at which the phase transition occurs. In the monotropic case, where the solubility curves do not cross, the polymorph with the higher solubility is the metastable form; in this case the metastable polymorph will retain higher solubility than the thermodynamic form over the full temperature range.

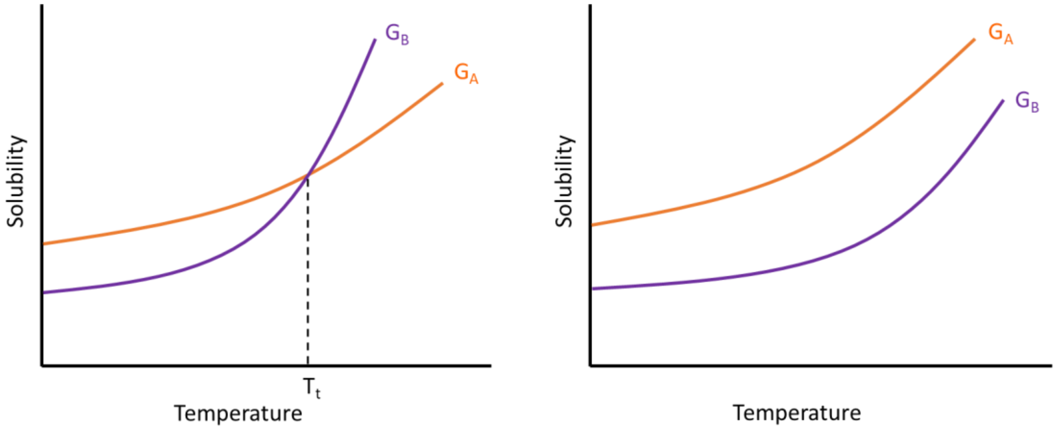

Figure 1.20. Solubility curves showing the relationship between two polymorphs enantiotropically related (left) and monotropically related (right) over a defined temperature range

1.7.2 Salts

Salts are formed due to proton transfer from an acidic component on one molecule to a basic component on the other. This is another way in which a co-crystalline system can be produced, through the formation of molecular salts. The major interaction in these systems is now an electrostatic interaction between a positively charged component and a negatively charged component, adding to the hydrogen bonding as seen with neutral co-crystals. Whether or not proton transfer is likely to occur will be determined by the pK_a difference between the acidic and basic group. While not a definitive rule, if ΔpK_a (= pK_a(base) – pK_a(acid)) is greater than 2-3 a salt is expected to form, while for $\Delta pK_a < 0$ a co-crystal is generally expected. Knowledge of these values can be used to guide the choice of an appropriate co-former to obtain the desired results. No prediction of what will form is possible using this method when the ΔpK_a value sits between 0 and 3.[148] It should be noted that pK_a is a solution characteristic, hence less relevant for the resulting solid state structure.

The formation of salts can again be useful in altering the physical properties, most significantly improvements to solubility, without affecting the activity of the drug itself. As a result, it is estimated over half of all drug molecules produced are administered as salts.[149]

1.7.3 Co-crystals

Co-crystals are defined as solid-state materials with two or more components creating a structurally homogeneous crystalline material.[150] Both components exist as neutrally charged species and are solids at room temperature. Interactions between the components within the crystalline structure are intermolecular and non-covalent interactions, primarily hydrogen bonds, rather than electrostatic attractions and covalent bonds. As a result, compounds used to form co-crystals do not require any ionisable sites. The driving force for the creation of co-crystals is the formation of stronger, more favourable hydrogen bonds between the two components than those existing in the original single component crystals.[151] Packing is also an important factor, the packing of the two components together must be favourable to allow the crystal to form. This change in the molecular arrangement with the addition of a second molecule can result in significant changes to the physical properties of the material.

Crystalline forms of pharmaceutical molecules are the most often utilised due to their stability and the ease with which they can be characterised. Co-crystals are of particular interest to the pharmaceutical industry due to this potential to improve the physical properties of APIs.[152] API molecules are good targets for co-crystallisation as, often, they contain an abundance of hydrogen bond donor and acceptor groups. Pharmaceutical co-crystals are formed by combining the target API with a GRAS additive which will not affect the therapeutic effect of the drug or cause any harmful secondary effects. The ability to alter physicochemical properties of a drug molecule without compromising its structural integrity, and as a result the bioactivity, has increased the interest in co-crystallisation research.[153] Co-crystallisation is not yet widely used in pharmaceutical production due to complications as a result of having extra components present. The introduction of additional components can result in difficulties tightly controlling the form produced and mixed phases are often created, from which separation is required and often difficult.

1.7.4 Solvates/hydrates

Solvates form as a direct result of the incorporation of solvent molecules into the crystal structure, forming a new multi-component crystal structure; they are sometimes inaccurately termed pseudopolymorphs, and this terminology remains commonplace. Hydrates are specific forms of solvates whereby the solvent being incorporated is water. The inclusion of solvent in the crystal structure changes the intermolecular interactions and therefore gives the new form unique physical properties. Particularly important for the pharmaceutical industry is the effect on solubility and bioavailability of the new form: often solvates possess a lower solubility than the unsolvated phases. Hydrates are more common than organic solvates.[10] It has been suggested that approximately 33% of all organic molecule are able to form hydrates, whereas solvates are reported to be much less prevalent (10%).[154] Water can often be readily incorporated into a structure due to small molecular size, adaptable hydrogen bonding and ability to stabilise structures by correcting imbalances present between number of donor and acceptor atoms.[155, 156] Although there appear to be benefits of hydrated crystalline systems, such as improved solubility, little research has been carried out into their long term stability, particularly their thermal stability. The variation of temperature can result in the loss of water from the crystal lattice, changing the properties and structure of the product. Co-crystal hydrates remain largely unexplored as a class of compounds.[154] As a result, it is important to determine whether new pharmaceutical molecules form solvates or hydrates for practical manufacturing decisions to be made. This is likely due to solvates being less desirable in the pharmaceutical industry as a very limited number of solvents are regarded as sufficiently safe as to be allowed to be present in stoichiometric quantities in pharmaceutical products.[157]

1.8 Aims and objectives

The aim of the work presented in this thesis is to produce a favourable morphology modification in an industrially relevant active pharmaceutical molecule. The method by which modifications were investigated involves changing the conditions of crystallisations, including the solvent systems and crystallisation methods used. Particular focus of the research involved the influence of intentionally added impurities on the resulting crystal morphology; both in additive quantities and for multi-component investigation. The major API of interest for this research was isoniazid (IZN), chosen due to its tendency to crystallise with a needle morphology. The isoniazid investigation was mirrored for another related API which also exhibits a preference for needle morphologies, pyridoxine (PYR).

The scale up of the impurity investigations is an importance consideration for assessing the potential for implementation into the pharmaceutical industry. As a result, a focus was placed on scale up of successful morphology modifications and, hopefully, transfer into a continuous platform.

During the course of the research, crystallisation workflows were produced for the investigation into additive effects on a crystallisation and the production of new multi-component materials. Another focus of the research, therefore, became the benchmarking and implementation of these workflows. These workflows have been applied to both IZN and PYR investigations, as well as a number of CMAC target molecules.

1.8.1 Isoniazid (IZN)

Isoniazid (IZN) is an anti-mycobacterial agent used in the treatment of latent tuberculosis (TB); the state whereby a patient is infected with TB bacteria but does not become ill or experience any adverse symptoms.[158] The clinical use of IZN to treat TB infections has been in circulation for over 60 years. Commonly patients are prescribed IZN in combination with further anti-TB drugs, including rifampicin, pyrazinamide and ethambutol or streptomycin. This is due to the increasing resistance of TB bacteria to the administration of IZN alone.[159, 160] In 1999, TB was recognised a global health problem by the World Health Organisation (WHO) and they dubbed the fixed-dose combination (FDC) tablet, consisting of the above mentioned molecules as active ingredients, an essential drug.[161]

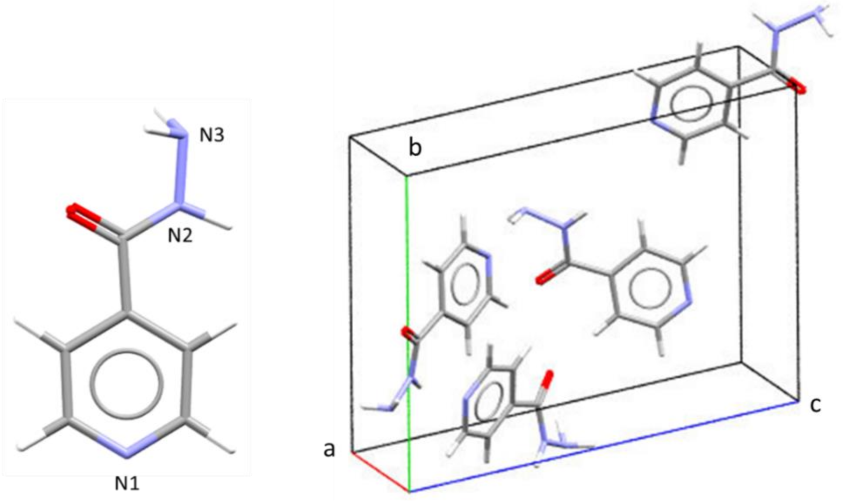

Figure 1.21. Labelled IZN molecule (left) and unit cell projection for IZN (INICAC02) (right)

IZN has been assumed to be monomorphic for the past 60 years. However, in March 2020 (by other researchers, but during the course of the investigations presented here) two new polymorphic forms of IZN were isolated from melt and nanoconfinement crystallisations. Both new forms of IZN are highly metastable; form II transforms to form I at room temperature within hours and form III is only stable at room temperature for less than a minute. [162] Due to the highly metastable nature of the newly discovered polymorphs, only the properties and structure of the stable form I will be discussed in this thesis.

The thermodynamic form I of IZN crystallises in the orthorhombic $P2_12_12_1$ space group (figure 1.21). An almost herringbone packing structure can be seen, creating a zig zag pattern of linked chains throughout the lattice (figure 1.22). The aromatic ring systems stack neatly on top of each other, resulting in the chains within the structure neatly packing on top of one another.

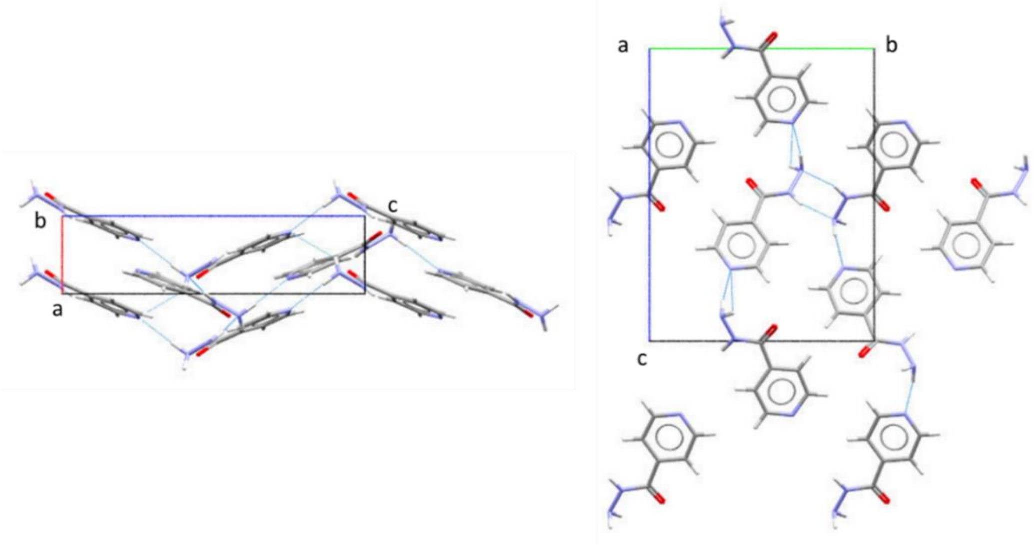

Figure 1.22. Packing of an IZN (INICAC02) crystal as viewed along the b axis (left) and a axis (right)

Chains of IZN molecules are connected via N3-H···N1 hydrogen bonds (table 1.2). Both hydrogen atoms on N3 donate to the pyridine N1 of two separate IZN molecules, creating a bifurcated interaction. One of the hydrogen bonds is observed in the same plane as the accepting IZN molecule, with the second occurring out of plane with the accepting IZN molecule. These interactions are illustrated in figure 1.23 (left). The chains are further connected to each other by a second hydrogen bond between the N2-H amide bond and the terminal amine nitrogen, N2-H···N3. This interaction is illustrated in the image in figure 1.23 (right).

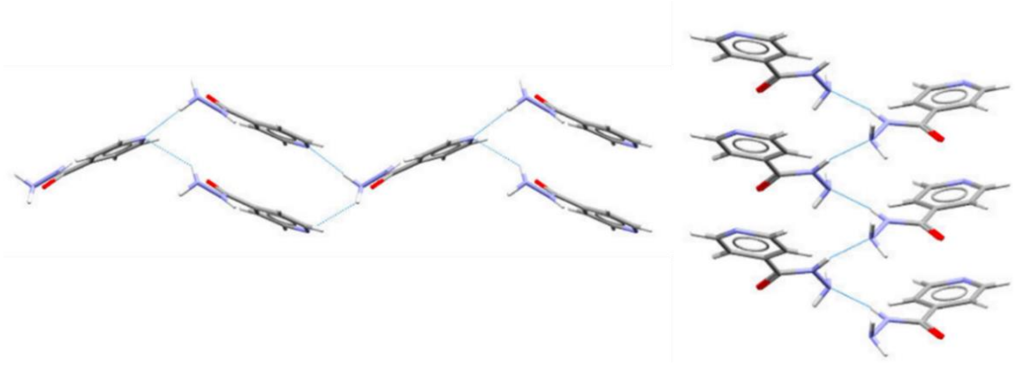

Figure 1.23. Hydrogen bonds present in IZN (INICAC02) crystal structure

Table 1.2. Hydrogen bond distances and angles for IZN form I crystal structure

D-H··A	d(D-H) (Å)	d(H··A) (Å)	d(D··A) (Å)	>(DHA) (°)
N3-H1··N1	0.92(2)	2.14(2)	3.046(2)	172(2)
N3-H2··N1	0.89(2)	2.58(2)	3.157(2)	123(2)
N2-H··N3	0.90(2)	2.05(2)	2.919(2)	163(2)

IZN most commonly crystallises in a needle morphology. As this tends to be unfavourable in the pharmaceutical industry it is a good target molecule for research into morphological modification. The BFDH morphology prediction tool in Mercury predicts an elongated crystal shape (figure 1.24), partially agreeing with the experimentally determined needles. The BFDH morphology seems to suggest a more rod-shaped crystal, despite the elongation being observed.

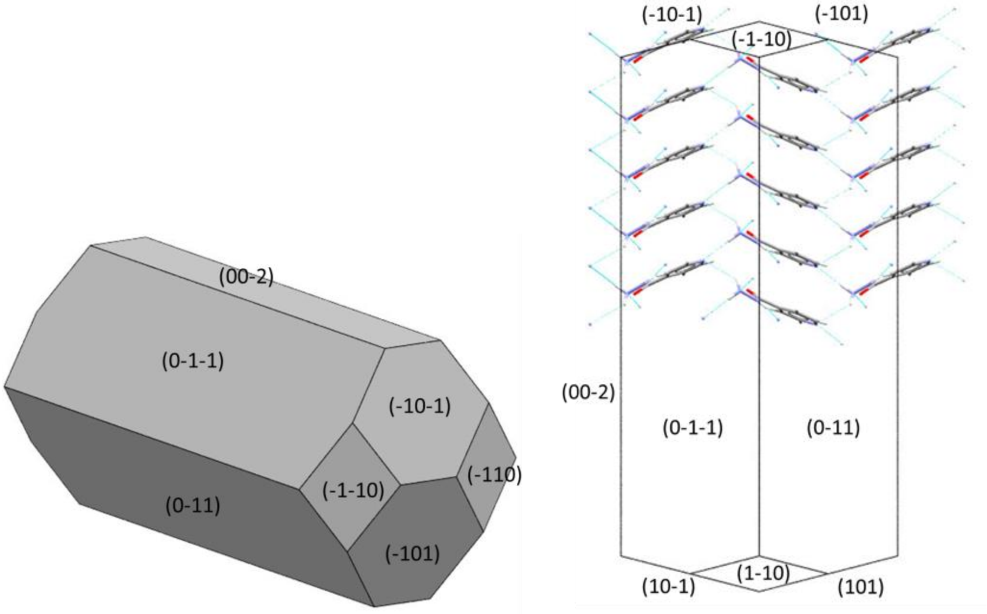

Figure 1.24. BFDH predicted morphology of IZN (INICAC02) (left) and associated packing (right)

In this calculated morphology there are four fast growing faces which lie close to perpendicular to the *a* axis ((101), (110), (1-10) and (10-1)). This results in elongation of the slow growing faces parallel to the crystallographic *a* axis. This suggests the more dominant hydrogen bonds are those between the amine N3-H bond and the N1 in the pyridine ring as they allow growth to occur parallel to the *a* axis. The elongation could also be rationalised as a result of π-stacking of the pyridine rings, these stack along the *a* axis (perpendicular to the slow growing faces) and are likely the dominant growth factor (figure 1.24; right). Carefully choosing an additive or solvent system that can interrupt these favourable interactions and slow the growth of the four fast growing faces could result in less elongation and a more equant morphology.

Crystals of the IZN starting material were also face indexed experimentally. Using the BFDH function in Mercury a schematic of the crystal was generated from this face-indexing (figure 1.25). Similarities to the predicted morphology are clear and the packing remains the same.

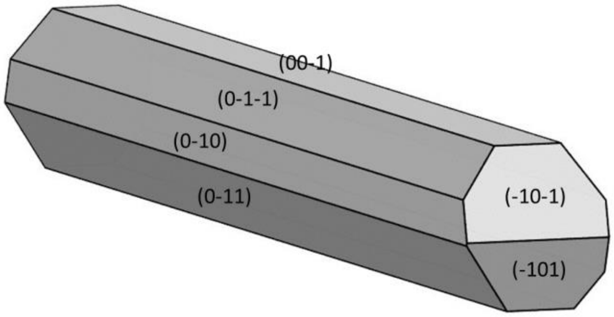

Figure 1.25. BFDH morphology schematic of IZN obtained from Sigma Aldrich, generated from face-indexing.

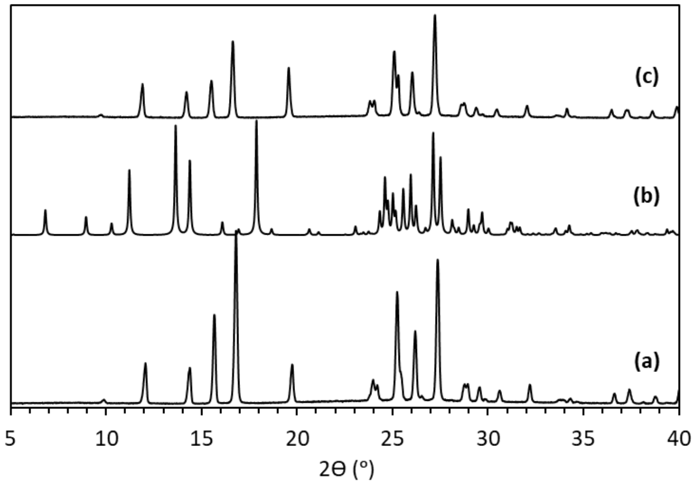

Figure 1.26. PXRD patterns of IZN: (a) form I calculated from SCXRD data (INICAC02), (b) form II calculated from SCXRD data (INICAC04) and (c) measured IZN starting material

Comparison of the calculated PXRD pattern with those of the thermodynamic form I of IZN and metastable form II, generated from the known SCXRD structure, to a measured pattern of IZN purchased from Sigma Aldrich confirms the purchased sample as pure form I; the patterns match well (figure 1.26). Form III has not been included as no structure solution has been achieved for this polymorph and therefore a PXRD pattern cannot be calculated. In future PXRD analyses discussed in this work, only the form I pattern will be used for analysis due to the highly unstable nature of the other two polymorphic forms.

The IZN material was also characterised using DSC. The trace achieved shows a sharp endothermic peak at 171 ^{0}C, which corresponds well to the literature value for the melting point of IZN; 170-

174 ^oC (figure 1.27).[163] The absence of other peaks in the trace and sharpness of the IZN melt peak also confirm the purity of the material purchased.

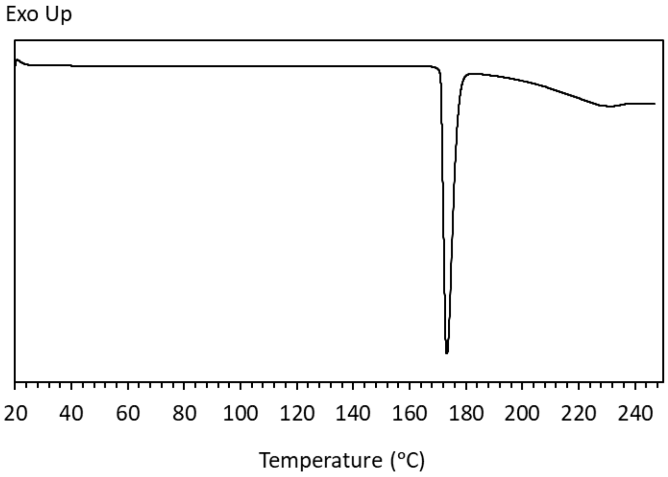

Figure 1.27. DSC trace of IZN material obtained from Sigma Aldrich

The solubility of IZN was determined in water (H_2O), ethanol (EtOH), propan-2-ol (IPA) and ethyl acetate (EtOAc) using observation methods (figure 1.28).

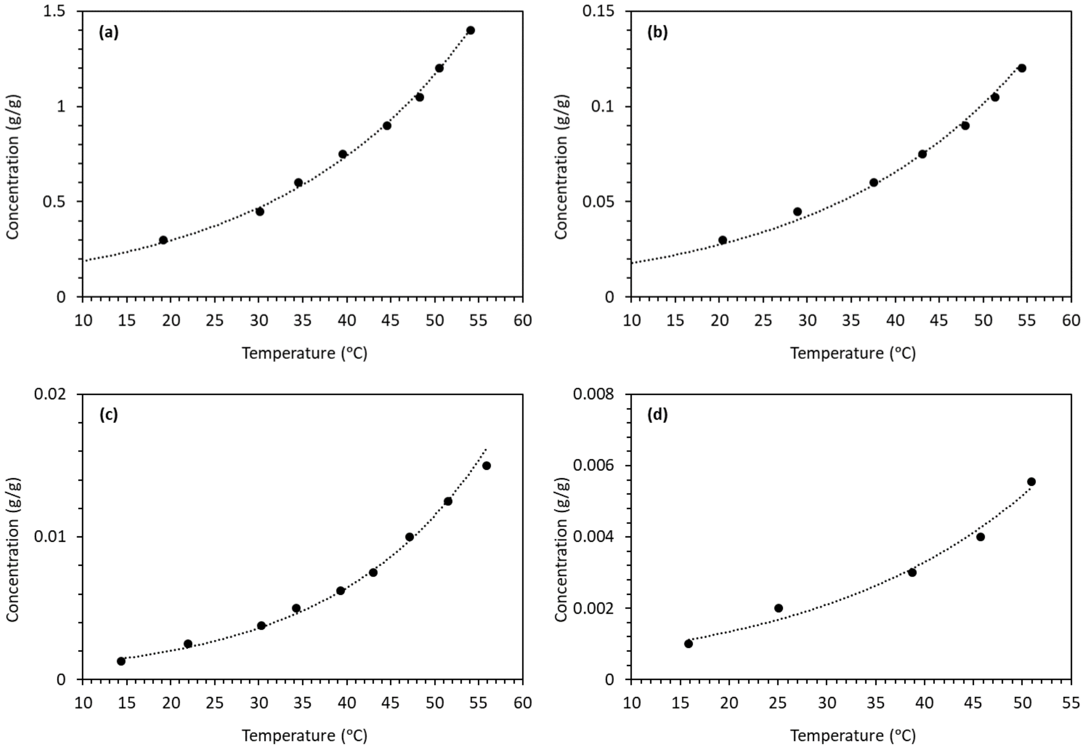

Figure 1.28. Solubility curves for IZN: Crystallised from (a) H_2O, (b) EtOH, (c) IPA and (d) EtOAc

1.8.2 Pyridoxine (PYR)

Pyridoxine (PYR) is one of six related components that make up vitamin B6. This vitamin functions in the body as a co-enzyme for the metabolism of amino acids, glycogen and sphingoid bases.[164] PYR is often prescribed alongside IZN to counteract some side effects associated with taking IZN. For example, it is knowns to prevent peripheral neuropathy associated with prolonged exposure to IZN and can also reduce other IZN toxicities. As a result, PYR is recommended to those in high risk groups and those being prescribed IZN for extended periods of time. In some cases, it is included in the FDC tablet, due to difficulties procuring and distributing the vitamin separately in some countries.[165]

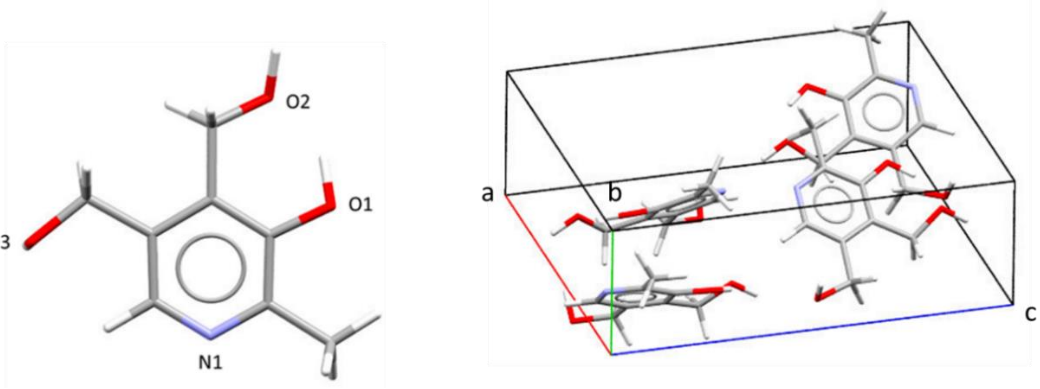

Figure 1.29. Labelled PYR molecule (left) and unit cell projection for PYR (BITZAF) (right)

Like IZN, PYR has no reported polymorphs, hydrates or solvates. The only reported structure for PYR crystallises in the orthorhombic Pna2_1 space group (figure 1.29). A zig-zag pattern is seen in the packing of the PYR crystal with the aromatic rings of the molecules stacking on top of one another creating layers (figure 1.30).

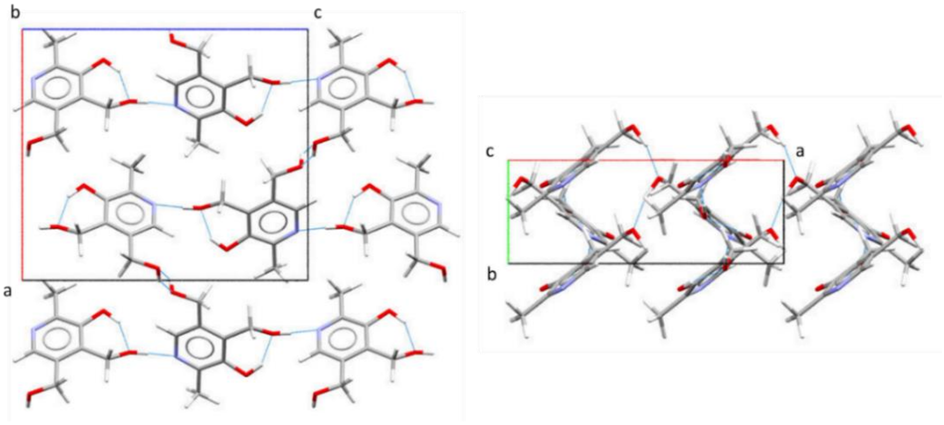

Figure 1.30. Packing in PYR (BITZAF) crystal

In this structure there are three intermolecular hydrogen bonds and one intramolecular interaction (table 1.3). The intramolecular interaction is between two terminal OH groups, donating from O1-H to O2, following the second general rule for hydrogen bonding: '*six membered intramolecular hydrogen bonds form in preference to intermolecular interactions*'.[126] An intermolecular hydrogen bond is seen to the N in the pyridine ring; donation occurs from O2-H to N1 acceptor in a second PYR molecule. The final oxygen, O3, acts as both an acceptor and a donor, forming hydrogen bonds to two different PYR molecules. O3 accepts a hydrogen bond donation from an O3-H on second PYR molecule and simultaneously is involved in the same hydrogen bond donation to a third PYR molecule (figure 1.31).

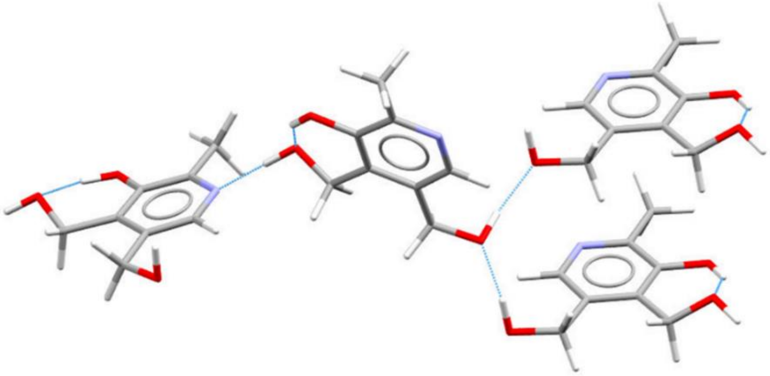

Figure 1.31. Hydrogen bonds present in PYR (BITZAF) crystal structure

Table 1.3. Hydrogen bond distances and angles in PYR crystal structure [i]

D-H··A	d(D-H) (Å)	d(H··A) (Å)	d(D··A) (Å)	>(DHA) (°)
O1-H··O2	0.96	1.73	2.58	147
O2-H··N1	0.99	1.74	2.73	177
O3-H··O3	0.99	1.75	2.70	157

Commonly, the resulting PYR crystals appear to have a needle morphology. Due to this morphology being unfavourable in the pharmaceutical industry, it is another good target molecule for research into morphological modification. The BFDH morphology prediction tool in Mercury predicts an elongated crystal shape (figure 1.32). This partially agrees with the experimentally observed needles, however, the prediction suggests a fatter rod-shaped crystal than achieved experimentally.

---

[i] Hydrogen bonding distances and angles are taken from published data (BITZAF). No errors are associated with the published data so could not be quoted in this table

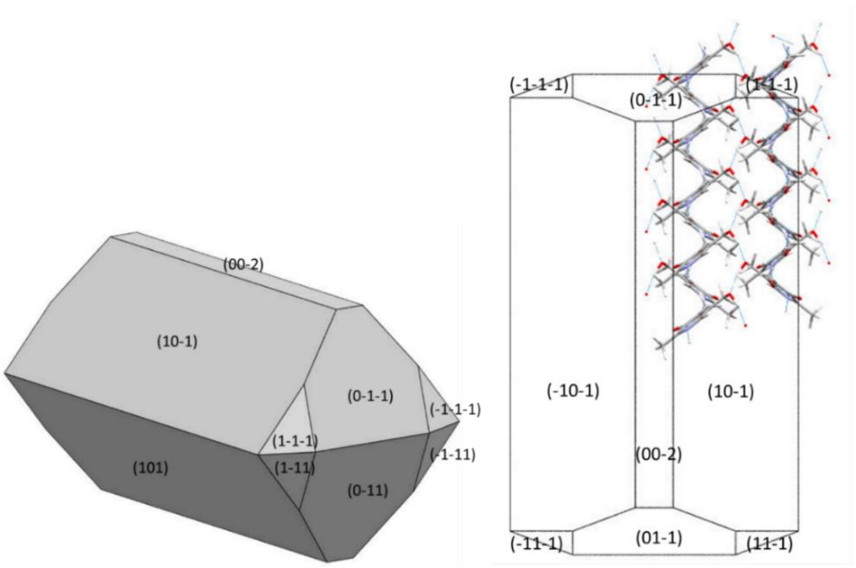

Figure 1.32. BFDH predicted morphology for PYR (BITZAF) (left) and associated packing (right)

In this calculated morphology there are six fast growing faces which lie almost parallel to the *a* axis ((0-1-1), (0-11), (1-1-1), (1-11), (-1-1-1) and (-1-11)). The fast growth observed on these faces results in the elongation observed for the slower growing faces surrounding the needle crystal, parallel to the crystallographic *b* axis. The hydrogen bonds contribute to growth in this direction, indirectly, due to the angled nature of the interactions. The elongation is most likely to be the direct result of the π-π interactions arising from the stacking of the aromatic rings (figure 1.32, right). These stack along the crystallographic *b* axis contributing to the fast growing faces. This is likely the dominant growth factor. Choosing an additive or solvent system that can effectively interrupt these favourable interactions, slowing the growth of the fast growing faces, could ultimately influence the overall morphology and create a more equant shape.

The starting material could not be face indexed due to the very thin, delicate nature of the needles.

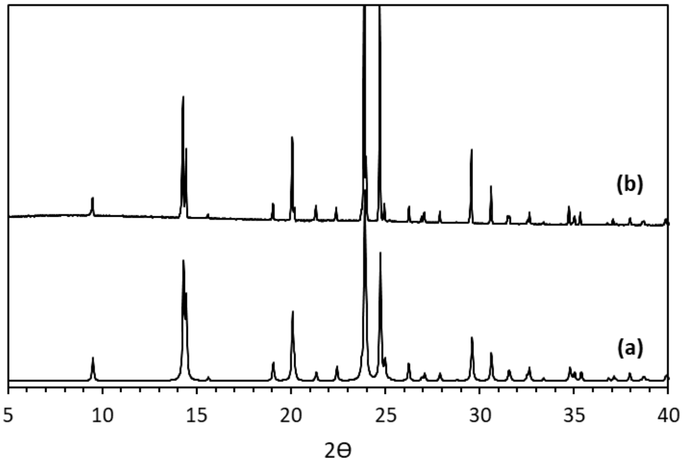

Figure 1.33. PXRD data for PYR: (a) calculated from SCXRD data (BITZAF) and (b) measured PYR starting material

The purity of the starting material, obtained from Sigma Aldrich, was determine by comparison of the calculated PXRD pattern, generated from the known SCXRD structure, to a measured PYR pattern; these match well (figure 1.33).

DSC characterisation of the starting material was also carried out. A sharp endothermic peak is observed at about 154 ^{o}C (figure 1.34). This agrees fairly well with the literature melting point for PYR, quoted as 159 ^{o}C.[166] The slight depression in melting point could be an indication of the presence of impurities, with these often causing the melting point of a solid to be lowered. The sharpness of the peak can indicate a high level of purity, and the absence of any further peaks confirms this. There is a small endothermic event shortly after the melting peak. This is likely to represent some decomposition of the sample once melting has occurred.

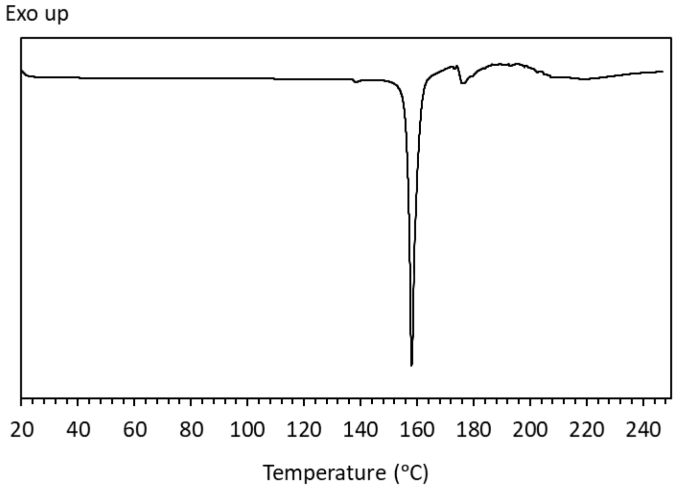

Figure 1.34. DSC trace for PYR starting material obtained from Sigma Aldrich

The solubility of PYR was determined in H_2O, EtOH and IPA using observation methods (figure 1.35).

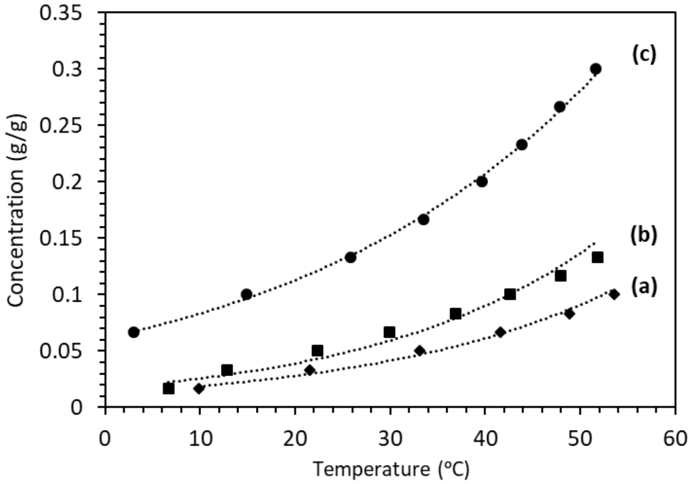

Figure 1.35. Solubility curves for PYR. Crystallised from (a) IPA, (b) EtOH and (c) H_2O

Chapter 2 Analytical methods

A range of analytical techniques were used in this research to characterise the structure and properties of the solid products produced from crystallisation experiments. These included a range of microscopy, thermal and crystallographic techniques.

2.1 Crystallography

2.1.1 Crystalline state

A crystalline solid comprises of constituent atoms, ions or molecules arranged in a precisely regular way repeated in all directions.[4, 167, 168] The official IUPAC definition of crystallinity is '*the presence of three-dimensional order on the level of atomic dimensions'*.[131] Perfectly crystalline materials consist of large numbers of identical molecules, or collection of a few molecules, arranged in this way, representing a form of symmetry known as translation, a fundamental characteristic of crystalline solids. Crystals demonstrate this translational symmetry in three dimensions.

Crystal structures can be described by combining the contents of one repeat unit with the way in which the defined unit is repeated by translation. By representing each molecule within the regular repeat unit as a single point, a pattern can be generated whereby each point is surrounded by the same environment: a regular infinite array of points in three dimensions results. This three dimensional array is known as a lattice, and the points as lattice points.[167] Whilst the lattice evidently shows the repeating nature of the structure, it gives no information about the contents of the repeat unit. Defining the repeat unit of a structure requires a parallelepiped to be drawn between eight chosen lattice points, giving rise to a unit cell (figure 2.1).[169] Many different possibilities are available to define the unit cell, however, at least one possible unit cell exists where the cell edges are the three shortest non-coplanar vectors of the lattice: generally, the unit cell with the highest internal symmetry and, therefore, the smallest repeating unit possible is chosen when defining the unit cell; this is known as the reduced cell. In three-dimensions a unit cell has three defined edges (a, b, c) and three defined angles (α, β, γ). The arrangement is such that angle α lies between edges b and c, i.e. opposite side a, and similarly for β and γ.

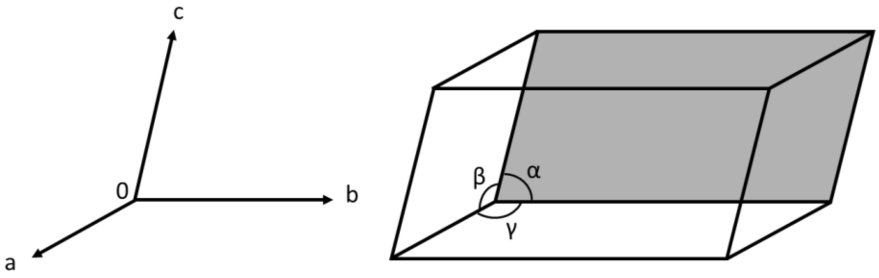

Figure 2.1. Unit cell defined by lengths (a, b, c) and angles (α, β, γ). The molecular components that comprise the crystal are contained within the unit cell.

Four lattice types exist for three-dimensional crystal structures; primitive (P), body centred (I), face centred (F) and centred (C) (figure 2.2). The type of lattice defined for a crystal system depends on the position of the lattice points within the unit cell. The simplest arrangement exists in the P type lattice, with only one lattice point; therefore, the only translational symmetry is that of the unit cell itself. The other three lattice types contain extra lattice points within the unit cell volume and, as a result, have additional translational symmetry within the unit cell.[170]

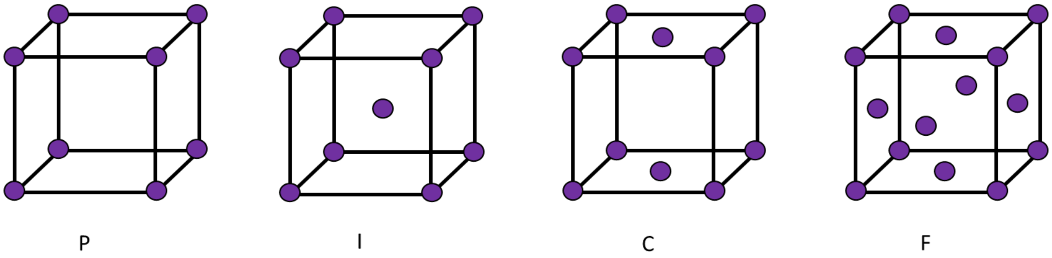

Figure 2.2. The four lattice types. P = primitive, I = body-centred, C = centred and F = face-centred

By introducing further symmetry elements, such as rotation and reflection, restrictions are applied to crystal structures giving rise to seven crystal systems.[167, 169] By combining the four lattice types with the seven crystal systems, fourteen Bravais lattices are formed (table 2.1). For all crystal structures, the unit cell determined will belong to one of the fourteen Bravais lattices.

Table 2.1. Seven crystal systems, their unit cell restrictions and the distribution of lattice types

Crystal System	**Unit cell parameters**	**Bravais Lattice**
Cubic	a=b=c, α=β=λ=90º	P, I, F
Hexagonal	a=b≠c, α=β=90º λ=120º	P
Trigonal	a=b≠c, α=β=90º λ=120º	P
Tetragonal	a=b≠c, α=β=λ=90º	P, I
Orthorhombic	a≠b≠c, α=β=λ=90º	P, I, C, F
Monoclinic	a≠b≠c, α=λ=90º β≠90º	P, C
Triclinic	a≠b≠c, α≠β≠λ≠90º	P

2.1.2 Molecular symmetry

Further symmetry operations can be applied within the unit cell to reduce it further to smaller symmetry-equivalent objects;[168] the smallest such unit is known as the asymmetric unit. Individual asymmetric units are related to one another by a set combination of symmetry operations, the outcome of which generates the unit cell contents, which when translated in three directions produces the full crystal structure. The asymmetric unit can consist of a fraction of a molecule, a whole molecule or more than one molecule depending on the symmetry present within the molecule in question.[167] There are a total of six different symmetry elements possible within the unit cell (figure 2.3), which can be split into two categories; translational and non-translational symmetry. There are four different types of non-translational symmetry; rotation (symbol = order of rotation), reflection across a mirror plane (symbol = m), inversion at a point (symbol = ◦) and rotation-inversion about an axis (symbol = order of rotation with “bar”). A translational symmetry element, as the name suggests, also includes a translation of the asymmetric unit. Two types of translational symmetry exist; glide planes and screw axes. A glide plane combines a translation and a mirror plane parallel to the translation axis. A screw axis combines a translation and a rotation around the translation axis.[171]

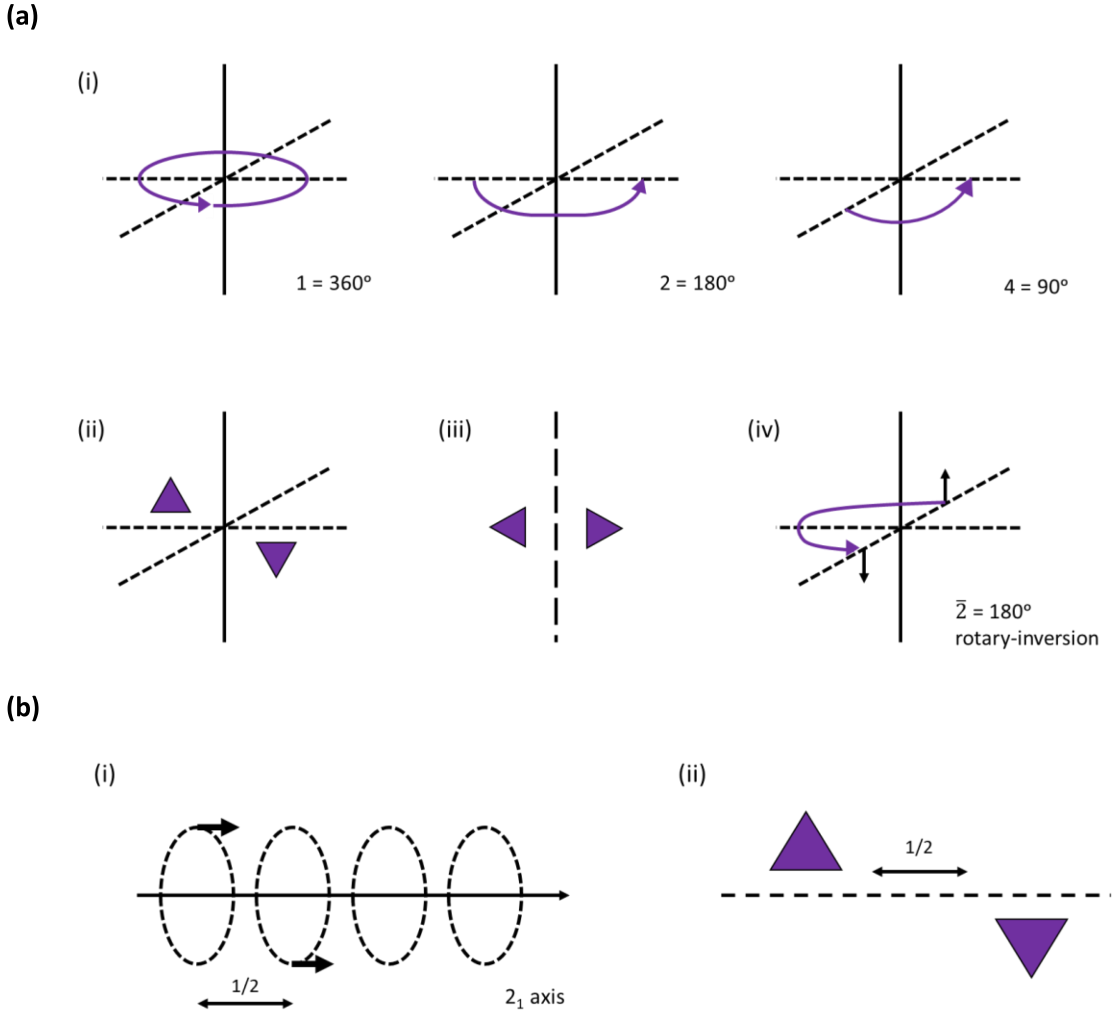

Figure 2.3. Pictorial representations of (a) non-translational symmetry elements: (i) rotation, (ii) inversion, (iii) reflection and (iv) rotary-inversion. (b) translational symmetry elements: (i) screw-axis and (ii) glide plane.

All of the crystal systems highlighted in table 2.1, except triclinic which imposes no restrictions, require a combination of essential symmetry elements in order to be generated correctly. Combining the essential symmetry elements of a crystal and its Bravais lattice type produces a space group for the structure.[172] The limited number of possible combinations of the six symmetry elements and the 14 Bravais lattice types generates a finite number of space groups; only 230 possible combinations exist. Space group symmetry describes all the symmetry operations necessary to generate the crystal from the initial asymmetric unit.[171]

2.1.3 X-ray diffraction

As stated above, crystalline solids are the result of a regular arrangement of atoms, molecules or ions that extends over three dimensions. This regularity enables crystalline structures to diffract X-rays and produce regular patterns interpretable using mathematical processes. The use of X-rays can provide an abundance of structural information; interatomic distances in molecules are comparable to the wavelength associated with X-rays. Commonly, copper and molybdenum X-ray target materials are used in lab X-ray diffraction experiments with characteristic wavelengths of 1.5418 Å and 0.71073 Å respectively.[167]

2.1.4 Bragg's Law

The regular arrangement of atoms in a crystal means the structure contains long range order, giving rise to parallel sets of planes present throughout. W. L. Bragg noted that diffraction could be interpreted as reflection from these sets of planes; the Bragg equations, or Bragg's law, describe diffraction in this way. These parallel planes within a crystal are known as Miller planes and assigned indices, a set of three integers, (*h k l*) which describe where a particular plane intercepts along the lattice vector. The (*h k l*) planes are separated by distances of d_{hkl}.[173]

When a crystal is exposed to a beam of X-rays, the electrons associated with each atom scatter the X-rays in all directions. The diffracted beams can undergo constructive and destructive interference; the occurrence of constructive interference is the consequence of crystal orientation and geometry. X-ray diffraction from adjacent planes must give rise to constructive interference for the reflection to be observed. The derivation of Bragg's law can be seen in figure 2.4. The view seen in the schematic shows the edge of a set of planes, horizontal lines, separated by distance d_{hkl}. The incoming X-ray beams are in phase. To achieve constructive interference, the diffracted waves must exit the crystal in phase with one another. For this to be possible, the path difference travelled by the waves must be equal to a whole number of wavelengths (equations 2.1 & 2.2):

$$AB + BC = n\lambda \qquad \text{Equation 2.1}$$

$$AB = BC \therefore 2(AB) = n\lambda \qquad \text{Equation 2.2}$$

Using basic trigonometry, it can be seen that:

$$AB = d_{hkl} sin\theta \qquad \text{Equation 2.3}$$

Therefore, the conditions under which constructive interference occurs and a reflection is observed is defined by Bragg's law:

$$n\lambda = 2d_{hkl}sin\Theta \qquad \text{Equation 2.4}$$

n denotes an integer value, λ refers to the wavelength of the X-ray beam and d_{hkl} corresponds to the distance between two planes in the same Miller set.[173]

If the incident X-ray wavelength satisfies the equation a diffraction spot will be observed (figure 2.4).

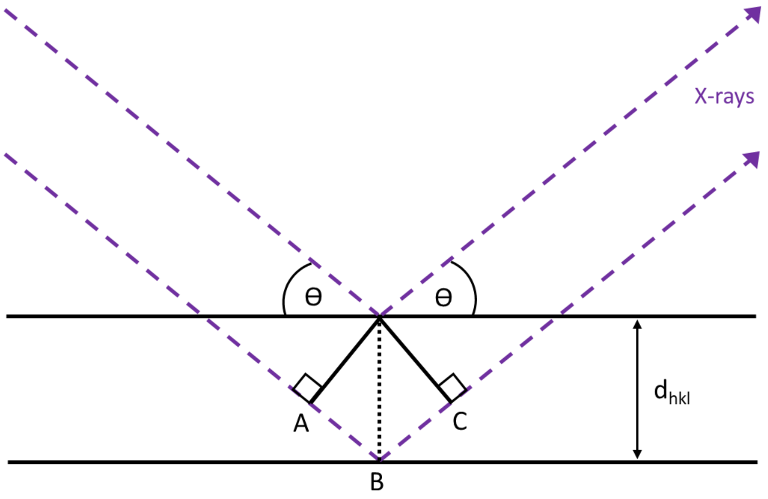

Figure 2.4. Schematic of Bragg's law. X-ray diffraction shown between parallel Miller planes (hkl) separated by a distance d_{hkl}

2.1.5 Diffraction patterns and reciprocal space

Due to the regularity of crystal structures, the diffraction patterns produced consist of an array of bright spots (Bragg reflections) that occur where Bragg's law is satisfied and possess a degree of symmetry and a definite geometry that reflect the underlying lattice structure. The crystal structure and diffraction pattern are related through the mathematical procedure of Fourier transformation. The diffraction pattern exists in 'reciprocal space', representing the 'reciprocal lattice' and has an inversely proportional relationship with the 'direct lattice' of the crystal in 'direct space'.[173]

Bragg's law can be rearranged to show that the distance d_{hkl} is inversely proportional to sinΘ:

$$\sin\theta = \frac{\lambda}{2} \times \frac{1}{d_{hkl}} \qquad \text{Equation 2.5}$$

The dimension of reciprocal space is, therefore, $\frac{1}{d_{hkl}}$. The mathematical relationship between reciprocal and direct space is well understood and Fourier transform calculations are used to reconstruct the crystal electron density from its diffraction pattern.[167, 174]

2.1.6 Scattering factors

Bragg's law does not give any information about the intensity of reflections observed in a diffraction experiment. A relationship exists between the number of electrons and the scattering observed. Therefore, the interaction between X-rays and electron clouds is characteristic of a particular element, due to the different numbers of electrons present in their electron clouds. As such, the ability of a neutral atom to scatter electrons, known as atomic scattering factor (f_j), is dependent on the element present. At low Bragg angles, the ability of an atom to scatter electrons is proportional to the number of electrons in the electron cloud. However, X-rays scatter from the extended electron cloud, thus at higher angles the path length difference between X-rays scattered from different parts of that extended scattering object will increase. As these shifts observed between different beams are larger at higher angles, a greater chance exists of destructive interference. Consequently, the scattering ability of the electrons drops off when reaching higher Bragg angles.[167] Scattering curves (figure 2.5) can be used to illustrate the change in diffraction intensity as a function of diffraction angle. Information on atomic scattering factors is obtained from quantum mechanical calculations and is often built into crystallographic software packages for commonly used wavelengths.[175]

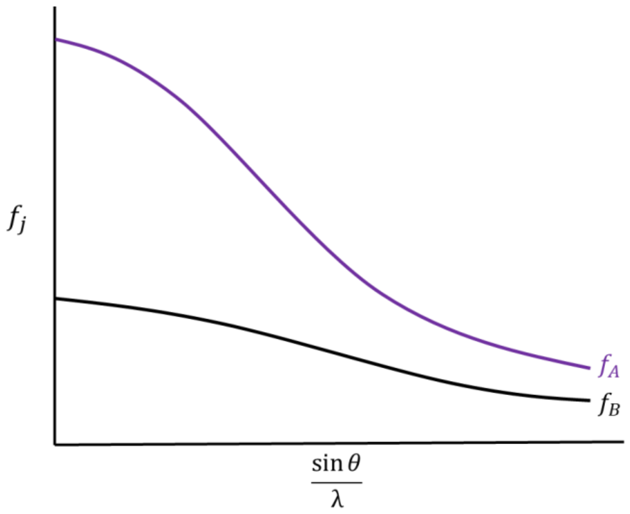

Figure 2.5. Representation of X-ray scattering factors f_j for atoms A and B.

2.1.7 Data collection

The combination of diffraction from a crystalline array of weakly diffracting molecules gives the detectable scattered intensity measured in a diffraction experiment. Scattering from different atoms in the structure have different individual contributions to the intensity of a particular Bragg intensity; the scattering power of a plane can be represented by the structure factor (F_{hkl}; equation 2.6). Structure factors contain information on Miller plane sets and the position and types of all atoms contained in the unit cell. As each F_{hkl} represents one set of Miller planes, measurement of a full set of reflections (complete diffraction pattern) is needed to achieve the most complete description of the structure; every reflection contains some information about the structure being probed.[175, 176]

$$F_{hkl} = \sum_{j=1}^{j=n} f_j \exp[2\pi i(hx + ky + lz)] \qquad \text{Equation 2.6}$$

Structure factors are complex numbers. Two numerical values are associated with each reflection in a diffraction pattern; the amplitude ($|F_{hkl}|$) and the phase (ϕ_{hkl}))(equation 2.7).[167]

$$F_{hkl} = |F_{hkl}| \exp(i\ \phi_{hkl}) \qquad \text{Equation 2.7}$$

During a SCXRD data collection the intensities (I_{hkl}) of the diffracted beams from each Miller plane set are measured. The amplitudes $|F_{hkl}|$ can be found using experimentally determined intensities by the relationship $|F_{hkl}|^2 \propto I_{hkl}$.[176] If the structure factors are fully determined, then performing an inverse Fourier transform, the electron density map can be constructed (equation 2.8). Electron density is expressed in units of electrons per cubic angstrom (e Å^{-3}). Analysis of an electron density map results in the location of all atoms at positions (x, y, z) within the unit cell.[175]

$$\rho_{xyz} = \frac{1}{V} \sum_h \sum_k \sum_l |F_{hkl}|\ \exp[-2\pi i(hx + ky + lz)] \qquad \text{Equation 2.8}$$

Equations 2.6 and 2.8 link the atomic positions to the electron density *via* the structure factor. However, phase information for different reflections cannot be recovered directly from the experimental data collected. Thus, for an unknown structure, it is not possible to simply calculate the electron density once the diffraction pattern has been recorded, due to this loss of phase information.[167, 175, 176] This is widely known as the phase problem.

2.1.8 Structure solution

The phase problem must be overcome before structure solution can be achieved; it is necessary to determine the phases, which can be done in a number of ways. The most common of these are Direct methods, Patterson methods and charge flipping.[177, 178]

2.1.8.1 Direct methods

The aim of Direct methods is to determine phases without any prior knowledge of the structure or information on crystal composition. This method is most often used for small molecule crystallography, including purely organic molecules or those containing only light atoms.

The method is based on statistical relations between the measured structure factors, whereby generation of possible electron density maps – and hence atomic coordinates – is attempted by mathematical approaches using a single set of X-ray intensities.[179] To solve the phase problem, mathematical relations between the experimental structure factor amplitudes and their phases are used. These give a set of probabilistic terms expressing relationships between sets of phases. The simplest of these relationships is the triplet relationship. A triplet is a set of three structure factors, such as $E(h)$, $E(k)$ and $E(h-k)$, whose related phases satisfy the probability relationship: [179, 180]

$$\phi(h) \approx \phi(k) + \phi(h-k) \qquad \text{Equation 2.9}$$

A higher probability of these conditions being satisfied occur for larger values of $|E_{hkl}|$. In automated Direct methods programs, a multi-solution permutation approach amongst the stronger reflections is adopted. Random sets of initial phases are assigned to a small starting set of reflections then triplets and higher order relationships are used to generate a set of possible solutions for the estimated phases of a wider set of structure factors. This in turn generates a set of potential electron density maps, from which the crystal structure can be solved.[179, 181]

2.1.8.2 Patterson methods

This method is an older technique, relying on the knowledge of a few atom positions. This method is utilised, in the majority, to solve structures containing a few heavy metal atoms, for example in coordination complexes, or when a substantial portion of a structure is expected to be well-defined and rigid.[180] Patterson synthesis generates a map of interatomic vectors; the peaks are proportional to the square of the atomic number of the atoms giving rise to them. This makes it easy to identify peaks due to vectors between heavy atoms.[182, 183] By using the known symmetry relations, the positions of these heavier atoms can be determined and structure factor phases calculated based on these known heavy atom coordinates, which are generally sufficiently accurate set to allow structure solution.[181]

2.1.8.3 Dual-space iterative methods

With the increase in availability of cheap computer power, new methods have been developed that are conceptually similar to the classical methods, with a requirement for more computation. Whilst these extensions to traditional methods exist, a new class of methods has also been developed, known as dual-space iterative methods.[184] These techniques are based on iterative modification of an image both in direct and reciprocal space. An example of dual-spaced iterative methods is charge-flipping; the use of alternating modifications in direct and reciprocal space to find a solution to the phase problem.[185] This dual-space algorithm is used in the computer software ShelXT to solve the phase problem observed in single-crystal reflection data.[178] Applications of this method can range beyond the standard structure solution. For example, it is possible to solve the structure of quasicrystals and crystals with incommensurately modulated structures. The combination of charge flipping with histogram matching, a density modification technique, can also allow the solution of complex structures to be obtained from powder diffraction patterns. Structures can also be solved from neutron scattering experiments using a band flipping variant of this method.[184]

2.1.9 Structure completion and refinement

Structural solution processes produce a reconstruction of the average electron density. This reconstruction is not the direct result of the diffraction experiment but uses the observed structure factor magnitudes with the initial phases calculated in the structure solution step.[186] From this, most structural solution programs will be able to output an approximate ‘trial structure’, if provided some information on the expected crystal composition. With this prior knowledge the atomic positions in the first trial structure can be assigned, however, the structure is often incomplete, and a series of calculations is carried out. Electron density maps are calculated from the known atoms to generate improved sets of phases, and hence improved maps, that will reveal more atoms until all heavier atoms (and often many of the hydrogen atoms) are located. This “Fourier recycling” process is carried out automatically in structure solution programs, usually in combination with refinements of the known atomic parameters.

A refinement process is then required to optimise the parameters of the trial model, ultimately achieving the best fit between the observed and calculated data.[187]

A number of important 'refinable parameters' require adjusting in order to improve the fit of the model, including: scale factor; isotropic or anisotropic displacement parameters; atomic site occupancies; and, most importantly, the fractional coordinates of individual atoms.[187, 188]

2.1.9.1 Least-squares refinement method

The aim of crystal structure refinement is to find the best model of the crystal structure, determining parameter values which give the best fit to the data collected and estimating the uncertainty of these parameters.[189] In most 'small-molecule' structure determinations, the refinement method used is called 'least-squares' refinement. This procedure involves the minimisation of the function

$$M = \sum w \ (Y_O - Y_C)^2 \qquad \text{Equation 2.10}$$

Where Y_O = the strength of an observed reflection (in terms of either F_O, F_O^2 or I), Y_C = the calculated value for the reflection based on the current model (either in terms of F_C or F_C^2) and w = an assigned weight which reflects the confidence in this particular data point.[187] The weight term is derived from the standard uncertainty of the measurement; frequently $w = 1/\sigma$.[186] The minimisation of M should result in optimal values for parameters, and their standard deviations σ, for that structural model. It is possible to carry out this minimisation by refining the model against either F_O, F_O^2 or I; refinement against F^2 is most commonly used.[186]

In order to improve the fit of the model it is possible to either increase or decrease the number of refinable parameters being dealt with. This is achieved by introducing constraints and restraints to the refinement model. Constraints are introduced to reduce the number or refinable parameters, which can be particularly useful when the quality of the data is poor. Constraints reduce the number of parameters by either expressing one parameter in terms of others, or by predetermining and fixing its value, removing the need to refine it.[187] One example is the position of hydrogen atoms within a structure. A constraint can be used to fix the bonding angles and distances of hydrogen atoms bonded to non-hydrogen atoms, treating them as a rigid group. This is known as the 'riding model' and results in hydrogen atoms moving with the atoms they are bonded to during refinement. Restraints can also be introduced; these are considered as additional experimental observations, helping include further chemical or physical information about a molecule into the refinement process. Examples include specifying bond lengths or angles, based on knowledge of similar structures, or fixing the planarity of aromatic groups using the knowledge they tend to be flat. Thus, using restraints indirectly increases the number of data points to refine against.[186, 187] As with constraints, the use of restraints can be advantageous when the data is poor, resulting in an unreasonable model.[189]

2.1.9.2 R-Factors

Least-squares refinement is an iterative process, cycling through recalculations of the model to improve the fit between the experimental and calculated diffraction patterns, proceeding towards convergence. The quality of a model is judged using calculated residual factors, or ‘R-factors’.[186] R-factors reduce in magnitude as the agreement between measurements and the parameterised model improves; a good refinement will have a low R factor.[181, 189] The ‘conventional’ R-factor (equation 2.11) is calculated during each refinement cycle, providing an assessment of the agreement of calculated structure factors with those determined experimentally.

$$R = \frac{\sum |F_o - F_c|}{\sum |F_o|} \qquad \text{Equation 2.11}$$

The final calculated R-factor is used to assess the quality of the final model, and is most often quoted in publications due to it almost always giving the lowest value.[189] A weighted R-factor, which is most closely related to refinement against F^2 values, can also be calculated:

$$wR = \sqrt{\left[\frac{\sum|w|(|F_o|^2 - |F_c|^2)^2}{\sum w|F_o|^2}\right]} \qquad \text{Equation 2.12}$$

This residual factor provides better comparisons for testing the significance of adding or removing parameters from the refinement; often the value is higher but statistically more valid. It is frequently used to monitor the progress of refinements.[186, 189]

2.1.9.3 Structure completion

It is often difficult to determine when a completed structure is a ‘good structure’. A structure is considered ‘good’ when the final refinement converges on a model that shows good agreement with the experimental data. A number of key values can be used to conclude whether the final structure reached is acceptable. As mentioned, the final R-factor is most frequently used with acceptable values, for small, molecular species, typically below <0.05. The standard uncertainties calculated for refined parameters can also be taken into account; small values indicate a good fit between model and experimental data. Any residual positive peaks present in the electron density map that have not been modelled must be taken into account. Generally, if these peaks are smaller than those calculated for hydrogen atoms the model is assumed to be a good fit. Finally, a good completeness of data must be attained. This requires that the diffraction data collected must cover at least the unique region of reciprocal space to allow the structure to be properly modelled.

2.1.10 Powder X-ray Diffraction (PXRD)

In comparison to the single-crystal analysis just discussed, powder X-ray diffraction techniques (PXRD) utilise a polycrystalline powder sample. Hence, this is considered an important analysis technique due to the difficulty obtaining good quality single crystals for some samples and under certain conditions. This technique also allows the bulk sample to be characterised, as opposed to individual crystals selected for SCXRD. The principles of PXRD are based on the interaction of a monochromatic X-ray beam with a sample capable of diffracting them, similarly to SCXRD. Within the polycrystalline sample all crystallites are orientated differently, with a random distribution. Diffraction peaks are therefore generated for each crystallite when its orientation is able to satisfy Bragg's law; the random distribution of orientations of very many crystallites ensures that the Bragg angle will be met for each reflection. Diffraction for a particular 2Θ value will consist of reflected X-rays occurring in varying directions depending on the crystallite orientations. As a result, cones of reflection are observed (figure 2.6); superimposing the diffraction from each crystallite gives a full diffraction pattern of the sample.[167, 169] The intensity is measured as the detector intersects these cones as it moves through all 2Θ angles, resulting in a plot of intensity verses 2Θ. Due to the random nature of the orientation of the crystallites, information on relative orientations of scattering vectors is lost, resulting in a 1D pattern.[124]

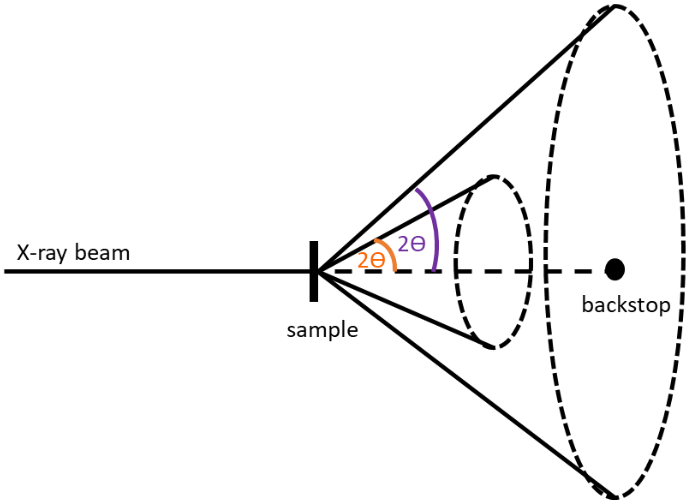

Figure 2.6. Cones of reflection observed when irradiating a polycrystalline sample during a powder X-ray diffraction experiment.

PXRD is a powerful diagnostic technique as the patterns produced are unique to different crystal structures: most importantly for the work presented here, peak positions are determined by the unit cell parameters. This unique nature means the technique can be used as a fingerprinting tool.

As a result, useful applications of PXRD involve the identification of unknown crystalline phases, determination of sample purity and investigating phase changes.[170] Structure solution and refinement is also possible with well-resolved powder diffraction data, using methods such as Rietveld refinement. As the peak positions in a diffraction pattern are determined by unit cell parameters, indexing the data can determine these for a structure. However, this indexation is made difficult, in less well-resolved data, by peak overlap and a low number of uniquely observed peaks. The intensities of peaks reflect the unit cell contents and can be used in structure refinement if very good data are available; this is not used in the research presented here. The intensity of peaks can be affected by other external factors. Preferred orientation effects can increase the intensity of some peaks irrespective of the structure. To mitigate these effects samples are often ground down before analysis and rotated for the duration of the PXRD experiment.[167, 169]

2.2 Thermal analysis

Knowing how different materials act under different temperature environments can be very important. Temperature can affect the stability and activity of materials, which can greatly affect their uses and methods for their production. Thermal analytical methods which measure a physical property, such as weight or the flow of heat energy, as a function or temperature or time are especially valuable for pharmaceutical applications.[190] In most thermal techniques, samples are subjected to a defined temperature program, involving linear heating and cooling. The thermal events that occur can be recorded and interpreted as physical or chemical changes. Thermal analytical techniques detect both exothermic processes, including crystallisation and some phase changes, and endothermic processes, such as melting, desolvation and some phase changes. They can also determine mass changes in a sample, such as during desolvation processes.

2.2.1 Differential Scanning Calorimetry (DSC)

Differential Scanning Calorimetry (DSC) '*measures the energy transferred as heat to or from a sample at constant pressure during a physical or chemical change'*.[191] A sample is measured into a sealed pan and subjected to a program of temperature changes and thermal events recorded. DSC is commonly used to identify the solid form of a sample and recognise the phase transitions that may occur as a function of temperature. There are two different forms of DSC, using different methods to maintain constant temperature between sample and reference during a temperature scan; power compensation and heat flux. During a power compensation DSC experiment, the temperature difference between the sample and the reference is maintained at a constant level.

The difference in power supplied to each to allow this to happen is measured and is proportional to heat flow. In a heat flux DSC, the temperature is allowed to vary slightly and then converted back rapidly by an input of power.

Thermal events are identified by the heat flows required to maintain the reference and sample at the same temperature: thermal events exhibit as a change in heat flow with respect to temperature. For example, in an endothermic event more heat will be required to keep the temperature of the sample increasing at the same rate relative to the empty reference pan. From a DSC plot (figure 2.7) the temperature at which a transition occurs can be determined by the position of endothermic and exothermic peaks and the enthalpy of the associated thermal event can be determined by integration of the area under the peak. Typically, DSC plots are presented as 'exo up' whereby exothermic events are plotted as positive on the graph with endothermic events being negative.

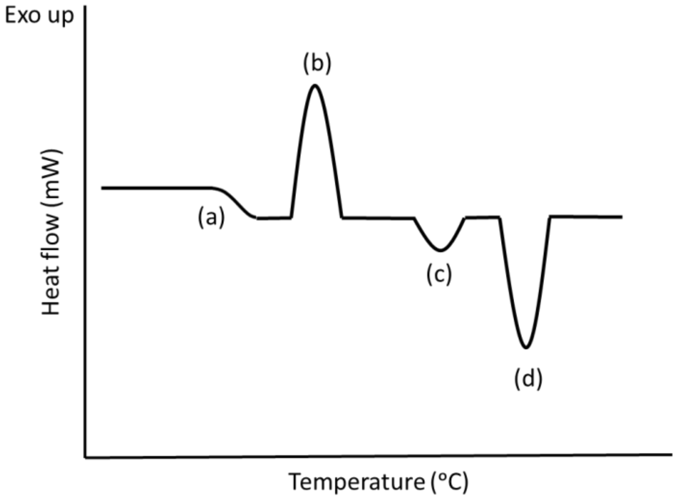

Figure 2.7. DSC schematic showing some commonly observed thermal events in pharmaceutical solids. (a) glass transition, (b) recrystallisation or decomposition, (c) desolvation or phase transition and (d) melting or decomposition.[190]

For pharmaceutical solids, the thermal events observed are often endothermic events. Most commonly melting points of crystalline solids can be determined. This helps identify the solid form achieved and the purity of the sample. Phase transitions, desolvation and dehydration of samples can also be hypothesised from endothermic events. Endothermic events can also correspond to decomposition and sublimation events. In pharmaceutical crystals, exothermic events often correspond to recrystallisation events, for example as the result of the formation of a new polymorphic form. Glass transitions are observed when there is amorphous content in the initial sample. It is not always clear exactly what is causing each peak observed in a DSC trace. As a result, further thermal analysis techniques should be used alongside DSC analysis to fully characterise each thermal event observed.

2.2.2 Thermogravimetric Analysis (TGA)

Thermogravimetric analysis (TGA) is a technique used to measure the change in mass of a sample, as determined by a thermobalance, as a function of temperature and/or time.[190] TGA is useful in determining many physical and chemical properties and is often used to investigate the decomposition of a sample with increasing temperature.[192] In pharmaceutical applications, TGA can be particularly useful in identifying solvate or hydrate samples and determining their stoichiometry. This technique can be coupled with mass spectrometry (TG-MS), allowing the identification of any products of the degradation process. Nitrogen flow into the sample chamber is often used to maintain an inert atmosphere, preventing any chemical reactions occurring during the programmed temperature changes. A known mass of sample is placed in a pan, either ceramic or aluminium, and suspended inside the sample chamber. As the temperature increases at the rate programmed the mass of the sample is recorded. Plots of the percentage mass change verses temperature allow the quantification of thermal events occurring within the sample (figure 2.8).

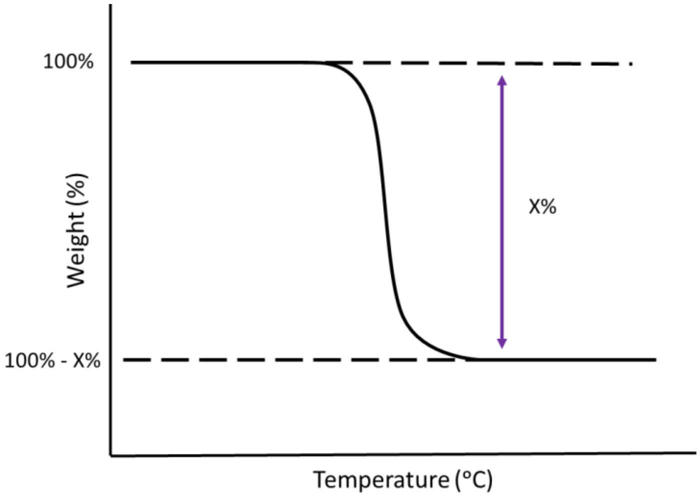

Figure 2.8. Typical TGA graph showing mass loss from a sample

2.2.3 Hot-stage Microscopy (HSM)

Hot-stage microscopy (HSM) uses optical microscopy to monitor a sample during a heating and/or cooling cycle; adding a hot-stage to a microscope allows thermal events to be recorded and visualised. This technique has important advantages to other thermal techniques already discussed: differentiation between thermal events that may exhibit similar energy profiles in other thermal techniques, for example distinguishing between melting and other phase transitions, such as the desolvation of a crystal structure, is possible through visualisation. Coupling this technique with DSC and TGA is particularly useful in aiding the interpretation of thermal events that may be unclear: this visualisation can confirm or contradict any conclusions drawn from a DSC or TGA trace. This method can assist in understanding the behaviour of hydrates, polymorphs and solvates, making it particularly useful in pharmaceutical research.[193] HSM can also be a useful tool when investigating other properties affected by temperature. One such example would be the identification of thermochromic materials which change colour with varying temperature.

2.3 Optical microscopy

Optical microscopy is a useful analytical tool in solid state chemistry. As noted above, this forms part of the HSM technique that is used as a complement to other analytical thermal methods; however, standard optical microscopy is also used. For crystal analysis it is particularly useful to use a microscope with a polarising lens. The polariser acts as a filter and allows light oscillating in only one orientation to pass through the lens. This phenomenon can be used to determine the crystallinity of a sample. Single crystals possess a property known as double refraction, where incoming light is split into different directions with differing speeds. Upon recombination of the light under a polarising microscope interference occurs, forming a black focal plane for the crystal. As a result, single crystals appear to ‘extinguish’ and become dark when the light is rotated. This allows the identification of possible samples for single crystal X-ray diffraction experiments.[194] Optical microscopy can also be useful to examine further properties of crystals, including the morphology, size and colour. In this work, optical microscopy was used mainly to examine the shapes of crystalline products and identify samples that may require further analysis.

2.4 Fourier Transform Infra-red spectroscopy (FTIR)

Infra-red spectroscopy probes molecular vibrations through the absorption of infra-red light by the sample. The percentage transmission is measured as a function of frequency; the transmission will be reduced (producing the characteristic infra-red bands) when strong absorption occurs at particular frequencies. The infra-red light is absorbed by a molecule when the vibrations of the bonds present match the frequency of light being used, allowing the energy to be absorbed through excitation to a higher vibrational energy state. This method allows for the identification of functional groups as specific bonds absorb with characteristic infra-red frequencies.

Most modern infra-red spectrometers use Fourier transform techniques. The infra-red beam in split into two and reflects off two mirrors within the spectrometer. One mirror is fixed in position whilst the second is movable and can be used to alter the path length of the beam, creating a path difference. The two beams are recombined giving an interference pattern, due to the constructive and destructive interference resulting from the path difference. The interference pattern can then be converted to a spectrum using a Fourier transformation. The use of FTIR allows multiple frequencies to be collected simultaneously and also increases the sensitivity of the measurements.[195]

The speed of data collection coupled with the non-destructive nature of the technique makes this a useful analysis technique. In pharmaceutical studies, it can be used to identify and monitor characteristic functional or hydrogen bonded groups, either during crystallisation processes or in product samples, notably allowing polymorphs to be distinguished.

2.5 Nuclear Magnetic Resonance spectroscopy (NMR)

Nuclear magnetic resonance (NMR) is an analysis technique that aids in the determination of the structure of a molecule. Many types of NMR spectroscopy are available, however, for the purpose of the work presented here only proton NMR spectroscopy (^{1}H-NMR spectroscopy) has been used.

NMR spectroscopy is a radiofrequency technique, with proton resonance occurring at about 400 MHz. An NMR spectrometer consists of a magnet producing an intense, uniform field and a radio frequency source. The magnetic field is often provided using an electromagnet or, in more advanced experiments, a superconducting magnet.[196]

In NMR spectroscopy the sample is placed within the strong magnetic field within the spectrometer. Certain nuclei within the sample which have a non-zero nuclear spin (notably including ^{1}H) can act as tiny magnets, aligning with or against the applied magnetic field. The different alignments of the nuclei are known as spin states and will be split in energy in the presence of the external magnetic field. Electromagnetic radiation is then used to irradiate the sample. The radiation is absorbed if it equals the difference in the energy of the spin states of the nuclei present. This absorption promotes the nuclei in the lower energy spin state to the higher energy spin state, producing resonance. The excited nuclei then relax back down to the lower energy state releasing energy. ^{1}H-NMR spectroscopy is a particularly valuable technique as the different protons in molecules will likely experience different magnetic fields, as effects caused by electronic environment close to a proton will result in the local magnetic field being slightly different from the applied field in the spectrometer, resulting in them absorbing different frequencies of the radio wave radiation. These differences (chemical shifts) are detected and give rise to the NMR spectrum; the knowledge gained of the proton environments often allows the molecular structure to de deduced.[197]

For the purposes of the work presented here, ^{1}H-NMR spectroscopy was used for confirmation of expected molecular structures rather than full analysis of unknown molecules.

Chapter 3 Experimental methods and analysis equipment

3.1 Solubility and metastable zone width measurements

Knowledge of the solubility of a material is essential to be able to control solution mediated crystallisation processes. It is also a key physical property that needs to be determined for pharmaceutical molecules in order not only to develop a production process, but also to formulate the final pharmaceutical product. Two methods have been used to determine solubility throughout this research, gravimetric analysis and solubility by observation. It is also important to determine the metastable zone in order to have better control over controlled cooling crystallisation methods. This was determined for some systems using the same observation method used for solubility determination.

3.1.1 Gravimetric solubility determination

Gravimetric solubility is based upon the measurement of mass, relating the mass of a solute dissolved to the mass of the solvent used. Slurries of excess solute are created in a given solvent and placed at different temperature intervals. The slurries are stirred continuously for 48 hours to aid dissolution and allow an equilibrium to be reached and the solvent to become saturated with the solute. Stirring is ceased and the remaining undissolved solute allowed to settle before an amount of solution is removed from the top of the vial, without disturbing the undissolved solute. The solution is decanted into a clean vial of known weight and the weight of solution determined. The solution is then left to completely evaporate, leaving behind any solute that was dissolved in the solvent. By calculating the mass of solution removed from the slurry and the mass of solute remaining after evaporation a solubility data point can be determined (with units of g of solute /g of solvent). Repeating this method for a range of different temperatures allows a solubility curve to be plotted.

The accuracy of this method can be called into question for a number of different reasons. There is the possibility that the solutions, while slurrying, could become supersaturated and as a result skewing the data and overestimating the solubility of the solute. The solubility measurement can also be affected when removing the solution from the vial. There is a high possibility of also removing some undissolved solute particles, exaggerating the mass of solute that could dissolve in the amount of solute. The reverse is also possible with solute dissolved at higher temperatures crashing out of solution when removed due to the change in temperature. This solute may remain behind in the pipette used and therefore an underestimation of the amount of solute that can be dissolved would result. Accuracy can be improved, however, by repeating each temperature measurement multiple times.

Whilst there are some accuracy concerns, this method is a reasonably time efficient way of determining the solubility of a compound.

3.1.2 Solubility and metastable zone width determination via observation

Solubility by observation is arguably a more accurate determination of solubility. The set up uses controlled heating to steadily increase the temperature of the solution. The method relies on observational determination of the clear point temperature of a solution, the point at which all solute dissolves in the solvent. To determine the MSZW the opposite method is used. Controlled cooling is used to steadily decrease the temperature of the solution and find the cloud point temperature, the point at which the solute crystallises back out of solution. These two points can be determined in tandem using a cycling mechanism. The concentration of the solution is known and the temperature is cycled up and down to determine the clear and cloud points of the solution. This cycle can happen multiple times to obtain repeated measurements for the same concentration. Tight control over the temperature of the solution is important for accurate results. Slow heating and cooling rates are required to give the system time to equilibrate and prevent the true temperature points being overshot.

In this research a Polar Bear Plus crystalliser from Cambridge Reactor Design was used to control the heating rate of the solvent (figure 3.1). Starting from the minimum temperature required, about 5 ^{o}C, solvent was heated in a 50 mL round bottom flask at a rate of 0.3 ^{o}C/minute to a maximum temperature, around 60 ^{o}C. An initial amount of solute was added and stirred continuously at 700 rpm using a magnetic bottom stirrer. The temperature at which the solute had fully dissolved was recorded and the concentration of the solution calculated. With the flask still heating this method was then repeated for set mass intervals until the maximum temperature required was reached. Plotting concentration against temperature from the data produces a solubility curve. This was repeated three times for each sample investigated, to increase the accuracy of the solubility curve obtained.

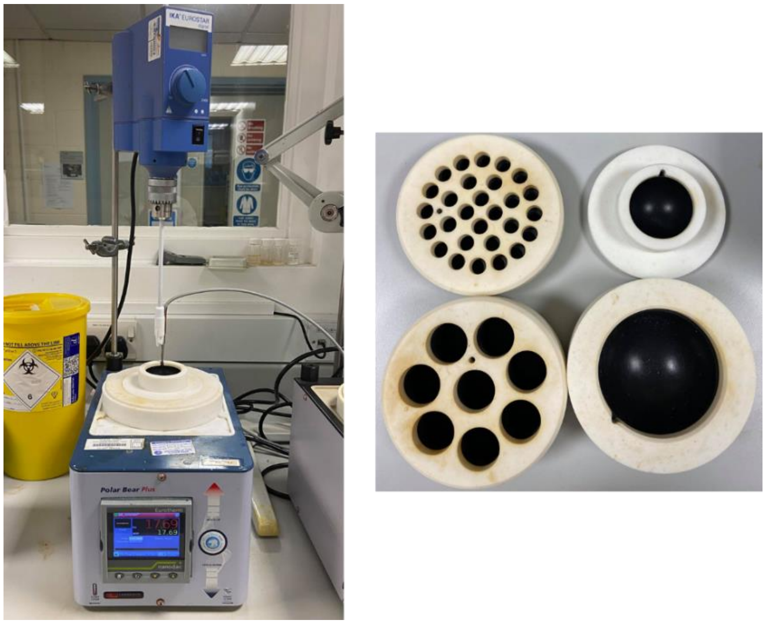

Figure 3.1. Cambridge Reactor Designs Polar Bear Plus crystalliser set up. Left: Polar Bear with overhead stirrer set up. Right: Different sized inserts for Polar Bear (top, left to right: 1 mL + 50 mL; bottom, left to right: 10 mL + 250 mL)

For MSZW measurements a cyclic approach was used. Again a Polar Bear Plus crystalliser was used to gain tight control over the temperature profile. Using a 50 mL round bottom flask of solvent, stirring at 700 rpm, approximate values of the clear and cloud points of each concentration being investigated were determined. A programme was then set up to heat and cool at 0.3 ^{0}C/minute in a cycle 5 ^{0}C above and below the approximate temperatures previously determined for each concentration, to achieve more accurate measurements of the clear and cloud points of the solution. The concentrations of the solutions were plotted against the clear and cloud point data obtained to give a solubility curve with corresponding MSZ. Again each measurement was repeated three times to obtain an accurate determination.

This method used to determine the solubility and MSZW of a solute is similar to that utilised in the crystal16 device (manufactured by Technobis crystallisation systems) often used in industry. In the crystal16 set up multiple solutions at different concentrations are cycled three times through a pre-set temperature profile. The clear and cloud points are determined using an FBRM probe to measure the turbidity of the solutions. The benefit of this method is the ability to carry out accurate experiments on a small amount of solute, ideal for an industry setting where typically there is an initially limited supply of the active ingredient being investigated.

It is important to note that while solubility is a thermodynamic property of the solute the MSZ is a kinetic factor. As a result, the MSZW will change depending on the conditions under which the experiment is being performed. This makes application of the results of a MSZW screen to different cooling crystallisation set ups very difficult, so it is often used only as an estimation.

The results of the solubility determination were used to determine the saturation point for future crystallisation experiments. The saturation temperature (T_{sat}) quoted in experimental sections of this thesis refers to the concentration of solute in g/g required to saturate the solvent at the temperature quoted.

3.2 Crystallisation methods

The crystallisation method used can have a significant effect on the resulting crystals, including their morphology. As a result, multiple different crystallisation methods were used during this research. Solvent-mediated methods were analysed for their ability to influence the morphology of the crystals produced. Some mechanochemical methods were also used in the investigation of new multi-component materials.

3.2.1 Evaporative crystallisation

Evaporative crystallisation was used as an initial screening method for both multi-component and additive crystallisations. Initial screening experiments to establish the effect of different solvents on crystal morphology were also carried out using this method. A small mass of target molecule, along with any co-former or additive required, is dissolved in solvent in a 7 mL glass vial. Usually the minimal amount of solvent required is used to prevent unnecessarily prolonged evaporation times. To aid dissolution, sonication and application of heat is sometimes used. PTFE lids were used to seal the vials and holes made in these to aid slow evaporation. Vials were left to crystallise at different temperatures, including room temperature, using feedback controlled hot plates. Using this method multiple crystallisations could be set up using various different conditions. Variables changed include solvent system, additive present, and ratios of target and additives/co-formers present.

3.2.2 Cooling crystallisation

Two different cooling crystallisation techniques were utilised in this research: uncontrolled crash cooling and controlled cooling.

3.2.2.1 Uncontrolled crash cooling

Uncontrolled crash cooling was sometimes used in the place of evaporative crystallisation to screen for multi-component crystals. The advantage of crash cooling over evaporative crystallisation is a faster crystallisation time is usually achieved. However, the resulting crystals are often of poorer quality and not ideally suited to analysis by SCXRD. Solubility data is not necessarily required to carry out this kind of cooling crystallisation. A mass of solid that exceeds the room temperature saturation in a given solvent was dissolved in 7 mL glass vials. Sonication with heating was utilised to aid dissolution of the saturated solution. Vials were transferred to the fridge, set at 4 ^{o}C, to create the fast cooling conditions. If no crystallisation is induced, slow evaporation can be adopted by piercing holes in the plastic lids, however this would then no longer be a purely crash cooled experiment.

3.2.2.2 Controlled cooling

For controlled cooling crystallisations a Polar Bear Plus crystalliser from Cambridge Reactor Design was used. The set up allows batch crystallisations to be carried out on a number of different scales, made possible by a number of different sized inserts (figure 3.1). Crystallisation on scales of 1 mL and 20 mL (vials) are possible as well as 50 mL, 100 mL and 250 mL (round bottom flasks). Heating and cooling profiles can be programmed to tightly control the crystallisation set up. Stirring is possible with both magnetic bottom stirring, in all sizes, and overhead stirring with an impellor, only in round bottom flasks. Overhead stirring is achieved using an overhead shaft and motor clamped above the round bottom flask crystallisations.

3.2.3 Grinding (mechanochemical)

Grinding was carried out to screen the formation of multi-component crystal systems and determine the more stable polymorphic form of co-crystals. A small amount, on the milligram scale, of the relevant materials were ground together by hand using a pestle and mortar. Experiments were carried out with the target molecule and corresponding stoichiometric ratio of co-former or a 1:1 stoichiometric ratio of two polymorphic forms were used. Liquid assisted experiments (LAG) were also carried out where a drop of solvent was added to aid formation of new intermolecular interactions. Neither method was used for the investigation of crystal morphology as grinding would be an additional influence on the crystal shape, resulting in crushed micro-crystallites.

3.2.4 Slurrying

Slurrying methods were also used in the formation of multi-component crystal systems. Excess starting materials were stirred in solvent for a prolonged period of time to allow for the transformation of starting materials into co-crystalline products. This method was used to scale up successful multi-component crystallisations to produce a bulk amount of a sample. This method was particularly beneficial for the scale up of production of PYR co-crystals (chapter 6) due to their low solubility. This method was not used to investigate crystal morphology as the continuous stirring often results in a microcrystalline powder.

3.2.5 Continuous crystallisation

Continuous crystallisations were carried out using a modified set up of the KRAIC, previously discussed in chapter 1. The adapted KRAIC set up is shown in figure 3.2.

Figure 3.2. Adapted KRAIC set up. 1. Air pump; 2. Galden pump; 3. Solution pump; 4. Feed/solution vessel; 5. Submerged cross piece; 6. Crystallisation coil; 7. Outlet; 8. Crystal collection; 9. Galden recovery.

The configuration detailed was developed to allow cooling crystallisations to be carried out within a fume hood. This enabled the use of solvents not suitable for use on the bench with an overhead extractor. The KRAIC can also be set up to achieve other crystallisations, such as anti-solvent, and chemical synthesis in flow. The set up utilises a continuous stream of solution split into discrete segments using air pumped into the tube. An inert organic carried fluid is also used to preferentially wet the walls of the tubing, further separating the solution segments, known as slugs, and preventing a solid/solution interface being available to induce nucleation. The solution cools as it travels through the tubing allowing nucleation and growth to occur before the solution is separated from the carrier fluid and crystals filtered from solution at the outlet.

The KRAIC is constructed from 15 m of fluorinated ethylene propylene (FEP) tubing with an internal diameter of 3.2 mm. The tubing is assembled into coils with a gentle ascending gradient between each coil. In the set up used here the tubing is coiled around one support only to allow it to fit inside a fume hood. Solution, carrier fluid and air are pumped into the coils using individual gear pumps. The solution is temperature controlled prior to entering the crystalliser to ensure all solute is fully dissolved. The inlets of the feed tubes are fitted with solvent filters to prevent small, undissolved nuclei or other foreign particles (such as dust) entering the crystallisation vessel. Any small particles entering would seed nucleation in the discrete segments, reducing the chance of primary nucleation occurring. Segmentation is created using a glass mixer cross piece with three inlets, one for each of solution, carrier fluid and air, and one outlet for the segmented flow.

Supersaturation is achieved via cooling crystallisation. Solution is saturated at an elevated temperature to allow a temperature gradient to be generated across the coiled tubing. Temperature control of the tubing after the mixer piece was not possible, however, temperature before this point is controlled in a number of ways. The feed vessels are temperature controlled using feedback controlled hot plates with Drysyn® formers to house the round bottom flasks. All the inlet tubing is jacketed using flexible tubing jackets connected to a circulator bath, allowing the temperature to be maintained before the mixer piece. The final step using temperature control is the mixing in the cross piece. The cross piece, three inlets and segmentation outlet are submerged in a water bath. This temperature is again feedback controlled using a hot plate. Temperature control at this point is very important to prevent nucleation induced by the mixing of the three phases; crystallisation at this point could block the flow. Finally, the set up finishes with an end piece designed to aid expulsion of the crystalline material from the KRAIC and recover the carrier fluid used in the experiment. The end piece feeds into a Buchner funnel to collect any crystals produced. Sometimes crystals remain in the inlet and a neutral solvent is required, to help flush the crystals out of the end piece without re-dissolving any of the product.

A typical KRAIC experiment follows the general process:

- The KRAIC set up is primed using pure solvent (same as used to make up the solution), air and carrier fluid for 1 hour. This is to ensure the system is at equilibrium and the temperature gradient is produced.
- The pump speeds are set to control the relative flow rates and ensure the segmentation is regular and well sized and also to fine tune the residence time, the time the solution takes to go through the length of the crystalliser.

- The primer inlet is switched to the feed solution and the crystallisation experiment starts.
- The solution cools over the length of the KRAIC, generating supersaturation and inducing primary nucleation in the segments.
- At the end of the crystalliser the carrier fluid is recovered and crystals collected using Buchner filtration.

3.2.6 Temperature cycling

Temperature cycling is often utilised to improve particle size distribution and crystal aspect ratio. Temperature cycling uses a defined temperature profile that both heats and cools at steady rates. Repeating the cycle multiple times can improve particle size distribution by re-dissolving small, fine particles produced with uncontrolled nucleation and allowing the larger crystals to act as seeds when cooling recommences. The dissolved molecules are then more likely to grow on existing crystals than nucleate to form new crystals. A similar argument can be made for improving aspect ratios, as all faces have different dissolution and growth rates.

Temperature cycling was carried out using the Polar Bear Plus crystalliser. A temperature profile was determined from solubility and MSZW data obtained for the materials. The cycle is designed around the determined solubility line. To initially nucleate the solution must be cooled to fall outside the MSZ (in the labile region). Following this the dissolution/recrystallisation cycle should remain either side of the solubility limit, from undersaturated to within the MSZ, to encourage crystal growth and limit further nucleation. The defined temperature cycle giving rise to the dissolution and recrystallisation of the solute is continued until the preferred outcome is achieved. Temperature profiles can be simple cycles, returning towards the minimum set immediately after reaching the maximum, or contain a hold step at set temperatures to allow more time for the system to equilibrate.

Temperature cycling is a more reliable technique when utilising direct feedback control. Using PAT probes, such as FBRM, the cycles can be monitored and an end point easily determined. When using PAT probes it is also easier to maintain the crystallisation parameters within the MSZ limits of the system.

3.3 Stability measurements

A range of experiments were used to characterise the stability of the multi-component crystal forms produced throughout the work discussed in this thesis.

3.3.1 Slurry

An excess sample of the multi-component product was slurried in water at 40 ^{o}C for a week. The samples were continuously stirred in solution for the duration of the experiment. Small amounts of each sample were removed throughout the process and analysed by PXRD to determine if any breakdown or transformations occurred. The conditions used were chosen to mimic the dissolution of the sample within the body.

3.3.2 Competitive slurrying

Competitive slurry experiments are used to help distinguish the thermodynamic polymorph from metastable polymorphic forms. An excess amount of a 1:1 mixture of two polymorphs was slurried in solvent for a week. Slurries were carried out at 20 ^{o}C and an elevated temperature of 40 ^{o}C. Samples were continuously stirred and samples were removed at intervals throughout the process. Analysis using PXRD was used to determine the transformations that occurred throughout the duration. The samples are expected to convert to the more stable polymorphic form over time.

3.3.3 Elevated temperature

Elevated temperature studies were also carried out to investigate the stability of the new solid forms to storage conditions throughout the supply chain. A temperature of 50 ^{o}C was chosen to accelerate any changes and degradation that may be observed when stored at higher than ideal temperatures. Samples of each form were left in an oven set to 50 ^{o}C for 3 weeks and tested periodically throughout using PXRD analysis. The results were compared to the starting materials and original form PXRD patterns to determine any degradation or form changes observed as the result of the increased storage temperature.

3.3.4 Humidity

Humidity studies can be used to investigate the potential stability of the multi-component crystals produced in storage conditions that may occur throughout the supply chain. A humidity chamber was created using a saturated solution of water and NaCl salt. Upon testing with a humidity probe the 70% humidity was maintained with an error of 3%. Samples were placed in 1 mL vials which were in turn placed in 20 mL vials before being sealed in the humidity chamber (figure 3.3). PXRD analysis was carried out on small amounts of each sample extracted at weekly intervals up to a limit of 9 weeks. The results were compared to the PXRD patterns of the individual components and original co-crystalline sample to determine if any changes occurred as the direct result of the conditions to which the sample was subjected.

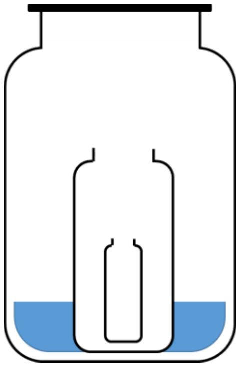

Figure 3.3. Humidity chamber set up with unsealed 1 mL vial inside an unsealed 20 mL vial

3.4 X-ray diffractometers

3.4.1 Single Crystal X-ray Diffraction (SCXRD)

The SCXRD data discussed in this thesis were collected on three different laboratory diffractometers; Rigaku Oxford Diffraction SuperNova, Rigaku Oxford Diffraction Xcaliber and a Rigaku Oxford Diffraction Gemini A Ultra (figure 3.4). Both the SuperNova and Gemini models are equipped with dual sources (Mo-Kα and Cu-Kα), with the Xcaliber only capable of analysis using Mo-Kα radiation. The SuperNova utilises a dual micro-focus source and the Gemini A Ultra a dual sealed tube source. Both are fitted with graphite monochromators. The Xcaliber has a sealed tube Mo-Kα source and a graphite monochromator.

All diffractometers possess the possibility of data collection at low temperatures using a liquid nitrogen stream (either an Oxford Instruments CryoJetXL or a Cryostream 700). Full structure analysis was carried out at 150 K using the flow of liquid nitrogen to control the temperature of the sample. It is also possible to heat the nitrogen stream, allowing the temperature to be controlled at higher temperatures. This presents the possibility of data collection at variable temperatures.

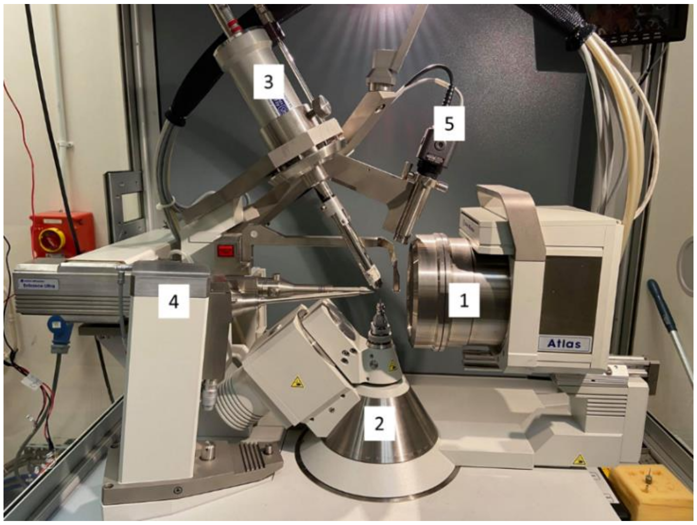

Figure 3.4. Rigaku Oxford Diffraction Gemini A Ultra diffractometer. 1. CCD area detector; 2. Goniometer; 3. Cryostream; 4. Cu and Mo X-ray tubes; 5. Camera. Backstop can be seen between the X-ray tubes and area detector

All diffractometers are equipped with a charge coupled device (CCD) area detector, the position of which can be altered to increase or decrease the distance from the mounted crystal. The goniometer on which the crystal is mounted also has the ability to move. Each diffractometer is equipped with a 4-circle kappa goniometer allowing movement through the angles κ, ϕ, ω and 2θ to produce a full data set for each collection.

CrysAlisPro[198] software was used for data collection and processing for all full structure determination experiments carried out. All structures were solved by direct methods using ShelXS[177] and refined using ShelXL[177] within Olex2[199] software. Following full resolution and refinement of the crystal structures, Mercury 3.10.2[135] was used to visualise the crystal structures. This software was also used to calculate the BFDH morphology for crystals where face indexing was carried out.

Face indexing experiments were carried out on the Rigaku Oxford Diffraction SuperNova, Rigaku Oxford Diffraction Xcaliber and Rigaku Oxford Diffraction Gemini A Ultra diffractometers. Face indexing can be performed on either full data collections or pre-experimental data. The analysis is carried out using CrysAlisPro software, using a movie collected of the mounted crystal on the diffractometer. Using the software to outline the edges of the crystal as it rotates, the faces and their hkl values can be determined. In order to analyse the resulting morphology further a face table is produced, which can be imported into Mercury 3.10.2 software and the BFDH function used for visualisation and comparison.

3.4.2 Powder X-ray Diffraction (PXRD)

PXRD data was collected in transmission mode using a Stoe Stadi P model diffractometer. The Stoe has a sealed tube equipped with a primary monochromator to produce pure $K_{\alpha1}$ radiation using a Cu source. The diffractometer was used in transmission mode with samples mounted using a high precision, two-circle goniometer and spun throughout the data collection. Spinning the sample produces more reliable intensities than would be achieved in flat plate mode, as it reduces the possibility of preferential orientation. Grinding of crystalline samples in a pestle and mortar, before being loaded into the sample holders, ensures a more homogeneous microcrystalline powder preventing a high background in the data. Data were collected between 2θ values of 2° and 75° at room temperature using a Dectris Mythen 1K detector. Data presented in this thesis are shown between 2θ values of 5° and 40°.

Variable temperature PXRD experiments were performed for one complex to develop a better understanding of a possible phase transition observed in previous DSC traces. Data were collected on beamline I11, situated at a synchrotron source (Diamond Light Source). Using a borosilicate glass capillary as the sample holder, the microcrystalline sample was loaded and held in a brass holder using glue. The sample is spun, similar to the laboratory PXRD experiments, to achieve more accurate peak intensities and prevent preferential orientation of the micro-crystallites having an effect. Radiation on the beamline, monochromated from a Si (111) source, has an energy of 15 keV (λ=~0.826 λ). The beamline utilises two detector arrays: the position-sensitive detector, used for high throughput experiments, and the multi-analyser crystal for high resolution. The position-sensitive detector was used to collect data for this experiment. The sample temperature was controlled using an Oxford Cryosystems Cryostream Plus, able to both heat and cool the samples measured.

3.5 Thermal analysis

3.5.1 Hot-stage Microscopy (HSM)

HSM was carried out on crystals to observe thermal phase transitions occurring when heat is applied. Using a Mettler Toledo FP82 hot-stage equipped with a Leica DM1000 microscope, crystals were subjected to a defined temperature profile from 30 ^{o}C to various maximum temperatures, dependent on the sample undergoing the test. A FP90 Central Processor was employed to control the heating rate, chosen at 10 ^{o}C/minute to correlate the results to those seen in DSC experiments.

Films of the crystals were captured using a Lumenera Infinity 2 microscopy camera and recorded using Studio Capture software version 4.0.1 © 2001-2010 Studio86Designs.

3.5.2 Differential Scanning Calorimetry (DSC)

The DSC instrument used was the Thermal Advantage Q20 DSC from TA Instruments. The instrument is operated with a dry nitrogen purge gas at a flow rate of 18 cm^3/minute to create an air free atmosphere. This prevents any water crystallisation occurring within the system when low temperatures are reached. 2-4 mg of sample is sealed in a Tzero aluminium pan and heated at a rate of 10 ^oC/minute to a maximum temperature, determined by the composition of the sample being investigated. Cooling is also possible using the DSC instrument and was utilised to determine whether recrystallisation was occurring. Data were collected using Advantage for Qseries software (version 5.4.0 © 2001-2011 TA Instruments-Waters LLC). Analysis of the peaks observed in the collected data was carried out using TA Universal Analysis software.

3.5.3 Thermogravimetric Analysis (TGA)

TGA experiments were carried out using a Perkin Elmer TGA4000. 2-5 mg of sample was placed in the sample holder and the temperature ramped to 250 ^oC at a rate of 5 ^oC/minute. The TGA system is maintained under a nitrogen atmosphere using a flow rate of 20 mL/minute.

3.6 Other analysis techniques

3.6.1 Fourier Transform Infra-red spectroscopy (FTIR)

The FTIR spectra obtained in this work were recorded using a Perkin Elmer FTIR Spectrometer in the range 4000–500 cm^{-1} with an attenuated total reflectance (ATR) sampling accessory. Samples were analysed at room temperature.

3.6.2 Nuclear Magnetic Resonance spectroscopy analysis (NMR)

Proton NMR spectra were obtained using an Agilent Technologies 300 MHz ^{1}H-NMR spectrometer. The samples were prepared by dissolving a small amount of crystalline material in a deuterated solvent. The experiments were conducted at 298 K. Resulting spectra were compared using MestReNova software.

Chapter 4 Morphology changes observed in pure isoniazid

4.1 Introduction and aims

Morphology is an important physical property to consider for pharmaceutical crystals due to the significant influence it can have both on surface-dependent particle properties such as dissolution rate and on downstream processing steps. In processing, controlling this property can not only make many crucial steps, such as filtration, easier, but also prevent extra steps, such as grinding, being required. Controlling morphology without changing the crystal structure of the active ingredient requires influencing the crystallisation process to result in a change in the growth of the crystal. The influences being investigated here come from the solvent system used and impurities present in the crystallisation.

The aim here is to achieve a morphology change of pure IZN through solvent choice or additive impurities. This means no changes should be observed to the crystal structure produced.

4.2 Solvent effects on isoniazid morphology

Early in the development of a pharmaceutical product there is likely to be significant freedom with solvent choice. Generally, in the early stages of development a large number of solvents would be screened for API solubility, the form of the crystalline product produced by recrystallisation from these (including the potential to form any solvates) and the quality of the crystals produced. Any solvents yielding the correct form of the product can also be screened for their morphological influence. It is widely accepted that different solvents can yield different growth mechanisms for the same molecule and crystal form, often resulting in changes to the overall morphology.

The aim of this research was to develop a solvent system for the crystallisation of IZN that produces a favoured crystal morphology. Avoidance of needle and plate shapes in favour of more block shaped crystals is preferred in pharmaceutical development. The transfer of any solvent effects between different crystallisation methods is also necessary, with the final goal in this investigation of eventual transfer into continuous crystallisation platforms. Crystal habits were characterised by indexation of the faces using SCXRD. As a key element of this investigation is to maintain the original form of IZN, without producing solvates, PXRD, DSC and NMR spectroscopy methods were also used to characterise the bulk sample.

4.2.1 Experimental information

The IZN and all solvents used in the following experiments were acquired from commercial sources and used without any further purification steps.

4.2.1.1 Choice of solvents for isoniazid crystallisations

When choosing the solvents for this investigation a variety of factors where considered. Lists of commonly used solvents in pharmaceutical production were consulted initially.[199] Considerations of the volatility of the solvent and ability to dissolve the target molecule were used to determine an initial list of solvents. The availability and safety of the solvents are also important concerns taken into account. The solvents chosen for these experiments came from a variety of different classifications for pharmaceutical production. The final solvents chosen were water (H_2O), alcohols ethanol (EtOH) and isopropanol (IPA), ethyl acetate (EtOAc) and acetonitrile (ACN).

A secondary list of esters was chosen as additional solvent options due to the successful morphology changes achieved with EtOAc. These esters had varying chain lengths and are shown in figure 4.1.

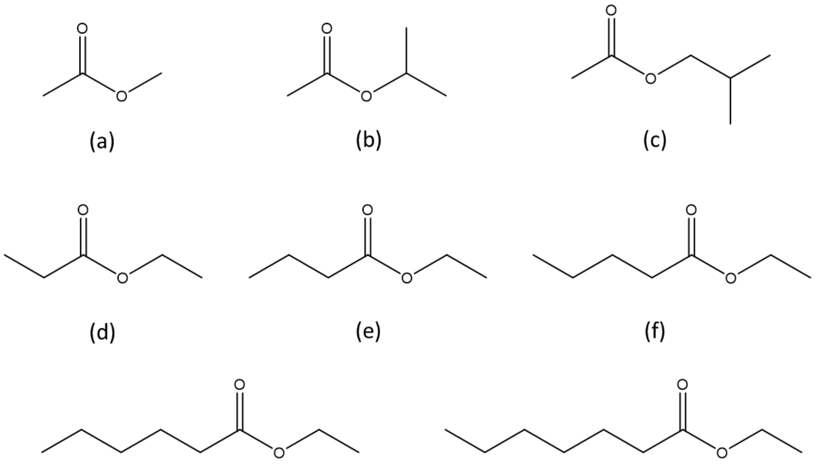
(a) (b) (c) (d) (e) (f) (g) (h)

Figure 4.1. Ester solvents used (a) methyl acetate, (b) isopropyl acetate, (c) isobutyl acetate, (d) ethyl propionate, (e) ethyl butyrate, (f) ethyl valerate, (g) ethyl hexanoate and (h) ethyl heptanoate

4.2.1.2 Evaporative screening of isoniazid in different solvent systems

Initial evaporative experiments were carried out using pure IZN in the four initial solvents. Approximately 0.01 g of IZN was dissolved in a minimal amount of solvent in 7 mL vials. Holes were pierced in plastic lids and the vials left to evaporate at room temperature and 40 ^oC.

Evaporative experiments from the broader range of ester solvents were carried out due to the success observed from initial screens carried out in EtOAc. Again a small amount of IZN, 0.01 g, was dissolved in a minimal amount of ester in 7 mL vials. The vials were sealed and sonication was used to aid full dissolution. Holes were poked in the top of the plastic lids to allow slow evaporation and the vials left at both room temperature and 40 ^oC.

Further experiments were carried out with solvent mixtures. The main solvents chosen were EtOAc and IPA, due to their reliability when producing the morphological changes observed with initial screens. Mixtures of either IPA or EtOAc with the esters in figure 4.1 in v/v ratios of 10%, 20%, 30%, 40% and 50% were investigated. In addition, solvent mixtures of IPA and EtOAc were prepared in 10%, 20%, 30%, 40%, 50%, 60%, 70%, 80% and 90% v/v ratios. A 7 mL vial was used to dissolve 0.01 g of IZN in the minimal amount of solvent mixture. After sonication, to aid dissolution, the vials were left at room temperature and 40 ^oC to fully evaporate.

4.2.1.3 Cooling crystallisations of isoniazid in different solvent systems

Controlled cooling experiments were carried out on IZN in the same five solvents; H_2O, EtOH, IPA, EtOAc and ACN. A T_{sat} of 30 ^oC was used for EtOH and H_2O, and a T_{sat} of 50 ^oC for IPA, EtOAc and ACN, due to low solubility of IZN in these solvents. A mass of 8 g of solvent was saturated for all solvents except water, where 4 g was saturated due to the very high solubility. Crystallisations were carried out in 20 mL vials without any stirring to prevent breaking/grinding of the resulting crystals. Cooling experiments were carried out from 55 ^oC with cooling rates of both 1 ^oC/minute and 0.1 ^oC/minute. Crystals were filtered at the end using a Buchner funnel and allowed to dry before analysis.

Further controlled cooling experiments were carried out with IPA and EtOAc on a 30 g and 150 g solvent scale with overhead stirring. The crystallisations were carried out in 50 mL and 250 mL round bottom flasks, respectively. T_{sat} of 50 ^oC was used. The solutions were heated to 55 ^oC and held for 30 minutes to allow for complete dissolution. Cooling was carried out at 1 ^oC/ minute to 5 ^oC and the solution held at 5 ^oC for a further hour. The samples were filtered and left to dry for analysis.

4.2.1.4 Isoniazid cooling crystallisations in the KRAIC continuous platform

Cooling experiments were also carried out in the KRAIC continuous platform, discussed in section 3.2.5. The cooling mechanism in this platform is uncontrolled as the tubing is not temperature controllable in the current set up.

Crystallisations were carried out in the KRAIC in both IPA and EtOAc solvent. A number of different crystallisations were carried out with different temperature profiles and starting saturations to optimise the process and achieve the best crystallisations. The temperature settings and saturation concentrations are shown in table 4.1.

Table 4.1. Conditions for crystallisations carried out in the KRAIC continuous platform in solvents IPA and EtOAC

Solvent system	Run number	Concentration (g/g)	Priming/feed temperature (˚C)	Cross piece temperature (˚C)	Circulator bath temperature (˚C)
IPA	1	0.006	50	50	50
	2	0.01	50	50	50
	3	0.015	55	55	55
	4	0.02	55	55	55
EtOAc	1	0.005	55	55	55
	2	0.005	55	55	60
	3	0.003	55	55	55

For both solvents, the KRAIC was primed for 1 hour using pure solvent, air and Galden (carrier fluid). Priming ensures that steady-state is reached before crystallisation experiments are carried out. A residence time is measured whilst priming; the time it takes for the solution to travel the length of the crystalliser. The residence time is directly influenced by the flow rates; all pumps were set to a flow rate of 2.40 mL/minute. After priming, the feed solution was introduced in place of the pure solvent. A temperature gradient is set up, with the feed solution introduced at an elevated temperature and allowed to cool to room temperature throughout the tubing. Crystals were collected from the end piece into a Buchner funnel and left to dry after the experiment for further analysis. Galden was recycled back into the crystalliser via separation through the carrier fluid recovery holes in the end piece. A further inlet is utilised above the end piece to allow for the introduction of a neutral solvent in the event of crystal build-up in the end piece. The neutral solvent is miscible with the crystallisation solvent and does not change the solubility; only increases the flow, pushing the built-up crystals through, reducing the opportunity for fouling to occur at the outlet.

4.2.1.5 Temperature cycling crystallisation of isoniazid from ethyl acetate

Two temperature cycling experiments were carried out in EtOAc to try to improve the morphology change already successfully achieved from that solvent. The experiments were carried out in the Polar Bear Plus crystalliser in a 50 mL round bottom flask. Magnetic bottom stirring at 700 rpm was used during the heating phases but turned off during the cooling phases. The solutions were made by saturating 30 g of EtOAc with IZN at 40 °C. The temperature cycling profiles are shown in figure 4.2. The ramp rates used in each experiment were 2 °C/minute during heating and 0.05 °C/minute during cooling. In both experiments the solution was first heated to 40 °C and held for 30 minutes to allow for full dissolution to occur. Following this, cooling was carried out to 5 °C. The cycling then occurred by heating to 5 °C below the previous highest temperature and cooling to 5 °C above the previous lowest temperature until eventually converging at 20 °C. The solution was then held at this final temperature for 30 minutes. In experiment 1, a short 30-minute dwell was added between the heating and cooling portions of the profile to allow for extended periods of growth and dissolution of the crystals produced.

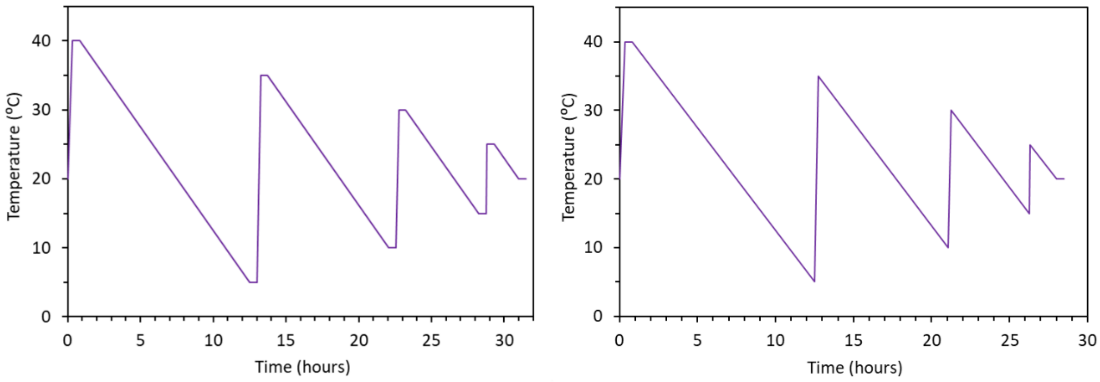

Figure 4.2. Temperature profiles for temperature cycling experiment 1 (left) and 2 (right)

4.2.1.6 Supersaturation experiments with isoniazid

A series of experiments were set up to investigate the effects of employing different starting saturations on the morphologies achieved in both IPA and EtOAc crystallisations. These were carried out in both evaporative and cooling crystallisation set ups.

In evaporative crystallisations, 3 g of solvent was saturated with IZN at 20 °C, 30 °C, 40 °C and 50 °C in a 7 mL vial. Each different saturation was then evaporated at a different temperature, using feedback controlled hot plates set at 20 °C, 30 °C, 40 °C and 50 °C, respectively. The effects of both saturation and the evaporation temperature were therefore investigated in parallel.

In cooling crystallisations, 8 g of solvent was saturated at 20 ^{o}C, 30 ^{o}C, 40 ^{o}C and 50 ^{o}C in a 20 mL vial. Solutions were heated to 55 ^{o}C and held for 30 minutes with magnetic bottom stirring at 700 rpm. Cooling was then carried out at rate of both 1 ^{o}C/minute and 0.1 ^{o}C/minute, without stirring, to a temperature of 5 ^{o}C and held for 1 hour.

4.2.1.7 Analytical methods

Microscope images of final crystal products were taken using a Nikon Coolpix P5100 camera through a Brunel Microscopes microscope. For smaller crystals a Leica DM1000 microscope with an Infinity 2 microscope camera was used as a higher zoom was able to be achieved with enhanced focus.

Analysis was also carried out via PXRD and DSC techniques, as explained in Chapter 3, to ensure the solid form of the crystals produced remained unchanged.

Face indexing was carried out using a Rigaku Oxford Diffraction Gemini A Ultra diffractometer with Mo-Kα radiation. Screening of unit cells were carried out at 298 K and pre-experimental data recorded. Face indexing was performed with CrysAlisPro software to determine the faces and overall shape of crystals produced. Crystal structure and morphology were visualized using the BFDH tool included in the Mercury software.

4.2.2 Effects of solvent on isoniazid morphology

Evaporative crystallisation of IZN from a variety of solvents was initially carried out to determine the effect of different solvents on the resulting crystal morphology. PXRD analysis confirms no form changes have occurred for the IZN (appendix A1). Initial evaporative crystallisations gave unreliable morphology changes for the majority of solvents (figure 4.3).

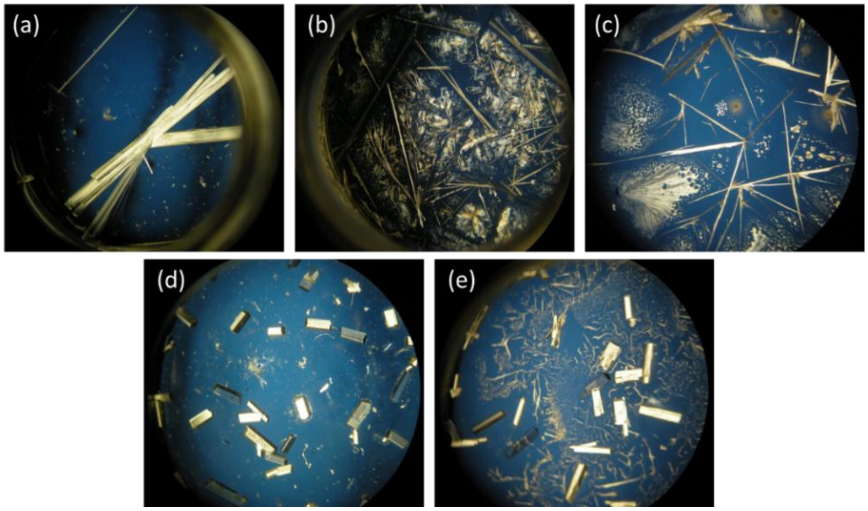

Figure 4.3. IZN crystals from evaporative crystallisations at 40 ^oC from solvents (a) H_2O, (b) EtOH, (c) IPA, (d) EtOAc and (e) ACN

Needle morphology was observed in samples from H_2O, EtOH and IPA evaporative crystallisations. However, more block shaped morphologies were observed from EtOAc and ACN. The morphology observed in both the EtOAc and ACN crystallisations are much more favourable in the pharmaceutical industry context than those observed in H_2O, EtOH and IPA.

The same experiments were also carried out in cooling crystallisations. Controlled cooling in the Polar Bear Plus crystalliser yielded further morphology changes not observed in evaporative crystallisation (figure 4.4).

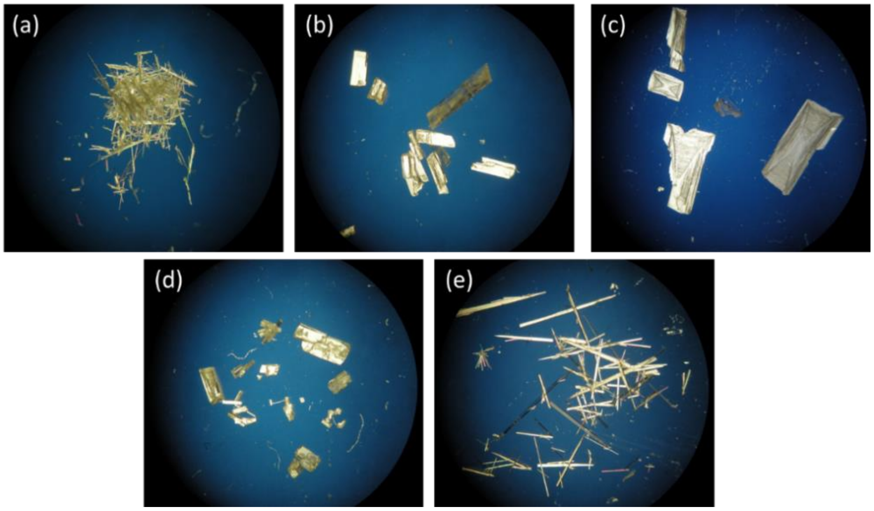

Figure 4.4. IZN crystals from cooling crystallisations at a rate of 1 ^oC/minute from (a) H_2O, (b) EtOH, (c) IPA, (d) EtOAc and (e) ACN

Again, water yields very thin needle shape IZN crystals which clump significantly upon filtration from the crystallisation solution. However, a difference is seen in the morphology produced from both EtOH and IPA compared with that seen in the evaporative crystallisations. Both these cooling crystallisations yield plate-shaped crystals, in contrast to the needles observed in evaporative. Although plates are not the most favourable crystal shape, they indicate the significant influence solvent can have on the morphology of IZN. More rod/block shaped crystals were again observed for EtOAc, however, the change was less significant and less controllable under these particular cooling conditions. It was not possible to achieve the evaporative experiment morphology from ACN in cooling crystallisation. Cooling experiments yielded long thin needle crystals in ACN cooling experiments, in contrast to the block shapes observed in evaporative crystallisations.

Face indexing experiments were not carried out for the needle-shaped products obtained in the crystallisations from H_2O. Needles are difficult to face index due to their length and limited thickness. Often the length of the needle crystals does not fit within the camera view on the XRD instrument and their faces cannot be distinguished due, mainly, to their very close proximity to one another. As a result, the growth habit is projected from the BFDH morphology calculations carried out. The fastest growing faces in crystals are those with the smallest surface area and so it is clear in needle crystals the fastest faces are those capping the tips of the needles. Using the predicted morphology, the major growth mechanism contributing to growth on these faces can be determined.

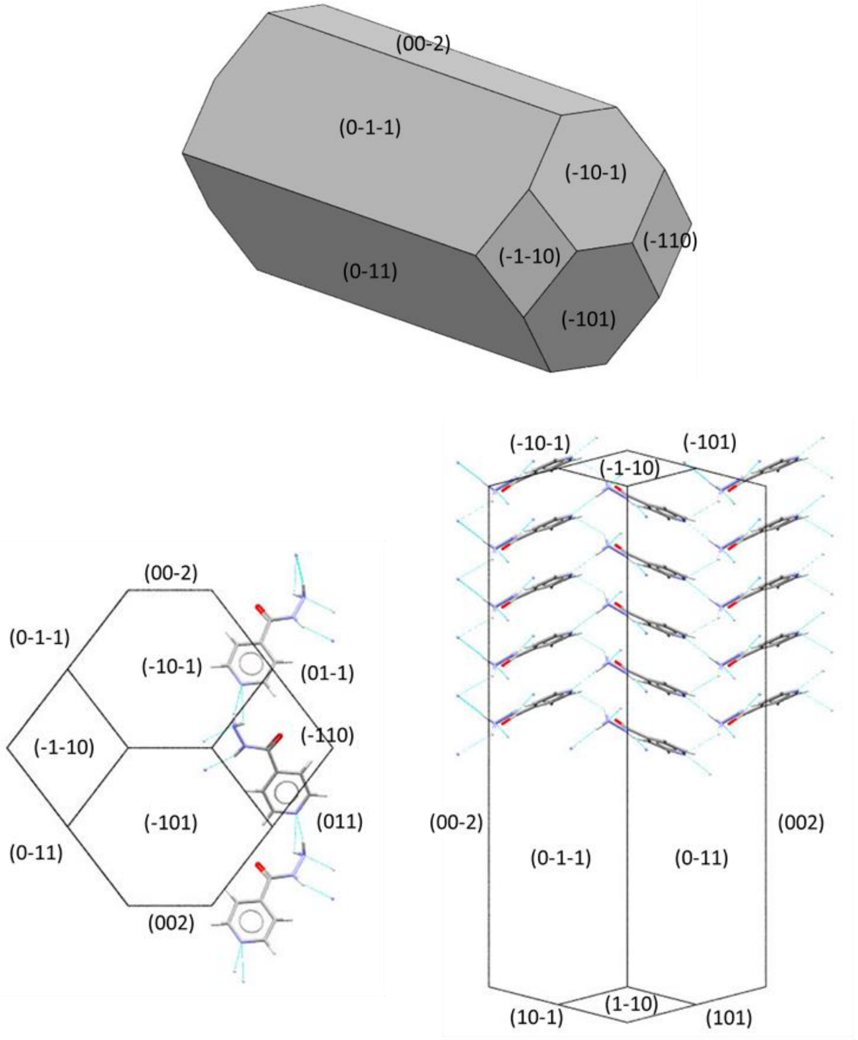

Figure 4.5. Top: BFDH predicted morphology for IZN (INICAC02). Bottom: Molecular packing with respect to BFDH morphology

This calculated morphology for IZN (figure 4.5) shows an elongated, rod-shaped crystal. Whilst the actual morphology achieved from H_2O is observed to be much thinner and more needle-like than that predicted, the calculated morphology does tell us the likely major growth mechanism occurring in the crystallisations. By visualising the molecular packing in the crystal with respect to this morphology, it can be clearly determined that the major growth mechanism in IZN is the interaction between the aromatic π-systems. The packing of the crystal structure allows the π-systems to overlap with one another, occurring parallel to the capping faces of the morphology. Due to the almost herringbone structure of the packing, the hydrogen bonds are also orientated slightly towards the capping faces, also contributing to the major growth. Examination of the predicted needle crystal morphology and the underlying packing show there are no hydrogen bonding interactions protruding from the capping faces. The long sides of the needle, however, are surrounded by different hydrogen bonding interactions. The interaction of H_2O with the growing crystal is therefore along the length of the needle crystal, through hydrogen bonding interactions. The ability of H_2O to hydrogen bond to these faces limits the ability of the solute molecules to adsorb to them, inhibiting growth in that direction and favouring further growth to extend the needle axis. The high polarity of the solvent makes it very successful in forming strong hydrogen bonds with the slower growing faces on the crystal surface. This strong solvent-surface interaction is likely responsible for directing the growth in the needle direction, increasing the aspect ratio of the crystal.

Face indexing experiments were carried out on the plates produced in EtOH and IPA to allow for a comparison of the faces. Examination of the faces can allow conclusions to be drawn about the changes in crystal growth achieved in each different solvent.

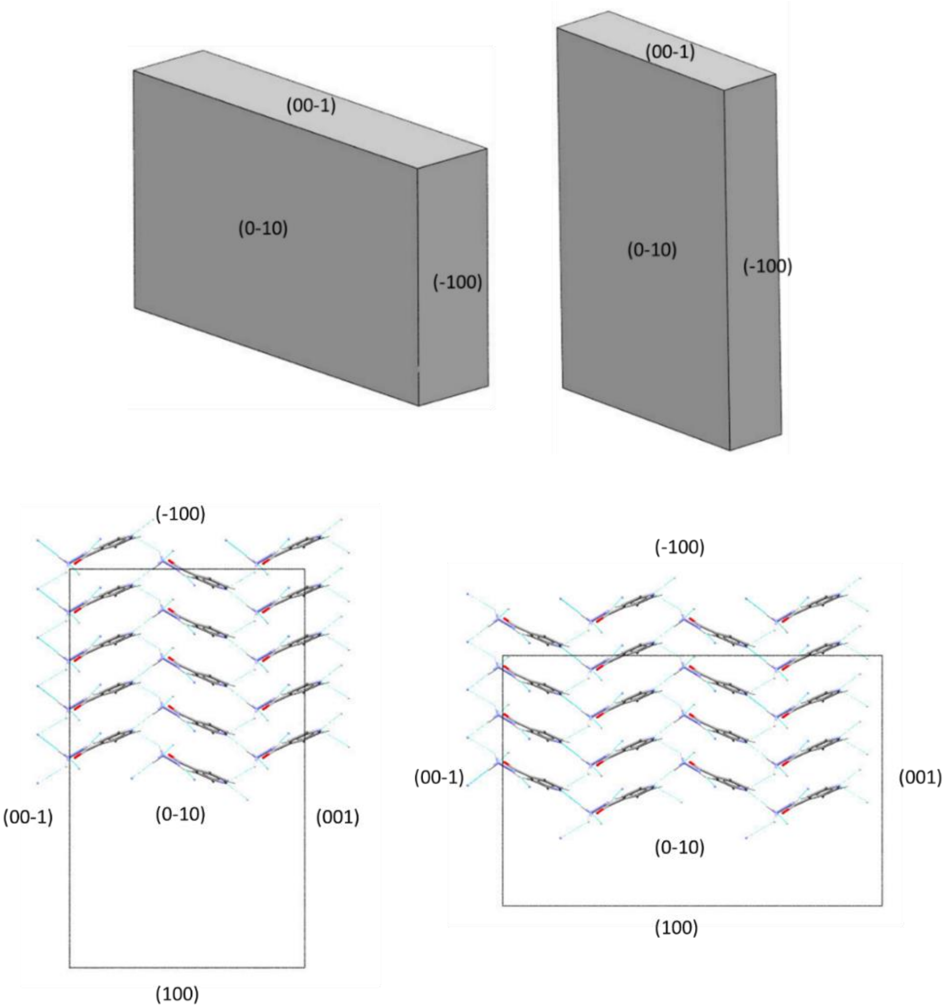

Figure 4.6. Top: Face indexed morphologies for IZN crystallised from EtOH (left) and IPA (right). Bottom: Molecular packing with respect to morphology for EtOH (left) and IPA (right).

Plates of IZN are observed from both EtOH and IPA (figure 4.6), but the major growth direction appears to differ slightly in each solvent system. In EtOH, the smallest face determined was the (-100) / (100). These faces grow as a result of the major growth interaction, π-system overlap. This is the same major growth as observed in the needle crystals. However, significant growth has also occurred in the (00-1) / (001) directions and these are the smallest faces observed in crystals grown from IPA (see below). The growth here is the result of hydrogen bond donation from the terminal NH_2 group and accepted by the N in the pyridine ring (figure 4.7).

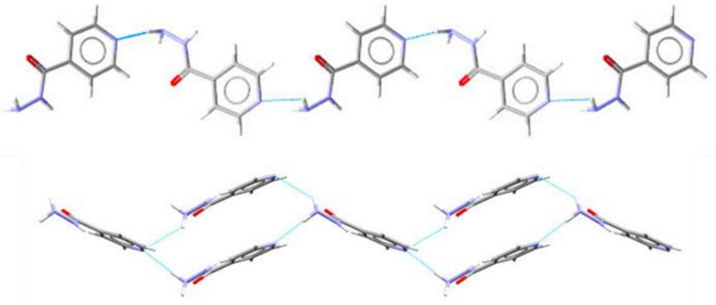

Figure 4.7. Hydrogen bonds contributing to elongation of plate crystals in IPA: viewed from (-100) face (top) and (0-10) face (bottom)

These hydrogen bonds connect in a zig-zag pattern, creating the herringbone structure observed in IZN crystals, and therefore also contribute to the growth on the needle axis and stacking of the aromatic rings in IZN. The growth on the (0-10) / (010) faces is the result of hydrogen bond donation from the NH group and accepted by the NH_2 nitrogen. This is a much weaker hydrogen bonding interaction than those previously discussed, resulting in the limited growth observed.

In IPA the major growth direction is different to that observed in EtOH, with the smallest faces now being (00-1) / (001), resulting from the hydrogen bond donation from the NH_2 group to the N in the pyrazine ring. There is still significant growth on the (-100) / (100) faces of the crystal, resulting from the π-system stacking. Despite the seeming shift of major growth mechanisms in IPA, the morphology observed is very similar to that seen in EtOH. Comparing the morphology produced in IPA to that produced from water, minimal growth occurs on the (0-10) / (010) faces, similar to the needle growth and the EtOH crystallisation. Again, this reflects a weaker hydrogen bonding interaction and explains the slower growth observed in this direction.

The differences observed between the major growth faces in the EtOH and IPA crystals are thus likely due to differences in the available interactions. Solvents can compete with solute at growth sites altering the growth mechanism occurring during crystallisation. Interactions between solvents and specific faces of a growing crystal are possible, limiting the growth of those with stronger interactions to a greater extent. The increased growth on the c-direction is probably the result of a reduction in the hydrogen bonding potential in the solvents used. EtOH is a more polar solvent than IPA, resulting in a higher propensity to hydrogen bond to the slower growing faces of the crystal. The lower polarity means the hydrogen bonding interactions between the solvent and the surface are weaker and there is a higher ability for the solute molecules to hydrogen bond where the solvent would otherwise block the growth.

The correlation between lower polarity and a more equant morphology can be further shown through the crystallisation carried out in EtOAc. EtOAc has a much lower polarity and causes a much more equant crystal morphology.

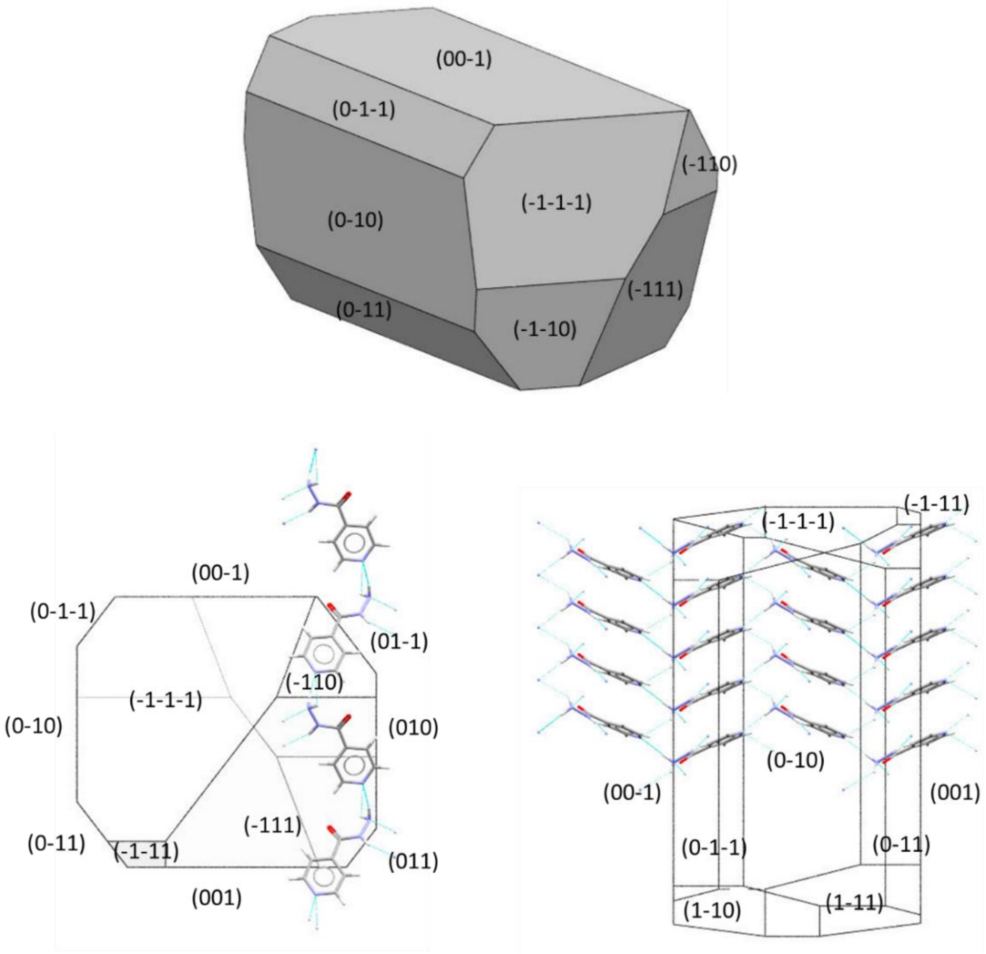

Figure 4.8. Top: Face indexed morphology for IZN crystallised from EtOAc. Bottom: Molecular packing with respect to morphology

The face indexed morphology achieved from crystallisations in EtOAc (figure 4.8) has a distinct similarity to that calculated using the simple BFDH approach (figure 4.5). The growth on the needle capping faces is significantly reduced in this solvent in comparison that observed in water. There is also an increase in the growth of the (0-10) / (010) faces when compared to crystallisations carried out in EtOH and IPA. The apparent reduction in the growth resulting from π-system stacking could be the result of a specific interaction between the face and the solvent. As the solvent does not possess an aromatic ring to interrupt this interaction, this is an unlikely method of disruption. It is more likely that an acceleration of growth on the slower faces is occurring, allowing this growth to 'catch up', producing more block shaped crystals. The lower polarity of the solvent system supports this potential mechanism. The lower polarity of EtOAc reduces its potential to block hydrogen bonding sites on the surface of the growing crystal. In addition to the reduced polarity, the structure of EtOAc also has an effect on its ability to hydrogen bond. The combination of these two factors reduces the ability of the solvent to interact with the growing surfaces and allows the solute molecules to bind preferentially instead.

The evaporative crystallisation carried out in ACN also results in a more favourable block shaped crystal morphology (figure 4.9). Again, ACN has a lower polarity than water, allowing the growth of the slow faces to catch up with that of the faster faces.

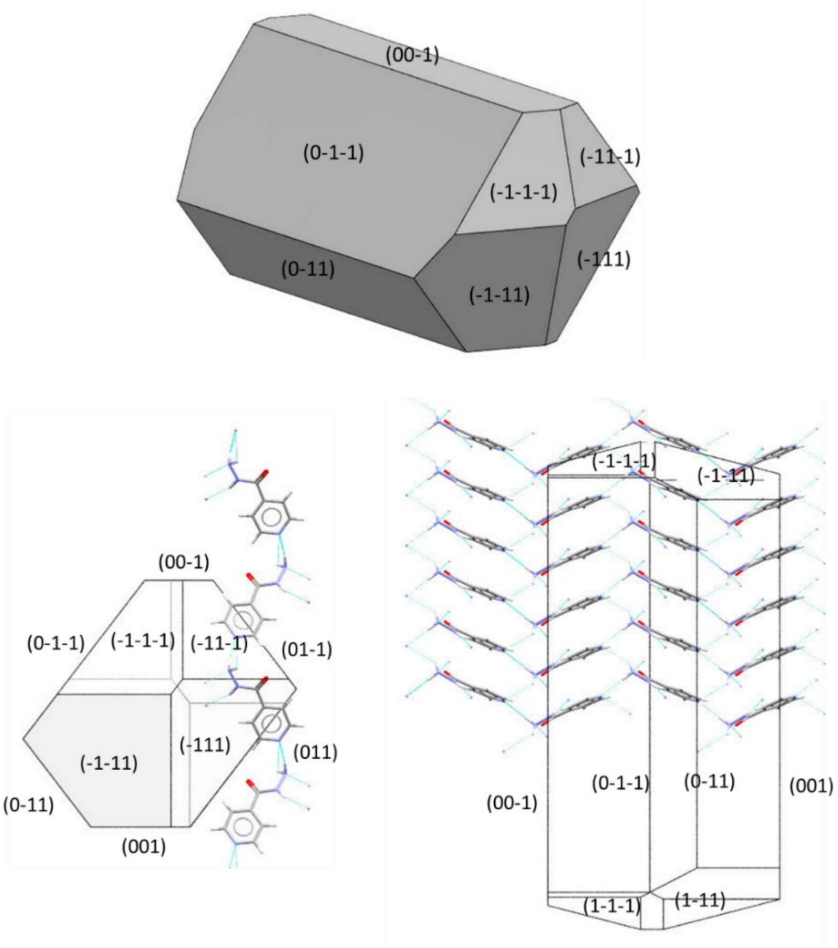

Figure 4.9. Top: Face indexed morphology for IZN crystallised from ACN. Bottom: Molecular packing with respect to morphology

The most significant growth is observed on the capping faces, as discussed above with respect to the needles produced. The π-stacking interactions have the strongest effect on the growth of the crystal in ACN, as in all the previous solvents discussed. This major growth mechanism is difficult to interrupt with aliphatic solvent systems. ACN contains functional groups that form weaker hydrogen bonds than the more polar solvents investigated. As a result, ACN has a low affinity for the growing surfaces of the crystal and does not efficiently block the approach of the solute growth units. Whilst the polarity of ACN is much lower than that of water, comparison of the solvent polarities alone would suggest the shape produced from ACN should be more similar to that observed for IPA. The more block shape obtained from ACN can therefore be attributed not only to the polarity of the solvent but must also be influenced by the structure.

The same results were not achieved in cooling crystallisation. Only needle crystals were achieved from cooling crystallisation in ACN, both with and without overhead stirring. As a result, ACN is not a reliable solvent for effecting reproducible morphology changes in IZN.

4.2.3 Transfer of isoniazid solvent experiments into the KRAIC continuous crystallisation platform

The KRAIC continuous platform was used to crystallise IZN from both IPA and EtOAc in order to determine whether the same morphology modifications could be achieved using a continuous crystallisation methodology.

Successful continuous crystallisation experiments were carried out in IPA at a concentration of 0.02 g/g. Experiments were also carried out at lower concentrations, but no nucleation was observed within the coils of the KRAIC for these experiments. At the concentration of 0.02 g/g, the crystallisation was run for three residence times (total of 42 minutes) before crystallisation was observed in the outlet of the solution pump. It is not possible to control the temperature of the solution as it goes through the pump in the current set up. This means there is the potential for nucleation in this part of the KRAIC due to the solution being highly saturated. The chosen concentration of 0.02 g/g resulted in the ability to achieve the correct level of supersaturation to allow for significant nucleation within the KRAIC coil, resulting in growth of the crystals in the coil (figure 4.10).

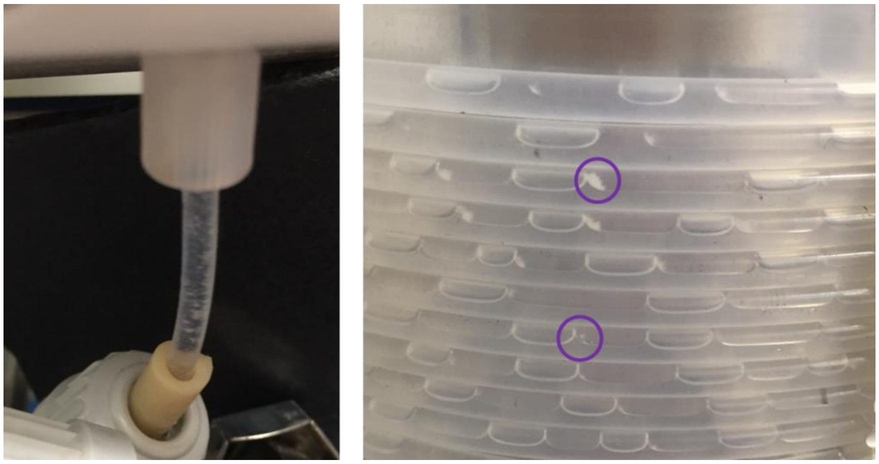

Figure 4.10. Crystallisation in feed pump outlet (left) and crystals in solution slugs in KRAIC tubing (right) for IZN crystallisation from IPA

The crystals extracted from the KRAIC (figure 4.11) showed the usual plate-shaped morphology discussed above for crystallisations carried out in IPA. The consistency in the morphology demonstrates the ability of the morphology change to be achieved in a continuous platform, a promising finding in terms of implementing morphology control as part of a continuous crystallisation approach to process development. Successful transfer of morphology control to continuous crystallisation has previously been achieved for an additive-enabled morphology change in a model compound (succinic acid).[63, 201]

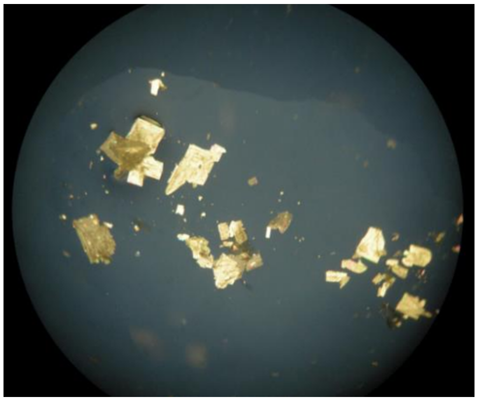

Figure 4.11. Crystals produced from continuous cooling crystallisations in IPA in the KRAIC set up

Face indexing experiments were carried out to allow comparison of the faces of the plates produced in the KRAIC (figure 4.12) to those previously produced in bulk cooling methods.

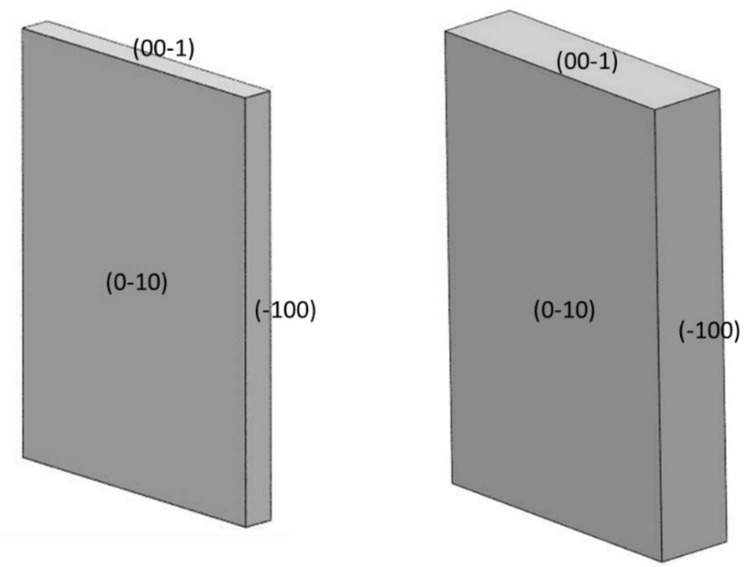

Figure 4.12. Face indexed crystals of IZN crystallised from IPA in the KRAIC continuous cooling (left) and batch cooling (right)

The faces indexed for the crystals produced in the KRAIC exactly mirror those determined for the crystals produced in bulk cooling methods from IPA. This validates the use of IPA solvent as a robust influence on changing the morphology of IZN. The ability to achieve the same morphology in the KRAIC demonstrates the transferability of the effects of IPA on the growth across different crystallisation methods and into continuous crystallisation platforms.

PXRD confirms the crystals to be pure IZN, with the peaks from the sample analysed matching the unique peaks for the pure IZN structure (figure 4.13). The absence of any distinctive peaks differing from those of the known IZN pattern confirms no form change has occurred upon the change in morphology and no solvate form has been produced.

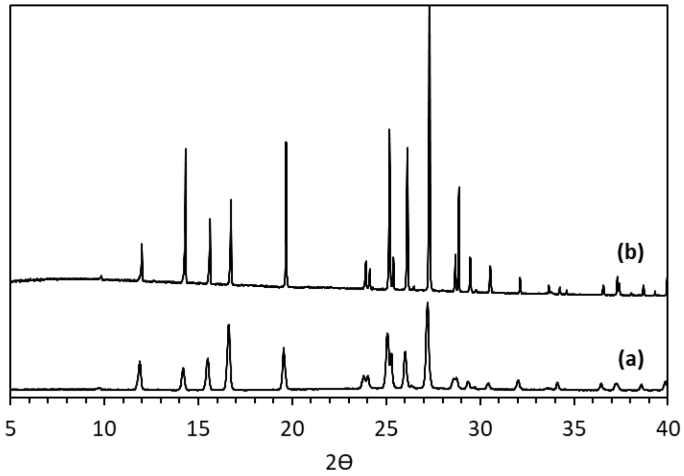

Figure 4.13. PXRD data for (a) IZN (INICAC02) and (b) IZN crystallised from IPA in the KRAIC continuous platform

KRAIC experiments were also carried out for IZN in EtOAc. Using a concentration of 0.005 g/g crystallisation of IZN was observed in the coils of the KRAIC (figure 4.14 right). However, significant crystallisation was also observed in the outlet of the solution pump (figure 4.14 left). This could result in blockages of the pump itself and significant increase of pressure in the system. As a result, the experiment was aborted after 21 minutes, within the second residence time of the experiment. Repeat runs were carried out with higher set temperatures for the jacketed tubing, resulting again in crystallisation in the outlet of the pump, and at lower starting saturations of IZN, resulting in no crystallisation within the KRAIC coil.

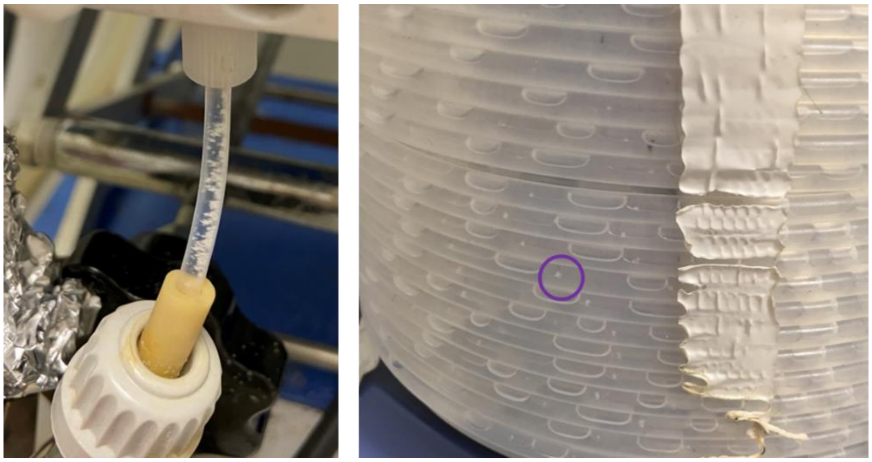

Figure 4.14. Crystallisations in the feed pump outlet (left) and crystals in solution slugs in KRACI tubing (right) for crystallisations of IZN from EtOAc

Despite the issues in optimising the crystallisation, the crystals produced within the KRAIC again exhibited a successful morphology change consistent with that observed for EtOAc in previous methods. Small, rod-shaped crystals were observed (figure 4.15), closely resembling those previously discussed in this chapter.

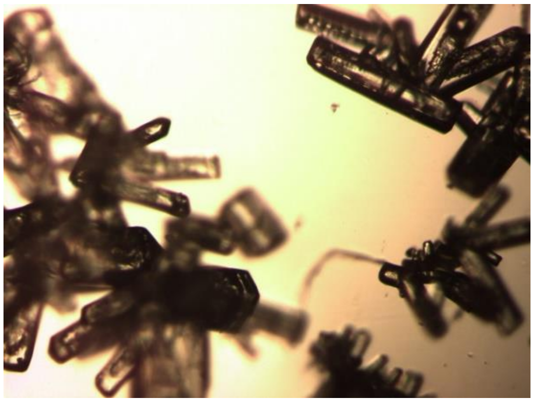

Figure 4.15. Crystals produced from continuous cooling crystallisations from EtOAc in the KRAIC set up

The transferability of this morphology change again suggests the KRAIC continuous crystallisation method could be a viable route to robustly creating IZN crystals on a large scale that display enhanced morphological characteristics. Face indexing was carried out for comparison with the morphology previously observed from evaporative and cooling crystallisations of IZN from EtOAc (figure 4.16).

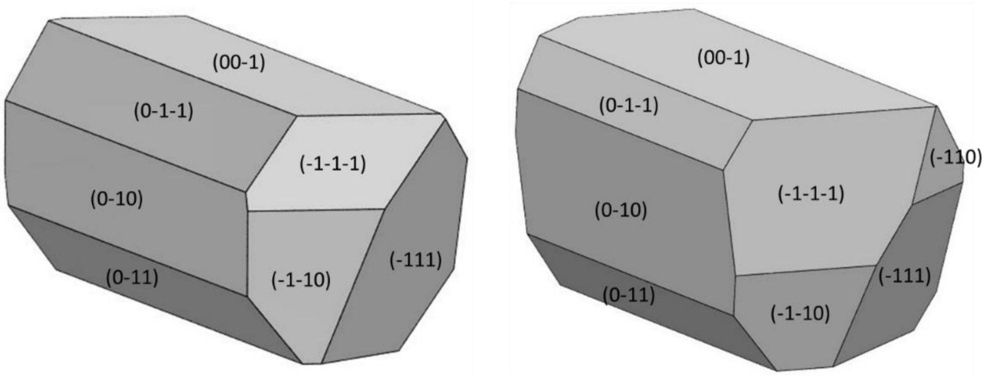

Figure 4.16. Face indexed crystals produced from EtOAc in KRAIC continuous cooling (left) and batch cooling (right)

The indexed faces of the crystals produced in the KRAIC are the same as those indexed in samples from the bulk crystallisation experiments. The shape achieved replicates the original morphology, with the exception of the capping faces on the end. The (-110) face is missing from the end of the crystal, which could be the result of a number of factors. The face could have been missed from the indexation of the KRAIC sample, due to its small size and lack of clarity in the movie taken of the crystal. The difference could also be the result of breakages to the ends of the crystal as it is moved from the vial and mounted onto the single crystal diffractometer. The final reason for the difference could be slightly different growth mechanisms occurring in the KRAIC and in the bulk crystallisation methods. The reproduction of the morphology confirms EtOAc has a significant influence which can be transferred between a number of different crystallisation methods and platforms.

PXRD analysis was used to confirm the absence of a solvate form or polymorphic change in the pure IZN crystals. The peak positions in the pattern measured for the IZN crystals produced in EtOAc match those for pure IZN (figure 4.17).

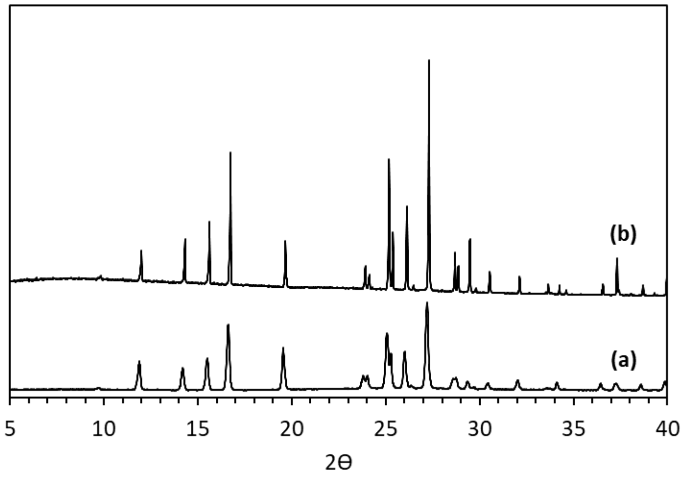

Figure 4.17. PXRD data for (a) IZN (INICAC02) and (b) IZN crystallised from EtOAc in the KRAIC continuous cooling platform

4.2.4 Temperature cycling effects on isoniazid morphology crystallised from ethyl acetate

Temperature cycling can be a useful tool to improve morphology. Heating and cooling cycles can allow the dissolution of fines in the solution and result in the growth of larger crystals with improved shapes. As different faces possess different growth and dissolution rates, prolonged cycling allows morphologies to be accessed that would otherwise be difficult to achieve.[64, 202] However, due to this extended cycling, it is a time consuming process.

Two experiments were carried out to see if the morphology changes in IZN crystals observed in EtOAc could be further improved using the cycling method. The resulting crystals show little change from those seen previously for crystallisations carried out in EtOAc (figure 4.18). PXRD analysis shows no solvates have formed during the cycling experiments (appendix A2).

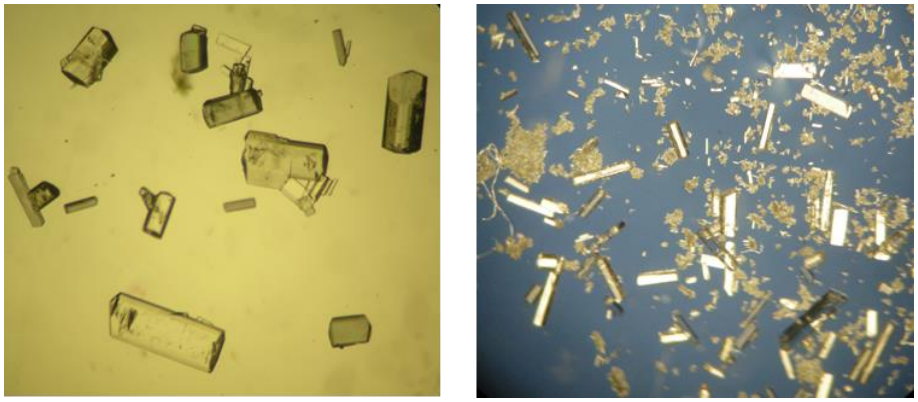

Figure 4.18. IZN crystals produced in temperature cycling experiment 1 where a 30 minute hold was included between cycles (left) and experiment 2 where no hold was utilised between heating and cooling (right)

Experiment 1 shows a slight improvement on the uniformity of the morphology achieved in cooling crystallisations and closer resembles the outcome of the evaporative crystallisations. The dwell periods between the ramping up and down in temperature has allowed the crystals to grow to be larger than seen in experiment 2 and less fines are produced. However, this experiment overall took 31.5 hours, compared to 13.5 hours for a standard cooling experiment using the same ramp rates and conditions. Experiment 2 has a slightly shorter experiment time, 28.5 hours, but does not produce as good results as seen in experiment 1. More fines can be seen and the crystals produced are longer, thinner and smaller.

Overall the more successful temperature cycling approach would be experiment 1, with the inclusion of the dwell periods between the heating and cooling profiles. However, the improvement compared to the shorter, linear cooling crystallisations is likely not enough to justify the significant increase in crystallisation time required.

4.2.5 The effect of supersaturation on isoniazid morphology

As some crystallisations did not produce the same morphologies in evaporative as they did in cooling, experiments were carried out to investigate the effects of starting saturation on the morphology achieved. In parallel, the effect of changing the temperature at which a sample is evaporated was also examined.

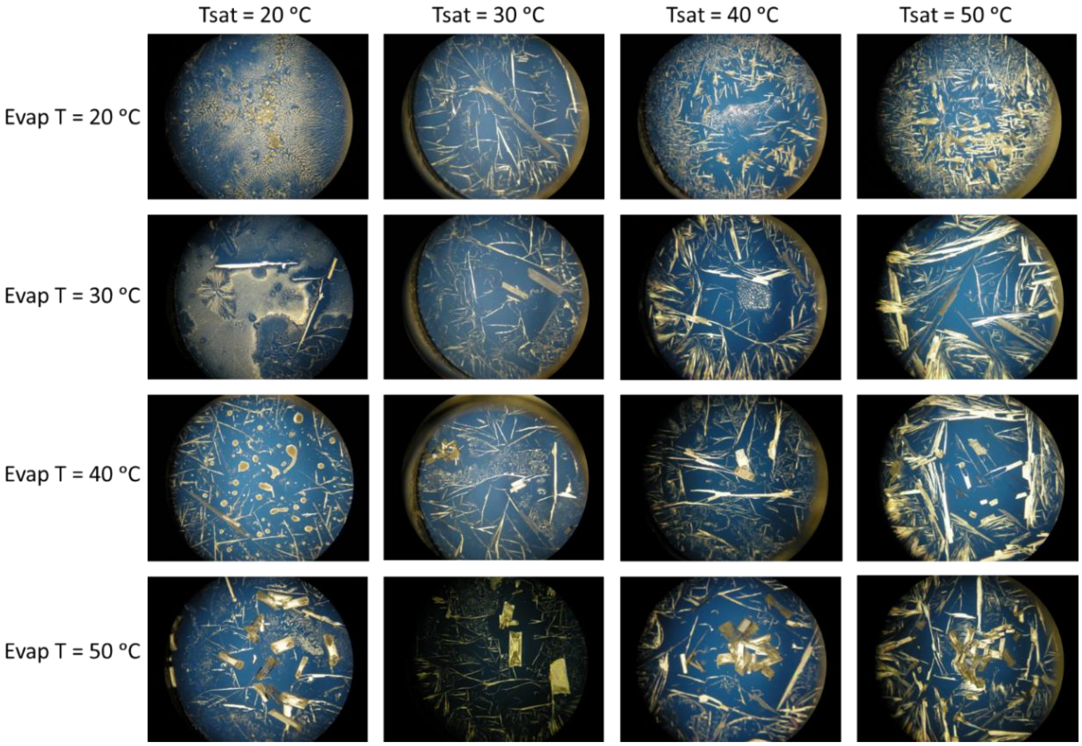

Figure 4.19. Evaporative experiments to investigate the effects of saturation and evaporation temperature on the morphology of IZN crystallised from IPA

For evaporative crystallisations carried out in IPA, evaporating at a faster rate seems to allow the formation of plates as seen in cooling crystallisations (figure 4.19). At all initial saturations, plates are produced when evaporated at a temperature of 50 ^{o}C. This suggests the fast evaporation rate prevents the formation of the needle crystals. Some plates can also be seen in the evaporative crystallisations carried out at 40 ^{o}C with higher starting saturations.

In EtOAc, the rod-shaped crystal morphology was obtained from both evaporative and cooling crystallisations. The effect of starting saturation and evaporative temperature was also investigated for crystallisation from EtOAc to determine the landscape of the conditions allowing for the successful morphology change to occur.

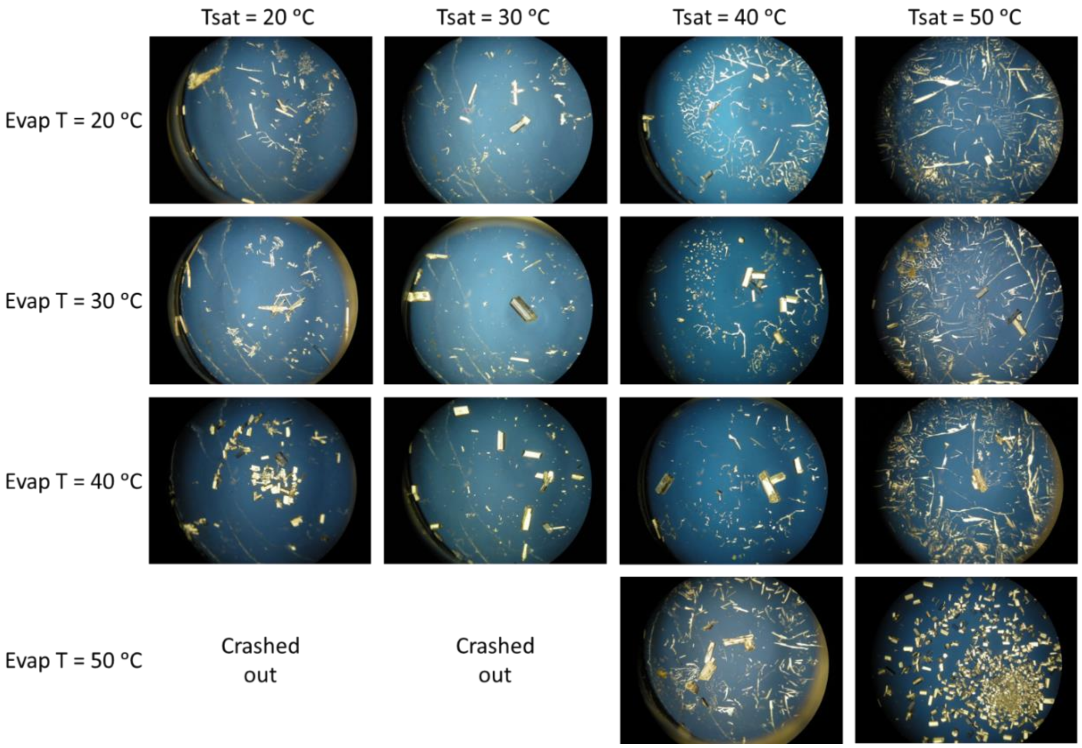

Figure 4.20. Evaporative experiments to investigate the effects of saturation and evaporation temperature on the morphology of IZN crystallised from EtOAc

The rod-shaped morphology is achieved in all crystallisations carried out in EtOAc (figure 4.20). The starting saturation and evaporative temperatures used appear to have no significant impact on the morphology of the crystals produced. No discernible pattern can be identified for the crystallisations carried out in EtOAc.

Supersaturation investigations were also carried out in cooling crystallisations, to examine the effects of cooling speed and starting saturation of the shapes of the crystals produced. No influence on the shape was observed. The only difference resulting from changing the starting saturation was the amount of crystals produced. As a result, it can be determined that saturation has little effect on the morphology produced under controlled cooling conditions.

4.2.6 Morphology changes of isoniazid in evaporative crystallisations with solvent mixtures

4.2.6.1 Ethyl acetate:propan-2-ol mixtures

Crystallisation of IZN from mixtures of IPA and EtOAc were investigated to determine whether the presence of a smaller percentage of EtOAc can have the same morphological effects as seen in experiments carried out in pure EtOAC. EtOAc was added to IPA in 10% intervals from 90:10 to 10:90

IPA:EtOAc solvent mixtures and evaporative IZN crystallisation carried out in each mixture, at 20 ^{o}C and 40 ^{o}C (figure 4.21).

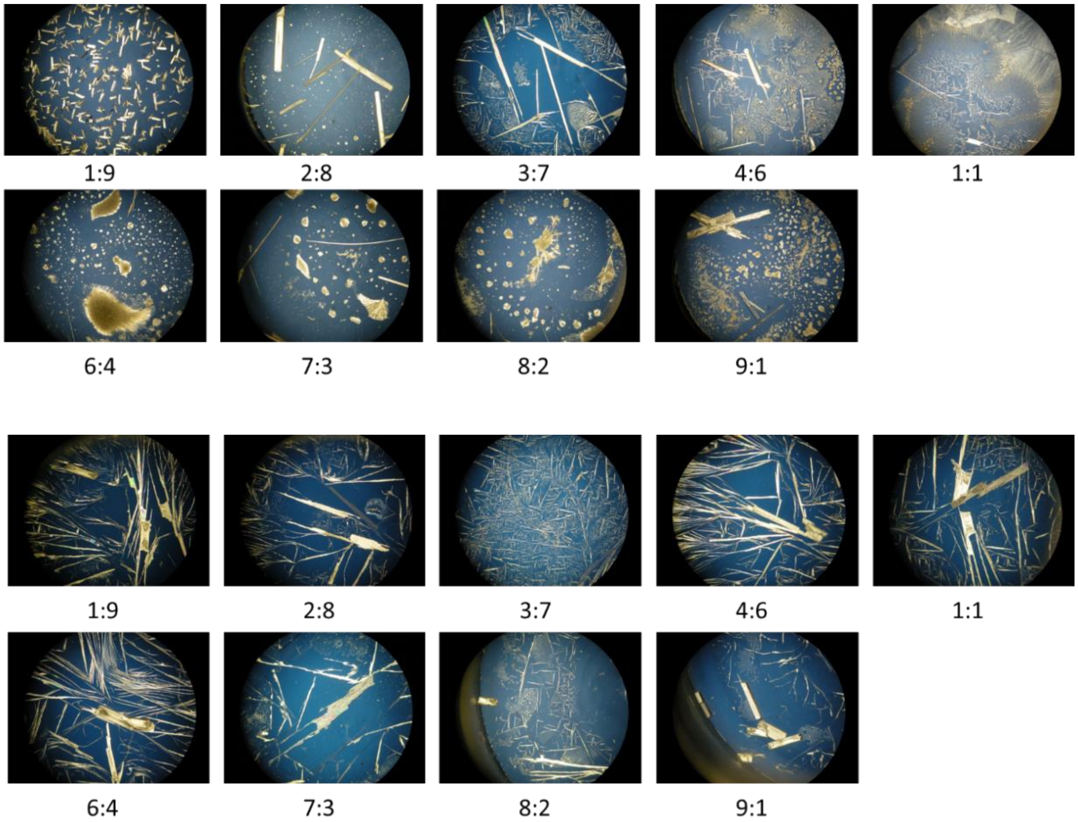

Figure 4.21. Evaporative experiments carried out at 20 ^{o}C (top) and 40 ^{o}C (bottom) to investigate effects of solvent mixtures of IPA:EtOAC on IZN morphology

The results show that successful morphology modifications are observed only at the higher percentages of EtOAc. Only those with 90% and 80% EtOAc have produced the rod-shaped crystals previously seen for crystallisations carried out in pure solvent. The other crystallisations show the plate-shaped crystals seen for pure IPA in both evaporative and cooling crystallisations. There is thus no evident benefit of using the mixed IPA:EtOAc solvent in achieving IZN morphology modification.

4.2.6.2 Ethyl acetate and ester mixtures

Initially, a selection of esters was chosen for use as the primary crystallisation solvent, with the aim of determining whether chain length of the ester had an effect on the morphology produced. The solubility of IZN in the esters was found to be minimal however, and the experiment was not successfully carried out. As a result, a series of solvent mixture experiments were set up as an alternative way to assess any effect of the longer chain length esters. The esters were used in 10% - 50% v/v ratios with both IPA and EtOAC.

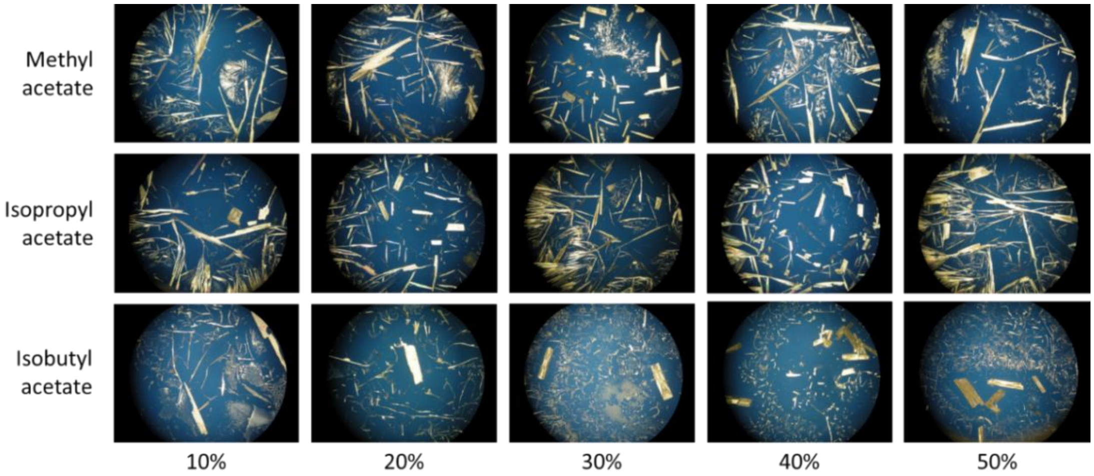

Figure 4.22. Evaporative experiments to investigate the effects of solvent mixtures of IPA and assorted esters (percentages given) on the morphology of IZN

Crystallisations of IZN from solvent mixtures of the branched esters with IPA show only plate-shaped crystals, as previously observed from IPA alone (figure 4.22). This indicates that the esters do not affect the crystallisation in the amounts added; however, no detrimental effects are observed.

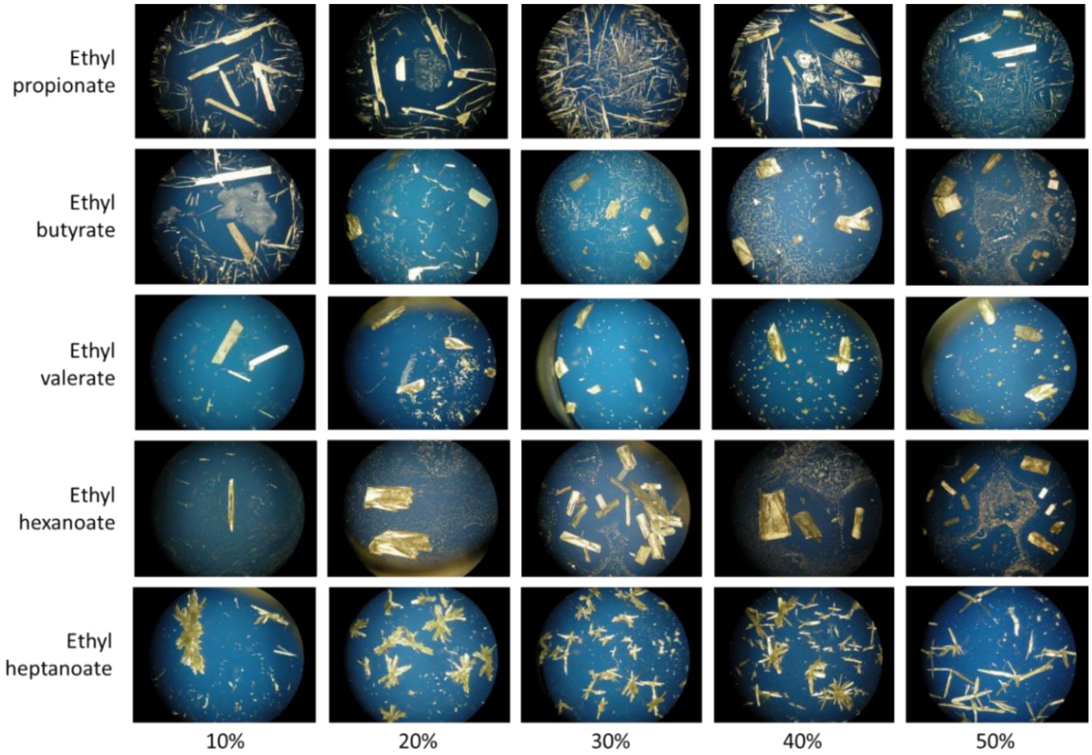

Figure 4.23. Evaporative experiments to investigate the effects of solvent mixtures of IPA and assorted esters (percentages given) on the morphology of IZN

The same can be concluded for the extended carbon chain esters used. Plate-shaped crystals, as usually observed for IPA crystallisations, can be seen for almost all of the mixed solvent experiments in this set (figure 4.23). The only exception is the IZN morphology produced from crystallisations carried out in ethyl heptanoate. The crystals produced in all experiments with ethyl heptanoate show needle-shaped crystals. This suggests the addition of the extended chain ester in the crystallisation solvent mixture produces less favourable conditions for the desired IZN morphology improvement, resulting in the return from plates to needles.

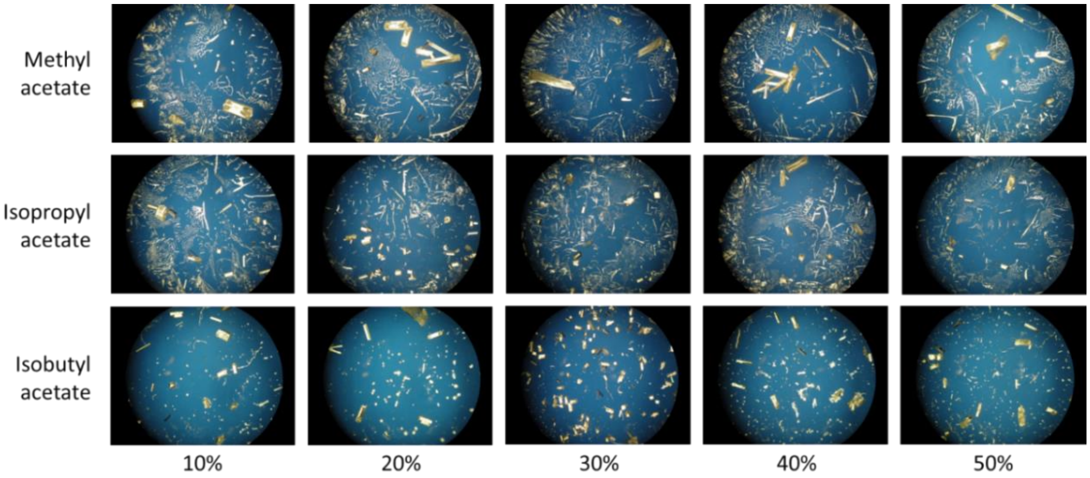

Figure 4.24. Evaporative experiments to investigate the effects of solvent mixtures of EtOAc and assorted esters (percentages given) on the morphology of IZN

The crystals produced from mixtures of EtOAc and the branched esters show similar rod-shaped morphologies as achieved from pure EtOAc crystallisations (figure 4.24). No change is observed upon the addition of the ester additives.

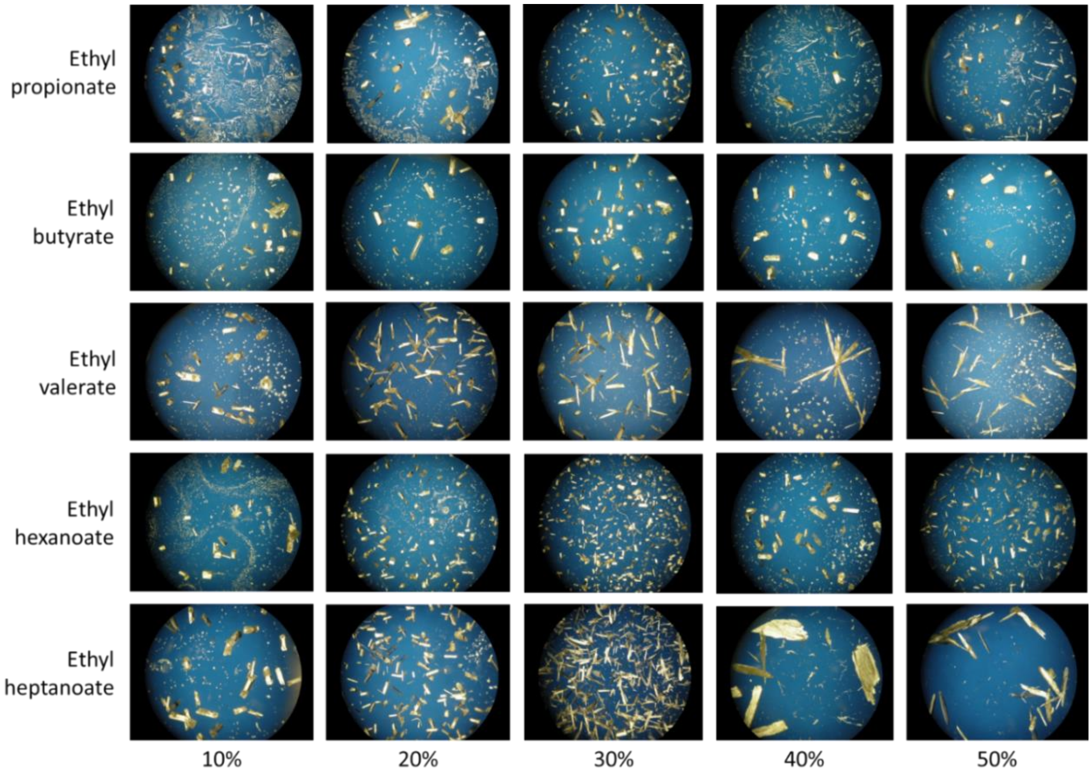

Figure 4.25. Evaporative experiments to investigate the effects of solvent mixtures of EtOAc and assorted esters (percentages given) on the morphology of IZN

Similarly, very little change is observed for crystallisations carried out with solvent mixtures of extended chain esters and EtOAc (figure 4.25). The exception to this is the return to needle shapes seen for solvent mixtures containing a higher percentages of ethyl valerate and ethyl heptanoate. These effects are detrimental to the morphology changes achieved in pure EtOAc.

The solvent mixture experiments suggest there is little benefit from using a solvent mixture to aid the changes in morphology of IZN. In IPA, no promising morphology changes were observed upon the addition of the esters. In EtOAc, no further morphology changes are observed that improve upon the changes originally achieved in pure EtOAc. As a result, it would not be beneficial to use a solvent mixture as the same results can be obtained in pure EtOAc.

4.3 Additive experiments with isoniazid

Additives are considered intentionally added impurities when being referred to in the context of crystallisation. Whilst many additives are used in pharmaceutical product formulation, it is not common to see them used in the crystallisation step. Regulations dictate that only very small amounts of impurity are allowed at the crystallisation stage to ensure these do not come through into the final drug product and cause potential harm to patients. As a result, research into the use of additives must focus on changes made by the presence of very small quantities. A good additive choice would be significantly more soluble that the API target in question in order to allow it to remain in solution after crystallisation has occurred and be removed in filtration steps.

The aim of this work is to identify an additive system that is successful in modifying the morphology of IZN when present in solution. The robustness of this control would then be verified by testing the system under various crystallisation conditions. As previously discussed, IZN often forms thin needle or plate-shaped crystals, the avoidance of which can offer significant benefits for pharmaceutical processing steps. Therefore, an additive would ideally yield more block shaped crystals with better aspect ratios. For this research two different types of materials have been chosen as additives; structurally similar/size-matched molecules and polymers. SCXRD was used to index the crystal faces of crystals exhibiting a morphology change to understand any changes occurring in the growth of the crystals. Unit cell determination and other bulk analysis techniques, including PXRD, NMR spectroscopy and DSC, are also used to confirm the same form of the API is being produced.

4.3.1 Selection of additives for isoniazid

Additive selection was carried out using molecular complementarity function in the Mercury program. All five molecular descriptors were enabled for the calculations. Molecular complementarity is a calculation usually designed to predict the compatibility of molecules for co-crystallisation. It is used here to guide the choice of additives. The additives used should be able to interact with the active ingredient in a way that changes the growth. Therefore, if a chosen molecule has propensity to make a co-crystal with the target API, it follows that there is a chance a small amount being present will interact to influence the growth of the API crystals. Two different lists of molecules were screened for complementarity; a list of GRAS molecules and a list of common molecules found to make co-crystals. The use of non-GRAS additives would not be favourable to the pharmaceutical industry, however, the knowledge gained from their use could help design a better additive process with safe molecules.

The molecules that passed the molecular complementarity check are further examined for their possible interactions with IZN and their structural similarities. As the major growth in IZN is influenced by the interaction between the aromatic rings, molecules containing an aromatic ring were favoured. The aim of choosing these would be to interrupt the major growth mechanism of the crystal, allowing the slower growing faces to catch up. By capping the fast growing faces it is hoped the resulting crystals will be shorter and fatter. The final consideration taken was to check if any of the additives that passed were already known to make co-crystals. This was again favoured as they are already known to interact well with the IZN molecules. The additive wt% used should be low enough to avoid co-crystal formation from these being present in the system. The final additive list chosen is shown in figure 4.26.

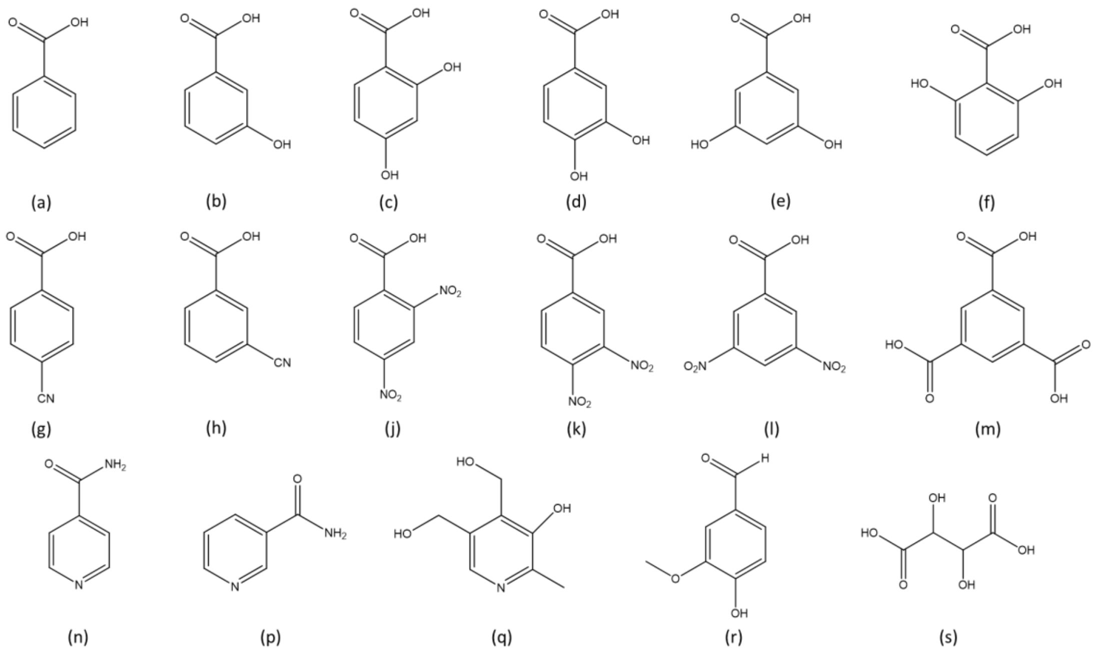

Figure 4.26. Additives list for screening with IZN (a) benzoic acid, (b) 3-hydroxybenzoic acid, (c) 2,4-dihydroxybenzoic acid, (d) 3,4-dihydroxybenzoic acid, (e) 3,5-dihydroxybenzoic acid, (f) 2,6-dihydroxybenzoic acid, (g) 4-cyanobenzoic acid, (h) 3-cyanobenzoic acid, (j) 2,4-dinitrobenzoic acid, (k) 3,4-dinitrobenzoic acid, (l) 3,5-dinitrobenzoic acid, (m) trimesic acid, (n) isonicotinamide, (p) nicotinamide, (q) pyridoxine, (r) vanillin and (s) L-tartaric acid

A selection of polymeric additives was chosen based on their hydrophilic or hydrophobic properties. The needle morphology of IZN has hydrogen bonding groups along the needle axis and no functional groups on the capping faces. In H_2O, it is observed that the molecules likely interact with the long axis faces, inhibiting growth perpendicular to these, resulting in growth units joining on the capping faces and extending the needle length. This would suggest that hydrophobic polymers could cap the major growth faces and allow the fattening of the needle morphologies to more favourable, equant shapes. By using a mixture of hydrophobic and hydrophilic polymers this hypothesis can be tested for IZN crystallisations; the polymers selected are shown in figure 4.27.

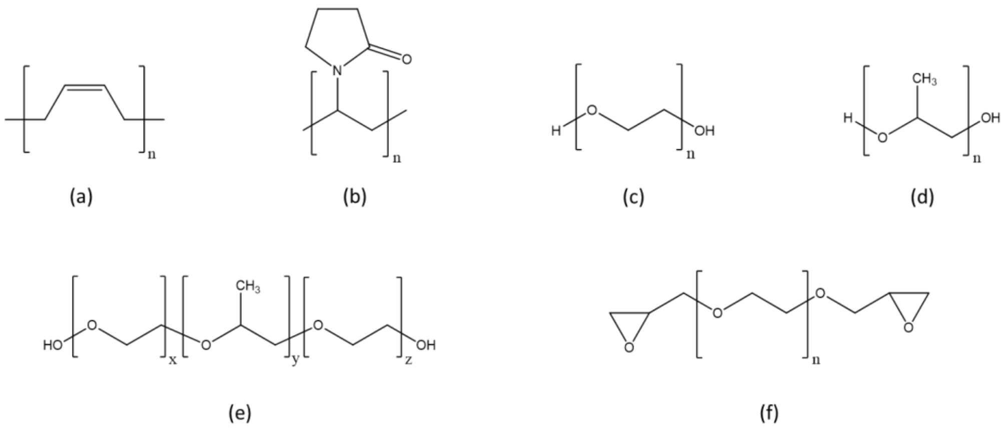

Figure 4.27. Polymeric additive list for screening with IZN (a) polybutadiene, (b) polyvinylpyrrolidone, (c) poly(ethylene glycol), (d) poly(propylene glycol), (e) pluronic P123 and (f) poly(ethylene glycol) diglycidyl ether

The hydrophobic polymers used were polybutadiene (PBD) and polypropylene glycol (PPG). The hydrophilic polymers used were polyvinylpyrrolidone (PVP), polyethylene glycol (PEG) and poly(ethylene glycol) diglycidyl ether (PDE). Pluronic P123 (PP123) is an amphiphilic polymer, with both a hydrophilic and hydrophobic section.

4.3.2 Experimental information

All materials and solvents used in these experiments were obtained from commercial sources. No further purification steps were carried out on the acquired starting materials.

4.3.2.1 Evaporative screening of isoniazid with different additives

Evaporative crystallisations were prepared in 7 mL vials by dissolving small quantities (0.01 g) of IZN and the corresponding wt% of additive in a minimal amount of solvent. To allow slow evaporation holes were pierced in the plastic lids. Evaporation was carried out at room temperature and an elevated temperature of 40 ^{o}C. The solvent chosen for this study was IPA, due to the repeatability of the plate morphology achieved in this solvent. Although this IZN morphology change was observed from IPA, the ideal crystal habit has not been achieved. Therefore, the additive investigation was carried out in IPA in an attempt to further improve the morphology change already observed. The additives were tested at a range of concentrations, at wt% values of 1%, 5% and 10%.

Polymers as additives were also investigated in evaporative crystallisations. Small quantities of IZN (0.01 g) and polymer additive were dissolved in IPA in 7 mL vials. Holes were pierced in the lids of the vials to allow for slow evaporation at both room temperature and an elevated temperature of 40 ^{o}C. Polymer additives were used in percentage mass ratios of 0.1% and 1%. A wt% of 1% was chosen due to success achieved with size-matched additives at this level, while the smaller mass ratio of 0.1% was used due to successes reported in literature of much smaller additive percentages.

4.3.2.2 Cooling crystallisation of isoniazid with different additives

Controlled cooling experiments were carried out for systems in which successful additive effects were observed in evaporative experiments. As transfer to cooling proved challenging, a wide variety of different experiments were carried out. The variables changed throughout the experiments include starting saturation, cooling rate, length of time held at low temperature and percentage of additive. T_{sat} values of 20 ^{o}C, 30 ^{o}C, 40 ^{o}C and 50 ^{o}C were used with respect to IZN in IPA. Cooling rates of 1 ^{o}C/minute and 0.1 ^{o}C/minute were used along with holds at low temperature of 1 hour, 5 hours and 10 hours. Percentages of (size-matched) additive chosen were 1%, 5% and 10%. A mass of 5 g of solvent was saturated in 20 mL glass vials. Stirring was implemented using a magnetic bottom stirrer during heating but turned off during cooling to avoid breaking/grinding of the resulting crystals. All crystallisations were heated to 55 ^{o}C and held for 30 minutes to allow for complete dissolution. Cooling was then carried out to a temperature of 5 ^{o}C at the chosen rate and held at this temperature for the chosen period of time.

Large scale cooling crystallisations were also carried out in a 250 mL round bottom flask using overhead stirring. 150 g of IPA was saturated at 40 ^{o}C and additive percentages of 1%, 5% and 10% were used. The crystallisations were again cooled from 55 ^{o}C, after being held for 30 minutes to achieve complete dissolution, at rates of 1 ^{o}C/minute and 0.1 ^{o}C/minute. Crystallisations were finished at 5 ^{o}C and held for 1 hour. Overhead stirring was used continuously throughout at a rate of 350 rpm.

Polymeric additives were also tested in cooling crystallisation. The same polymer percentages used in evaporative were investigated in cooling, 1% and 0.1%. Crystallisations were carried out in 20 mL glass vials and 5 g of solvent was saturated with IZN at 40 ^{o}C. Samples were heated to 55 ^{o}C and held for 30 minutes with stirring to ensure full dissolution. Cooling was carried out at 1 ^{o}C/minute and 0.1 ^{o}C/minute to 5 ^{o}C without stirring. The samples were held for an hour to allow nucleated crystals to grow.

4.3.2.3 Transfer of isoniazid additive crystallisations into the KRAIC continuous platform

Uncontrolled cooling crystallisations of IZN were carried out in the KRAIC in IPA with both 3-hydroxybenzoic acid (3-HBA) and 3,4-dinitrobenzoic acid (3,4-DNBA) additives. A number of different crystallisation runs were carried out to optimise the temperature profile and starting concentration of the solution. The optimised conditions are shown in table 4.2.

Table 4.2. Conditions for crystallisations carried out in the KRAIC continuous platform in solvents IPA and EtOH

Concentration IZN (g/g)	Priming/feed temperature (˚C)	Cross piece temperature (˚C)	Circulator bath temperature (˚C)
0.0175	55	55	55

The crystallisations were carried out for additive ratios of 1%, 5% and 10%. The KRAIC was primed for 1 hour using IPA, air and Galden (carrier fluid) to ensure steady-state was reached. The flow rate of all pumps was set to 2.40 mL/minute. After priming, the feed solution was introduced in place of the pure IPA. Crystals were collected from the end piece of the crystalliser tubing into a Buchner funnel and left to dry after the experiment for further analysis. Galden was recycled back into the crystalliser via separation through the carrier fluid recovery holes in the end piece. If a build-up of crystals occurred in the end piece a syringe of neutral solvent, pure IPA, was used to flush the crystals into the funnel.

4.3.2.4 Analytical methods

Microscope images of final crystal products were taken using a Nikon Coolpix P5100 camera through a Brunel Microscopes microscope.

Analysis was also carried out via PXRD and DSC techniques, as explained in Chapter 3, to ensure the form of the crystals produced remained the same. NMR spectroscopy analysis techniques were also used to help determine whether any additive was incorporated into the crystal structure in small amounts.

Face indexing was carried out using a Rigaku Oxford Diffraction Gemini A Ultra diffractometer with Mo-Kα radiation. Screening of unit cells were carried out at 298 K and pre-experimental data recorded. Face indexing was performed with CrysAlisPro software to determine the faces and overall shape of crystals produced. Crystal structure and morphology were visualized using the BFDH tool included in Mercury software.

4.3.3 Effect of size-matched and structurally similar additives on isoniazid morphology achieved via evaporative crystallisation

Plate or needle-shaped crystals resulted from the majority of the additive experiments carried out (appendix A3). However, two successful additive candidates were identified that gave more equant morphology; 3-HBA and 3,4-DNBA. Both of these additives are capable of producing multi-component crystalline materials with IZN; the co-crystal structure for 3-HBA is available via the CSD and the structure for IZN:3,4-DNBA is reported later in this thesis (chapter 5). The presence of these additives in the crystallisation mixture results in formation of more rod-shaped crystals (figure 4.28), in contrast to the original plates, without incorporation of the additive molecule into the crystal structure.

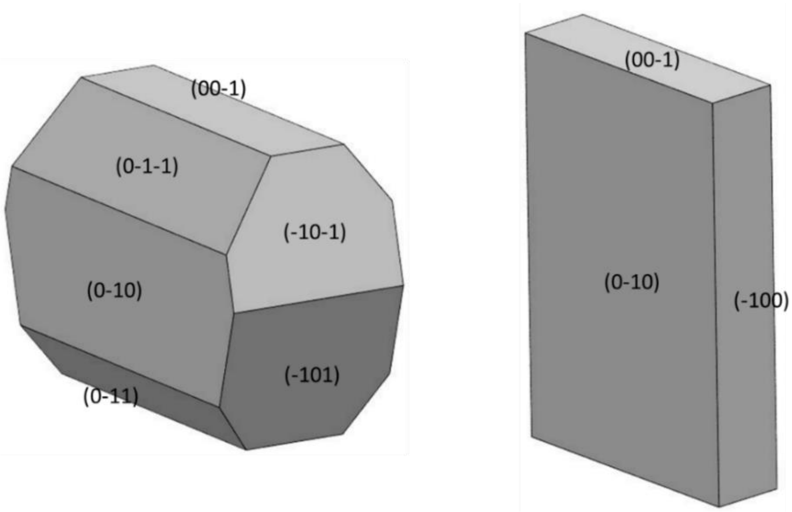

Figure 4.28. Face indexed crystals of IZN crystallised from IPA in the presence of 1% 3-HBA (left) and in the absence of additives (right)

The morphology achieved in the presence of 3-HBA (from IPA solvent) is similar to that observed for crystallisations carried out in EtOAc. Significant growth is observed on the (-10-1) and (-101) faces, resulting from the stacking and interaction between the aromatic rings of the IZN molecules. This growth is also seen in the morphology achieved in EtOAc. The growth on the (00-1) face is the result of the hydrogen bonding interaction between the terminal NH_2 group and the N in the pyridine ring. These chains of molecules are also responsible for the elongation in the plates obtained from IPA cooling crystallisations in the absence of additive. These similarities are observed in most of the solvent influenced crystal morphologies. The differences between the IPA crystal morphology and the additive influenced morphology are characterised by the fattening of the morphology and increased growth on the (0-10) face. The (0-10) face is only lightly influenced by hydrogen bonding interactions, explaining the slower growth along this crystallographic axis. The weaker interactions appear to have been overcome slightly in the presence of the additive. The additive is likely to interact with the IZN crystal structure in two ways. Firstly, the 3-HBA is an aromatic, planar molecule, allowing it to interrupt the aromatic interactions causing the major growth in the IZN molecule. By partially blocking this face the joining IZN molecules are forced to attach to different faces. Secondly, the 3-HBA is likely to form some favourable hydrogen bonding interactions with the N in the pyridine ring. Interactions between the COOH and pyridine N are seen in the majority of co-crystals published for IZN, including for the published IZN:3HBA co-crystal structure. This potential interaction will act as a capping interaction for the growth in this direction; whilst other hydrogen bonding interactions are possible with the 3-HBA, the chain growth is the most likely to be interrupted. This capping of the hydrogen bonds responsible for the growth on the (00-1) face coupled with the aromatic stacking interruption is likely responsible for the increased growth on the (0-10) face. This growth face is less heavily influenced by the presence of the additive and, therefore, an easier pathway for IZN molecules to join the structure.

The absence of the additive in the final crystal structure was confirmed using SCXRD, PXRD and DSC analysis techniques (appendix A4). A detection limit exists in the analysis techniques used to determin absence of the additive in the crystals produced in these crystallisations. In the case of PXRD and DSC the detection limit is potentially too high to determine the purity of the crystals produced to the level required by regulatory bodies.

Similar morphology is achieved with the additive 3,4-DNBA (figure 4.29). A rod crystal shape is achieved, again resembling the morphology achieved from EtOAc.

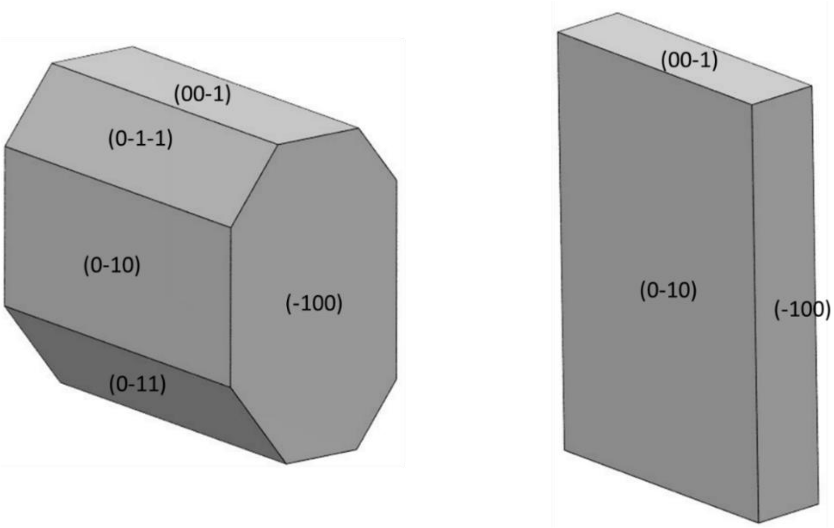

Figure 4.29. Face indexed crystals of IZN crystallised from IPA in the presence of 1% 3,4-DNBA (left) and in the absence of additives (right)

Despite the presence of 3,4-DNBA, significant growth is still observed on the (-100) / (100) faces. This is the result of π-π stacking between IZN aromatic rings and is also seen in the morphology achieved from IPA in the absence of additive. Hydrogen bonding interactions between terminal NH_2 groups and the heterocyclic N in the pyridine ring contribute to the growth on the (00-1) / (001) faces. These interactions form chains of molecules and are also responsible for the elongation observed in the plates obtained from IPA cooling crystallisations. These two interactions cause similar results in the majority of the solvent-influenced morphologies. The difference observed in the presence of the 3,4-DNBA additive is again the fattening of the crystal, to form the rod morphology observed. This suggests extra growth is occurring on the (0-10) and (010) faces of the crystal. There is only a small influence from hydrogen bonds on this axis, resulting in the slower growth observed in the solvent-mediated morphology. The presence of the additive is allowing extra growth to occur on this face either by increasing the interactions occurring on this face, or by weakening the interactions on the faster growing faces, allowing the slower growth to catch up. The latter explanation is perhaps more likely in the presence of this additive. The additive has a similar structure to 3-HBA and is therefore likely to interact with the IZN crystal structure in a similar way. The aromatic portion of the 3,4-DNBA can interact with the aromatic ring in the IZN, capping the (-100) and (100) faces. By blocking molecules from joining this face the major growth mechanism can be significantly reduced, allowing the slower faces to catch up and a less needle-like morphology to result. The carboxylic acid group in the 3,4-DNBA will also be able to hydrogen bond with the N in the IZN pyridine ring. This interaction blocks the primary hydrogen bonding interaction for incoming IZN molecules, forcing the weaker interactions to play a larger role in the growth mechanism. The 3,4-DNBA does not have any further hydrogen bonding donors or acceptors, therefore, the capping of these interactions will not result in any further growth from this site. It is probable the combination of these two capping interactions with the growing IZN crystal are causing the increased growth on the (0-10) and (010) faces; the incoming IZN molecules will be favoured to join these faces as they will not need to overcome the interactions between IZN and additive on the other faces.

PXRD and DSC analysis were carried out to confirm the absence of any additive in the resulting crystal structure (appendix A5). Again, the detection limit needs to be considered for both PXRD and DSC analysis techniques. The absence cannot be confirmed to the level of purity potentially required for regulatory approval. This was also confirmed by SCXRD analysis of the crystal structure.

4.3.4 Effect of size-matched and structurally similar additives on isoniazid morphology achieved via cooling crystallisation

Transfer of these successful additive crystallisations to cooling proved not to be straightforward. Multiple cooling crystallisation experiments were carried out with both 3-HBA and 3,4-DNBA additives under various conditions. The cooling profile variables changed throughout the investigations were: the cooling rate used; the dwell time at the end of the crystallisation process; the scale of the crystallisation; and stirring mechanism. The cooling method used was also changed and included controlled cooling in the Polar Bear Plus crystalliser, at two different scales, and uncontrolled cooling in the KRAIC continuous crystallisation platform. Different percentages of additive used were investigated, despite the evaporative crystallisations suggesting 1% was the optimal amount, and, where possible, the starting saturation of IZN was also altered between experiments. This extensive set of variables were investigated as there is evidence of these variables proving strongly influential in similar examples in the past.[63]

4.3.4.1 Cooling crystallisations at 10 g solvent scale

The crystallisations carried out for each additive at this small scale were unsuccessful. No stirring was used during the cooling profile in the 10 g scale experiments; only magnetic bottom stirring is possible at this small scale and would result in a powder product due to the grinding of the crystals. Due to the lack of stirring used, lower starting saturations produced little to no crystallisation. Those where crystallisation did occur gave only plate-shaped crystals, the morphology that usually results in IZN cooling crystallisations from IPA. Under the conditions used at this scale the additive appeared to have little if any effect on the morphology of the crystals produced.

In cooling experiments such as these, carried out without stirring, crystals took much longer to nucleate after cooling. Experiments were therefore held for longer periods after reaching the final temperature to attempt to allow more nucleation and growth and, hopefully, achieve the desired morphology change towards rod-like crystals. However, this increase in hold time after the full cooling profile was achieved had no effect on the morphology of the crystals produced. Plate-shaped crystals were still observed for all additive and saturation percentages. Some experiments with higher additive percentages even moved the morphology outcome back towards more needle-shaped crystals. (appendix A6 to A17).

4.3.4.2 Cooling crystallisations at 150 g solvent scale

Despite the lack of success in small scale, larger scale cooling crystallisations were carried out; these have the benefit of allowing overhead stirring to be utilised. Stirring will change the nucleation kinetics of the crystallisation being carried out, creating the potential for a successful morphology change to be observed that was not accessed in the small scale crystallisations. The two different cooling rates used at small scale were also used at this scale, however, the starting saturation of IZN was unchanged between crystallisations (T_{sat} of 40 ^{o}C).

For the 3-HBA additive, successful morphology changes were observed on this larger scale (figure 4.30).

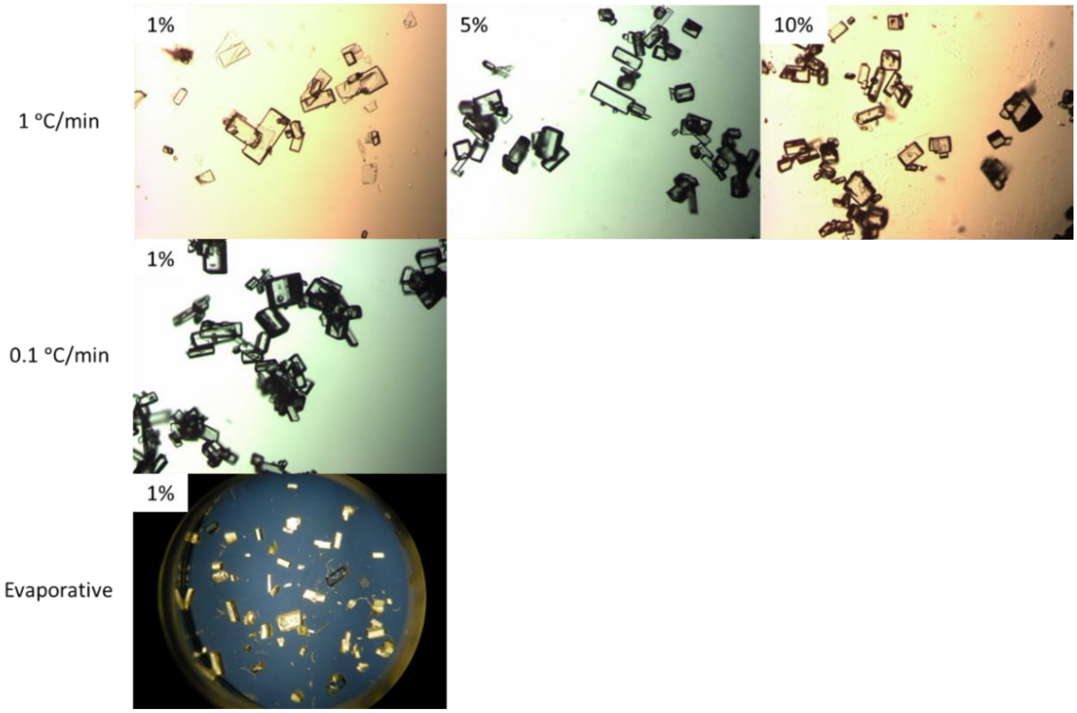

Figure 4.30. Microscope images comparing the morphology of IZN crystallised from IPA with 3-HBA additive in 150 g cooling with overhead stirring (top and middle) and evaporative crystallisations (bottom)

At a cooling rate of 1 ^{o}C/minute, all additive percentages produced mainly plate-shaped crystals, similar to those normally produced in additive-free IPA cooling crystallisations. Some more rod-shaped crystals were observed in the crystallisation carried out with 5% and 10% additive, however, as these were a minority of the crystals produced this was still determined as a failed procedure. The major success is seen for a cooling rate of 0.1 ^{o}C/minute with an additive percentage of 1%. This is the same additive content that achieved the most success in the original evaporative process. The crystals produced are of consistently fat, hexagonal rod-shaped morphology. The shape achieved is the same as seen in the successful additive-mediated evaporative crystallisation from IPA and similar to that seen for additive free crystallisations in EtOAc. Due to the success of the crystallisation with 1% 3-HBA additive, the experiment was not repeated with higher additive percentages.

PXRD analysis was carried out on the samples to confirm pure IZN was formed in the crystallisations (figure 4.31).

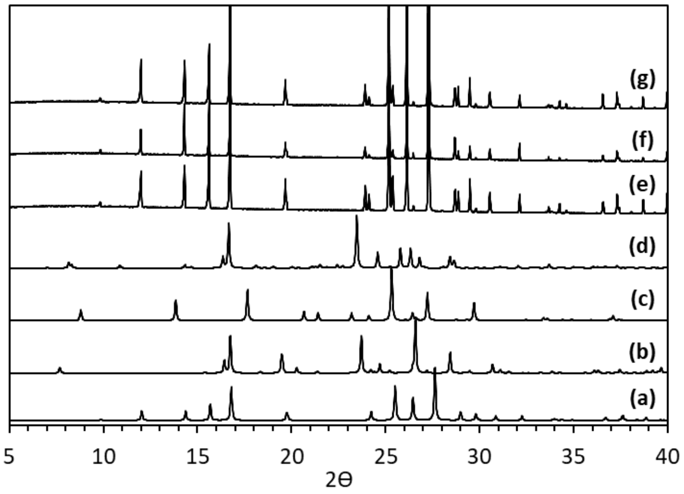

Figure 4.31. PXRD data for (a) IZN (INICAC02), (b) 3-HBA form I (BIDLOP), (c) 3-HBA form II (BIDLOP01), (d) 3-HBA hydrate (BOMCAJ), (e) IZN 1% 3-HBA, (f) IZN 5% 3-HBA and (g) IZN 10% 3-HBA

No trace of the additive is observed at any of the additive percentages attempted, however, this analysis technique is not particularly sensitive. DSC analysis also showed only one peak, corresponding to the melting point of IZN. Again, the detection limit of this technique is potentially not sensitive enough to detect the additive amounts of impurity present (appendix A18). NMR spectroscopy analysis was thus carried out in an attempt to determine whether any additive was present within the sample (appendix A19). NMR spectroscopy is a more sensitive technique than either DSC or PXRD, with a better detection limit for the additives present. ^{1}H-NMR spectroscopy was carried out for both IZN 1% 3-HBA and pure IZN were carried out in D_2O (peak observed at 4.8

ppm), with 3-HBA carried out in DMSO (observed at 2.5 ppm). Stacking of the three patterns shows that the products from IZN 1% 3-HBA and pure IZN have the same NMR spectroscopy patterns; no peaks relating to pure 3-HBA are observed in the additive crystallisation NMR spectra. At this detection limit, it can be concluded no additive is present in the product from the additive crystallisations.

Face indexing of the IZN crystals produced with 1% 3-HBA at a cooling rate of 0.1 ºC/minute at 150 g scale was carried out to allow comparison with the morphology produced from additive evaporative crystallisations (figure 4.32).

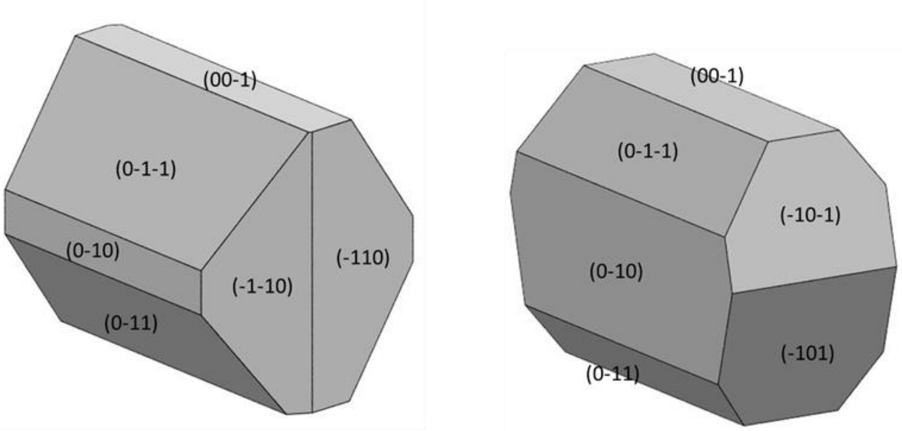

Figure 4.32. Face indexed crystals of IZN from 150 g cooling crystallisation (left) and evaporative crystallisations (right) in IPA with 1% 3-HBA additive

The morphologies are very similar to each other, with only slight differences in the size of the faces. The end faces differ but this is a likely region of breakage when removing crystals from the vial or upon contact with the impeller. The overall octagonal shape of the crystal is still observed, with the same faces surrounding both crystals. The dominant growth direction is still along the crystallographic *a* axis of the crystal, caused by the aromatic stacking of the rings. The area of the (0-10) face has decreased under cooling crystallisation conditions, suggesting growth perpendicular to this face is faster under these conditions than in evaporative crystallisation. This results in a less uniform octagonal morphology when compared to that achieved in evaporative crystallisation. However, the face indexing experiments are carried out on a very small subset of the crystals produced, and the differences in the sizes of the faces may not be significant and may be less pronounced if a larger number of crystals were sampled. The presence to a significant extent of particular indexed faces is the more important factor to take into account. Overall, the additive-mediated morphology change to thick rods has been successfully reproduced in cooling crystallisation with a high level of similarity achieved between cooling and evaporative methods.

The crystals produced have been changed significantly from the needles originally observed in H_2O and the plates observed from crystallisations in IPA, to a much more favourable morphology for pharmaceutical manufacturing.

For the second additive, 3,4-DNBA, successful morphology changes were again observed on this larger 150 g solvent scale (figure 4.33).

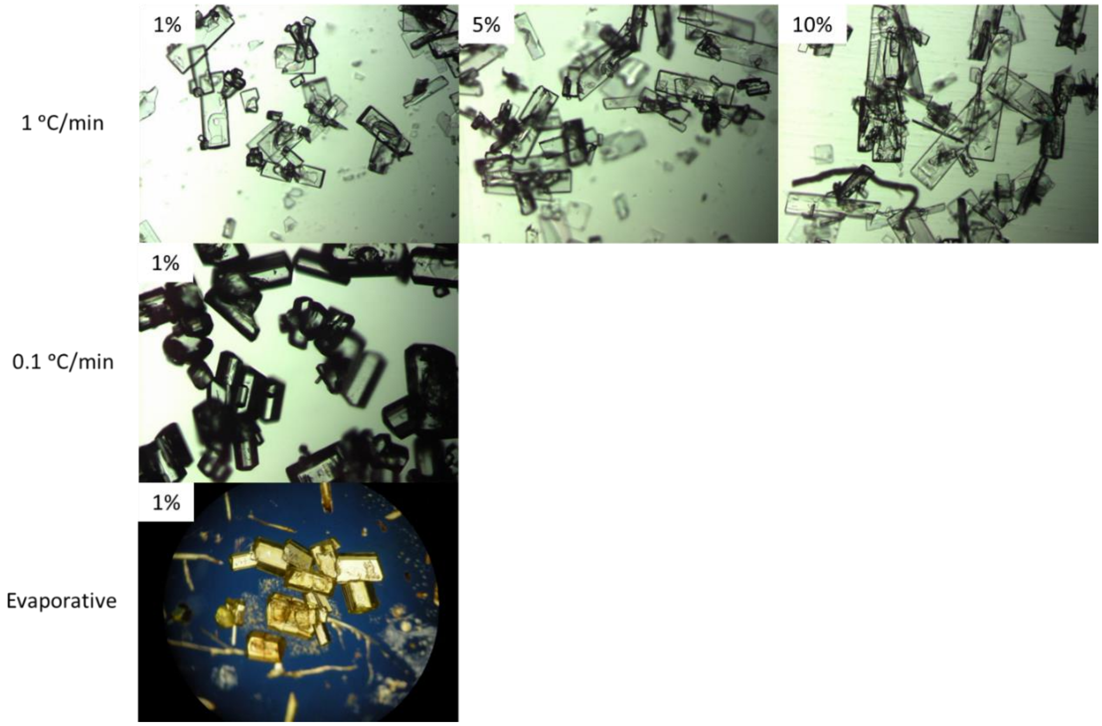

Figure 4.33. Microscope images comparing the morphology of IZN crystallised from IPA with 3,4-DNBA additive in 150 g cooling with overhead stirring (top and middle) and evaporative crystallisation (bottom

When a cooling rate of 1 ^{o}C/min was used, all three additive percentages produced plate-shaped crystals, similar to those normally produced in IPA. No rod-shaped crystals seem to be produced in the crystallisations carried out at this cooling rate. This is a similar result to that observed in smaller scale crystallisations. When cooled at a rate of 0.1 ^{o}C/min with an additive percentage of 1%, rod-shaped crystals were produced. The morphology observed mirrors that seen in the evaporative additive crystallisations originally carried out. The morphology modification is uniform throughout the sample, with no plate-shaped crystals observed. The shape achieved is also the same as seen for additive-free crystallisations in EtOAc. Due to the success of the crystallisation with 1% 3,4-DNBA additive, the experiment was not repeated with higher additive percentages.

The crystals produced in the additive cooling crystallisation had the same yellow tinge as seen in the samples from the evaporative crystallisation also shown in figure 4.33. PXRD analysis was carried out to confirm that the morphology-modified samples were of pure IZN without the presence of co-crystal or residual additive (figure 4.34).

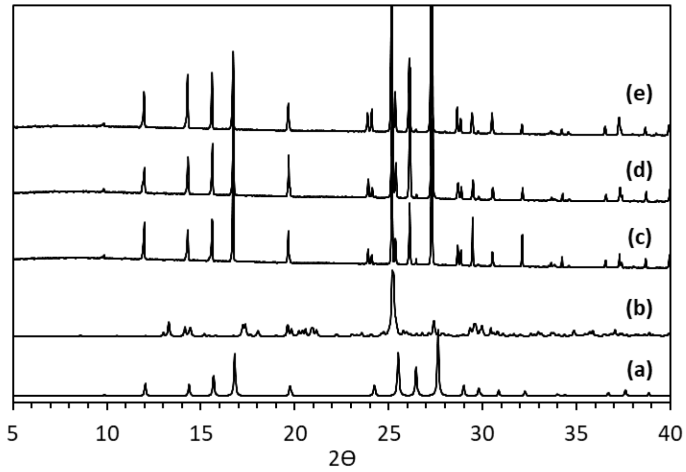

Figure 4.34. PXRD data for (a) IZN (INICAC02), (b) 3,4-DNBA (YADKOF), (c) IZN 1% 3,4-DNBA, (d) IZN 5% 3,4-DNBA and (e) IZN 10% 3,4-DNBA

The resulting PXRD pattern shows no peaks corresponding to the 3,4-DNBA and matches that of pure IZN, strongly suggesting no additive has been incorporated into the structure. DSC also confirmed the absence of the additive, with only one sharp endotherm corresponding to the melt point for IZN (appendix A20). Further experiments were carried out with NMR spectroscopy to determine whether any trace additive remained in the sample (appendix A21). Again, the analyses of the product from the additive crystallisation and the pure IZN sample were carried out in D_2O and that of the additive, 3,4-DNBA, was carried out in DMSO. The ^{1}H-NMR spectroscopy pattern for pure IZN and the product from IZN 1% 3,4-DNBA are identical, with no peaks observed that correspond to the pure 3,4-DNBA NMR spectrum. At the detection limit of the NMR spectroscopy experiment, it can be determined that the IZN crystals produced from the additive crystallisation method are pure, with no additive content.

Face indexing of the crystals of IZN produced with 1% 3,4-DNBA at a cooling rate of 0.1 °C/minute was carried out (figure 4.35) to allow comparison with the morphology produced from the additive-mediated evaporative crystallisations.

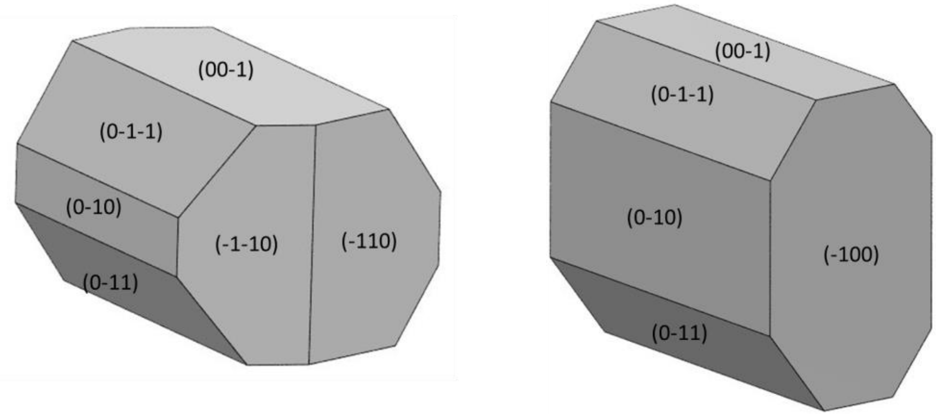

Figure 4.35. Face indexed crystals of IZN from 150 g cooling crystallisation (left) and evaporative crystallisations (right) in IPA with 1% 3,4-DNBA additive

The morphologies produced from cooling and evaporative appear very similar in the photos of the crystals shown in figure 4.33. The face indexing confirms this similarity. The overall octagonal shape of the crystal is still observed, with the same faces surrounding both crystals. Dominant growth is still occurring along the crystallographic *a* axis of the crystal, although there is a slight difference in the hkl values determined for the capping faces. The capping faces are often hard to distinguish when face indexing the crystals, and sometimes their indexing requires simplifying due to breakages which occur during crystallisation and when extracting and mounting the crystals. Thus, despite the faces not being indexed the same, the direction of major growth remains the same. This growth is still the result of the aromatic interactions between the individual IZN molecules within the structure. The area of the (00-1) face has increased under cooling crystallisation conditions, suggesting this face is not growing as fast under these conditions as in evaporative crystallisation. Similarly, the area of the (0-10) face has decreased indicated faster growth possibly occurring in the direction perpendicular to this face. The results of these changes give the crystal morphology obtained from cooling crystallisation a more uniform octagonal shape, when compared to that of the morphology produced in evaporative crystallisation. As for the samples produced with the 3-HBA additive, while this difference seems significant from the above face indexed crystals, this represents only one crystal from the bulk product sample, therefore, it is likely this difference is not necessarily significant and the consistent production of the rod-like morphology is the most important finding. Overall, the morphology changes originally seen in evaporative experiments in the presence of the additive have been successfully reproduced in cooling crystallisation with a high level of similarity between the two. The crystals produced in bulk are significantly changed from those observed from pure IPA and exhibit a much more favourable morphology to take forward into future processing steps.

4.3.4.3 Transfer of successful additive experiments into the KRAIC continuous platform

The transfer of the additive-assisted crystallisations into the KRAIC showed little success in achieving the altered morphology. Experiments were carried out at three different additive percentages, despite the previous experiments determining 1% to be the most successful additive concentration. This strategy was adopted due to other variables being more difficult to control in the continuous set up.

For 3-HBA additive no successful morphology change was observed in the KRAIC set up. Plate-shaped IZN crystals, as observed from IPA cooling crystallisations in the absence of additive, were produced at all additive percentages (figure 4.36). PXRD analysis was used to confirm the formation of pure IZN crystals, with no evidence of the co-crystal form being present in the final product.

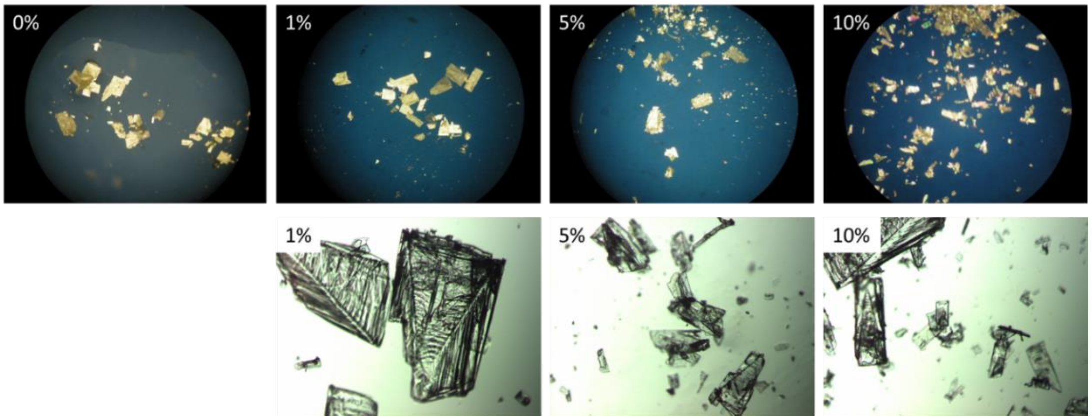

Figure 4.36. Microscope images of crystals achieved from IPA KRAIC crystallisations with different additive percentages of 3-HBA

For 3,4-DNBA additive, a similar result was achieved. Plate-shaped crystals were obtained for all additive percentages (figure 4.37), with the slight yellow tinge usually observed when this additive is present. These plates closely resemble the IZN morphology achieved in cooling crystallisations from IPA in the absence of additive. PXRD analysis was carried out and confirmed the formation of pure IZN crystals, with no evidence of the formation of co-crystals.

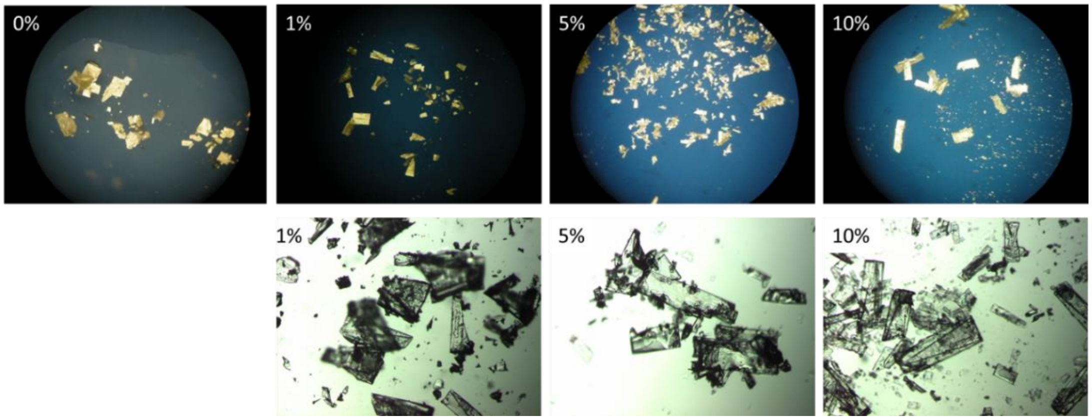

Figure 4.37. Microscope images of crystals achieved in IPA KRAIC crystallisations with different additive percentages of 3,4-DNBA

The design of the KRAIC continuous crystallisation platform gives limitations on the number of crystallisation conditions available for variation. The starting saturation of IZN could potentially be altered in this set up, however, it was found that doing so greatly affected the point of nucleation; an IZN starting saturation of 0.0175 g/g was determined necessary to achieve controlled crystallisation within the coils of the KRAIC. Reducing the starting saturation resulted in no nucleation being observed in the coil, although some crystallisation did occur on contact with the filter paper on extraction from the KRAIC. Increasing the starting concentration caused significant crystallisation to occur in the outlet of the SF10 solution pump. The inlet, pump head, and outlet of the solution pump cannot be temperature controlled, causing this to become a possible nucleation site at high saturations. This position is before segmentation occurs and can cause significant problems, with the pump head becoming blocked and a pressure increase occurring. As a result, the starting saturation of IZN cannot be varied for this particular continuous crystallisation procedure.

It is also not possible to control the cooling rate of the crystallisation in this platform set up, due to the coil not being temperature controlled. This variable seemed to have a significant influence on the cooling crystallisations carried out in batch at larger scale, suggesting favourable morphology changes may be possible in a temperature controlled continuous crystalliser.

Although these two variables cannot be controlled, their effects could be mitigated by altering the length of time the solution takes to travel through the length of the coil, the residence time. Changing the flow rate by adjusting the speed of the pumps allows shorter or longer residence times to be achieved for the platform. Increasing the residence time could potentially result in crystallisation occurring within the coil at lower starting saturations. It also has the potential to allow more time for growth to occur once the lower temperature is reached, allowing successful morphology changes to be achieved.

4.3.5 Effect of polymer additives on isoniazid morphology achieved via evaporative and cooling crystallisation

The concentration of polymer additives used was 1%, due to the success observed using this concentration of size-matched additives, and 0.1%, from evidence in literature of lower polymer concentrations being more successful.[63]

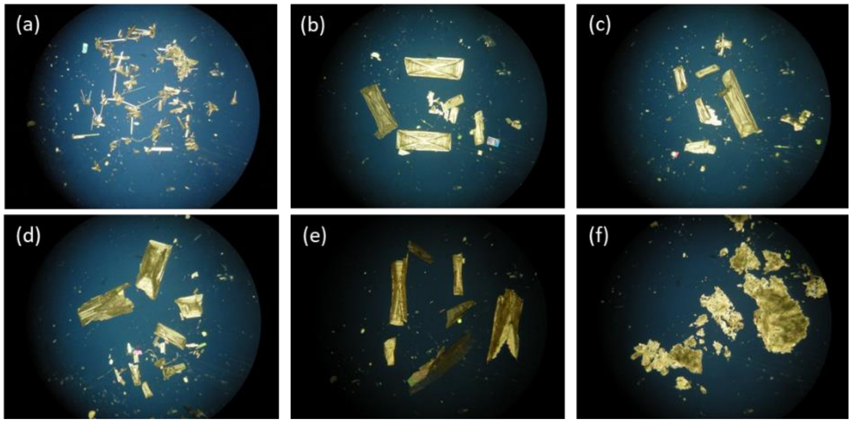

Figure 4.38. Cooling crystallisations of IZN with 1% polymer additives in IPA at a rate of 0.1°C/minute. (a) PP123, (b) PEG, (c) PPG, (d) PBD, (e) PVP and (f) PDE

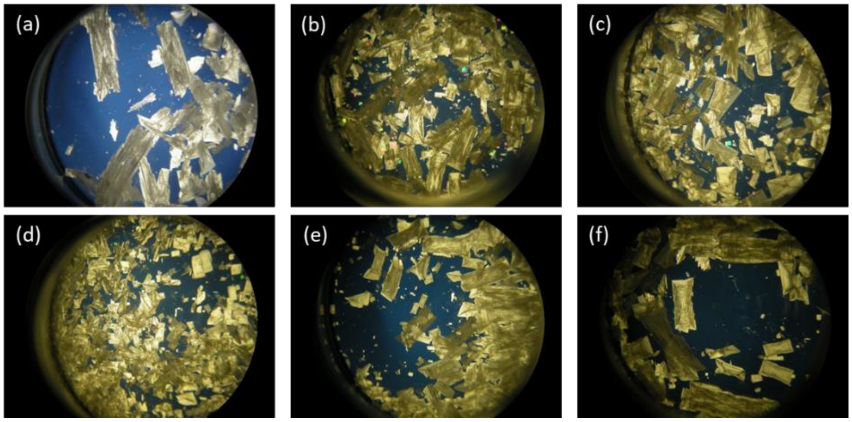

Figure 4.39. Cooling crystallisations of IZN with 0.1% polymer additives in IPA at rate of 0.1 °C/minute. (a) PP123, (b) PEG, (c) PPG, (d) PBD, (e) PVP and (f) PDE

Most of the 1% polymer additive cooling crystallisations produced plate-shaped crystals (figure 4.38), similar to those seen for cooling crystallisations from IPA without the polymer present. The crystals produced in the presence of P123 polymer show smaller, almost needle-shaped crystals. This suggests the presence of this polymer is working against the effect of the solvent system and reverting back to the least favourable crystal morphology for IZN. Crystals produced in the presence of PDE are also much smaller and significantly clumped. The morphology is still small, thin plates and this crystallisation clearly demonstrates the problem with this crystal morphology in terms of downstream crystal processing steps. The same results were seen for faster cooling rates of 1 °C/minute: no improvements to the morphology are observed in these crystallisations (appendix A22 and A23).

Crystallisations with 0.1% polymer additive also showed no improvement in the morphology achieved (figure 4.39). For all polymers the same plate-shaped crystals were observed as those from cooling crystallisations from IPA in the absence of polymers.

The same polymer additive percentages were used in a set of evaporative crystallisations, which were carried out at 20 °C (appendix A24 and A25) and 40 °C.

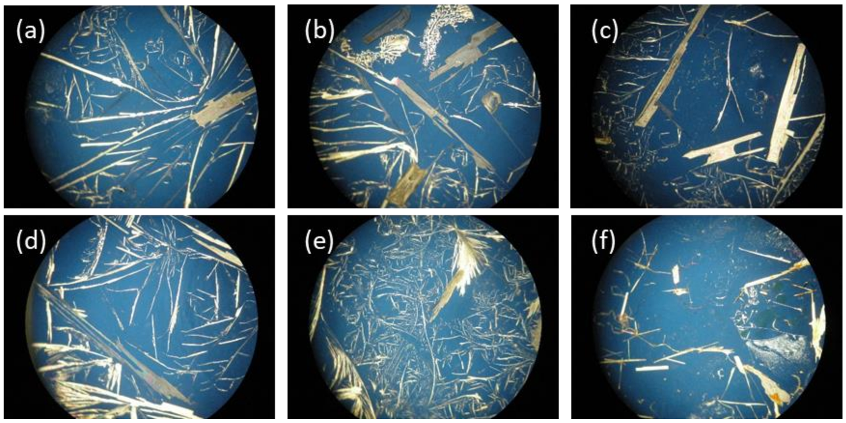

Figure 4.40. 40 °C evaporative crystallisations of IZN with 1% polymer additives from IPA. (a) PP123, (b) PEG, (c) PPG, (d) PBD, (e) PVP and (f) PDE

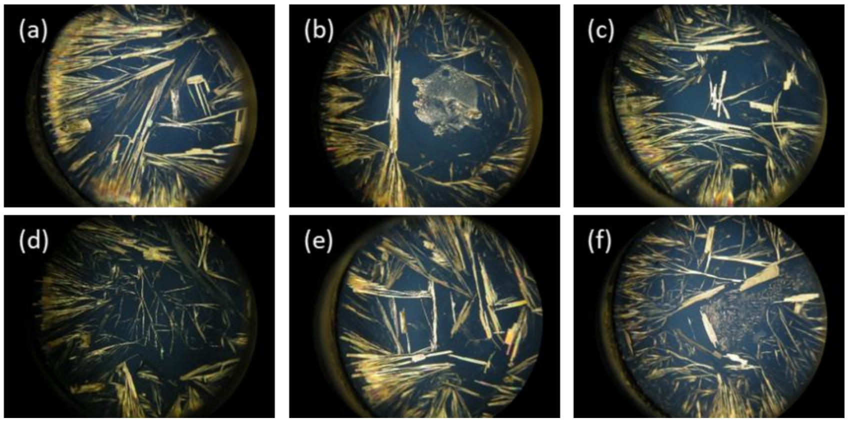

Figure 4.41. 40 °C evaporative crystallisations of IZN with 0.1% polymer additives from IPA. (a) PP123, (b) PEG, (c) PPG, (d) PBD, (e) PVP and (f) PDE

The overriding morphology observed in the evaporative crystallisations is needle-shaped crystals (figures 4.40, 4.41). This is again the same as that predominantly observed for evaporative crystallisation from IPA in the absence of polymers. Some plates are observed in some samples but no improvement on the usual morphology achieved from IPA is observed.

In summary, none of the polymers trialed as additives in this work have a positive effect on the morphology produced.

4.4 Conclusions

Crystallisation of IZN from different solvent systems has proven to be successful in producing favourable morphology modifications from the needle shape normally observed for this API. IZN crystals are clearly susceptible to solvent effects on the growth mechanisms present. A minor positive morphology change was observed in both EtOH and IPA solvents, with thin plate-shaped crystals forming. Whilst this is a significant morphology change from the needles originally observed in crystallisations from H_2O, it is still not a favoured morphology. Crystallisations in EtOAc, however, form thick, rod-shaped crystals. This is close to the block shaped morphology favoured in most processing steps in the manufacturing process.

Achieving these morphology modifications is easily repeatable through a number of different cooling crystallisation scales and methods. The modifications can be recreated in the KRAIC continuous cooling platform as well as in batch methods of different volumes. This makes the observed solvent effects potentially useful for pharmaceutical applications as the versatility across crystallisation conditions will allow for easier design of crystallisation and implementation into already existing crystallisation processes.

The effects of saturation concentration on the shape of the crystals produced was significant in the evaporative crystallisations carried out, with some concentrations resulting in needles and others the modified morphologies. However, these same effects were not observed in cooling crystallisations. The starting saturation of the solution had no effect on the morphology achieved in cooling, only affecting the yield of the product produced. This lack of influence on the results of a cooling crystallisation confirms the robust nature of this method in this case. Implementation into existing processes will also be aided by the fact that starting concentration has little effect on the final morphology achieved from each solvent when crystallised via cooling.

In an attempt to determine how much EtOAc must be present to observe the changes, solvent mixtures were investigated. The results of these crystallisations showed that a high content of EtOAc was required in these mixtures to reproduce the desired morphology, indicating essentially no improvement over the use of pure EtOAc. Different chain length esters were also used as solvents and in mixtures and showed no improvement in morphology modification from that achieved with EtOAc alone.

In addition to successful solvent effects, two size-matched additives also offered promising morphology changes. Both 3-HBA and 3,4-DNBA additives in a 1% ratio allowed crystals produced from IPA to form the same thick, rod-shaped crystals as seen in crystallisations from EtOAc. This favourable morphology change was originally observed in evaporative additive crystallisations but successful scale up was achieved in cooling.

Recreating the same effects of the additive in cooling proved tricky with the effects only being observed when carried out on a 150 g solvent scale with overhead stirring. Whilst the scale may be affecting the morphology observed, it is more likely to be caused by the change in kinetics due to the introduction of overhead stirring. These effects could be investigated on smaller volume scales if the ability to implement overhead stirring were possible. The attempts to transfer these additive effects into the KRAIC continuous platform were also unsuccessful. Given the effect of the overhead stirring in batch cooling this could be down to the kinetics and mixing profiles achievable in the KRAIC set up. Whilst transfer to continuous was unsuccessful in this platform the possibility still remains for successful transfer into other reactors such as the COBC and cSTR. cSTR's in particular have the capacity for overhead stirring to be implemented and so are much more likely to offer the same successful morphology modification.

Analysis of the crystals produced from additive crystallisations with SCXRD, PXRD, NMR spectroscopy and DSC show that no trace of the additive remains in the crystalline product. However, there could be a small amount present as point defects within the crystal or sitting on the surface of the crystals. This is a particular concern for samples produced in the presence of 3,4-DNBA additive as the final product is yellow as opposed to white. Further analysis would be needed in the case of pharmaceutical applications to ensure the products fit the regulatory requirements and the inclusion of any additive impurities is below the threshold set by regulatory bodies. A good technique to use could be HPLC as this has a much lower detection limit than the analysis techniques already used.

The polymeric additives tested to date have proven unsuccessful in producing morphology modification. No improvement on morphologies achieved in pure solvent was observed with any of the polymers used. However, there is substantial literature precedent for the general success of polymer additives in changing morphology so further polymer candidates could be tested to find an appropriate system.

Overall, the use of solvent choice and additives to change the morphology of IZN has been very successful with good results seen in both cases. Both methods are suitable for manufacturing applications, however, the success of solvent choice alone is possibly the best route to choose. This method is uncomplicated and shows the same results that have been achieved using additives. The use of solvent also reduces the possibility of impurities being incorporated into the crystal structure and would be easier to implement and be approved by regulators.

Chapter 5 Morphology changes observed in multi-component crystals of isoniazid

5.1 Introduction

Co-crystallisation can have many positive effects on the physical properties of pharmaceutical materials. The benefits of co-crystals can include improved solubility and stability as well as crystal habit modification. As noted previously, IZN is known for not only its poor crystal shape but also its reduced stability as part of the FDC tablet. This combination tablet formulation was developed to combat the increasing resistance of TB to doses of IZN alone.[159, 160] IZN is therefore a good candidate for research into multi-component crystal systems in an attempt to combat this reduction in stability. Co-crystallisation also changes the crystal structure and, often, macroscopic crystal parameters; a new morphology is a possible additional effect of the introduction of a secondary molecule into the structure and thus co-crystal formation can also be a route to morphology modification of IZN-containing crystals. A large number of co-crystal structures are already published due to extensive research into co-crystallisation of IZN. An improved morphology is predicted using BFDH for some reported co-crystals, however, as this was not the main focus of most of the research carried out on IZN co-crystallisation, the morphology is often not reported in the literature. The aim of this work was to investigate the formation of new multi-component crystalline materials, not previously reported in the literature, with an emphasis on possible morphology changes. It is hoped that in any new co-crystal structures the morphology of the crystal will be positively altered with an improved aspect ratio.

5.2 Selection of co-formers for isoniazid

The co-former selection process is important to narrow down the potential list of molecules to screen for the production of multi-component materials. Designing a robust prediction method is vital in reducing the extent of the costly and time-consuming screening process. In this work two predictive methods have been used in parallel to obtain a short list of potential co-former molecules.

Initially the molecular structure of the target molecule is considered to identify potential sites for hydrogen bonding. IZN is a weak base with two major functional groups, a hydrazide and a pyridine ring, giving rise to two hydrogen bond donor sites, the NH_2 and NH group, and four hydrogen bond acceptors, three N atoms and a carbonyl group. Further information on the hydrogen bonding nature of the target molecule can be obtained by investigating the multi-component materials (co-crystals) already published in the CSD. A search within the CSD provides 81 hits for IZN, including 56 co-crystal structures. Of the total reported co-crystals only 12 contain a co-former without a carboxylic acid group. Of the 44 co-crystals formed with carboxylic acid containing co-formers, 19 are formed with dicarboxylic acids. There are only two reported co-crystals with co-formers that have neither a carboxylic acid group nor a hydroxyl group. Analysis of the carboxylic acid containing co-crystals indicated the predominant hydrogen bonding interaction occurs via donation from the co-former carboxylic acid to the N in the pyridine ring. The main hydrogen bonding interactions seen in IZN co-crystal structures containing carboxylic acids are shown in figure 5.1.

The following discussion focusses on the hydrogen bonding interactions illustrated in figure 5.1. The carboxylic−pyridine synthon, (vi), is reported in co-crystals with 4-aminosalicylic acid and other co-formers containing hydroxybenzoic and dicarboxylic acids; a total of 11 structures show this interaction, often with proton transfer to the pyridine N. Hydrazide−hydrazide hydrogen bonds, (i) – (v), can be seen in 31 co-crystals with dicarboxylic acids and hydroxybenzoic acids.[203] A series of co-crystals with mono- and dicarboxylic acid co-formers was reported with the conclusion that the dominant interaction in all cases was (iv).[125] A further study extended this to include co-crystallisation with an aromatic carboxylic acid, terephthalic acid. The co-crystal produced was isostructural to the adipic acid co-crystal previously published and, again, contained the COO-H··$N_{heterocyclic}$ hydrogen bond as the major interaction between the molecules. However, the presence of the aromatic ring also resulted in interactions between the overlapping π-systems.[204]

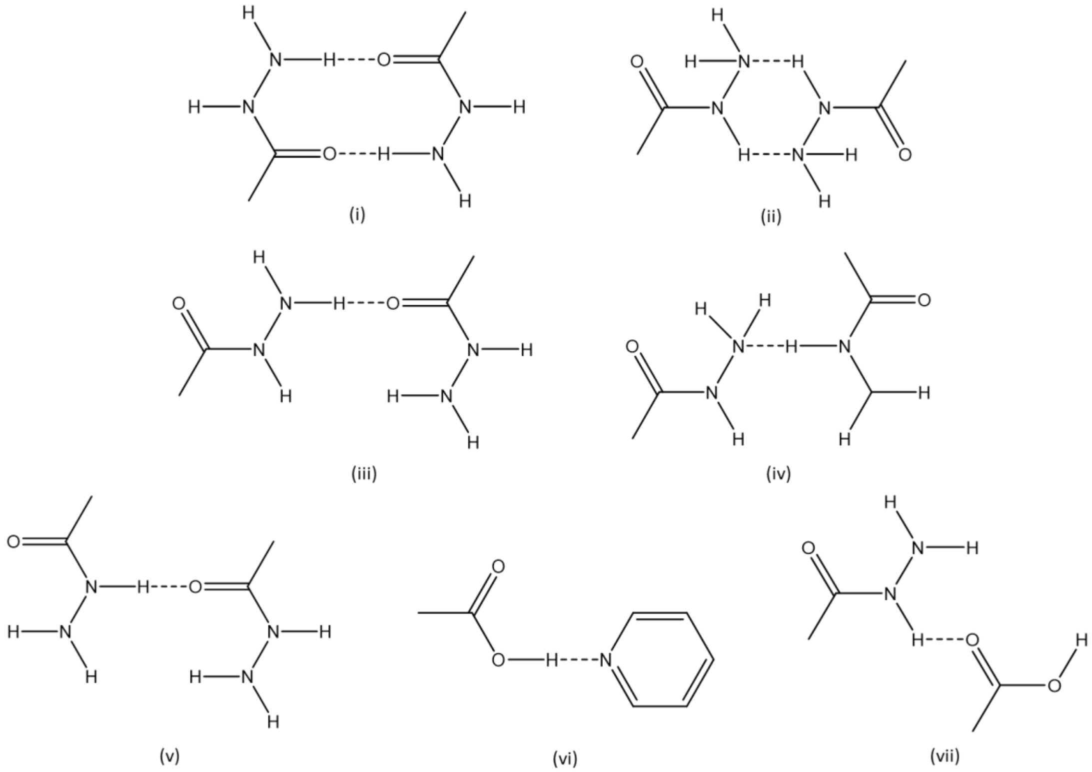

Figure 5.1. Supramolecular synthons observed in IZN co-crystals in the CSD [203]

Of the above interactions, the chain link interactions (iii, iv, v, vi and vii) are the most commonly observed. For the dimeric interactions, nine co-crystals exhibit (ii) and 12 contain (i). These dimeric interactions are not observed in pure IZN; interactions in the structure of IZN are (iv) and a second interaction between the NH_2 group and the ring N (not illustrated here). The ability of the IZN molecules to form dimeric interactions in the presence of secondary molecules in the structure could suggest the existence of other polymorphic forms of IZN that require very specific conditions to encourage their formation. This hypothesis was confirmed in mid-2020 with the discovery of a second IZN polymorph showing these dimeric interactions. The new polymorph can only be obtained through confined crystallisations and is only stable for less than an hour at room temperature and pressure.[162]

Using the information obtained from examination of the published structures in the CSD, an initial list was drafted of potential co-formers for IZN co-crystallisation experiments. The molecules chosen included at least one carboxylic acid group and some also contained aromatic ring centers. The co-formers were chosen from either the GRAS list or the list of common co-formers found in published structures in the CSD.

A computational approach was used to narrow down the lists further, using calculations carried out using the molecular complementarity tool in the CCDC Mercury software. This tool calculates the likelihood of two molecules interacting to form a multi-component material by taking into account the size and shape of the two molecules and their crystal structures. A comparison is made and a pass or fail verdict reached, with those that are most similar resulting in a pass. Five different criteria can be used to carry out these calculations, which can be used in any combination; in this work all five descriptors were used. The calculations produce a full list of potential candidates. The final list was decided by elimination of molecules that are already known to form co-crystals published in the CSD. The set of co-formers screened in the resulting experiments is shown in figure 5.2.

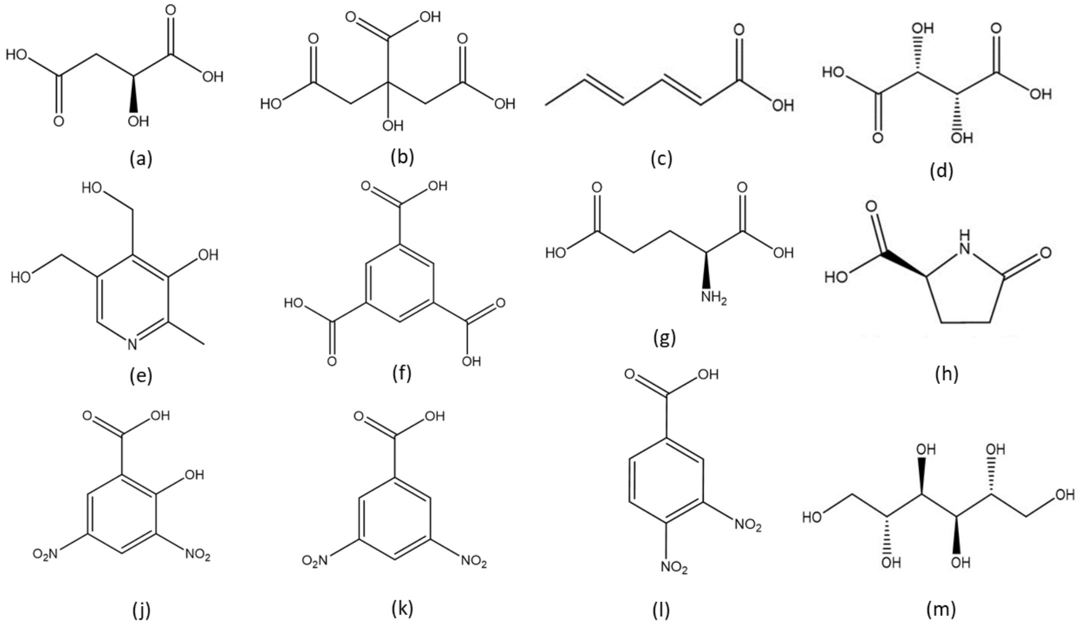

Figure 5.2. Structure of co-formers determined from initial molecular complementarity calculations with IZN (a) malic acid, (b) citric acid, (c) sorbic acid, (d) (L)-tartaric acid, (e) pyridoxine, (f) trimesic acid, (g) glutamic acid, (h) (L)-pyroglutamic acid, (j) 3,5-dinitrosalicylic acid, (k) 3,5-dinitrobenzoic acid, (l) 3,4-dinitrobenzoic acid, (m) D-mannitol

5.3 Experimental information

All solvent and materials used in this research were obtained from commercial sources. No further purification was carried out prior to any experimental procedure outlined.

5.3.1 Evaporative screening for isoniazid co-crystals

Evaporative crystallisations were carried out from solutions containing 1:1 stoichiometric ratios of API and co-former. A small amount of IZN, 0.01 g, and the corresponding mass of co-former were dissolved in minimal solvent in 7 mL glass vials. Solvents used were H_2O, EtOH, IPA and EtOAc. Vials were sealed with PTFE lids containing pierced holes, to allow slow evaporation, and left to evaporate at both room temperature and 40 ^oC.

5.3.2 Crash cooling of isoniazid co-crystals

Crash cooling crystallisations were carried out in the fridge at 4 ^oC. Crystallisations were set up in all four solvents with a saturation temperature arbitrarily chosen as 30 ^oC (T_{sat}= 30 ^oC). For both H_2O and EtOH, the crystallisations were carried out in only 1 g of solvent. For IPA, 2 g of solvent was used due to the saturation concentration being much lower. Similarly, in EtOAc the limited solubility led to 3 g of solvent being used. Crystallisations were prepared in 7 mL vials in a 1:1 ratio of IZN and the corresponding molar ratio of the additive. Each sample was sonicated at an elevated temperature to allow full dissolution of the IZN and additive starting materials. Once full dissolution had been observed the solutions were transferred to the fridge until crystallisation occurred. If no crystallisation occurred, holes were pierced in the lids to allow for some very slow evaporation.

5.3.3 Isoniazid single crystal structures

Crash cooling and evaporative crystallisations from solutions of IZN in a 1:1 ratio with a number of co-formers resulted in the formation of new multi-component crystalline materials. Single crystal structures were determined for all five new materials. All structures were solved using ShelXS and refined using ShelXL within Olex2 software. Crystallographic data for all new complexes are shown in table 5.1.

(1) Isoniazid with (L)-tartaric acid (IZN:LTA)

A 1:1 molar ratio of IZN (0.160 g) and LTA (0.175 g) were dissolved in H_2O in a 7 mL glass vial. Crash cooling produced clumped plate-shaped crystals. Single crystal data were collected using a Rigaku Oxford Diffraction Xcaliber diffractometer with Mo-Kα radiation (λ=0.70173 Å) at 150 K.

(2) Isoniazid with (D)-tartaric acid (IZN:DTA)

A second complex was produced with IZN (0.160 g) and DTA (0.175 g). Crash cooling in H_2O was again carried out and clumped plate crystals produced. Single crystal data were collected using a Rigaku Oxford Diffraction Xcaliber diffractometer with Mo-Kα radiation (λ=0.70173 Å) at 150 K.

(3) Isoniazid with (DL)-tartaric acid (IZN:DLTA:H_2O)

A hydrated salt system of IZN (0.160 g) and DLTA (0.175 g) was produced via crash cooling in the fridge in H_2O. The crystals produced take on a plate like morphology and clump together. Single crystal data were collected using a Rigaku Oxford Diffraction Gemini A Ultra diffractometer with Mo-Kα radiation (λ=0.70173 Å) at 150 K.

(4) Isoniazid with (DL)-tartaric acid (IZN:DLTA)

The hydrated salt of (IZN:DLTA:H_2O) was heated using a hot stage microscope to 120 ^{o}C to drive off the H_2O included in the crystal lattice and isolate the anhydrous co-crystal. The crystal morphology remained plate like. Single crystal data were collected using a Rigaku Oxford Diffraction Gemini A Ultra diffractometer with Mo-Kα radiation (λ=0.70173 Å) at 150 K.

(5) Isoniazid with 3,4-dinitrobenzoic acid (IZN:3,4-DNBA)

A 1:1 molar ratio of IZN (0.02 g) and 3,4-DNBA (0.031 g) was crystallised from IPA in a 7 mL glass vial. Evaporative cooling produced plate-shaped crystals. Single crystal data were collected using a Rigaku Oxford Diffraction Gemini A Ultra diffractometer with Mo-Kα radiation (λ=0.70173 Å) at 150 K.

Table 5.1. Crystallographic parameters for newly discovered co-crystal structures formed with IPA IZN [ii]

	1	2	3	4	5
Code	IZN:LTA	IZN:DTA	IZN:DLTA:H_2O	IZN:DLTA	IZN:3,4DNBA
Formula	$C_{20}H_{26}N_6O_{14}$	$C_{20}H_{26}N_6O_{14}$	$C_{10}H_{15}N_3O_8$	$C_{10}H_{13}N_3O_7$	$C_{13}H_{11}N_5O_7$
M / g mol^{-1}	575.47	575.47	305.25	287.24	349.27
T (K), radiation	149.99(10), Mo Kα	156(9), Mo Kα	150.00(10), Mo Kα	150.00(10), Mo Kα	150.00(10), Mo Kα
Space group	$P2_12_12_1$	$P2_12_12_1$	$P\bar{1}$	$P2_1/c$	$P\bar{1}$
a (Å)	7.8134(3)	7.82710(10)	7.3170(8)	12.394(4)	6.7471(7)
b (Å)	15.1461(5)	15.1575(2)	7.3838(6)	7.1835(10)	7.6631(9)
c (Å)	19.7911(9)	19.7998(2)	12.6567(13)	22.554(8)	14.9606(16)
α (°)	90	90	78.380(8)	90	76.604(10)
β (°)	90	90	74.540(9)	143.53(8)	86.936(9)
γ (°)	90	90	88.874(11)	90	71.072(10)
Volume (Å^3)	2342.13(16)	2349.03(5)	646.27(14)	1193.5(15)	711.58(14)
Z	4	4	2	4	2
ρ_{cal}/ g cm^{-3}	1.629	1.624	1.571	1.598	1.630
μ/ mm^{-1}	0.140	0.139	0.137	0.137	0.135
2Θ range/°	5.866 – 60.866	5.86 – 60.72	5.78 – 57.314	6.078 – 59.078	6.912 – 60.6
Completeness	95%	98%	99%	100%	100%
Refln. Collected	10167	9783	4459	6071	12192
Independent refln.	5602	5696	2670	2850	3763
Rint	3.87%	2.86%	5.58%	9.59%	6.99%
GooF	1.096	1.098	1.053	0.963	1.054
R_1 (obs)	7.58%	6.41%	8.10%	7.93%	7.21%
R_1 (all)	10.02%	7.34%	15.30%	23.29%	16.14%
wR_2 (all)	18.39%	15.79%	19.98%	24.43%	16.99%
$P_{max,min}$/e Å^{-3}	1.37/-0.54	1.18/-0.58	0.49/-0.39	0.29/-0.31	0.47/-0.31

[ii] Molecular formula and molecular mass correspond to the asymmetric unit of the crystal structure

5.3.4 Further preparations of isoniazid co-crystals

To investigate whether the formation of the co-crystals was robust, further crystallisation techniques were used in an attempt to repeat their production.

5.3.4.1 Isoniazid co-crystal production using mechanochemical grinding

Mechanochemical crystallisation was carried out via grinding of IZN and co-formers in a pestle and mortar. A small quantity of IZN (0.01 g) and the corresponding molar ratio of additive were ground together in the absence of solvent for 30 minutes. Grinding was carried out in a 1:1 IZN:co-former ratio.

LAG experiments were also carried out for the successful solvent-mediated crystal screens. A small quantity of IZN (0.01 g) and the corresponding (1:1) molar ratio of additive were ground in a pestle and mortar with a few drops of solvent until it had fully evaporated. The solvent used for these crystallisations was H_2O for the TA family and IPA for the 3,4-DNBA.

5.3.4.2 Isoniazid co-crystal production via slurrying

An excess amount of IZN and co-former, in a 1:1 molar ratio, were weighed into a 7 mL glass vial. The amount of solvent added is crucial, it must not be enough to fully dissolve the material added to the vial. The solutions were continuously stirred at room temperature, using a magnetic bottom stirrer at 250 rpm, for 2 hours. Again, the TA family (0.5 g IZN, 0.55 g TA) were slurried in H_2O (3 g) and 3,4-DNBA (0.12 g IZN, 0.186 g 3,4-DNBA) in IPA (3 g).

This production was also scaled up in the Polar Bear Plus crystalliser. For new materials with LTA, DTA and DLTA, H_2O was used as the solvent on a 60 g scale (in a 100 mL round bottom flask). For the 3,4-DNBA co-crystal a slurry was carried out on a 200 g scale (in a 250 mL round bottom flask) in IPA. Slurrying was maintained at 20 ^oC with overhead stirring at 350 rpm.

5.3.4.3 Scale up of isoniazid co-crystals using controlled cooling

Scaled up production of the co-crystals was achieved using controlled cooling profiles set up on the Polar Bear Plus crystalliser. Scale up was achieved for all new multi-component materials, to 10 g and 30 g (for TA co-crystals) and 200 g (for 3,4-DNBA co-crystal).

For multi-component materials of LTA, DTA and DLTA, H_2O was used as the solvent. H_2O was saturated at a temperature of 30 ^oC with respect to IZN (T_{sat} = 30 ^oC). For the co-crystal formed with 3,4-DNBA, IPA was used as the solvent system. IPA was saturated at a temperature of 30 ^oC with respect to IZN (T_{sat} = 30 ^oC). For each different scale a different insert and vessel were used for the crystallisation; 20 mL glass vial with screw lid (for 10 g), 50 mL round bottom flask (for 30 g) and 250 mL round bottom flask (for 200 g). The 1:1 molar ratio of IZN and co-former were added to the vessel. In the glass vials magnetic bottom stirring at 350 rpm was used, whereas, in the round bottom flasks overhead stirring at 350 rpm was used. All solutions were heated to 50 ^{o}C and held for an hour to allow complete dissolution. Cooling was programmed at a rate of 1 ^{o}C/minute to a minimum of 5 ^{o}C and held there for a further hour.

5.3.5 Solubility determination of isoniazid co-crystals

The solubility of the co-crystals was determined using observational heating techniques. Using the Polar Bear Plus crystalliser, a heating profile was set up to heat from 5 ^{o}C to 60 ^{o}C at a rate of 0.3 ^{o}C/minute. In 50 mL round bottom flask, 20 g of solvent was stirred at 700 rpm using a magnetic bottom stirrer. An initial mass of co-crystal was added to the stirring solution and observed as it was slowly heated. When the co-crystal had fully dissolved the temperature was recorded and a second pre-determined mass added to the round bottom flask. This was repeated, recording the temperature and adding an additional amount of co-crystal every time full dissolution was observed. This method was repeated three times for each co-crystal system. The co-crystal solubility was determined in the solvent from which it was originally produced.

5.3.6 Stability testing of isoniazid co-crystals

Three different stability tests were carried out for each new multi-component material. Stability at high temperatures was determined by placing small amounts of each co-crystal on a watch glass in an oven held at 50 ^{o}C. Samples were analysed using PXRD after 24 hours, 48 hours, 73 hours, 1 week, 2 weeks and 3 weeks. Humidity studies were carried out in a 70% humidity chamber formed using NaCl salt and H_2O. Each co-crystal was placed in a 1 mL vial and then into a 20 mL vial, to prevent any H_2O/salt mixture from entering the smaller vial (figure 3.3). The vials were sealed in the humidity chamber and samples analysed by PXRD every week for 9 weeks. The final stability study saw all the co-crystals slurried in H_2O at 40 ^{o}C for a week. An excess amount of co-crystal was continuously stirred in 3 mL of H_2O in a 7 mL glass vial. The vials were kept on a heated stirrer plate and a magnetic bottom stirrer was used. A sample of the suspended powder was taken at 2 hours, 4 hours, 6 hours, 8 hours, 24 hours, 48 hours, 72 hours and 1 week. Once each sample had dried it was analysed using PXRD.

5.3.7 Analytical methods

Images of the crystals were taken using a Nikon Coolpix P5100 camera through a Brunel Microscopes microscope. Images of the phase transition occurring from IZN:DLTA:H_2O to form anhydrous IZN:DLTA were taken using an Infinity 2 microscope camera connected to a Leica DM1000 microscope with an attached hot-stage mount.

Crystal structure data were collected using CrysAlisPro software and calculations and refinement carried out using Olex2.0. Mercury software was utilised to analyse the structure of the new multi-component crystals.

Face indexing was executed with CrysAlisPro software to determine the faces and overall shape of crystals produced. Crystal structure and morphology were visualized using the BFDH tool included in Mercury software.

Analysis was also carried out via PXRD, DSC, TGA and IR techniques in the manner outlined in Chapter 3. Variable temperature PXRD was used exclusively in the investigation of IZN:DLTA:H_2O and is outlined below.

5.3.7.1 Variable temperature Powder X-ray Diffraction (vtPXRD)

Analysis of samples via vtPXRD was carried out at Diamond Light Source on the I11 high resolution powder diffraction beamline. A sample of IZN:DLTA:H_2O was ground and loaded into a borosilicate capillary. The sample was heated to 75 ^{o}C and PXRD patterns recorded at 2 ^{o}C intervals from 75 ^{o}C to 100 ^{o}C, by which temperature complete transformation to the anhydrous phase had been observed.

5.4 Crystallisation of isoniazid with tartaric acid enantiomers

Three new co-crystalline structures were discovered between TA and IZN. Discussion of the hydrogen bonding interactions in all three structures will use the numbering system shown in figure 5.3.

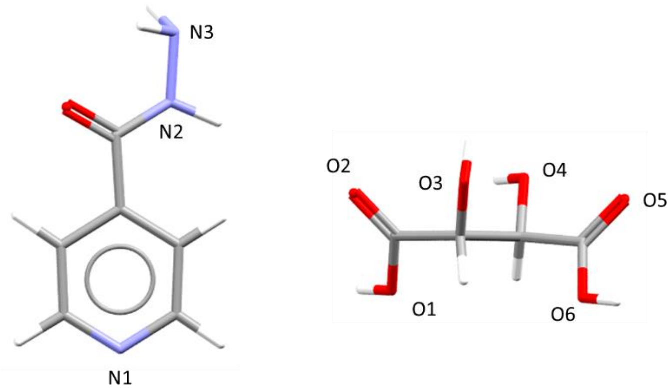

Figure 5.3. Structure of IZN and TA showing the numbering system used in hydrogen bonding discussions.

5.4.1 Crystallisation of isoniazid with (L)-tartaric acid and (D)-tartaric acid [iii]

Evaporative crystallisations from H_2O of (L)-tartaric acid (LTA) and IZN in a 1:1 molar ratio yielded a pale yellow suspension that would not dissolve without significant heating. Filtration and initial PXRD analysis of the remaining powder suggested a new multi-component form may have been produced. As a result, crash cooling crystallisation was utilised to grow single crystals and characterise the new form. These crash cooling crystallisations yielded a multi-component salt form with a 1:1 ratio of LTA and IZN. The complex crystallises in the $P2_12_12_1$ space group with an asymmetric unit consisting of two protonated IZN molecules and two deprotonated LTA molecules. Proton transfer has occurred from one carboxylic acid group on the LTA molecules, resulting in a deprotonated carboxylic acid group and a protonated N in the pyridyl ring. Protonation of the N in the ring is commonly observed within IZN multi-component structures.

After the initial successful co-crystallisation of IZN with LTA, experiments were also carried out with equimolar amounts of (D)-tartaric acid (DTA). These were again carried out via crash cooling crystallisations from H_2O and were also successful in producing a new multi-component salt form. The complex again crystallises in the $P2_12_12_1$ space group with the same asymmetric unit as the LTA salt. As expected the LTA and DTA co-crystals are isostructural with opposing chirality: the two structures with the opposite enantiomers are mirror images of each other. Proton transfer is again observed with a carboxylic acid group on DTA being deprotonated and the pyridyl N in IZN protonated. A search of the CSD highlighted 11 structures with a protonated IZN at the N in the ring, six of which contained a deprotonated carboxylic acid. There was only one example of proton

---

[iii] The structure for the DTA multi-component crystal has been added to the CSD (WETZAZ) since this research was carried out. A paper was published in 2019 describing the structure of the (D)-tartaric acid co-crystal.

transfer occurring from a carboxylic acid group that was not directly involved in a hydrogen bond with the IZN ring.

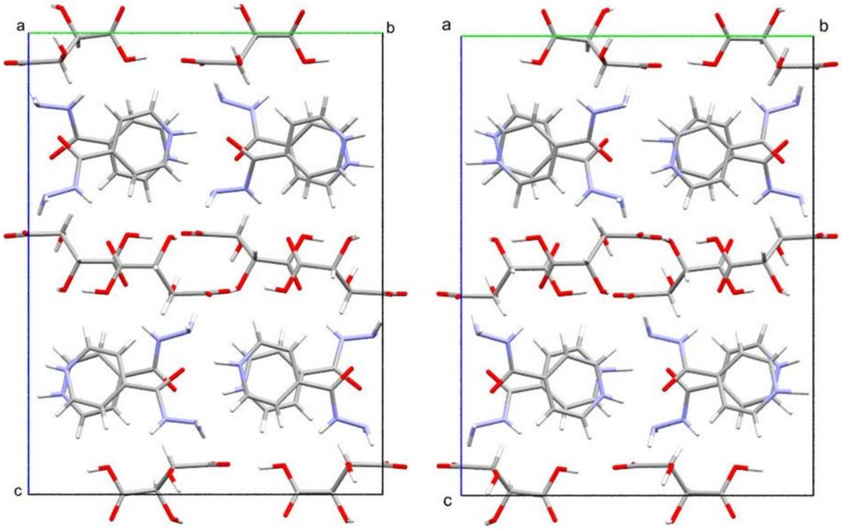

Figure 5.4. View along the crystallographic a axis of IZN:LTA (left) and IZN:DTA (right)

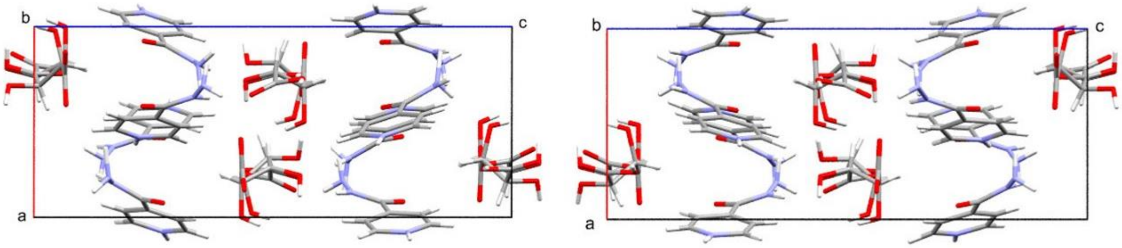

Figure 5.5. View along the crystallographic b axis of IZN:LTA (left) and IZN:DTA (right)

The structure of these two co-crystals consists of chains of TA co-formers and chains of IZN alternating throughout (figures 5.4 and 5.5). Due to the enantiomeric nature of the acid co-former the orientation of the IZN flips, resulting in the mirror image crystal structures observed. The aromatic rings of the IZN molecule are slightly eclipsed, overlapping with each other to form π-stacking interactions. The stacked IZN molecules result in s-shaped spirals (figure 5.5), illustrating the 2_1 screw axis present, parallel to the crystallographic *a* axis.

There are a large number of hydrogen bonds present in this crystal structure (table 5.2 for IZN:LTA and table 5.3 for IZN:DTA), holding the TA co-formers and the IZN molecules in chains throughout. The IZN molecules form a bifurcated hydrogen bonding interaction to each other, creating the chains that form along the crystallographic *c* axis. Donation occurs from the protonated N in the pyridyl ring to the NH_2 group and carbonyl on the neighbouring IZN molecule. The involvement of the IZN carbonyl is not seen in pure IZN crystals. In IZN-containing structures in the CSD, the carbonyl bond is involved in hydrogen bonding interactions in 21 different co-crystals; 12 of these are due to dimeric interactions between the carbonyl on one IZN to the NH_2 group on a second molecule. The bifurcated hydrogen bond interaction observed in this structure is present in four other co-crystals that show a proton transfer to the pyridyl N. None of these co-crystals involve a carboxylic acid group.

The IZN molecules form hydrogen bonds to a total of four different TA molecules (figure 5.6). The NH in the IZN donates a hydrogen bond to the carbonyl of the protonated carboxylic acid group. Further hydrogen bonds form from the NH_2 group to the central hydroxyl groups on two TA molecules and the deprotonated carboxylic acid on the final TA molecule. Hydrogen transfer has occurred in this structure, but the route of transfer is not clear. The deprotonated carboxylic acid is hydrogen bonded the NH_2 group, but the transferred proton lies on the pyridyl ring N. The ring N forms an intramolecular interaction with the NH_2 group indicating further transfer of a proton has occurred. This suggests two proton transfers have occurred, one from the TA molecule to the NH_2 group and one from the NH_2 group to the pyridyl ring. The lack of direct interaction between the deprotonated co-former and protonated site on IZN has only been observed previously in structures that do not contain a carboxylic acid group. Four structures show the suspected indirect proton transfer whilst six feature the deprotonated carboxylic acid with a direct interaction to the protonated N in the ring.

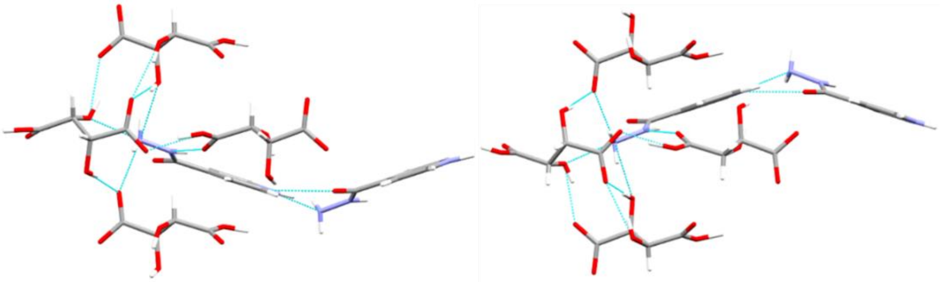

Figure 5.6. Hydrogen bonding interactions formed with IZN molecules in the LTA co-crystal structure (left) and DTA co-crystal structure (right)

The chains of TA molecules are linked together between the deprotonated carboxylic acid group on one end and the protonated carboxylic acid on the second TA (figure 5.7). The rotation of the central hydroxyl groups in the TA molecules shifts slightly down the chain, resulting in alternating molecules experiencing different hydrogen bonding interactions. In one TA molecule both central hydroxyl groups form a bifurcated hydrogen bond by donating to the oxygen in the deprotonated carboxylic acid group. The TA molecule accepting this hydrogen bond donates back to the deprotonated carboxylic acid group from O3 to a third TA molecule and from O4 back to the original TA molecule.

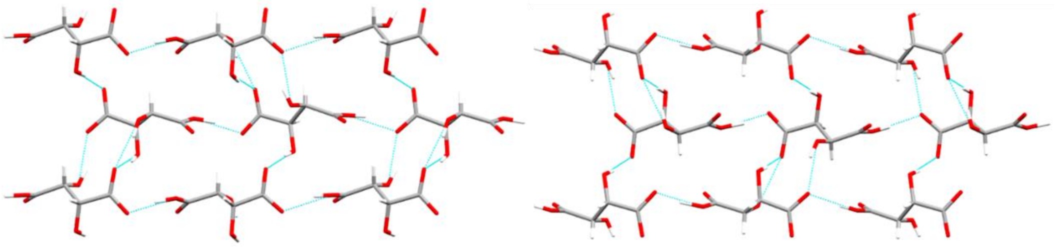

Figure 5.7. Hydrogen bonding interactions between TA molecules: LTA co-crystal (left) and DTA co-crystal (right)

Table 5.2. Hydrogen bond distances and angles for IZN:LTA[iv]

D-H··A	d(D-H) (Å)	d(H··A) (Å)	d(D··A) (Å)	>(DHA) (°)
N1a-H··N3a^{1}	0.93(9)	0.71(5)	1.9(1)	160(9)
N1a-H··Oa^{1}	0.93(9)	2.41(9)	3.013(4)	123(8)
N1b-H··N3b^{3}	0.87(9)	1.92(9)	2.756(6)	160(8)
N2b-H··O5a	0.76(6)	2.08(7)	2.783(6)	154(7)
N3b-H··O1a^{2}	0.85(6)	2.16(6)	2.848(7)	138(5)
N3a-H··N1a^{6}	0.97(7)	1.92(7)	2.857(11)	162(6)
O6b-H··O2a^{5}	0.55(7)	2.02(7)	2.562(6)	173(11)
O3b-H··O1a^{2}	1.00(8)	1.74(9)	2.741(6)	176(8)
O6a-H··O2b	1.18(8)	1.34(8)	2.498(5)	165(7)
O4a-H··O1b^{2}	0.94(9)	1.79(9)	2.713(5)	170(8)
O4b-H··O2a^{4}	0.89(6)	1.81(6)	2.659(5)	159(5)

[iv] ^{1}2-X,-1/2+Y,1/2-Z ^{2}-1/2+X,3/2-Y,1-Z ^{3}1-X,-1/2+Y,1/2-Z ^{4}1/2+X,3/2-Y,1-Z
^{5}+X,1+Y,+Z ^{6}2-X,1/2+Y,+Z

Table 5.3. Hydrogen bond distances and angles for IZN:DTA[v]

D-H··A	d(D-H) (Å)	d(H··A) (Å)	d(D··A) (Å)	>(DHA) (°)
N1a-H··N3a^1	0.71(5)	2.11(5)	2.768(5)	154(6)
N1a-H··Oa^1	0.71(5)	2.49(5)	3.022(4)	134(5)
N1b-H··N3b^2	0.78(7)	2.03(7)	2.764(5)	156(7)
N2b-H··O5a^2	0.78(5)	20.4(5)	2.785(5)	159(5)
N3b-H··O1a^3	0.88(5)	2.12(5)	2.854(5)	141(4)
N3a-H··N1a^7	0.88(9)	1.97(9)	2.848(7)	176(8)
O6b-H··O2a^4	0.71(7)	1.87(7)	2.565(4)	168(7)
O3b-H··O1a^5	0.91(5)	1.86(6)	2.749(4)	168(5)
O6a-H··O2b^6	1.06(8)	1.45(8)	2.500(4)	168(7)

In addition to SCXRD analysis, PXRD analysis was carried out to examine the bulk product and determine the phase purity of this multi-component crystallisation.

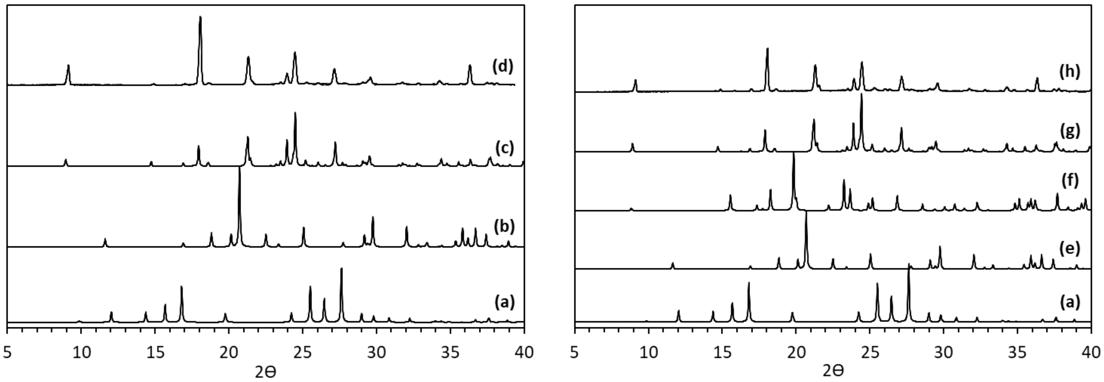

Figure 5.8. PXRD data for IZN:LTA (left) and IZN:DTA (right): (a) IZN (INICAC02), (b) LTA (TARTAL), (c) IZN:LTA co-crystal calculated from SCXRD, (d) IZN:LTA co-crystal from H_2O crash cooling, (e) DTA (TARTAC), DTA form II (TARTAC24), (g) IZN:DTA co-crystal calculated from SCXRD and (h) IZN:DTA co-crystal from H_2O crash cooling experiment

Some small traces of the starting materials can be seen in the data for both crystallisations (figure 5.8). Despite this, reasonably good phase purity was achieved for this crystallisation. Both co-crystals result in the same PXRD pattern just as they show the same SCXRD structure. It is not possible to differentiate between the enantiomers from the location of the peaks alone.

---

[v] ^{1}1-X,-1/2+Y,1/2-Z ^{2}-X,-1/2+Y,1/2-Z ^{3}-1/2-X,-Y,-1/2+Z ^{4}1/2+X,-1/2-Y,1-Z
^{5}1+X,+Y,+Z ^{6}-1/2+X,1/2-Y,1-Z ^{7}1-X,1/2+Y,1/2-Z

DSC analysis was used to determine the thermal behaviour of the new crystalline form (figure 5.9).

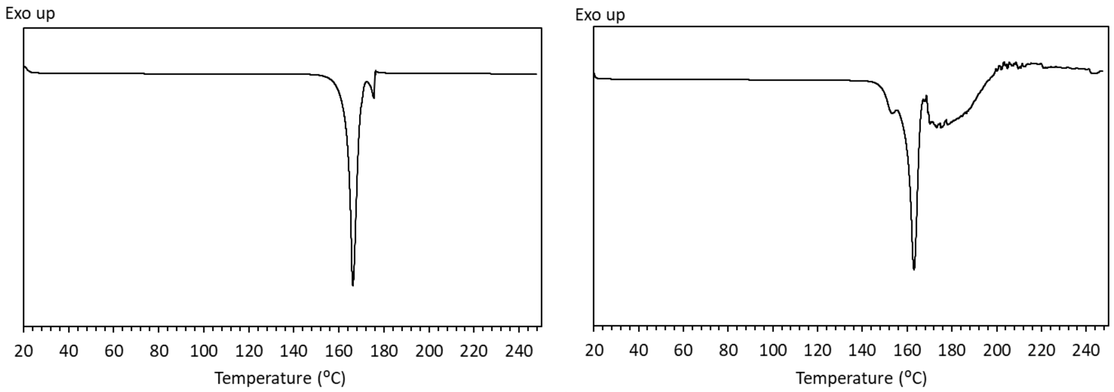

Figure 5.9. DSC data for IZN:LTA co-crystal (left) and IZN:DTA co-crystal (right). IZN melting point = 171-174 °C [163], TA melting point = 170-172 °C [205]

An endothermic event is observed at 166 °C for the LTA multi-component crystal and 163 °C for the DTA multi-component crystal. These differ from the melting points of the starting materials, occurring at lower temperatures than both IZN and the TA enantiomers. This suggests the multi-component forms are less thermodynamically stable than the initial starting materials.

Attempts at reproducing the formation of these co-crystals across multiple crystallisation methods were also carried out. Successful transformations were achieved for both solvent-mediated methods and mechanochemical grinding (appendix A26 – A29). Grinding in the absence of solvent was less successful than LAG. Some evidence in PXRD data was seen of partial transformation of the starting materials but the phase purity was low. Higher conversion was observed with LAG, suggesting the solvent may be required to allow for successful proton transfer and hydrogen bond formation. Attempts to form the co-crystal via slurrying in H_2O were successful with high conversion and phase purity. In addition, controlled cooling crystallisation of both materials was achieved on 10 g and 30 g scales (appendix A30 and A31). Co-crystallisation was not carried out at a 200 g scale due to the high solubility of the pure starting material phases.

The solubility of the co-crystal was determined using observational analysis. Although not reflecting a phase transition, the solubility relationship between the co-crystal and the pure IZN starting material can be classed as being analogous to monotropic in nature (figure 5.10); pure IZN is more soluble than the co-crystal system in H_2O. Co-crystallisation is often carried out to increase the solubility, which is not the case in this co-crystal. Co-crystallisation is of interest for IZN as it could be used to increase the stability of the FDC tablet: the reduced solubility may be an acceptable compromise if increased stability was achieved in the FDC formulation. Other interests associated with co-crystallisation, such as improved flow and compressibility, could also provide benefits that outweigh the reduction in solubility observed.

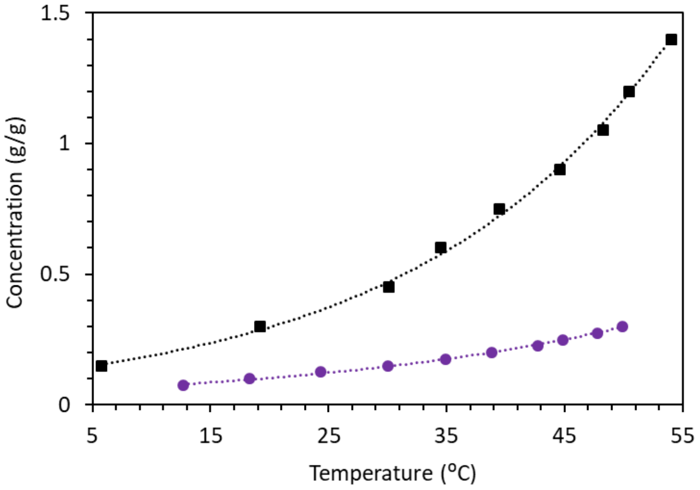

Figure 5.10. Solubility plot for IZN:TA co-crystal (purple circle marker) and pure IZN (black square marker) measured by observation in H_2O

The stability of the new solid forms was tested via all three techniques noted above: annealing, slurrying and humidity, with outcomes characterised by PXRD (figure 5.11). Samples kept in the oven at 50 °C for 3 weeks showed no change in the PXRD patterns. Slurry experiments in H_2O showed no visible breakdown after 1 week and samples stored at 70% humidity showed no change after 9 weeks.

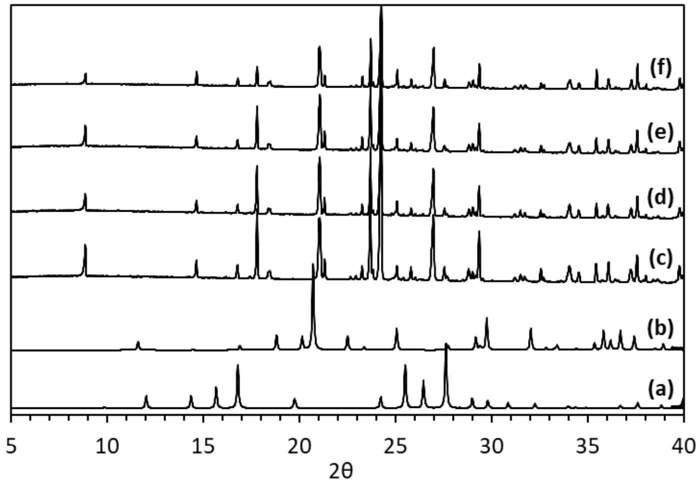

Figure 5.11. PXRD data for (a) IZN (INICAC02), (b) LTA (TARTAL), (c) IZN:LTA co-crystal calculated from SCXRD, (D) IZN:LTA co-crystal slurry 1 week, (e) IZN:LTA co-crystal 50 °C 3 weeks and (f) IZN:LTA co-crystal 70% humidity 9 weeks

The co-crystals exhibit a plate morphology when crystallised from H_2O (figure 5.12). This is a contrast to the needles usually observed for crystallisations of pure IZN from H_2O. The co-crystal formation has thus successfully produced a morphology change, one of the main targets of this research.

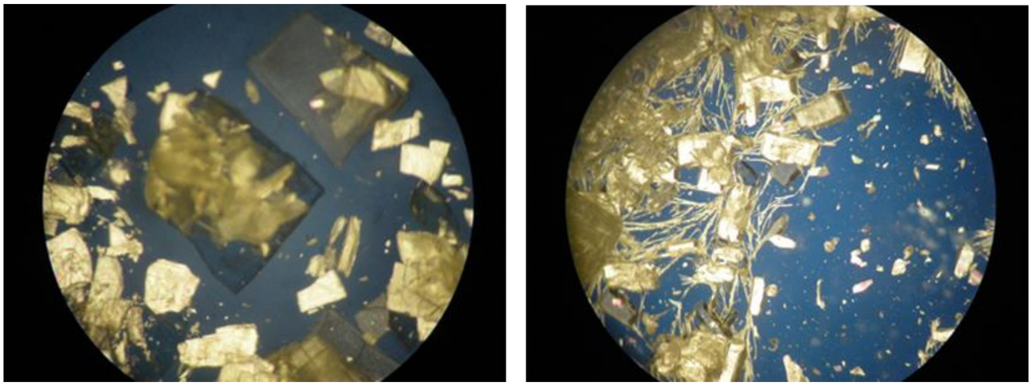

Figure 5.12.Plate-shaped crystals of IZN:LTA co-crystal (left) and IZN:DTA co-crystal (right) crystallised from H_2O

The crystals were face indexed using SCXRD and then compared to the predicted morphology for this crystal system (figure 5.13).

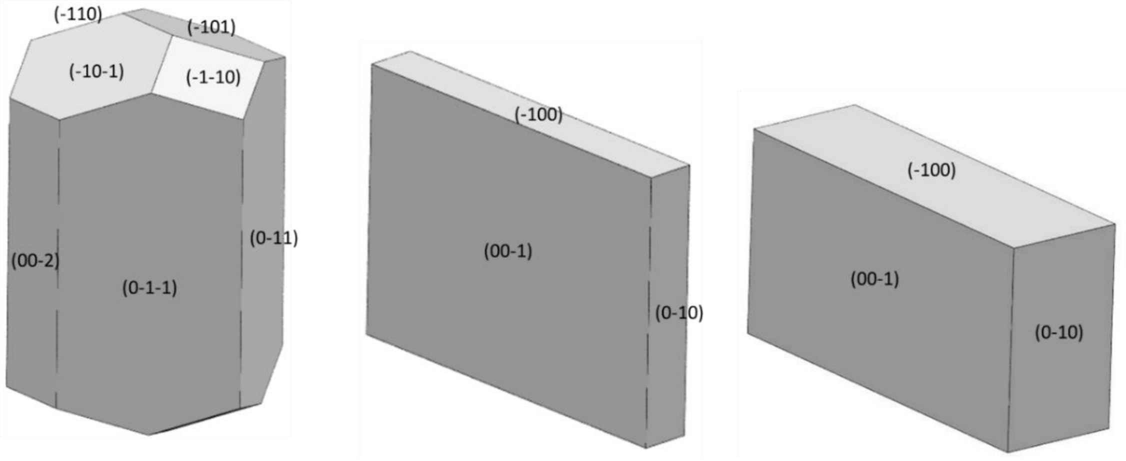

Figure 5.13. Predicted BFDH morphology for IZN:TA (left); observed morphology for IZN:LTA (middle) and IZN:DTA (right)

The predicted BFDH morphology for the new crystalline system is the same as that of pure IZN. This is due to pure IZN and the new multi-component salts crystallising in the same space group ($P2_12_12_1$), with similar unit cell parameters. BFDH calculations use the inter-planar spacing of crystals to predict morphology and, as the same space group is achieved with very similar unit cell parameters, the same result when calculating the morphology using this simple methodology is likely (as described in 1.3.1). In contrast, the observed morphology shows very thin plate crystals. The π-stacking interactions are responsible for the growth on the (100) and (-100) faces, corresponding to the edge where the (-10-1) and (-101) faces meet in the predicted morphology. Significant growth is also observed on the (010) and (0-10) faces. These faces would sit directly across the apex of the (011) and (01-1) and the apex of the (0-1-1) and (0-11) faces, observed in the predicted morphology, respectively. The interactions contributing to this growth are the hydrogen bonds that increase the length of the chains of IZN molecules. The elongation of the crystal structure in this direction is similar to that contributed to by the π-π interactions creating the overall plate shape with a relatively square cross-section. Very little growth occurs on the (001) and (00-1) faces, equivalent to the (002) and (00-2) faces observed in the predicted structure. This direction is dependent on the interaction between individual chains of IZN molecules and TA molecules. Whilst there are a number of hydrogen bonding interactions linking the chains, they are weaker than those seen making up each chain. Between IZN molecules the interactions are bifurcated and between the TA molecules there are significant numbers of hydrogen bonds contributing to the overall strength of interaction. However, between the two there are only single hydrogen bonds between NH groups and either OH or CO groups, significantly weaker than the other hydrogen bonds present. This coupled with the fast growth of the strong π-π interactions causes the plate morphology to arise. The elongation of existing layers is more favourable than the building up of adjacent layers.

Whilst the predicted structure appears to be a more favourable block shape, the calculations do not take into account any additional influences on the growth, such as solvent. Comparing the observed co-crystal morphology to that observed for pure IZN crystallisations in H_2O there is a significant change. Production of the plate shape, in contrast to long thin needles, illustrates the potential to modify morphology, alongside other significant crystal properties, using multi-component crystallisation. Further improvements could be made to the morphology observed in multi-component crystals using techniques such as temperature cycling, by changing the solvent or using additives.

5.4.2 Crystallisation of isoniazid with (DL)-tartaric acid forming a hydrate

Following the successful co-crystallisations of IZN with LTA and DTA, further experiments were carried out with the racemic mixture (DL)-tartaric acid (DLTA). Crash cooling crystallisation of a 1:1 molar ratio of IZN and DLTA from H_2O yielded a hydrated co-crystalline salt form with the three components in a 1:1:1 ratio. The structure is in space group $P\overline{1}$, an achiral space group confirming the presence of the racemic DLTA in this crystal structure. The asymmetric unit consists of one IZN molecule, one DLTA molecule and one H_2O molecule (figure 5.14). Again, proton transfer has occurred resulting in formation of a multi-component salt. The proton transfer differs from that in the LTA and DTA structures as it occurs between a carboxylic acid group on the DLTA and the terminal NH_2 group of the IZN, forming an NH_3^+ terminal group. The pyridyl N is hydrogen bonded to DLTA, however, the bond is with a central hydroxyl instead of the terminal carboxylic acid, as seen in the enantiomeric structures. This hydroxyl group is much less easily polarisable than the terminal carboxylic acid and, as a result, limited proton transfer occurs towards the N. The hydrogen bond distances are 0.94(6) Å for the O-H and 1.79(6) Å for the H··N interaction (table 5.4). Analysis of the co-crystals already published in the CSD show one structure with proton transfer to the NH_2 group. This structure also contains IZN molecules with proton transfer to the pyridyl N. There are no reported IZN structures where proton transfer to the NH_2 group is the only proton transfer observed.

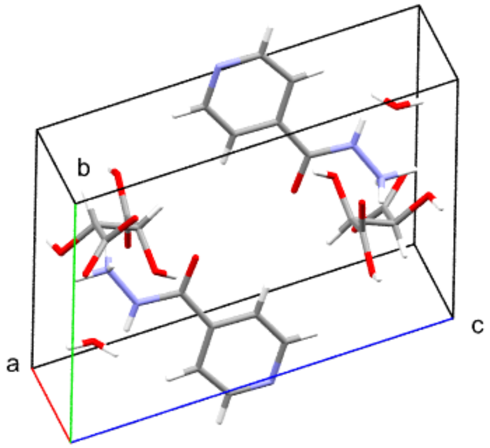

Figure 5.14. Unit cell for IZN:DLTA:H_2O co-crystal structure

The IZN molecules again stack via the interactions between their aromatic rings, however these lie in alternate directions (figure 5.15). This alternating sequence is not seen for the single enantiomers and is the result of having the racemic mixture present. The DLTA molecules form chains between the IZN molecules, again with alternating geometries. This is due to the two enantiomeric conformations and their differing interactions with the IZN molecules. The result of these is a loss of symmetry throughout the structure. An inversion center is still present due to the chirality of the DLTA.

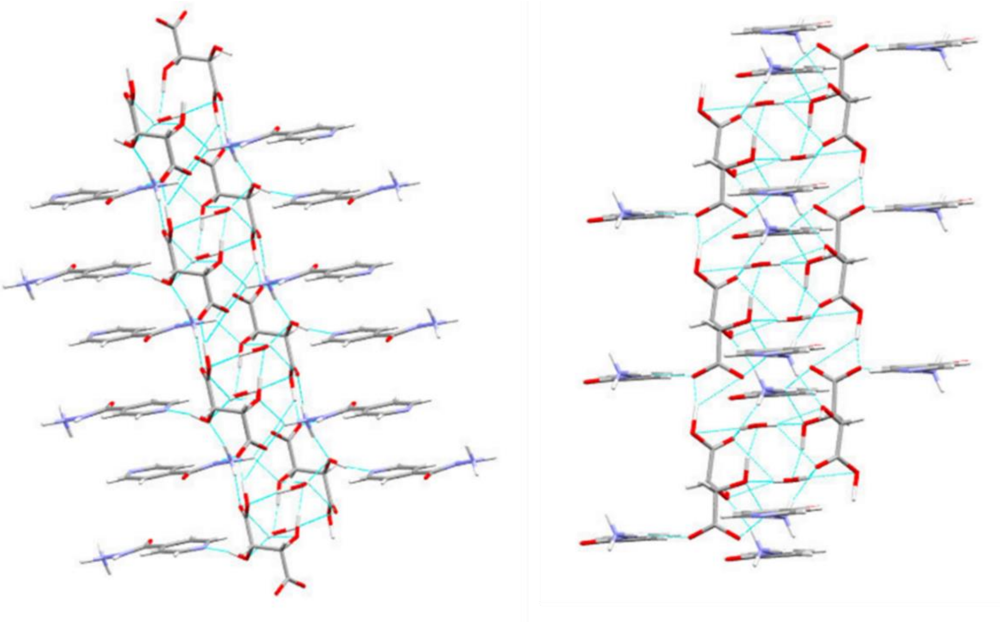

Figure 5.15. Hydrogen bonding interactions present in the IZN:DLTA:H_2O co-crystal showing the alternating nature of the IZN stacking and the chains of DLTA

A number of hydrogen bonding interactions are present between the three components present in the crystal structure (table 5.4). The H_2O molecule in the structure becomes part of the DLTA chain, with each H_2O molecule forming six hydrogen bonds to two separate DLTA molecules. No direct hydrogen bonding interactions exist between the IZN molecules in the structure; instead these are linked by aromatic interactions. Chains are formed with DLTA bridging the gaps in between, which are stacked in layers of alternating directions. The ring systems in the IZN overlap, enabling the interactions between the aromatic rings. IZN molecules form six hydrogen bond interactions with five different DLTA molecules. The N in the pyridyl ring accepts a hydrogen bond from a central hydroxyl group on the first DLTA molecule. As the donor is a hydroxyl group in this structure and not a carboxylic acid the hydrogen bond formed is weaker and proton transfer does not occur. The NH group on the IZN donates a hydrogen bond to the carbonyl group of the unprotonated carboxylic acid group on a second DLTA molecule. The NH_3^+ group forms four hydrogen bonding interactions with three separate DLTA molecules. A bifurcated hydrogen bond forms, consisting of an interaction from the NH_3^+ group to the deprotonated carboxylic acid group and an interaction to the central hydroxyl group on the next carbon along in the same molecule. The final hydrogen bond is donated from the NH_3^+ to the carbonyl in the protonated carboxylic acid group. In addition to hydrogen bonding to five different IZN molecules and three H_2O molecules, the DLTA forms a final hydrogen bond to a second DLTA molecule creating the chain. This interaction is a donation from the protonated carboxylic acid group in one molecule to the deprotonated carboxylic acid group in the neighbouring molecule.

Table 5.4. Hydrogen bond distances and angles for IZN:DLTA:H_2O co-crystal [vi]

D-H··A	d(D-H) (Å)	d(H··A) (Å)	d(D··A) (Å)	>(DHA) (°)
O4-H··N1	0.94(6)	1.79(6)	2.693(5)	162(6)
N2-H··O1^{2}	0.81(5)	2.00(5)	2.797(5)	174(4)
N3-H··O4^{4}	0.96(7)	1.86(7)	2.807(6)	168(5)
N3-H··O5^{5}	0.76(6)	2.06(6)	2.805(6)	170(6)
N3-H··O2^{3}	0.99(8)	1.90(8)	2.782(6)	146(6)
N3-H··O3^{3}	0.99(8)	2.14(8)	2.879(6)	130(7)
O6-H··O1^{1}	1.22(6)	1.37(6)	2.571(5)	166(5)
O3-H··OH$_2$	1.11(6)	1.57(6)	2.661(5)	167(5)
HO-H··O2^{1}	0.80(6)	2.59(6)	3.157(4)	129(6)

H_2O can be incorporated into crystal structures in a number of diverse ways. The three classes of hydrate are isolated site hydrates, channel hydrates and ion-associated hydrates (figure 5.16). In isolated site hydrates it is characteristic for the incorporated H_2O molecules not to interact with one another, instead forming hydrogen bonds to the API molecules (or co-former in the case of co-crystals). The H_2O molecules in channel hydrates form chains, hydrogen bonding to each other along a given crystal axis. Upon dehydration, the H_2O molecules can be removed without affecting the structure of the original hydrate. This results in void spaces remaining within the crystal which can be filled again with either H_2O or another solvent molecule, whilst still maintaining the original crystal structure. Finally the third class of hydrate, ion-associated hydrates, see the H_2O molecules ion-coordinated with the API molecules.[206]

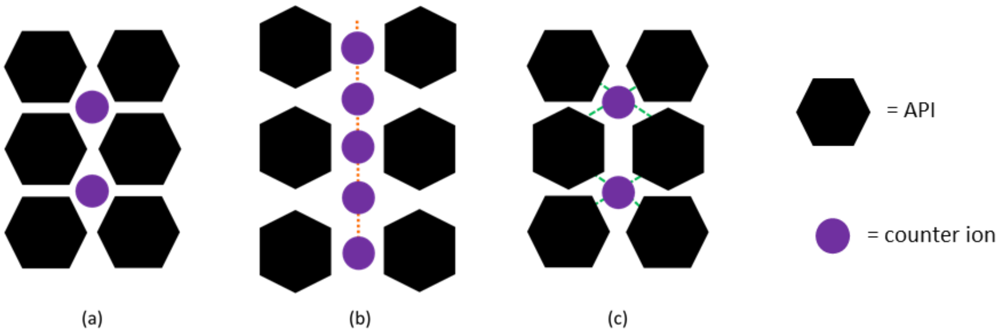

Figure 5.16. Schematic demonstrating (a) an isolated site hydrate, where H_2O molecules do not interact. (b) a channel hydrate, where H_2O molecules hydrogen bond to each other in a channel (orange dashed line). (c) an ion-associated hydrate, where the H_2O molecules are ion coordinated with the API (green dashed lines)

[vi] ^{1}1+X,+Y,+Z ^{2}-X,1-Y,1-Z ^{3}+X,-1+Y,1+Z ^{4}-X,-Y,1-Z ^{5}1-X,-Y,1-Z

From observation of the structural data for the IZN:DLTA:H_2O co-crystal, the hydrate is likely to fall under the classification of an isolated site hydrate. Analysis of the hydrogen bonding interactions present shows no direct interaction between individual H_2O molecules, with no chains forming throughout the structure, eliminating the possibility of it being a channel hydrate. There also does not appear to be an ion-coordinating interaction between the H_2O molecules and the API or co-former molecules in the structure ruling out the ion-assisted hydrate classification.

The class of a pharmaceutical hydrate can be further confirmed using a variety of analysis techniques, namely DSC, TGA and IR spectroscopy. Isolated site hydrates show sharp dehydration endotherms (showing sharp peaks in DSC traces), narrow weight loss regions (in TGA) and sharp OH bands (in IR spectroscopy). Channel hydrates also show sharp OH bands but, in contrast to isolated site hydrates, show wide TGA weight loss ranges and broad endothermic peaks in DSC, often observed at lower temperatures. Finally, ion-associated hydrates show high dehydration temperatures due to the ionic interactions between the H_2O and crystal molecule.[206] Characterisation of the bulk was also carried out using PXRD.

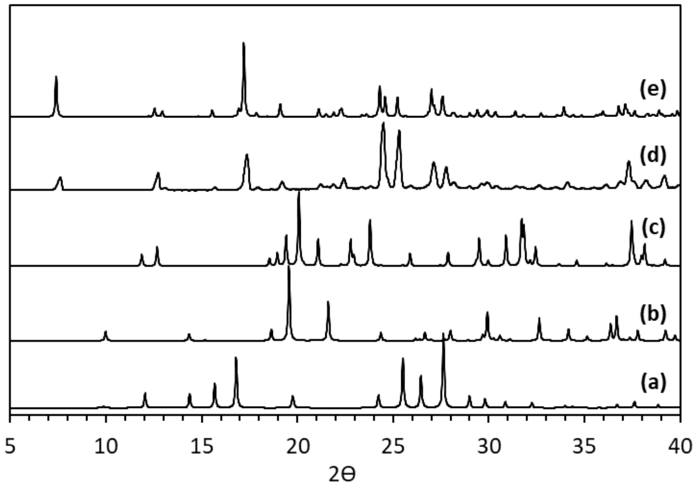

Figure 5.17. PXRD data for (a) IZN (INICAC02), (b) DLTA (ZZZDUI01), (c) DLTA monohydrate (TARTDL), (d) IZN:DLTA:H_2O co-crystal calculated from SCXRD and (e) IZN:DLTA:H_2O co-crystal from H_2O crash cooling

As expected, the PXRD data shows a new crystalline form when compared to the raw starting materials (figure 5.17). The calculated pattern from single crystal data matches that of the bulk with very little deviation suggesting a high level of phase purity has been achieved.

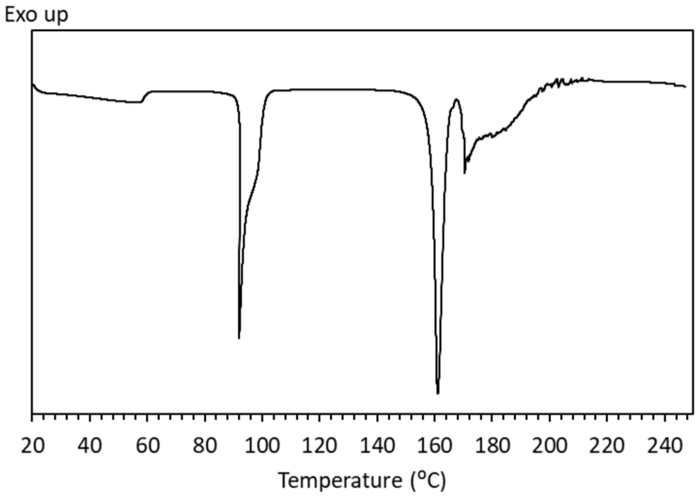

Figure 5.18. DSC trace for IZN:DLTA:H_2O co-crystal. IZN melting point = 171-174 °C[163]*, DLTA melting point = 210-212 °C*[207]

DSC analysis also confirms the formation of a new crystalline form. The DSC trace of the multi-component structure (figure 5.18) shows two sharp endotherms, one at 92 °C and one at 161 °C. The endotherm at 92 °C could be the result of H_2O being eliminated from the system. The sharpness of this endotherm suggests the hydrated structure can be classified as an isolated site hydrate, in agreement with the analysis of the structural data. This interpretation is supported by observation of a second endotherm, suggesting a stable anhydrous crystalline form of the multi-component crystal has been formed. The second endotherm at 161 °C falls in the same place as that of the single enantiomer co-crystals. This could indicate the anhydrous structure formed is the same as that previously reported for the single enantiomers.

The formation of the hydrated co-crystal was attempted in a number of solvent-mediated methods as well as using mechanochemical grinding (appendix A32 and A33). Grinding in the absence of solvent and LAG showed PXRD patterns that differ from that of the co-crystal, containing many peaks not corresponding to the starting materials, but which did not correspond to the known hydrated co-crystal. The LAG experiments showed higher conversion to the potential new phase than the grinding in the absence of solvent. These results suggest a second form exists of this crystal system. The PXRD interpretation is confirmed by the DSC data obtained for both the grinding and LAG experiments; both showing a single melt at approximately the same temperature, matching the second endotherm observed in the crash cooling analysis. This could take the form of a hemi-hydrate or, more likely, an anhydrous form. Attempts to form the hydrated co-crystal via slurrying in H_2O were successful with high conversion and phase purity. In addition, controlled cooling crystallisation yielded the hydrated co-crystal on 10 g and 30 g solvent scales (appendix A34).

Crystallisation on larger 200 g solvent scales were not carried out due to the high solubility of the starting materials in H_2O.

Co-crystal solubility was determined using observation techniques. The IZN:DLTA:H_2O co-crystal and pure IZN starting material have a relationship that can be regarded as analogous to monotropic (figure 5.19): the co-crystal is less soluble over the full temperature range. As a result, this co-crystal form is also a potential candidate for improving other physical properties of IZN, notably the stability of IZN in the FDC tablet. The presence of more intermolecular interactions could result in an overall increase in crystal stability, when formulated into the FDC table, and therefore a reduction in solubility would be a worthwhile compromise.

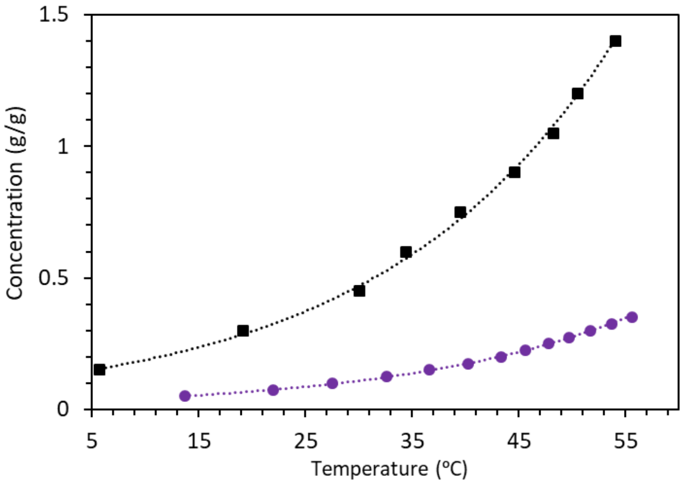

Figure 5.19. Solubility plot for IZN:DLTA:H_2O co-crystal (purple circle marker) and pure IZN (black square marker) measured by observation in H_2O

The effects of the inclusion of H_2O into pharmaceutical crystals is also important to consider. Hydrates can possess different dissolution profiles to anhydrous forms, however this is also affected by a number of other factors. They can also experience a change in mechanical properties. It is possible for these changes to be a positive result for the crystal system in question but does require careful investigation. Chemical stability is one property that can be affected that needs to be considered very carefully. The inclusion of the H_2O in the structure during crystallisation could pose the problem of dehydration during storage, depending on the type of hydrate that has been formed. Later processing steps often involve the use of heat, giving rise to the possibility for dehydration to occur. This could result in a change in an unstable product leading to unfavourable properties due to variation in hydrate content or uncontrolled hydrate formation and dehydration processes. Therefore, in order to be considered as a viable option, the structural (crystallographic) aspects of hydrates, the mechanism for their formation and the effects on the properties of the API must be fully understood.[206]

Confirmation of the H_2O stoichiometry in the crystal structure was carried out by TGA analysis.

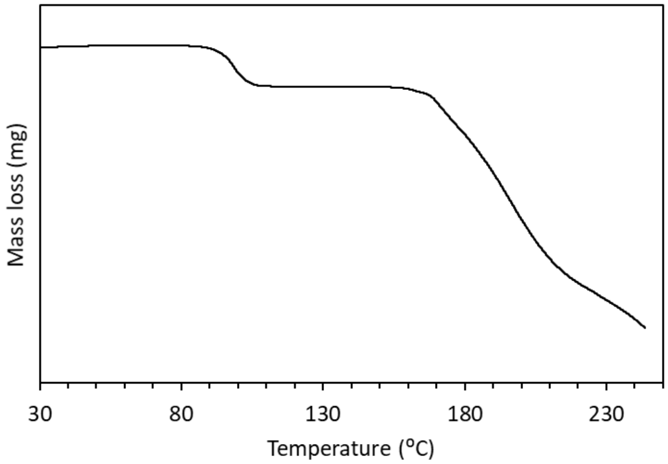

Figure 5.20. TGA trace for IZN:DLTA:H_2O co-crystal showing the mass loss with increasing temperature

The TGA trace of this crystalline form confirmed the loss of H_2O hypothesised from the DSC analysis (figure 5.20). The first mass loss is 0.7 mg, about 5.1% of the total mass of the crystal added. The molecular mass of a 1:1:1 co-crystal would be 305 g/mol, with 18 g/mol corresponding to H_2O. This would correspond to the crystal being in a 1:1:0.84 ratio, assuming all H_2O in the structure has been fully eliminated. This is close to the 1:1:1 ratio originally hypothesized for the crystal structure. The loss of mass corresponding to H_2O occurs between 77 °C and 116 °C, matching the endotherm observed in the DSC experiment. The mid-point of the initial mass loss corresponds to 98 °C, close to the boiling point of H_2O. The small deviation in the temperatures between DSC and TGA are due to the DSC pan being sealed and the TGA sample holder being open to the atmosphere. The second loss of mass starts at about 160 °C. This is comparable to the second thermal event observed in the DSC and shows full decomposition of the remaining crystal structure. The weight loss region corresponding to the dehydration is relatively narrow, spanning about 20 °C. This narrow weight loss region would, again, suggest the hydrate formed falls into the class of isolated site hydrate. This agrees with the DSC and the structural analysis.

The use of FTIR analysis to confirm the type of hydrate is complicated in this case, due to the structure of the co-former present. As well as the H_2O molecules the co-former has two COOH functional groups and two OH functional groups; the IR bands from these all overlap in the spectrum (figure 5.21), making differentiation between them difficult.

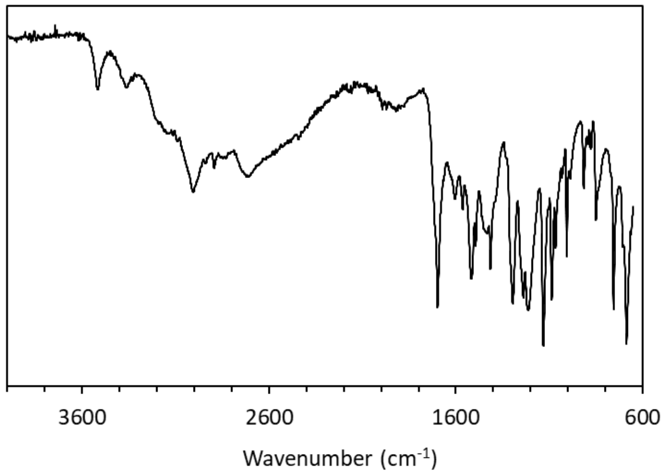

Figure 5.21. FTIR scan of IZN:DLTA:H_2O co-crystal

The broad set of peaks between 3600 cm^{-1} and 2200 cm^{-1} is due to the OH functional groups present in the DLTA co-former and H_2O molecules. Within this region, OH peaks from alcohol groups and the H_2O molecules are present at the top end of the peak, between 3600 cm^{-1} and 3400 cm^{-1}, OH peaks from COOH functional groups are present between 3300 cm^{-1} and 2500 cm^{-1}, and peaks caused by the N-H bonds within the molecule, between 3500 cm^{-1} and 3300 cm^{-1}. Isolated site hydrates show sharp OH peaks and, whilst it is difficult to determine exactly which part of the peak the H_2O is responsible for, the initial high wavenumber part of the peak does begin sharply. When combined with the DSC and TGA data, this helps confirm the presence of the isolated site hydrate; however, in isolation from the other data, the IR spectrum would not allow definitive determination of the type of hydrate in this case.

Whilst the DSC trace (figure 5.18) suggested a dehydrated crystalline structure may exist, determination of whether this second structure was fully crystalline was necessary. HSM and variable temperature PXRD analysis were carried out to examine this.

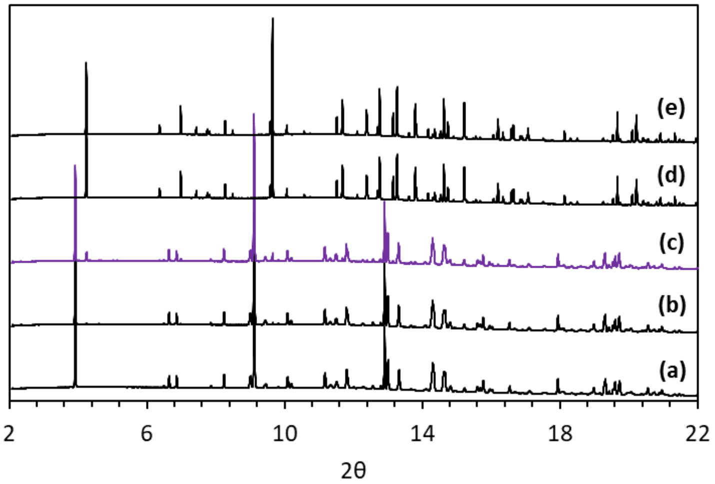

Figure 5.22. Variable temperature PXRD data obtained from beamline I11 at Diamond light source showing the conversion from the hydrated co-crystal to a secondary crystal structure. (a) initial collection at 75 ^{o}C, (b) collection at 79 ^{o}C, (c) collection at 81 ^{o}C showing the transition, (d) collection at 83 ^{o}C and (e) collection at 85 ^{o}C

The variable temperature PXRD data were collected on beamline I11 at Diamond Light Source (figure 5.22). In pattern (c), the beginning of a transition from the initial crystal structure can be observed. At around 81 ^{o}C the pattern remains mostly similar to the hydrated co-crystal pattern but with the emergence of a small peak at 8° 2θ. This peak signifies the start of the transition to the secondary structure with full transformation having occurred by 83 ^{o}C (pattern (d)). This temperature corresponds well to the onset of the H_2O loss observed in both DSC and TGA analysis. The second, dehydrated, structure is confirmed as fully crystalline by its sharp PXRD pattern. The substantial change in structure is further evidence that the hydrate is not a channel hydrate, as eliminating H_2O from channels within a structure would tend to result in little or no change in the crystal parameters.

The co-crystal stability was investigated in slurry techniques for up to 1 week. No conversion was observed in PXRD (figure 5.23), with the co-crystal remaining stable without any degradation or additional uptake of H_2O. However, the co-crystal stability at high temperatures was found to be reduced. From the data produced in vtPXRD, DSC, TGA and solubility experiments it has been suggested the co-crystal becomes less stable as the temperature is increased, eventually converting to a second, assumed anhydrous, form. Conversion of the co-crystal system begins to be observed after only 24 hours at an elevated temperature of 50 ^{o}C. The second (anhydrous) structure is fully achieved after 48 hours at 50 ^{o}C. This reduced stability at elevated temperatures is directly related to the inclusion of H_2O in the crystal structure and provides a good example of the problems with using hydrated crystals in the pharmaceutical industry. Samples subjected to increased humidity remained stable for the full 9 weeks of the analysis.

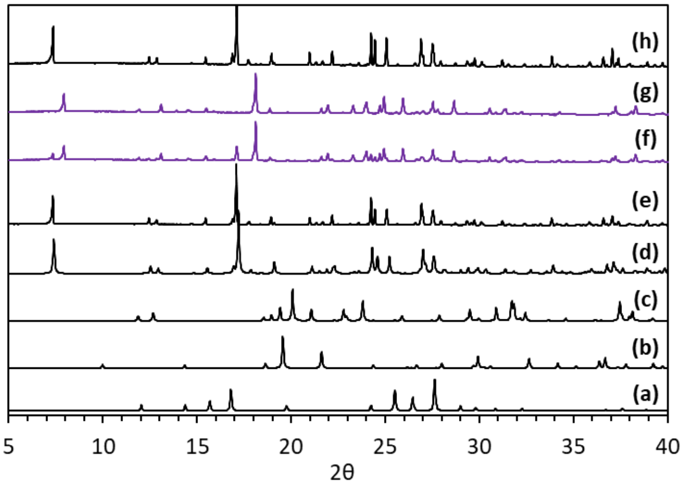

Figure 5.23. PXRD data for (a) IZN (INICAC02), (b) DLTA (ZZZDUI05), (c) DLTA monohydrate (TARTDL), (d) IZN:DLTA:H_2O co-crystal calculated from SCXRD, (d) IZN:DLTA:H_2O slurry 1 week, (e) IZN:DLTA:H_2O co-crystal 50 °C 24 hours, (f) IZN:DLTA:H_2O co-crystal 50 °C 1 week and (g) IZN:DLTA:H_2O co-crystal 70% humidity 9 weeks

The new hydrated salt form has a plate like morphology (figure 5.24). The addition of co-former and H_2O molecules has influenced the structure and growth of the crystal to significantly change the morphology seen in pure IZN crystallisations from H_2O.

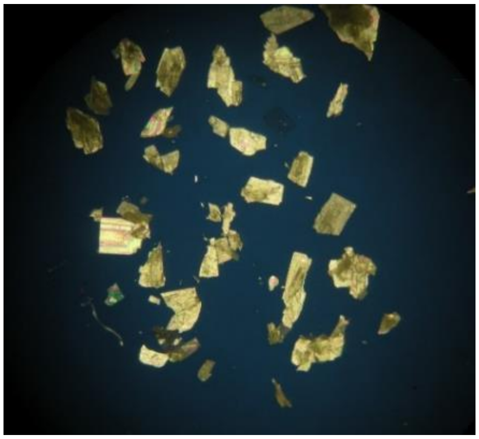

Figure 5.24.Plate-shaped IZN:DLTA:H_2O co-crystals crystallised from H_2O

Plate-shaped crystals are still not favoured by the pharmaceutical industry but, as previous research has shown, a change of solvent could in turn result in more favourable block shaped crystals forming rather than flat plates.

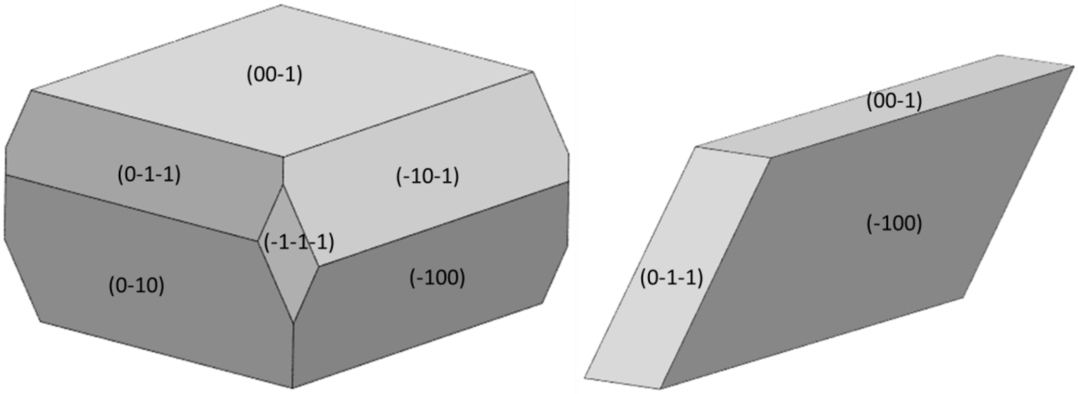

Figure 5.25. Predicted BFDH morphology for IZN:DLTA:H_2O (left); observed morphology for IZN:DLTA:H_2O (right)

The BFDH morphology is different from the observed face-indexed morphology of the crystals produced (figure 5.25). Whilst the face indexed crystal is a thin plate, the calculated morphology appears thicker and closer to a block. The calculated morphology still suggests the major growth mechanism occurs in the (100) and (101) directions with the π-π interactions contributing to the major growth. In the experimental morphology, the plate-shaped crystals show the major growth occurring on the (011) / (0-1-1) faces. The major growth interaction has shifted from those between the aromatic rings to the hydrogen bonds between the IZN, TA and H_2O components, illustrated mainly in the right image of figure 5.15. Little growth is seen parallel to the crystallographic *a* axis as very few interactions exist between the layers of IZN and TA in this direction. The π-systems alternate their orientation between layers. As a result, fewer π-stacking interactions are present causing the significant reduction of growth observed in this direction. The incorporation of H_2O molecules and the two different orientations of TA involved in the structure could explain the alternating nature of the IZN π-systems.

Comparison of the resulting morphology with that observed for pure IZN gives credibility to the approach of changing morphology using multi-component crystallisation. Again a plate shape crystal is observed as opposed to the thin needle usually crystallised from H_2O. This co-crystal not only has a different morphology but also a different major growth mechanism. This could be beneficial in attempting to alter this crystal habit with further techniques, for example the weakening of the aromatic interactions could result in greater ease of alteration using different solvent and additive techniques.

5.4.3 Dehydration of isoniazid and (DL)-tartaric acid hydrate to give an anhydrous form [vii]

Attempts were made to isolate a single crystal for the second crystal structure observed in the variable temperature PXRD data for the DLTA hydrated co-crystal. A single crystal was successfully isolated using the HSM set up. Single crystals of the hydrated DLTA co-crystal were heated on the hot stage to a temperature just above the first thermal event observed in the DSC and TGA data. To ensure the H_2O had fully left the structure the temperature chosen was 130 °C. The remaining crystals were then analysed using the Rigaku Oxford Diffraction Gemini A ultra to determine the crystal structure. The new crystal structure has a different space group to the hydrated co-crystal. This anhydrous form has space group $P2_1/c$ and exhibits extra symmetry without the H_2O present. This is again an achiral space group, confirming the presence of the racemic form DLTA. The asymmetric unit consists of one IZN molecule and one DLTA molecule (figure 5.26). The hydrogen bonding distances again show the transferred proton sitting closer to midway between the donor and acceptor atoms: N3-H distance is 1.2(2) Å; H··O2 distance is 1.6(1) Å (table 5.5). Again, unlike the enantiomeric crystal structures, the pyridyl N is hydrogen bonded to a central hydroxyl group on the DLTA. Consequently, no proton transfer occurs towards the N in this structure.

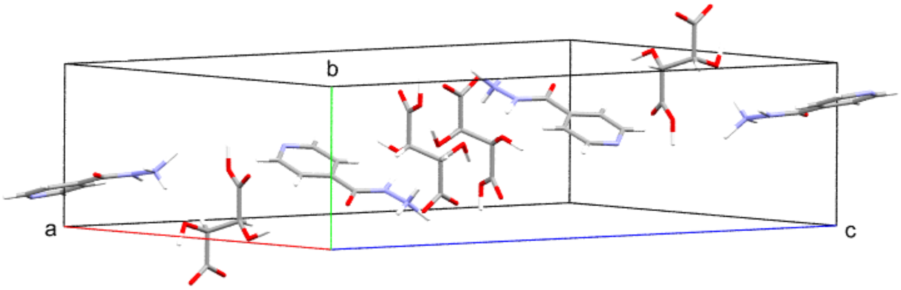

Figure 5.26. Unit cell of IZN:DLTA anhydrous co-crystal

The packing of this co-crystal is very similar to that of the hydrated co-crystal. The unit cell volume has reduced due to the loss of H_2O. IZN molecules stack via the interactions between their aromatic rings with the molecules alternating directions. Therefore, the direct overlap occurs between every other IZN molecule looking down the crystallographic *b* axis. This alternation is the same as observed in the hydrated structure. The DLTA chains observed in the hydrated structure are again seen here

---

[vii] The structure for the anhydrous DL-tartaric acid co-crystal has been added to the CSD (BOPHOG) since this research was carried out with a paper published in 2019.

and lie between the stacked IZN molecules. The loss of H_2O in the structure has led to the adoption of a higher symmetry in the unit cell (figure 5.27).

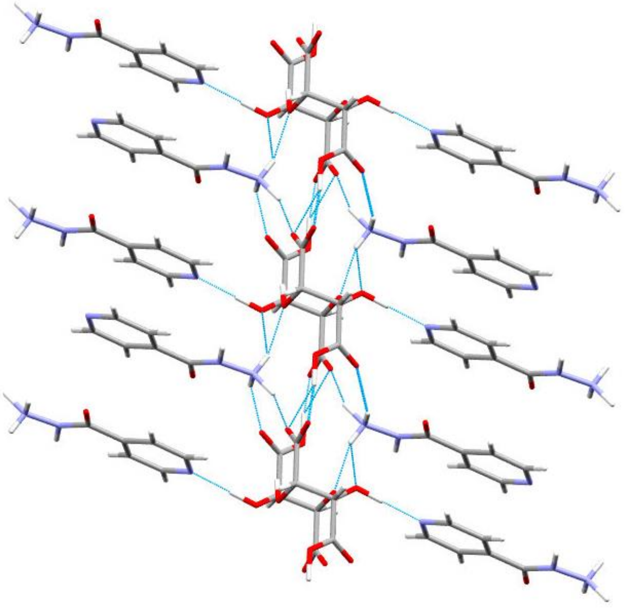

Figure 5.27. Hydrogen bonding interactions present in IZN:DLTA co-crystal showing the alternating nature of the IZN stacking and chains of the DLTA molecules

The hydrogen bonds present are listed in table 5.5. Each IZN molecule accepts a hydrogen bond at the pyridyl ring N, donated from a central hydroxyl group on a DLTA molecule. Due to the low polarizability of the hydroxyl group no proton transfer is observed. Each IZN molecule then hydrogen bonds to a further four DLTA molecules. The NH donates to the carbonyl group of the deprotonated carboxyl on a second DLTA molecule. The NH_3^+ donates to three separate DLTA molecules; one to a central hydroxyl group, one to the carbonyl of the protonated carboxylic acid group and the final bond is between the deprotonated carboxylic acid where proton transfer has occurred. Each DLTA molecule is bonded to five separate IZN molecules through the five interactions previously discussed. The DLTA molecules are also hydrogen bonded to each other through the terminal carboxylic acid groups to form the chains. The deprotonated end of the DLTA molecule accepts a hydrogen bond donated from the protonated end of a second DLTA creating a chain through the structure. No direct hydrogen bonding interactions are observed between IZN molecules in this geometry.

Table 5.5 Hydrogen bond distances and angles for IZN:DLTA co-crystal [viii]

D-H··A	d(D-H) (Å)	d(H··A) (Å)	d(D··A) (Å)	>(DHA) (°)
O4-H··N1	1.01(7)	1.71(7)	2.706(5)	167(6)
N2-H··O1[4]	1.01(6)	1.80(6)	2.809(7)	178(7)
N3-H··O2[3]	1.2(2)	1.6(1)	2.73(1)	157(7)
N3-H··O3[2]	0.83(6)	2.08(6)	2.811(7)	146(5)
N3-H··O5[1]	0.95(6)	1.99(6)	2.761(7)	137(5)
O6-H··O1[5]	1.07(8)	1.47(8)	2.538(5)	171(6)

Bulk analysis for this co-crystal was carried out on a sample of the preparation of hydrated IZN:DLTA co-crystal that had undergone dehydration in the oven at 50 ^{o}C. PXRD analysis was carried out to compare the calculated pattern with the bulk-produced sample and determine the phase purity and conversion (figure 5.28).

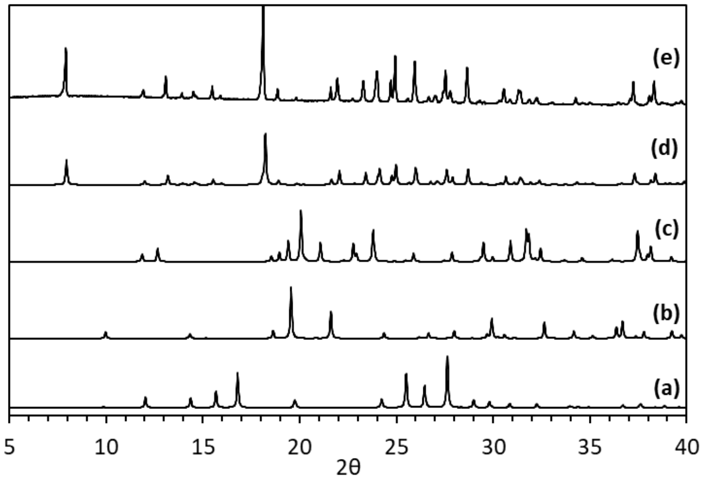

Figure 5.28. PXRD data for (a) IZN (INICAC02), (b) DLTA (ZZZDUI05), (c) DLTA monohydrate (TARTDL), (d) IZN:DLTA co-crystal calculated from SCXRD and (e) IZN:DLTA co-crystal produced by dehydrating the hydrated form at 50 ^{o}C

Full conversion to the dehydrated co-crystal is found to be possible without significant degradation back to starting materials. The new dehydrated crystalline form is confirmed with no discernable traces of the hydrated co-crystal or further decomposition of the crystalline structure.

Thermal techniques were also used to characterise the thermal behavior of the new anhydrous co-crystal structure and confirm the crystal structure to be fully dehydrated. This would allow for the

---

[viii] [1]-X,-Y,1-Z [2]-1+X,+Y,+Z [3]-1+X,-1+Y,+Z [4]1-X,-1/2+Y,3/2-Z [5]+X,-1+Y,+Z

possibility that a hemi-hydrate could have formed in the bulk from incomplete evaporation of the H_2O present.

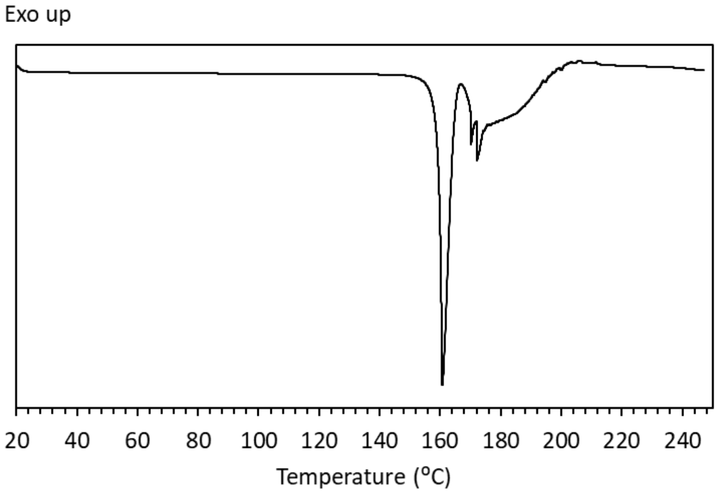

Figure 5.29. DSC trace for IZN:DLTA co-crystal. IZN melting point = 171-174 °C [163]*, DLTA melting point = 210-212 °C* [207]

The DSC trace shows a sharp endothermic peak at 155 °C (figure 5.29), representing the melting point of the new co-crystal structure. This is lower than both starting materials suggesting that the anhydrous co-crystal is less stable than the pure forms are individually. The melting endotherm and the complex endothermic peak directly following match the trace observed for the equivalent thermal events in the hydrated IZN:DLTA co-crystal, confirming the hypothesis that the dehydrated co-crystal is formed upon heating of the hydrated crystal.

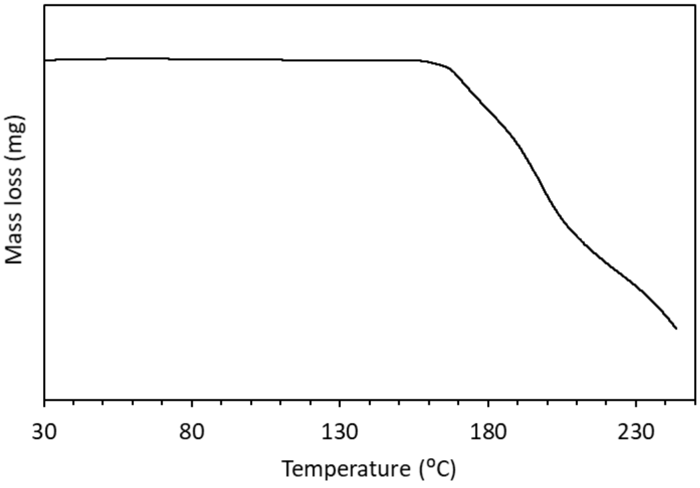

Figure 5.30. TGA trace for IZN:DLTA co-crystal confirming the absence of H_2O in the structure

TGA analysis confirms the anhydrous form of the crystal and discounts the possibility of a second, hemi-hydrate being formed (figure 5.29). No mass loss is observed in the TGA data until 160 °C where decomposition of the co-crystal structure begins to occur. There is no mass loss observed that would be attributed to H_2O as seen in the hydrated crystal, confirming the absence of H_2O in this form.

FTIR analysis of the dehydrated form was carried out in an attempt to confirm further the absence of H_2O (figure 5.31). Again the presence of many OH groups in the co-former makes this determination difficult.

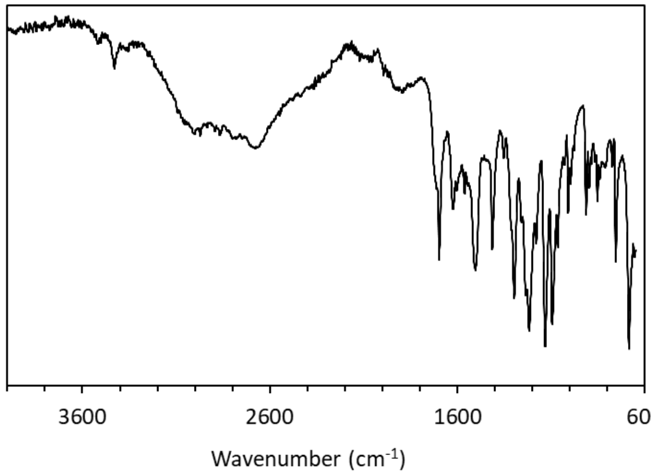

Figure 5.31. FTIR scan of IZN:DLTA co-crystal

A broad OH peak is observed between 3300 cm^{-1} and 2500 cm^{-1} caused by the OH group in the carboxylic functional groups observed in the co-crystal. Also falling within this region is a peak corresponding to the N-H bonds present in IZN and formed due to donation of the H from a carboxylic acid group to the N in the pyridine ring, between 3500 cm^{-1} and 3300 cm^{-1}, and from the alcohol groups also present in the co-former. Comparison of this broad peak with that seen in figure 5.20 shows that the broad peak starts at a slightly lower wavenumber, around 3300 cm^{-1} compared to 3600 cm^{-1}, suggesting the absence of the H_2O molecules in this structure. While it is difficult to determine with certainty from these data that the H_2O has been eliminated within this structure, when combined with the DSC, TGA and structural analysis it can be determined that no H_2O remains within the structure.

The dehydrated co-crystal solubility was determined using observation techniques. A monotropic relationship between pure IZN and the co-crystal is observed (figure 5.32, left). The solubility of the co-crystal is lower than pure IZN, indicating the co-crystal has good stability. Thus, the potential exists for this form to improve the stability of IZN in the FDC tablet. The solubility of the hydrated and dehydrated co-crystal are very similar, almost identical at low temperatures. At higher temperatures, slight deviation is observed with the hydrated co-crystal becoming slightly less soluble (figure 5.32, right). Whilst this agrees with the general finding that hydrated co-crystals tend to be less soluble than their anhydrous counter parts, due to the changes in intermolecular interactions leading to a reduction in Gibbs free energy[205], the differences are likely negligible when taking into account the error of the experimental procedure. The similarity could be the result of the anhydrous form re-hydrating in solution and, therefore, the experiment is just measuring the solubility of the hydrated co-crystal once again.

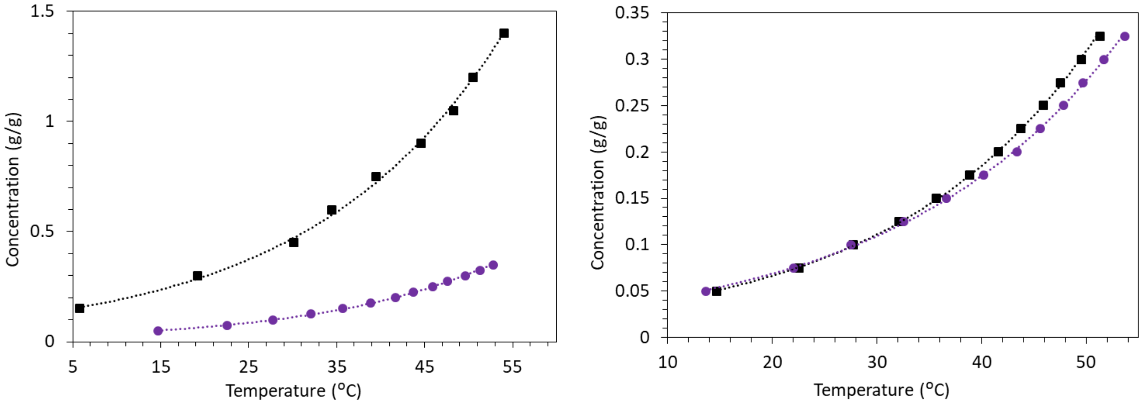

Figure 5.32. Left: Solubility plot for IZN:DLTA co-crystal (purple circle marker) and pure IZN (black square marker) measured by observation in H_2O. Right: comparison of IZN:DLTA co-crystal solubility (purple circle marker) and IZN:DLTA:H_2O co-crystal (black square marker)

Stability testing of the dehydrated crystal structure was again carried out via slurrying, high temperature studies and increased humidity, with outcomes monitored by PXRD (figure 5.33). The co-crystal was stable for three weeks when stored at 50 °C with no degradation to the starting materials observed. However, in slurry experiments a conversion back to the hydrated form of the co-crystal was witnessed. This conversion occurred completely after 48 hours of continuous mixing in H_2O at 40 °C. No changes were observed after 9 weeks in the humidity chamber, indicating the need for dissolution to allow for the reintroduction of H_2O into the crystal structure.

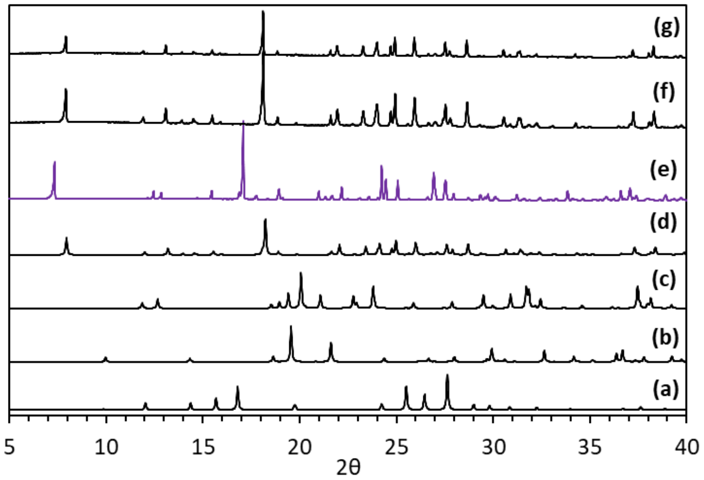

Figure 5.33. PXRD data for (a) IZN (INICAC02), (b) DLTA (ZZZDUI05), (c) DLTA monohydrate (TARTDL), (d) IZN:DLTA co-crystal calculated from SCXRD, (e) IZN:DLTA co-crystal slurry 48 hours, (f) IZN:DLTA co-crystal 50 ℃ 3 weeks and (g) IZN:DLTA co-crystal 70% humidity 9 weeks

Further experiments showed that H_2O elimination and re-uptake are not reversible; it is not possible to rehydrate the anhydrous structure. This was to be expected due to the classification of the hydrate as an isolated site hydrate. If a channel hydrate were formed, the re-uptake of H_2O would be possible. Cycling experiments on the DSC and HSM instruments were carried out with no successful recrystallisation of the hydrated form of the co-crystal (appendix A35). Slurrying on the other hand, can induce rehydration, assisting the transition through the continuous dissolution and recrystallisation of the co-crystal over time. The significant reduction in unit cell volume observed on dehydration further confirms the irreversible nature of the transformation observed on heating the hydrated crystal.

The crystal morphology for this structure remains a plate due to the method of isolation used to achieve this crystal form. Obtaining the crystal via heating in HSM causes the morphology to remain the same as the original hydrated form of the co-crystal (figure 5.34)

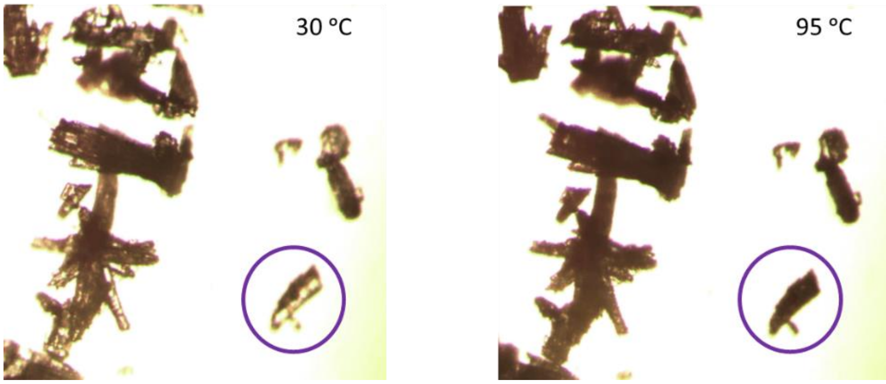

Figure 5.34. Images isolated from HSM video footage showing the morphology retention when IZN:DLTA:H_2O co-crystal (left) transforming to IZN:DLTA co-crystal (right) upon heating

The overall BFDH predicted morphology for this crystal structure is similar to that calculated for the hydrated co-crystal, but with significantly different growth faces as expected given the different unit cell parameters. The block-like morphology has an overall predicted hexagonal shape in comparison to the square shape predicted for the hydrated co-crystal. The predicted morphology still shows an overlap of the aromatic rings after the elimination of H_2O, however, the growth from hydrogen bonding is predicted to be more equal throughout the structure.

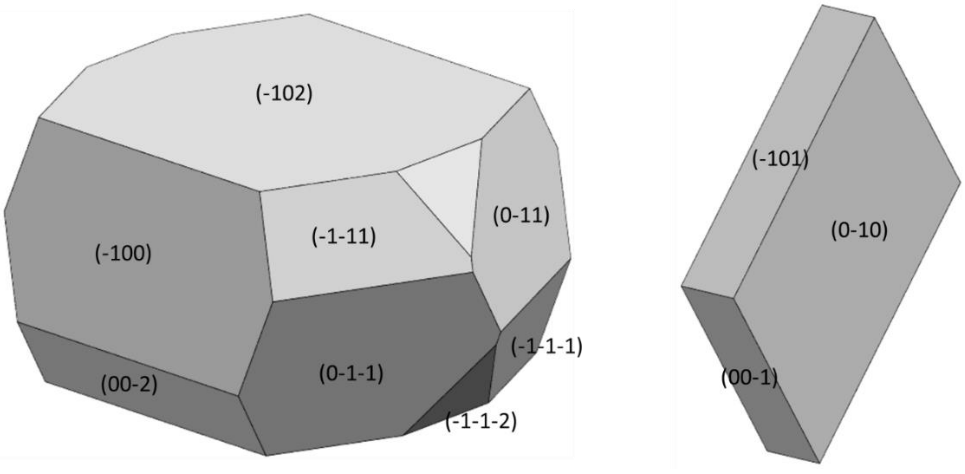

Figure 5.35. Predicted BFDH morphology for IZN:DLTA (left); observed morphology for IZN:DLTA (right)

The observed plate-shaped crystals share the same major growth as the hydrated crystal structure (figure 5.35). The fastest growing faces are now the (00-1) and (001) faces, due to hydrogen bonding. From this observed morphology, it would appear that the aromatic ring interaction is not responsible for the major growth of the crystal, as predicted in the BFDH morphology. In this interpretation, the overall contribution from the many hydrogen bonds in this structure could potentially outweigh the strength of the aromatic interactions. It is more likely, however, that this morphology is purely the result of the method of isolation used. This is further confirmed by Sarma et al., in a paper published in 2019 since this work was carried out. The research successfully crystallised the anhydrous co-crystal using solvent-mediated techniques. In both ACN and EtOH crystallisations needle-shaped crystals resulted for this form.[207] It is likely in this case that the major growth mechanism is again the π-π interactions between the aromatic rings in the IZN, resulting in the same needle morphology observed in crystallisations of pure IZN. This is a good example of different crystallisation methods resulting in different crystal morphologies. By eliminating the H_2O from the hydrated co-crystal through dehydration, a significantly different morphology can be obtained to that produced from solution methods. It may be possible to alter this further using additives in the crystallisation process.

5.5 Crystallisation of isoniazid with 3,4-dinitrobenzoic acid

A co-crystal of IZN was also obtained from a 1:1 ratio of IZN and 3,4-dinitrobenzoic acid (3,4-DNBA) in IPA (figure 5.36).

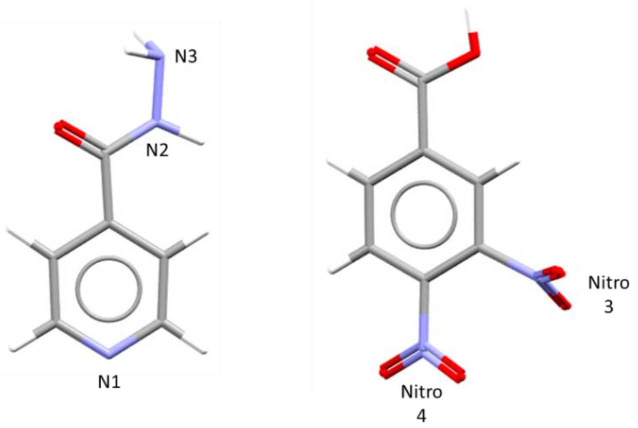

Figure 5.36. Structure of IZN and 3,4-DNBA showing the numbering system used in hydrogen bonding discussions

The new form crystallises in the $P\overline{1}$ space group with an asymmetric unit consisting of one IZN and one 3,4-DNBA molecule (figure 5.37). In this structure no proton transfer is observed between the IZN and the co-former molecule.

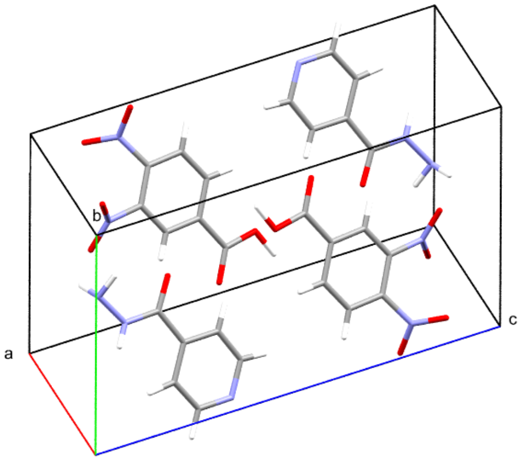

Figure 5.37. Unit cell of co-crystal IZN:3,4-DNBA

The hydrogen bonding interactions occurring in this structure (table 5.6) create discrete 1D chains of molecules (figure 5.38). The first creates a link between the pyridyl N on the IZN to the carboxylic acid group on the 3,4-DNBA. Unlike the other co-crystal structures discussed in this chapter, this hydrogen bond does not appear to show transfer of the H from the carboxylic acid group to the N. However, there appears to be significant elongation of the O-H distance and corresponding shortening of the N··H distance: the N··H distance is 1.46(4) Å and O-H distance is 1.10(4) Å. This could suggest the hydrogen is not strongly held on the carboxylic acid in this structure and the hydrogen could migrate or transfer as observed in other structures. The data for this co-crystal structure shows significant errors (ESD's) for the bond lengths measured. As a result the position of the hydrogen is essentially undetermined. Examination of the CSD database shows there are 19 crystals with this hydrogen bond interaction with 13 occurring without a shift in the proton. Further hydrogen bonds form between the NH and NH_2 groups in the IZN molecules. These interact head on with each other and create dimeric ring interactions. This is an unusual interaction for IZN. In the CSD, only nine co-crystalline structures form this type of interaction of 56 co-crystalline structures published in total. This is a stark contrast to the carboxylic acid/pyridyl N interaction previously discussed. These interactions form chains through the molecule in an alternating fashion, 3,4-DNBA··IZN··IZN··3,4-DNBA. The IZN and 3,4-DNBA singularly bonded heterodimers exist in the same plane as each other, with the aromatic rings flat. The ring interactions between the two heterodimers result in a slight offset and do not occur in the same plane (figure 5.38). The aromatic rings of the second heterodimer still remain flat with respect to the first. The chains do not form hydrogen bonds to neighbouring chains; these are instead held together by weaker intermolecular interactions.

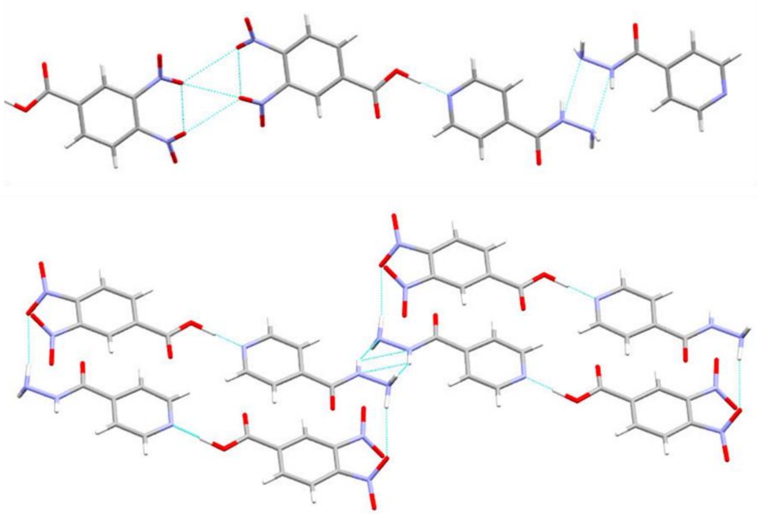

Figure 5.38. Hydrogen bonding and close interactions of IZN:3,4-DNBA co-crystal

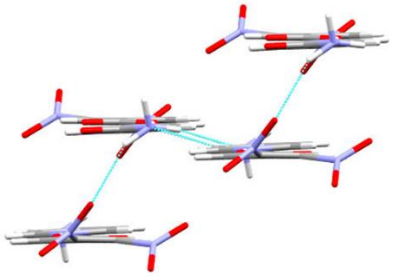

Figure 5.39. Offset of dimeric hydrogen bonding interactions

The 1D layers produced by the discrete hydrogen bonded chains in turn interact to form the 2D crystal. One hydrogen bond exists to link the stacked chains together (figure 5.38 and 5.39). This hydrogen bond occurs between the IZN NH_2 group and the NO_2 group in position four of the 3,4-DNBA molecule. The link influences the arrangement of the chains in comparison to one another. A slight shift occurs between each stacked chain meaning the ring interactions are not directly stacked and the molecules alternate when stacked. Due to the rings being planar to each other, the π-systems present a face-stacked geometry contributing to the intermolecular interactions holding the structure together.

Table 5.6. Hydrogen bond distances and angles for co-crystal IZN:3,4-DNBA [ix]

D-H··A	d(D-H) (Å)	d(H··A) (Å)	d(D··A) (Å)	>(DHA) (°)
O-H··N1[1]	1.10(4)	1.46(4)	2.561(3)	178(3)
N2-H··N3[4]	0.82(3)	2.20(3)	2.966(4)	155(3)
N3-H··O(Nitro-3)[3]	0.94(3)	2.27(3)	3.148(3)	155(2)

When visualising the structure using Mercury software, further interactions are suggested between the nitro groups on the 3,4-DNBA. The distances calculated are between 2.8 Å and 3.9 Å, but no hydrogens are present between these two functional groups; a different interaction may be occurring. In the literature, there is mention of interactions, similar to hydrogen bonds, existing between two nitro groups. A study conducted by Daszkiewicz[209] observed N··O interactions between nitro groups on adjacent molecules. However, these interactions were only detected for nitro groups arranged perpendicular to each other. The nitro groups within the present co-crystal structure are parallel, figure 5.38, suggesting this interaction is not present here. Further evidence to suggest this interaction is not present comes from the bond distances. In all structures noting the NO_2-NO_2 interaction, the intermolecular N···O distance is below 3 Å; here the N··O intermolecular distances between adjacent 3,4-DNBA molecules is much larger (table 5.7). The incorrect orientation of nitro groups and this long distance strongly suggests the interactions discussed by Daszkiewicz are not present between nitro groups within this crystal structure.

Table 5.7. Distances and angles for interactions between nitro groups

N··O	Nitro-group position	d(N··O) (Å)	>(NOO) (°)
Intermolecular N··O	Nitro 3 to 3	3.842(3)	114.6(2)
Intermolecular N··O	Nitro 3 to 4	3.652(3)	126.5(2)

PXRD analysis was used to collect data from the bulk and determine the phase purity of the product from this crystallisation. A comparison was made to the raw starting materials as well as the pattern calculated from the SCXRD data obtained (figure 5.40).

[ix] [1]+X,1+Y,+Z   [3]-X,-Y,1-Z   [4]-X,-Y,-Z

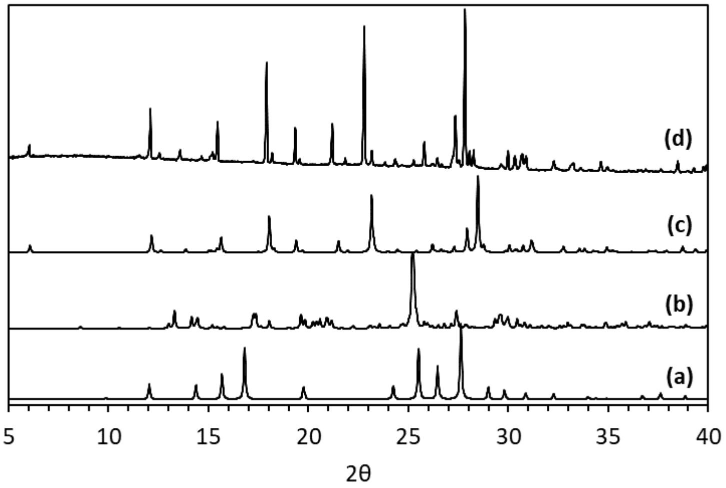

Figure 5.40. PXRD data for (a) IZN (INICAC02) (b) 3,4-DNBA (YADKOF), (c) IZN:3,4-DNBA calculated from SCXRD and (d) IZN:3,4-DNBA crystals from evaporative crystallisation in IPA

The calculated and experimental patterns for the co-crystal system match well; they are slightly offset from one another due to the calculated data being generated from structural parameters collected at 150 K and the experimental pattern being collected at 298 K. The lower temperature will be reflected in a smaller unit cell size and hence the PXRD data shift slightly in 2θ. There are no unassigned peaks in the experimental pattern corresponding to any starting material so phase purity can be considered quite high.

The thermal behaviour of the co-crystal was investigated using DSC analysis (figure 5.41). The DSC trace for the new co-crystal form has a sharp endothermic peak at 152 ^{o}C, a lower temperature than the melting points of IZN and 3,4-DNBA, confirming the formation of a new co-crystal. The lower presumed melting point suggests the co-crystal is less stable than the two starting materials.

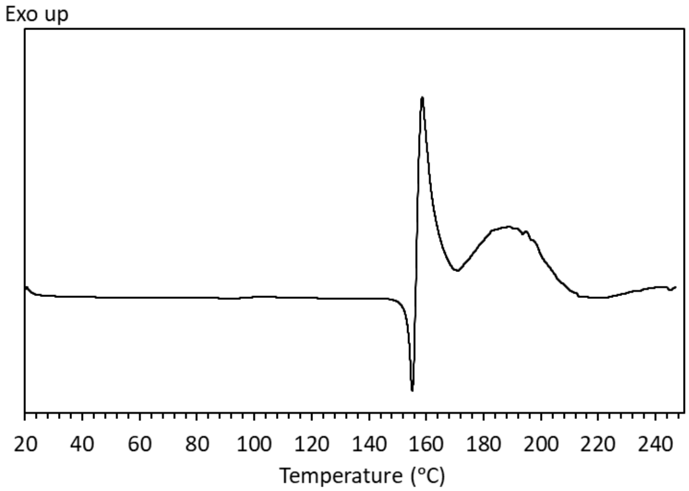

Figure 5.41. DSC trace for IZN:3,4-DNBA co-crystal. IZN melting point = 171-174 °C[163]*, 3,4-DNBA melting point = 165 °C*[210]

After the sharp endotherm the trace immediately shows a sharp exothermic peak. The close proximity of these two peaks in a crystalline sample suggests a recrystallisation after the initial melt. The exothermic peak could be the result of either a new form of the co-crystal recrystallising or, perhaps more likely, one of the starting components recrystallising. However, as no further melting is observed, the exothermic peak is less likely to correspond to a recrystallisation. HSM was carried out on the sample to characterise further the events observed in the DSC trace. Melting of the crystals was witnessed at 152 ^{o}C, corroborating the assignment of the endotherm in the DSC data. However, no recrystallisation was observed following the melt so is not the cause of the sharp exothermic peak. Another possible explanation for the exothermic peak is a liquid rearrangement. From experiments on the HSM it is known that the sample remains a liquid until its eventual decomposition, therefore the peak could be the result of the liquid rearranging to a slightly more ordered material without reaching full crystallinity. The broader peak following the sharp exotherm is indicative of an exothermic decomposition. This could be due to the hydrazine group decomposing within the IZN, reported as exothermic in the literature. This is not observed in the DSC trace of pure IZN, but it may be occurring at a lower temperature in this mixture as a result of reduced stability due to the presence of 3,4-DNBA.

The co-crystal system was also subjected to TGA analysis to understand further the potential exothermic decomposition.

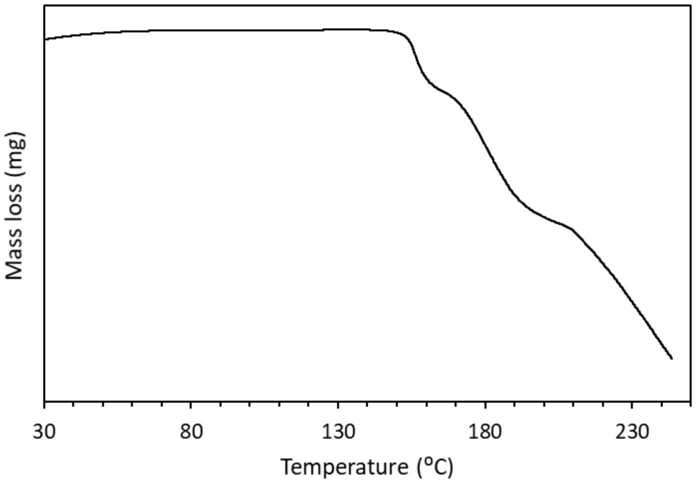

Figure 5.42. TGA trace for IZN:3,4-DNBA co-crystal

The TGA data (figure 5.42) shows a number of mass loss events, occurring above 152 °C, corresponding to the melting point of the co-crystal. Analysis of the masses lost can allow the nature of the decomposition to be studied. The first mass loss occurs at 156 °C, at a temperature close to the melting endotherm. This mass loss could also potentially be attributed to the initial exothermic peak, as the temperature range of the full loss overlaps with this peak. The first mass loss is 8.1% of the total mass and one possible explanation is that this could be the result of a loss of remaining crystallisation solvent from the bulk system. Although no solvent was incorporated into the crystal structure some may have remained in the sample, for example on the surface. However, the boiling point of IPA, 82 °C, is much lower than the temperature at which the mass loss occurs. Whilst the temperature could be higher if the solvent is being held in the crystal structure there is no evidence of this from crystallographic studies so can likely be discounted. A second mass loss 16% of the total mass is observed at 179 °C, the same temperature as the broad exothermic peak. This mass loss supports the rapid decomposition theory discussed above, but gives no further information as to which groups may be lost to cause the mass loss.

Further crystallisation methods were attempted to produce this co-crystalline form on different scales (appendix A36 and A37). Grinding mechanochemical methods in the absence of solvent did not successfully form the new co-crystal to an acceptable level of phase purity. The addition of a small amount of solvent, LAG, achieved better conversion with minimal evidence of the initial starting materials remaining. Slurry techniques were also attempted with good conversion from starting materials to co-crystal after stirring for 24 hours in IPA. Crash cooling also exhibited good results with the co-crystal produced at the same purity as achieved in evaporative crystallisation.

Scale up of this crystallisation was carried out using the Polar Bear Plus crystalliser. Using inserts for 20 mL and 250 mL vessels the crystallisation process was successfully scaled to 10 g and 200 g (solvent mass). The 30 g scale was not attempted for this co-crystal in light of the success at these two scales. Production of the co-crystal was also achieved through slurry crystallisations in IPA (appendix A38).

The solubility of the co-crystal was determined using observation techniques. The data show that the co-crystal is more soluble in IPA than pure IZN (figure 5.43). The relationship appears to be monotropic, within the temperature range sampled; it cannot be determined with certainty with the data provided. This increased solubility suggests the co-crystal is less stable than pure IZN in the temperature range examined. This increase in solubility and associated decrease in thermodynamic stability differs from that observed in the other multi-component materials discussed in this chapter. This co-crystal differs from those with TA derivatives in that there is no hydrogen transfer; this structure is a neutral co-crystal not a co-crystalline salt. The combination of intermolecular forces within this structure is different and the overall strength of interactions is likely lower, which may explain the reduction in stability for this co-crystal system. With respect to the instability of IZN in the FDC tablet, this co-crystal would thus not be a favoured candidate to provide an improvement. The reduced stability could be an appropriate compromise to achieve increased solubility; however, due to the use of a non-GRAS co-former in this structure, its potential in pharmaceutical applications are limited. Thus, the IZN:TA co-crystals would be favoured.

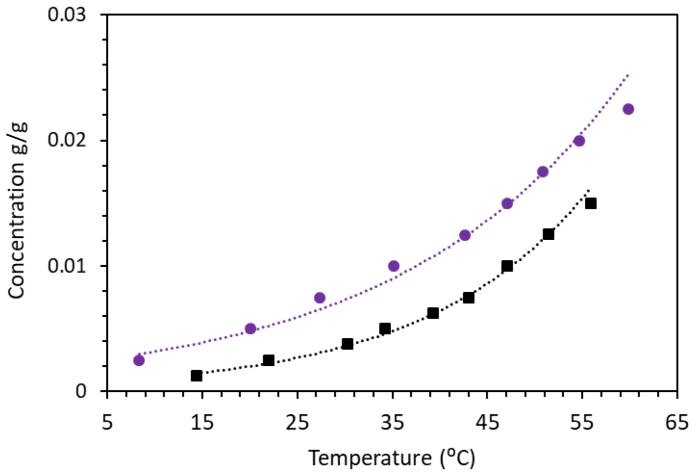

Figure 5.43. Solubility plot for IZN:3,4-DNBA co-crystal (purple circle marker) and pure IZN (black square marker) measured by observation in IPA

The stability of the co-crystal was tested by all three stability methods; exposure to high temperatures for prolonged periods, slurrying at a temperature of 40 ^{o}C and humidity studies; the outcomes were monitored by PXRD (figure 5.44). This co-crystal system remained stable at 50 ^{o}C for three weeks with no conversion into a second form or decomposition back to the starting materials. Slurrying experiments showed no changes in the PXRD data after a week. No significant amount of solvent became incorporated into the crystal structure and no significant decomposition occurred back to the starting materials. Finally, no significant decomposition or changes were observed in the PXRD data for the co-crystal when held in a 70% humidity chamber for 9 weeks.

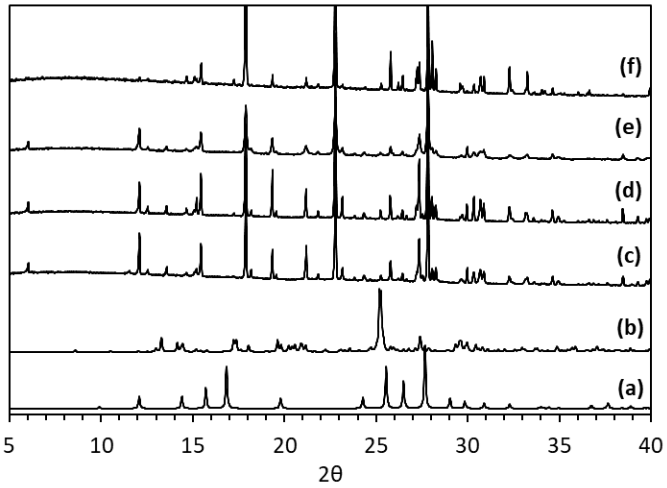

Figure 5.44. PXRD data for (a) IZN (INICAC02), (b) 3,4-DNBA (YADKOF), (c) IZN:3,4-DNBA calculated from SCXRD, (d) IZN:3,4-DNBA co-crystal slurry 1 week, (e) IZN:3,4-DNBA co-crystal 50 ^{o}C 3 weeks and (f) IZN:3,4-DNBA co-crystal 70% humidity 9 weeks

Crystallisation of the IZN:3,4-DNBA co-crystal from IPA yields a plate-shaped crystal (figure 5.45). The morphology observed for pure IZN in IPA is also plate-shaped crystals. A significant change in morphology has thus not been observed for this co-crystal under the given crystallisation conditions.

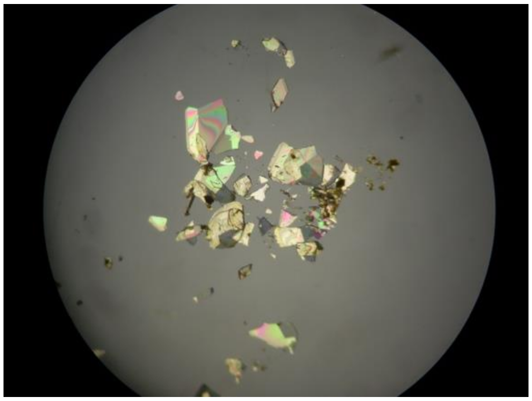

Figure 5.45. Plate-shaped IZN:3,4-DNBA co-crystals crystallised from IPA

The calculated BFDH morphology for the co-crystal structure is a fat, hexagonal plate, verging on a block shaped crystal (figure 5.46, left). The major growth occurs on the (100) and (-100) faces, the same direction as observed in most of the structures reported here. The major interaction contributing to the growth in this direction is, again, the π-π interactions between the aromatic rings in the two molecular components in the crystal. The hydrogen bonding interactions are likely responsible for the growth in the (00-1) and (001) directions associated with the calculated morphology.

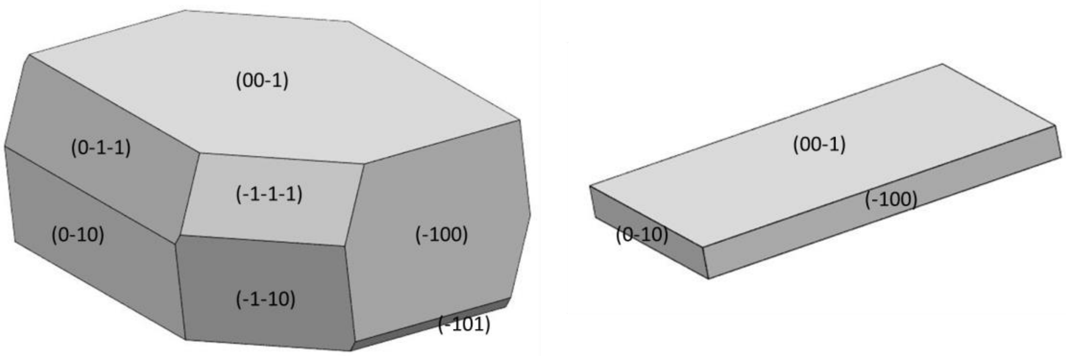

Figure 5.46. Predicted morphology for IZN:3,4-DNBA (left); observed morphology for IZN:3,4-DNBA (right)

The plates produced in the crystallisation are extremely thin and delicate, making face indexing a challenge; the result highlights the thin nature of the crystals when compared to the calculated morphology (figure 5.46, right). The major growth direction for the calculated morphology appears to be perpendicular to the (-100) and (100) faces. This differs from the observed morphology, which suggests the major growth is perpendicular to the (0-10) and (010) faces. The major contribution of the π-system interactions acts on the (-100) / (100) face set: whilst this is still responsible for some growth in the predicted structure it does not show the level of growth that has been seen in other IZN co-crystal structures discussed. The hydrogen bonding contribution is greatly diminished in the predicted structure, with very little growth seen on the (00-1) face. External factors within the crystallisation, such as solvent effects or impurities present, may be influencing the hydrogen bonding interactions and preventing their formation. An increase in the favourability of the hydrogen bonding interactions would tend to drive the predicted morphology and the calculated morphology towards looking more similar.

5.6 Conclusions

The work discussed in this chapter is focussed on the formation of new multi-component solid forms (co-crystals) of IZN and characterising their physical properties. The overall aim was to determine whether the morphology can be improved through the formation of new co-crystalline structures.

IZN was found to form three new structures with different enantiomeric combinations of tartaric acid. New multi-component crystal structures were found with L-TA, D-TA and DL-TA, with a hydrate of the latter also accessed. The solubility of each of the new crystal forms produced was less than that observed for pure IZN, a possible negative effect of the formation of the multi-component structures. However, IZN has a BCS (biopharmaceutics classification system) class of 1, due to its high solubility, suggesting a reduction in solubility would be acceptable for this API.[211] In addition, the potential improvements in other physical properties, such as solid form stability, compressibility and flowability, may outweigh the reduction in solubility. In depth stability analysis showed that each new form was stable for up to 9 weeks at 70% humidity. All forms were stable for at least 3 weeks at 50 ^{o}C except the hydrate, which had fully converted to the dehydrated form after 1 week. Slurry experiments in H_2O also proved the stability of the co-crystals for up to 1 week, with the exception of the dehydrated DLTA co-crystal which converted back to the hydrated version through dissolution: the dehydration is not a reversible process without this dissolution step.

IZN:TA co-crystals were all found to crystallise in a plate-shaped morphology. All crystallisations were carried out in H_2O, which gives needle-shaped crystals for pure IZN. The morphology change upon the addition of the co-formers into the crystal structure is significant. The needles are no longer formed due to the co-former allowing for more hydrogen bonding interactions to occur, diminishing the strength of the π-π-interactions between the aromatic rings. Whilst the morphology change is significant, the plate-shaped morphologies achieved are still undesirable for the downstream processing steps required for a pharmaceutical ingredient.

A further multi-component crystal for IZN was produced with 3,4-DNBA. The solubility of the new form in this case was found to have increased when compared to pure IZN, which is potentially favourable. However, this co-former is non-GRAS, meaning the application of this co-crystal to pharmaceutical production is highly unlikely compared to those with TA. Stability tests again show the new form is significantly stable under numerous conditions. The co-crystal remained stable for 9 weeks at 70% humidity, 3 weeks at 50 ^{o}C and 1 week when slurried.

The IZN:3,4-DNBA co-crystal was crystallised from IPA and gave a thin plate morphology. The crystals were extremely thin, verging on flakes. The morphology usually achieved through crystallising pure IZN from IPA is a plate-shaped morphology, therefore no improvement was observed upon the formation of this co-crystal structure. The very thin flakes would likely cause significant problems for downstream processing steps. Given the lack of positive morphology change and the use of the non-GRAS co-former this multi-component form would not be favoured as a potential solution to the IZN morphology problem.

Overall, the creation of multi-component materials of IZN has resulted in morphology changes of the crystals. This is especially clear when comparing the needles previously achieved from crystallisations in H_2O to the plates achieved when co-crystallised with the GRAS co-former TA. However, the plate-shaped morphology is not necessarily sufficient to have a significant improvement on the ease of downstream processing steps. Given the difficulty in obtaining FDA approval for the secondary component, this approach would be unlikely to be worthwhile in practice as the improvements in the morphology are not substantial enough. In all co-crystals, apart from the IZN:3,4-DNBA, the addition of the secondary component has also significantly reduced the solubility when compared to pure IZN, often extremely unfavourable in the pharmaceutical industry. More significant improvements in IZN morphology were reported in chapter 4, with the use of different solvents and additives. As a result, the formation of new multi-component materials would not be suggested as the best route to improving the morphology of IZN for pharmaceutical applications.

Chapter 6 Changing the morphology of pyridoxine

6.1 Introduction

Following the success of changing the morphology of IZN by variation of solvent, use of additives and the creation of multi-component materials, an equivalent set of experiments were attempted with a structurally similar molecule, pyridoxine (PYR). PYR (figure 6.1) has a similar structure to IZN, with the aromatic ring containing an N atom and a range of R groups. PYR also forms a needle crystal morphology, with the major growth attributed to the stacking of the aromatic rings within the structure.

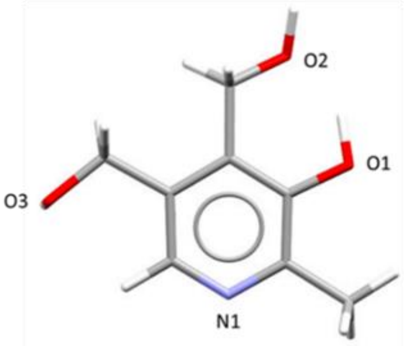

Figure 6.1. Labelled PYR molecule showing the functional groups present

The aim of the investigation on PYR was to achieve similar morphology modifications to those discussed for IZN in chapters 4 and 5.

6.2 Selection of co-formers and additives for pyridoxine

Additive selection was carried out using the molecular complementarity function in the Mercury program. Calculations were carried out with all five molecular descriptors enabled. Two different lists of molecules were screened for complementarity; a list of GRAS molecules and a list of common molecules found to make co-crystals. Using GRAS additives would be more favourable to the pharmaceutical industry, however, the knowledge gained from non-GRAS additives can be useful in helping to design an additive process with safe molecules.

Molecules that passed the molecular complementarity check were further examined for their possible interactions with PYR and their structural similarities. In PYR, the major growth is influenced by the interaction between the aromatic rings, causing the needle crystals most often observed. The rings stack on an angle along the crystallographic *b* axis and contributing to the growth on the fast growing faces (figure 1.32). Therefore, molecules containing an aromatic ring were favoured as potential additives. For such aromatic ring-containing additives it is predicted they will cap the fast growing faces, interrupting the major growth mechanism of the crystal, and allowing the slower growing faces to catch up, resulting in shorter, fatter, more block shaped crystals. Finally, the possibility that any of the additives passing the complementary calculations were already known to form co-crystals with PYR was considered. Those that formed co-crystals were favoured as they are already known to interact well with the PYR molecules. In the context of morphology control targeted here, the additive wt% used should be low enough to avoid co-crystal formation.

The final additive list chosen is shown in figure 6.2.

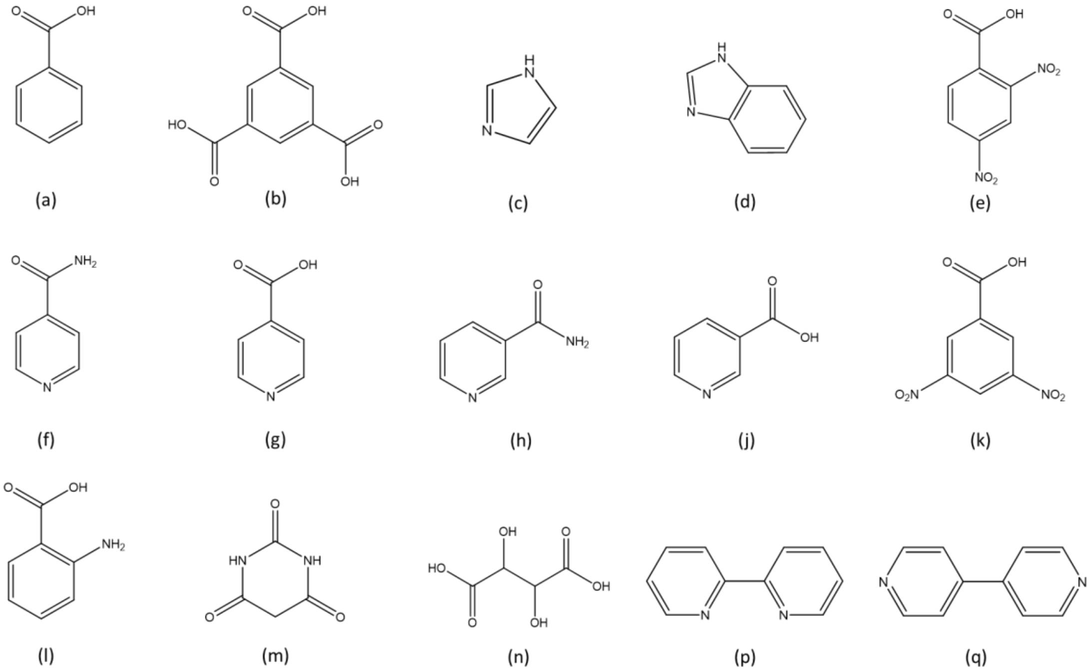

(a) (b) (c) (d) (e)

(f) (g) (h) (j) (k)

(l) (m) (n) (p) (q)

Figure 6.2. Additive list for screening with PYR (a) benzoic acid, (b) trimesic acid, (c) imidazole, (d) benzimidazole, (e) 2,4-dinitrobenzoic acid, (f) isonicotinamide, (g) isonicotinic acid, (h) nicotinic acid, (j) nicotinamide, (k) 3,5-dinitrobenzoic acid, (l) 2-aminobenzoic acid, (m) barbituric acid, (n) tartaric acid, (p) 2,2'-bipyridine and (q) 4,4'-bipyridine

Co-former choices for co-crystal formation followed the same molecular complementarity calculations as used to determine additive candidates, which are in fact more generally used in the design of new co-crystalline materials. Prior to the complementarity calculations, the molecular structure of PYR was examined to identify possible sites for hydrogen bonding and identify a potential list of co-formers to utilise.

PYR has two major functional groups, three alcohol groups and a pyridine ring. This gives rise to three hydrogen bond donor sites, the three OH groups, and four hydrogen bond acceptors, the N in the ring and the three O atoms. The OH group directly bonded to the aromatic ring donates a hydrogen bond to the neighbouring OH group. Investigating the multi-component materials already published in the CSD can give further information on the hydrogen bonding nature of the target molecule. Less research has been published on PYR than was the case for IZN; a search within the CSD provides only 18 hits. This consists of 15 different materials, which includes 12 different co-crystal structures and two halogenated salts. Of the reported co-crystals, all result from hydrogen transfer to the N in the aromatic ring forming co-crystalline salts. Of the 12 co-crystalline salts formed, seven form with carboxylic acid containing co-formers and two are formed with alcohol containing co-formers. There are only three reported co-crystals with co-formers that have neither a carboxylic acid group nor a hydroxyl group. Analysis of the carboxylic acid containing co-crystals indicated that the predominant hydrogen bonding interaction occurs between the co-former carboxylic acid and the N in the pyridine ring. The main hydrogen bonding interactions seen in PYR co-crystal structures containing carboxylic acids are shown in figure 6.3. All interactions observed are chain link hydrogen bonding, with only one published co-crystal showing the bifurcated hydrogen bonding interaction (ii).

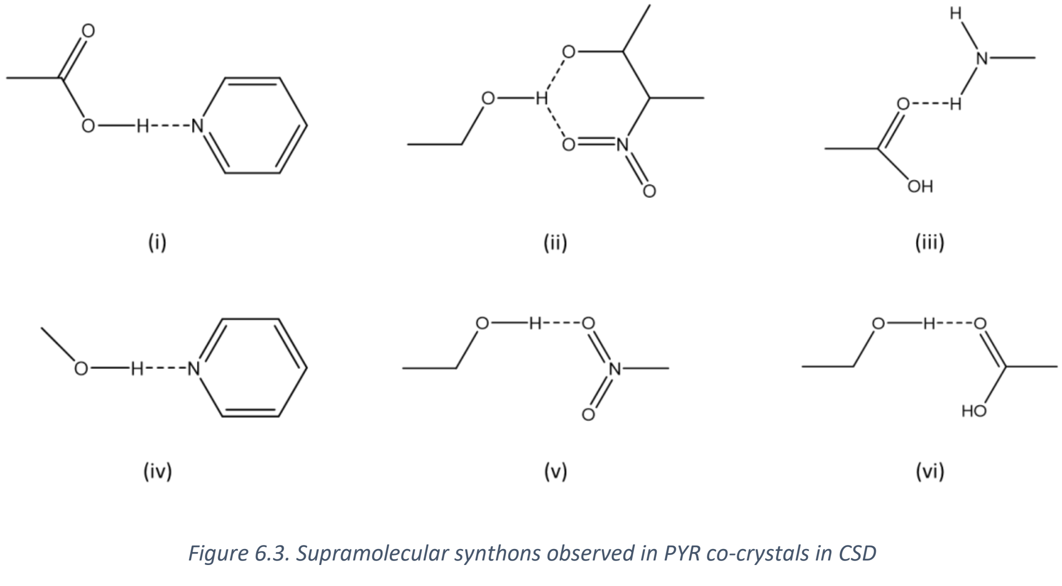

(i) (ii) (iii)

(iv) (v) (vi)

Figure 6.3. Supramolecular synthons observed in PYR co-crystals in CSD

From this analysis of published PYR co-crystal structures, an initial list of co-formers can be created. The common functional groups in published structures include alcohol, carboxylic acid and nitro groups; all of these were incorporated into the initial co-former list, shown in figure 6.4. Due to the similarities in the hydrogen bonding between PYR and IZN, the majority of the co-formers used were the same in both cases.

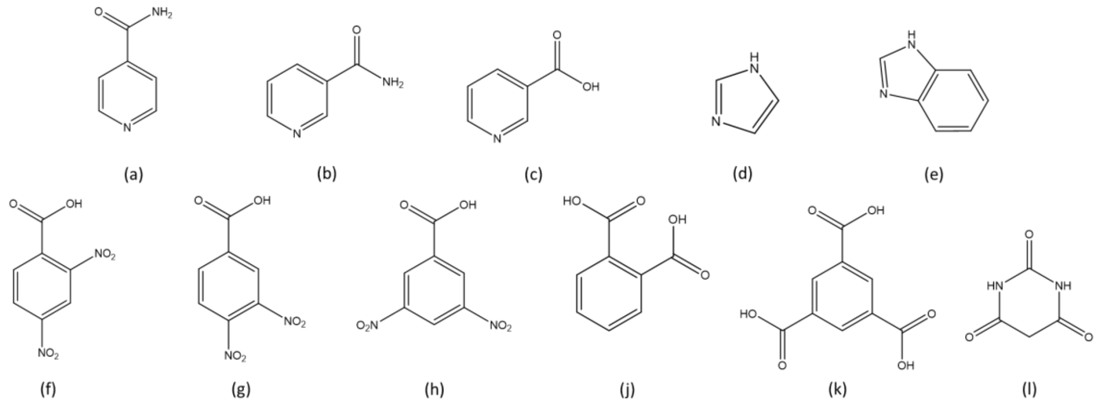

Figure 6.4. Co-formers used in multi-component crystallisation screening (a) isonicotinamide, (b) nicotinamide, (c) nicotinic acid, (d) imidazole, (e) benzimidazole, (f) 2,4-dinitrobenzoic acid, (g) 3,4-dinitrobenzoic acid, (h) 3,5-dinitrobenzoic acid, (j) phthalic acid, (k) trimesic acid and (l) barbituric acid

Polymer additives chosen for experiments with PYR are the same as those used for experiments with IZN (discussed in chapter 5; shown here in figure 6.5). The needle morphology of PYR predominantly resulting from aromatic interactions shows the potential for hydrophilic interaction along the long axis of the needle, with the potential for hydrophobic interactions on the capping faces. This suggests hydrophobic polymers could be utilised to cap the fast growing faces, preventing the major growth mechanism from occurring, allowing the crystals to become fatter and more equant in shape. A selection of hydrophobic and hydrophilic polymers was utilised to examine the effects of both on the morphology achieved.

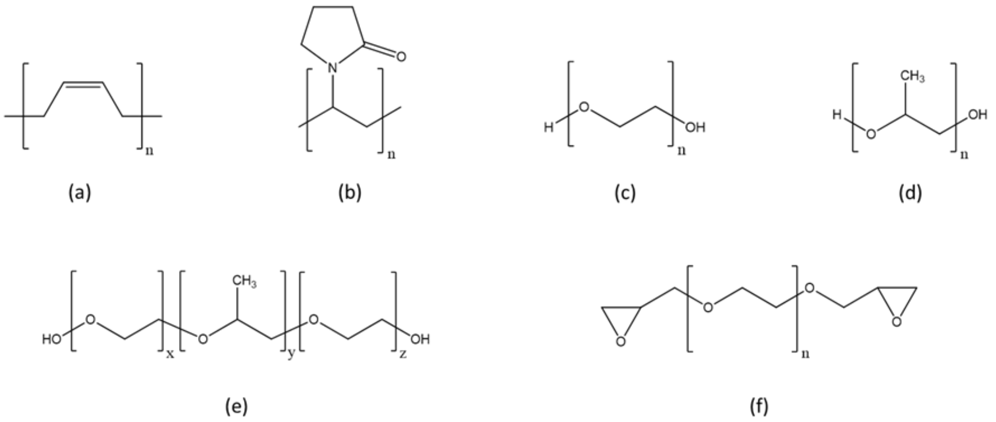

Figure 6.5. Polymer additives used (a) Polybutadiene, (b) polyvinylpyrrolidone, (c) poly(ethylene glycol), (d) poly(propylene glycol), (e) pluronic P123 and (f) poly(ethylene glycol) diglycidyl ether

The hydrophobic polymers employed are polybutadiene (PBD) and polypropylene glycol (PPG). The hydrophilic polymers are polyvinylpyrrolidone (PVP), polyethylene glycol (PEG) and poly(ethylene glycol) diglycidyl ether (PDE). The block co-polymer pluronic P123 (PP123) is amphiphilic and has both a hydrophilic and hydrophobic section.

6.3 Experimental information

All solvents and materials utilised in this research were obtained from commercial sources and used without any further purification being carried out.

6.3.1 Additive and solvent experiments with pyridoxine

6.3.1.1 Evaporative screening of pyridoxine with different solvents and additives

Initial evaporative experiments were carried out using pure PYR in H_2O, IPA and EtOH. 0.01 g of PYR was dissolved in a minimal amount of solvent in 7 mL vials. Holes were pierced in plastic lids and the vials left to evaporate at room temperature and 40 ^oC.

Evaporative crystallisations were also carried out with additives present. Small quantities of PYR (0.01 g) were dissolved in minimal solvent with the corresponding wt% of additive using a minimal amount of solvent. Holes were pierced in the plastic lids to allow slow evaporation. Evaporation was carried out at room temperature and an elevated temperature of 40 ^oC. These experiments were carried out in IPA only. IPA was chosen arbitrarily as no influence of solvent was identified on the morphology of PYR. The additives were tested in wt% of 1%, 5% and 10%.

Polymer additives were also investigated in evaporative crystallisation. 0.01 g of PYR with the corresponding wt% of additive were dissolved in 7 mL vials. The crystallisations were carried out in 3 g of IPA. Holes were pierced in the lids of the vials to allow for slow evaporation at both room temperature and an elevated temperature of 40 ^oC. Polymer additives were used in percentage mass ratios of 0.1% and 1%.

6.3.1.2 Cooling crystallisation of pyridoxine with different solvents and additives

Controlled cooling experiments were carried out for PYR in three different solvents: H_2O, EtOH and IPA. A mass of 8 g for each solvent was saturated at 40 ^oC with PYR. Crystallisations were carried out in 20 mL vials without magnetic bottom stirring to prevent breaking/grinding of the resulting crystals. Cooling rates of 1 ^oC/minute and 0.1 ^oC/minute were used with each solvent, with cooling occurring between 55 ^oC and 5 ^oC. Crystals were filtered at the end using a Buchner funnel and allowed to dry before analysis.

Cooling crystallisations were carried out with 1% wt ratio of additives. This percentage was chosen due to the success of this percentage in IZN crystallisations. Cooling experiments were carried out using cooling rates of 1 ^{0}C/minute and 0.1 ^{0}C/minute. 20 mL vials were used without any magnetic bottom stirring to prevent breaking/grinding of the resulting crystals. Crystals were filtered at the end using a Buchner funnel and allowed to dry before analysis.

6.4 Multi-component experiments with pyridoxine

6.4.1 Evaporative screening for pyridoxine co-crystals

All evaporative crystallisations were initially carried out in 1:1 stoichiometric ratios of API and co-former. 0.01 g of PYR and the corresponding mass of co-former were dissolved in minimal solvent in 7 mL glass vials. Solvents used were H_2O, EtOH and IPA. Vials were sealed with PTFE lids with holes pierced in, to allow slow evaporation, and left to evaporate at both room temperature and 40 ^{0}C. Experiments with trimesic acid (TRI) co-former were also repeated at 2:1 stoichiometry, in IPA, due to the formation of a new co-crystalline system of the same stoichiometric ratio.

6.4.2 Pyridoxine single crystal structures

Evaporative crystallisations of PYR in a 1:1 ratio with a number of co-formers resulted in the formation of new multi-component crystalline materials. Single crystal structures were determined for these new co-crystal materials. All structures were solved using ShelXS and refined using ShelXL within Olex2 software. Crystallographic data for all complexes are shown in table 6.1.

(1) Pyridoxine with 2,4-dinitrobenzoic acid (PYR:2,4-DNBA)

A 1:1 molar ratio of PYR (0.010 g) and 2,4-DNBA (0.012 g) were dissolved in IPA in a 7 mL glass vial. Evaporative crystallisation produced thick plate-shaped crystals. Single crystal data were collected using a Rigaku Oxford Diffraction Xcaliber diffractometer with Mo-Kα radiation (λ=0.70173 Å) at 150 K.

(2) Pyridoxine with 2,4-dinitrobenzoic acid (PYR:2,4-DNBA II)

A second polymorph of PYR:2,4-DNBA was formed via slurrying form I in H_2O. Single crystal data were collected using a Rigaku Oxford Diffraction Supernova diffractometer with Cu-Kα radiation (λ=1.5406 Å) at 150 K.

(3) Pyridoxine with 3,5-dinitrobenzoic acid (PYR:3,4-DNBA)

A second complex was produced with PYR (0.010 g) and 3,5-DNBA (0.012 g). Evaporative crystallisation in H_2O was carried out and produced block shaped co-crystals. Single crystal data were collected using a Rigaku Oxford Diffraction Xcaliber diffractometer with Mo-Kα radiation (λ=0.70173 Å) at 150 K.

(4) Pyridoxine with trimesic acid (2PYR:TRI)

The third novel co-crystal complex was formed from a 1:1 molar ratio of PYR (0.010 g) and TRI (0.012 g). However, the resulting crystal structure is a 2:1 co-crystalline salt. The crystal was produced via evaporative crystallisation from IPA and produced plate-shaped crystals. Single crystal data were collected using a Rigaku Oxford Diffraction Supernova diffractometer with Mo-Kα radiation (λ=0.70173 Å) at 150 K.

(5) Pyridoxine with phthalic acid (PYR:PtA)

The fourth novel co-crystal complex was formed from a 1:1 molar ratio of PYR (0.010 g) and TRI (0.0081 g). The structure shows a 1:1 stoichiometry and the plate-shaped single crystals were produced via evaporative crystallisation in EtOH. Single crystal data were collected using a Rigaku Oxford Diffraction Supernova diffractometer with Cu-Kα radiation (λ=1.5406 Å) at 150 K.

Table 6.1. Crystallographic parameters of newly discovered co-crystal structures formed with API PYR [x]

	1	2	3	4	5
Code	PYR:2,4-DNBA I	PYR:2,4-DNBA II	PYR:3,5-DNBA	PYR:TRI	PYR:PtA
Formula	$C_{15}H_{15}N_3O_9$	$C_{15}H_{15}N_3O_9$	$C_{15}H_{15}N_3O_9$	$C_{50}H_{56}N_4O_{24}$	$C_{16}H_{17}NO_7$
M / g mol^{-1}	381.30	381.30	381.30	1096.98	335.30
T (K), radiation	150.00(10), Mo Kα	150.00(10), Cu Kα	150.01(10), Mo Kα	150.00(10), Mo Kα	150.00(10), Cu Kα
Space group	C2/c	$P\bar{1}$	$P2_1/c$	$P\bar{1}$	$P2_1/n$
a (Å)	28.7601(13)	6.9759(3)	9.1930(19)	7.3526(4)	8.1175(2)
b (Å)	12.6869(6)	9.6261(4)	14.1287(7)	17.3839(10)	12.1753(3)
c (Å)	9.7150(4)	12.1988(4)	17.299(4)	20.0646(12)	15.0049(3)
α (°)	90	82.507(3)	90	107.653(5)	90
β (°)	111.029(5)	83.219(3)	135.54(4)	98.762(5)	90.353(2)
γ (°)	90	86.892(3)	90	97.736(5)	90
Volume (Å^3)	3308.7(3)	805.85(6)	1573.7(9)	2370.4(2)	1473.87(6)
Z	8	2	4	2	4
ρ_{cal}/ g cm^{-3}	1.531	1.571	1.609	1.537	1.511
μ/ mm^{-1}	0.129	1.145	0.136	0.124	1.018
2Θ range/°	7.104-56.556	7.356-142.724	6.954-56.636	5.444-60.69	9.378-142.39
Completeness	100%	100%	100%	100%	100%
Refln. Collected	7185	4962	6347	22015	5216
Independent refln.	3407	3051	3225	11992	2803
Rint	1.76%	1.24%	2.86%	3.02%	2.49%
GooF	1.029	0.968	1.044	1.031	1.041
R_1 (obs)	3.64%	3.41%	5.13%	5.93%	4.78%
R_1 (all)	5.07%	3.65%	8.28%	11.19%	5.36%
%wR_2 (all)	9.04%	9.70%	12.82%	15.94%	13.9%
$P_{max,min}$/e Å^{-3}	0.19/-0.23	0.23/-0.23	0.24/-0.27	0.44/-0.29	0.29/-0.37

---

[x] Molecular formula and molecular mass correspond to the asymmetric unit of the crystal structure

6.4.3 Further pyridoxine co-crystal preparation

6.4.3.1 Mechanochemical grinding of pyridoxine co-crystals

Grinding of PYR with successful co-crystallisation co-formers was carried out in a pestle and mortar. A small quantity of PYR (0.01 g) and the corresponding molar ratio of additive were ground together in both the absence of solvent and via liquid assisted grinding (LAG) for 30 minutes. Grinding was carried out on a 1:1 ratio for 2,4-DNBA, 3,5-DNBA and PtA, and a 2:1 ratio was used for TRI. Solvents used for each LAG experiment corresponded to those used in the successful evaporative crystallisations.

6.4.3.2 Pyridoxine co-crystal production via slurrying

PYR and co-former in chosen stoichiometric ratios (1:1 molar ratio for 2,4-DNBA, 3,5-DNBA and PtA; 2:1 molar ratio of TRI) were weighed into a 7 mL glass vial. The amount of solvent added is crucial, it must allow the amount of solid used to be in excess in the solution, but not be enough to fully dissolve the material added to the vial. The solutions were continuously stirred at room temperature, using a magnetic bottom stirrer at 250 rpm, for 2 hours.

6.4.3.3 Scale up of pyridoxine co-crystals using controlled cooling

A Polar Bear Plus crystalliser was used to scale up production of the co-crystals. Scale up to 10 g and 30 g of solvent was carried out for all new multi-component materials.

Each multi-component material was crystallised from a different solvent system: PYR:2,4-DNBA form I was crystallised from IPA; PYR:2,4-DNBA form II was crystallised in H_2O; PYR:3,5-DNBA was crystallised in H_2O; PYR:PtA was crystallised in EtOH; and PYR:TRI was crystallised in IPA. All solvents were saturated at $T_{sat} = 40\ ^{o}C$. For each different scale a different insert and vessel were used for the crystallisation: 20 mL glass vial with screw lid and 50 mL round bottom flask. The correct molar ratio of PYR and co-former were added to the vessel. In the glass vials magnetic bottom stirring at 700 rpm was used, whereas in the round bottom flasks overhead stirring at 350 rpm was used. All solutions were heated to 55 ^{o}C and held for 30 minutes to allow complete dissolution. Cooling was programmed at a rate of 1 ^{o}C/minute to a minimum of 5 ^{o}C and the system held for a further hour at that final temperature.

6.4.4 Solubility determination of pyridoxine co-crystals

Observational solubility techniques were used to determine the solubility of the co-crystals, using the Polar Bear Plus crystalliser. The heating profile used was set to heat from 5 ^{o}C to 60 ^{o}C at a rate of 0.3 ^{o}C/minute. Using a 20 mL glass vial, 3 g of solvent was stirred at 700 rpm using a magnetic bottom stirrer. An initial mass of co-crystal was added to the stirring solution and observed as it was slowly heated. When the co-crystal had fully dissolved the temperature was recorded and a second pre-determined mass added to the round bottom flask. This was repeated, recording the temperature and adding an additional amount of co-crystal every time full dissolution was observed. This method was repeated three times for each co-crystal system. The co-crystal solubility was determined in the solvent from which it was produced.

6.4.5 Analytical methods

Crystal images were taken using a Nikon Coolpix P5100 camera through a Brunel Microscopes microscope.

Crystal structure data were collected using CrysAlisPro software and calculations and refinements were carried out using Olex2.0. Mercury software was utilized to analyse the structures of the new multi-component crystals.

Face indexing was executed with CrysAlisPro software to determine the faces and overall shape of crystals produced. Crystal structure and morphology were visualized using the BFDH tool included in Mercury software.

Analysis was also carried out via PXRD and DSC techniques in the manner outlined in Chapter 3.

6.5 Solvent effects on pyridoxine morphology

Crystallisations were carried out in three main solvents; H_2O, EtOH and IPA. No form changes occurred in the solvents chosen (appendix A39) and no morphology changes were observed in either cooling crystallisation or evaporative crystallisation (figure 6.6 and 6.7, respectively).

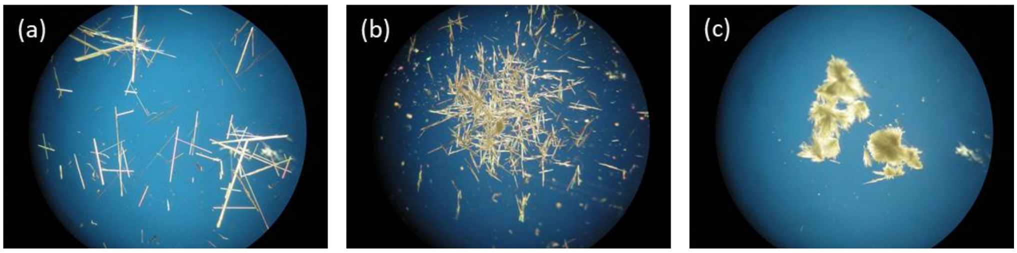

Figure 6.6. PYR morphology achieved in cooling crystallisations carried out in (a) H_2O, (b) EtOH and (c) IPA

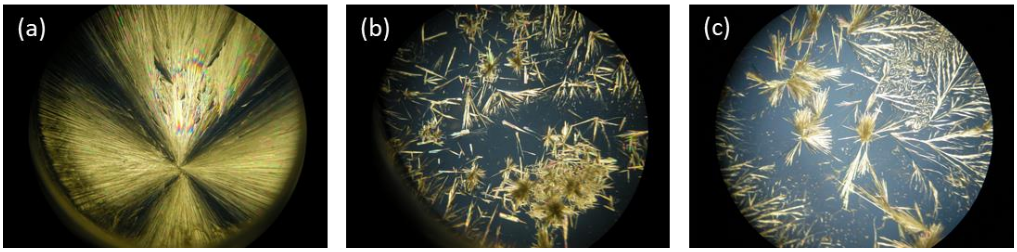

Figure 6.7. PYR morphology achieved in evaporative crystallisations carried out in (a) H2O, (b) EtOH and (c) IPA

All crystallisations yielded very thin needle crystals with significant clumping observed. PYR thus shows significantly less susceptibility than IZN to influence from different solvents.

6.6 Effect of additives on pyridoxine morphology

6.6.1 Effect of size-matched and structurally similar additives in evaporative and cooling crystallisation

A number of different additives were investigated in an attempt to change the morphology of PYR. The crystallisations were carried out in IPA. As no significant changes were observed in any particular solvent, IPA was chosen to remain in line with the experiments carried out with IZN.

Optical microscopy analysis of the final crystals produced showed that all crystallisations resulted in needle crystals, as seen in the absence of additives (appendix A40). No morphology modifications have been achieved with any of the additives attempted. As no modifications can be seen for neither solvent nor size-matched additives, it stands that this form of morphology modification is not a viable route for influencing the growth morphology of PYR crystals.

6.6.2 Effect of polymeric additives in evaporative and cooling crystallisation

The polymeric additive experiments were carried out in both evaporative and cooling crystallisations, with the additives in both a 1% and 0.1% ratio.

In cooling, neither percentage of additive resulted in a morphology change. Experiments carried out at 1 ^{o}C/minute resulted in no crystallisation. The faster cooling rate does not give the system enough time to grow to an appropriate size before the end of the experiment. As the result, there are no images for these crystallisations. However, cooling at the slower rate of 0.1 ^{o}C/minute allows the crystals to grow sufficiently to allow the morphology to be observed (figure 6.8 and appendix A41). Again, no morphology modification is observed and only needle-shaped crystals are achieved.

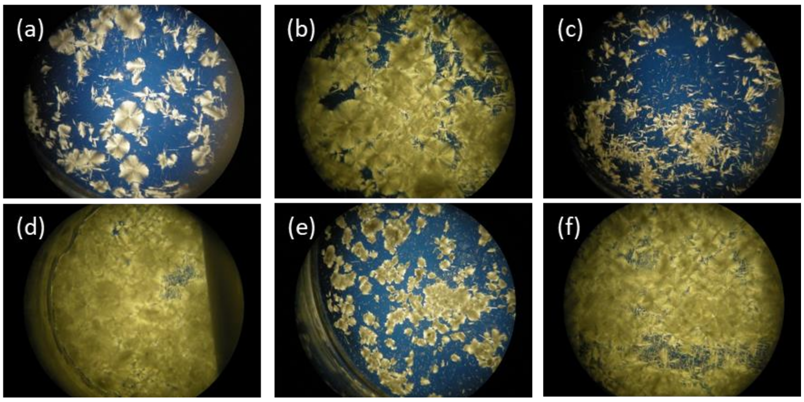

Figure 6.8. Cooling crystallisations of PYR with 0.1% polymer additives in IPA at rate of 0.1 ^oC/minute. (a) PP123, (b) PEG, (c) PPG, (d) PBD, (e) PVP and (f) PDE

Evaporative experiments also showed no changes in the morphology in the presence of the polymeric additives, neither at a 1% ratio nor a 0.1% ratio (figure 6.9 and 6.10 respectively). Only needle-shaped crystals were observed when evaporated at both 20 ^oC (appendix A42 and A43) and 40 ^oC.

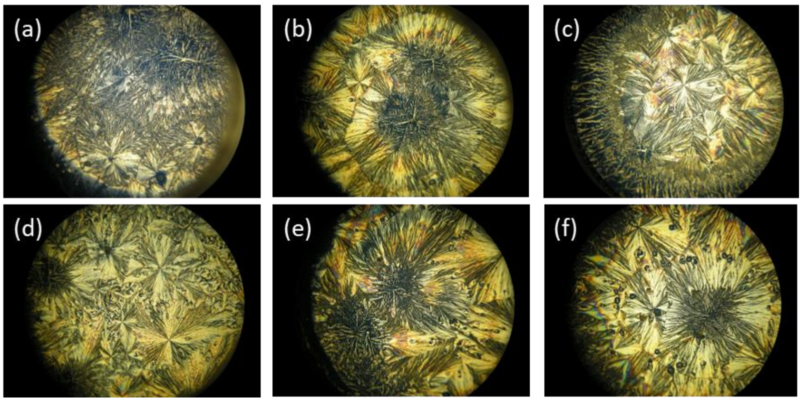

Figure 6.9. 40 ^oC evaporative crystallisations of PYR with 1% polymer additives in IPA. (a) PP123, (b) PEG, (c) PPG, (d) PBD, (e) PVP and (f) PDE

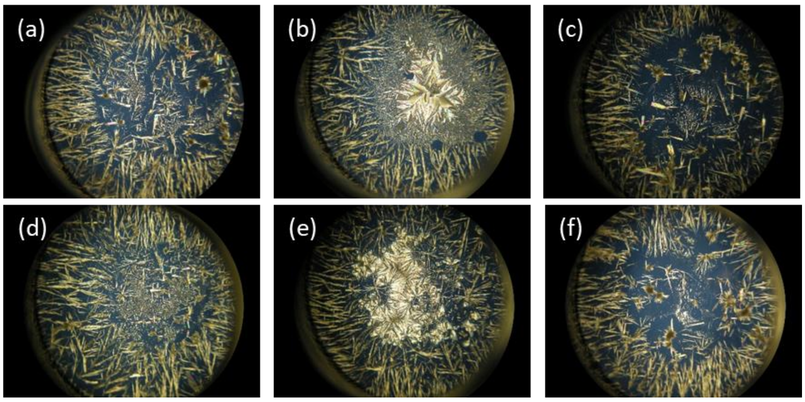

Figure 6.10. 40 ^oC evaporative crystallisations of PYR with 0.1% polymer additives in IPA. (a) PP123, (b) PEG, (c) PPG, (d) PBD, (e) PVP and (f) PDE

None of the polymers attempted so far appear to have any effect on the morphology of the PYR crystals produced. This suggests their use for morphology modification is not worth pursuing for PYR crystallisations. However, further investigations could be carried out with other polymers to rule the approach out entirely. In addition, other methods of crystallisation could be attempted, including temperature cycling, if this route of modification were to be investigated further.

6.7 Multi-component crystallisations with pyridoxine

6.7.1 Crystallisation of pyridoxine with 2,4-dinitrobenzoic acid

A successful co-crystallisation was achieved from a 1:1 ratio of PYR and 2,4-DNBA (figure 6.11) in IPA.

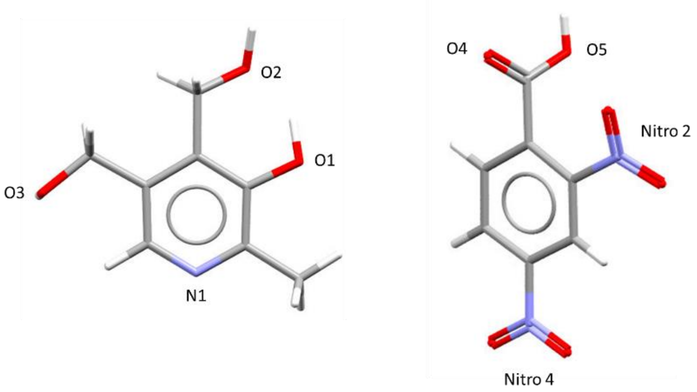

Figure 6.11. Structure of PYR and 2,4-DNBA showing the numbering system used in hydrogen bonding discussions

The new form crystallises in the monoclinic C2/c space group (figure 6.12). The asymmetric unit contains one PYR and one 2,4-DNBA molecule. Proton transfer occurs between the two molecules, resulting in a deprotonated carboxylic acid group on the 2,4-DNBA and a protonated N in the ring of the PYR molecule.

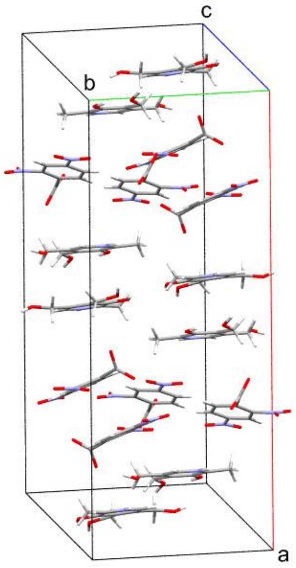

Figure 6.12. Unit cell of co-crystal PYR:2,4-DNBA

The PYR molecules stack on a diagonal with a slight overlap of the aromatic rings in their structure (figure 6.13, left). The 2,4-DNBA molecules also stack on a diagonal with again an overlap of their aromatic rings, forming the layers within the structure. Two asymmetric units, each consisting of one PYR and one 2,4-DNBA molecule, on two different layers are hydrogen bonded together to form a ring structure (figure 6.13, right). Each ring is then hydrogen bonded to the next via a chain link to the next asymmetric unit on the same level.

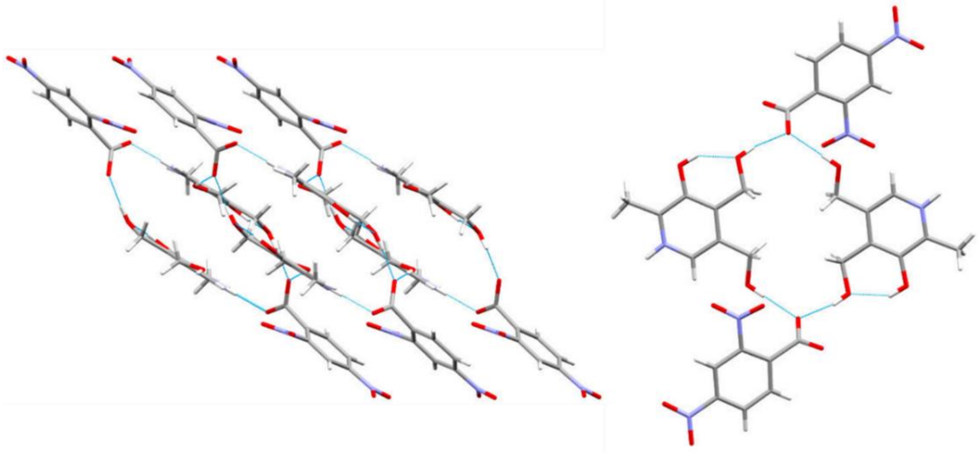

Figure 6.13. Hydrogen bonding interactions present in PYR:2,4-DNBA co-crystal showing the nature of the stacking

The hydrogen bonding network within the structure is reasonably simple, with only four different interactions occurring (table 6.2). Bifurcated hydrogen bonds allow the ring structure to form within the structure. Each 2,4-DNBA carboxylic acid group accepts a hydrogen bond from two different PYR molecules, O3-H··O4 from one PYR molecule and O2-H··O4 from a second molecule. These hydrogen bonds are then repeated with a second 2,4-DNBA molecule, ultimately creating a four membered ring (shown in figure 6.13). The ring exists on two different layers, with the PYR molecules in one and the 2,4-DNBA molecules being above and below. Chain link hydrogen bonds connect the rings together between the N in the PYR ring and the 2,4-DNBA carboxylic hydroxyl. Proton transfer occurs in this interaction, resulting in a protonated PYR molecule and a 2,4-DNBA molecule with a deprotonated carboxylic acid group. This proton transfer can be confirmed by analysis of the hydrogen bonding distances: N^+··H has a distance of 0.97(2) Å and the O··H has a distance of 1.74(2) Å, confirming salt formation. These chain link hydrogen bonds are in the same plane as the PYR molecules, in comparison to the ring hydrogen bonds which are perpendicular to the plane of the PYR molecules. This is possible due to the geometry of the carboxylic acid groups in the 2,4-DNBA with respect to the hydroxyl groups in the PYR molecule. The O2 hydroxyl group in the PYR molecule has a fixed geometry due to an intramolecular hydrogen bonding interaction. This interaction exists between O1-H··O2, ensuring the geometry of the PYR molecule remains planar.

Table 6.2. Hydrogen bond distances and angles for PYR:2,4-DNBA co-crystal [xi]

D-H··A	**d(D-H) (Å)**	**d(H··A) (Å)**	**d(D··A) (Å)**	**>(DHA) (°)**
O2-H··O4[2]	0.89(2)	1.76(2)	2.646(2)	170(2)
O3-H··O4	0.85(2)	1.87(2)	2.714(2)	175(2)
O1-H··O2	0.89(2)	1.69(2)	2.520(2)	155(2)
N1-H··O5[1]	0.97(2)	1.74(2)	2.715(1)	175(2)

Characterisation of the bulk product was carried out using PXRD and DSC techniques.

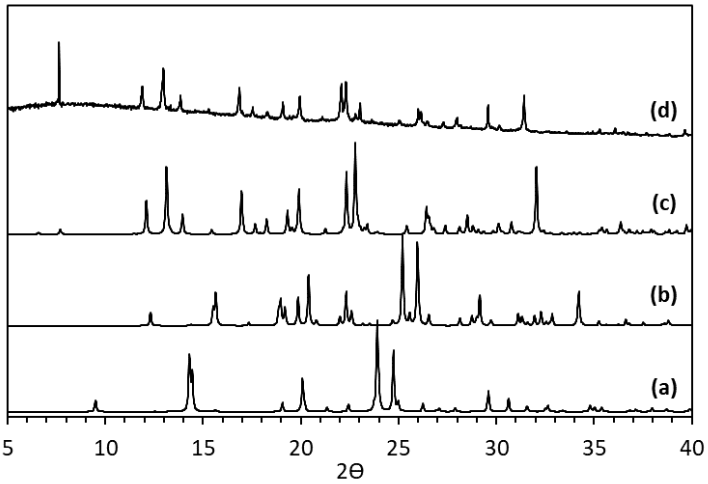

Figure 6.14. PXRD data for (a) PYR (BITZAF), (b) 2,4-DNBA (BAQLUD), (c) PYR:2,4-DNBA co-crystal calculated from SCXRD data and (d) PYR:2,4-DNBA co-crystal from evaporative crystallisation in IPA

[xi] [1]+X,1-Y,1/2+Z [2]-X,1-Y,1-Z

The new co-crystal system is confirmed by the PXRD pattern for the sample (figure 6.14). The experimental PXRD pattern (d) is significantly different to that of the two starting materials. The experimental pattern also matches the calculated pattern for the co-crystal structure. Some subtle differences can be seen between the two patterns as a result of the temperatures the experiments were carried out at. PXRD experiments were carried out a room temperature, whilst SCXRD was carried out at 150 K. The crystal structure is slightly contracted at the lower temperatures resulting in a slight expansion of the 2Θ values in the calculated pattern. There are no obvious unassigned peaks in the experimental pattern corresponding to any starting material. Phase purity can be considered relatively high in this crystallisation.

Thermal analysis by DSC, also confirms the formation of a new co-crystalline structure (figure 6.15).

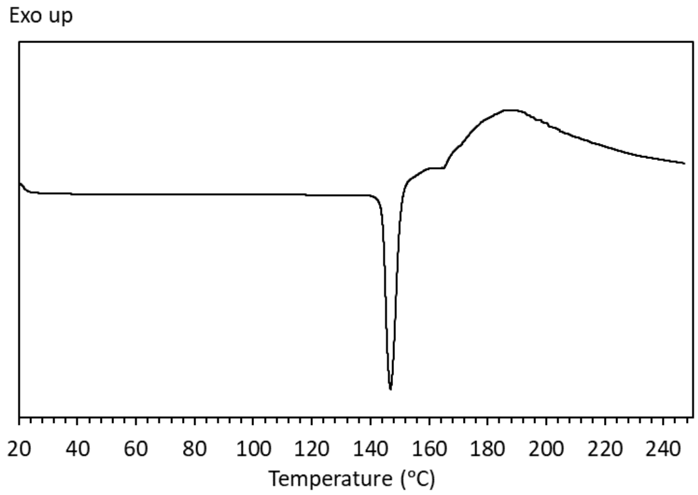

Figure 6.15. DSC trace of co-crystal PYR:2,4-DNBA. PYR melting point = 159-162 °C [166], 2,4-DNBA melting point = 182 °C [210]

DSC analysis produces an endothermic peak at about 140 ^{o}C, yielding the melting point of the new co-crystal structure. This is at a different temperature to the melting points of the two starting materials, confirming the formation of the new structure. The high phase purity is also confirmed due to the absence of any peaks relating to the starting materials, suggesting conversion to the co-crystal was complete, and the sharpness of the melting peak. A small, broad exothermic peak occurs after the initial melt. This broad exotherm is similar to that observed in the DSC of the IZN:3,4-DNBA complex reported in chapter 5. It was hypothesized the endotherm was as a result of a decomposition of the nitro groups in the co-former. The similarity here could help confirm this hypothesis. Due to the broad nature of the peak it is unlikely this peak is the result of a recrystallisation. The nature of the exothermic peak could be confirmed using HSM.

Mechanochemical grinding experiments carried out appear to show some successful formation of the co-crystal in DSC and PXRD analysis (appendix A44 and A45). The grinding experiment in the absence of solvent shows peaks corresponding to both the starting materials and the new co-crystal form. The LAG experiments using IPA show better conversion of starting materials to the co-crystal. The peaks corresponding to the starting materials reduce in intensity and the co-crystal peaks have increased in intensity. Full conversion has not been achieved in either case, although the presence of some conversion could suggest grinding for increased periods of time could result in full conversion. Attempts to make the co-crystal via slurry experiments in IPA were successful, with full conversion of starting materials to new co-crystal form. In addition, controlled cooling crystallisation was achieved on 10 g and 30 g solvent scales (appendix A46).

The solubility of the co-crystal was determined via observation methods (figure 6.16). The co-crystal and the pure PYR have a monotropic relationship in IPA with the co-crystal solubility being significantly lower than that of pure PYR in IPA, suggesting the co-crystal is highly stable. This stability is further confirmed by the difficulties arising when attempting to form the co-crystal via cooling crystallisation. Initial attempts were unsuccessful as the starting materials converted to the co-crystal too quickly to allow for complete dissolution. The increased hydrogen bonding interactions are likely responsible for the increased stability. The ease of formation of the co-crystal suggests the hydrogen bonds within the co-crystal are highly favoured in comparison to those found in the pure PYR crystal structure; the strength of the hydrogen bonding interactions is expected to have increased from the pure PYR structure to the co-crystalline structure. A decrease in solubility is not often favoured in the pharmaceutical industry, due to the probable reduction this causes in the bioavailability of the drug. However, reduction in solubility is potentially advantageous in pharmaceuticals that require slow release, if it is linked to dissolution rate. Fast dissolution can result in dosages needing to be taken in quick succession, meaning lower solubility could be a benefit to highly water-soluble pharmaceutical, such as PYR.

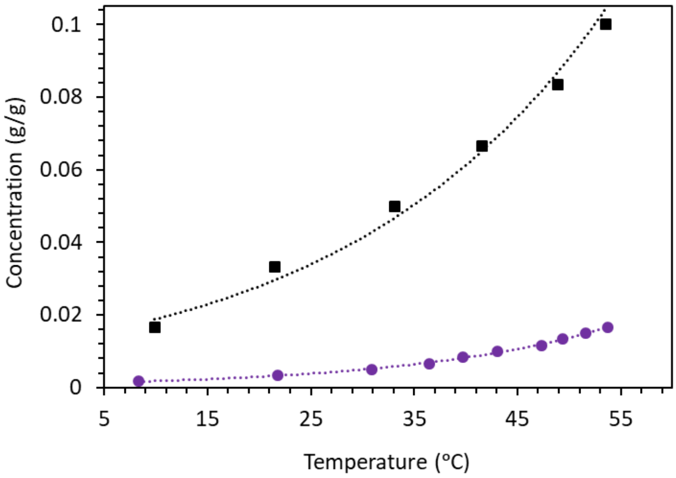

Figure 6.16. Solubility plot for PYR:2,4-DNBA co-crystal (purple, circle marker) and pure PYR (black, square marker) from observation in IPA

In order to determine the stability of the new co-crystalline form, three different experiments were carried out (figure 6.17). Samples were stored at an elevated temperature of 50 °C and in a 70% humidity chamber for extended periods of time and also slurried continuously in H_2O at 40 °C.

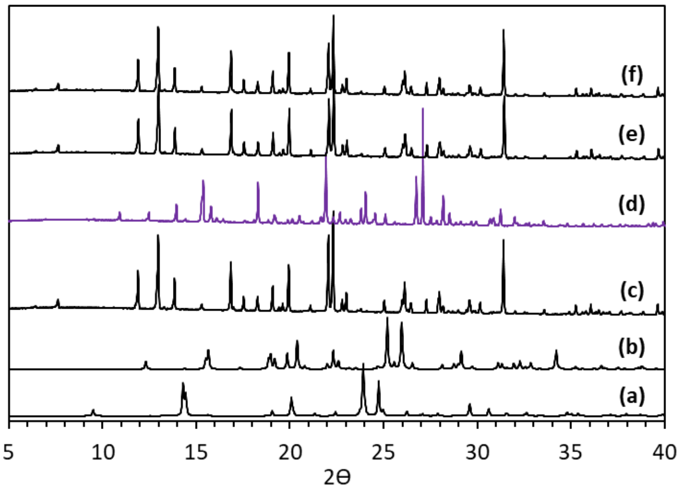

Figure 6.17. PXRD data for (a) PYR (BITZAF), (b) 2,4-DNBA (BAQLUD), (c) PYR:2,4-DNBA form I calculated from SCXRD, (d) PYR:2,4-DNBA form I slurry 1 week, (e) PYR:2,4-DNBA form I 50dc 3 weeks and (f) PYR:2,4-DNBA form I humidity 9 weeks

No changes in the PXRD pattern were observed for the samples subjected to elevated temperature or humidity. This form of the co-crystal is stable up to three weeks under both these conditions. However, a change in the sample taken from the slurry in H_2O after 6 hours shows a change in the PXRD pattern to a potential new form. This pattern was maintained up to the week limit of the slurry. The new PXRD pattern does not match the peaks seen in the starting material patterns shown below, ruling out a break-down of the co-crystal form to its single molecule counterparts. The product is therefore likely to be a new form of the PYR:2,4-DNBA co-crystal. This new crystal could be a number of potential forms: a hydrate, formed from the continuous slurrying in H_2O, a new polymorph of the original co-crystal or a co-crystal consisting of a different stoichiometry. To determine the nature of the new co-crystalline form DSC analysis and SCXRD experiments were carried out (discussed in section 6.7.2.)

The PYR-2,4-DNBA co-crystal from IPA shows a significant change in morphology from the needles previously seen in PYR crystallisations (figure 6.18). These are fattened, with a much improved aspect ratio when compared to a needle. However, it is difficult to describe the shape of the crystals as they all have significant irregularities.

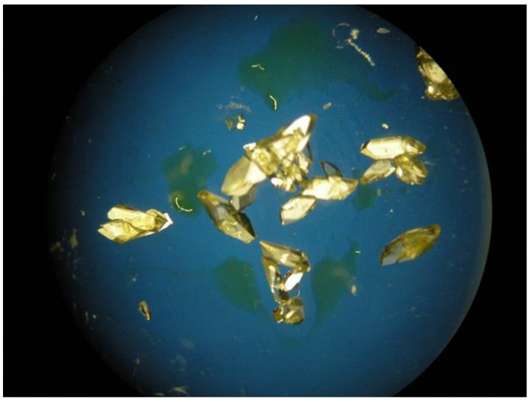

Figure 6.18. Thickened crystals of PYR:2,4-DNBA form I co-crystal crystallised from IPA

Face indexing the crystals also posed significant difficulties due to the size of the crystals produced. Most crystals were too big to be able to face index properly. This resulted in smaller, likely broken crystals having to be face indexed to determine which faces are present in the new co-crystal system.

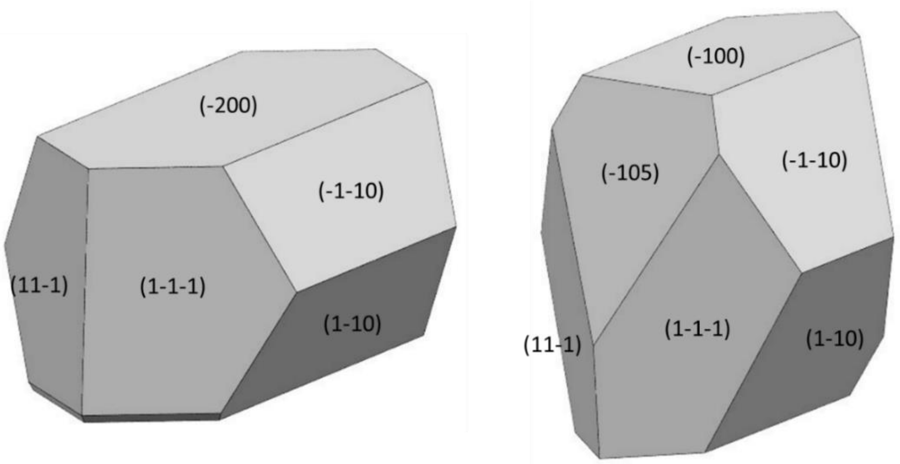

Figure 6.19. Predicted BFDH morphology for PYR:2,4DNBA form I (left); observed morphology for PYR:2,4-DNBA form I (right)

The BFDH predicted morphology is similar in shape to that of a number of crystals observed in figure 6.17. The predicted shape is also very similar to that achieved from face indexing crystals from the sample (figure 6.19). The experimental morphology has an extra plane of faces, (-105) and (10-5), which could be the result of breakages in the crystals. The hydrogen bonding interactions contribute to the growth on both the (-105) / (10-5) set and the (-100) / (100) set. The (-100) and (100) faces are parallel to the crystallographic *c* axis and this direction is where the most significant growth occurs. As well as the hydrogen bonding interactions present on the surface of this face there is some influence from the interactions between aromatic rings within the structure. The overlap between the π systems is limited, due to the offset of the positions of the aromatic rings, but, there is likely still to be some influence from these interactions allowing the faster growth on the (-100) and (100) faces.

The morphology of the co-crystals produced here is a substantial improvement on the needle crystals previously produced for pure IZN, suggesting that co-crystallisation could be a viable solution for improving the morphology of PYR.

6.7.2 Determining the structure of the second polymorph of the PYR:2,4-DNBA co-crystal

Due to the change in the PXRD pattern after slurrying the PYR:2,4-DNBA co-crystal in H_2O for 24 hours, a SCXRD experiment was carried out to determine the nature of the possible new form produced.

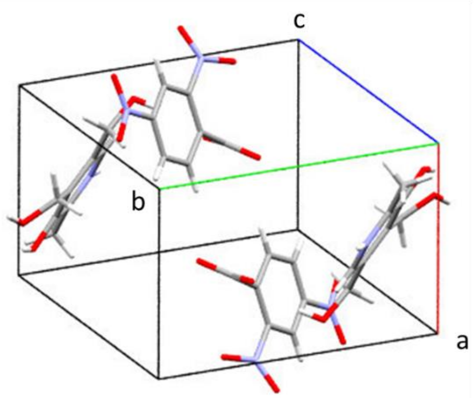

Figure 6.20. Unit cell of PYR:2,4-DNBA form II co-crystal

The second form crystallises in the triclinic $P\bar{1}$ space group, with an asymmetric unit containing one PYR and one 2,4-DNBA molecule (figure 6.20).

The PYR molecules are all in plane with each other, with the 2,4-DNBA molecules at an, approximately, 45° angle to those (figure 6.21). This differs from the original polymorph observed, in which the PYR and 2,4-DNBA molecules remain in the same plane. The aromatic ring centers of the PYR molecules overlap in an alternating step pattern due to the inversion center present in the structure. The two asymmetric units are hydrogen bonded together to form a 4 membered ring system, with the center of inversion in the middle. The same ring type hydrogen bonding structure is seen in the original polymorph, with slightly different bonding distances and angles between the molecules. These ring systems are then hydrogen bonded to each other via donation from a PYR molecule in one ring system to a 2,4-DNBA molecule in the neighbouring system.

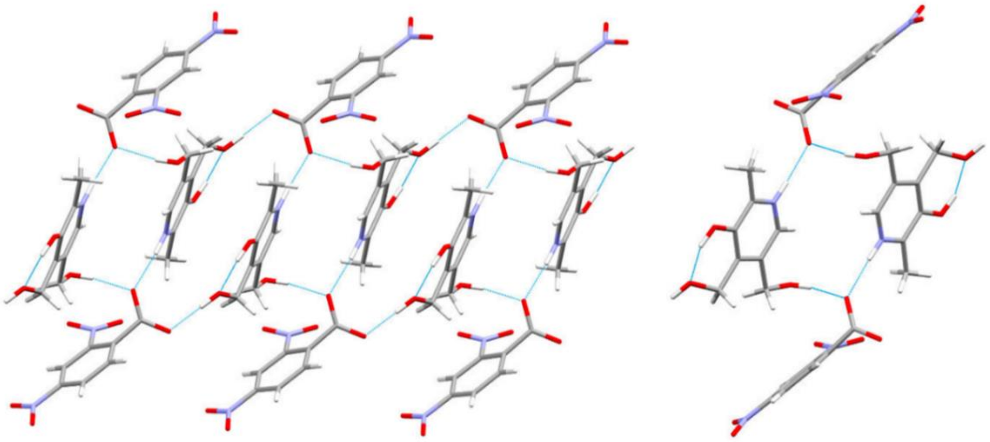

Figure 6.21. Hydrogen bonding interactions present in PYR:2,4-DNBA form II co-crystal showing the ring interactions formed between the API and co-former and the chain links between the rings.

The hydrogen bonding network within this new polymorphic structure remains simple, with only four different interactions occurring within the structure (figure 6.21; table 6.3). The hydrogen bonding closely mimics that observed in polymorph I, with some subtle differences as the result of the change in the orientation of the PYR molecules (numbering system used is the same as shown in figure 6.11). A bifurcated hydrogen interaction is present with O5 at the center, allowing the ring system to form. The 2,4-DNBA carboxylic acid group donates a hydrogen to the N in the PYR ring, O5··H-N, and simultaneously accepts a hydrogen bond donated from O3 in a second PYR molecule, O3-H··O5. This differs from that observed in form I, where the carbonyl group (O4) accepts a hydrogen bond donation from an OH group on two different PYR molecules. In form I the N within the PYR ring is not involved in the bifurcated hydrogen bond or the formation of the 4-membered hydrogen bonded ring system. The molecules present in the ring systems formed in form II do not lie within the same plane, as is seen in form I; the 2,4-DNBA molecules are twisted by approximately 45°. The hydrogen bond connecting the rings together forms between the remaining alcohol group on the PYR molecules and the carbonyl group on a 2,4-DNBA molecule in the neighbouring ring formation, O2-H··O4. This interaction in form I involves the donation of the H from the carboxylic acid group within the 2,4-DNBA molecule to the N in the PYR ring. The final hydrogen bonding interaction observed within the structure is the intramolecular hydrogen bond within the PYR molecule, O1-H··O2.

Table 6.3. Table of distances and angles for PYR:2,4-DNBA form II co-crystal [xii]

D-H··A	d(D-H) (Å)	d(H··A) (Å)	d(D··A) (Å)	>(DHA) (°)
N1-H··O5[1]	0.93(2)	1.84(2)	2.753(1)	163(2)
O3-H··O5[2]	0.88(2)	1.83(2)	2.706(1)	163(2)
O1-H··O2	0.91(2)	1.74(2)	2.549(1)	148(2)
O2-H··O4	0.91(2)	1.72(2)	2.630(1)	179(2)

The structure of form II sees the same hydrogen transfer as observed in form I, with differing hydrogen bonding distances. In form II the N··H distance is 0.93(2) Å and the O··H distance is 1.86(2) Å, confirming the formation of the salt and transfer of the hydrogen. In form I, the distances are N··H, 0.97(2) Å and O··H, 1.74(2) Å. The slightly decreased N··H distance and slightly increases O··H distance in form II suggests the H is held more strongly by the N in this structure. This could potentially be the result of the H transfer taking part in the bifurcated hydrogen bonding interaction within the ring in form II but not in form I.

A comparison of the calculated PXRD pattern for the above crystal structure and that of the bulk formed in the stability slurry test was made to ensure the single crystal picked out of the sample was representative of the bulk product (figure 6.22).

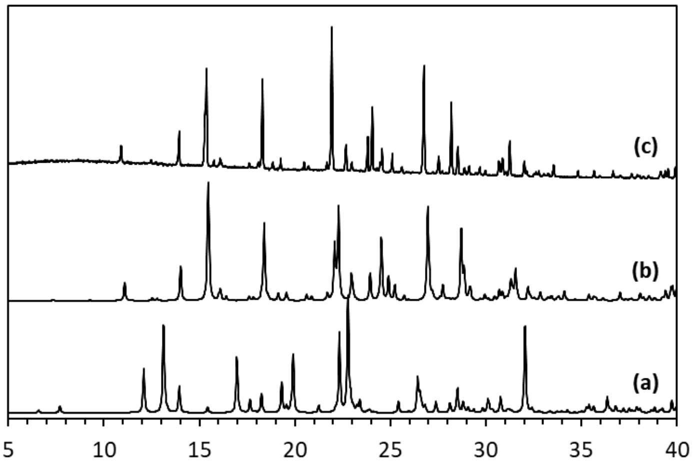

Figure 6.22. PXRD data for (a) PYR:2,4-DNBA form I calculated from SCXRD, (b) PYR:2,4-DNBA form II calculated from SCXRD and (c) PYR:2,4-DNBA form II co-crystal from slurry of PYR:2,4-DNBA form I in H_2O

Comparison of the PXRD patterns confirms the bulk product from slurrying matches that predicted from the SCXRD data for the crystal selected. This confirms that slurrying PYR:2,4-

---

[xii] [1] 1-X,2-Y,-Z [2] +X,1+Y,+Z

DNBA form I in H_2O at 40 °C for 6 hours facilitates the conversion to PYR:2,4-DNBA form II. This suggests the second form found is the more thermodynamically stable form.

DSC analysis was carried out in an attempt to confirm the more thermodynamically stable of the two polymorphs and determine the melting point of the newly discovered form II (figure 6.23).

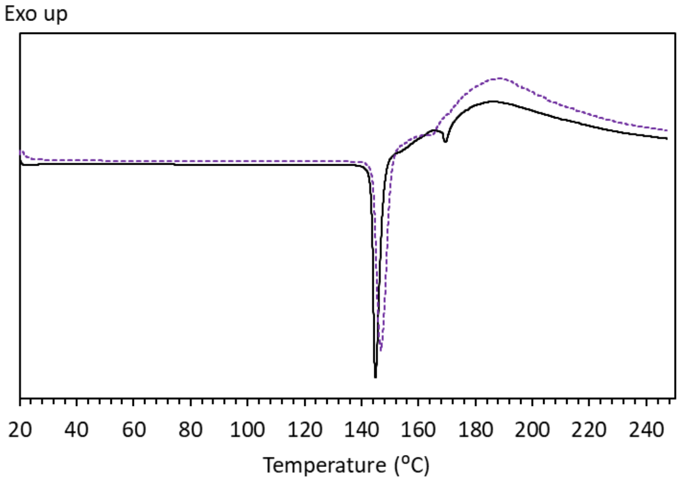

Figure 6.23. DSC trace of co-crystal PYR:2,4-DNBA form II (solid black line) compared to form I (dotted purple line). PYR melting point = 159-162 °C [166], 2,4-DNBA melting point = 182 °C [210]

The trace shows a sharp endothermic peak at 140 °C, corresponding to the melt of the new polymorphic form. No peaks corresponding to the melt temperatures of the starting materials are observed in the trace. The melt peak falls at the same temperature as that of form I of the co-crystal, making determination of the thermodynamically stable polymorphs difficult via this method. When closely inspecting the two traces, a slight decrease in the onset of the melt from form I to form II has been observed. Although the melting points are very close to each other, this could possibly suggest that form I may be slightly more thermodynamically stable than form II. However, this is in contrast to the prediction made based on the conversion to form II during slurry experiments. A similar situation to this was recently discussed in polymorphic co-crystals of the material urea-barbituric acid, where form I and form III show very similar thermal events.[212]

Formation of form II was attempted in evaporative, in order to determine the morphology, and cooling crystallisations. The products from initial evaporative crystallisations set up in H_2O were not tested using PXRD and DSC due to an amorphous oil like substance being formed. As a result, cooling crystallisations were used to determine the morphology of the new crystal form.

Cooling crystallisation from H_2O yielded form II of the co-crystal with a high level of purity (figure 6.24). Cooling was carried out in an identical manner to the scale up crystallisations in IPA, which previously produced form I of the co-crystal.

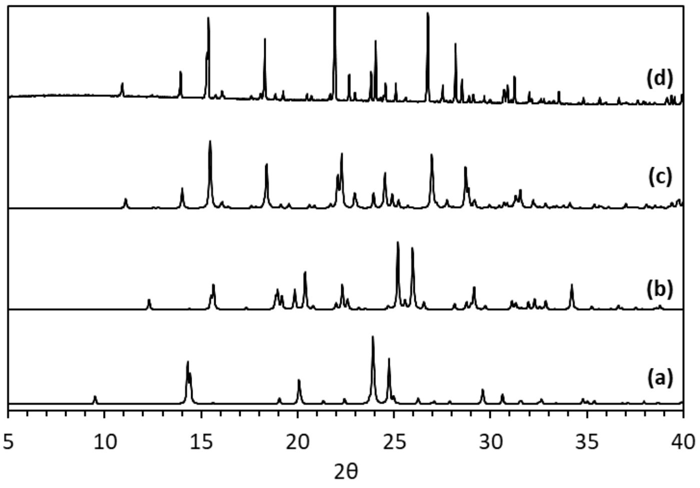

Figure 6.24. PXRD data for (a) PYR (BITZAF), (b) 2,4-DNBA (BAQLUD), (c) PYR:2,4-DNBA form II co-crystal calculated from SCXRD data and (d) PYR:2,4-DNBA co-crystal form II from cooling crystallisation in H_2O

Mechanochemical grinding experiments carried out appear to show some successful formation of the form I co-crystal in DSC and PXRD analysis. The experiments were repeated for form II (appendix A47). The PXRD analysis shows that grinding the starting materials in the absence of solvent does not form either of the two forms, producing only a mixture of the starting materials. The LAG experiments were carried out in H_2O and again in IPA. Both LAG experiments show the formation of form I as the major component. Attempts to make the co-crystal via solvent-mediated methods were more successful. Slurrying the starting materials in H_2O produced form II of the co-crystal purely and controlled cooling on both 10 g and 30 g scales in H_2O also yielded form II of the co-crystal (appendix A48).

The solubility of the new polymorphic form was determined via observation methods, in H_2O (figure 6.25). Form II also shows a monotropic relationship with pure PYR in H_2O, with the co-crystal solubility being significantly lower. This suggests the co-crystalline form is very stable. The hydrogen bonding interactions are very similar between form I and form II and are likely responsible for the elevated stability. This polymorph forms with ease in H_2O crystallisations, indicating the hydrogen bonds within the co-crystal are highly favoured: the strength of the hydrogen bonding interactions is expected to have increased from the pure PYR structure to the co-crystalline structure. As previously discussed, a decrease in solubility is not often favoured in the pharmaceutical industry, however, reduction in solubility is potentially advantageous in pharmaceuticals that require slow release, if it is related also to dissolution rate.

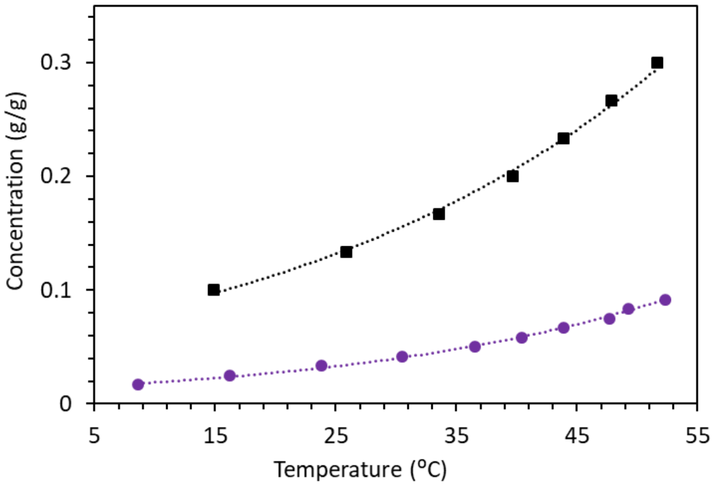

Figure 6.25. Solubility plot for PYR:2,4-DNBA form II co-crystal (purple, circle marker) and pure PYR (black, square marker) from observation in H_2O

The stability of the new polymorph was also analysed using the three different methods (figure 6.26). No change was observed in the PXRD data in any of the humidity studies carried out. After 3 weeks, samples taken from the humidity chamber and those from elevated temperature studies remain as form II of the co-crystal. After slurrying the form II co-crystal in H_2O for 1 week no changes in the form was observed and no breakdown of the co-crystal has occurred. This is in contrast to the transformation observed when form I is slurried in H_2O; after 6 hours of slurry in H_2O form I transforms to form II. This suggests that form II is more stable than the originally discovered form I. Under the stability experiments carried out no breakdown of the co-crystal can be detected, suggesting the form is stable for a prolonged period of time.

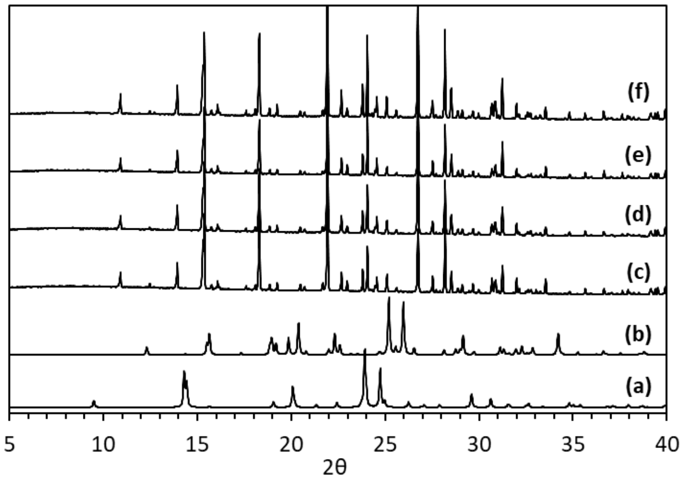

Figure 6.26. PXRD data for (a) PYR (BITZAF), (b) 2,4-DNBA (BAQLUD), (c) PYR:2,4-DNBA form II calculated from SCXRD, (d) PYR:2,4-DNBA form II slurry 1 week, (e) PYR:2,4-DNBA form II 50dc 3 weeks and (f) PYR:2,4-DNBA form II humidity 9 weeks

The new polymorphic form of the co-crystal could not be made via evaporative crystallisation in H_2O; form I was instead achieved. As a result, cooling crystallisation had to be used to determine the morphology of this polymorphic form. The morphology achieved (figure 6.27) is significantly different to the needles usually seen for pure PYR and closely resembles that of the form I co-crystals produced in IPA. The shape is fatter than a needle, with a much improved aspect ratio, but is hard to describe due to the irregular nature of the crystalline product.

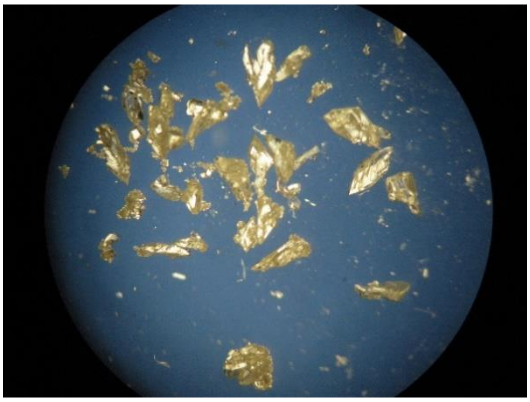

Figure 6.27. Irregular shaped crystals of PYR:2,4-DNBA form II from cooling in H_2O

As a result, face indexing the crystals posed similar difficulties to those seen in the form I co-crystals. Most crystals were too large or broken to be successfully indexed. An attempt was made, but it is unlikely to be representative of all the crystals in the bulk sample. However, the results give an idea of which faces are important in the new co-crystalline form (figure 6.28).

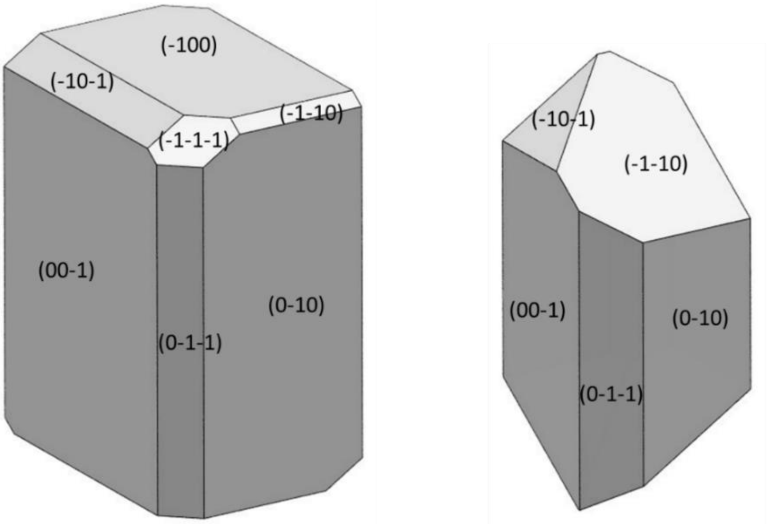

Figure 6.28. Predicted BFDH morphology for PYR:2,4-DNBA form II (left); observed morphology for PYR:2,4-DNBA form II (right)

The predicted morphology shows a block shaped crystal. The molecules in the structure are orientated in the same plane as the (011) and (0-1-1) faces, albeit on a slight angle. As a result, the hydrogen bonding groups extend from the molecules towards the (-100) and (100) faces, the fastest growing faces in the crystal structure. However, most of the hydrogen bonds are not in the same plane as the molecules. The hydrogen bonds contribute also to the growth of the surrounding faces. This is likely the reason for the more block shaped crystal predicted by BFDH calculations. If any aromatic interactions are present in this crystal structure, their contribution would be to the growth of the (011) and (0-1-1) faces. However, due to the angles of the molecules, no complete overlap is likely to be present. The experimental morphology is similar to the calculated morphology. The slower growing, surrounding faces are the same as observed in predicted morphology. The major difference in the two shapes is the (-100) and (100) faces, these are not observed in the experimental morphology. The likelihood of that the capping faces have broken in the process of removing the crystals from the vial and mounting them on the goniometer is high, potentially distorting the shape of the experimental crystal. The high similarity in general suggests the prediction is good for this co-crystalline form. The suggestion from face indexing is the final morphology achieved would be favourable for pharmaceutical applications due to the increased block like nature of the crystals produced.

6.7.3 Identifying the thermodynamically stable polymorphic form of the PYR:2,4-DNBA co-crystal

In an attempt to determine the thermodynamically stable polymorph, two experiments were carried out. First, additional solubility measurements were made for both forms in the solvent system from which it was not initially crystallised, form I in H_2O and form II in IPA, for comparison (figure 6.29).

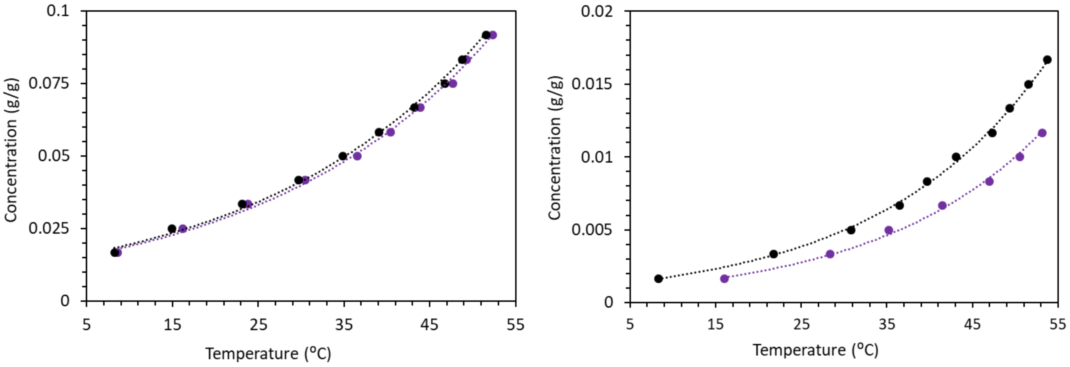

Figure 6.29. Solubility of PYR:2,4-DNBA form I (black) and form II (purple) in H_2O (left) and IPA (right) from observation methods

In both solvents, the polymorph with the lower solubility is form II. This suggests form II is the more thermodynamically stable of the two polymorphs. In H_2O, the solubility of the two different forms is almost indistinguishable and likely falls within the error of the measurements. In IPA, the differences are more noticeable, with the solubility difference seeming to increase with increasing temperature. The solubility measurements for the forms do not cross over throughout the temperature range sampled, suggesting the polymorphs have a monotropic relationship with each other. The solubility data does not give any indication as to why form I can be formed selectively from crystallisations in IPA and form II can be formed selectively from crystallisations in H_2O; understanding these further would involve more detailed kinetic considerations in the nucleation and crystallisation process.

The second experiment carried out was competitive slurrying of the two polymorphic forms in both IPA and H_2O. The experiments were carried out at 20 ^{o}C. Over time, it is expected that the metastable polymorph would convert to the thermodynamically stable form. Competitive slurry experiments allow this process to be expedited due to the solvent medium, the use of a continuous stirring environment.

After slurrying the two forms together for 2 hours, complete transformation from the initial mixture to form II was achieved (figure 6.30). Form II is therefore determined to be the thermodynamically stable form.

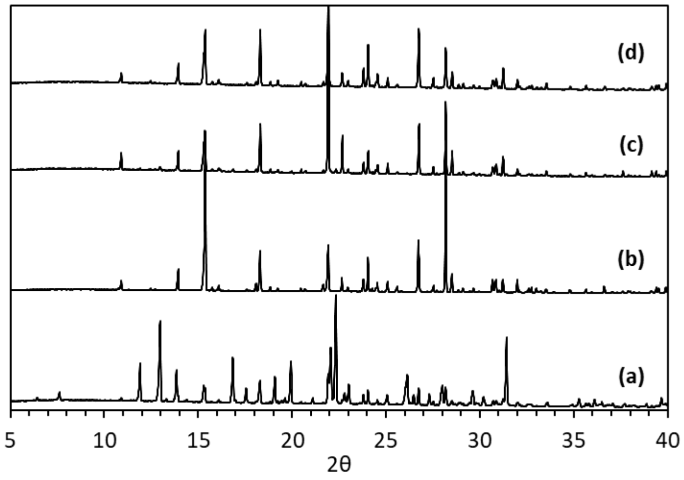

Figure 6.30. PXRD data for (a) PYR:2,4-DNBA form I calculated from SCXRD, (b) PYR:2,4-DNBA form II calculated from SCXRD, (c) competitive slurry of 1:1 form I:form II mixture in IPA and (d) competitive slurry of 1:1 form I:form II mixture in H_2O

Due to the very rapid conversion in competitive slurry methods further experiments were carried out that, hopefully, have a slower conversion time. To achieve this, the two forms were mixed together in the absence of any solvent medium and sampled every 24 hours. In addition, the two forms were ground together to determine whether phase transformations can occur using this method. Co-grinding the two forms together also results in conversion to form II of the co-crystal (figure 6.31).

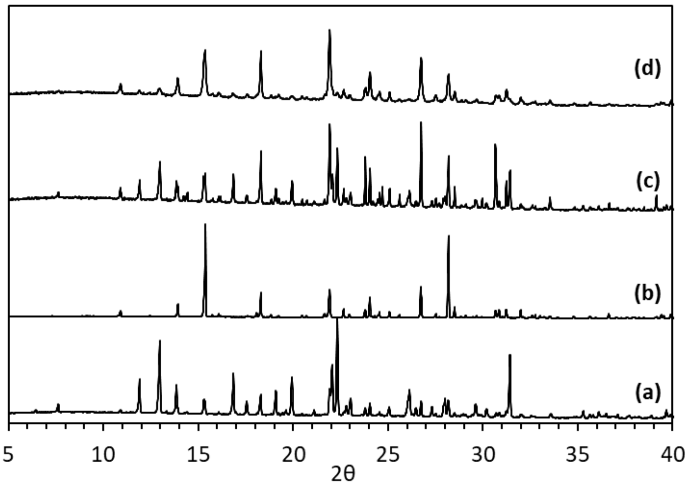

Figure 6.31. PXRD data for (a) PYR:2,4-DNBA form I calculated from SCXRD, (b) PYR:2,4-DNBA form II calculated from SCXRD, (c) mixture of form I and form II after 3 months and (d) co-grinding experiment of 1:1 form I:form II PYR:2,4-DNBA co-crystal

The forms remain stable for a long period of time when isolated from one another, as well as when kept as a physical mixture; further suggesting the thermodynamic stability of both forms is very similar. The conversion to form II appears to be favourable when the system is ground together, the addition of energy allowing complete conversion. Fast conversion is also observed in solvent-mediated slurry experiments, when both forms are present and when form I is slurried in H_2O. This suggests that form II is the thermodynamically stable form. It is unknown for how long form I can remain stable in the dry physical mixture, however, experiments suggest it would remain stable for an extended period of time unless given some form of energy to allow for the conversion.

6.7.4 Crystallisation of pyridoxine with 3,5-dinitrobenzoic acid

A second successful co-crystallisation was achieved with a 1:1 ratio of PYR:3,5-DNBA (figure 6.32).

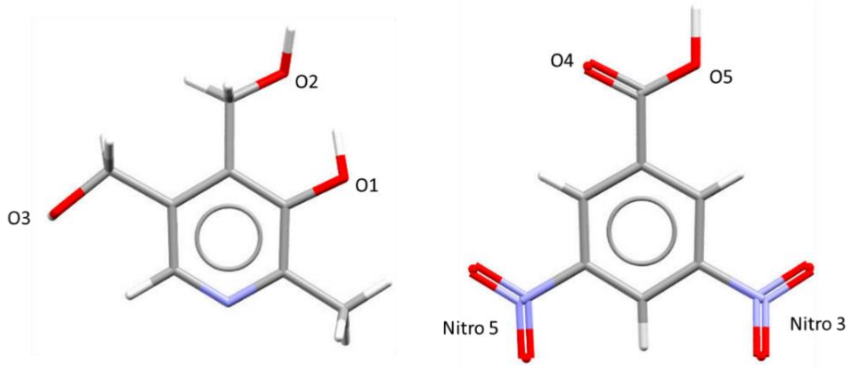

Figure 6.32. Structure of PYR and 3,5-DNBA showing the numbering system used in hydrogen bonding discussions

This new co-crystalline form crystallises in the monoclinic P2$_1$/c space group, with an asymmetric unit consisting of one PYR and one 3,5-DNBA molecule.

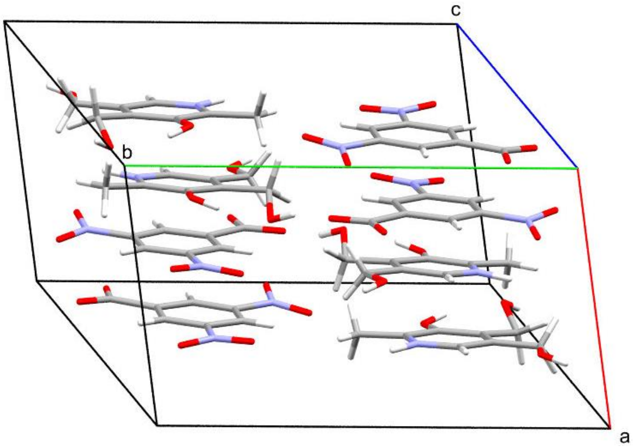

Figure 6.33. Unit cell of co-crystal PYR:3,5-DNBA

The packing of the co-crystal is made up of discrete sheets of molecules in the crystallographic *bc* plane (figure 6.33). These sheets of molecules stack on top of each other in the direction of the *a* axis as a result of the overlap of the aromatic rings present in the two molecules. The ring overlap alternates between the two molecular species throughout the structure, ··PYR··3,5-DNBA··PYR··. No hydrogen bonds exist between the discrete sheets, with π-ring overlap and other intermolecular interactions being responsible for holding the layers together. All the molecules within the structure are in the same plane, with all the hydrogen bonding interactions existing within this plane (figure 6.34). Each PYR molecule is surrounded by, and hydrogen bonded to, three different 3,5-DNBA molecules. In return, each 3,5-DNBA molecule is hydrogen bonded to three different PYR molecules.

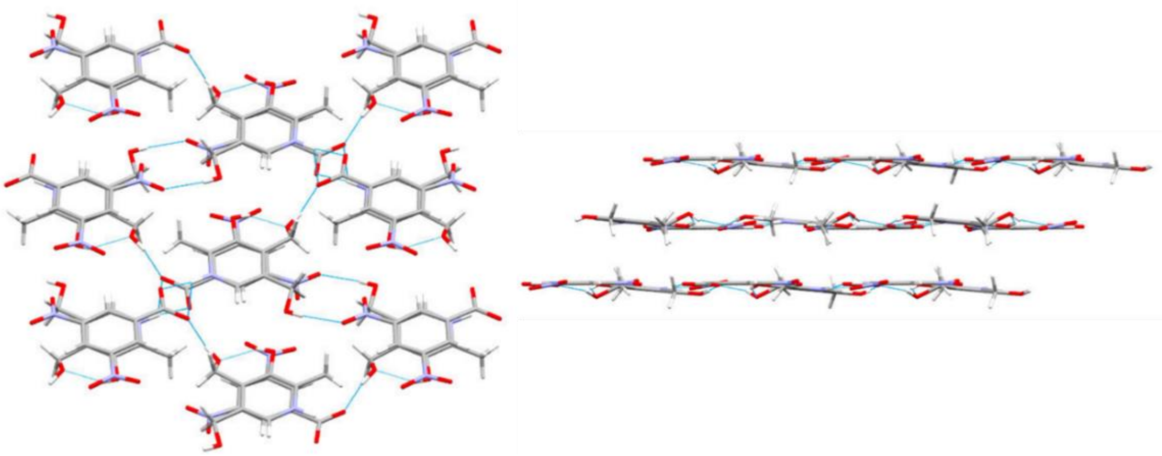

Figure 6.34. Hydrogen bonding interactions present in PYR:3,5-DNBA co-crystal showing the discrete layers of hydrogen bonded molecules and the overlap of the aromatic rings (left) and the stacking of the discrete planes of molecules (right)

The hydrogen bonding network within this structure is relatively straightforward to describe, as all the interactions exist within the same plane (figure 6.34). An internal hydrogen bond is present within the PYR molecule between two hydroxyl groups, O1-H··O2. This intramolecular interaction helps fix the geometry of the PYR molecules and maintains their planar conformation. A bifurcated hydrogen bond interaction exists between the N in the PYR ring and the carboxylic acid group in the 3,5-DNBA. Hydrogen transfer is again observed in this structure, with the bond distances (table 6.4) confirming the proton presence on the PYR ring: The N1-H distance is 1.03(3) Å and the H··O distance is 1.60(3) Å. The transfer appears less distinct in this structure, with a slightly elongated N-H distance in comparison to the other structures previously discussed. The data has quite significant ESDs associated with these bond lengths, resulting in a large possible distance range for the hydrogen to sit in. Ultimately, it is not possible to state exactly where the hydrogen is residing. Further hydrogen bonds are donated from each of the PYR hydroxyl groups to two separate co-former molecules. The second hydroxyl group donates a hydrogen bond to the deprotonated carboxylic acid group, O2-H··O4, and the third hydroxyl group donates a hydrogen bond to the nitro-group of another co-former molecule, O3-H··O(Nitro3). Similar hydrogen bond interactions between a nitro group and the PYR molecule are observed in other co-crystal structures consisting of co-formers containing nitro-groups. All three of the reported PYR structures in the CSD containing co-formers including nitro-groups show a similar interaction to that observed here, but this interaction is not seen in the PYR-2,4-DNBA structure. The presence of this interaction is likely the result of the differing geometry of the nitro-groups in the co-former molecule. There are five different hydrogen bonding interactions within this structure, however, none exist between the same molecular entity.

Table 6.4. Hydrogen bond distances and angles for PYR:3,5-DNBA co-crystal [xiii]

D-H··A	**d(D-H) (Å)**	**d(H··A) (Å)**	**d(D··A) (Å)**	**>(DHA) (°)**
O1-H··O2	0.91(3)	1.74(3)	2.569(2)	149(3)
O2-H··O4^2	0.83(3)	1.80(3)	2.600(2)	162(3)
N1-H··O4^1	1.03(2)	1.60(3)	2.626(3)	172(3)

[xiii] ^{1}1-X,1-Y,2-Z ^{2}1-X,1/2+Y,3/2-Z

Analysis via PXRD and DSC, confirms the bulk of material produced in the crystallisation has formed the new co-crystal structure.

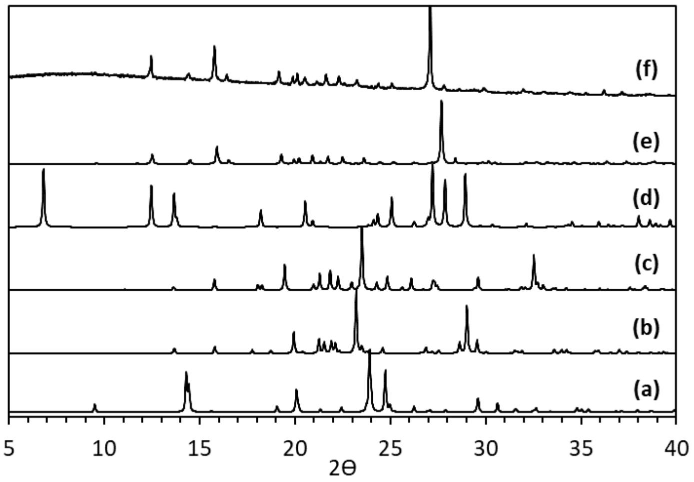

Figure 6.35. PXRD data for (a) PYR (BITZAF), (b) 3,5-DNBA form I (CUKCAM01), (c) pure 3,5-DNBA form II (CUKCAM02), (d) 3,5-DNBA hydrate (OKEMAT), (e) PYR:3,5-DNBA co-crystal calculated from SCXRD data and (f) PYR:3,5-DNBA co-crystal from evaporative crystallisation

The calculated and experimental PXRD patterns show the same peaks across the 2Θ value range (figure 6.35). At higher 2Θ values there is a slight disagreement between the peaks due to the differences in temperature at which the samples were analysed; the low 150 K analysis temperature for SCXRD results in a shift along the 2Θ axis. The agreement between the two patterns suggests there are no unassigned peaks in the experimental PXRD corresponding to any unconverted starting material. The phase purity of the sample can, therefore, be considered relatively high.

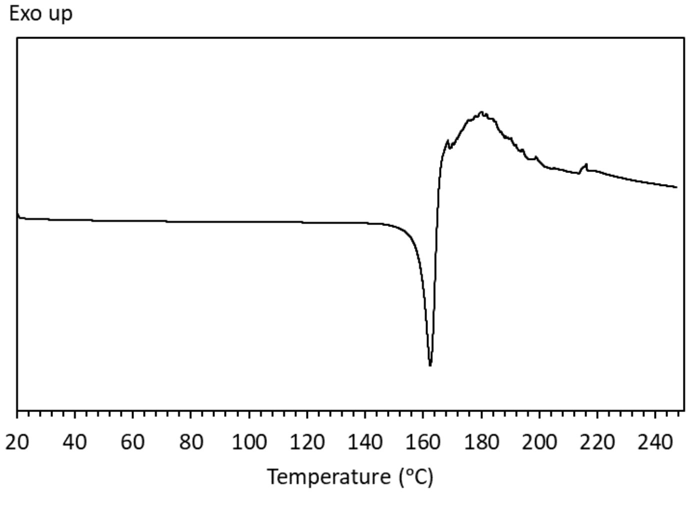

Figure 6.36. DSC trace of PYR:3,5-DNBA co-crystal. PYR melting point = 159-162 °C [166], 3,5-DNBA melting point = 204-206 °C [213]

DSC analysis shows one endothermic peak at 152 ^{o}C, giving the melting point of the new co-crystalline form (figure 6.36). The melting point is very similar to that of pure PYR, causing the DSC analysis alone to be insufficient to confirm the conversion to a new crystalline form. The peak is sharp, suggesting purity, but due to the closeness of the melting temperatures it is a less clear indicator. No endothermic peak is observed at around 205-207 ^{o}C, strongly indicating the full incorporation of the co-former into the co-crystalline structure. A small, broad exotherm is again observed after the initial melt of the co-crystal. As previously discussed, this could be due to decomposition of the nitro-groups in the co-former. This exothermic peak has been observed in all three co-crystals containing the dinitro-groups; the continued appearance in co-crystals containing dinitro groups increases the probability the hypothesis is correct.

Again, the mechanochemical grinding of the starting materials showed some success in forming the co-crystal (appendix A49 and A50). Grinding in the absence of solvent shows three endothermic peaks corresponding to the melting points of both the starting materials and the new co-crystal form. The LAG experiment still shows three peaks, however, those relating to the starting materials are significantly reduced in their intensity. Better conversion of starting materials to co-crystal was thus achieved using LAG methods, the presence of solvent clearly aiding the conversion. Full conversion was not achieved in the time frame of the grinding carried out, but with an increased grinding time full conversion may be possible. Slurry experiments were also successful in forming the co-crystal system, with good conversion and high phase purity achieved. In addition, controlled cooling crystallisation was achieved on 10 g and 30 g solvent scales (appendix A51).

Determination of the co-crystal solubility, again by observation methods, shows a substantial reduction in comparison to the pure PYR crystals (figure 6.37). Solubility determination for the PYR:3,5-DNBA co-crystal was carried out in H_2O. The lower solubility is indicative of a stable structure forming. The favourable nature of this co-crystal was also confirmed by the rapid precipitation of the new multi-component crystal structure from solution at higher temperatures, before the intended cooling could commence in initial cooling experiments. As a result of this precipitation, slurries were initially used to create bulk products of the co-crystal; achieving full dissolution without solubility data proved difficult. The reduction in solubility, in addition to the ease of formation, suggests the hydrogen bonding interactions in the co-crystal are stronger and more favoured than those in the pure PYR co-crystal, resulting in their formation in preference to the pure PYR crystal. Despite crystal engineering usually being utilised to increase the aqueous solubility of poorly soluble APIs, the reduction in solubility for extremely soluble pharmaceutical target molecules could prove useful in some applications.

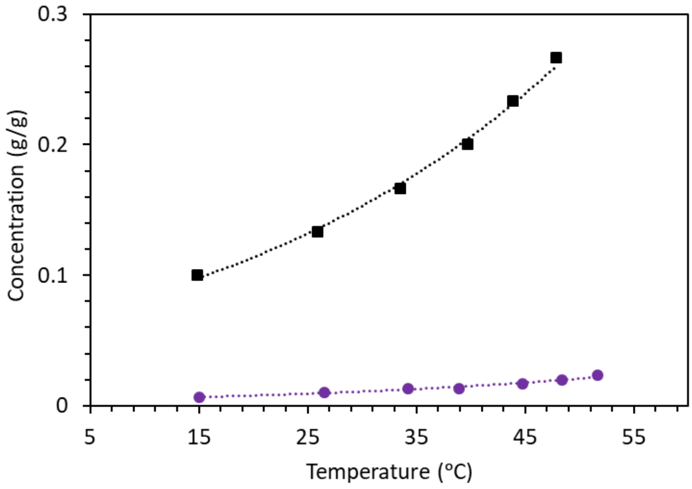

Figure 6.37. Solubility plot for PYR:3,5-DNBA co-crystal (purple, circle marker) and pure PYR (black, square marker) from observation in H_2O

The stability of the 3,5-DNBA co-crystal was determined using slurry, elevated temperature and humidity studies (figure 6.38).

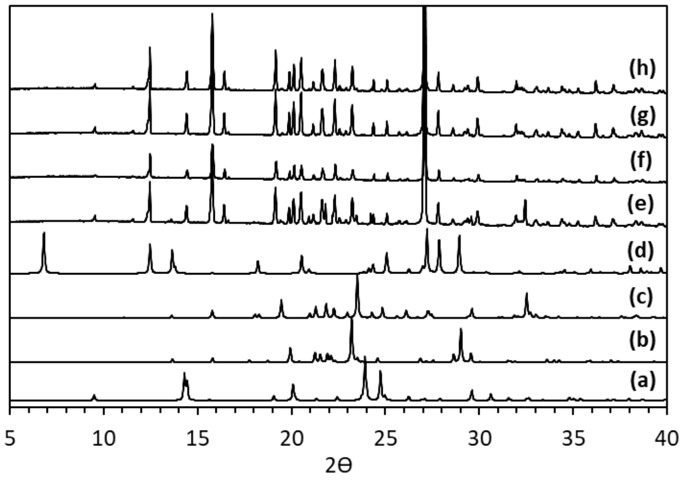

Figure 6.38. PXRD data for (a) PYR (BITZAF), (b) 3,5-DNBA form I (CUKCAM01), (c) 3,5-DNBA form II (CUKCAM02), (d) 3,5-DNBA hydrate (OKEMAT), (e) PYR:3,5-DNBA co-crystal calculated from SCXRD, (f) PYR:3,5-DNBA co-crystal slurry 1 week, (g) PYR:3,5-DNBA 50 ^{o}C 3 weeks and (h) PYR:3,5-DNBA 70 % humidity 9 weeks.

The PXRD patterns for samples taken from the slurry solution after 1 week, the humidity study after 3 weeks and the elevated temperature after 3 weeks all matched the initial pattern taken for the co-crystalline sample. The patterns do not show any degradation of the samples after the allocated periods of time, indicating the new co-crystalline product is stable under these conditions. This is a good indication in the case of elevated temperature and humidity studies that the co-crystal would not degrade when stored for prolonged periods of time, as is often the case in the pharmaceutical supply chain. The lack of conversion in slurrying suggests a hydrated form of the co-crystal is not likely to be formed. As the co-crystal does not break down this also tells us it is likely more stable under these conditions than the individual starting materials.

Upon co-crystallisation, a morphology change is observed from that often observed for PYR. The shape of the crystals produced closer resembles a block shaped crystal (figure 6.39).

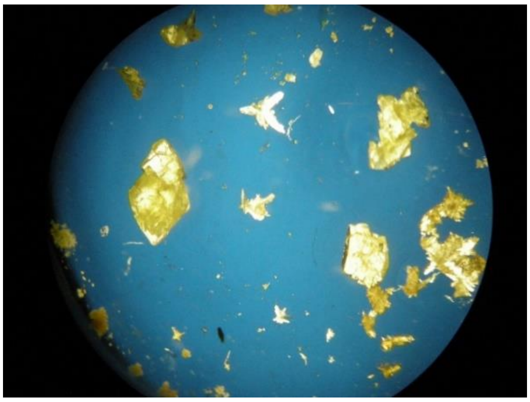

Figure 6.39. Fat, plate-shaped crystals of PYR:3,5-DNBA co-crystal crystallised from H_2O

Face indexing experiments carried out determine that the crystals produced are plates (figure 6.40). The plates produced are fattened, rather than very thin and breakable. This change is favourable in comparison to the needles usually observed. Although plates are not always a favourable crystal morphology, the fattening of these crystals moves them closer to blocks than plates.

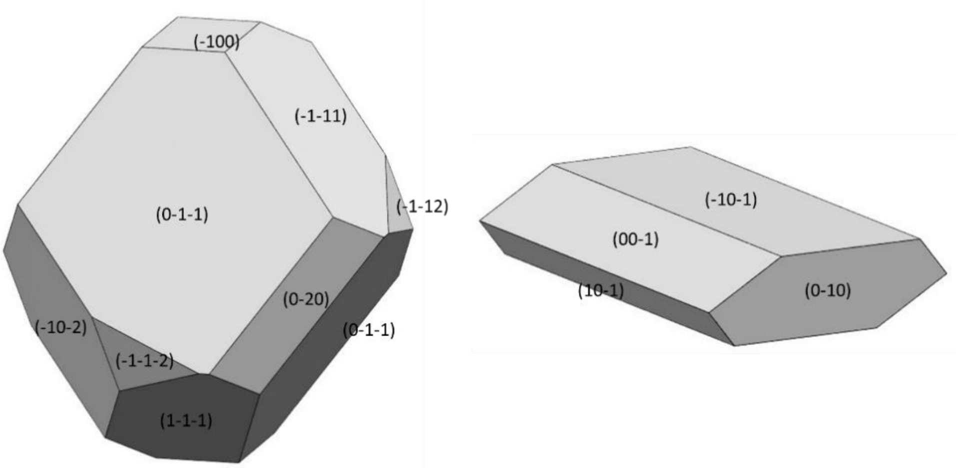

Figure 6.40. Predicted BFDH morphology for PYR:3,5-DNBA form II (left); observed morphology for PYR:3,5-DNBA form II (right)

The observed morphology does not resemble the predicted morphology in this case. The predicted morphology shows a block shaped crystal whose development is governed by the aromatic rings of the molecules stacking parallel to the (-100) and (100) faces. These faces are the smallest, suggesting they are the fastest growing faces. The hydrogen bonding interactions are, therefore, observed on the surrounding faces of the crystal structure. Whilst the prediction would indicate the π-π interactions are responsible for the major growth, the predicted morphology shows fairly even growth throughout the whole structure. The major differences observed in the predicted and observed crystal structure are likely the result of external influences not being taken into account in the BFDH calculations. The fattened plate shape crystal shows the major growth direction to be on the (0-10) and (010) faces. This growth direction is influenced by hydrogen bonding interactions occurring along the crystallographic *b* axis, which is perpendicular to the face. Hydrogen bonding interactions are also responsible for the growth on the (00-1) and (001) faces. These faces are perpendicular to the crystallographic *c* axis, where the further extending on the hydrogen bonded network occurs. The stacking of the layers of hydrogen bonded molecules occurs parallel to the apex between the (00-1) and (-101) faces. The limited growth on the (-10-1) face could be the result of reduced π-π interactions within the growing structure. The solvent could potentially be reducing the strength of these interactions in favour of the hydrogen bonding, explaining the plate shape observed instead of the block shape predicted.

6.7.5 Crystallisation of pyridoxine with trimesic acid

The third new co-crystal system was initially achieved from a 1:1 molar ratio of PYR and TRI (figure 6.41).

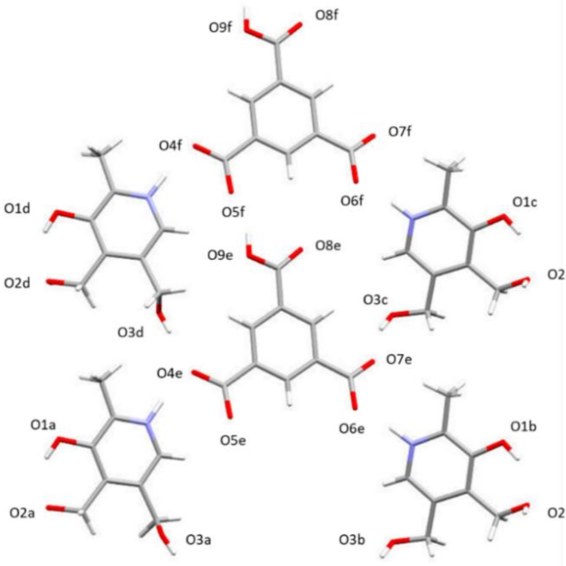

Figure 6.41. Structure of PYR and TRI molecules and positions in the co-crystal showing the numbering system used in hydrogen bonding discussions

The new crystalline form has a 2:1 stoichiometry of PYR:TRI, despite being crystallised from a 1:1 molar ratio. The crystal structure belongs to the triclinic $P\overline{1}$ space group, with an asymmetric unit containing four PYR molecules and two TRI molecules (figure 6.42).

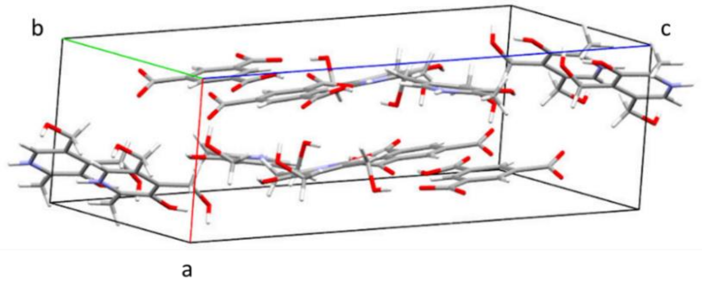

Figure 6.42. Unit cell of 2:1 PYR:TRI co-crystal

The packing of the co-crystal is similar to that observed for the PYR:3,5-DNBA co-crystal, with sheets of molecules aligned in the *bc* crystallographic plane (figure 6.43). The sheets are not perfectly planar due to the angles required for hydrogen bonding interactions between the two aromatic molecules, however, the layers can be clearly seen. The sheets of molecules stack on top of each other in the direction of the crystallographic *a* axis due to the overlap of the aromatic rings present in the two molecules. The ring overlap is slightly offset, giving the structure an off-set parallel stacking arrangement. In contrast to the PYR:3,5-DNBA co-crystal, the layers of molecules are not discrete, with hydrogen bonds existing between molecules of different layers. This hydrogen bond, with π-ring overlap and other intermolecular interactions, is responsible for holding the layers together.

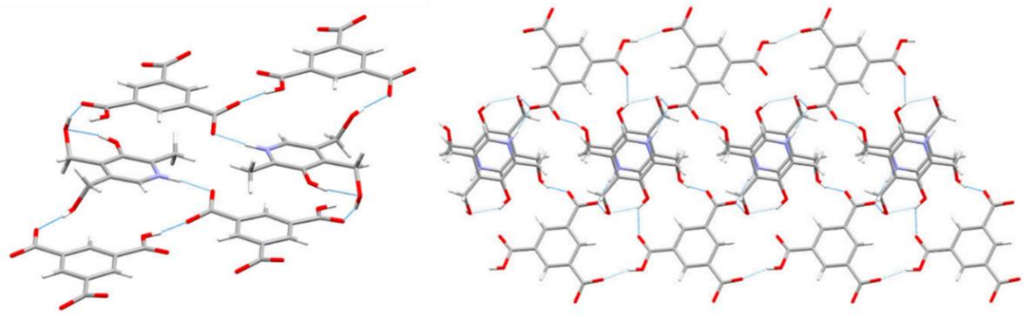

Figure 6.43. Hydrogen bonding interactions present in PYR:TRI co-crystal: All hydrogen bonds for PYR molecule (right) and all hydrogen bonds to a central TRI molecule (left)

The hydrogen bonding network within this structure is extensive, with multiple links between PYR and TRI molecules (figure 6.43). Due to the 2:1 stoichiometry and the nature of the structure, with four different PYR and two different TRI molecules in the asymmetric unit, there are a significant number of unique bonding interactions within the structure. There are no direct intermolecular hydrogen bonds between PYR molecules within the structure, however, the intramolecular hydrogen bond donated from O1-H to O2 is still present in all four PYR molecules. In general, each PYR molecule partakes in three different intermolecular hydrogen bonds, donating from the O2, O3 and accepting a H transfer at N. The exception is PYR molecule b, which donates an extra hydrogen bond from O1. The N in the pyridine ring, in all PYR molecules, accepts a hydrogen donation from one of the deprotonated acid groups; PYRa is protonated by

O4e, PYRb is protonated by O6e, PYRc is protonated by O6f and PYRd is protonated by O4f. The donation of the hydrogen bonds is confirmed by the bond lengths in table 6.5, with the N-H bond length being significantly shorter than the O-H bond length. The TRI molecules donate one hydrogen bond from O9e to O5f and O9f to O5e, creating a chain of PYR molecules. This is the only H bond forming between two TRI molecules. All the other H bonds involving the TRI molecules are donated by the surrounding PYR molecules; due to the already donated H atoms from two acid groups the only functional groups remaining are acceptors. The TRI molecules both accept a total of seven hydrogen bonds from surrounding PYR molecules and donate one to the neighbouring TRI molecule. The donation from TRI to TRI is within the same plane. Four bifurcated hydrogen bonds are observed within the structure; all involve the H transfer from a deprotonated acid group and two separate PYR molecules. These are unconventional bifurcated hydrogen bonds as they result from the hydrogen transfer from the acid groups, with the N to which the H has been transferred acting as the donor.

Table 6.5. Hydrogen bond distances and angles for PYR:TRI co-crystal [xiv]

D-H··A	d(D-H) (Å)	d(H··A) (Å)	d(D··A) (Å)	>(DHA) (°)
O1a-H··O2a	0.94(3)	1.90(3)	2.752(3)	149(3)
O2a-H··O8e[1]	0.85(3)	1.93(3)	2.752(2)	164(3)
O3a-H··O4f[2]	1.02(4)	1.72(4)	2.717(3)	166(3)
Na-H··O4e	0.98(3)	1.71(3)	2.676(2)	166(3)
O1b-H··O2b	0.92(4)	1.73(4)	2.576(3)	152(3)
O2b-H··O6e[4]	0.84(3)	1.82(3)	2.647(2)	172(3)
O3b-H··O7f[2]	0.84(3)	1.87(3)	2.685(2)	162(3)
Nb-H··O6e	1.01(3)	1.64(3)	2.628(3)	168(3)
O1c-H··O2c	0.91(4)	1.74(4)	2.575(3)	150(3)
O2c-H··O6f[5]	0.91(3)	1.75(3)	2.649(2)	176(3)
O3c-H··O7e	0.82(3)	1.89(3)	2.681(2)	162(3)
Nc-H··O6f	0.94(3)	1.71(3)	2.637(3)	170(3)
O1d-H··O2d	0.90(3)	1.89(3)	2.687(3)	146(3)
O2d-H··O8f[3]	0.88(3)	1.88(3)	2.747(2)	166(3)
O3d-H··O4e	1.03(4)	1.74(4)	2.771(3)	176(3)
Nd-H··O4f	1.03(3)	1.70(3)	2.721(3)	170(3)
O9e-H··O5f	0.80(4)	1.81(4)	2.569(3)	157(3)
O9f-H··O5e[6]	0.88(3)	1.73(4)	2.568(3)	158(3)

[xiv] [1]1-X,1-Y,1-Z [2]+X,1+Y,+Z [3]1-X,-Y,1-Z [4]-X,1-Y,-Z [5]-X,-Y,-Z [6]+X,-1+Y,+Z

Analysis via PXRD and DSC confirms the bulk of material produced in the crystallisation has formed the new co-crystal structure.

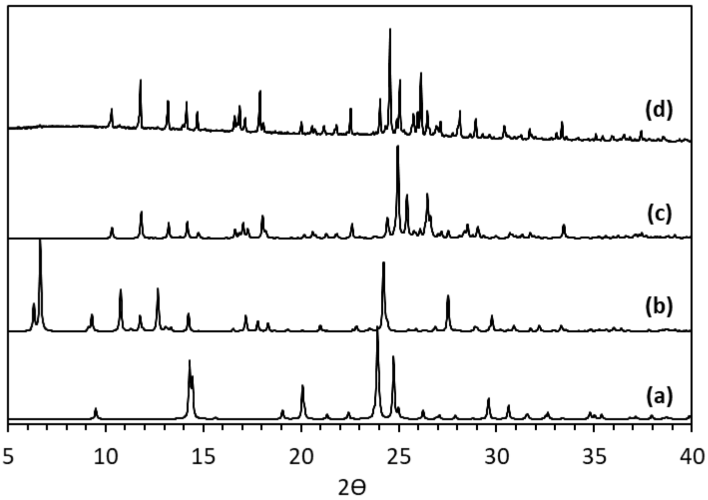

Figure 6.44. PXRD data for (a) PYR (BITZAF), (b) TRI (BTCOAC), (c) PYR:TRI co-crystal calculated from SCXRD and (d) PYR:TRI co-crystal from IPA evaporative crystallisation

Whilst the experimental and calculated patterns for the co-crystal match, there are possibly some residual peaks from the excess PYR starting material in the sample (figure 6.44). As the crystallisation was set up in a 1:1 stoichiometry and the resulting co-crystal formed has a 2:1 stoichiometry, there will be some PYR left over in the bulk product from the crystallisation, which is likely to show up in the pattern observed. However, it is less likely there will be any unconverted TRI, due to it being the limiting mass in the crystallisation. The significant peaks observed for TRI at 6-7° 2Θ are correspondingly completely absent from the experimental data, suggesting it is no longer present in the final bulk sample and has been fully utilised in co-crystal formation.

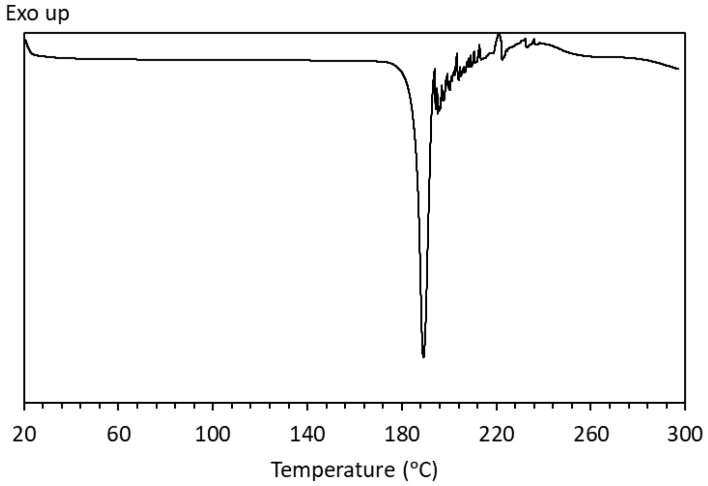

Figure 6.45. DSC trace of PYR:TRI co-crystal. PYR melting point = 159-162 °C [166], TRI melting point = >300 °C [214]

The DSC data for the co-crystal shows a sharp endothermic peak at about 180 ^{o}C, indicating the melting point of the new co-crystal system (figure 6.45). There is no endothermic peak seen at around 160 ^{o}C, indicating there is no PYR remaining in the bulk product of the crystallisation, in contrast to the indications of possible residual PYR from the PXRD. There is also little indication of any residual TRI in the bulk, though only the lower limit of the melting point range of TRI has been reached in this scan. Taken together, the DSC confirms the formation of a co-crystal structure, but not necessarily the complete conversion of all starting materials.

Grinding experiments for the PYR:TRI co-crystal were carried out in 2:1 molar ratios, due to the stoichiometric nature of the co-crystal (appendix A52 and A53). The DSC data for grinding in the absence of solvent shows a peak for the PYR starting material and a second melting point at 170 ^{o}C. This is slightly lower than the melting of the co-crystal. Comparing this to the LAG grinding experiment, a peak for unconverted PYR starting material and a peak at 170 ^{o}C are observed, but in addition there is a small peak seen at 180 ^{o}C, corresponding to the co-crystal 2:1 form. The peaks observed at 170 ^{o}C could potentially be due to a second multi-component form of a different stoichiometry. The LAG experiment is the only grinding experiment to show evidence of the formation of the 2:1 co-crystal form, however, full conversion is not achieved. Both experiments show an unknown peak and suggest a different stoichiometric form is possible using this co-crystal preparation method. Full conversion has not been achieved in either case. Slurry experiments were also carried out at a 2:1 molar ratio, achieving full conversion to the 2:1 co-crystal form characterised above. In addition, production of this co-crystal was achieved by controlled cooling crystallisation on 10 g solvent scale (appendix A54). Crystallisation at 30 g solvent scale was not achieved due to precipitation of the co-crystalline form before cooling could occur. Experiments at lower saturations resulted in no crystallisation being observed.

Observational solubility experiments for the 2:1 PYR:TRI co-crystal in IPA were carried out in the Polar Bear Plus crystalliser (figure 6.46). The multi-component crystal was determined to be more stable than the pure PYR crystal structure with a significantly reduced solubility profile. The solubility for this co-crystal is very similar to that seen for the PYR:2,4-DNBA co-crystal in IPA. The increased stability is due to the substantial increase in hydrogen bonding interactions within the structure. There could also be some significance in the 2:1 stoichiometry of the structure, although it is likely the effects of this will be increased strength of intermolecular interactions. As with the other two co-crystalline structures, initial formation of the multi-component structure was achieved through slurry techniques. The ease at which this co-crystal forms in solution is further testament to the favoured interactions within the structure and the increased stability this affords. The creation of a less soluble form of PYR could be of use in some pharmaceutical applications as the pure PYR has a very high solubility. However, this is often not the goal of co-crystal formation.

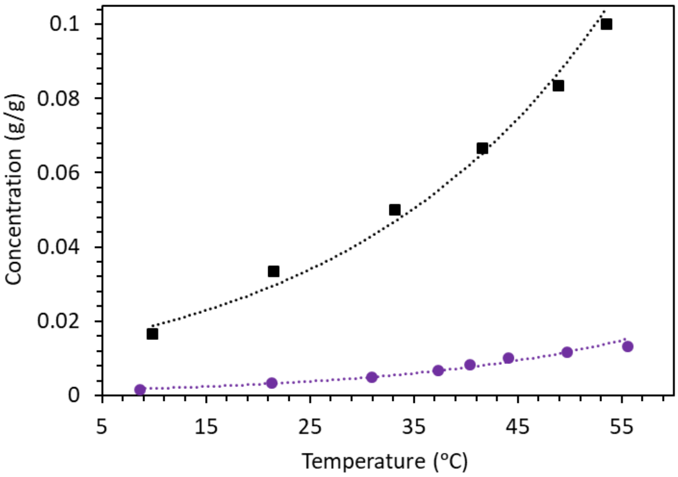

Figure 6.46. Solubility plot for PYR:TRI co-crystal (purple, circle marker) and pure PYR (black, square marker) from observation in IPA

The same three stability tests as for previous co-crystals were carried out on samples of the PYR:TRI co-crystal.

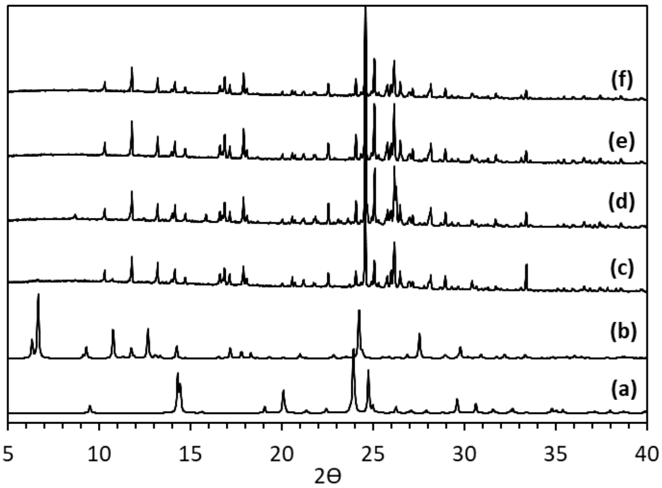

Figure 6.47. PXRD data for (a) PYR (BITZAF), (b) TRI (BTCOAC), (c) PYR:TRI co-crystal calculated from SCXRD, (d) PYR:TRI slurry 1 week, (e) PYR:TRI 50 °C 3 weeks and (f) PYR:TRI 70% humidity 9 weeks.

The PXRD patterns for all three stability studies match that of the original co-crystal (figure 6.47). No degradation is seen over the duration of the studies. The stability at increased humidity and elevated temperature suggests that storage of the co-crystal in the pharmaceutical supply chain would not be a problem, with no conversion to a different form or degradation back to the individual components. The lack of hydrate formation in the slurry suggests this is not likely to form over time, which is beneficial for storage. The absence of any breakdown of the co-crystal suggests the co-crystal structure is more stable than the individual components under these conditions.

The morphology of the co-crystals produced has changed significantly from the needles normally observed for PYR crystallisations.

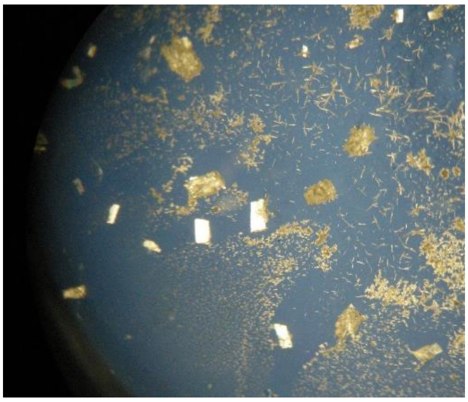

Figure 6.48. Plate-shaped crystals of PYR:TRI co-crystal crystallised from IPA

The crystals produced from the crystallisation show a plate-shaped morphology (figure 6.48). This is an improvement on the usual morphology observed, although not as significant as observed with the other two co-crystals discovered.

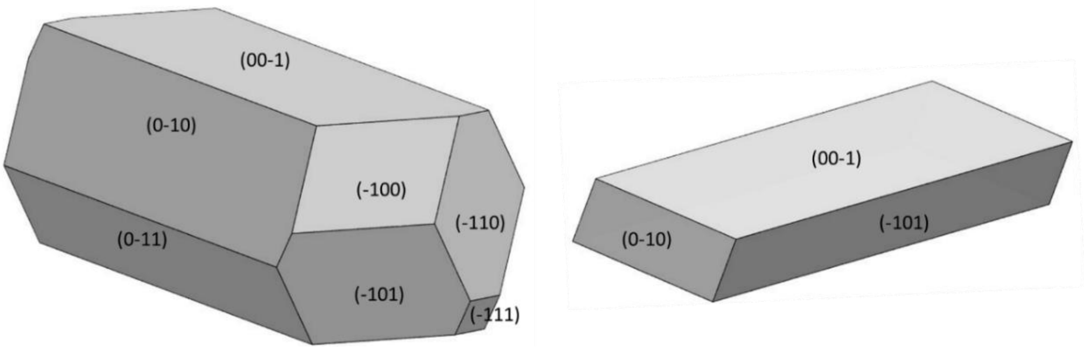

Figure 6.49. Predicted BFDH morphology for PYR:TRII (left); observed morphology for PYR:TRII (right)

The predicted morphology is similar to that observed for pure PYR (figure 6.49). It suggests the morphology should be a slightly fattened needle. The major growth direction is highly influenced by the π-interactions between the aromatic rings within the structure. However, as with pure PYR, it is likely the expected morphology would be closer to a needle. The observed morphology shows a plate-shaped crystal that has different interactions contributing to the major growth. The major growth face is the (0-10) face, making the major growth interactions the hydrogen bonds between molecules. This is in contrast to the predicted morphology and is most likely the result of the solvent interactions not being taken into account in the prediction calculations. The second major growth face, (-101), is contributed to by the aromatic rings stacking within the structure. The two major growth directions are likely to be very equally matched, with the differences being difficult to distinguish between when many different crystals are face indexed. Very slow growth occurs on the (00-1) faces. Analysis of the interactions show the intramolecular hydrogen bond within the PYR molecules lies directly along this face, limiting the number of possible interactions that allow growth in this direction. The creation of a co-crystal has achieved a new morphology, plate-shaped crystals as opposed to the commonly seen needles formed in EtOH. Whilst plate crystals are not the favoured morphology in the pharmaceutical industry, they are deemed an improvement from needle crystals. Further investigation could be carried out into the crystallisation conditions under which the co-crystal is formed in an attempt to alter the morphology even further and obtain a more block shaped morphology.

6.7.6 Crystallisation of pyridoxine with phthalic acid

A fourth co-crystal was discovered from an initial crystallisation of a 1:1 molar ratio of PYR and PtA (figure 6.50).

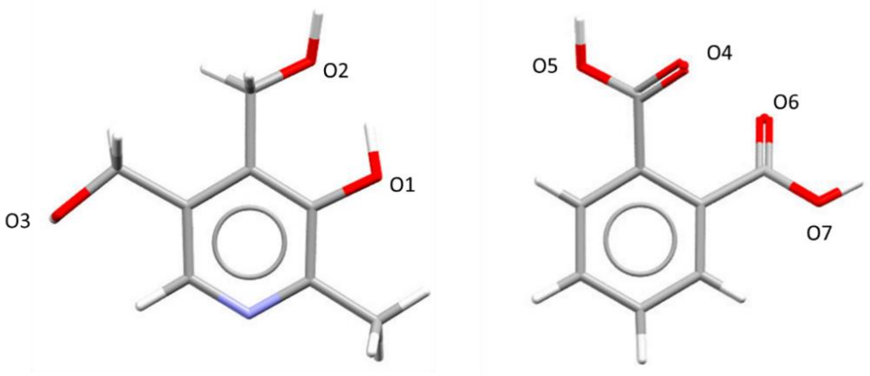

Figure 6.50. Structure of PYR and PtA showing the numbering system used in hydrogen bonding discussions

This co-crystalline material crystallises in the monoclinic $P2_1/n$ space group, with an asymmetric unit consisting of one PYR and one PtA molecule.

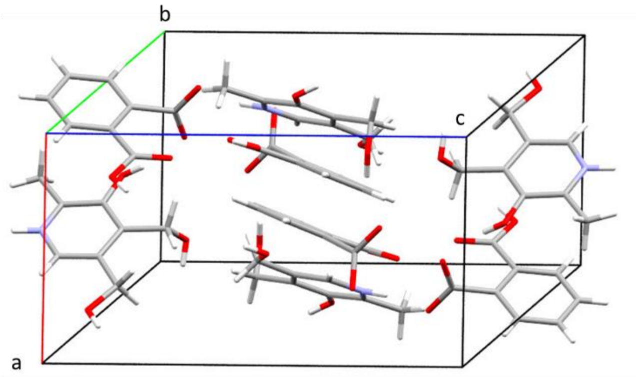

Figure 6.51. Unit cell of 1:1 PYR:PtA co-crystal

The packing of the co-crystal shows an overall zig-zag pattern, when viewed along the crystallographic *c* axis (figure 6.51). The molecules within the structure are not co-planar, with pairs of molecules alternating their orientation. The aromatic rings in each molecule stack parallel to the crystallographic *a* axis. This stacking occurs in an alternating pattern of PYR-PtA-PYR-PtA etc.; within each stack the aromatic rings remain at the same angle.

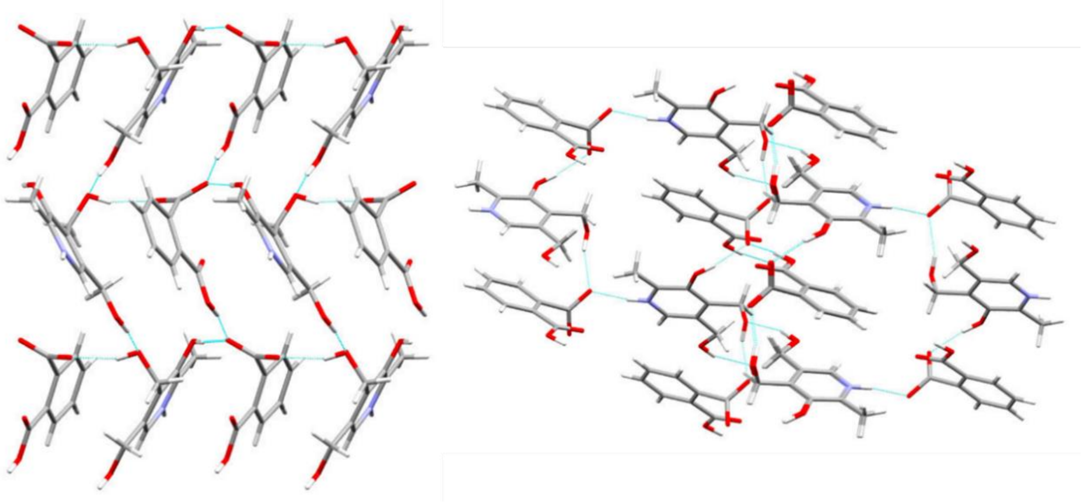

Figure 6.52. Hydrogen bonding interactions present in PYR:PtA co-crystal

The hydrogen bonding in the structure looks more complicated due to the zig-zag orientation of the molecules (figure 6.52). The PYR molecules donate a hydrogen bond from each alcohol group in the structure, with O2 also accepting a hydrogen bond from a neighbouring PYR molecule. The hydrogen bonding distances (table 6.6) suggest proton transfer has again occurred in this co-crystalline form: transfer has occurred from one of the carboxylic acid groups on PtA to the N in the pyridine ring of the PYR molecule. The N-H bonding distance is 0.92(2) Å and the H··O5 bonding distance is 1.85(2) Å. Each PtA molecule forms hydrogen bonds to three different PYR molecules and one PtA molecule. One carboxylic acid forms two bifurcated hydrogen bonding interactions; O5 accepts a hydrogen bonding interaction donated by O2-H on a PYR molecule and is also involved in the proton transfer with the N in a second PYR molecule; O4 accepts donation from both O1 in a third PYR molecule and O7 from another PtA molecule. This carboxylic acid group is out of plane with the aromatic ring system of the PtA and is responsible for the hydrogen bonds linking the stacking of alternating ··PYR··PtA··PYR·· molecules together. The second carboxylic acid group is in plane with the PtA aromatic ring and is only involved in one hydrogen bonding interaction: O7 donates to another PtA molecule. This structure differs from all the other PYR co-crystals discovered as there is no intramolecular hydrogen bond between O1-H··O2; this intramolecular hydrogen bond is also observed in the pure PYR crystal structure. Its absence in the PYR:PtA co-crystal contradicts the second general rule for hydrogen bonding, as described by Etter: '*six membered intramolecular hydrogen bonds form in* *preference to intermolecular interactions'*.[126] The creation of the co-crystal has required a change in the angles of the O1-H and O2-H groups and therefore moved the structure away from a favoured 6-membered ring geometry, eliminating the intramolecular interaction. Inspection of the published structures in the CSD shows only one example where this intramolecular hydrogen bond does not form, PYR:p-aminobenzoic acid co-crystal (VUKPIC).[215]

Table 6.6. Hydrogen bond distances and angles for PYR:PtA co-crystal [xv]

D-H··A	d(D-H) (Å)	d(H··A) (Å)	d(D··A) (Å)	>(DHA) (°)
N-H··O5[4]	0.92(2)	1.85(2)	2.768(2)	171(2)
O1-H··O4[1]	0.87(3)	1.83(3)	2.695(2)	172(2)
O2-H··O5	0.86(2)	1.88(2)	2.680(2)	154(2)
O3-H··O2[2]	0.89(3)	1.96(3)	2.814(2)	159(3)
O7-H··O4[3]	0.93(3)	1.70(3)	2.616(2)	170(2)

Analysis via PXRD and DSC was used to determine that the bulk of material produced in the crystallisation has formed the new co-crystal structure.

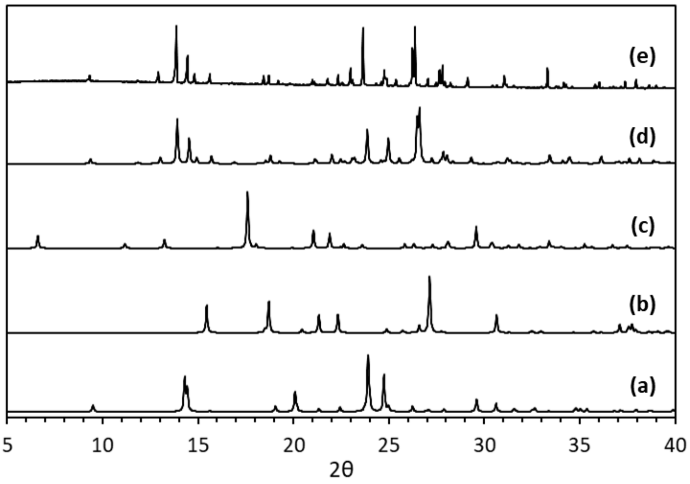

Figure 6.53. PXRD data for (a) PYR (BITZAF), (b) PtA (PHTHAC), (c) PtA hydrate (WODVAN), (d) PYR:PtA co-crystal calculated from SCXRD data and (e) PYR:PtA co-crystal from EtOH evaporative crystallisation

The calculated and experimental PXRD patterns show good agreement, with no extra peaks observed in the experimental pattern (figure 6.53). The agreement between the two patterns suggests no unconverted starting material remains and no other forms are present in the crystallisation. The phase purity of the sample is therefore relatively high.

[xv] [1]1+X,+Y,+Z [2]3/2-X,-1/2+Y,1/2-Z [3]1/2-X,-1/2+Y,1/2-Z [4]1/2+X,3/2-Y,1/2+Z

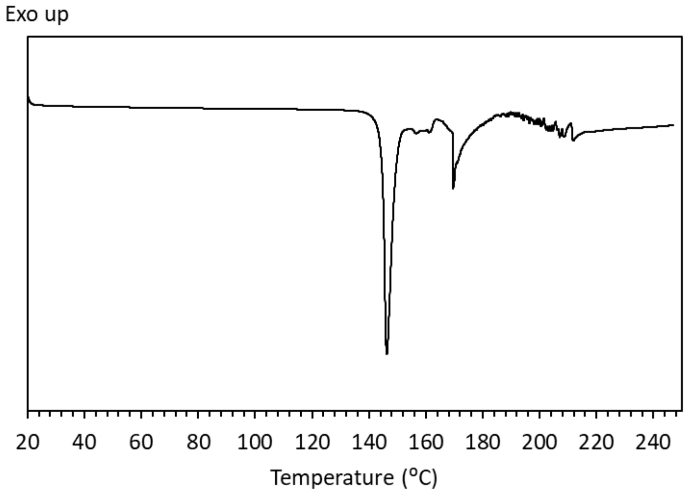

Figure 6.54. DSC trace of PYR:PtA co-crystal. PYR melting point = 159-162 °C [166], PtA melting point = 210-211 °C [216]

The DSC trace shows one endothermic peak at 140 °C, determining the melting point of the new co-crystalline form (figure 6.54). The peak is sharp, confirming the high conversion of the crystalllisation to the new form at high purity. A further, small endothermic event is observed at 169 °C. This could be caused by residual PYR in the sample with a slightly increased melting point due to the presence of the co-crystal. It could also be a second form of the co-crystalline structure, however, this is not supported by the PXRD data shown in figure 6.53.

Further crystallisation methods were carried out to determine how the co-crystalline form can be made (appendix A55 – A57). Mechanochemical grinding of the starting materials showed little success in forming the co-crystal, with the PXRD pattern resembling a mixture of PYR and PtA starting materials. In DSC no sharp peaks are observed. The LAG experiment with EtOH is more promising, showing a PXRD pattern that resembles the calculated pattern for the co-crystal structure. Some small impurity peaks remain suggesting full conversion was not obtained in this technique. Again, the DSC shows no sharp peaks in the trace resulting in no conclusions being able to be drawn from this data. Further solvent-mediated methods, namely slurry cooling experiments, showed good conversion to the new co-crystal system with high phase purity. Scale up was achieved to 10 g and 30 g solvent scales in cooling crystallisation.

Observation methods were used to determine the solubility of the new PYR:PtA co-crystal (figure 6.55). The solubility of the co-crystal is lower than that of PYR in EtOH, but the difference is less significant than with some of the other co-crystals and the co-crystal has a lower melting point. The data shown here is an average, therefore reducing the potential significance in the difference between the two further. However, the co-crystal forms favourably, indicating the stability of the co-crystal structure in general. The observed reduction is solubility is often unfavoured in the pharmaceutical industry, with the formation of co-crystals usually employed to increase the aqueous solubility of poorly soluble APIs.

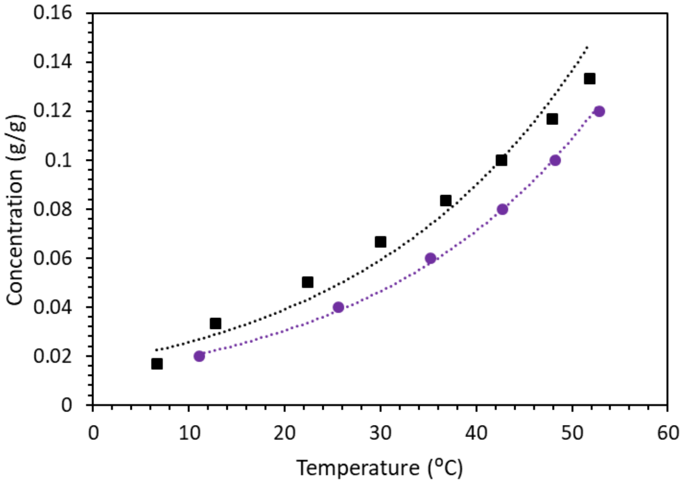

Figure 6.55. Solubility plot for PYR:PtA co-crystal (purple, circle marker) and pure PYR (black, square marker) from observation in EtOH

Three stability tests were carried out on samples of the PYR:PtA co-crystal; humidity, slurry and high temperature studies.

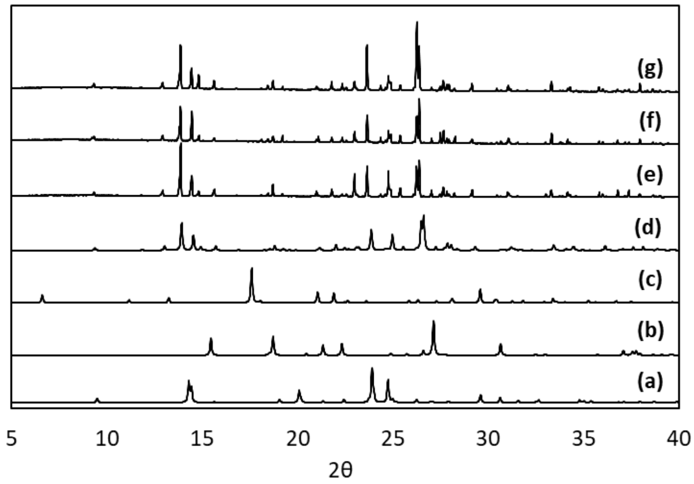

Figure 6.56. PXRD data for (a) PYR (BITZAF), (b) PtA (PHTHAC), (c) PtA hydrate (WODVAN), (d) PYR:PtA co-crystal calculated from SCXRD, (d) PYR:PtA slurry 1 week, (e) PYR:PtA 50 °C 3 weeks and (f) PYR:PtA 70% humidity 9 weeks.

The PXRD patterns for samples resulting from all three stability studies match that calculated for the co-crystalline form (figure 6.56). The confirmation of stability of the co-crystal at increased humidity and elevated temperature suggest that storage of the co-crystal would be possible for long periods of time without conversion to a different form or degradation back to the individual components. In the slurry, a hydrated form is not formed and the original structure is maintained, which is also beneficial for long term storage. The absence of any breakdown of the co-crystal suggests the hydrogen bonding in the co-crystal structure is sufficiently favourable under these conditions.

Again, the morphology change on formation of this co-crystal is significant: the co-crystal forms plate-shaped crystals in EtOH, a significant improvement on the needles usually observed for PYR (figure 6.57).

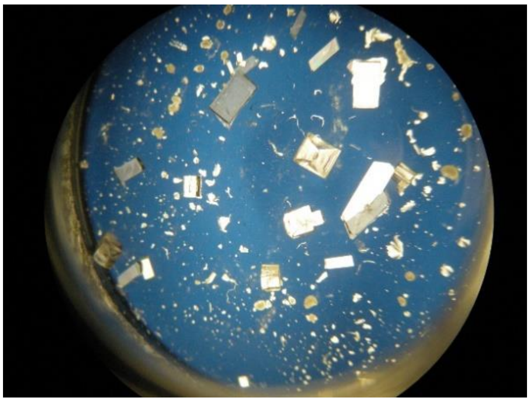

Figure 6.57. Plate-shaped crystals of PYR:PtA co-crystal produced from IPA

The plates produced here are much more substantial than those observed for PYR:TRI co-crystals. Although the change is more favourable, the optimal morphology for pharmaceutical processing has still not been achieved. Optimisation of this co-crystal form may be possible with further investigation. Face indexing experiments could not be carried out in this co-crystalline form to determine the major growth mechanisms due to equipment unavailability at the end of the project.

6.7.7 Crystallisation of further multi-component materials of pyridoxine

An investigation into the formation of PYR co-crystals with a set of aliphatic di-carboxylic acids was carried out under the author's supervision by Dave Collins (MChem student) towards the end of this research project. A number of new, co-crystalline forms are indicated to have been found; confirmed through PXRD and DSC analysis. Full single crystal XRD structure determination was carried out on some of these new co-crystals, confirming the formation of PYR:succinic acid 2:1, PYR:succinic acid:H_2O 2:1:2 and PYR:fumaric acid 1:1. Structure elucidation was not possible for the other promising forms due to breakdown of equipment. The full analysis of these co-crystals was not included in this thesis as they do not appear to show favourable morphology changes and further research would be required to achieve full structure determination of all forms in the series.

6.8 Conclusion

The modification of the morphology of PYR using different solvents was not achieved with the selection of solvents utilised in this research. Little influence can be seen on the growth morphology in different solvents, indicating that the potential to access a better morphology through changing the solvent is limited. It may be that an appropriate solvent is yet to be discovered. There are many computational modelling projects being carried out to attempt to predict the morphology achievable from a particular solvent, without the need to carry out excess screening experiments. In the case of PYR, this would be a good place to start if the influence of solvent were to be further investigated.

In terms of additive effects, both polymeric and size-matched additives were unsuccessful in changing PYR morphology under the conditions used in these experiments. In both cases, the additives and conditions utilised have not been exhaustive and further investigation could be carried out. Further size-matched and polymeric additives could be screened for their influence on the growth of PYR crystals in numerous different wt% ratios. The additives used in the screening discussed here could also be investigated in different wt% ratios than those already attempted. In addition, the option to screen the additives in different solvent systems also exists and could be investigated if a solvent system allowed the PYR to be more susceptible to morphological modification. The scope of additive screening could be large, covering a wide range of different variables. However, as no change has been observed in PYR to date, further screening could also prove fruitless for morphology modification. As a result, further screening would not be advised as the best method to improve the morphology of this particular API.

Some success was observed in changing the morphology of PYR upon the creation of multi-component materials. Four new co-crystalline structures of PYR were discovered (one of these in two polymorphic forms), all with morphology changes compared with pure PYR crystals. New multi-component crystal structures were found with 2,4-DNBA (two forms), 3,5-DNBA, TRI and PtA. The physical properties of each new co-crystalline structure were determined, along with the resulting crystal structures. In addition, the morphology was analysed and the faces determined using SCXRD and face indexing methods.

The solubility of each of the new crystal forms produced was less than that of pure PYR, a possible negative effect of the formation of the multi-component structures. Usually higher solubility is more favourable in pharmaceutical applications, however, the lower solubility could be a compromise worth making if the morphology improvement has significant effects on the processing steps. In depth stability analysis carried out determined each new form was stable for up to 9 weeks at 70% humidity. All forms were also stable for at least 3 weeks at 50 ^{0}C. Slurry experiments in H_2O also proved the stability of the co-crystals for up to 1 week, with the exception of the 2,4-DNBA form I co-crystal which converted to a second form (form II) of the co-crystalline structure under slurrying.

Determining the thermodynamic polymorphic form of the PYR:2,4-DNBA co-crystal was not possible using melting points or solubility data; the difference in stability between the two polymorphs appears to be small and likely within the error of the experiments carried out. Form II showed a slightly reduced solubility so was hypothesised to be the more stable form, supported by the fact that competitive slurry experiments showed full conversion of the sample to form II within 2 hours. In addition, co-grinding the two forms together also yields complete conversion to form II. Whilst both forms have very similar stabilities, the experiments carried out confirm form II of the co-crystal to be slightly more thermodynamically stable than form I and conversion to form II is possible through grinding and slurrying methods.

PYR:2,4-DNBA co-crystals show an irregular block shaped crystal, a significant improvement on the shape seen for PYR under most crystallisation conditions. The needles no longer form as the co-former allows different hydrogen bonding interactions to occur, reducing the strength of the π-π-interactions between the aromatic rings. The morphology change observed in the production of this co-crystal is much more favourable for downstream processing.

The PYR:3,5-DNBA co-crystal forms a fattened-plate-shaped crystal morphology. Again, this is a significant improvement on the usual needle morphology observed for pure PYR crystals. Whilst plate-shaped crystals are often unfavourable in processing, the fattened nature of those produced here suggests they could significantly improve the downstream processing steps required for production. The PYR:TRI co-crystal also forms plate-shaped crystals. The plates produced here are much thinner than observed for the PYR:3,5-DNBA co-crystal and are a much less favourable change. The change is still a major difference from the needles usually observed, however, the thin nature of the plates would makes them also difficult to process into a final pharmaceutical product. The PYR:PtA co-crystal also shows a plate morphology. The plates are more substantial than those produced with TRI co-former, but still thinner than those produced with 3,5-DNBA. Although plates are more favoured than needles, they still cause difficulties in processing steps, therefore, these three co-crystals would be less desirable to the pharmaceutical industry: the inclusion of a secondary molecule is likely not giving a large enough morphology improvement to justify exploring these co-crystal systems as a pharmaceutical crystal system for PYR.

Overall, the creation of PYR co-crystals has resulted in positive morphology changes not previously observed in additive or solvent experiments. The improvement is particularly beneficial in the case of the PYR:2,4-DNBA co-crystal, where an almost block shape is achieved. Although there would be difficulty obtaining FDA approval for crystals involving a secondary component, this would be the most promising method to utilise to change the morphology of the PYR crystals. No improvement was seen for either of the methods attempted which do not change the crystal structure of the API; neither additives nor solvent were shown to influence the growth shapes of pure PYR. In contrast to the conclusions reached about IZN, the formation of multi-component crystal structures is more successful in morphology modification for PYR and would be a promising route for further investigation, despite the difficulties potentially faced when seeking approval for these co-crystalline API materials.

Chapter 7 Benchmarking CMAC workflows

7.1 Introduction

This strand of the project is carried out in the broader context of the CMAC Future Manufacturing Hub. The CMAC consortium as a whole focuses on tackling the optimisation of pharmaceutical manufacturing through adopting continuous crystallisation methods.[217] This provides the opportunity to improve product quality and improve cost effectiveness, sustainability, energy usage and other environmental benefits. Moving towards continuous manufacturing processes presents new technical and economic challenges that need to be overcome to enable their implementation.[111, 218] To address this, CMAC has developed a microfactory approach. This involves the implementation of modular lab scale process steps, the choice and optimisation of which for a particular target process-product combination are based on an underpinning set of workflows developed within CMAC. The workflows rely on a combination of experimental and digital approaches which can be implemented and linked to allow for rapid evaluation of the feasibility of potential methods for the production of a given target molecule.[219]

The work presented in this chapter was published in part as Hatcher, Burgess, Payne and Wilson, "*From structure to crystallisation and pharmaceutical manufacturing: the CSD in CMAC workflows*", 2020, CrystEngComm, **22**, 7475; doi: https://doi.org/10.1039/D0CE00898B.

7.2 Importance of workflows

Standardised workflows are important within collaborative environments such as CMAC, and in cross-industry approaches, to ensure research is being carried out in a reproducible way. Workflows can also be useful for researchers carrying out research and development in areas in which they are not expert. When interlinked, they also offer advantages in developing integrated process approaches such as the CMAC microfactories, giving a standardised approach in which the compatibility and effectiveness of overall end-to-end process can be developed with respect to optimised individual unit processes; workflows also offer key decision points to aid such process development. The workflows developed at the University of Bath, by Dr. Lauren Hatcher, relate to two different primary crystallisation screening techniques used to modify the primary crystalline particle properties to control/change a chosen physical property – **multi-component crystal** screening and **additive crystallisation** screening.

Both workflows were designed to drive the decision-making process surrounding the screening of potential new multi-component materials (MCM) and additive crystallisations in order to achieve a change in the physical properties of the primary API crystals. Included in the workflows are a number of check points to help navigate the decision points where challenges are often presented in crystallisation screening.

7.3 Outline of workflows

7.3.1 Multi-component (MC) workflow

MCM screening is often considered in the early stages of primary processing as a way to improve physical properties both of the particle, for example size and shape, and the API itself (as a co-crystal or salt), including solubility/dissolution and bioavailability. MC crystal screening should only be considered in situations where the composition of the crystal of the delivered API can be varied (i.e. co-crystals or salts are acceptable). This method of investigation is often already well established in laboratories, but usually without a formalised workflow/decision point structure. Figure 7.1 shows the workflow produced for CMAC on multi-component material screening.

Figure 7.1 CMAC MCM screening workflow driven by the decision points capturing key elements to indicate successes. Decision 1: is crystallinity retained following evaporation?; Decision 2: is there evidence for a new product from the PXRD and DSC analysis?; Decision 3: are there single crystals formed from the evaporation?; Decision 4: is there good diffraction from the single crystal and can a structure be solved?; Decision 5: is the product material stable to slurrying in solution?; Decision 1a: is crystallinity retained after grinding?; Decision 2a: is there evidence for a new product from the PXRD and DSC analysis?; Decision 3a: is the new product pure, or is there a mixture of product and starting materials present?

Before commencing any experiments, the key API property to be targeted should be outlined, along with the criteria to decide the success of the screening. Additionally, molecules for potential co-formers need to be determined. This can be done in a number of ways, including computational calculations and analysis of potential intermolecular interactions possible with the API, for example using the CCDC Mercury molecular complementarity tool. Finally, any solubility data relating to the target API or potential co-formers should be available for workflow evaluation; this is often found in literature or from previous experimental studies. These decisions are included in the pre-requisite section of the workflow.

The first three stages focus on discovery experiments at a small scale. The workflow suggests a parallel approach using both mechanochemical and evaporative screening methods to enable a wider range of possibilities to be investigated in a shorter period of time. Decisions made at this point are used to decide if a new co-crystalline product has been accessed and can be characterised. The following stages move towards developing the new MCM on a larger scale and determine whether any improvement has been achieved to the initial physical property outlined in the pre-requisites. These stages also include further investigation into determining other important physical property information, such as solubility and stability. The goal of the workflow is to produce a new MC crystalline form that is well characterised and deliverable at a meso-scale in either a microcrystalline powder or single crystal form.

7.3.2 Additive workflow

In contrast to the MCM discovery, it is less common for additive intervention to be implemented into crystallisation processes, in spite of the potential benefits of this approach.[219] Additive screening may be considered early in the primary processing stages as a way to improve physical particle attributes, including particle size, crystal habit/morphology and polymorphic form. Additive interventions are particularly worthy of consideration in situations where the API is only acceptably delivered in its pure form (i.e. salts or co-crystals are not acceptable). Much of the additive workflow (figure 7.2) follows the same process as the MC workflow, with an emphasis on the concentrations of the secondary component being much lower than the stoichiometric amounts used in the discovery of MC materials, and of course with a different outcome targeted.

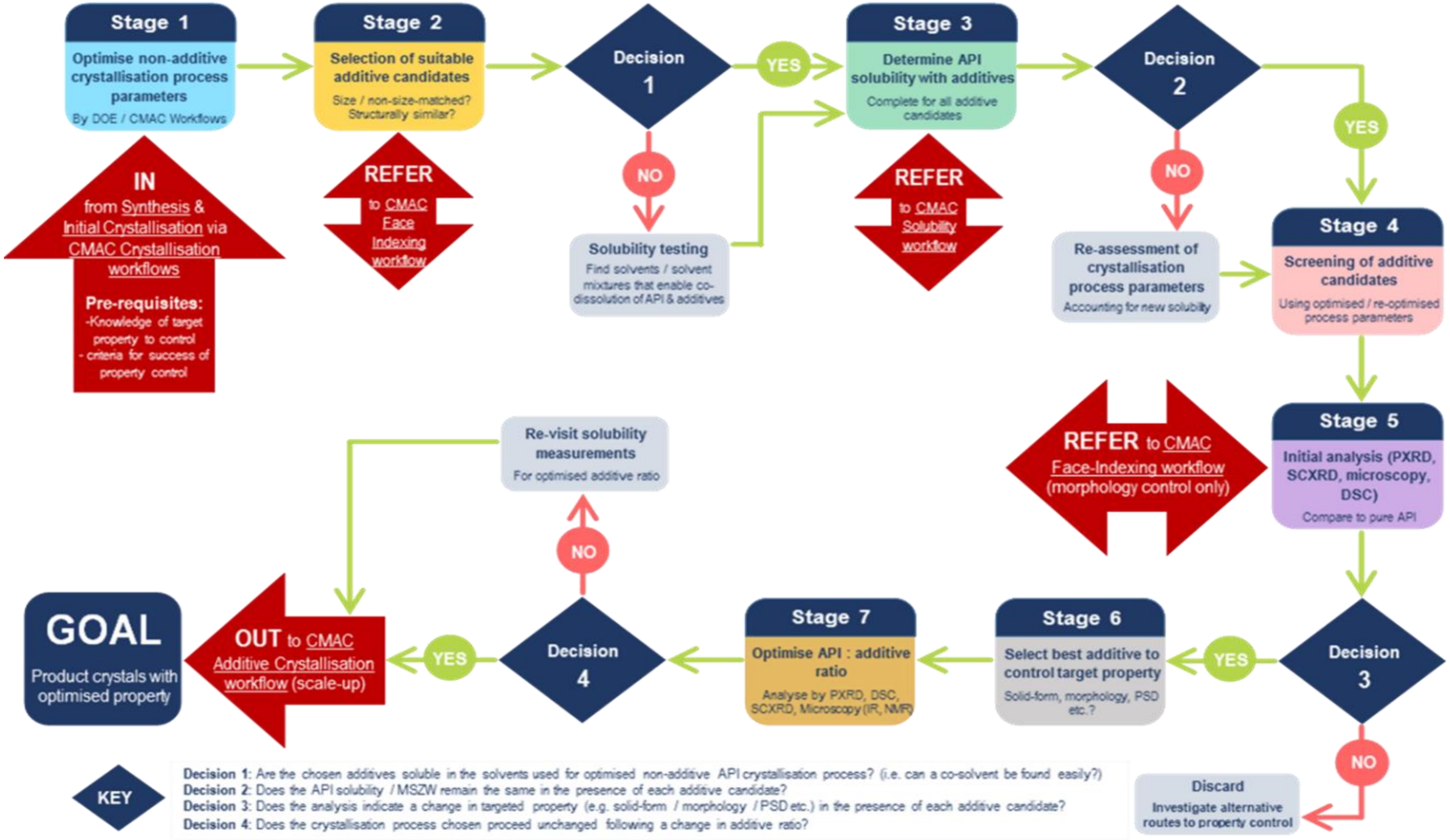

Figure 7.2. CMAC additive screening workflow driven by the decision points capturing key elements to indicate successes. Decision 1: are the chosen additives soluble in the solvents used for optimised non-additive API crystallisation process? (i.e. can a co-solvent be found easily?); Decision 2: does the API solubility/MSZW remain the same in the presence of each additive candidate?; Decision 3: does the analysis indicate a change in targeted property (e.g. solid-form/morphology/PSD etc.) in the presence of each additive candidate?; Decision 4: does the crystallisation process chosen for the product proceed unchanged following a change in additive ratio?

The workflow again begins with a similar pre-requisite section to that of the MC workflow. The API property being targeted must be outlined, along with the key criteria that must be met to be deemed successful. As the additive intervention does not intend to change the composition of the API material, the physical properties being targeted tend to be crystal particle attributes, such as particle size distribution (PSD), shape/morphology etc.

Stage 1 of the workflow is concerned with ensuring the crystallisation of the target API is optimised, including solvent choice and solubility. This is particularly important for investigating the effects of additives due to the choice of target properties often being primary particle attributes. It is important to know the outcome of the crystallisation process in the absence of additives to ensure any changes observed are the result of the additives present and not due to changes in the experimental set up. The next two stages (2 and 3) are concerned with choosing suitable additive candidates and understanding their solubility. This can again be done via computational approaches, similar to those utilised in the MC workflow, or other empirical methods. One important additional element in the additive workflow is use of SCXRD data to enable face indexing methods to determine the surrounding faces of the crystal. By visualising this information using the BFDH morphology function in the CSD Mercury software, the interactions responsible for the major growth of a crystal and functional groups present on each of the faces can be determined.

Stages 4 and 5 begin the screening process of the additives in small scale crystallisations. All decisions included in these stages focus on whether an enhancement of the target property has been observed or whether no significant changes have been observed. It is also important to confirm at this stage that no additive has become incorporated into the structure and no form changes have been induced by the presence of the additive. Once an additive has been deemed successful, the final stages focus on optimising the crystallisation conditions with the additive present to achieve the best and most reproducible enhancement possible. This includes identifying the best additive concentration (stage 6) and maintaining other important crystallisation parameters at an optimal level, for example the solvent choice, API concentration, etc.

The overall goal of the workflow is to determine an additive candidate that has the potential to deliver an API crystallisation process with enhanced particle properties, without any unwanted inclusion of additive into the final product crystal or solid form changes of the target API. Any information obtained in this screening process would be used in the design of a scaled-up version of the additive crystallisation route.

7.4 Multi-component workflow benchmarking

The benchmarking of the multi-component workflow was carried out largely by Dr. Lauren Hatcher and Bath MChem student Ayrton Burgess, using the CMAC target molecule of mefenamic acid (MFA) and other members of the fenamic acid (FA) family. A new co-crystal form of flufenamic acid and 2,2'-bipyridine was discovered using the workflow discussed.[219] The discovery and further analysis of PYR co-crystals, discussed in chapter 6, was also carried out using the MC workflow, by the present author. The MC work carried out with IZN, presented in chapter 5, was undertaken before the workflow was formalised; however, it followed essentially the same methodology.

7.5 Additive workflow benchmarking

The additive workflow was used to determine whether additive crystallisations were a suitable consideration for morphology modification in a number of target molecules. Experiments were carried out on FA and its derivative MFA. Both form plate-shaped crystals which can cause problems with downstream processing steps in the manufacturing process. By introducing additives into the crystallisations in small quantities the potential exists to modify the growth and resulting morphology of the crystals without incorporating the perceived impurity into the crystal structure.

7.5.1 Fenamic acid (FA) and mefenamic acid (MFA)

FA is a monomorphic material which crystallises in the triclinic space group $P\overline{1}$. The hydrogen bonding interactions show an intermolecular dimeric ring interaction between the carboxylic acid groups on the molecule (figure 7.3). There is also an intramolecular hydrogen bonding interaction between the N-H group in the centre of the FA and the C=O group within the carboxylic acid group. This intramolecular hydrogen bond plays a role in fixing the geometry of the molecule and means there is no free rotation around the N between the aromatic rings.

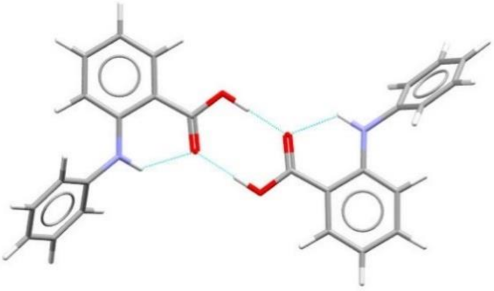

Figure 7.3. Dimeric hydrogen bonding interaction between FA molecules

The solvent utilised in the benchmarking process was IPA; crystallisation from this solvent resulted in a plate morphology with a parallelogram shaped end face (figure 7.4).

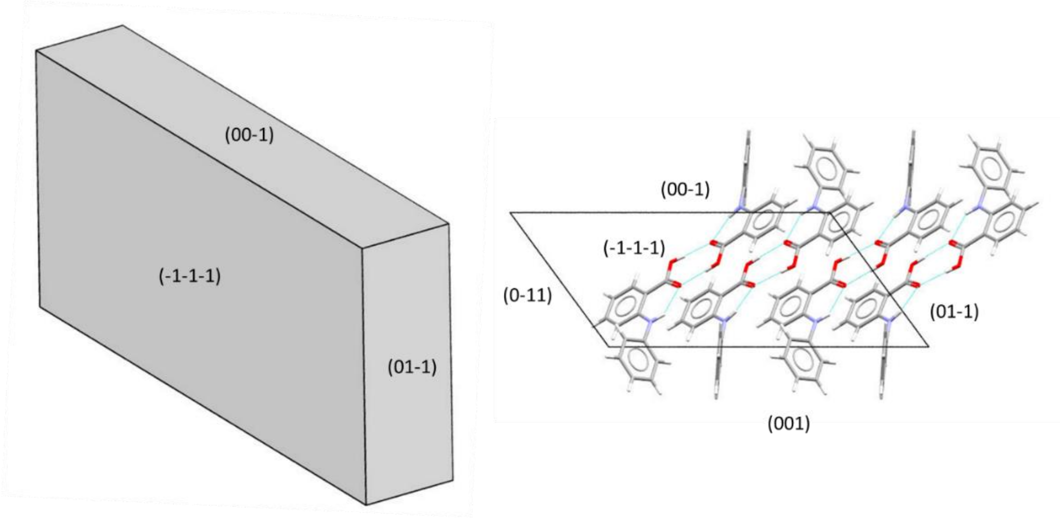

Figure 7.4. Face indexed morphology for FA crystallised from IPA and molecular packing with respect to morphology

The major growth faces are (01-1) / (0-11). Stacking of one of the aromatic rings in the FA structure contributes to this growth direction, while the dimeric hydrogen bonding is present along these faces. The second aromatic ring is at 90° to the other and contributes to growth in the (-1-1-1) / (111) direction; from the observed morphology growth in this direction is less pronounced.

MFA has three polymorphic forms, which show distinct PXRD patterns (figure 7.5). Form I is the most stable at room temperature with form II and form III the metastable forms. Form II becomes the most stable form at higher temperatures.

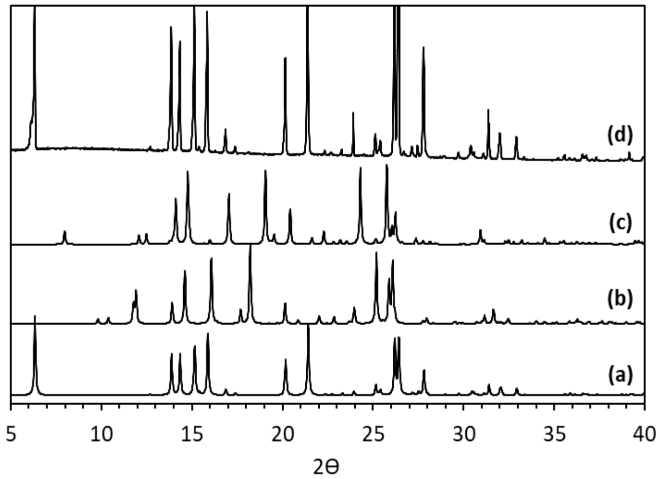

Figure 7.5. PXRD data for (a) MFA form I, (b) MFA form II, (c) MFA form III and (d) MFA crystallised from IPA

Form 1 also crystallises in the $P\overline{1}$ space group with a similar hydrogen bonding structure to that of FA, showing an inter-molecular dimeric ring interaction between the carboxylic acid groups on the molecule (figure 7.6). The intra-molecular hydrogen bond is also observed between the N-H group and the C=O group, as seen in the FA structure, fixing the geometry of the molecule. The MFA molecule features two methyl groups not observed in FA.

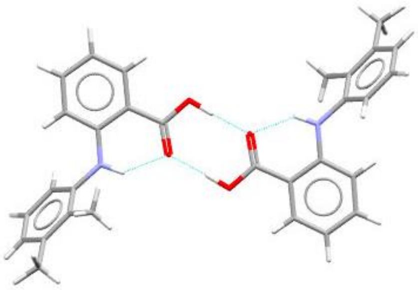

Figure 7.6. Dimeric hydrogen bonding interaction between MFA molecules

The use of IPA as a solvent allows the stable form I of MFA to form, without the presence of the metastable forms, as evidenced from the PXRD (figure 7.5). Using additives in the system has the potential to allow a metastable polymorph to form more favourably due to the influence it may have on the packing and growth of the crystals. As additives can also affect growth, the morphology of resulting crystals was also analysed.

The morphology observed for MFA in IPA shows a very thin plate with the faces forming a hexagonal shape (figure 7.7).

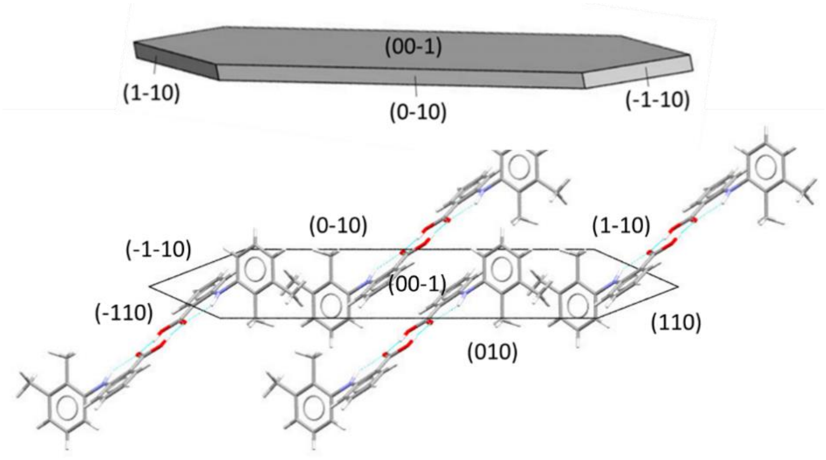

Figure 7.7. Face indexed morphology for MFA crystallised from IPA and molecular packing with respect to morphology

The major growth direction appears to benefit from major contributions from π-π interactions between the aromatic rings in neighbouring MFA molecules.

7.5.2 Workflow benchmarking for fenamic acid and mefenamic acid

Workflow inputs/pre-requisites

Initial CSD data mining with ConQuest

The possible solid forms already reported and their structures must first be identified for each API. This can be effectively achieved via a structure search in ConQuest. The structures of the target molecules are shown in figure 7.8. Similar to the searches carried out for the MC workflow, the following filters were used for the CSD search:

- 3D coordinates must be determined
- No polymeric structures
- Only organic structures.

Adding explicit hydrogen assignment on COOH groups prevents the return of salt structures for this search.

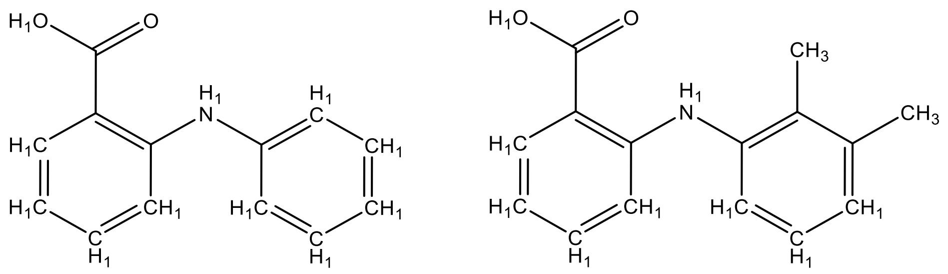

Figure 7.8. Structure of target molecules used in ConQuest structure search with all the hydrogens explicitly assigned: FA (left), MFA (right)

The search for FA returned five hits, of which two were structure determinations of the single polymorphic form isolated so far (QQQBTY). The remaining three consist of two MC materials with co-formers acridine and 4,4'-bipyridine. The CSD search carried out for MFA returned 26 hits in the data base. Seven of these were determinations (and re-determinations) of the three polymorphic forms that exist for the structure (form I = XYANAC). The remaining 19 structures consist of 14 different MC materials with various co-former molecules.

Stage 1: Optimisation of non-additive crystallisation parameters

Small scale evaporative crystallisation experiments were used to determine the parameters to be used for each target API. This stage can also be carried out in cooling crystallisation if the equipment is available. The solvent chosen for this set of experiments was IPA due to the ease of dissolution of each target in the solvent system. 10 mg of API was dissolved in a minimum amount of solvent (based on solubility data available) and allowed to evaporate slowly at a constant temperature of 40 ^{0}C.

The resulting product materials were analysed by optical microscopy and in each case the morphology determined. Face indexing experiments were also carried out on the crystals using SCXRD platforms to determine the faces contributing to the external morphology.

Stage 2: Selection of suitable additive candidates

Selection of additives was carried out using the molecular complementarity screening tool (previously discussed in chapter 4). This calculation is primarily used to design MC materials, however, it also has the potential to be useful in the determination of possible additive molecules. This relies on the fact that if a material was likely to form a MC material with the target molecule it may also, in smaller quantities, have a sufficiently significant interaction with the growing crystal to influence the morphological outcome.

For this benchmarking study both the GRAS list and the list of non-GRAS co-formers, discussed previously in chapter 4, were used. Incorporation of the additives into the final crystal structure is not the aim of this screening process, therefore the use of non-GRAS materials should be less problematic in these experiments than when focusing on the creation of MC materials. Screening searches were performed for both target molecules with all five molecular descriptors enabled. In addition to these screening experiments, the CSD searches previously carried out were further analysed to identify any potential additives that already form MC materials with the target molecules. The formation of a MC material confirms there is a strong interaction between the target API and the chosen co-former, suggesting this may be successful as an additive when present in smaller quantities in the crystallisation. As a result of these investigations, a total of eight additives were short listed for both FA and MFA: isonicotinamide (EHOWIH), nicotinamide (NICOAM), flufenamic acid (FPAMCA), tolfenamic acid (KAXXAI), adipic acid (ADIPAC), 4,4'-bipyridine (HIQWEJ), 2,2'-bipyridine (BIPYRL) and sorbic acid (ZZNWQ). All the chosen additive candidates either pass the screening tests carried out or are known to form a MC material with one/both of the target molecules. MFA has reported MC material crystals with nicotinamide, flufenamic acid, tolfenamic acid and 4,4'-bipyridine. By contrast, FA only shows a MC material with 4,4'-bipyridine.

At this stage in the workflow we have reached decision 1: *Are the chosen additives soluble in the solvents used for the optimised non-additive API crystallisation?'.* This is an important consideration when choosing the additives. All eight candidates shortlisted for each target were chosen in part due to their solubility in IPA, the chosen solvent for this experiment set.

Stage 3: Determine API solubility with additives

During the benchmarking process, the position of this stage of the workflow was called into question. The initial draft of the workflow suggests solubility testing needs to be carried out at this point, to determine any changes to the solubility of the API with an additive present. The presence of the additive could significantly affect the solubility profile of the API in the solvent system chosen, therefore, identifying this at an early stage could save time in later steps of the workflow. However, determining the solubility for every additive at this stage is a time-consuming process, especially if there are a large number of potential additives chosen for screening. In reality, most additives investigated are likely to be unsuccessful in improving the chosen target property, with this stage resulting in the generation of a lot of surplus data that will not be required. In addition, at this stage of the workflow the concentration of the additive required for optimal enhancement of target properties has yet to be identified, making it difficult to know for what percentage of additive it would be relevant to carry out the solubility determination. As additives are often used in small quantities, frequently ≤ 1% of the API weight, the influence on the solubility may be negligible. As a result, spending time investigating the solubility at this point is likely to be time consuming without necessarily adding significantly to the investigation.

Decision 2 would be considered at this point: *Does the API solubility/MSZW remain the same in the presence of each additive candidate?* Due to the nature of the workflow, decision 2 is made redundant if stage 3 is removed. As a result of the benchmarking studies presented here, it is suggested that stage 3 and decision 2 would be moved to later in the workflow when optimisation of successful additives is being considered. It is likely this stage would be more appropriate after stage 7, where decision 4 already indicated the potential for a change in solubility due to optimisation of the additive concentration.

Stage 4: Screening of additive candidates

Small scale evaporative crystallisations were set up for each target molecule to mimic those carried out in stage 1. 10 mg of target molecule with 1% wt/wt of the additive molecule added to each crystallisation. Each crystallisation was then allowed to evaporate at a constant temperature of 40 ^{o}C.

This stage should be carried out using identical conditions to those determined in stage 1 of the workflow and optimised for each target molecule. By using identical conditions, the results from stage 1 can be used as a control experiment during comparison to the crystallisations carried out at this stage. In this benchmarking study, the morphology is being probed and as a result the morphology of the crystals achieved in the presence of additive will be compared to those observed in stage 1, in the absence of additive.

Stage 5: Initial analysis of results

The analysis methods chosen will depend on the desired particle property for control. In this benchmarking exercise the property being controlled is particle morphology, thus the first analysis method utilised is optical microscopy. This helps determine if any shape changes have occurred.

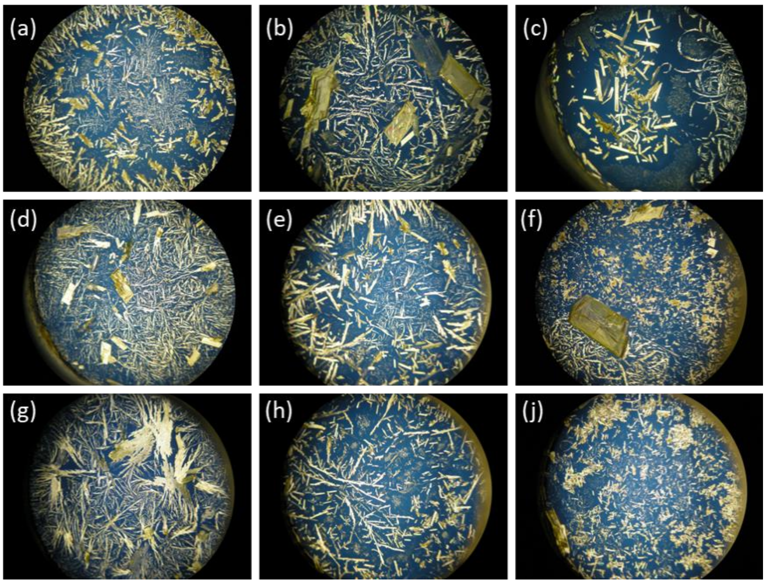

Figure 7.9. The morphology of FA crystals from IPA observed in the presence of additives. (a) absence of additive, (b) nicotinamide, (c) isonicotinamide, (d) flufenamic acid, (e) tolfenamic acid, (f) adipic acid, (g) 4,4'-bipyridine, (h) 2,2'-bipyridine and (j) sorbic acid

Analysis of the FA crystals produced show minimal additive effects on the morphology achieved (figure 7.9). Despite this, large differences can be seen between the pictures. Some show larger crystals with many fine crystallites, whilst others show more uniformity with some smaller fines present. This is likely due to changes in the nucleation of the samples. Evaporative crystallisation is uncontrolled and therefore not the best method to get reproducible crystallisation conditions. The crystallisations show mainly elongated plate-like crystals similar to the shape observed from IPA alone.

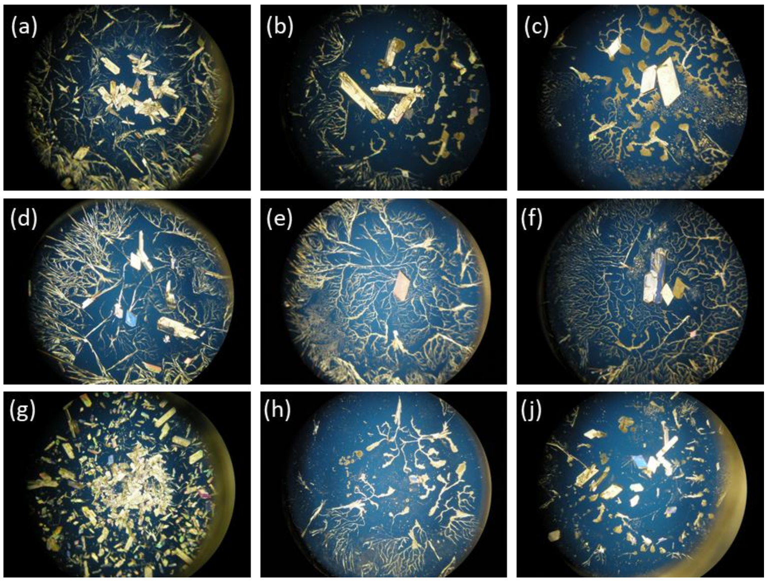

Figure 7.10. The morphology of MFA crystals from IPA observed in the presence of additives. (a) absence of additive, (b) isonicotinamide, (c) nicotinamide, (d) flufenamic acid, (e) tolfenamic acid, (f) adipic acid, (g) 4,4'-bipyridine, (h) 2,2'-bipyridine and (j) sorbic acid

The microscopy analysis of the MFA crystals also shows no influence of the additives on the morphology achieved (figure 7.10). Most crystallisations show elongated, plate-shaped crystals similar to the shape observed from IPA alone. Again some crystallisations show an increased number of smaller crystallites due to the uncontrolled nature of evaporative crystallisation.

As MFA has more than one known polymorphic form, further analysis is necessary to confirm the experiments all yield the same polymorph. Using PXRD analysis, the products of each crystallisation were analysed and compared to calculated patterns from published structures in the CSD database. All crystallisations were confirmed to produce MFA form I (figure 7.11).

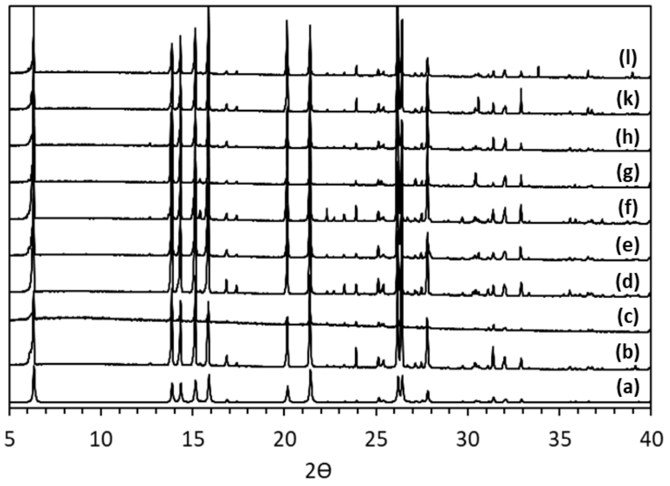

Figure 7.11. PXRD data for (a) MFA form I calculated for SCXRD, (b) MFA crystallised from IPA in absence of additive, (c) with isonicotinamide, (d) with nicotinamide, (e) with flufenamic acid, (f) with tolfenamic acid, (g) with adipic acid, (h) with 4,4'-bipyridine, (k) with 2,2'-bipyridine and (l) with sorbic acid

Further analysis that can be carried out at this point includes face indexing experiments to determine the nature of the morphology changes observed.

At this point in the workflow we arrive at another decision point: *Does analysis indicate a change in the targeted property (e.g. solid form/morphology/PSD etc) in the presence of each additive candidate?* In the case of FA and MFA, the answer at this decision point would be no. The influences of the additive in the crystallisations carried out is minimal and does not achieve a significant morphology change. As a result, these additives would be discarded. At this point, further investigations could be carried out using a different set of additives identified in stage 2 or the conclusion can be drawn that additive intervention is not a viable method to achieve a morphology change in these target molecules.

An example of a successful morphology change due to additive interventions can be seen in chapter 4 for IZN. If the workflow had been established when the IZN investigation was undertaken, stages 6 and 7 could be carried out as follows.

Stage 6: Select best additive to control target property.

As discussed in chapter 4, IZN shows a favourable morphology change with two additives: 3-HBA and 3,4-DNBA. Repetition of any successful additive crystallisations in cooling could potentially aid the decision as to which additive to choose. Another consideration to make at this point would be the safety of the potential candidates for the use in pharmaceutical products. As there are only two potential additives it would be possible to continue the research on both until one could be ruled out.

Stage 7: Optimise API to additive ratio

Experiments carried out on IZN showed that a ratio of 1% additive is sufficient to change the morphology. More experiments could be carried out in an industrial setting to determine further the optimal ratio between these two concentrations. This would be particularly important in the case where the lowest concentration of additive possible is favourable in the crystallisation process.

7.6 Conclusions

The benchmarking experiments showed that both workflows provide structured and logical approaches to the challenges they have been developed to solve. The decision points work well within the experimental process, allowing for the research to move on in a smooth and effective way. The workflows offer a reproducible approach to process design, harnessing the strength of experimental data alongside the computational modelling elements included in the steps. The use of early intervention, at the primary particle stage of development in pharmaceutical manufacturing, can result in a reduction of process steps, including downstream processing requirements, and allow for the design of optimised particle properties. Evaluation of the potential of any additional steps at the primary particle stage is necessary as they may not be considered the ‘first choice fix’ in process development but may offer significant benefits over other downstream interventions. The approach from the workflows discussed places an increased importance on the early stage design of a crystallisation processes. In addition, the workflows allow a more targeted screening approach, reducing the experimental screening required before an appropriate decision can be made, saving both time and money for the researchers and manufacturers.

Benchmarking with both MFA and FA have demonstrated the versatility of the workflows created and confirmed the decision points are appropriately placed within the workflow. Whilst the research on additive intervention in changing morphology was unsuccessful with both target molecules investigated here, the workflow allowed for this decision to be made and the research to cease in a timely manner. It was also evident that the successful additive-induced morphology modification produced for IZN in chapter 4 followed and exemplified the first five stages of the workflow methodology. The benchmarking research highlighted a possible change that would need to be made in step 3 of the additive workflow; 'Determine API solubility with additives'. This step would be better placed towards the end of the workflow, after step 7, due to the unnecessary time this step would take and the excess data it would have the potential to generate. Moving step 3 would also require decision 2 to be moved and result in a potential re-wording of decision 4. This change was discussed with other researchers and industry members, confirming the step was not completely necessary in the early stages of the workflow and could be moved as suggested. As the workflow is a guide document, this step could be included at the discretion of the researchers carrying out the screening, depending on their specific requirements.

Further benchmarking tests could be useful to gain a more detailed understanding of the workflows. These could include research into controlling other physical properties, such as polymorphic form or PSD. In addition, initial screening steps should be carried out using different crystallisation methods, such as small scale controlled cooling crystallisation. Evaporative crystallisation is quick to set up and allows many screening experiments to be carried out in parallel, however, is not a controllable method of crystallisation and often gives a large variation of results in the same experiment. Whilst this is often enough to suggest where a success may occur, it can cause useful results to be missed. Carrying out benchmarking tests using small scale controlled cooling crystallisations may allow for more repeatable experiments/results and allow for easier scale-up procedures in the later steps of the workflow. Finally, the development of some standard operating procedures for the key steps in the workflow may be beneficial in allowing researchers to carry out easily repeatable experiments and ensure uniformity between different researchers and companies.

Chapter 8 Conclusions and future work

8.1 Conclusions

The work presented in this thesis shows the results of investigations into optimising the particle morphology of pharmaceutically active ingredients IZN and PYR, with the particular aim of achieving a more block shaped crystal as opposed to the needles usually produced for IZN and PYR. Various methods were utilised to influence the morphology of the crystals produced, including additives and solvent effects. Both size-matched and polymeric additives were used in small quantities as intentionally added impurities in the crystallisations. In addition, an investigation into the creation of new multi-component materials was also carried out in an attempt to form more block shaped morphologies.

The solvent effects on IZN are significant, with a number of morphological changes achieved. Initial evaporative crystallisations in EtOAc and ACN produced thickened rod block shaped crystals, a significant change from the thin needles previously observed in H_2O. In cooling crystallisations, EtOH and IPA showed thin plate-shaped crystals; a significant morphology change but not as favourable. The rod-shaped crystals achieved in EtOAc could also be accessed in cooling crystallisations, however, the ACN effects were not observed in cooling, with needle-shaped crystals resulting. Further research was carried out on EtOAc, which showed the most favourable change, and IPA solvent effects. It was proven that the morphology changes observed were repeatable via a number of different cooling crystallisation methods, including in the KRAIC continuous platform. The ease of transfer from evaporative to small scale cooling to large scale continuous methods shows the versatility of the changes achieved using different solvents. This is particularly useful for pharmaceutical applications as it allows for easier implementation into already existing crystallisation processes.

The effect of supersaturation on the morphology was investigated using the above solvents. It was determined to be possible to achieve the same morphology observed in cooling in evaporative crystallisations, depending on the starting saturation used. Plate-shaped crystals were observed for IPA in evaporative crystallisations at higher starting concentrations of IZN. The same effects were not observed in cooling crystallisation. The increase in starting supersaturation in cooling only serves to increase the amount of crystallisation occurring, not the morphology achieved. The lack of influence on cooling morphologies also points to the robust nature of this method and the ease of the potential implementation into already existing pharmaceutical manufacturing processes.

The most favourable solvent effect can be attributed to EtOAc crystallisations. Upon indexing the faces, the morphology closely resembles that predicted using BFDH calculations. The major growth mechanism seems to still be as a result of the aromatic interactions between the rings in the IZN molecules. The solvent prevents this happening as fast as observed in H_2O, meaning the needle does not grow as long and can fatten up; the slow growing faces have been allowed to catch up. This is likely due to the reduction in polarity of the solvent. In contrast, H_2O is a strongly polar solvent and is therefore likely to interact with the polar, hydrogen bonding groups that exist on the slow growing faces. This blocks the approach of growth units, meaning they are more likely to join the growing crystal on the fast growing face. In a less polar solvent such as EtOAc, there is less interruption to growth on the slower growing faces from the solvent molecules, allowing these faces to catch up a bit with the fast growing needle axis faces.

Studies carried out in solvents with PYR show very little influence of the solvent used on the morphology achieved. All solvents used give needle crystals. Due to low solubility in other solvents, the number of solvents used in this screen was limited. A wider screen is necessary to rule this out definitively as a possible route. This could initially be done computationally using methods currently employed with CMAC.

Investigations into size-matched additives effects on IZN yielded two potential candidates for further experimentation: 3-HBA and 3,4-DNBA. Initial evaporative investigations carried out will small additive percentages of 1%, 5% and 10% showed positive morphology changes with 1% of the additive. The addition of these additives allowed thickened, rod-shaped crystals to result, where previously thin plate-shaped crystals were observed. The morphology achieved in IPA in the presence of these additives closely resembles the morphology observed from crystallisations in EtOAc. Transfer of these effects from evaporative crystallisation to cooling crystallisation proved difficult, with a number of different conditions and platforms attempted. The scale up was eventually achieved at a 200 mL scale in the Polar Bear Plus crystalliser, with the 250 mL round-bottomed flask insert. The success of the crystallisation can be attributed to the use of overhead stirring. Cooling crystallisations at the same scale without overhead stirring still yielded plate-shaped crystals observed in IPA alone. The stirring with influence the kinetics of the crystallisation, potentially responsible for the more favourable morphology change achieved. More research into the kinetics is required to fully understand the influence of the stirring on the growth morphologies achieved in the presence of additives in cooling crystallsations. Transfer of the size-matched additive effects into continuous cooling platform the KRAIC, was also unsuccessful. Conventional stirring is also not possible in this continuous platform, considered the likely reason for the limited success given the outcomes of the batch cooling investigation. As a result, further experiments into other continuous methods should be carried out.

A condition the pharmaceutical industry must consider when investigating the use of additives to influence morphology, is the possible inclusion of the additive into the crystal structure. As the additives used here are size-matched the possibility exists that the additive could be included into the crystal structure, forming a new multi-component material. This would be an unfavourable outcome as the new crystal form would need to go through rigorous testing and approval before being marketed to the public. As such, additives are treated as impurities and must be below the threshold set up by the regulatory bodies. Upon using SCXRD, PXRD, DSC and NMR spectroscopy to analyse the final crystal products, no trace of the additive was determined in the crystal structure or left behind in the bulk sample. These results suggest the additive was in sufficiently low concentrations to remain in solution and be filtered out when the crystals were isolated from the mother liquor. However, these analysis techniques are not the most sensitive ones that could be carried out. As a result, to take this forward a pharmaceutical company would need to use other techniques to quantify exactly how much, if any, of the additive remained in the crystalline samples produced.

No influence of polymeric additives on the morphology of IZN has been determined within the scope of the screens carried out in this thesis. For the selection of additives investigated here, no successful morphology change was observed. The polymers showed no sign of influencing the morphology in either cooling or evaporative platforms. The correct polymer may not yet have been found and so further investigation into this could be considered.

Crystallisations carried out in the presence of both size-matched and polymeric additives were deemed unsuccessful with PYR, showing no evidence of any morphology changes being achieved in their presence. This closely mimics what was observed in the different solvent screens attempted for PYR. This further suggests PYR is less prone to changes to the growth mechanisms present. Further additives could be investigated for PYR, however, care should be taken not to spend too much time as the screens already carried out point to this being an unsuccessful venture.

Research into the creation of new multi-component materials of IZN found three new structures with different enantiomeric combinations of tartaric acid and a new co-crystalline structure with 3,4-DNBA. All the new multi-component forms with IZN were determined to have thin plate morphologies. The change seen in the TA co-crystals was significant as the crystallisations were carried out in water, which previously only yielded very thin needle crystals. The 3,4-DNBA co-crystal was crystallised from IPA, which also yields a plate-shaped crystal without the co-former molecule. Upon analysing other physical properties of the new co-crystals, their solubility was determined to be lower than that observed for pure IZN. This could be considered a possible negative effect of the formation of the multi-component structures. All new co-crystals showed a solubility relationship mimicking that of monotropic polymorphs. Stability analysis experiments, humidity studies, slurry studies and temperature studies, confirmed all forms were stable with respect to the conditions subjected to for extended periods of time. The exception being the DLTA hydrated crystal. When subjected to high temperatutes the crystal structure fully converted to a dehydrated crystalline form after approximately 1 week. This dehydrated crystal was shown to rehydrate when slurried in water. However, this transition is believed not to be fully reversible due to the shrinking in the crystal unit cell parameters on dehydration. The rehydration is likely the result of the dehydrated co-crystal dissolving and reincorporating the water molecules upon recrystallisation.

The co-crystalline products produced with IZN were all easily scaled up in batch cooling crystallisations and large scale slurry experiments. In addition, the crystallisation products of the scaled up experiments maintained a good conversion of starting materials, with no trace remaining in the DSC or PXRD data obtained.

Whilst limited success was observed in attempts to change the morphology of PYR using additives and solvent, some success was observed upon the creation of multi-component materials. Throughout the research presented here three new co-crystalline structures of PYR were discovered, all exhibiting favourable morphology changes. New multi-component crystal structures were found with 2,4-DNBA, 3,5-DNBA, TRI and PtA.

Similar to the co-crystals produced with IZN, the solubility of each of the new PYR crystal forms produced was much lower than pure PYR. Whilst a reduction in solubility is generally considered detrimental to pharmaceutical applications, if it remains over a certain threshold it may be a compromise worth considering to achieve a beneficial morphology change that will improve manufacturing processes. The co-crystals were all determined to be stable with respect to the studies carried out, high temperature, high humidity and slurry experiments, with the exception of the PYR:2,4-DNBA co-crystal. During slurry experiments in water a new polymorphic form of the co-crystal (form II) was discovered. It was not possible to determine the thermodynamic form using traditional physical properties, such as melting points or solubility, as the difference between the two polymorphs was negligible. As a result, competitive slurry and co-grinding experiments were carried out. These both showed full conversion from form I to form II (within 2 hours for the slurry experiment). Consequently, form II was determined to be thermodynamically more stable. Although it should be noted their stabilities are very similar and another, more stable, form could be possible.

The morphology change observed for the PYR:2,4-DNBA co-crystals was significant, with an irregular block shaped crystal as opposed to the needles previously observed in IPA. The co-former causes a different hydrogen bonding network to be present in the structure reducing the strength of the π-π-interactions between the aromatic rings. A fattened, plate-shaped crystal is observed for PYR:3,5-DNBA co-crystals. This is much closer to a block shape and is a significant improvement on the usual needle morphology observed for pure PYR crystals. Whilst plate-shaped crystals are often unfavourable in processing, the fattened nature of those produced here suggests they could significantly improve the downstream processing steps required for production. The least beneficial morphology change was observed for the PYR:TRI co-crystal. Plate-shaped crystals are also seen here, although much thinner than for 3,5-DNBA. Whilst the change is still a major difference from the needles usually observed, the thin nature of the plates makes them difficult to process into the final pharmaceutical product. Finally, the PYR:PtA co-crystal also showed a plate shape morphology. It was not possible to face index these within the time constraints of this work due to equipment failure in the last 3 months of research.

Overall, the creation of PYR co-crystals has resulted in positive morphology changes not previously observed in additive or solvent experiments. The improvement is particularly beneficial in the case of the PYR:2,4-DNBA co-crystal, where an almost block shape is achieved. Although there would be difficulty obtaining FDA approval for crystals involving a secondary component, this would be the most promising method to utilise to change the morphology of the PYR crystals. No improvement was seen for either of the methods attempted which do not change the crystal structure of the API; both additives and solvent showed no influence on the growth shapes. In contrast to the conclusions made about IZN, the formation of multi-component crystal structures is more successful in morphology modification and would be a good route for further investigation, despite the difficulties potentially faced when seeking approval.

Overall, the creation of multi-component materials of IZN and PYR has resulted in morphology changes of the crystals. This is especially clear when comparing the needles previously achieved from crystallisations in. In terms of PYR the changes seen upon co-crystallisation are a major improvement, particularly in the case of PYR:2,4-DNBA. No changes were observed for additive crystallisations with PYR so the creation of multi-component materials would be the best method to pursue for this API. An attempt should be made to find some successful GRAS co-formers in order to allow their approval by the FDA. For IZN, the plate-shaped morphologies achieved as not as beneficial in easing the downstream processing steps as the morphology changes achieved via solvent and additive interventions. The difficulty obtaining FDA approval for the secondary component would not be a worthwhile venture for IZN, as the improvements in the morphology are not substantial enough. The addition of the secondary component has also significantly reduced the solubility when compared to pure IZN, this is often extremely unfavourable in the pharmaceutical industry. More significant improvements for IZN were seen with the additives 3-HBA and 3,4-DNBA and in the solvent EtOAc. One of these routes would be best to take forward into pharmaceutical processes. When considering regulatory approval, the solvent effects may be favoured as there are no impurities to quantify in the final product. However, once the amount of additive remaining is quantified, and if this falls below the threshold, this may be the more favoured route due to better reproducibility of the morphologies achieved.

8.2 Future work

In the research carried out here, it was shown significant morphological changes in IZN crystals could be achieved in the presence of small wt% of both 3-HBA and 3,4-DNBA additives, when crystallised from IPA. In the process of scaling up these crystallisations the influence of overhead stirring was determined to have a significant impact on the success of the crystallisations carried out. Further, in depth research into the reasons behind this could help achieve similar outcomes in other similar molecules, for example PYR. Experiments which probe the kinetics of the crystallisation could help determine why the stirring has such an influence on the morphology achieved in cooling.

Determining the influence of the stirring may also aid in the transfer of the additive effects into continuous platforms. The research carried in the KRAIC continuous crystallisation platform was unsuccessful in achieving the desired morphology change in the presence of additives. Due to the apparent importance of stirring, the potential for success exists in a platform such as a cSTR. As this set up involves a series of stirred tanks it could allow for the correct kinetic conditions to be achieved which allow the crystal growth to achieve the desired morphology change.

It is also important to quantify whether any additive remains within the crystal structure or on the surface of the crystals, particularly in the case where pharmaceutical applications are being considered. DSC, PXRD and NMR spectroscopy studies were carried out and showed no presence of the additives, however, there are other methods with better detection limits which could prove otherwise. A series of HPLC experiments should be carried out to help determine the percentages of additive, if any, that remain within the crystalline sample after filtration and drying. If a successful polymeric additive was determined, SEM could be used to investigate whether any additive remains on the surface. This would not be necessary in the case of IZN as the successful additives were all size-matched and, therefore, more prone to inclusion in the crystal structure.

Further research could also be carried out on PYR. None of the additives, size-matched or polymer, used so far have succeeded in causing a morphology change to occur. Other polymers and additives could be investigated in an attempt to achieve this. However, care should be taken as extensive screening has already been carried out with little success suggesting further screening would also be unsuccessful.

Finally, if one of the co-crystalline products developed during the course of this research was deemed to have beneficial morphological and other physical properties for a pharmaceutical application, further research into the production via continuous methods should be attempted. The different conditions in the continuous platforms could cause properties such as morphology to change and would need to be quantified before moving forward with the choice into pharmaceutical applications.

Bibliography

1. B. M. Couillaud, P. Espeau, N. Mignet and Y. Corvis, *ChemMedChem*, 2019, **14**, 8-23.
2. https://www.cmac.ac.uk/Hub_Research.htm, (accessed 22/11/18, 2018).
3. D. B. Amabilino and X. Obradors, *Chemical Society Reviews*, 2009, **43**, 2009-2012.
4. R. J. Davey and J. Garside, *From Molecules to Crystallizers: An Introduction to Crystallization*, Oxford University Press Inc., New York, United States, 2000.
5. X-W. Ni, *The Chemical Engineer*, 2008, 36-38.
6. W. Beckmann, in *Crystallization: Basic Concepts and Industrial Applications*, ed. W. Beckmann, Wiley-VCH Weinheim, Germany, 2013, ch. 2, pp. 7-34.
7. S. Lawton, G. Steele, P. Shering, L. Zhao, I. Laird and X-W. Ni, *Organic Process Research & Development*, 2009, **13**, 1357–1363.
8. F. Pfannkuch, H. Rettig and P. H. Stahl, in *Handbook of Pharmaceutical Salts: Properties, Selection and Use*, eds. P. H. Stahl and C. G. Wermuth, Wiley-VCH, Weinheim, Germany, 2002, ch. 5, pp. 117-134.
9. S. S. Kadam, H. J. M. Kramer and J. H. ter Horst, *Crystal Growth & Design*, 2011, **11**, 1271-1277.
10. S. Lohani and D. J. W. Grant, in *Polymorphism in the Pharmaceutical Industry*, ed. R. Hilfiker, Wiley-VCH Weinham, Germany, 2006, ch. 2, pp. 21-42.
11. R. J. Davey, S. L. M. Schroeder and J. H. ter Horst, *Angewandte Chemie*, 2013, **52**, 2166-2179.
12. H-H. Tung, E. L. Paul, M. Midler and J. A. McCauley, in *Crystallization of Organic Compounds: An Industrial Perspective*, John Wiley & Sons, Hoboken, New Jersey, 2009, ch. 4, pp. 77-100.
13. J. W. Mullin, in *Crystallization*, Butterworth-Heinmann, Oxford, 4 edn., 2001, ch. 5, pp. 181-215.
14. M. Mazzotti, T. Vetter, D. R. Ochsenbein, G. M. Maggioni and C. Lindenberg, in *Polymorphism in the Pharmaceutical Industry: Solid From and Drug Development*, eds. R. Hilfiker and M. V. Raumer, Wiley-VCH Weinhein, Germany, 2018, ch. 9, pp. 261-283.
15. G. Coquerel, in *Polymorphism in the Pharmaceutical Industry: Solid Form and Drug*, eds. R. Hilfiker and M. v. Raumer, Wiley-VCH Weinham, Germany, 2018, ch. 4, pp. 91-132.
16. L. Cronin, P. J. Kitson and C. C. Wilson, in *Process Understanding: For Scale-Up and Manufacture of Active Ingredients*, ed. I. Houson, Wiley-VCH Weinham, Germany, 2011, ch. 7, pp. 199-225.
17. J. W. Mullin, in *Crystallization*, Butterworth-Heinemann, Oxford, 4 edn., 2001, ch. 6, pp. 216-284.
18. A. S. Myerson and R. Ginde, in *Handbook of Industrial Crystallization*, ed. A. S. Myerson, Butterworth-Heinemann, 2002, ch. 2, pp. 33-65.
19. M. A. Lovette, A. Robben Browning, D. W. Griffin, J. P. Sizemore, R. C. Snyder and M. F. Doherty, *Industrial & Engineering Chemistry Research*, 2008, **47**, 9812 - 9833.
20. P. Dandekar, Z. B. Kuvadia and M. F. Doherty, *Annual Review of Materials Research*, 2013, **43**, 359-386.
21. M. A. Lovette and M. F. Doherty, *Crystal Growth & Design*, 2013, **13**, 3341-3352.
22. S. Datta and D. J. W. Grant, *Nature Reviews Drug Discovery*, 2004, **3**, 42-57.
23. D. R. Ochsenbein, T. Vetter, S. Schorsch, M. Morari and M. Mazzoti, *Crystal Growth & Design*, 2015, **15**, 1923-1933.
24. N. Pudasaini, P. P. Upadhyay, C. R. Parker, S. U. Hagen, A. D. Bond and J. Rantanen, *Organic Process Research & Development*, 2017, **21**, 571-577.
25. S. Mirza, I. Miroshnyk, J. Heinamaki, O. Antikainen, J. Rantanen, P. Vuorela, H. Vuorela and J. Yliruusi, *AAPS PharmSciTech*, 2009, **10**, 113-119.
26. P. York, *International Journal of Pharmaceuticals*, 1983, **14**, 1-28.

27. Z. Berkovitch-Yellin, *Journal of American Chemical Society*, 1985, **107**, 8239 - 8253.
28. H. A. Moynihan and D. E. Horgan, *Organic Process Research & Development*, 2017, **21**, 689-704.
29. R. J. Davey, N. Blagdon, G. D. Potts and R. Docherty, *Journal of American Chemical Society*, 1997, **119**, 1767-1772.
30. S. K. Poornachary, P. S. Chow and R. B. H. Tan, *Crystal Growth & Design*, 2008, **8**, 179-185.
31. X. He, J. G. Stowell, K. R. Morris, R. R. Pfeiffer, H. Li, G. P. Stahly and S. R. Byrn, *Crystal Growth & Design*, 2001, **1**, 305-312.
32. E. Simone, G. Steele and Z. K. Nagy, *CrystEngComm*, 2015, **17**, 9370-9379.
33. A. D. Franklin, in *Point defects in crystals*, eds. J. H. Crawford and L. M. Slifkin, Springer, Boston, 1972, ch. 1, pp. 1-101.
34. J. D. Wright, in *Molecular Crystals*, Cambridge University Press, Cambridge, 2nd edn., 1995, ch. 4, pp. 50-70.
35. A. S. Narang and S. H. S. Boddu, in *Excipient Applications in Formulation Design and Drug Delivery*, eds. A. S. Narang and S. H. S. Boddu, Springer, Switzerland, 2015, ch. 1, pp. 1-10.
36. Z. B. Kuvadia and M. F. Doherty, *Crystal Growth & Design*, 2013, **13**, 1412-1428.
37. C. Schmidt, M. J. Jones and J. Ulrich, in *Crystallization: Basic Concepts and Industrial Principles*, ed. W. Beckmann, Wiley-VCH Weinheim, Germany, 2013, ch. 6.
38. M. Salvalaglio, T. Vetter, F. Giberti, M. Mazzotti and M. Parrinello, *Journal of American Chemical Society*, 2012, **134**, 17221-17233.
39. L. Addadi, Z. Berkovitch-Yellin, N. Domb, E. Gati, M. Lahav and L. Leiserowitz, *Nature*, 1982, **296**, 21-26.
40. L. Addadi, Z. Berkovitch-Yellin, I. Weissbuch, M. Lahav, L. Leiserowitz and S. Weinstein, *Journal of American Chemical Society*, 1982, **104**, 2075-2077.
41. Z. Berkovitch-Yellin, L. addadi, M. Idelson, M. Lahav and L. Leiserowitz, *Angewandte Chemie*, 1982, **21**, 1336-1345.
42. L. Addadi, Z. Berkovitch-Yellin, I. Weissbuch, M. Lahav and L. Leiserowitz, *Molecular Crystals and Liquid Crystals*, 1983, **96**, 1-17.
43. Z. Berkovitch-Yellin, J. v. Mil, L. Addadi, M. Idelson, M. Lahav and L. Leiserowitz, *Journal of American Chemical Society*, 1985, **107**, 3111-3122.
44. C. Thompson, M. C. Davies, C. J. Roberts, S. J. B. Tendler and M. J. Wilkinson, *International Journal of Pharmaceuticals*, 2004, **280**, 137-150.
45. B. A. Hendrikson, D. J. W. Grant, P. Meenan and D. A. Green, *Journal of Crystal Growth*, 1998, **183**, 629-640.
46. G. M. Clydesdale, K. J. Roberts and R. Docherty, *Journal of Crystal Growth*, 1994, **135**, 331-340.
47. R. Davey, W. Fila and J. Garside, *Journal of Crystal Growth*, 1986, **79**, 607-613.
48. C-H. Gu, K. Chatterjee, V. Y. Jr. and D. J. W. Grant, *Journal of Crystal Growth*, 2002, **235**, 471-481.
49. L. Yu, S. M. Reutzel-Edens and C. A. Mitchell, *Organic Process Research & Development*, 2000, **4**, 396-402.
50. M. Kitamura and T. Ishizu, *Journal of Crystal Growth*, 1998, **192**, 225-235.
51. L. H. Thomas, C. Wales, L. Zhao and C. C. Wilson, *Crystal Growth & Design*, 2011, **11**, 1450-1452.
52. L. R. Agnew, T. McGlone, H. P. Wheatcroft, A. Robertson, A. R. Parsons and C. C. Wilson, *Crystal Growth & Design*, 2017, **17**, 2418-2427.
53. Y. Liu, B. Gabriele, R. J. Davey and A. J. Cruz-Cabeza, *Journal of American Chemical Society*, 2020, **142**, 6682-6687.
54. C. J. Schram, S. P. Beaudoin and L. S. Taylor, *Crystal Growth & Design*, 2016, **16**, 2094-2103.

55. D. E. Alonzo, S. Raina, D. Zhou, Y. Gao, G. G. Z. Zhang and L. S. Taylor, *Crystal Growth & Design*, 2012, **12**, 1538-1547.
56. G. A. Ilevbare, H. Liu, K. J. Edgar and L. S. Taylor, *CrystEngComm*, 2012, **14**, 6503-6514.
57. C. J. Schram, S. P. Beaudoin and L. S. Taylor, *Langmuir*, 2015, **31**, 171-179.
58. C. J. Schram, L. S. Taylor and S. P. Beaudoin, *Langmuir*, 2015, **31**, 11279-11287.
59. T. Vetter, M. Mazzotti and J. Brozio, *Crystal Growth & Design*, 2011, **11**, 3813-3821.
60. G. A. Ilevbare, H. Liu, K. J. Edgar and L. S. Taylor, *Crystal Growth & Design*, 2012, **12**, 6050-6060.
61. G. A. Holder and J. Winkler, *Nature*, 1965, **207**, 719-721.
62. S. Xie, S. K. Poornachary, P. S. Chow and R. B. H. Tan, *Crystal Growth & Design*, 2012, **10**, 3363-3371.
63. A. R. Klapwijk, E. Simone, Z. K. Nagy and C. C. Wilson, *Crystal Growth & Design*, 2016, **16**, 4349-4359.
64. E. Simone, A. R. Klapwijk, C. C. Wilson and Z. K. Nagy, *Crystal Growth & Design*, 2017, **17**, 1695-1706.
65. E. Simone, M. V. Cenzato and Z. K. Nagy, *Journal of Crystal Growth*, 2016, **446**, 50-59.
66. E. Staab, L. Addadi, L. Leiserowitz and M. Lahav, *Advanced Materials*, 1990, **2**, 40-43.
67. V. López-Mejías, J. W. Kampf and A. J. Matzger, *Journal of American Chemical Society*, 2009, **131**, 4554-4555.
68. M. Lang, A. L. Grzesiak and A. J. Matzger, *Journal of American Chemical Society*, 2002, **124**, 14834-14835.
69. C. P. Price, A. L. Grzesiak and A. J. Matzger, *Journal of American Chemical Society*, 2005, **127**, 5512-5517.
70. J. Ulrich and C. Strege, *Journal of Crystal Growth*, 2002, **237**, 2130-2135.
71. N. Rodríguez-Hornedo and D. Murphy, *Journal of Pharmaceutical Sciences*, 1999, **88**, 651-660.
72. A. Saleemi, I. I. Onyemelukwe and Z. K. Nagy, *Frontiers of Chemical Science and Engineering*, 2013, **7**, 79-87.
73. R. Duro, C. Souto, J. L. Gómez-Amoza, R. Martínez-Pacheco and A. Concheiro, *Drug Development and Industrial Pharmacy*, 1999, **25**, 817-829.
74. R. J. Davey, *Journal of Crystal Growth*, 1976, **34**, 109-119.
75. R. J. Davey and J. W. Mullin, *Journal of Crystal Growth*, 1974, **26**, 45-51.
76. N. Kubota and J. W. Mullin, *Journal of Crystal Growth*, 1995, **152**, 203-208.
77. N. Kubota, *Crystal Research and Technology*, 2001, **36**, 749-769.
78. N. Kubota, M. Yokota, L. A. Guzman, S. Sasaki and J. W. Mullin, *Crystal Growth & Design*, 2003, **3**, 397-402.
79. T. A. Land, T. L. Martin, S. Potapenko, G. T. Palmore and J. J. D. Yoreo, *Nature*, 1999, **399**, 442-445.
80. L. N. Rashkovich and N. V. Kronsky, *Journal of Crystal Growth*, 1997, **182**, 434-441.
81. P. M. Martins, F. A. Rocha and P. Rein, *Crystal Growth & Design*, 2006, **2006**, 12.
82. K. Sangwal, *Journal of Crystal Growth*, 1999, **203**, 197-212.
83. P. M. Martins, F. Rocha, A. M. Damas and P. Rein, *CrystEngComm*, 2011, **13**, 1103-1110.
84. A. Borsos, A. Majumder and Z. K. Nagy, *Crystal Growth & Design*, 2016, **16**, 555-568.
85. P. Hartman and P. Bennema, *Journal of Crystal Growth*, 1980, **49**, 145-156.
86. R. Docherty, G. Clydesdale, K. J. Roberts and P. Bennema, *Journal of Applied Physics D: Applied Physics*, 1991, **24**, 89-99.
87. J. P. Sizemore and M. F. Doherty, *Crystal Growth & Design*, 2009, **9**, 2637-2645.
88. R. L. M. Robinson, D. Geatches, C. Morris, R. Mackenzie, A. G. P. Maloney, K. J. Roberts, A. Moldovan, E. Chow, K. Pencheva and D. R. M. Vatvani, *journal of Chemical Information and Modeling*, 2019, **59**, 4778-4792.

89. C. J. Tilbury, D. A. Green, W. J. Marshall and M. F. Doherty, *Crystal Growth & Design*, 2016, **16**, 2590-2604.
90. Y. Wang and Z. Liang, *CrystEngComm*, 2017, **19**, 3198-3205.
91. R. Adhiyaman and S. K. Basu, *International Journal of Pharmaceutics*, 2006, **321**, 27-34.
92. Z. Liang, J-F. Chen, Y. Ma, W. Wang, X. Han, C. Xue and H. Zhao, *CrystEngComm*, 2014, **16**, 5997-6002.
93. S. K. A. Mudalip, M. R. A. Bakar, P. Jamal, F. Adam, R. C. Man, S. Z. Sulaiman, Z. I. M. Arshad and S. M. Shaarani, *MATEC Web of Conferences* 2018, **150**, 1-6.
94. T. B. Hansen, A. Taris, B-G. Rong, M. Grosso and H. Qu, *Journal of Crystal Growth*, 2016, **450**.
95. C-H. Gu, V. Y. Jr. and D. J. W. Grant, *Journal of Pharmaceutical Sciences*, 2001, **90**, 1878-1890.
96. H. Gu, R. Li, Y. Sun, S. Li, W. Dong and J. Gong, *Journal of Crystal Growth*, 2013, **373**, 146-150.
97. I. Rosbottom, C. Y. Ma, T. D. Turner, R. A. O'Connell, J. Loughrey, G. Sadiq, R. J. Davey and K. J. Roberts, *Crystal Growth & Design*, 2017, **17**, 4151-4161.
98. J. H. ter Horst, R. M. Geertman and G. M. v. Rosmalen, *Journal of Crystal Growth*, 2001, **230**, 277-284.
99. T. T. H. Nguyen, I. Rosbottom, I. Marziano, R. B. Hammond and K. J. Roberts, *Crystal Growth & Design*, 2017, **17**, 3088-3099.
100. D. Han, T. Karmakar, Z. Bjelobrk, J. Gong and M. Parrinello, *Chemical Engineering Science*, 2018, **In Press**.
101. J. D. H. Donnay and D. Harker, *American Mineralogist*, 1937, **22**, 446-467.
102. V. Bisker-Leib and M. F. Doherty, *Crystal Growth & Design*, 2001, **1**, 455-461.
103. V. Bisker-Leib and M. F. Doherty, *Crystal Growth & Design*, 2003, **3**, 221-237.
104. P. Hartman and W. G. Perdock, *Acta Crystallographica*, 1995, **8**, 49-52.
105. D. Wieckhusen, in *Crystallization: Basic Concepts and Industrial Approach*, ed. W. Beckmann, Wiley-VCH, Weinheim, Germany, 2013, ch. 10, pp. 187-201.
106. T. Friscic and W. Jones, *Crystal Growth & Design*, 2008, **9**, 1621-1637.
107. D. R. Weyna, T. Shattock, P. Vishweshwar and M. J. Zaworotko, *Crystal Growth & Design*, 2009, **9**, 1106-1123.
108. T. Rager and R. Hilfiker, *Crystal Growth & Design*, 2010, **10**, 3237-3241.
109. W. Beckmann, in *Crystallization: Basic Concepts and Industrial Applications*, ed. W. Beckmann, Wiley-VCH Weinham, Germany, 2013, ch. 1, pp. 1-6.
110. B. Nienhaus, in *Crystallization: Basic concepts and Industrial Applications*, ed. W. Beckmann, Wiley-VCH, Weinheim, Germany, 2013, ch. 13, pp. 247-273.
111. K. Plumb, *IChemE*, 2005, **83**, 730-738.
112. J. Chen, B. Sarma, J. M. B. Evans and A. S. Myerson, *Crystal Growth & Design*, 2011, **11**, 887-895.
113. T. McGlone, N. E. B. Briggs, C. A. Clark, C. J. Brown, J. Sefcik and A. J. Florence, *Organic Process Research & Development*, 2015, **19**, 1186-1202.
114. K. Robertson, P.-B. Flandrin, A. R. Klapwijk and C. C. Wilson, *Crystal Growth & Design*, 2016, **16**, 4759-4764.
115. J. Leng and J-B. Salmon, *Lab on a Chip*, 2009, **9**, 24-34.
116. H-H. Tung, E. L. Paul, M. Midler and J. A. McCauley, in *Crystallization of Organic Compounds: an Industrial Perspective*, John Wiley & Sons Hoboken, New Jersey, 2009, ch. 1, pp. 1-13.
117. M. D. Cohen, G. M. J. Schmidt and F. I. Sonntag, *Journal of the Chemical Society - Chemical Communications*, 1964, 2000-2013.
118. G. R. Desiraju, *Journal of the American Chemical Society*, 2013, **135**, 9952-9967.
119. B. Moulton and M. J. Zaworotko, *Chemical Reviews*, 2001, **101**, 1629-1658.
120. G. R. Desiraju, *Journal of Molecular Structure*, 2003, **656**, 5-15.

121. K. Biradha, *CrystEngComm*, 2003, **5**, 374-384.
122. A. Burrows, J. Holman, A. Parsons, G. Pilling and G. Price, *Chemistry^3*, Oxford University Press, Oxford, 2nd edn., 2013.
123. E. Arunan, G. R. Desiraju, R. A. Klein, J. Sadlej, S. Scheiner, I. Alkorta, D. C. Clary, R. H. Crabtree, J. J. Dannenberg, P. Hobza, H. G. Kjaergaard, A. C. Legon, B. Mennucci and D. J. Nesbitt, *Pure and Applied Chemistry*, 2011, **83**, 1637-1641.
124. C. E. Housecroft and A. G. Sharpe, *Inorganic Chemistry*, Pearson Education Ltd, Harlow, Essex, 4th edn., 2012.
125. A. Lemmerer, J. Bernstein and V. Kahlenbergb, *CrystEngComm*, 2010, **12**, 2856-2864.
126. M. C. Etter, *Accounts of Chemical Research*, 1990, **23**, 120-126.
127. G. A. Jeffrey, *An Introduction of Hydrogen Bonding*, Oxford University Press, New York, 1 edn., 1997.
128. G. R. Desiraju and T. Steiner, in *The Weak Hydrogen Bond: In Structural Chemistry and Biology*, Oxford University Press, New York, 1999, pp. 1-28.
129. C. A. Hunter and J. K. M. Sanders, *Journal of American Chemical Society*, 1990, **112**, 5535-5534.
130. C. R. Martinez and B. L. Iverson, *Chemical Science*, 2012, **3**, 2191–2201.
131. A. D. McNaught and A. Wilkinson, *IUPAC. Compendium of Chemical Terminology - Gold book XML on-line corrected version 2.3.3*, Blackwell Scientific Publications, Oxford, 1997.
132. P. Atkins and J. de Paula, in *Elements of Physical Chemistry*, Oxford University Press, New York, 7 edn., 2017, ch. 10, pp. 427-446.
133. L. R. Agnew, D. L. Cruickshank, T. McGlone and C. C. Wilson, *Chemical Communications*, 2016, **52**, 7368-7371.
134. C. B. Aakeroy and N. Schultheiss, in *Making Crystals by Design: Methods, Techniques and Applications*, eds. D. Braga and F. Grepioni, Wiley-VCH, Weinheim, Germany, 2007, ch. 2.5, pp. 209-235.
135. C. F. Macrae, I. J. Bruno, J. A. Chisholm, P. R. Edgington, P. McCabe, E. Pidcock, L. Rodriguez-Monge, R. Taylor, J. v. d. Streek and P. A. Wood, *Journal of Applied Crystallography*, 2008, **41**, 466-470.
136. C. R. Groom, I. J. Bruno, M. P. Lightfoot and S. C. Ward, *Acta Crystallographica*, 2016, **B72**, 171-179.
137. I. J. Bruno, J. C. Cole, P. R. Edgington, M. Kessler, C. F. Macrae, P. McCabe, J. Pearson and R. Taylor, *Acta Crystallographica*, 2002, **B58**, 389-397.
138. C. F. Macrae, I. Sovago, S. J. Cottrell, P. T. A. Galek, P. McCabe, E. Pidcock, M. Platings, G. P. Shields, J. S. Stevens, M. Towler and P. A. Wood, *Journal of Applied Crystallography*, 2020, **53**, 226-235.
139. P. T. A. Galek, F. H. Allen, L. Fábián and N. Feeder, *CrystEngComm*, 2009, **11**, 2634-2639.
140. P. T. A. Galek, L. Fábián and F. H. Allen, *CrystEngComm*, 2010, **12**, 2091-2099.
141. P. T. A. Galek, L. Fábián, W. D. S. Motherwell, F. H. Allen and N. Feeder, *Acta Crystallographica*, 2007, **63**, 768-782.
142. L. Fábián, *Crystal Growth & Design*, 2009, **9**, 1436-1443.
143. S. Karki, T. Friščić, L. Fábián and W. Jones, *CrystEngComm*, 2010, **12**, 4038-4041.
144. E. Pidcock and W. D. S. Motherwell, *Chemical Communications*, 2003, **24**, 3028-3029.
145. H-H. Tung, E. L. Paul, M. Midler and J. A. McCauley, in *Crystallization of Organic Compounds: an Industrial Perspective*, John Wiley & Sons, Hoboken, New Jersey, 2009, ch. 3, pp. 49-76.
146. H. G. Brittain, in *Polymorphism in Pharaceutical Solids*, ed. H. G. Brittain, Informa Healthcare USA, Inc, New York, USA, 2009.
147. J. Bauer, S. Spanton, R. Henry, J. Quick, W. Dziki, W. Porter and J. Morris, *Pharmaceutical Research*, 2001, **18**, 859-866.

148. S. L. Childs, G. P. Stahly and A. Park, *Molecular Pharmaceutics*, 2007, **4**, 323-338.
149. C. G. Wermuth and P. H. Stahl, in *Handbook of Pharmaceutical Salts: Properties, Selection and Use*, eds. P. H. Stahl and C. G. Wermuth, Wiley-VCH, Weinheim, Germany, 2008, ch. Introduction, pp. 1-8.
150. C. B. Aakeroy and D. J. Salmon, *CrystEngComm*, 2005, **7**, 439-448.
151. G. R. Desiraju, *Journal of Chemical Sciences*, 2010, **122**, 667-675.
152. S. Aitipamula, R. Banerjee, A. K. Bansal, K. Biradha, M. L. Cheney, A. R. Choudhury, Gautam R. Desiraju, A. G. Dikundwar, R. Dubey, N. Duggirala, P. P. Ghogale, S. Ghosh, P. K. Goswami, N. R. Goud, R. R. K. R. Jetti, P. Karpinski, P. Kaushik, D. Kumar, V. Kumar, B. Moulton, A. Mukherjee, G. Mukherjee, A. S. Myerson, V. Puri, A. Ramanan, T. Rajamannar, C. M. Reddy, N. Rodriguez-Hornedo, R. D. Rogers, T. N. G. Row, P. Sanphui, N. Shan, G. Shete, A. Singh, C. C. Sun, J. A. Swift, R. Thaimattam, T. S. Thakur, R. K. Thaper, S. P. Thomas, S. Tothadi, V. R. Vangala, N. Variankaval, P. Vishweshwar, D. R. Weyna and M. J. Zaworotko, *Crystal Growth & Design*, 2012, **12**, 2147-2152.
153. N. Schultheiss and A. Newman, *Crystal Growth & Design*, 2009, **9**, 2950-2967.
154. H. D. Clarke, K. K. Arora, H. Bass, P. Kavuru, T. T. Ong, T. Pujari, L. Wojtas and M. J. Zaworotko, *Crystal Growth & Design*, 2010, **10**, 2152-2167.
155. G. R. Desiraju, *Journal of the Chemical Society - Chemical Communications*, 1991, 426-428.
156. A. L. Gillon, N. Feeder, R. J. Davey and R. Storey, *Crystal Growth & Design*, 2003, **3**, 663-673.
157. V. S. Minkov, A. A. Beloborodova, V. A. Drebushchak and E. V. Boldyreva, *Crystal Growth & Design*, 2014, **14**, 513-522.
158. World Health Organization, https://www.who.int/tb/areas-of-work/preventive-care/ltbi_faqs/en/, (accessed 16th July, 2020).
159. Y. L. Janin, *Bioorganic & Medicinal Chemistry*, 2007, **15**, 2479-2513.
160. D. J. Klein, S. Boukouvala, E. M. McDonagh, S. R. Shuldiner, N. Laurierie, C. F. Thorn, R. B. Altman and T. E. Klein, *Pharmacogenet Genomics*, 2016, **26**, 436-444.
161. WHO Expert Committee on the Use of Essential Drugs, *The Use of Essential Drugs: Ninth Report of the WHO Expert Committee (including the Revised Model List of Essential Drugs)*, World Health Organization, 2000.
162. K. Zhang, N. Fellah, A. G. Shtukenberg, X. Fu, C. Hu and M. D. Ward, *CrystEngComm*, 2020, **22**, 2075-2078.
163. G. A. Brewer, *Analytical Profiles of Drug Substances*, 1977, **6**, 183-258.
164. Institute of Medicine (US) Standing Committee, in *Dietary Reference Intakes for Thiamin, Riboflavin, Niacin, Vitamin B6, Folate, Vitamin B12, Pantothenic Acid, Biotin, and Choline*, National Academies Press, Washington (DC), USA, 1998, ch. 7.
165. 18th Expert Committee on the Selection and Use of Essential Medicines, *Inclusion of Fixed-dose combination tablet: isoniazid (INH) 300 mg + pyridoxine (Vitamin B6) 25 mg + sulfamethoxazole 800 mg + trimethoprim 160 mg*, World Health Organisation, 2011.
166. Sigma Aldrich, Pyridoxine, https://www.sigmaaldrich.com/catalog/product/sigma/p5669?lang=en&region=GB, (accessed 13th Oct, 2020).
167. W. Clegg, *Crystal Structure Determination*, Oxford University Press Inc., New York, United States, 1998.
168. C. Giacovazzo, in *Fundamentals of Crystallography*, ed. C. Giacavazzo, Oxford University Press Inc., New York, United States, 2002, ch. 1, pp. 1-64.
169. W. Clegg, *X-ray Crystallography*, Oxford University Press Inc, New York, United States, 2015.
170. M. T. Weller, *Inorganic Materials Chemistry*, Oxford University Press Inc, New York, United States, 1994.

171. A. Bond and W. Clegg, in *The 17th BCA/CCG Intensive Teaching School in X-Ray Structure Analysis*, Durham Univeristy, UK, 2019, ch. 4, pp. 4.1-4.22.
172. W. Clegg, A. J. Blake, R. O. Gould and P. Main, in *Crystal Structure and Analysis: Principles and Practice*, ed. W. Clegg, Oxford University Press Inc., New York, United States, 2001, ch. 3, pp. 24-41.
173. H. J. Shepherd, in *The 17th BCA/CCG Intensive Teaching School in X-Ray Structure Analysis*, Durham University, UK, 2019, ch. 6, pp. 6.1-6.29.
174. W. Clegg, A. J. Blake, R. O. Gould and P. Main, in *Crystal Structure and Analysis: Principles and Practice*, ed. W. Clegg, Oxford University Press Inc., New York, United States, 2001, ch. 4, pp. 42-49.
175. W. Clegg, A. J. Blake, R. O. Gould and P. Main, in *Crystal Structure and Analysis: Principles and Practice*, ed. W. Clegg, Oxford University Press Inc., New York, United States, 2001, ch. 1, pp. 1-9.
176. S. Parsons, in *The 17th BCA/CCG Intensive Teaching School in X-Ray Structure Analysis*, Durham University, UK, 2019, ch. 10, pp. 10.11-10.22.
177. G. M. Sheldrick, *Acta Crystallographica*, 2008, **A64**, 112-122.
178. G. M. Sheldrick, *Acta Crystallographica*, 2015, **A71**, 3-8.
179. W. Clegg, A. J. Blake, R. O. Gould and P. Main, in *Crystal Structure Analysis: Principles and Practice*, ed. W. Clegg, Oxford University Press Inc, New York, United States, 2001, ch. 9, pp. 102-118.
180. L. Palatinus, in *The 17th BCA/CCG Intensive Teaching School in X-Ray Structure Analysis*, Durham University, UK, 2019, ch. 12, pp. 12.11-12.19.
181. D. Viterbo, in *Fundamentals of Crystallography*, ed. C. Giacovazzo, Oxford University Press Inc., New York, United States, Second edn., 2002, ch. 6, pp. 413-503.
182. W. Clegg, S. Parsons and S. Moggach, in *The 17th BCA/CCG Intensive Teaching School in X-Ray Structure Analysis*, Durham University, UK, 2019, ch. 11, pp. 11.11-11.20.
183. W. Clegg, A. J. Blake, R. O. Gould and P. Main, in *Crystal Structure and Analysis: Principles and Practice*, ed. W. Clegg, Oxford University Press Inc., New York, United States, 2001, ch. 8, pp. 90-100.
184. L. Palatinus, in *The 17th BCA/CCG Intensive Teaching School in X-Ray Structure Analysis*, Durham University, UK, 2019, ch. 13, pp. 13.11-13.12.
185. L. Palatinus, *Acta Crystallographica*, 2013, **B69**, 1-16.
186. P. Muller, in *Crystal Structure Refinement: A Crystallographers Guide to SHELX*, ed. P. Muller, Oxford University Press, New York, United States, 2006, ch. 2, pp. 7-25.
187. R. Cooper and S. Parsons, in *The 17th BCA/CCG Intensive Teaching School in X-Ray Structure Analysis*, Durham University, UK, 2019, ch. 16, pp. 16.11-16.26.
188. S. Parsons, in *The 17th BCA/CCG Intensive Teaching School in X-Ray Structure Analysis*, Durham, UK, 2019, ch. 15, pp. 15.11-15.18.
189. R. Cooper, in *The 17th BCA/CCG Intensive Teaching School in X-Ray Structure Analysis*, Durham, UK, 2019, ch. 17, pp. 17.12-17.36.
190. D. Giron and D. J. W. Grant, in *Handbook of Pharmaceutical Salts: Properties, Selection and Use*, eds. P. H. Stahl and C. G. Wermuth, Wiley-VCH, Weinheim, Germany, 2008, ch. 3, pp. 41-82.
191. P. Atkins and J. de Paula, in *Atkins' Physical Chemistry*, Oxford University Press, New York, 9th edn., 2010, ch. 1, pp. 17-209
192. A. W. Coats and J. P. Redfern, *Analyst*, 1963, **88**, 906-924.
193. R. A. Carlton, in *Pharmaceutical Microscopy*, Springer, New York, United States, 2011, pp. 65-84.
194. R. A. Carlton, in *Pharmaceutical Microscopy*, Springer, New York, United States, 2011, ch. 2, pp. 7-64.
195. P. Atkins and J. de Paula, in *Elements of Physical Chemistry*, Oxford University Press, Oxford, 7th edn., 2017, ch. 11, pp. 448-497

196. P. Atkins and J. de Paula, in *Elements of Physical Chemistry*, Oxford University Press, Oxford, 7th edn., 2017, ch. 13, pp. 523-546
197. A. Burrows, J. Holman, A. Parsons, G. Pilling and G. Price, in *Chemistry^3*, Oxford University Press, Oxford, 2009, ch. 13, pp. 605 - 659.
198. Agilent, *CrysAlis PRO*, Agilent Technologies Ltd., Yarnton, Oxfordshire, England, 2014.
199. O. V. Dolomanov, L. J. Bourhis, R. J. Gildea, J. A. K. Howard and H. Puschmann, *Journal of Applied Crystallography*, 2009, **42**, 339-341.
200. K. Grodowska and A. Parczewski, *Acta Poloniae Pharmaceutica* 2010, **67**, 3-12.
201. A. R. Klapwijk, Doctor of Philosophy, University of Bath, 2016.
202. L. E. Hatcher, W. Li, P. Payne, B. Benyahia, C. D. Rielly and C. C. Wilson, *Crystal Growth & Design*, 2020, **20**, 5854-5862.
203. I. Sarcevica, L. Orola, M. V. .Veidis, A. Podjava and S. Belyakov, *Crystal Growth & Design*, 2013, **13**, 1082-1090.
204. A. Lemmerer, J. Bernstein and V. Kahlenberg, *Journal of Chemical Crystallography*, 2011, **41**, 991-997.
205. Sigma Aldrich, L-(+)-tartaric acid, https://www.sigmaaldrich.com/catalog/product/sial/251380?lang=en&region=GB, (accessed 13th Oct, 2020).
206. F. Tian, H. Qua, A. Zimmermann, T. Munk, A. C. Jørgensen and J. Rantanen, *Journal of Pharmacy and Pharmacology*, 2010, **62**, 1534-1546.
207. Sigma Aldrich, DL-tartaric acid, https://www.sigmaaldrich.com/catalog/product/aldrich/t400?lang=en&region=GB, (accessed 13th Oct, 2020).
208. K. K. Sarma, T. Rajbongshi, A. Bhuyan and R. Thakuria, *Chemical Communications*, 2019, **55**, 10900-10903.
209. M. Daskiewicz, *CrystEngComm*, 2013, **15**, 10427-10430.
210. S. Vecchio and B. Brunetti, *Journal of Chemical Thermodynamics*, 2009, **41**, 880-887.
211. C. Becker, J. B. Dressman, G. L. Amidon, H. E. Junginger, S. Kopp, K. K. Midha, V. P. Shah, S. Stavchansky and D. M. Barends, *Journal of Pharmaceutical Sciences*, 2007, **96**, 522-531
212. R. A. Lunt, PhD, University of Bath, 2019.
213. Sigma Aldrich, 3,5-dinitrobenzoic acid, https://www.sigmaaldrich.com/catalog/product/aldrich/121258?lang=en&region=GB, (accessed 13th Oct, 2020).
214. F. H. Herbstein, M. Kapon and G. M. Resiner, *Acta Crystallographica*, 1985, **b41**, 348-354.
215. R. Ganduri, S. Cherukuvada and T. N. G. Row, *Crystal Growth & Design*, 2015, **15**, 3474-3480.
216. Sigma Aldrich, Pthalic Acid, https://www.sigmaaldrich.com/catalog/product/sial/p39303?lang=en&region=GB, (accessed 10th Mar, 2021).
217. C. J. Brown, T. McGlone, S. Yerdelen, V. Srirambhatla, F. Mabbott, R. Gurung, M. L. Briuglia, B. Ahmed, H. Polyzois, J. McGinty, F. Perciballi, D. Fysikopoulos, P. MacFhionnghaile, H. Siddique, V. Raval, T. S. Harrington, A. D. Vassileiou, M. Robertson, E. Prasad, A. Johnston, B. Johnston, A. Nordon, J. S. Srai, G. Halbert, J. H. ter Horst, C. J. Price, C. D. Rielly, J. Sefcik and A. J. Florence, *Molecular Systems Design and Engineering*, 2018, **3**, 518-549.
218. S. D. Schaber, D. I. Gerogiorgis, R. Ramachandran, J. M. B. Evans, P. I. Barton and B. L. Trout, *Industrial & Engineering Chemistry Research*, 2011, **50**, 10083-10092.
219. L. E. Hatcher, A. J. Burgess, P. Payne and C. C. Wilson, *CrystEngComm*, 2020.
220. Sigma Aldrich, 3-hydroxybenzoic acid, https://www.sigmaaldrich.com/catalog/product/aldrich/h20008?lang=en&region=GB, (accessed 15th Jan, 2021).

Appendix

Chapter 4

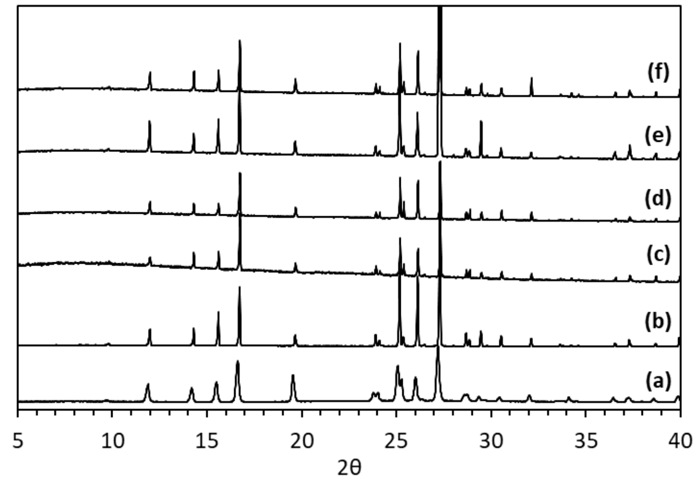

A 1. PXRD data for (a) IZN (INICAC02), (b) IZN crystallised from H_2O, (c) IZN crystallised from EtOH, (d) IZN crystallised from IPA, (e) IZN crystallied from EtOAc and (f) IZN crystallised from ACN

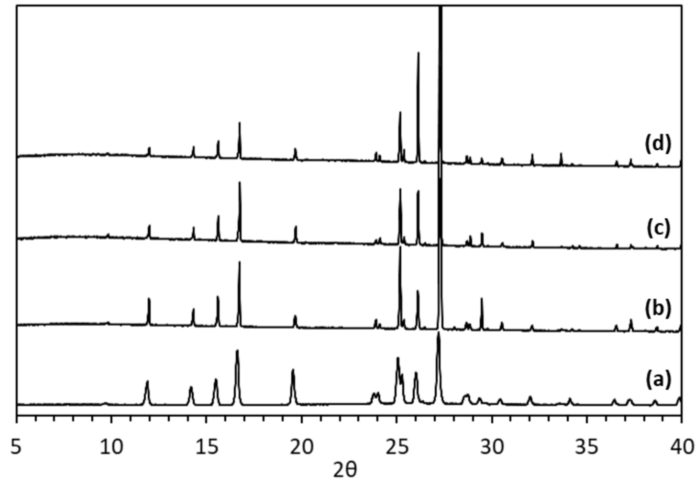

A 2. PXRD data for (a) IZN (INICAC02), (b) IZN crystallised from EtOAc, (c) IZN temperature cycling experiment 1 in EtOAc and (d) IZN temperature cycling experiment 2 in EtOAc

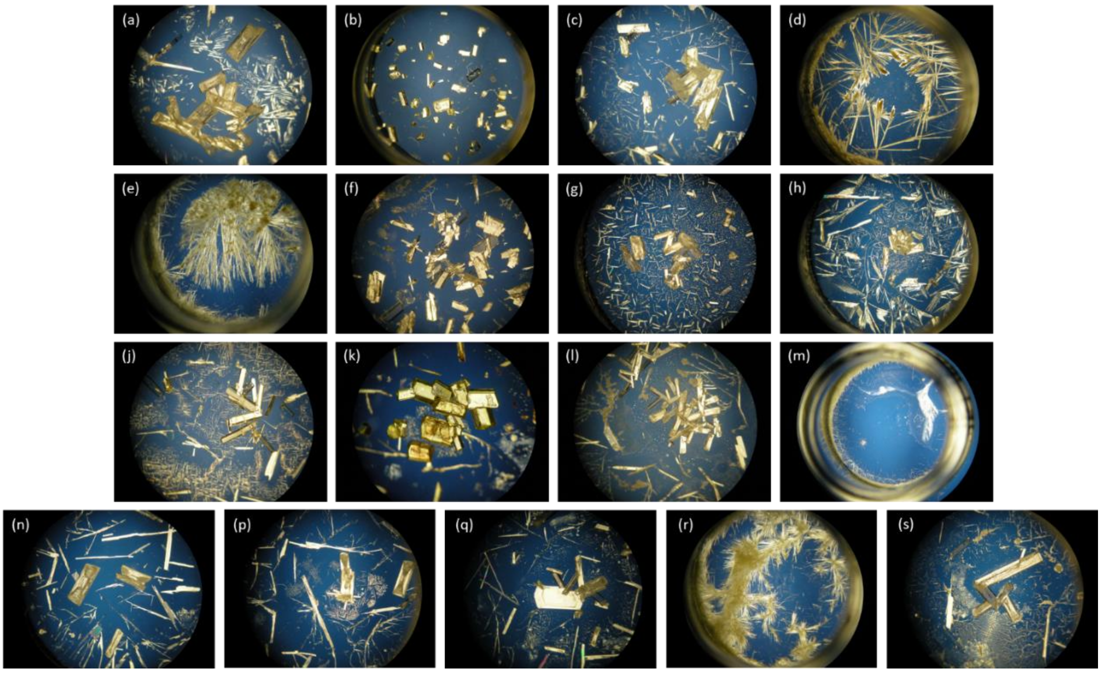

A 3. Evaporative crystallisations at 40 °C with 1% additives (a) benzoic acid, (b) 3-hydroxybenzoic acid, (c) 2,4-dihydroxybenzoic acid, (d) 3,4-dihydroxybenzoic acid, (e) 3,5-dihydroxybenzoic acid, (f) 2,6-dihydroxybenzoic acid, (g) 4-cyanobenzoic acid, (h) 3-cyanobenzoic acid, (j) 2,4-dinitrobenzoic acid, (k) 3,4-dinitrobenzoic acid, (l) 3,5-dinitrobenzoic acid, (m) trimesic acid, (n) isonicotinamide, (p) nicotinamide, (q) pyridoxine, (r) vanillin and (s) L-tartaric acid

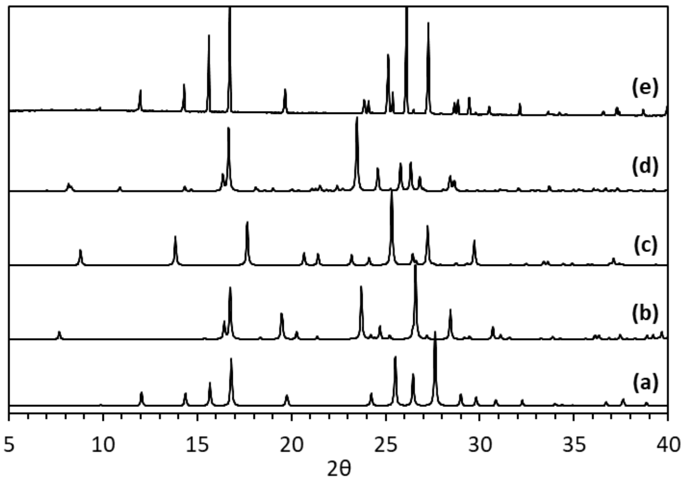

A 4. PXRD data for (a) IZN (INICAC02), (b) 3-HBA form I (BIDLOP), (c) 3-HBA form II (BIDLOP01), (c) 3-HBA hydrate (BOMCAJ) and (d) IZN evaporative with 1% 3-HBA from IPA

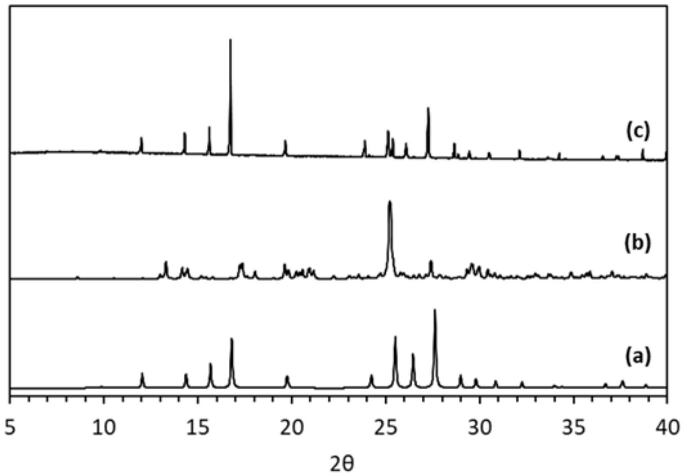

A 5. PXRD data for (a) IZN (INICAC02), (b) 3,4-DNBA (YADKOF) and (c) IZN evaporative with 1% 3,4-DNBA from IPA

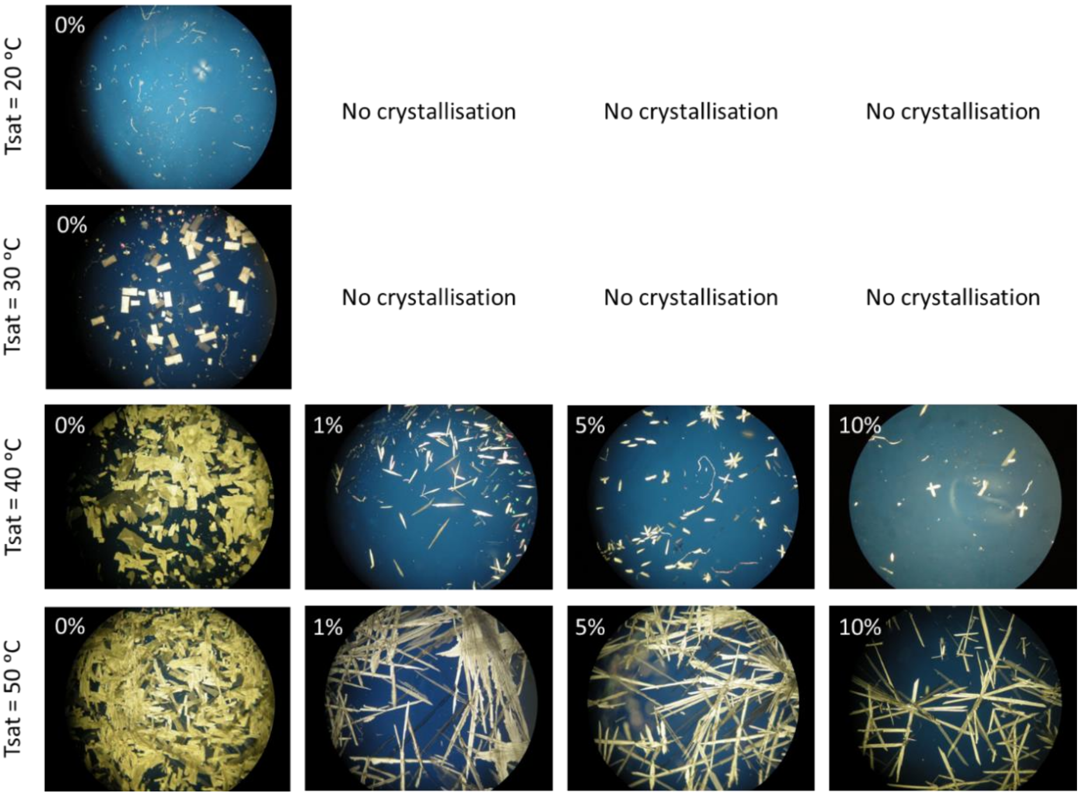

A 6. Cooling crystallisations of IZN with 3-HBA additive. Scale: 10 g, cool rate: 1 ^{o}C/minute, final dwell: 1 hour

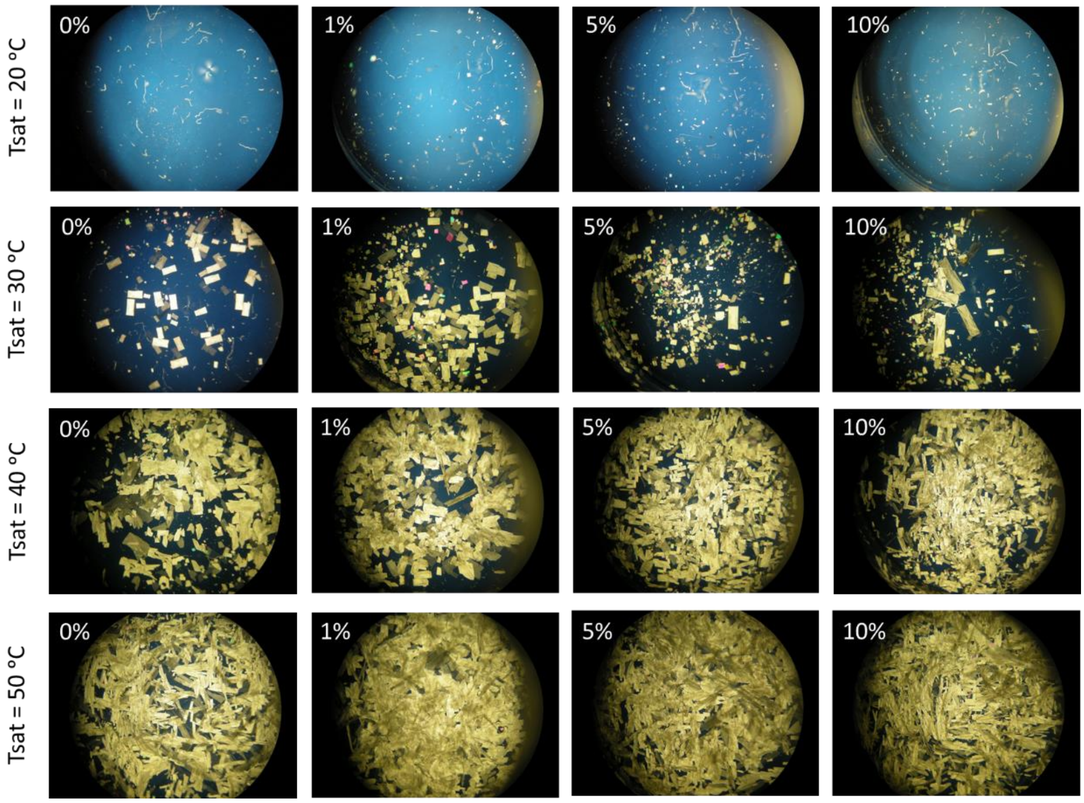

A 7. Cooling crystallisations of IZN with 3-HBA additive. Scale: 10 g, cool rate: 1 °C/minute, final dwell: 5 hour

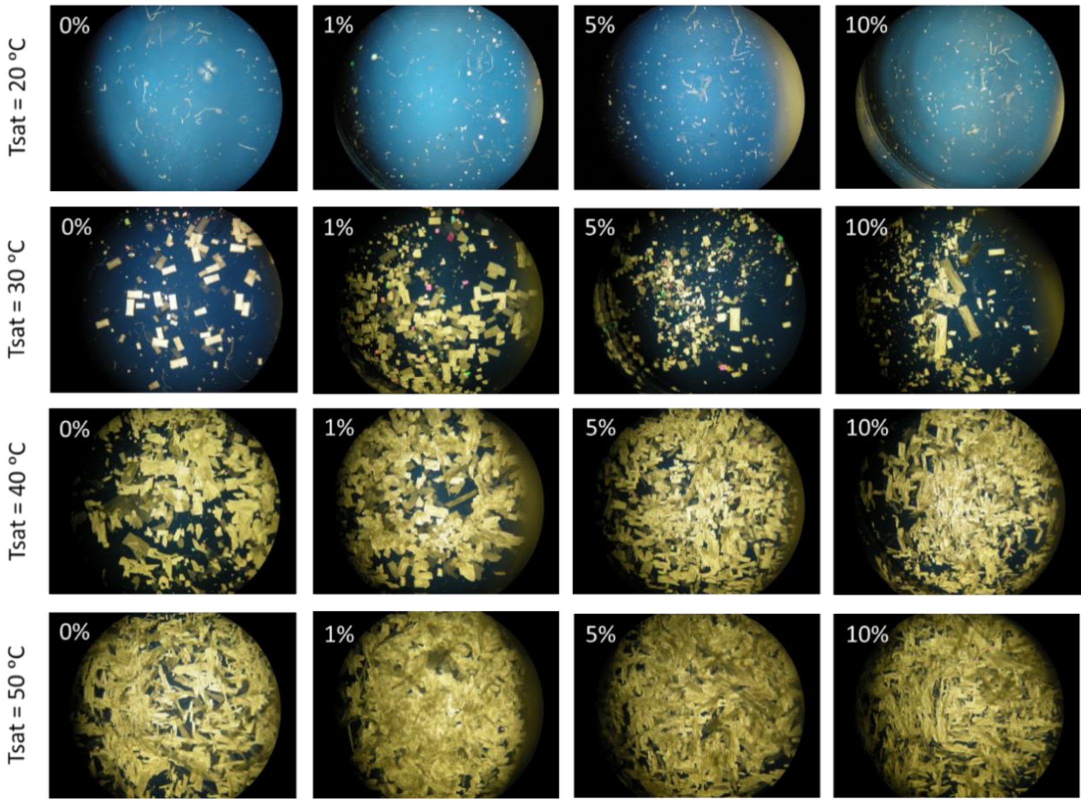

A 8. Cooling crystallisations of IZN with 3-HBA additive. Scale: 10 g, cool rate: 1 °C/minute, final dwell: 10 hour

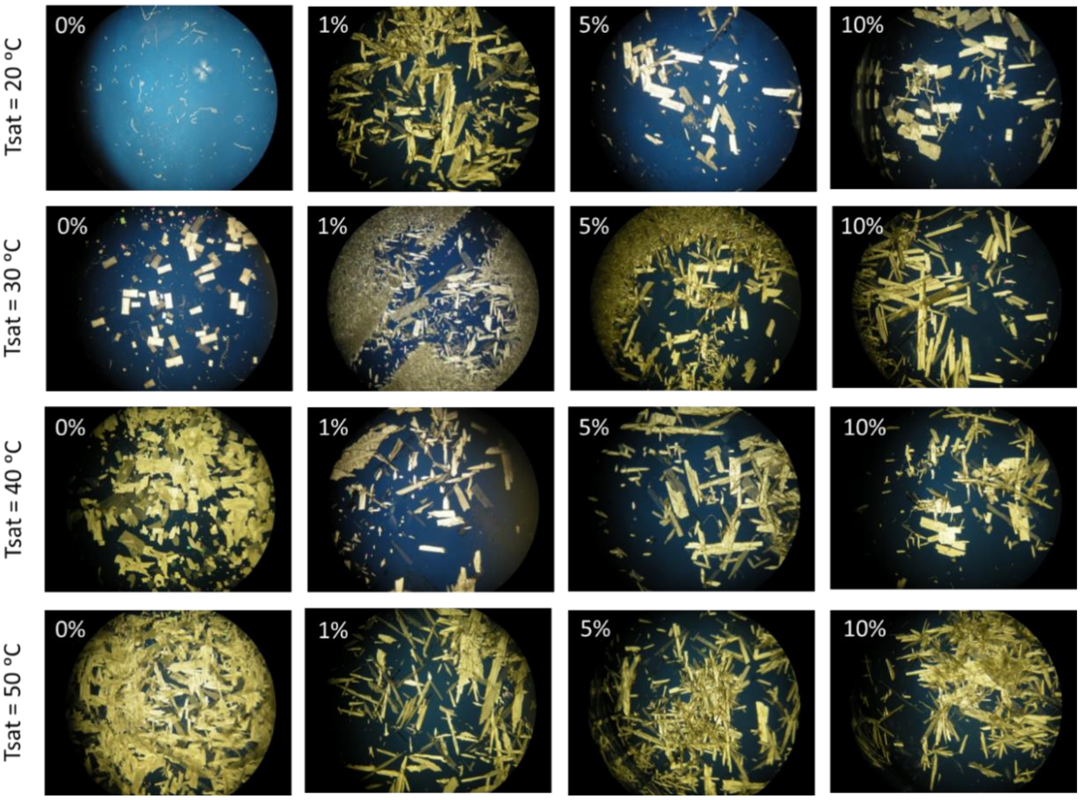

A 9. Cooling crystallisations of IZN with 3-HBA additive. Scale: 10 g, cool rate: 0.1 ^{o}C/minute, final dwell: 1 hour

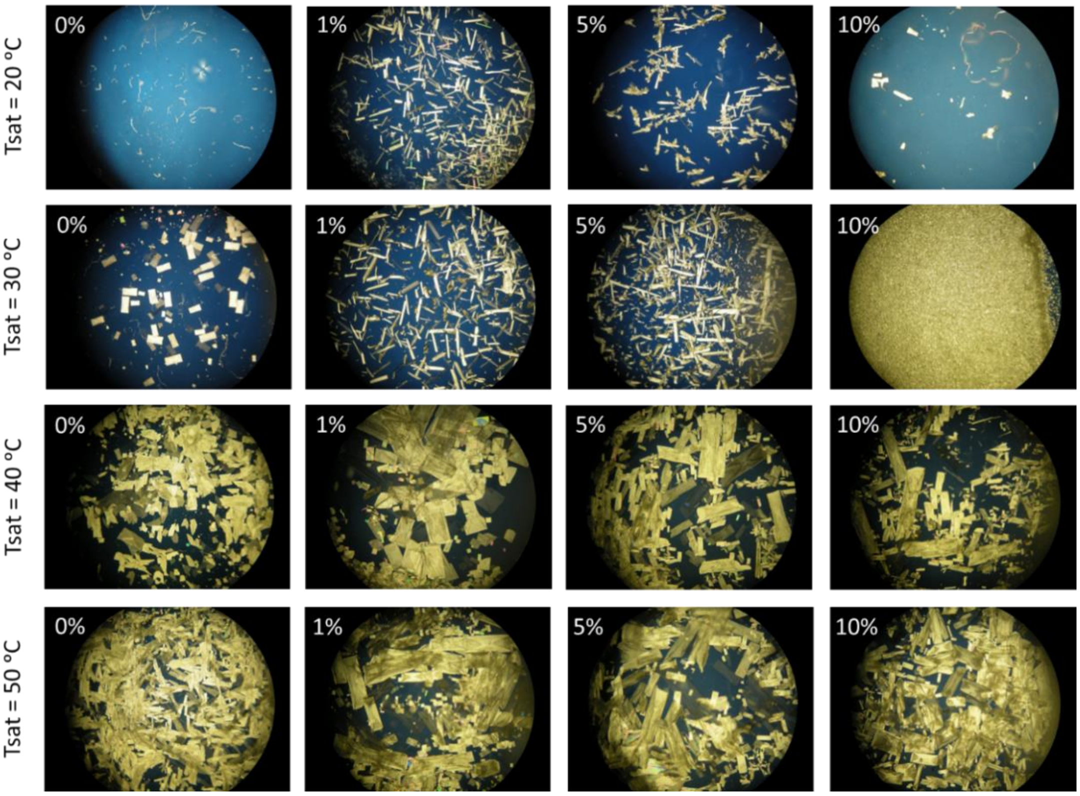

A 10. Cooling crystallisations of IZN with 3-HBA additive. Scale: 10 g, cool rate: 0.1 ^{o}C/minute, final dwell: 5 hour

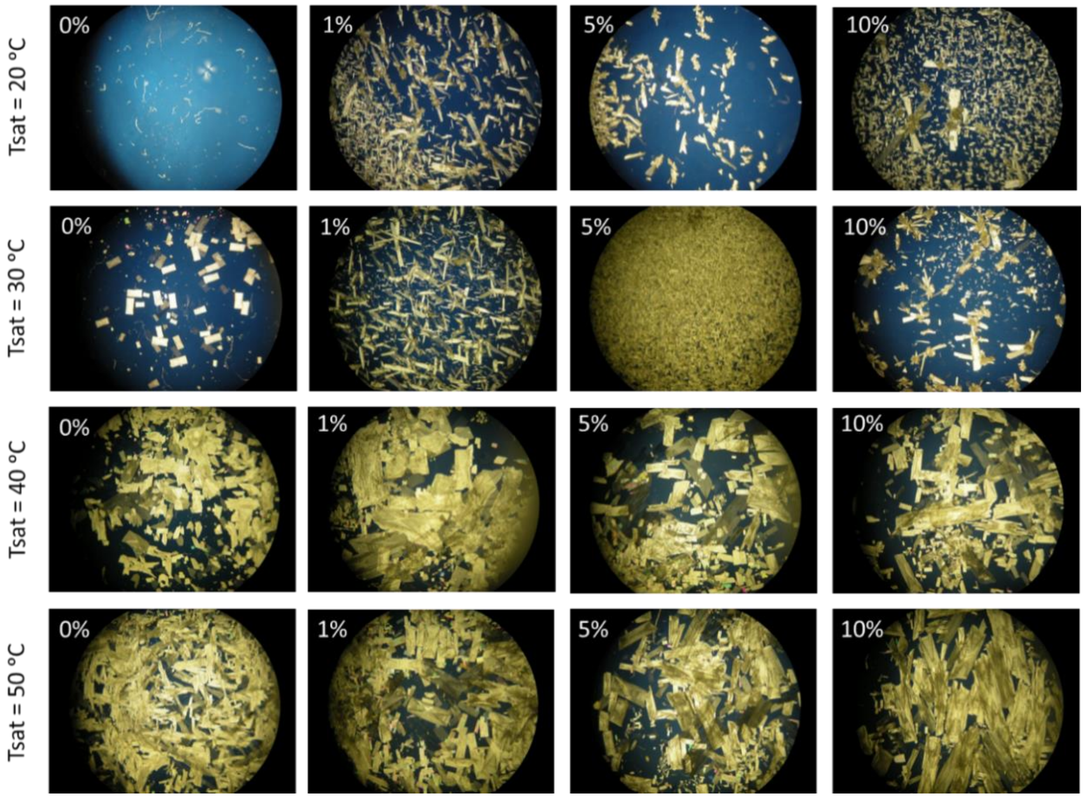

A 11. Cooling crystallisations of IZN with 3-HBA additive. Scale: 10 g, cool rate: 0.1 °C/minute, final dwell: 10 hour

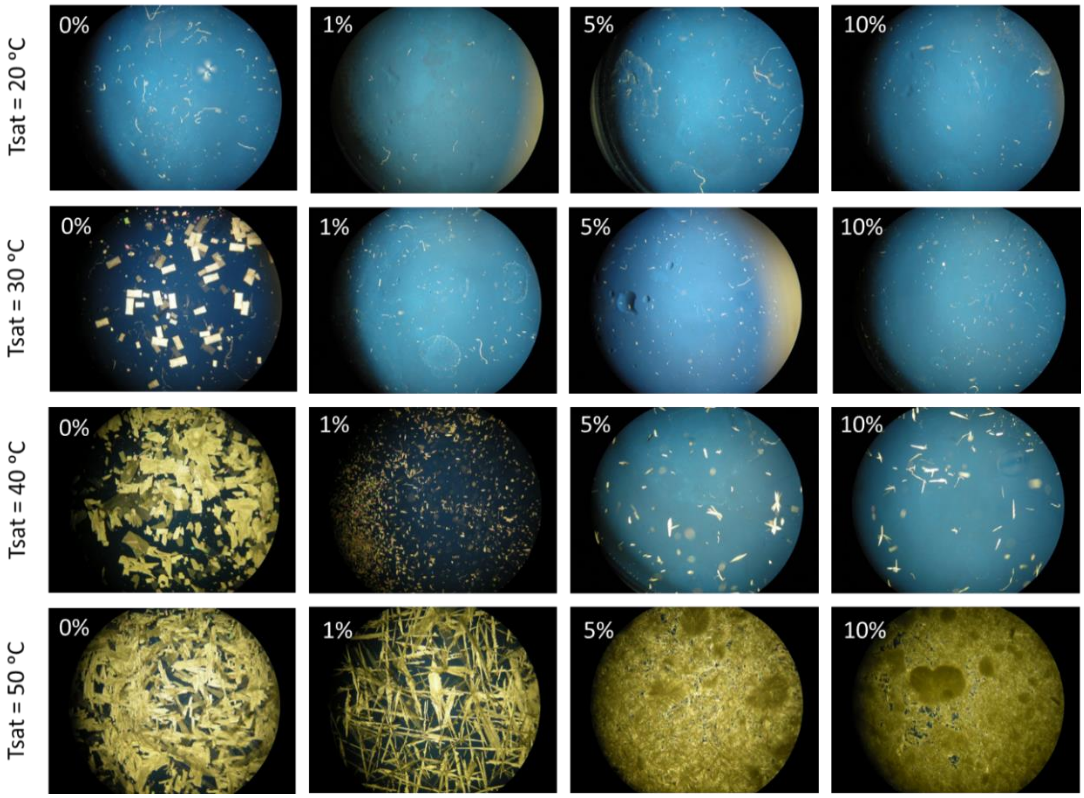

A 12. Cooling crystallisations of IZN with 3,4-DNBA additive. Scale: 10 g, cool rate: 1 °C/minute, final dwell: 1 hour

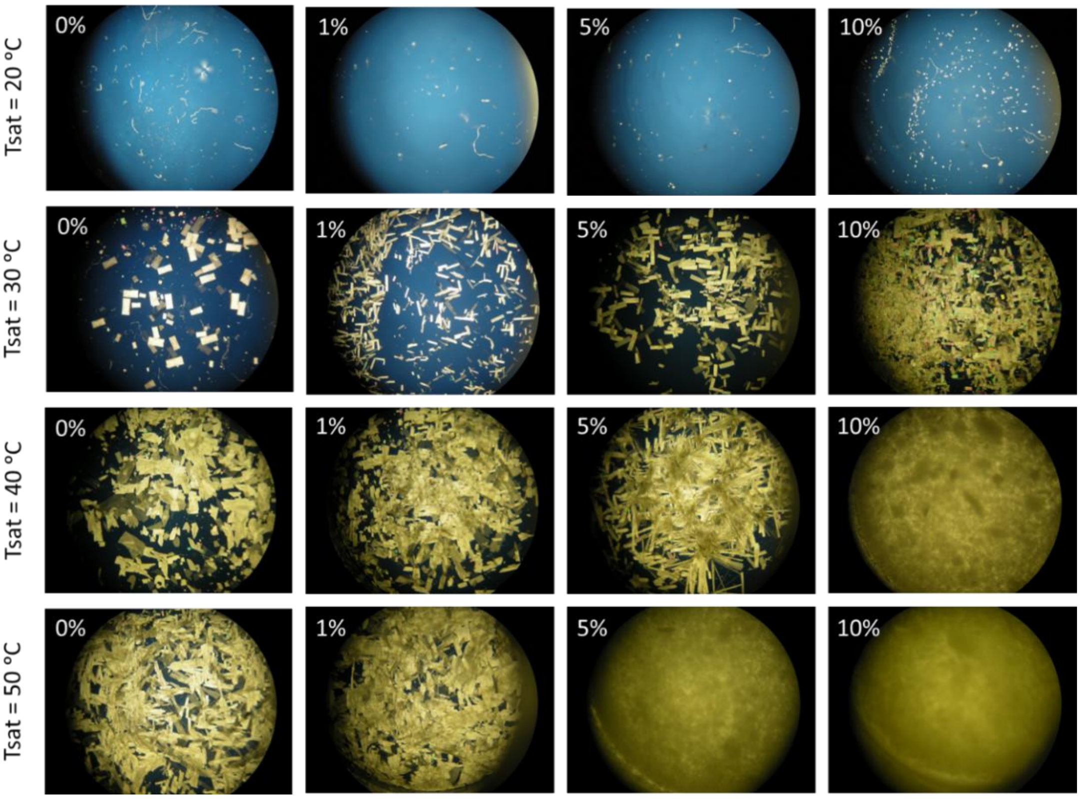

A 13. Cooling crystallisations of IZN with 3,4-DNBA additive. Scale: 10 g, cool rate: 1 ^{o}C/minute, final dwell: 5 hour

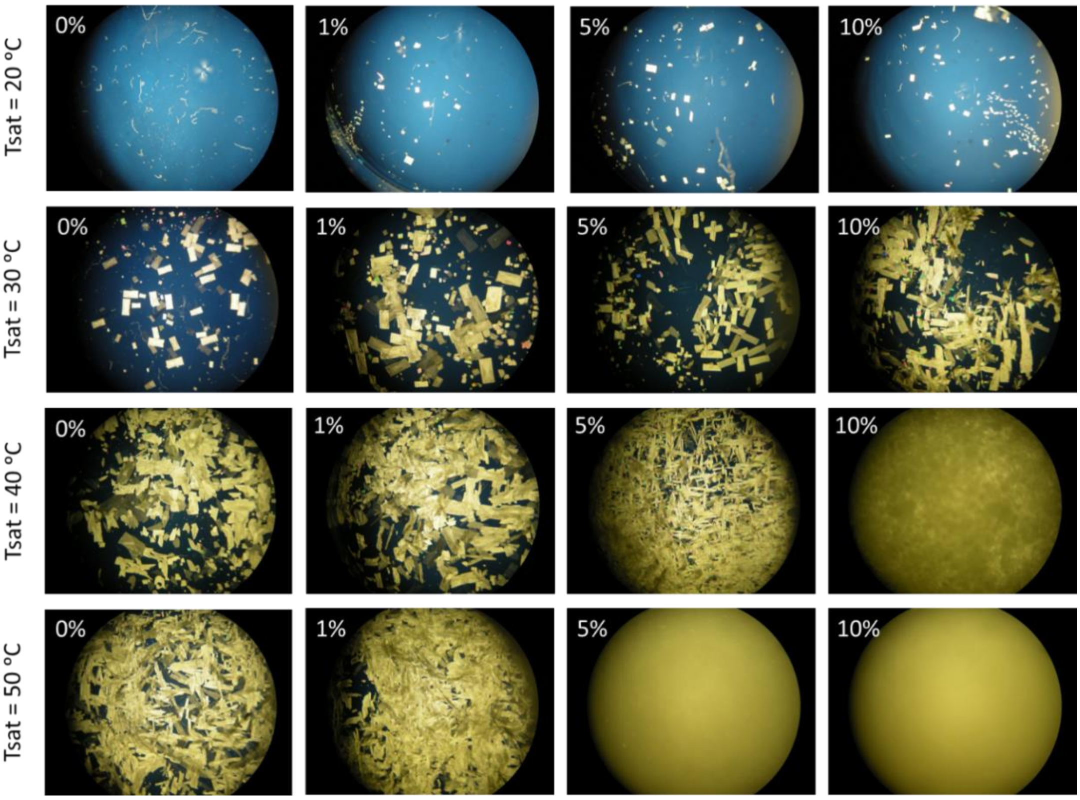

A 14. Cooling crystallisations of IZN with 3,4-DNBA additive. Scale: 10 g, cool rate: 1 ^{o}C/minute, final dwell: 10 hour

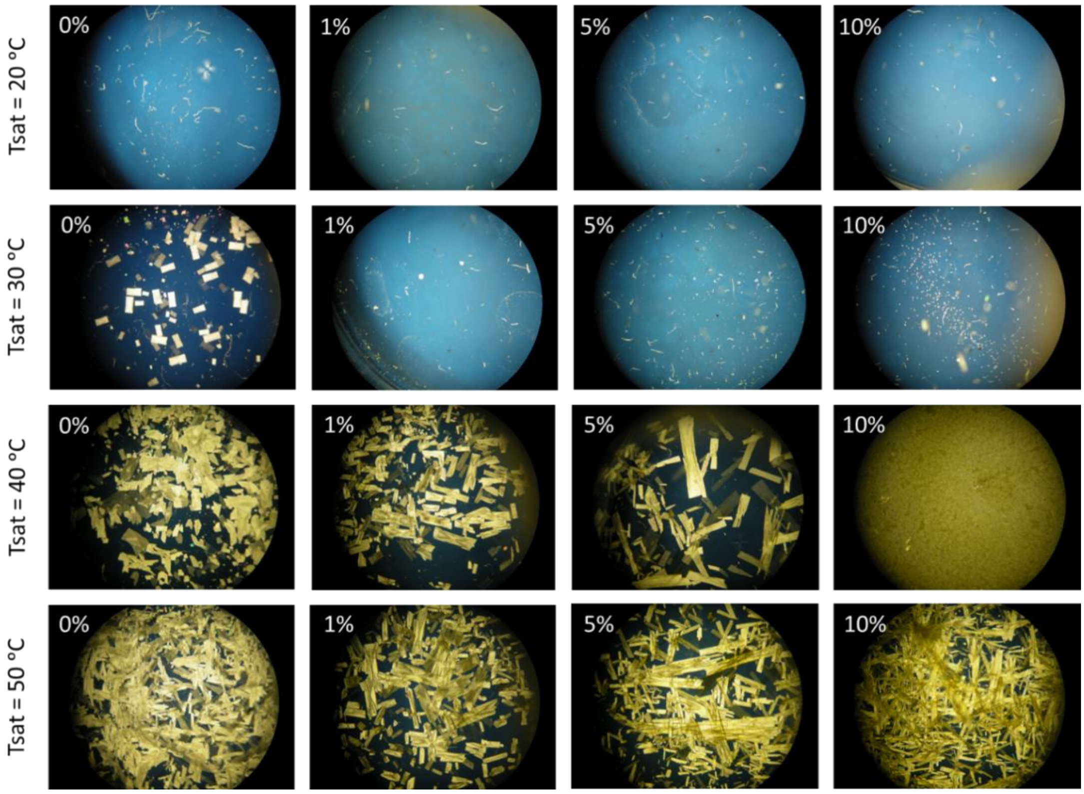

A 15. Cooling crystallisations of IZN with 3,4-DNBA additive. Scale: 10 g, cool rate: 0.1 ^{o}C/minute, final dwell: 1 hour

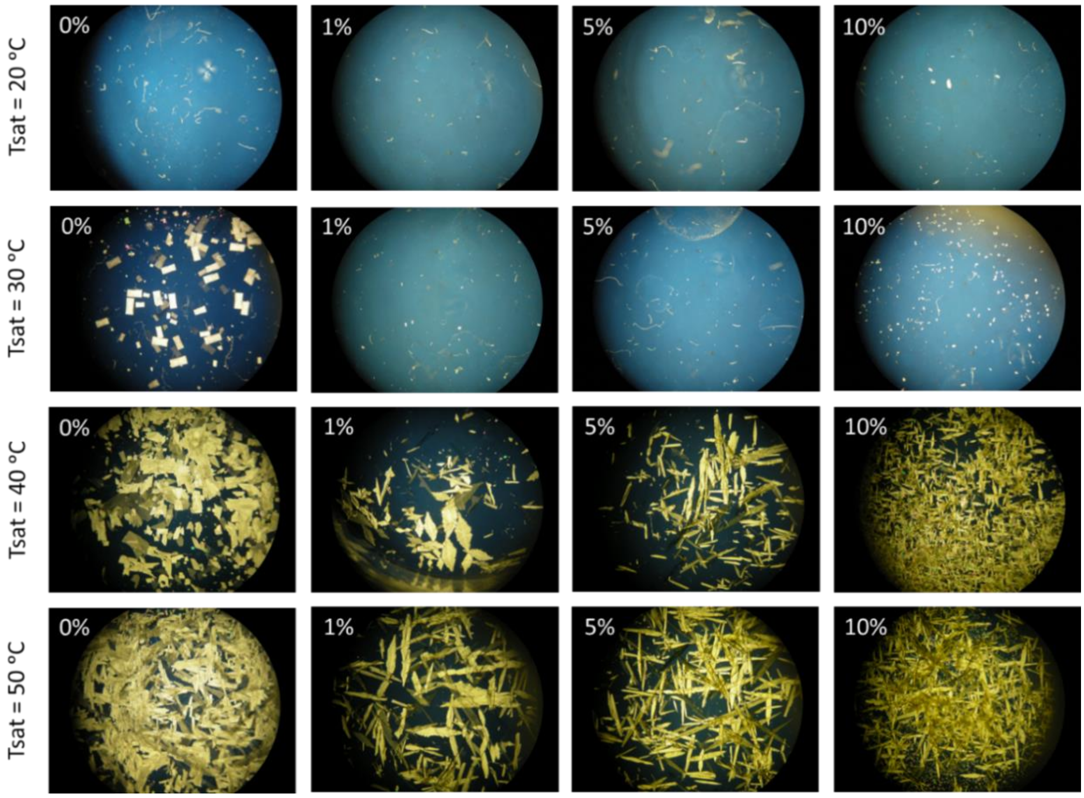

A 16. Cooling crystallisations of IZN with 3,4-DNBA additive. Scale: 10 g, cool rate: 0.1 ^{o}C/minute, final dwell: 5 hour

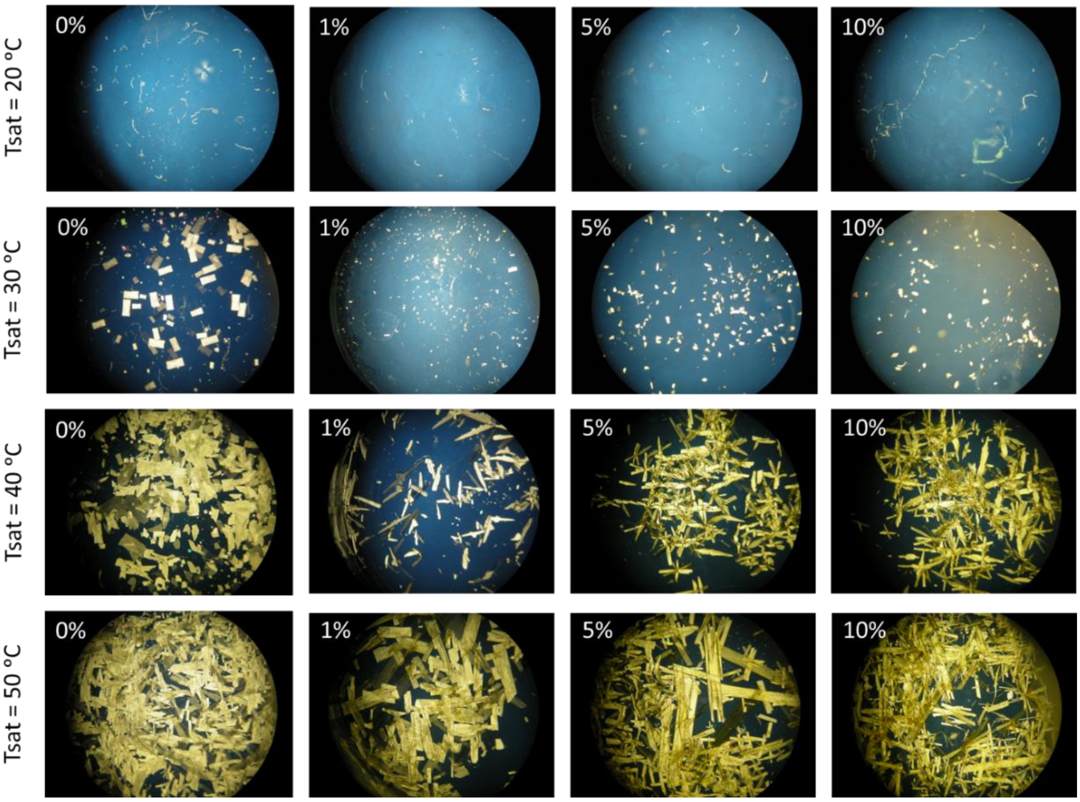

A 17. Cooling crystallisations of IZN with 3,4-DNBA additive. Scale: 10 g, cool rate: 0.1 °C/minute, final dwell: 10 hour

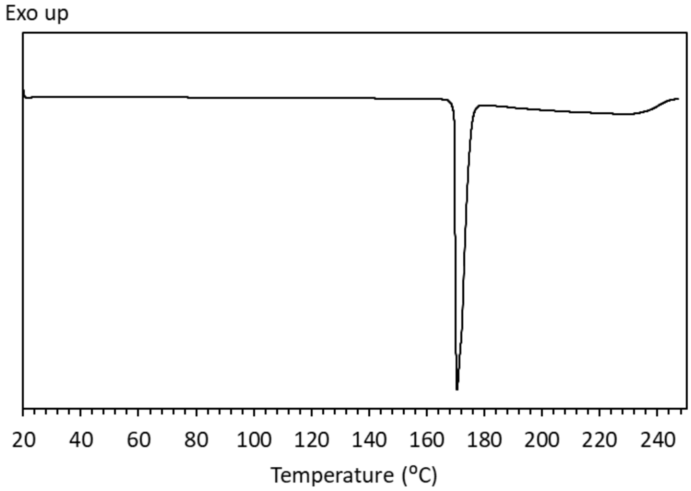

A 18. DSC trace for IZN crystallised via 200 mL cooling crystallisation in IPA with 1% 3-HBA additive. IZN melting point = 171-174 °C [163]*, 3-HBA melting point = 200-203 °C* [220]

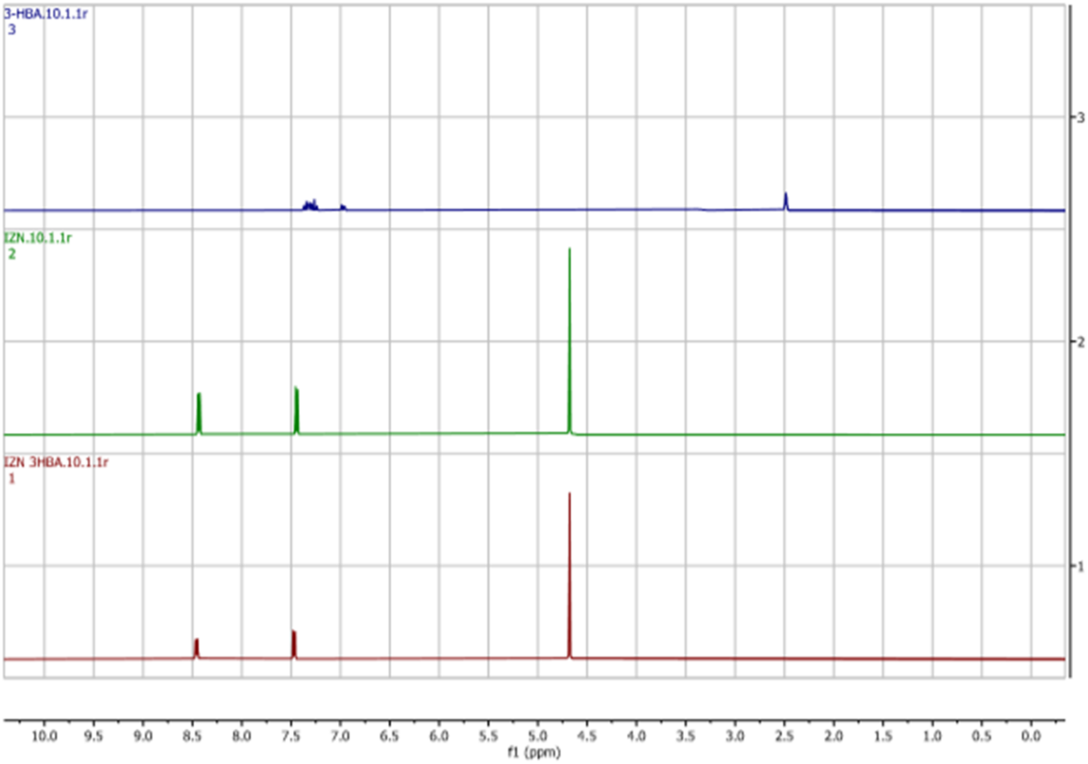

A 19. NMR spectroscopy experimental data for IZN crystallised via 200 mL cooling crystallisation in IPA with 1% 3-HBA additive (red) compared to pure IZN (green) and pure 3-HBA (blue).

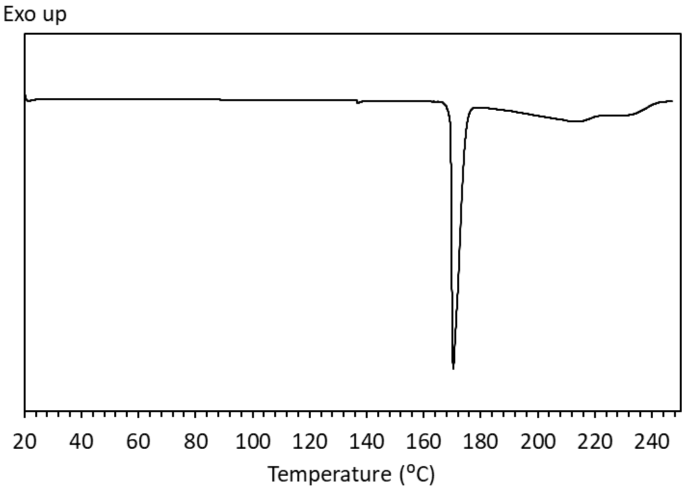

A 20. DSC trace for IZN crystallised via 200 mL cooling crystallisation in IPA with 1% 3,4-DNBA additive. IZN melting point = 171-174 °C [163]*, 3,4-DNBA melting point = 165 °C* [210]

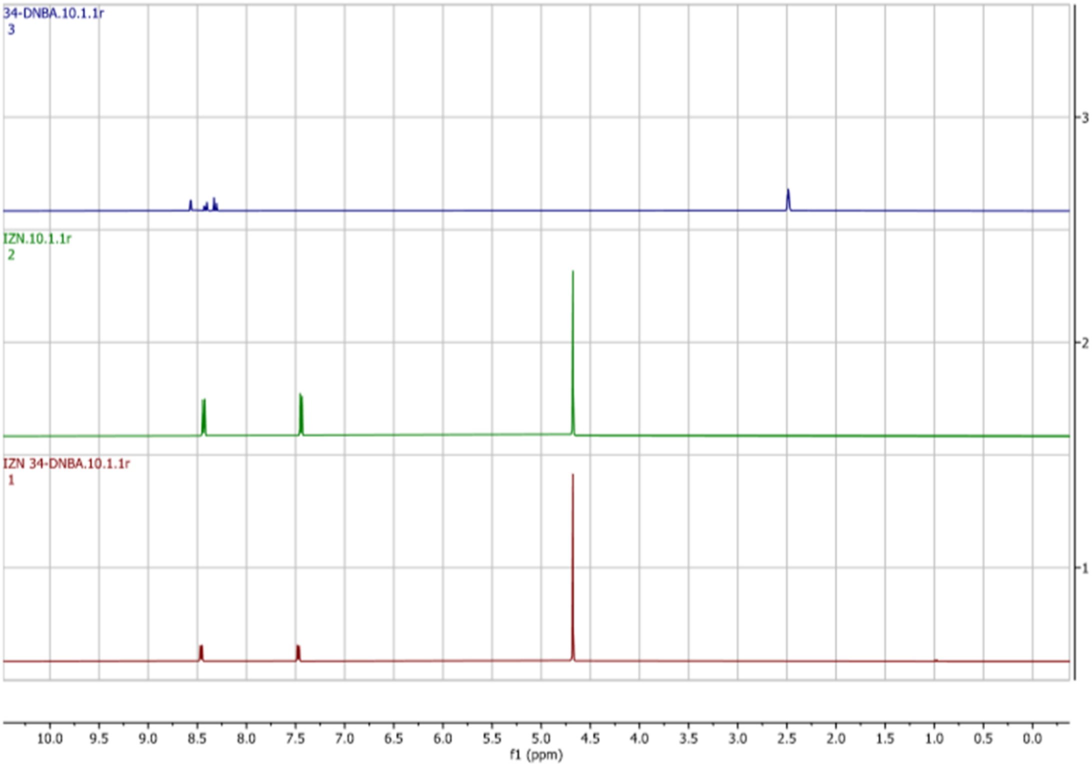

A 21. NMR spectroscopy experimental data for IZN crystallised via 200 mL cooling crystallisation in IPA with 1% 3,4-DNBA additive (red) compared to pure IZN (green) and pure 3,4-DNBA (blue).

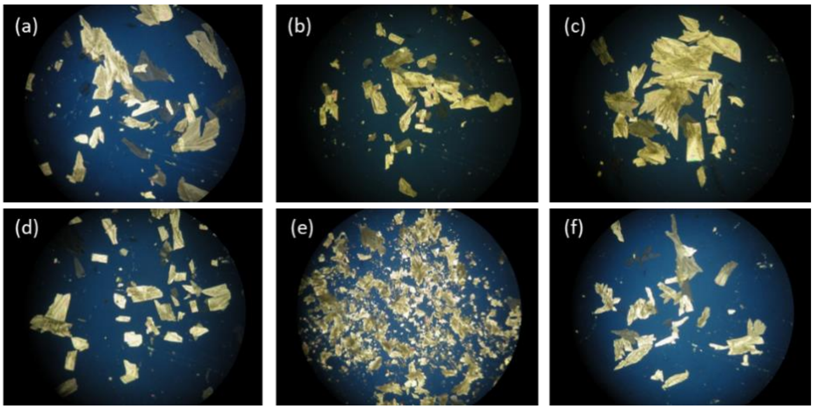

A 22. Cooling crystallisations of IZN with 1% polymer additives from IPA at a rate of 1°C/minute. (a) PP123, (b) PEG, (c) PPG, (d) PBD, (e) PVP and (f) PDE

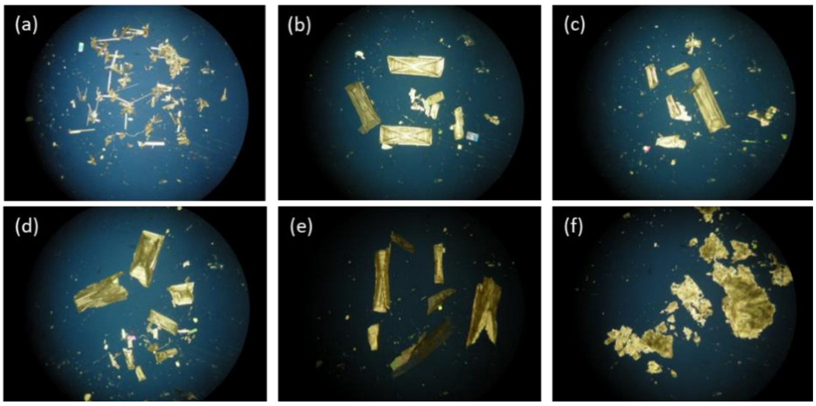

A 23. Cooling crystallisations of IZN with 0.1% polymer additives from IPA at a rate of 1^{o}C/minute. (a) PP123, (b) PEG, (c) PPG, (d) PBD, (e) PVP and (f) PDE

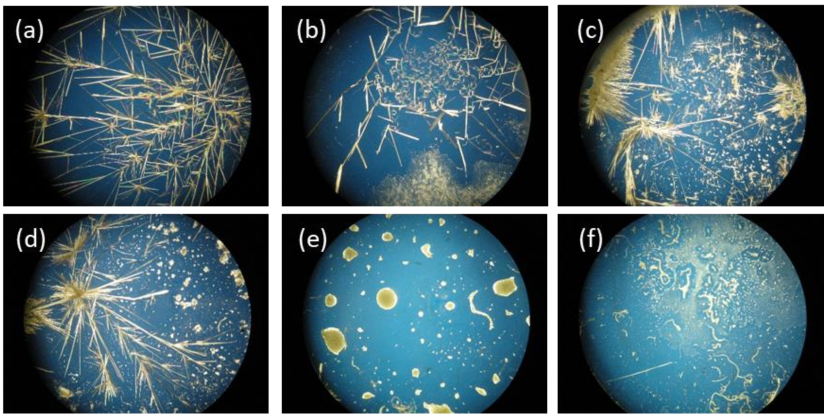

A 24. 20 ^{o}C evaporative crystallisations of IZN with 1% polymer additives in IPA. (a) PP123, (b) PEG, (c) PPG, (d) PBD, (e) PVP and (f) PDE

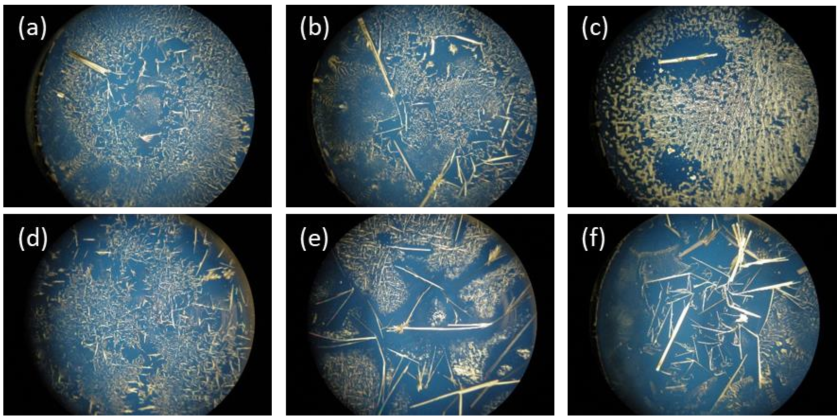

A 25. 20 ^{o}C evaporative crystallisations of IZN with 0.1% polymer additives from IPA. (a) PP123, (b) PEG, (c) PPG, (d) PBD, (e) PVP and (f) PDE

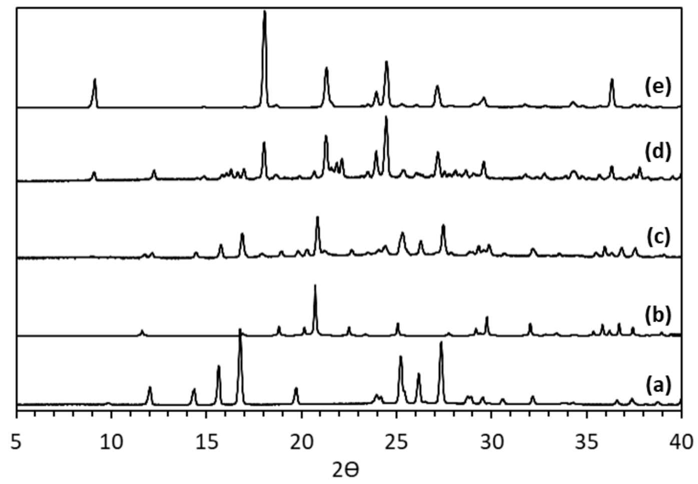

A 26. PXRD data for (a) IZN (INICAC02), (b) LTA (TARTAL), (c) 1:1 IZN:LTA grinding, (d) 1:1 IZN:LTA LAG with H_2O and (e) IZN:LTA co-crystal produced via crash cooling from H_2O

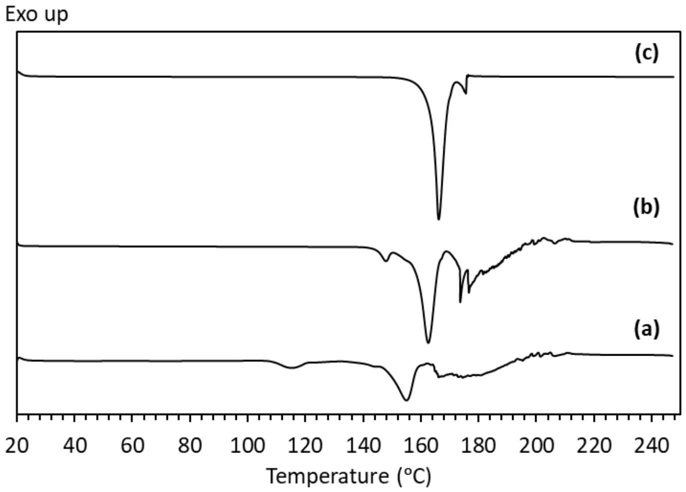

A 27. DSC trace for (a) 1:1 IZN:LTA grinding, (b) 1:1 IZN:LTA LAG with IPA and (c) IZN:LTA co-crystal produced via crash cooling from H_2O

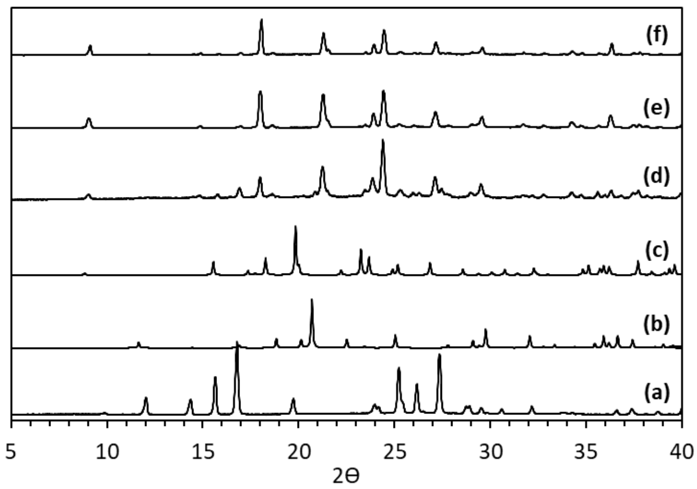

A 28. PXRD data for (a) IZN (INICAC02), (b) DTA (TARTAC), (c) DTA (TARTAC24), (d) 1:1 IZN:DTA grinding, (e) 1:1 IZN:DTA LAG with H_2O and (f) IZN:DTA co-crystal produced via crash cooling from H_2O

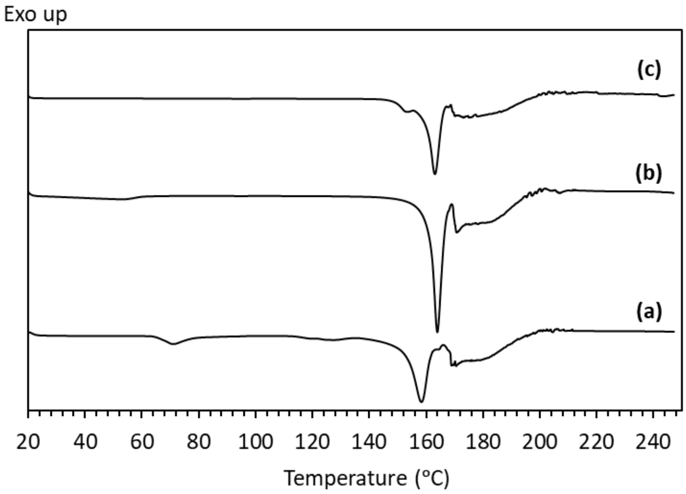

A 29. DSC trace for (a) 1:1 IZN:DTA grinding, (b) 1:1 IZN:DTA LAG with H_2O and (c) IZN:DTA co-crystal produced via crash cooling from H_2O

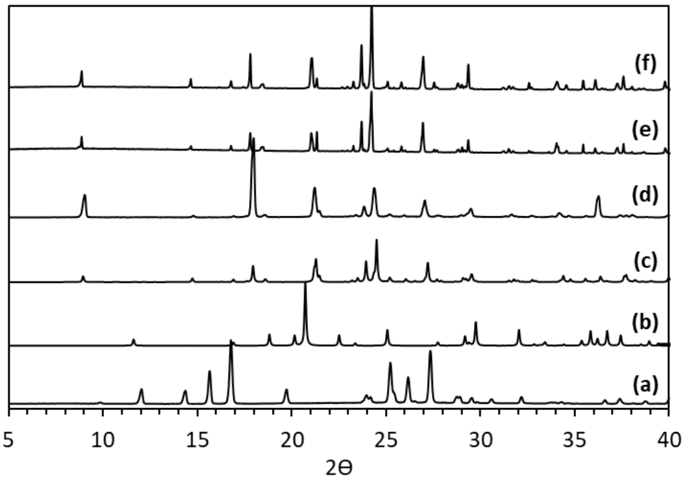

A 30. PXRD data for (a) IZN (INICAC02), (b) LTA (TARTAL), (c) IZN:LTA co-crystal calculated from SCXRD, (d) 10 g cooling in H_2O, (e) 30 g cooling in H_2O and (f) 60 mL slurry in H_2O

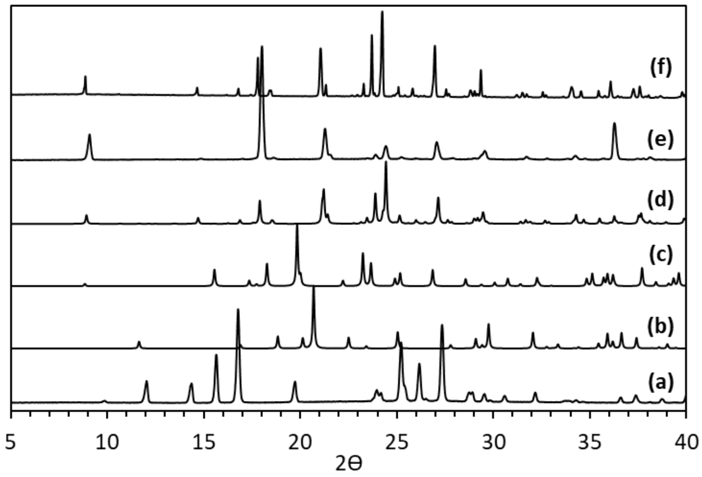

A 31. PXRD data for (a) IZN (INICAC02), (b) DTA (TARTAC), (c) DTA (TARTAC24), (d) IZN:DTA co-crystal calculated, (e) 10 g cooling in H_2O and (f) 30 g cooling in H_2O

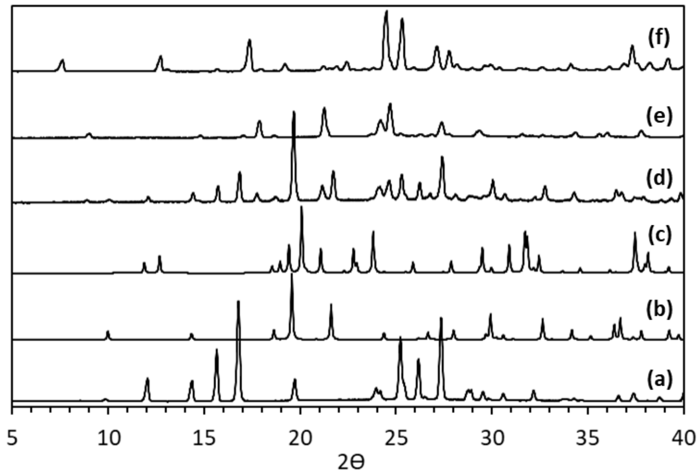

A 32. PXRD data for (a) IZN (INICAC02), (b) DLTA (ZZZDUI01), (c) DLTA monohydrate (TARTDL), (d) 1:1 IZN:DLTA grinding, (e) 1:1 IZN:DLTA LAG with H_2O and (f) IZN:DLTA co-crystal produced via crash cooling from H_2O

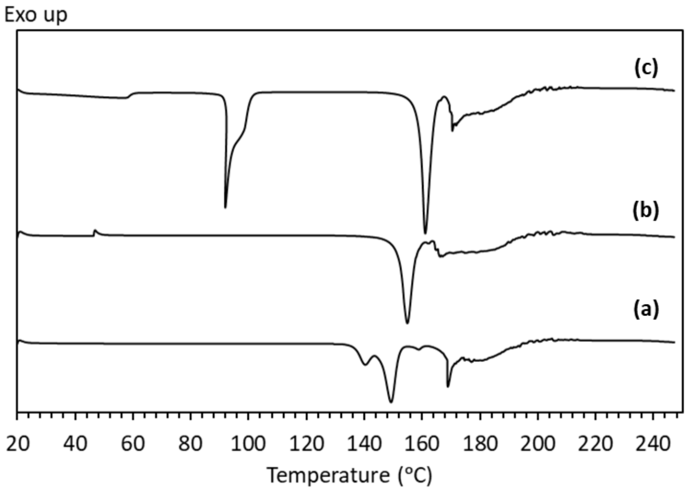

A 33. DSC trace for (a) 1:1 IZN:DLTA grinding, (b) 1:1 IZN:DLTA LAG with H_2O and (c) IZN:DLTA co-crystal produced via crash cooling from H_2O

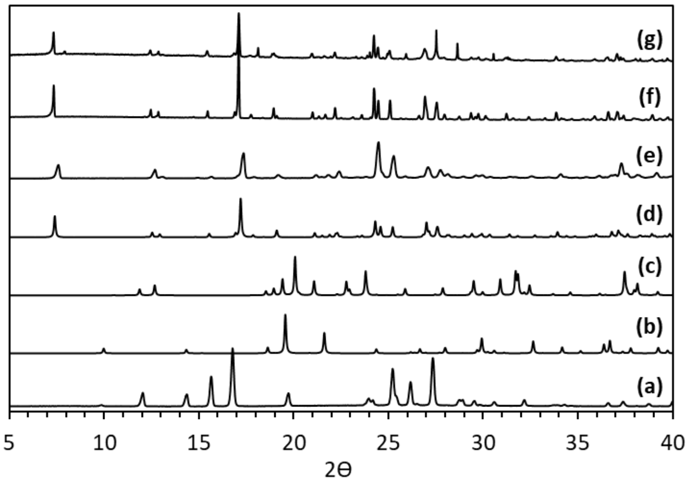

A 34. PXRD data for (a) IZN (INICAC02), (b) DLTA (ZZZDUI01), (c) DLTA monohydrate (TARTDL), (d) IZN:DLTA co-crystal calculated, (e) 10 g cooling in H_2O, (f) 30 g cooling in H_2O and (g) 60 mL slurry in H_2O

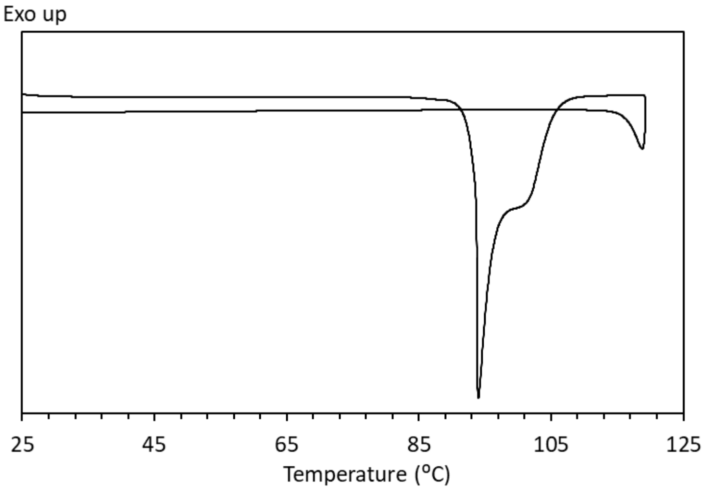

A 35 DSC trace for IZN:DLTA:H_2O cycled experiment

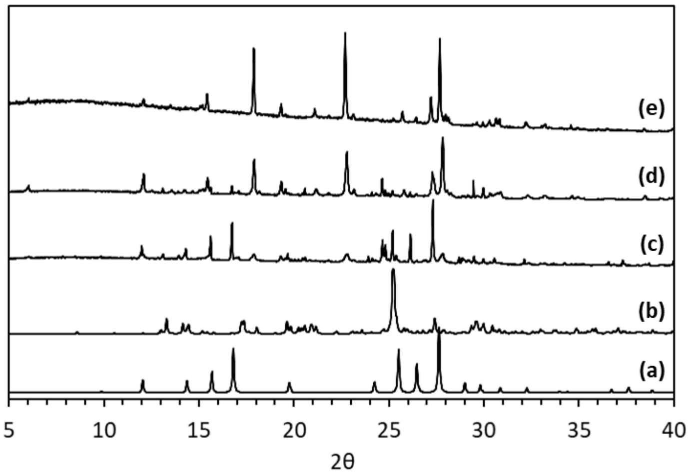

A 36. PXRD data for (a) IZN (INICAC02), (b) 3,4-DNBA (YADKOF), (c) 1:1 IZN:3,4-DNBA grinding, (d) 1:1 IZN:3,4-DNBA LAG with IPA and (e) IZN:3,4-DNBA co-crystal produced via crash cooling from IPA

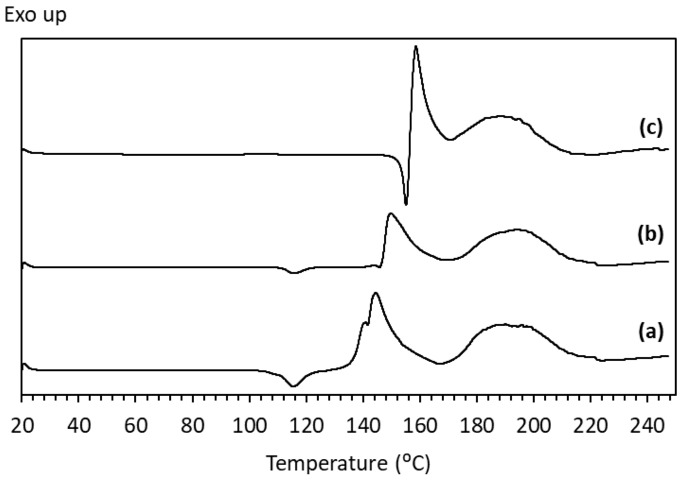

A 37. DSC trace for (a) 1:1 IZN:3,4-DNBA grinding, (b) 1:1 IZN:3,4-DNBA LAG with IPA and (c) IZN:3,4-DNBA co-crystal produced via crash cooling from IPA

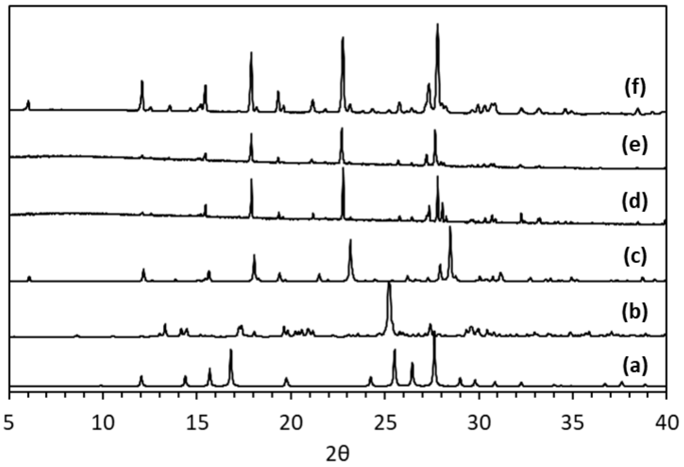

A 38. PXRD data for IZN:3,4-DNBA co-crystal scale up. (a) IZN (INICAC02), (b) 3,4-DNBA (YADKOF), (c) IZN:3,4-DNBA co-crystal calculated, (d) 10 g cooling in IPA, (e) 200 g cooling in IPA and (f) 200 g slurry in IPA

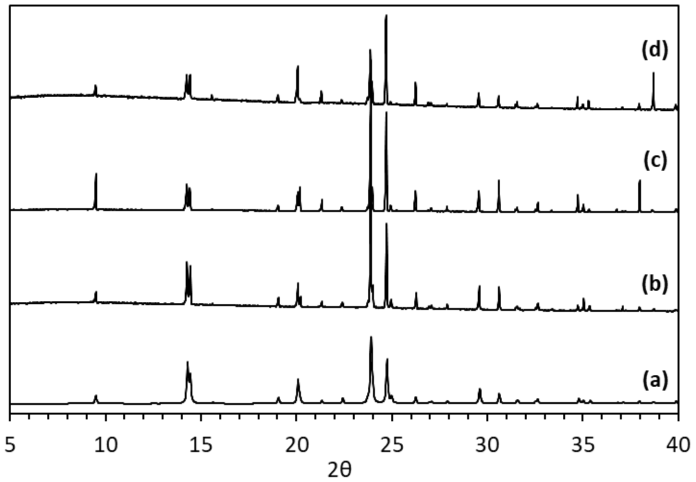

A 39 PXRD data for (a) PYR (BITZAF), (b) PYR crystallised from H_2O, (c) PYR crystallised from EtOH and (d) PYR crystallised from IPA

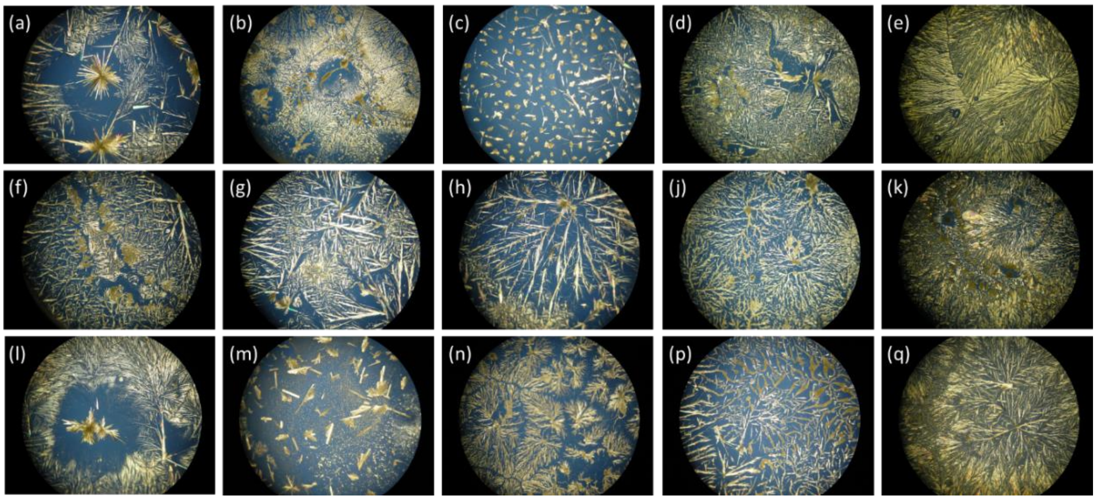

A 40. Evaporative crystallisations for PYR in IPA at 40 °C with 1 % additive (a) benzoic acid, (b) trimesic acid, (c) imidazole, (d) benzimidazole, (e) 2,4-dinitrobenzoic acid, (f) isonicotinamide, (g) isonicotinic acid, (h) nicotinic acid, (j) nicotinamide, (k) 3,5-dinitrobenzoic acid, (l) 2-aminobenzoic acid, (m) barbituric acid, (n) tartaric acid, (p) 2,2'-bipyridine and (q) 4,4'-bipyridine.

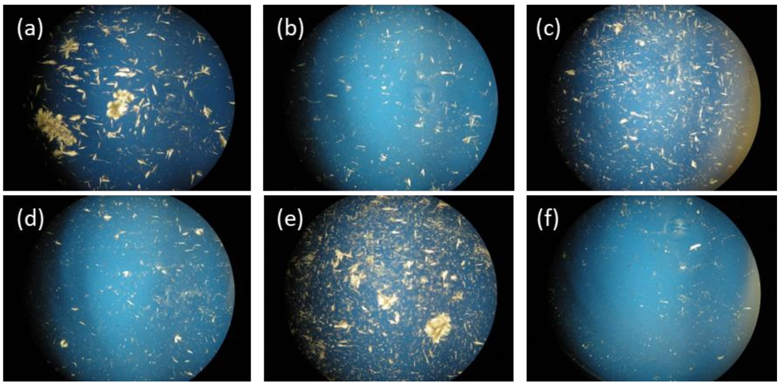

A 41. Cooling crystallisations of PYR with 1% polymer additives from IPA at rate of 0.1 °C/minute. (a) PP123, (b) PEG, (c) PPG, (d) PBD, (e) PVP and (f) PDE

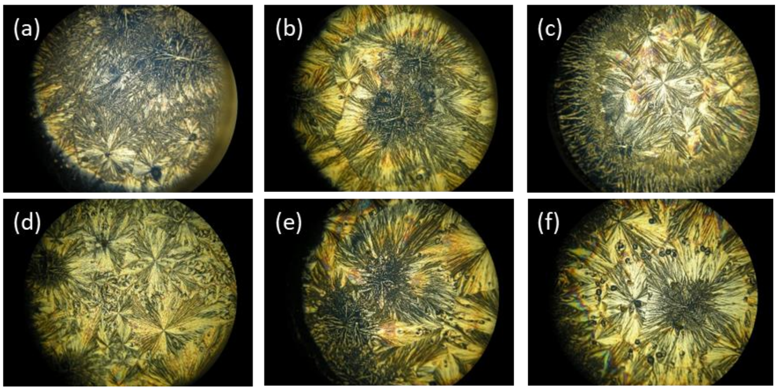

A 42. 20 °C evaporative crystallisations of PYR with 1% additives from IPA. (a) PP123, (b) PEG, (c) PPG, (d) PBD, (e) PVP and (f) PDE

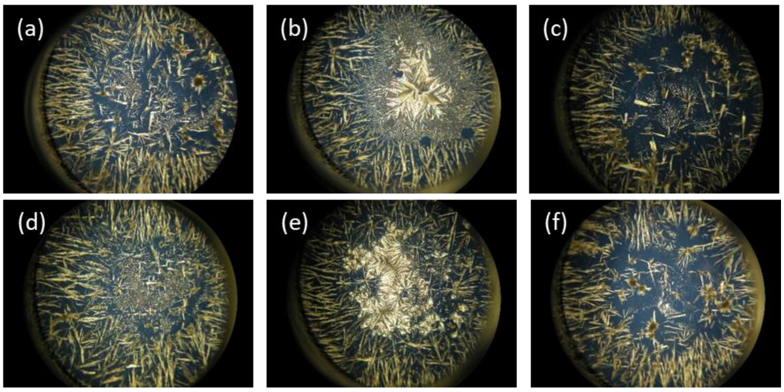

A 43. 20 °C evaporative crystallisations of PYR with 0.1% additives from IPA. (a) PP123, (b) PEG, (c) PPG, (d) PBD, (e) PVP and (f) PDE

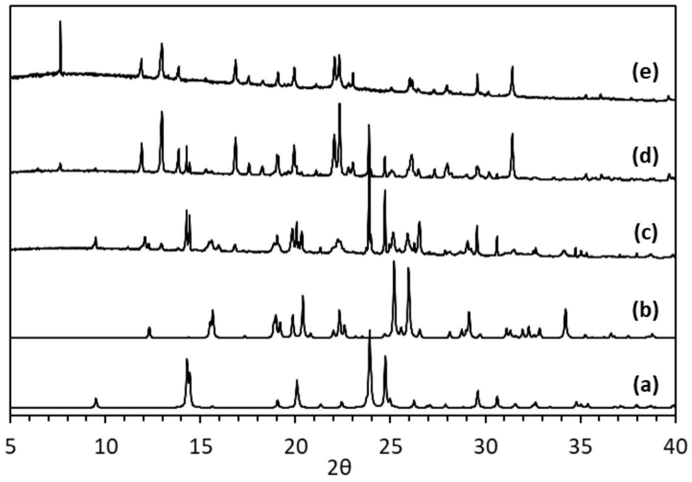

A 44. PXRD data for (a) PYR (BITZAF), (b) 2,4-DNBA (BAQLUD), (c) 1:1 PYR:2,4-DNBA grinding, (d) 1:1 PYR:2,4-DNBA LAG with IPA and (e) PYR:2,4-DNBA form I co-crystal produced from evaporative from IPA

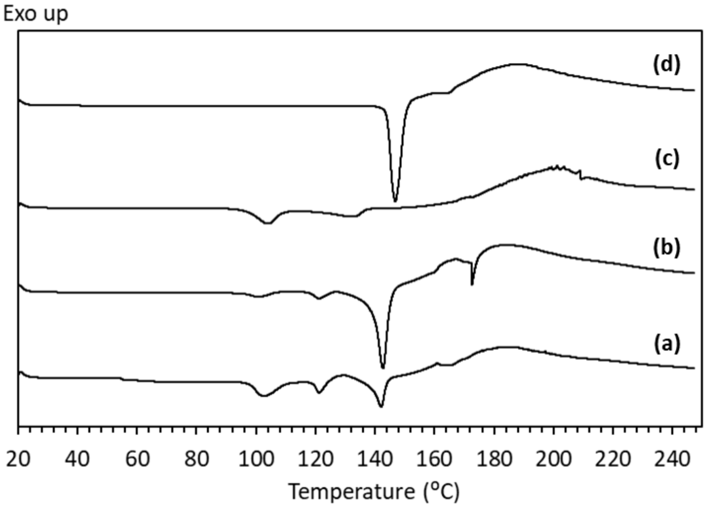

A 45. DSC trace for (a) 1:1 PYR:2,4-DNBA grinding, (b) 1:1 PYR:2,4-DNBA LAG with IPA, (c) 1:1 PYR:2,4-DNBA LAG with H_2O and (d) PYR:2,4-DNBA co-crystal produced via evaporative from IPA

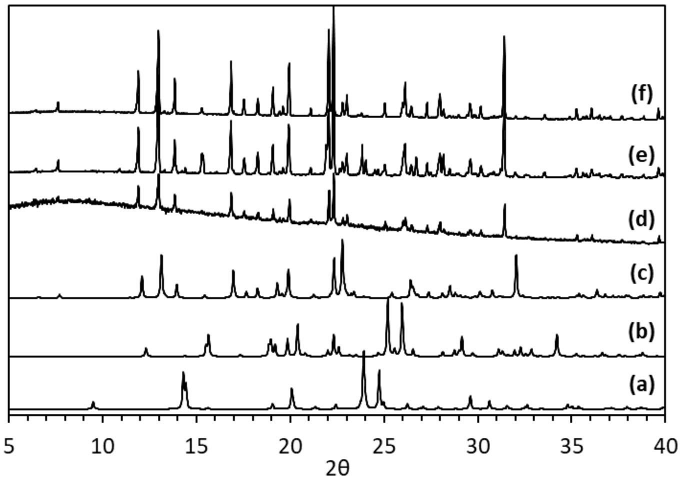

A 46. PXRD data for (a) PYR (BITZAF), (b) 2,4-DNBA (BAQLUD), (c) PYR:2,4-DNBA form I co-crystal calculated from SCXRD, (d) 10 g cooling in IPA, (e) 30 g cooling in IPA and (f) 10 g slurry in IPA

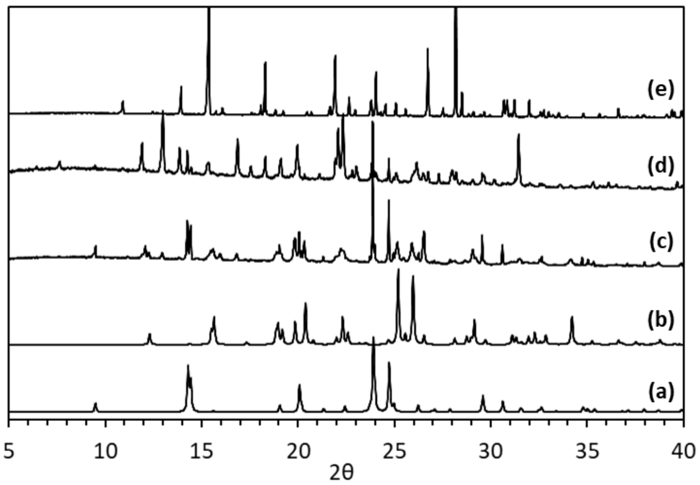

A 47. PXRD data for (a) PYR (BITZAF), (b) 2,4-DNBA (BAQLUD), (c) 1:1 PYR:2,4-DNBA grinding, (d) 1:1 PYR:2,4-DNBA LAG with H_2O and (e) PYR:2,4-DNBA form II co-crystal produced from cooling in H_2O

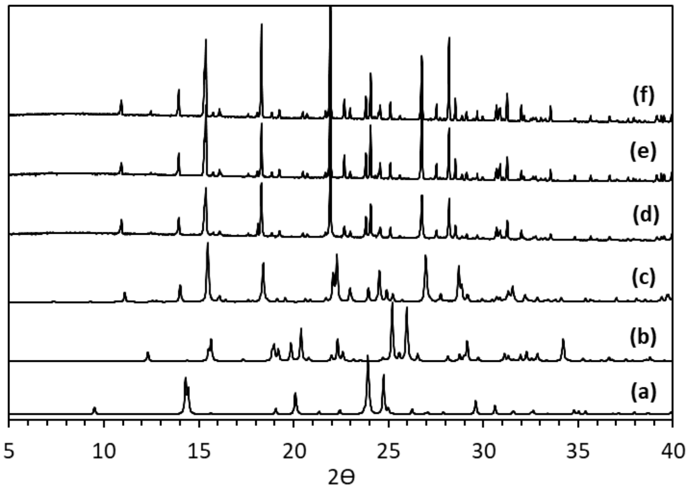

A 48. PXRD data for (a) PYR (BITZAF), (b) 2,4-DNBA (BAQLUD), (c) PYR:2,4-DNBA form II co-crystal calculated from SCXRD, (d) 10 g cooling in H_2O, (e) 30 g cooling in H_2O and (f) 10 g slurry in H_2O

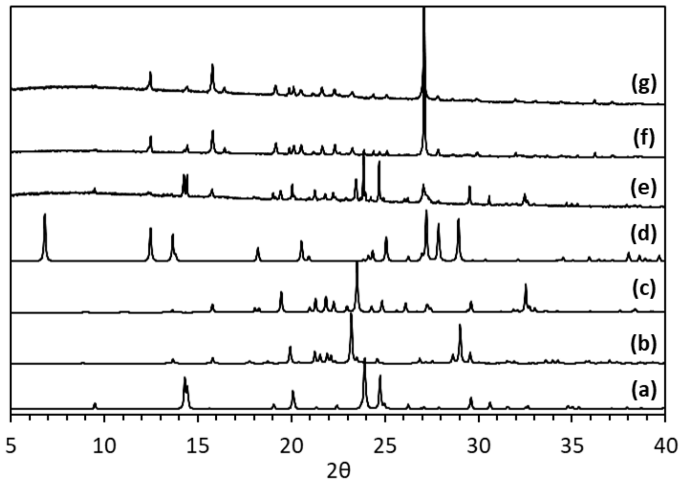

A 49. PXRD data for (a) PYR (BITZAF), (b) 3,5-DNBA form I (CUKCAM01), (c) 3,5-DNBA form II (CUKCAM02), (d) 3,5-DNBA hydrate (OKEMAT), (e) 1:1 PYR:3,5-DNBA grinding, (f) 1:1 PYR:3,5-DNBA LAG with H_2O and (g) PYR:3,5-DNBA co-crystal produced via evaporative from H_2O

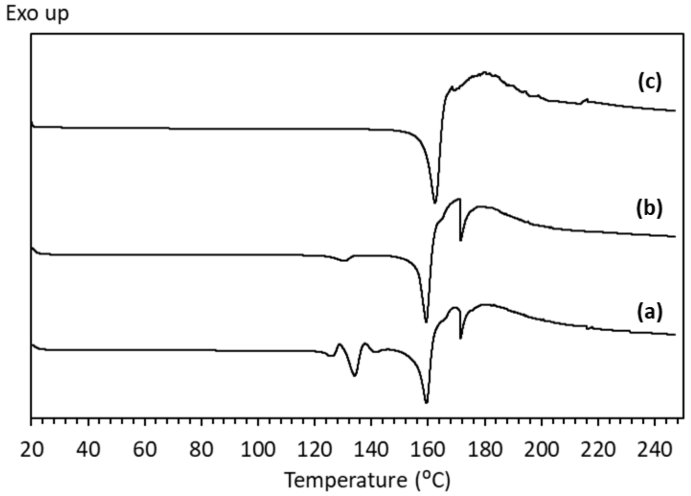

A 50. DSC trace for (a) 1:1 PYR:3,5-DNBA grinding, (b) 1:1 PYR:3,5-DNBA LAG with H_2O and (c) PYR:3,5-DNBA co-crystal produced via evaporative from H_2O

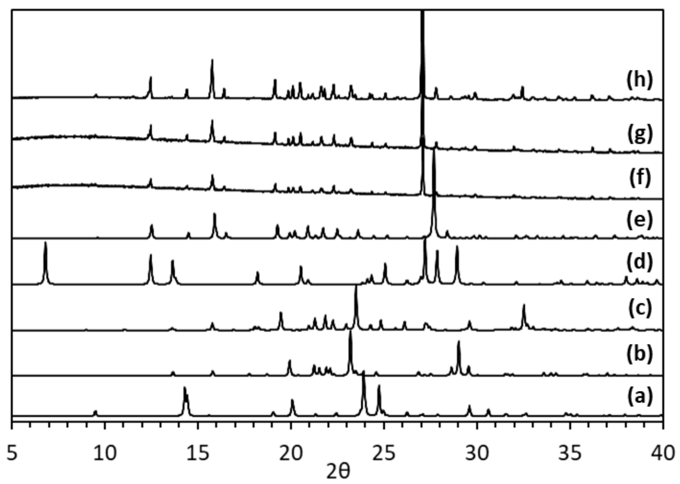

A 51. PXRD data for (a) PYR (BITZAF), (b) 3,5-DNBA form I (CUKCAM01), (c) 3,5-DNBA form II (CUKCAM02), (d) 3,5-DNBA hydrate (OKEMAT), (e) PYR:3,5-DNBA co-crystal calculated from SCXRD, (f) 10 g cooling in H_2O, (g) 30 g cooling in H_2O, and (h) 10 g slurry in H_2O

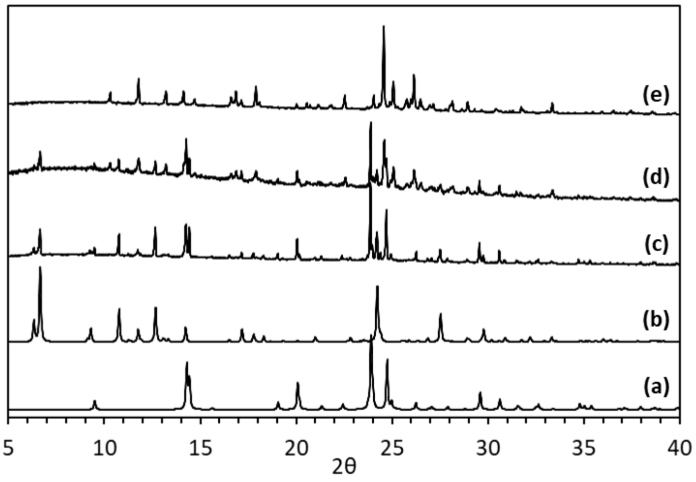

A 52. PXRD data for (a) PYR (BITZAF), (b) TRI (BTCOAC), (c) 2:1 PYR:TRI grinding, (d) 2:1 PYR:TRI LAG with IPA and (e) PYR:TRI co-crystal produced via evaporative from IPA

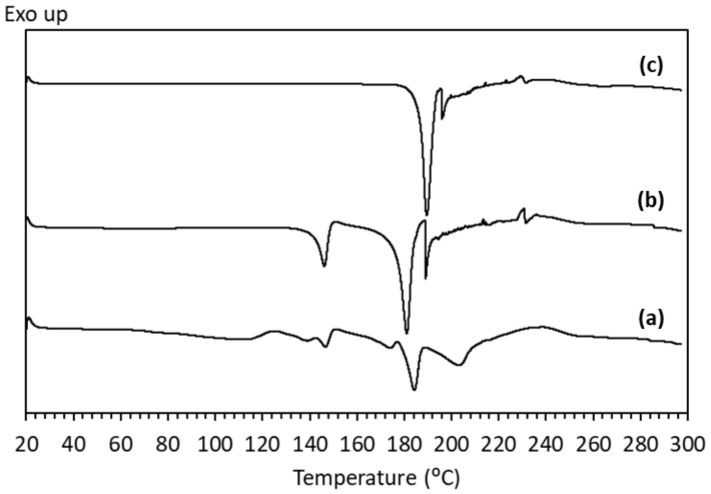

A 53. DSC trace for (a) 2:1 PYR:TRI grinding, (b) 2:1 PYR:TRI LAG with IPA and (c) PYR:TRI co-crystal produced via evaporative from IPA

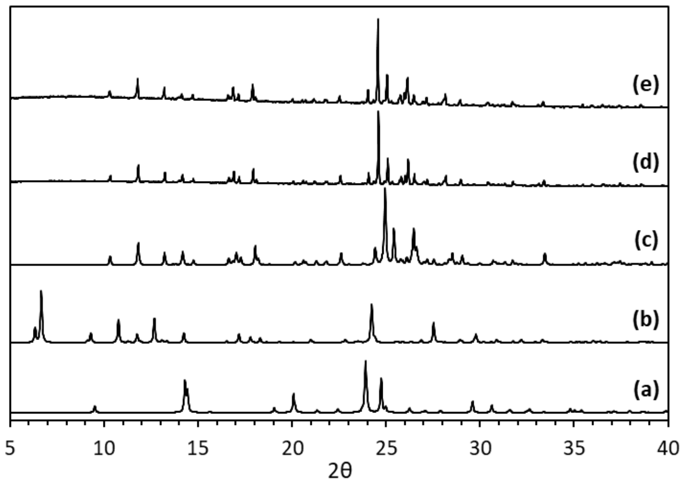

A 54. PXRD data for (a) PYR (BITZAF), (b) TRI (BTCOAC), (c) PYR:TRI co-crystal calculated from SCXRD, (d) PYR:TRI co-crystal calculated from SCXRD, (e) 10 g cooling in IPA and (f) 10 g slurry in IPA

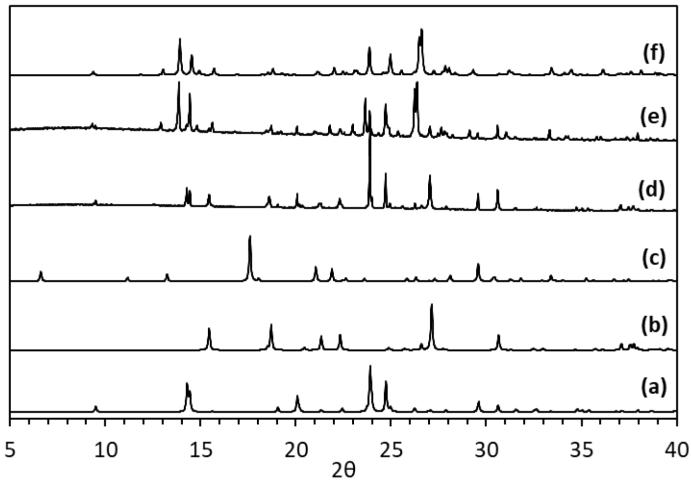

A 55. PXRD data for (a) PYR (BITZAF), (b) PtA (PHTHAC), (c) PtA hydrate (WODVAN), (d) 1:1 PYR:PtA grinding, (e) 1:1 PYR:PtA LAG with EtOH and (f) PYR:PtA co-crystal produced via evaporative from EtOH

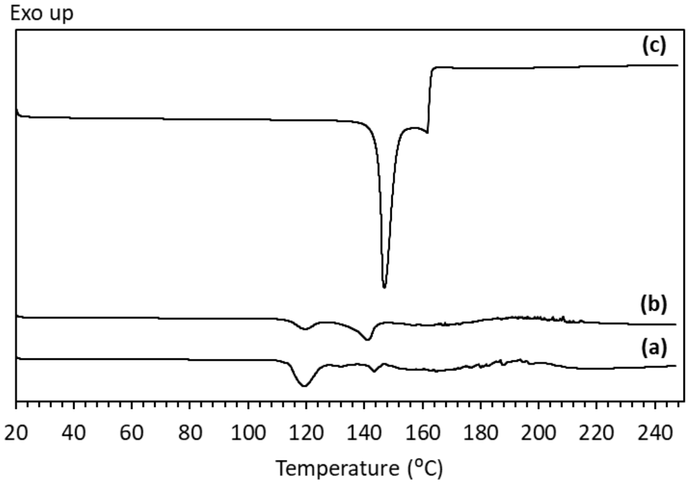

A 56. DSC trace for (a) 1:1 PYR:PtA grinding, (b) 1:1 PYR:PtA LAG with EtOH and (c) PYR:PtA co-crystal produced via evaporative from EtOH

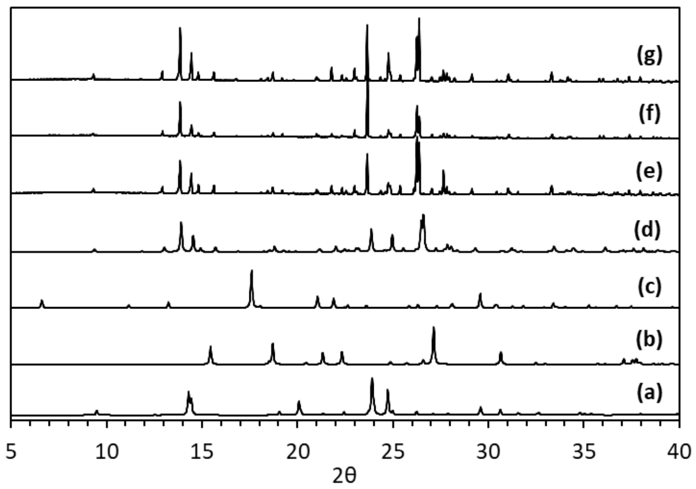

A 57. PXRD data for (a) PYR (BITZAF), (b) PtA (PHTHAC), (c) PtA hydrate (WODVAN), (d) PYR:PtA co-crystal calculated from SCXRD, (e) PYR:PtA 10 g cooling in IPA, (f) PYR:PtA 30 g cooling in IPA and (g) PYR:PtA 10 g slurry in IPA